



ScuDo

Scuola di Dottorato ~ Doctoral School

WHAT YOU ARE, TAKES YOU FAR

Doctoral Dissertation

Doctoral Program in Mechanical Engineering (29th cycle)

Development of computational efficient shell formulation for analysis of multilayered structures subjected to mechanical, thermal, and electrical loadings

By

Stefano Valvano

Supervisors:

Prof. Erasmo Carrera

Prof. Maria Cinefra

Doctoral Examination Committee:

Dr. Giunta Gaetano, Referee, Luxembourg Institute of Science and Technology

Prof. Alaimo Andrea, Referee, Università degli Studi Enna "Kore"

Prof. Lorenzo Dozio, Politecnico di Milano

Dr. Fiorenzo Fazzolari, University of Cambridge

Prof. Roberto Marsilio, Politecnico di Torino

Politecnico di Torino

27 June 2017

I hereby declare that, the contents and organization of this dissertation constitute my own original work and does not compromise in any way the rights of third parties, including those relating to the security of personal data.

Stefano Valvano
2017

Quibus firmissime me iuvaverunt,
quibus enixe me fulserunt,
quibusque me singulari patientia tulerunt.

A quelli che fermamente mi hanno aiutato,
a quelli che premurosamente mi hanno sostenuto,
a quelli che con straordinaria pazienza mi hanno sopportato.

Summary

The aim of this work is the development of robust finite shell model suitable for numerical applications in solid mechanics with a remarkable reduction in computational cost. Two-dimensional (2D) structural models, commonly known as plates/shells, are for instance used in many applications to analyze the structural behavior of thin and slender bodies such as panels, domes, pressure vessels, and wing stiffened panels amongst others. These models reduce the three-dimensional 3D problem into a two-dimensional 2D problem, where variables depend on the in-plane axis coordinates. Two-dimensional elements are simpler and computationally more efficient than 3D (solid) models. This feature makes plate/shell theories still very attractive for the static, dynamic response, free vibration, thermo-mechanical and electro-mechanical analysis, despite the approximations which they introduce in the simulation. Nevertheless, analytical solutions for three-dimensional elastic bodies are generally available only for a few particular cases which represent rather coarse simplifications of reality. In most of the practical problems, the solution demands applications of approximated computational methods. The Finite Element Method (FEM) has a predominant role among the computational techniques implemented for the analysis of layered structures. The majority of FEM theories available in the literature are formulated by axiomatic-type theories. In this thesis, attention is focused on weak-form solutions of refined plate/shell theories. In particular, higher-order plate/shell models are developed within the framework of the Unified Formulation by Carrera, according to which the three-dimensional displacement field can be expressed as an arbitrary expansion of the generalized displacements. A robust finite shell element for the analysis of plate and shell structures subjected to mechanical, thermal, and/or electrical loadings is developed. A wide range of problems are considered, including static analysis, free vibration analysis, different boundary conditions and different laminations schemes, distributed pressure loads, localized pressure loads or concentrated loads are taken into account.

The high computational costs represent the drawback of refined plate/shell theories or three-dimensional analyses. In recent years considerable improvements have been obtained towards the implementation of innovative solutions for improving the analysis efficiency for a global/local scenario. In this manner, the limited computational resources can be distributed in an optimal manner to study in detail only those parts of the structure that require an accurate analysis.

In the second part of the thesis two different methodology are presented to improve the analysis efficiency, and at the same time keeping the finite higher-order plate/shell element accuracy. The two approaches can be collocated in the simultaneous multi-model methodologies. The first is the Mixed ESL/LW variable kinematic method, where the primary variables are described along the shell thickness selecting some plies with an ESL description and others with a LW behaviour by using the Legendre polynomials for both the assembling approaches. The second approach is a new simultaneous multi-model, here presented as Node-Dependent Variable Kinematic method. The shell element with node-dependent capabilities enables one to vary the kinematic assumptions within the same finite element. The expansion order (along the shell thickness) of the shell element is, in fact, a property of the FE node in the present approach. Different kinematics can be coupled without the use of any mathematical

artifice.

The theories developed in this thesis are validated by using some selected results from the literature. The analyses suggest that Unified Formulation furnishes a reliable method to implement refined theories capable of providing almost three-dimensional elasticity solution, and that the two simultaneous multi-theories methods are extremely powerful and versatile when applied to composite or sandwich structures subjected to various multifield loadings.

Contents

Summary	ix
Contents	xi
List of Figures	xv
List of Tables	xxiii
Introduction	31
I Shell Structural Formulation	35
2 Constitutive and Geometrical relations	37
2.1 Generalized Hooke law for mechanical case	37
2.2 Costitutive equations for multifield problems	42
2.3 Geometry of the shell	47
2.4 Geometrical shell relations for multifield problems	51
3 Classical, refined and hierarchical theories	53
3.1 Classical and refined theories	53
3.2 Unified Formulation	55
3.3 Modelling Approaches	60
4 Variational Principles	61
4.1 Principle of Virtual Displacements for multifield problems	61
4.2 PVD for mechanical problems	63
4.3 PVD for partially coupled thermo-mechanical problems	63
4.4 PVD for electro-mechanical problems	64
4.5 Reissner Mixed Variational Theorem for multifield problems	64
4.6 RMVT for mechanical problems	64
4.7 RMVT for electro-mechanical problems	65
5 Weak formulation for shell problems	67
5.1 Finite Element Method	67
5.2 MITC9 Finite Shell Element	69
5.3 Governing Equations for shell weak formulation	71
5.3.1 PVD for mechanical problems	71
5.3.2 PVD for partially coupled thermo-mechanical problems	75
5.3.3 PVD for electro-mechanical problems	76

6	Results on Mechanical Problems	81
6.1	Doubly-Curved Shell	81
6.1.1	Assessment	81
6.1.2	FEM benchmark solutions	86
6.2	Trigonometric and Exponential Thickness Functions	93
6.2.1	Three-layer cross-ply square plate ($0^\circ/90^\circ/0^\circ$)	93
6.2.2	Two-layer ($0^\circ/90^\circ$) and four-layer ($0^\circ/90^\circ/90^\circ/0^\circ$) cross-ply square plate	103
6.2.3	Three-layer rectangular sandwich plate	105
7	Results on Thermo-Mechanical Problems	107
7.1	Heat conduction problem in layered structures	107
7.2	Thermal Profile Assumed Linear	109
7.2.1	Multilayered plate	109
7.2.2	Multilayered cylindrical panel	113
7.2.3	Multilayered spherical panel	117
7.3	Calculated Thermal Profile	120
7.3.1	Temperature profile evaluation	121
7.3.2	Assessment	122
7.3.3	FEM benchmark solutions	131
8	Results on Electro-Mechanical Problems	137
8.1	Static piezo-composite plates and shells	137
8.1.1	Multilayered plate	138
8.1.2	Multilayered piezoelectric cylinder.	144
8.2	RMVT-Dz for shells	151
8.3	Plate with piezoelectric Patches	157
8.3.1	Cantilevered plate with piezo-patches	158
II	Efficient Shell FEM Formulation	165
9	Variable Kinematic Mixed ESL/LW	167
9.1	Modeling Approaches Comparison	168
9.1.1	ESL models	168
9.1.2	LW models	168
9.1.3	Variable kinematics Mixed ESL/LW	169
9.2	Mechanical Analysis Results	171
9.2.1	Three-layer composite plate	171
9.2.2	Eight-layer composite beam	178
9.2.3	Three-layer sandwich plate	182
9.2.4	Five-layer composite sandwich plate	183
9.2.5	Three-layer composite cylinder	186
9.2.6	Ten-layer composite cylinder	193
9.2.7	Composite spherical panel	198
9.2.8	Eleven-layer sandwich cylindrical panel	201
9.3	Thermo-Mechanical Analysis Results	207
9.3.1	Three-layer plate	207
9.3.2	Ten-layer cylindrical panel	213
9.3.3	Sandwich composite spherical panel	217
9.4	Electro-Mechanical Analysis Results	225
9.4.1	Four-layer plate	225
9.4.2	Three-layer cylindrical shell	236
9.4.3	Four-layer cylindrical shell	239

10 Node-Dependent Variable Kinematic	249
10.1 Models Coupling	250
10.2 Finite elements with node-dependent kinematics	251
10.2.1 Fundamental nucleus of the stiffness matrix	253
10.3 Mechanical Analysis Results	257
10.3.1 Simply-supported isotropic plate under localized pressure load	257
10.3.2 Eight-layer cantilever plate	266
10.3.3 Composite plates simply-supported	271
10.3.4 Sandwich rectangular plates simply-supported	279
10.4 Electro-Mechanical Analysis Results	287
10.4.1 Simply-supported cross-ply composite plates with piezoelectric skins	287
10.4.2 Sandwich cantilever plate shear-actuated in mode-15	294
10.4.3 Sandwich cantilever plate under mechanical loading	302
 Conclusions	 311
 Appendix A Fundamental Nuclei with the MITC method	 313
A.1 PVD for mechanical problems	313
A.2 PVD for electro-mechanical problems	316
 Appendix B Publications & Talks	 319
 Bibliography	 323

List of Figures

2.1	Representation of Cauchy stress tensor components in a material body.	38
2.2	General problem coordinate system and material reference system of an unidirectionally reinforced lamina.	40
2.3	Representation of piezoelectric actuation modes taken into account. Transverse extension mode (3-1 mode), and the shear mode (1-5 mode)	44
2.4	Displacements on the shell reference surface.	47
2.5	General reference system and notations for shells.	50
3.1	Geometrical representation of the Kirchoff's assumptions.	53
3.2	Geometrical representation of the Reissner-Mindlin theory.	53
3.3	Geometrical representation of the Higher Order Theories.	54
3.4	Equivalent-Single-Layer behaviour of the primary variables along the thickness of the shell.	60
3.5	Layer-Wise behaviour of the primary variables along the thickness of the shell.	60
5.1	9-node element, local reference system.	67
5.2	Tying points location for the MITC9 <i>shell</i> element.	69
6.1	Three-layered shell, symmetric lamination, $R/a = 1$ and $a/h = 5$. Transverse shear and normal stresses $\bar{\sigma}_{\alpha z}$, $\bar{\sigma}_{zz}$	85
6.2	Three-layered shell, symmetric lamination, $R/a = 5$ and $a/h = 100$. Transverse shear and normal stresses $\bar{\sigma}_{\alpha z}$, $\bar{\sigma}_{zz}$	85
6.3	Four-layered shell, symmetric lamination, $R/a = 1$ and $a/h = 5$. Transverse shear and normal stresses $\bar{\sigma}_{\alpha z}$, $\bar{\sigma}_{zz}$	86
6.4	Four-layered shell, symmetric lamination, $R/a = 5$ and $a/h = 100$. Transverse shear and normal stresses $\bar{\sigma}_{\alpha z}$, $\bar{\sigma}_{zz}$	86
6.5	Two-layered shell, lamination $(45^\circ, -45^\circ)$, $R/a = 1$. Transverse shear stress $\bar{\sigma}_{\alpha z}$ for aspect ratios $a/h = 5$ and $a/h = 100$	89
6.6	Two-layered shell, lamination $(45^\circ, -45^\circ)$, $R/a = 5$. Transverse normal stress $\bar{\sigma}_{zz}$ for aspect ratios $a/h = 5$ and $a/h = 100$	90
6.7	Three-layered shell, clamped-free boundary conditions, $R/a = 1$. Transverse shear stress $\bar{\sigma}_{\alpha z}$ for aspect ratios $a/h = 5$ and $a/h = 100$	90
6.8	Three-layered shell, clamped-free boundary conditions, $R/a = 5$. Transverse normal stress $\bar{\sigma}_{zz}$ for aspect ratios $a/h = 5$ and $a/h = 100$	91
6.9	Three-layered shell, concentrated load, by varying a/h for $R/a = 2$. Transverse shear and normal stresses $\bar{\sigma}_{\alpha z}$ and $\bar{\sigma}_{zz}$	91
6.10	Three-layered shell, concentrated load, by varying R/a for $a/h = 10$. Transverse shear and normal stresses $\bar{\sigma}_{\alpha z}$ and $\bar{\sigma}_{zz}$	92
6.11	Reference system of the plate with a bi-sinusoidal loading.	94
6.12	Three-layered plate, transverse displacement \mathbf{w} along the thickness, with thickness ratio $(a/h) = 100$	97
6.13	Three-layered plate, transverse shear stress $\boldsymbol{\sigma}_{xz}$ along the thickness, with thickness ratio $(a/h) = 100$	97

6.14	Three-layered plate, transverse normal stress σ_{zz} along the thickness, with thickness ratio $(a/h) = 100$	98
6.15	Three-layered plate, transverse displacement w along the thickness, with thickness ratio $(a/h) = 4$	99
6.16	Three-layered plate, in-plane stress σ_{xx} along the thickness, with thickness ratio $(a/h) = 4$	99
6.17	Three-layered plate, transverse shear stress σ_{xz} along the thickness, with thickness ratio $(a/h) = 4$	100
6.18	Three-layered plate, transverse normal stress σ_{zz} along the thickness, with thickness ratio $(a/h) = 4$	100
6.19	Three-layered plate, transverse normal stress σ_{zz} along the thickness, with thickness ratio $(a/h) = 10$	103
7.1	Reference system of the plate.	109
7.2	Three-layered plate, by varying a/h . Transverse shear stress $\bar{\sigma}_{\alpha z}$	112
7.3	Three-layered plate, by varying a/h . Transverse normal stress $\bar{\sigma}_{zz}$	112
7.4	Reference system of the cylindrical shell.	114
7.5	Two-layered cylindrical shell, by varying R/h . Transverse shear stress $\bar{\sigma}_{\alpha z}$	117
7.6	Two-layered cylindrical shell, by varying R/h . Transverse normal stress $\bar{\sigma}_{zz}$	117
7.7	Reference system of the spherical shell.	118
7.8	Two-layered spherical shell, by varying R/h . Transverse shear stress $\bar{\sigma}_{\alpha z}$	120
7.9	Two-layered spherical shell, by varying R/h . Transverse normal stress $\bar{\sigma}_{zz}$	120
7.10	Temperature Profiles for different thickness ratios (a/h) . Composite plate.	121
7.11	Temperature Profiles for different radius to thickness ratios (R/h) . Composite cylinder.	122
7.12	Three-layered plate, by varying a/h . Transverse displacement w	125
7.13	Three-layered plate, by varying a/h . Transverse shear stress $\sigma_{\alpha z}$	126
7.14	Cylindrical panel, by varying R/h . Transverse displacement w	128
7.15	Cylindrical panel, by varying R/h . Transverse shear stress $\sigma_{\alpha z}$	128
7.16	Spherical panel, by varying R/h . Transverse displacement w	131
7.17	Spherical panel, by varying R/h . Transverse shear stress $\sigma_{\alpha z}$	131
8.1	Multilayered plate structure. Sensor Case, and Actuator Case configuration.	138
8.2	Four-layered plate, with thickness ratio $(a/h) = 100$. Transverse shear stress $\sigma_{\alpha z}$	143
8.3	Four-layered plate, with thickness ratio $(a/h) = 2$. Transverse normal stress σ_{zz}	143
8.4	Four-layered plate, with thickness ratio $(a/h) = 2$. Electric potential Φ	144
8.5	Four-layered plate, with thickness ratio $(a/h) = 100$. Electric displacement \mathcal{D}_z	144
8.6	Multilayered cylindrical shell. Sensor Case, and Actuator Case configuration.	145
8.7	Four-layered cylinder, with radius to thickness ratio $(R/h) = 100$. Transverse shear stress $\sigma_{\alpha z}$	150
8.8	Four-layered cylinder, with radius to thickness ratio $(R/h) = 2$. Transverse normal stress σ_{zz}	150
8.9	Four-layered cylinder, with radius to thickness ratio $(R/h) = 2$. Electric potential Φ	151
8.10	Four-layered cylinder, with radius to thickness ratio $(R/h) = 100$. Electric displacement \mathcal{D}_z	151
8.11	Three-layered cylinder, with radius to thickness ratio $(R/h) = 100$. Transverse normal stress σ_{zz}	156
8.12	Three-layered cylinder, with radius to thickness ratio $(R/h) = 2$. Transverse normal stress σ_{zz}	156

8.13	Three-layered cylinder, with radius to thickness ratio $(R/h) = 2$. Electric potential Φ	157
8.14	Three-layered cylinder, Sensor Case. Transverse electric displacement \mathcal{D}_z . . .	157
8.15	Geometry of the plate.	158
8.16	Isotropic plate with piezo patches, mesh grid representation.	160
8.17	Natural frequency 7.5639 Hz. Mode 1.	162
8.18	Natural frequency 25.312 Hz. Mode 2.	162
8.19	Natural frequency 45.718 Hz. Mode 3.	162
8.20	Natural frequency 90.236 Hz. Mode 4.	162
9.1	Equivalent-Single-Layer behaviour of the primary variables along the thickness of the shell.	168
9.2	Equivalent-Single-Layer assembling scheme for a second-order ($N = 2$) plate model: The fundamental nucleus of the stiffness matrix, $\mathbf{K}^{k\tau s}$, is expanded for each layer k . The laminate stiffness matrix is then obtained by summing, term by term, the contribution of each layer. The dimension of the global matrix does not depend on the number of layers.	168
9.3	Layer-Wise behaviour of the primary variables along the thickness of the shell.	169
9.4	Layer-Wise assembling scheme for a second-order ($N = 2$) plate model: The fundamental nucleus of the stiffness matrix, $\mathbf{K}^{k\tau s}$, is expanded for each layer k . The laminate stiffness matrix is then obtained by assembling the contribution of each layer at the layer/layer interface. The dimension of the global matrix depends on the number of layers.	169
9.5	Variable-Kinematics behaviour of the primary variables along the thickness of the shell.	170
9.6	Variable-kinematic assembling scheme for a second-order ($N = 2$) plate model: The fundamental nucleus of the stiffness matrix, $\mathbf{K}^{k\tau s}$, is expanded for each layer k . Depending on the modelling choice, the laminate stiffness matrix is then obtained by adopting a combined ESL/LW approach. In this example, layers 2 and 3 are homogenized by ESL and then assembled with layer 1 by LW. The dimension of the global matrix depends on the modelling choice. . .	170
9.7	Transverse shear stress σ_{xz} along the thickness, with thickness ratio $(a/h) = 4$. Composite plate.	173
9.8	Transverse normal stress σ_{zz} along the thickness, with thickness ratio $(a/h) = 4$. Composite plate.	173
9.9	Transverse displacement w along the thickness, with thickness ratio $(a/h) = 100$. Composite plate.	173
9.10	In-plane stress σ_{xx} along the thickness, with thickness ratio $(a/h) = 100$. Composite plate.	173
9.11	Variable Kinematic Models for the three-layer plate. Case 1 and Case 2. . . .	174
9.12	Transverse displacement w along the thickness, with thickness ratio $(a/h) = 100$. Composite plate.	176
9.13	In-plane stress σ_{xx} along the thickness, with thickness ratio $(a/h) = 100$. Composite plate.	176
9.14	Transverse normal stress σ_{zz} along the thickness, with thickness ratio $(a/h) = 100$. Composite plate.	176
9.15	Transverse shear stress σ_{xz} along the thickness, with thickness ratio $(a/h) = 100$. Composite plate.	176
9.16	Transverse shear stress σ_{xz} along the thickness, with thickness ratio $(a/h) = 100$. Composite plate.	177
9.17	Transverse displacement w along the thickness, with thickness ratio $(a/h) = 4$. Composite plate.	177

9.18	In-plane stress σ_{xx} along the thickness, with thickness ratio $(a/h) = 4$. Composite plate.	177
9.19	Transverse normal stress σ_{zz} along the thickness, with thickness ratio $(a/h) = 4$. Composite plate.	177
9.20	Transverse shear stress σ_{xz} along the thickness, with thickness ratio $(a/h) = 4$. Composite plate.	178
9.21	Transverse shear stress σ_{xz} along the thickness, with thickness ratio $(a/h) = 4$. Composite plate.	178
9.22	Reference system of the eight-layer beam with a concentrated load. The material lamination scheme is indicated with label 1 and label 2.	180
9.23	Transverse displacement w along the thickness, with thickness ratio $(a/h) = 9$. Composite beam.	180
9.24	In-plane stress σ_{xx} along the thickness, with thickness ratio $(a/h) = 9$. Composite beam.	181
9.25	Transverse normal stress σ_{zz} along the thickness, with thickness ratio $(a/h) = 9$. Composite beam.	181
9.26	Transverse shear stress σ_{xz} along the thickness, with thickness ratio $(a/h) = 9$. Composite beam.	181
9.27	Transverse displacement w along the thickness. Composite Sandwich Plate.	185
9.28	In-plane stress σ_{xx} along the thickness. Composite Sandwich Plate.	185
9.29	Transverse shear stress σ_{xz} along the thickness. Composite Sandwich Plate.	185
9.30	Variable-kinematic assembly schemes for the three-layered cylindrical shell.	189
9.31	Composite three-layered cylinder, by varying R/h . Transverse displacement w	192
9.32	Composite three-layered cylinder, by varying R/h . In-plane stress $\sigma_{\beta\beta}$	192
9.33	Composite three-layered cylinder, by varying R/h . Transverse shear stress $\sigma_{\alpha z}$	193
9.34	Composite three-layered cylinder, by varying R/h . Transverse normal stress σ_{zz}	193
9.35	Composite ten-layered cylinder, by varying R/h . Transverse displacement w	197
9.36	Composite ten-layered cylinder, by varying R/h . In-plane stress $\sigma_{\beta\beta}$	197
9.37	Composite ten-layered cylinder, by varying R/h . Transverse shear stress $\sigma_{\alpha z}$	198
9.38	Composite ten-layered cylinder, by varying R/h . Transverse normal stress σ_{zz}	198
9.39	Sandwich eleven-layered cylinder. Transverse displacement w along the thickness, with axis length to circumferential length ratio $b/a = 1$ and circumferential length to thickness ratios $a/h = 10$	204
9.40	Sandwich eleven-layered cylinder. In-plane stress $\sigma_{\alpha\alpha}$ along the thickness, with axis length to circumferential length ratio $b/a = 1$ and circumferential length to thickness ratios $a/h = 10$	204
9.41	Sandwich eleven-layered cylinder. In-plane stress $\sigma_{\beta\beta}$ along the thickness, with axis length to circumferential length ratio $b/a = 1$ and circumferential length to thickness ratios $a/h = 10$	204
9.42	Sandwich eleven-layered cylinder. In-plane shear stress $\sigma_{\alpha\beta}$ along the thickness, with axis length to circumferential length ratio $b/a = 1$ and circumferential length to thickness ratios $a/h = 10$	204
9.43	Sandwich eleven-layered cylinder. Transverse shear stress $\sigma_{\alpha z}$ along the thickness, with axis length to circumferential length ratio $b/a = 1$ and circumferential length to thickness ratios $a/h = 10$	205
9.44	Reference system of the composite plate with section of thermal load applied.	207
9.45	Three-layered plate. Temperature Profiles Comparison.	209
9.46	Variable Kinematic Cases. Compact example of assembling scheme.	209
9.47	Three-layered plate, transverse mechanical displacement \hat{w} , $a/h = 100$ (a), $a/h = 2$ (b).	212

9.48	Three-layered thin plates $a/h = 100$, transverse shear and normal stresses, $\hat{\sigma}_{xz}$ (a), $\hat{\sigma}_{zz}$ (b).	212
9.49	Three-layered thick plates $a/h = 2$, in-plane stress $\hat{\sigma}_{xx}$, T_a assumed linear (a), T_c calculated via Fourier heat law (b).	213
9.50	Reference system of the quarter of the composite cylindrical shell panel with symmetry condition applied.	214
9.51	Ten-layered cylindrical shell panel. Temperature Profiles Comparison.	214
9.52	Ten-layered cylindrical shell panel $R/a = 50$, transverse shear stress $\hat{\sigma}_{\alpha z}$, T_a assumed linear.	217
9.53	Ten-layered cylindrical shell panel $R/a = 5$, transverse normal stress $\hat{\sigma}_{zz}$, T_c calculate via Fourier heat conduction law.	217
9.54	Reference system of the quarter of the sandwich spherical shell panel with symmetry condition applied.	218
9.55	Five-layered sandwich spherical shell panel. Temperature Profiles Comparison. $a/h = 100$ (a), $a/h = 4$ (b)	219
9.56	Five-layered sandwich spherical panel transverse displacement \hat{w} with an assumed linear temperature profile T_a , $R/a = 5$ and $a/h = 100$ (a), $R/a = 20$ and $a/h = 4$ (b)	223
9.57	Five-layered sandwich spherical panel transverse shear stress $\hat{\sigma}_{\alpha z}$ with an assumed linear temperature profile T_a , $R/a = 5$ and $a/h = 100$.	223
9.58	Five-layered sandwich spherical panel transverse normal stress $\hat{\sigma}_{zz}$ with an assumed linear temperature profile T_a , $R/a = 5$ and $a/h = 100$.	224
9.59	Reference system of the composite plate with piezoelectric skins.	225
9.60	Variable Kinematic Cases. Compact example of assembling scheme.	228
9.61	Four-layered plate, Sensor case, transverse mechanical displacement \hat{w} , $a/h = 100$ (a), $a/h = 2$ (b).	232
9.62	Four-layered plate, Sensor case, transverse mechanical stresses, $\hat{\sigma}_{xz}$ for $a/h = 100$ ratio (a), $\hat{\sigma}_{zz}$ for $a/h = 2$ ratio (b).	232
9.63	Four-layered plate, Sensor case, Electric Potential $\hat{\Phi}$, $a/h = 100$ (a), $a/h = 2$ (b).	233
9.64	Four-layered plate, Sensor case, transverse electric displacement \hat{D}_z , $a/h = 100$ (a), $a/h = 2$ (b).	233
9.65	Four-layered plate, Actuator case, transverse mechanical displacement \hat{w} , $a/h = 100$ (a), $a/h = 2$ (b).	234
9.66	Four-layered plate, Actuator case, transverse mechanical stresses, $\hat{\sigma}_{xz}$ for $a/h = 100$ ratio (a), $\hat{\sigma}_{zz}$ for $a/h = 2$ ratio (b).	234
9.67	Four-layered plate, Actuator case, electric potential and electric transverse displacement, $\hat{\Phi}$ for $a/h = 100$ ratio (a), \hat{D}_z for $a/h = 2$ ratio (b).	235
9.68	Reference system of the composite cylinder with piezoelectric skins.	236
9.69	Four-layered cylinder, Sensor case, transverse mechanical displacement and in-plane stress, \hat{w} for $R/h = 100$ (a), $\hat{\sigma}_{\alpha\alpha}$ for $R/h = 2$ (b).	244
9.70	Four-layered cylinder, Sensor case, transverse mechanical stresses, $\hat{\sigma}_{\alpha z}$ for $R/h = 100$ ratio (a), $\hat{\sigma}_{zz}$ for $R/h = 2$ ratio (b).	244
9.71	Four-layered cylinder, Sensor case, electric potential and transverse electric displacement, $\hat{\Phi}$ for $R/h = 100$ (a), and \hat{D}_z for $R/h = 2$ (b).	245
9.72	Four-layered cylinder, Actuator case, transverse mechanical displacement and in-plane stress, \hat{w} for $R/h = 100$ (a), $\hat{\sigma}_{\alpha\alpha}$ for $R/h = 2$ (b).	245
9.73	Four-layered cylinder, Actuator case, transverse mechanical stresses, $\hat{\sigma}_{\alpha z}$ for $R/h = 100$ ratio (a), $\hat{\sigma}_{zz}$ for $R/h = 2$ ratio (b).	246
9.74	Four-layered cylinder, Actuator case, electric potential and transverse electric displacement, $\hat{\Phi}$ for $R/h = 100$ (a), and \hat{D}_z for $R/h = 2$ (b).	246

9.75	Four-layered cylinder, Actuator case, Euclidean Norm Error of the transverse mechanical displacement, \hat{w} for $R/h = 2$	247
10.1	Coupling example scheme of finite elements with different kinematics.	250
10.2	Example of finite element with node-dependent kinematics.	251
10.3	Example of finite element with node-dependent kinematics applied to multifield analysis of a multilayered structure with piezoelectric patches.	251
10.4	Displacement field at the nodal level of the finite element with node-dependent kinematics.	252
10.5	Assembling scheme of a 9-node finite element with node-dependent kinematics. Highlights of the influence of the cubic term of a 3^{rd} order Taylor expansion model in the FE stiffness.	255
10.6	Reference system of the isotropic plate (a), and placement of the evaluation points on the transverse section (b).	258
10.7	Subdivision zones for the isotropic plate, final mesh grid chosen after convergence study, and graphical description of the multi-theory models.	259
10.8	Transverse displacement $w(x; y) = w(a/2; b/2)$. Isotropic plate.	262
10.9	In-plane stress $\sigma_{xx}(x; y) = \sigma_{xx}(a/2; b)$. Isotropic plate.	262
10.10	Transverse shear stress $\sigma_{xz}(x; y) = \sigma_{xz}(0; b)$. Isotropic plate.	262
10.11	Transverse normal stress $\sigma_{zz}(x; y) = \sigma_{zz}(a/2; b)$. Isotropic plate.	263
10.12	Transverse shear stress $\sigma_{xz}(y; z) = \sigma_{xz}(b; 0)$ along the beam axis. Isotropic plate.	264
10.13	Transverse normal stress $\sigma_{zz}(y; z) = \sigma_{zz}(b/2; h/2)$ along the beam axis. Isotropic plate.	264
10.14	Convergence analysis of the transition elements for the transverse shear and normal stresses along the beam axis.	264
10.15	Three-dimensional representation of the transverse shear stress σ_{xz} . Isotropic plate.	265
10.16	Three-dimensional representation of the transverse normal stress σ_{zz} . Isotropic plate.	266
10.17	Eight-layered plate with concentrated loading. Reference system and material lamination scheme.	267
10.18	Eight-layered plate. Mesh scheme of the adopted multi-theory models with node-dependent kinematics.	268
10.19	Eight-layer composite plate. Transverse displacement $w(x; y) = -10^2 \times w(a; b/2)$	270
10.20	Eight-layer composite plate. Transverse shear stress $\sigma_{xz}(x; y) = -10^2 \times \sigma_{xz}(a/2; b/2)$	271
10.21	Cross-ply laminate subjected to localized pressure load and related FE mesh discretization into 3 zones.	272
10.22	Non-uniform adopted mesh on quarter of the plate, and graphical representation of the multi-theory models of the cross-ply plate structure.	274
10.23	Composite plate. Transverse displacement $w(x; y) = -10^5 \times w(a/2; b/2)$, and transverse shear stress $\sigma_{xz}(x; y) = -10 \times \sigma_{xz}(5a/12; b/2)$	276
10.24	Composite plate. Transverse shear stress $\sigma_{xz}(x; y) = -10 \times \sigma_{xz}(5a/12; b/2)$. Multi-theories with ESL model by Taylor Polynomials combined with LW model by Legendre Polynomials.	277
10.25	Composite plate. In-plane stress $\sigma_{xx}(y; z) = \sigma_{xx}(b/2; -h/2)$, and transverse shear stress $\sigma_{xz}(y; z) = -10 \times \sigma_{xz}(b/2; 0)$ along the in-plane direction X , the axis X is expressed in $[mm]$. Single and Multi-theory models.	278
10.26	Composite plate. Transverse normal stress $\sigma_{zz}(y; z) = -\sigma_{zz}(b/2; +h/2)$ along the in-plane direction X , the axis X is expressed in $[mm]$. Single and Multi-theory models.	278

10.27	Composite plate, three-dimensional view of a quarter of the plate. Transverse shear stress σ_{xz} for single models.	279
10.28	Composite plate, three-dimensional view of a quarter of the plate. Transverse shear stress σ_{xz} for multi-models.	279
10.29	Reference system of the sandwich plate. Three-dimensional deflection representation of a quarter of the plate.	280
10.30	Non-uniform adopted mesh and graphical representation of the multi-model cases, for a quarter of the sandwich plate.	281
10.31	Unsymmetrically laminated rectangular sandwich plate. Transverse displacement $w(x; y)$, and transverse normal stress $\sigma_{zz}(x; y)$ evaluated at $(a/2, b/2)$ by various single- and multi-theory models.	283
10.32	Unsymmetrically laminated rectangular sandwich plate. In-plane stress σ_{xx} , three-dimensional view of a quarter of the plate, and in-plane stress along the in-plane axis direction X evaluated at $(y, z) = (b/2, +h/2)$, for single and multi-models.	284
10.33	Unsymmetrically laminated rectangular sandwich plate, three-dimensional view of a quarter of the plate. Transverse normal stress σ_{zz} for single models. . . .	284
10.34	Unsymmetrically laminated rectangular sandwich plate, three-dimensional view of a quarter of the plate. Transverse normal stress σ_{zz} for multi-models. . . .	285
10.35	Reference system of the composite plate with piezoelectric skins.	287
10.36	Mesh zones of the composite plate with piezoelectric skins and graphical representation of the multi-theory models, based on layer-wise models.	289
10.37	Composite plate with piezoelectric skins. Transverse displacement $\bar{w}(x; y) = 10^{11} \times w(a/2; b/2)$. Sensor and Actuator Cases. Single and Multi-theory models.	292
10.38	Composite plate with piezoelectric skins. Transverse shear stress $\bar{\sigma}_{xz}(x; y) = (10) \times \sigma_{xz}(0, b/2)$ for the Actuator Case, and transverse electric displacement $\bar{D}_z(x; y) = (10^{10}) \times \mathcal{D}_z(a/2, b/2)$ for the Sensor Case. Single and Multi-theory models.	292
10.39	Composite plate with piezoelectric skins. In-plane stress $\bar{\sigma}_{xx}(y; z) = \sigma_{xx}(b/2; +h/2)$ for the Actuator Case, and transverse electric displacement $\bar{D}_z(y; z) = (10^{10}) \times \mathcal{D}_z(b/2; +h/2)$ for the Sensor Case, along the in-plane direction X , the axis X is expressed in $[mm]$. Single and Multi-theory models.	293
10.40	Composite plate with piezoelectric skins, three-dimensional view of a quarter of the plate. Transverse normal stress σ_{zz} for single and multi-model. Sensor Case.	294
10.41	Composite plate with piezoelectric skins, three-dimensional view of a quarter of the plate. Transverse shear stress σ_{xz} for single and multi-model. Actuator Case.	294
10.42	Reference system of the sandwich plate with piezoelectric patch, and three-dimensional representation of the deformation under the electric load.	295
10.43	Mesh zone subdivisions of the sandwich plate with piezoelectric patch, for the convergence study.	296
10.44	Sandwich plate with piezoelectric patch, tip transverse displacement $w(x, y, z) = 10^8 \times w(a, b/2, +h/2)$ for several position of the piezoelectric patch along the x-axis direction.	297
10.45	Graphical representation of the multi-theory models, based on layer-wise models, of the sandwich plate with piezoelectric patch, for the node-variable kinematic study.	298
10.46	Sandwich cantilever plate, transverse displacement $w(x, y) = 10^8 \times w(a, b/2)$, and electric potential $\Phi(x, y) = \Phi(d, b/2)$. Single and Multi-theory models. . .	300
10.47	Sandwich cantilever plate, three-dimensional view of the electric potential Φ , on deformed structure. 3D Abaqus C3D20RE and mono-model <i>LW4</i>	301

10.48	Sandwich cantilever plate, in-plane stress $\sigma_{xx}(x, y) = \sigma_{xx}(d, b/2)$, and transverse normal stress $\sigma_{zz}(x, y) = \sigma_{zz}(d, b/2)$. Single and Multi-theory models.	301
10.49	Sandwich cantilever plate, three-dimensional view of the transverse shear stress σ_{xz} , on undeformed structure. 3D Abaqus C3D20RE and mono-model <i>LW4</i>	302
10.50	Sandwich cantilever plate, transverse shear stress σ_{xz} . Three-dimensional view on undeformed structure by multi-model <i>Case C</i> , and behaviour along the thickness $\sigma_{xz}(x, y) = \sigma_{xz}(d, b/2)$ for single and multi-theory models.	302
10.51	Reference system of the sandwich plate with piezoelectric patch under the concentrated mechanical load.	303
10.52	Non-uniform adopted mesh and graphical representation of the multi-model cases, for the sandwich plate.	304
10.53	Sandwich cantilever plate under concentrated mechanical load. Transverse displacement $\bar{w}(x; y) = 10^5 \times w(a; b/2)$, and transverse shear stress $\bar{\sigma}_{xz}(x; y) = 10^{-5} \times \sigma_{xz}(a/2; b/2)$ along the plate thickness. Single and Multi-theory models.	306
10.54	Sandwich cantilever plate under concentrated mechanical load. Electric potential $\bar{\Phi}(x; y) = \Phi(3a/4; b/2)$, and transverse electric displacement $\bar{\mathcal{D}}_z(x; y) = 10^6 \times \mathcal{D}_z(a/2; b/2)$ along the plate thickness. Single and Multi-theory models.	306
10.55	Sandwich cantilever plate under concentrated mechanical load. Transverse shear stress $\bar{\sigma}_{xz}(y; z) = 10^{-5} \times \sigma_{xz}(b/2; +h/6)$, and transverse normal stress $\bar{\sigma}_{zz}(y; z) = 10^{-5} \times \sigma_{zz}(b/2; +h/6)$ along the in-plane x-axis. Single and Multi-theory models.	307
10.56	Sandwich cantilever plate under concentrated mechanical load. Electric potential $\bar{\Phi}(y; z) = \Phi(b/2; +h/6)$, and transverse electric displacement $\bar{\mathcal{D}}_z = 10^5 \times \mathcal{D}_z(b/2; +h/6)$ along the in-plane x-axis. Single and Multi-theory models.	308
10.57	Sandwich cantilever plate under concentrated mechanical load. Three-dimensional view of the electric potential Φ , on undeformed structure. 3D Abaqus C3D20RE and mono-model <i>LW4</i>	309
10.58	Sandwich cantilever plate under concentrated mechanical load. Three-dimensional view of the in-plane electric displacement \mathcal{D}_x , on undeformed structure. 3D Abaqus C3D20RE and mono-model <i>LW4</i>	309
10.59	Sandwich cantilever plate under concentrated mechanical load. Three-dimensional view of the transverse electric displacement \mathcal{D}_z , on undeformed structure. 3D Abaqus C3D20RE and mono-model <i>LW4</i>	310

List of Tables

6.1	Elastic and Geometrical properties	81
6.2	Transversal displacement $\bar{w}(z = 0)$. Three-layered shell, symmetric lamination $(0^\circ, 90^\circ, 0^\circ)$	82
6.3	Transversal displacement $\bar{w}(z = 0)$. Four-layered shell, antisymmetric lamination $(0^\circ, 90^\circ, 0^\circ, 90^\circ)$	83
6.4	Transversal displacement $\bar{w}(z = 0)$. Five-layered shell, symmetric lamination $(0^\circ, 90^\circ, 0^\circ, 90^\circ, 0^\circ)$	83
6.5	In-plane stress $\bar{\sigma}_{\alpha\alpha}(z = -h/2)$. Three-layered shell, symmetric lamination $(0^\circ, 90^\circ, 0^\circ)$	84
6.6	Shear stress $\bar{\sigma}_{\alpha z}$ evaluated in $(z = 0)$ for $N_l = 3, 5$ and $(z = -h/8)$ for $N_l = 4$. Curvature ratio $R/a = 2$	84
6.7	Antisymmetric lamination $(45^\circ / -45^\circ)$ with simply-supported boundary conditions and bi-sinusoidal load. Theory LW4.	88
6.8	Symmetric lamination $(0^\circ/90^\circ/0^\circ)$ with clamped-free boundary conditions and bi-sinusoidal load. Theory LW4.	88
6.9	Symmetric lamination $(90^\circ/0^\circ/90^\circ)$ with simply-supported boundary conditions and concentrated load. Theory LW4.	89
6.10	Expansion terms of the proposed theories.	93
6.11	Convergence study. Plate with lamination $[0^\circ/90^\circ/0^\circ]$ and with thickness ratio $a/h = 100$	94
6.12	Locking study. Plate with lamination $[0^\circ/90^\circ/0^\circ]$ and with thickness ratio $a/h = 100$. All the cases are computed with a mesh of 10×10 elements.	95
6.13	Plate with lamination $[0^\circ/90^\circ/0^\circ]$. Transverse displacement $\hat{w} = \hat{w}(a/2, b/2, +h/2)$, in-plane principal stress $\hat{\sigma}_{xx} = \hat{\sigma}_{xx}(a/2, b/2, \pm h/2)$, transverse shear stress $\hat{\sigma}_{xz} = \hat{\sigma}_{xz}(a, b/2, 0)$ and $\hat{\sigma}_{yz} = \hat{\sigma}_{yz}(a/2, b, 0)$	96
6.14	Plate with lamination $[0^\circ/90^\circ/0^\circ]$ and thickness ratio $a/h = 10$. Transverse displacement $\hat{w} = \hat{w}(a/2, b/2, 0)$, in-plane principal stress $\hat{\sigma}_{xx} = \hat{\sigma}_{xx}(a/2, b/2, \pm h/2)$, transverse shear stress $\hat{\sigma}_{xz} = \hat{\sigma}_{xz}(a, b/2, 0)$ and $\hat{\sigma}_{yz} = \hat{\sigma}_{yz}(a/2, b, 0)$	102
6.15	Plate with lamination $[0^\circ/90^\circ]$. Transverse displacement $\hat{w} = \hat{w}(a/2, b/2, +h/2)$, in-plane principal stress $\hat{\sigma}_{xx} = \hat{\sigma}_{xx}(a/2, b/2, \pm h/2)$, transverse shear stress $\hat{\sigma}_{xz} = \hat{\sigma}_{xz}(a, b/2, 0)$ and $\hat{\sigma}_{yz} = \hat{\sigma}_{yz}(a/2, b, 0)$	104
6.16	Plate of 4 layers $[0^\circ/90^\circ/90^\circ/0^\circ]$ with various thickness ratios a/h . Transverse displacement $\hat{w} = \hat{w}(a/2, b/2, 0)$	105
6.17	Sandwich rectangular plate. Transverse displacement $w = w(a/2, b/2, \pm h/2)$, in-plane principal stresses $\sigma_{xx} = \sigma_{xx}(a/2, b/2)$ and $\sigma_{yy} = \sigma_{yy}(a/2, b/2)$	106
7.1	Material data for multilayered plate, cylindrical and spherical shell.	110
7.2	Plate with lamination $(0^\circ/90^\circ/0^\circ)$. Transverse displacement $w = w(a/2, b/2) * h_{tot}$ and principal in-plane stress $\sigma_{\alpha\alpha} = \sigma_{\alpha\alpha}(a/2, b/2)$, evaluated at $z = \pm h/2$. Transverse shear stress $\sigma_{\alpha z} = \sigma_{\alpha z}(a, b/2)$, evaluated at $z = +h/6$	111

7.3	Constant thermal profile. Plate with lamination (0°/90°/0°) and cylindrical and spherical panel with lamination (0°/90°), transverse displacement $w = w(a/2, b/2)$, in-plane stress $\sigma_{\alpha\alpha} = \sigma_{\alpha\alpha}(a/2, b/2)$, transverse shear stress $\sigma_{\alpha z} = \sigma_{\alpha z}(a, b/2)$, transverse normal stress $\sigma_{zz} = \sigma_{zz}(a/2, b/2)$. Only for the cylindrical and spherical panel the transverse displacement $w = w 10$, transverse shear stress $\sigma_{\alpha z} = \sigma_{\alpha z} 10^2$, transverse normal stress $\sigma_{zz} = \sigma_{zz} 10^2$	113
7.4	Cylindrical panel with 1 layer made of isotropic materials Aluminum, $N_l = 1$. Transverse displacement $w = w(a/2, b/2) * 10 h_{tot} / \alpha_{Al} a^2 \Delta T$, evaluated along the thickness in $z = 0$. Cylindrical panel with 2 layers made of isotropic materials Aluminum-Titanium, $N_l = 2$. Transverse displacement $w = w(a/2, b/2) * 10 h_{tot} / \alpha_{Al} a^2 \Delta T$, evaluated along the thickness in $z = +h/4$	115
7.5	Cylindrical panel with lamination (0°/90°). Transverse displacement $w = w(a/2, b/2)$, in-plane stress $\sigma_{\alpha\alpha} = \sigma_{\alpha\alpha}(a/2, b/2) * 10$, transverse shear stress $\sigma_{\alpha z} = \sigma_{\alpha z}(a, b/2) * 10^2$, transverse normal stress $\sigma_{zz} = \sigma_{zz}(a/2, b/2) * 10^3$. The variables are evaluated at $z = 0$	116
7.6	Spherical panel with lamination (0°/90°). Transverse displacement $w = w(a/2, b/2)$, in-plane stress $\sigma_{\alpha\alpha} = \sigma_{\alpha\alpha}(a/2, b/2) * 10$ and transverse normal stress $\sigma_{zz} = \sigma_{zz}(a/2, b/2) * 10^3$ evaluated at $z = 0$, transverse shear stress $\sigma_{\alpha z} = \sigma_{\alpha z}(a, b/2) * 10^2$ evaluated at $z = -h/4$	119
7.7	Physical data for multilayered plate, cylindrical and spherical shell.	122
7.8	Convergence study. Plate with thickness ratio $a/h = 100$, cylindrical panel and spherical panel with radius to thickness ratio $R/h = 500$. All the cases are computed for the calculated temperature profile T_c and with a <i>LW4</i> theory.	123
7.9	Locking study. Plate with thickness ratio $a/h = 100$. All the cases are computed for the calculated temperature profile T_c , with a mesh of 10×10 elements.	123
7.10	Plate with lamination (0°/90°/0°). Transverse displacement $w = w(a/2, b/2) * h_{tot}$, evaluated at $z = \pm h/2$. Transverse shear stress $\sigma_{\alpha z} = \sigma_{\alpha z}(a, 0)$, evaluated at $z = +h/6$	124
7.11	Cylindrical panel with lamination (0°/90°). Transverse displacement $w = w(a/2, b/2)$, transverse shear stress $\sigma_{\alpha z} = \sigma_{\alpha z}(a, 0) * 10^2$, evaluated at $z = 0$	127
7.12	Spherical panel with lamination (0°/90°). Transverse displacement $w = w(a/2, b/2)$, evaluated at $z = 0$, transverse shear stress $\sigma_{\alpha z} = \sigma_{\alpha z}(a, 0) * 10^2$ evaluated at $z = -h/4$	130
7.13	Benchmark problems. Case 1 with anti-symmetric lamination $\pm 45^\circ$. Plate, cylindrical and spherical panel, transverse displacement $w = 10 w(a/2, b/2, +h/2)$ and transverse shear stress $\sigma_{\alpha z} = 10^2 \sigma_{\alpha z}(a, b/2, 0)$	133
7.14	Benchmark problems. Case 2 with clamped-free boundary condition. Plate, cylindrical and spherical panel, transverse displacement $w = 10 w(a/2, b/2, +h/2)$ and transverse shear stress $\sigma_{\alpha z} = 10^2 \sigma_{\alpha z}(a, b/2, 0)$	135
8.1	Physical data for multilayered plate and cylindrical shell.	138
8.2	Transverse normal displacement $\mathbf{w} * 10^{11}$ evaluated along the thickness in ($z = 0$). Electric potential $\Phi * 10^3$ evaluated along the thickness in ($z = 0$). Transverse normal electric displacement $\mathcal{D}_z * 10^9$ evaluated along the thickness at <i>top</i> ($z = +h/2$). Plate with 4 layers. Sensor case.	139
8.3	Transverse normal displacement $\mathbf{w} * 10^{11}$ evaluated along the thickness in ($z = 0$). Electric potential Φ evaluated along the thickness in ($z = 0$). Transverse normal electric displacement $\mathcal{D}_z * 10^9$ evaluated along the thickness at <i>top</i> ($z = +h/2$). Plate with 4 layers. Actuator case.	140
8.4	Principal stresses $\sigma_{\alpha\alpha}$, σ_{zz} evaluated along the thickness at <i>top</i> ($z = +h/2$) and shear stress $\sigma_{\alpha z}$ evaluated along the thickness in ($z = 0$). Plate with 4 layers. Sensor case.	141

8.5	Principal stresses $\sigma_{\alpha\alpha}$, σ_{zz} evaluated along the thickness at <i>top</i> ($z = +h/2$) and shear stress $\sigma_{\alpha z}$ evaluated along the thickness in ($z = 0$). Plate with 4 layers. Actuator case.	142
8.6	Transverse normal displacement $w * 10^9$, electric potential Φ , shear stresses $\sigma_{\alpha z}$, $\sigma_{\beta z}$ evaluated along the thickness in ($z = 0$). Transverse normal electric displacement $\mathcal{D}_z * 10^9$ evaluated along the thickness at <i>top</i> ($z = +h/2$). In-plane stresses $\sigma_{\alpha\alpha}$, $\sigma_{\beta\beta}$, $\sigma_{\alpha\beta}$ and transverse normal stress σ_{zz} evaluated along the thickness at ($z = \pm h/2$). Shell mono-layered piezoelectric cylinder. <i>Mesh</i> (10×10). Sensor case.	146
8.7	Transverse normal displacement $w * 10^{11}$, electric potential Φ , shear stresses $\sigma_{\alpha z}$, $\sigma_{\beta z}$ evaluated along the thickness in ($z = 0$). Transverse normal electric displacement $\mathcal{D}_z * 10^{11}$ evaluated along the thickness at <i>top</i> ($z = +h/2$). In-plane stresses $\sigma_{\alpha\alpha}$, $\sigma_{\beta\beta}$, $\sigma_{\alpha\beta}$ and transverse normal stress σ_{zz} evaluated along the thickness at ($z = \pm h/2$). Shell mono-layered piezoelectric cylinder. <i>Mesh</i> (10×10). Actuator case.	147
8.8	Transverse normal displacement $w * 10^{11}$, electric potential Φ , shear stress $\sigma_{\alpha z}$ and transverse normal stress σ_{zz} evaluated along the thickness in ($z = 0$). Transverse normal electric displacement $\mathcal{D}_z * 10^{11}$ evaluated along the thickness at <i>top</i> ($z = +h/2$). Shell cylinder with 3 layers. Sensor case.	148
8.9	Transverse normal displacement $w * 10^{11}$, electric potential Φ , shear stress $\sigma_{\alpha z} * 10^4$ and transverse normal stress $\sigma_{zz} * 10^4$ evaluated along the thickness in ($z = 0$). Transverse normal electric displacement $\mathcal{D}_z * 10^{11}$ evaluated along the thickness at <i>top</i> ($z = +h/2$). Shell cylinder with 3 layers. Actuator case.	149
8.10	Convergence study for transverse mechanical displacement $w * 10^{11}$, electric potential $\Phi * 10^2$ and transverse normal stress $\sigma_{zz} * 10^4$ evaluated at the midsurface ($z = 0$), and electric displacement $\mathcal{D}_z * 10^{11}$ evaluated at <i>top</i> ($z = +h/2$). All the variables are evaluated in ($\alpha = \frac{a}{2m}$; $\beta = \frac{b}{2n} \pm r \frac{b}{n}$), $r = 0, \dots, n - 1$. Thickness ratio (R/h) = 100. Actuator case.	153
8.11	Convergence study for transverse mechanical displacement $w * 10^{11}$, electric potential $\Phi * 10^4$ and transverse normal stress $\sigma_{zz} * 10$ evaluated at the midsurface ($z = 0$), and electric displacement $\mathcal{D}_z * 10^{12}$ evaluated at <i>top</i> ($z = +h/2$). All the variables are evaluated in ($\alpha = \frac{a}{2m}$; $\beta = \frac{b}{2n} \pm r \frac{b}{n}$), $r = 0, \dots, n - 1$. Thickness ratio (R/h) = 2. Sensor case.	153
8.12	Transverse normal displacement $w * 10^{11}$, electric potential $\Phi * 10^4$ and transverse normal stress $\sigma_{zz} * 10$ evaluated at the midsurface ($z = 0$). Transverse normal electric displacement $\mathcal{D}_z * 10^{12}$ evaluated at <i>top</i> ($z = +h/2$). All the variables are evaluated in ($\alpha = \frac{a}{2m}$; $\beta = \frac{b}{2n} \pm r \frac{b}{n}$), $r = 0, \dots, n - 1$. Sensor case. Mesh 6×22	154
8.13	Transverse normal displacement $w * 10^{11}$, electric potential $\Phi * 10^2$ and transverse normal stress $\sigma_{zz} * 10^4$ evaluated at the midsurface ($z = 0$). Transverse normal electric displacement $\mathcal{D}_z * 10^{11}$ evaluated at <i>top</i> ($z = +h/2$). All the variables are evaluated in ($\alpha = \frac{a}{2m}$; $\beta = \frac{b}{2n} \pm r \frac{b}{n}$), $r = 0, \dots, n - 1$. Actuator case. Mesh 6×22	155
8.14	Material and geometrical data for cantilevered plate with piezoelectric patches	159
8.15	Frequency of cantilevered Plate with piezo-patches. Open Circuit case. Convergence study. LW4 model.	159
8.16	Frequency of cantilevered Plate with piezo-patches comparing different locking correction methods. For all the cases a LW4 model is adopted.	160
8.17	Frequency of cantilevered Plate with piezo-patches. Pure Mechanical case.	161
8.18	Frequency of cantilevered Plate with piezo-patches. Short Circuit case.	162
8.19	Frequency of cantilevered Plate with piezo-patches. Open Circuit case.	163

9.1	Convergence study. Composite plate with lamination $[0^\circ/90^\circ/0^\circ]$ and with thickness ratio $a/h = 100$	171
9.2	Locking study. Composite plate with lamination $[0^\circ/90^\circ/0^\circ]$ and with thickness ratio $a/h = 100$. All the cases are computed with a mesh of 10×10 elements.	172
9.3	Composite plate with lamination $[0^\circ/90^\circ/0^\circ]$. Transverse displacement $\hat{w} = \hat{w}(a/2, b/2, +h/2)$, in-plane stress $\hat{\sigma}_{xx} = \hat{\sigma}_{xx}(a/2, b/2, \pm h/2)$, transverse shear stress $\hat{\sigma}_{xz} = \hat{\sigma}_{xz}(a, b/2, 0)$ and $\hat{\sigma}_{yz} = \hat{\sigma}_{yz}(a/2, b, 0)$. Taylor vs Legendre models.	172
9.4	Composite plate with lamination $[0^\circ/90^\circ/0^\circ]$. Transverse displacement $\hat{w} = \hat{w}(a/2, b/2, +h/2)$, in-plane stress $\hat{\sigma}_{xx} = \hat{\sigma}_{xx}(a/2, b/2, \pm h/2)$, transverse shear stress $\hat{\sigma}_{xz} = \hat{\sigma}_{xz}(a, b/2, 0)$ and $\hat{\sigma}_{yz} = \hat{\sigma}_{yz}(a/2, b, 0)$. Variable kinematic models.	175
9.5	Convergence study. Eight-layer cantilever beam. Transverse displacement $w = -10^2 w(a, b/2, 0)$, in-plane stress $\sigma_{xx} = 10^3 \sigma_{xx}(a/2, b/2, +h/2)$, transverse shear stress $\sigma_{xz} = 10^2 \sigma_{xz}(a/2, b/2, 0)$	178
9.6	Eight-layer cantilever beam. Transverse displacement $w = w(a, b/2, 0)$, in-plane stress $\sigma_{xx} = \sigma_{xx}(a/2, b/2, +h/2)$, transverse shear stress $\sigma_{xz} = \sigma_{xz}(a/2, b/2, 0)$.	179
9.7	Sandwich rectangular plate. Transverse displacement $w = w(a/2, b/2, \pm h/2)$, in-plane stresses $\sigma_{xx} = \sigma_{xx}(a/2, b/2)$ and $\sigma_{yy} = \sigma_{yy}(a/2, b/2)$	182
9.8	Composite sandwich plate. Transverse displacement $\hat{w} = \hat{w}(a/2, b/2, +h/2)$, in-plane stress $\hat{\sigma}_{xx} = \hat{\sigma}_{xx}(a/2, b/2, \pm h/2)$, transverse shear stress $\hat{\sigma}_{xz} = \hat{\sigma}_{xz}(a, b/2, 0)$ and transverse normal stress $\hat{\sigma}_{zz} = \hat{\sigma}_{zz}(a/2, b/2, +h/2)$. Variable kinematic models.	184
9.9	Convergence study. Composite cylinder with lamination $[90^\circ/0^\circ/90^\circ]$ and with radius to thickness ratio $R/h = 500$. The mesh is referred to one octave of the cylinder.	187
9.10	Locking study. Composite cylinder with lamination $[90^\circ/0^\circ/90^\circ]$ and with radius to thickness ratio $R/h = 500$. All the present FEM analyses are computed with a mesh of 8×32 elements.	187
9.11	Composite three-layered cylinder with lamination $[90^\circ/0^\circ/90^\circ]$. Taylor vs Legendre models.	188
9.12	Composite three-layered cylinder with $[90^\circ/0^\circ/90^\circ]$ lamination. Comparison of various models for thin cylinders.	190
9.13	Composite three-layered cylinder with $[90^\circ/0^\circ/90^\circ]$ lamination. Comparison of various models for thick cylinders.	191
9.14	Composite ten-layered cylinder with $[90^\circ/0^\circ/90^\circ/0^\circ/90^\circ]_S$ lamination. Comparison of various models for thin cylinders.	195
9.15	Composite ten-layered cylinder with $[90^\circ/0^\circ/90^\circ/0^\circ/90^\circ]_S$ lamination. Comparison of various models for thick cylinders.	196
9.16	Convergence study. Composite spherical panel with lamination $[0^\circ/90^\circ/0^\circ]$. Radius-to-side length ratio $R/a = 10$ and side length-to-thickness ratio $a/h = 10$.	199
9.17	Composite spherical panel with $[0^\circ/90^\circ/0^\circ]$ and $[0^\circ/90^\circ/90^\circ/0^\circ]$ laminations. Transverse displacement $\hat{w} = \hat{w}(a/2, b/2, 0)$. Results presented for different R/a and a/h ratios.	200
9.18	Composite spherical panel with $[0^\circ/90^\circ/0^\circ]$ and $[0^\circ/90^\circ/90^\circ/0^\circ]$ laminations. Transverse shear stress $\hat{\sigma}_{\alpha z} = \hat{\sigma}_{\alpha z}(a/2, b/2, 0)$, and transverse normal stress $\hat{\sigma}_{zz} = \hat{\sigma}_{zz}(a/2, b/2, +h/2)$. Results presented for different R/a and a/h ratios.	200
9.19	Convergence study. Composite sandwich cylindrical panel with circumferential length-to-thickness ratio $a/h = 5$ and side length ratio $b/a = 1$	201
9.20	Sandwich eleven-layered cylinder. Transverse displacement $\hat{w}(\alpha, \beta) = \hat{w}(a/2, b/2)$, in-plane stresses $\hat{\sigma}_{\alpha\alpha}(\alpha, \beta) = \hat{\sigma}_{\alpha\alpha}(a/2, b/2)$, $\hat{\sigma}_{\beta\beta}(\alpha, \beta) = \hat{\sigma}_{\beta\beta}(a/2, b/2)$, in-plane shear stress $\hat{\sigma}_{\alpha\beta}(\alpha, \beta) = \hat{\sigma}_{\alpha\beta}(0, 0)$ and transverse shear stress $\hat{\sigma}_{\alpha z}(\alpha, \beta) = \hat{\sigma}_{\alpha z}(0, b/2)$	203

9.21	Convergence study. Composite three layered plate with thickness ratio $a/h = 100$. All the cases are computed with a <i>LW4</i> model.	208
9.22	Locking study. Composite three layered plate with thickness ratio $a/h = 100$. The <i>Temperature Assumed Linear</i> and the <i>Temperature Calculated</i> cases are computed with a mesh of 32×32 elements and with a <i>LW4</i> model. . . .	208
9.23	Three-layer composite plate with lamination $[0^\circ/90^\circ/0^\circ]$. Mechanical variables described by Mono-models and Variable kinematic models for various aspect ratios a/h . Evaluation position for transverse displacement $\hat{w}(x, y, z) = \hat{w}(a/2, b/2, +h/2)$, in-plane stress $\hat{\sigma}_{xx}(x, y, z) = \hat{\sigma}_{xx}(a/2, b/2, +h/2)$, transverse shear stress $\hat{\sigma}_{xz}(x, y, z) = \hat{\sigma}_{xz}(0, b/2, +h/6)$, transverse normal stress $\hat{\sigma}_{zz}(x, y, z) = \hat{\sigma}_{zz}(a/2, b/2, +h/6)$	211
9.24	Ten-layer composite cylindrical shell panel with lamination $[0^\circ/90^\circ]_5$. Mechanical variables described by Mono-models and Variable kinematic models for various radius to length side ratios R/a . Evaluation position for transverse displacement $\hat{w}(x, y, z) = \hat{w}(a/2, b/2, 0)$, in-plane stress $\hat{\sigma}_{\alpha\alpha}(x, y, z) = \hat{\sigma}_{\alpha\alpha}(a/2, b/2, +h/2)$, transverse shear stress $\hat{\sigma}_{\alpha z}(x, y, z) = 10 \times \hat{\sigma}_{\alpha z}(a, b/2, +\frac{2}{5}h)$, transverse normal stress $\hat{\sigma}_{zz}(x, y, z) = 10^2 \times \hat{\sigma}_{zz}(a/2, b/2, 0)$	216
9.25	Five-layer sandwich spherical shell panel with lamination $[0^\circ/90^\circ/Core/90^\circ/0^\circ]$. Mechanical variables described by Mono-models and Variable kinematic models for various radius to length side ratios R/a and various aspect ratios a/h . Evaluation position for transverse displacement $\hat{w}(x, y, z) = \hat{w}(a/2, b/2, 0)$, in-plane stress $\hat{\sigma}_{\alpha\alpha}(x, y, z) = \hat{\sigma}_{\alpha\alpha}(a/2, b/2, +h/2)$, transverse shear stress $\hat{\sigma}_{\alpha z}(x, y, z) = 10 \times \hat{\sigma}_{\alpha z}(a, b/2, +\frac{9}{20}h)$, transverse normal stress $\hat{\sigma}_{zz}(x, y, z) = 10^2 \times \hat{\sigma}_{zz}(a/2, b/2, 0)$. The temperature profile is assumed linear T_a	221
9.26	Five-layer sandwich spherical shell panel with lamination $[0^\circ/90^\circ/Core/90^\circ/0^\circ]$. Mechanical variables described by Mono-models and Variable kinematic models for various radius to length side ratios R/a and various aspect ratios a/h . Evaluation position for transverse displacement $\hat{w}(x, y, z) = \hat{w}(a/2, b/2, 0)$, in-plane stress $\hat{\sigma}_{\alpha\alpha}(x, y, z) = \hat{\sigma}_{\alpha\alpha}(a/2, b/2, +h/2)$, transverse shear stress $\hat{\sigma}_{\alpha z}(x, y, z) = 10 \times \hat{\sigma}_{\alpha z}(a, b/2, +\frac{9}{20}h)$, transverse normal stress $\hat{\sigma}_{zz}(x, y, z) = 10^2 \times \hat{\sigma}_{zz}(a/2, b/2, 0)$. The temperature profile is calculated via Fourier heat conduction equation T_c	226
9.27	Material data for multilayered plate and shell.	226
9.28	Convergence study. Composite four layered plate with thickness ratio $a/h = 100$.	227
9.29	Locking study. Composite four layered plate with thickness ratio $a/h = 100$. The Sensor cases are computed with a mesh of 40×40 elements, the Actuator cases are computed with a mesh of 24×24 elements.	227
9.30	Four-layer square plate with a cross-ply composite core $[0^\circ/90^\circ]$ and piezoelectric external skins. Mechanical and electrical variables described by Mono-models and Variable kinematic models for various aspect ratios a/h . Sensor case.	230
9.31	Four-layer square plate with a cross-ply composite core $[0^\circ/90^\circ]$ and piezoelectric external skins. Mechanical and electrical variables described by Mono-models and Variable kinematic models for various aspect ratios a/h . Actuator case.	231
9.32	Four-layer square plate with a cross-ply composite core $[0^\circ/90^\circ]$ and piezoelectric external skins. Euclidean norm of the error respect to the reference solution <i>LW4</i> for mechanical and electrical variables described by Mono-models and Variable kinematic models for various aspect ratios a/h . Sensor and Actuator cases.	235
9.33	Convergence study. Composite three layered cylindrical shell with radius to thickness ratio $R_\beta/h = 100$	237

9.34	Three-layer cylinder with a composite core and piezoelectric external skins. Mechanical and electrical variables described by Mono-models and Variable kinematic models for various radius to thickness ratios R/h . Sensor case. . . .	238
9.35	Three-layer cylinder with a composite core and piezoelectric external skins. Mechanical and electrical variables described by Mono-models and Variable kinematic models for various radius to thickness ratios R/h . Actuator case. . .	239
9.36	Four-layer cylinder with a composite core and piezoelectric external skins. Mechanical and electrical variables described by Mono-models and Variable kinematic models for various radius to thickness ratios R/h . Sensor case. . . .	242
9.37	Four-layer cylinder with a composite core and piezoelectric external skins. Mechanical and electrical variables described by Mono-models and Variable kinematic models for various radius to thickness ratios R/h . Actuator case. . .	243
10.1	Convergence study according to the <i>ET4</i> model of the isotropic plate structure.	260
10.2	Simply-supported metallic plate. Displacement and stress components from single-theory, multi-theory and reference models.	261
10.3	Convergence study of single-theory models of the eight-layer cantilever plate. Transverse displacement $w = -10^2 \times w(a, b/2, 0)$, in-plane principal stress $\sigma_{xx} = 10^3 \times \sigma_{xx}(a/2, b/2, +h/2)$, transverse shear stress $\sigma_{xz} = -10^2 \times \sigma_{xz}(a/2, b/2, 0)$.	268
10.4	Eight-layer cantilever plate. Transverse displacement $w = -10^2 \times w(a, b/2, 0)$, in-plane normal stress $\sigma_{xx} = 10^3 \times \sigma_{xx}(a/2, b/2, +h/2)$, transverse shear stress $\sigma_{xz} = -10^2 \times \sigma_{xz}(a/2, b/2, 0)$ by various single- and multi-theory models. . .	269
10.5	Convergence study with a <i>ET4</i> plate element. Composite plate with $(0^\circ/90^\circ/0^\circ)$ lamination, a quarter of the plate is taken into account.	273
10.6	Composite plate with $[0^\circ/90^\circ/0^\circ]$ lamination. Transverse displacement $w = (-10^5) \times w(a/2, b/2, -h/2)$, in-plane normal stresses $\sigma_{xx} = \sigma_{xx}(a/2, b/2, -h/2)$ and $\sigma_{yy} = \sigma_{yy}(a/2, b/2, -h/2)$, transverse shear stress $\sigma_{xz} = (-10) \times \sigma_{xz}(5a/12, b/2, 0)$, and transverse normal stress $\sigma_{zz} = -\sigma_{zz}(a/2, b/2, +h/2)$ by various single- and multi-theory models.	275
10.7	Unsymmetrically laminated rectangular sandwich plate. Transverse displacement w , in-plane normal stresses σ_{xx} and σ_{yy} , and transverse normal stress σ_{zz} evaluated at $(a/2, b/2)$ by various single- and multi-theory models.	282
10.8	Material data for multilayered plate.	288
10.9	Composite four-layered plate with piezoelectric skins. Transverse displacement $\bar{w} = (10^{11}) \times w(a/2, b/2, 0)$, in-plane stress $\bar{\sigma}_{xx} = \sigma_{xx}(a/2, b/2, +h/2)$, transverse shear stress $\bar{\sigma}_{xz} = \sigma_{xz}(0, b/2, 0)$, transverse normal stress $\bar{\sigma}_{zz} = (10) \times \sigma_{zz}(a/2, b/2, 0)$, electric potential $\bar{\Phi} = (10^2) \times \Phi(a/2, b/2, 0)$, and transverse electric displacement $\bar{\mathcal{D}}_z = (10^{10}) \times \mathcal{D}_z(a/2, b/2, +h/2)$ by various single- and multi-theory models. Sensor Case.	290
10.10	Composite four-layered plate with piezoelectric skins. Transverse displacement $\bar{w} = (10^{11}) \times w(a/2, b/2, 0)$, in-plane stress $\bar{\sigma}_{xx} = \sigma_{xx}(a/2, b/2, +h/2)$, transverse shear stress $\bar{\sigma}_{xz} = (10) \times \sigma_{xz}(0, b/2, 0)$, transverse normal stress $\bar{\sigma}_{zz} = (10^3) \times \sigma_{zz}(a/2, b/2, 0)$, electric potential $\bar{\Phi} = \Phi(a/2, b/2, 0)$, and transverse electric displacement $\bar{\mathcal{D}}_z = (10^9) \times \mathcal{D}_z(a/2, b/2, +h/2)$ by various single- and multi-theory models. Actuator Case.	291
10.11	Convergence study versus the number of elements of the <i>LW4</i> single-theory model of the sandwich cantilever plate. Transverse displacement $w = 10^8 \times w(a, b/2, +h/2)$, electric potential $\Phi = \Phi(d, b/2, -h/2)$, in-plane principal stress $\sigma_{xx} = \sigma_{xx}(d, b/2, -h/2)$, transverse shear stress $\sigma_{xz} = \sigma_{xz}(d, b/2, 0)$, with the center of the piezoelectric patch placed at $d = 85 \text{ mm}$	296

10.12	Single-theory and multi-theory models of the sandwich cantilever plate. Transverse displacement $w = 10^8 \times w(a, b/2, +h/2)$, electric potential $\Phi = \Phi(d, b/2, -h/2)$, in-plane principal stress $\sigma_{xx} = \sigma_{xx}(d, b/2, -h/2)$, transverse shear stress $\sigma_{xz} = \sigma_{xz}(d, b/2, 0)$, transverse normal stress $\sigma_{zz} = \sigma_{zz}(d, b/2, -h/2)$, transverse electric displacement $\mathcal{D}_z = 10^4 \times \mathcal{D}_z(d, b/2, 0)$, with the center of the piezoelectric patch placed at $d = 85 \text{ mm}$	299
10.13	Single-theory and multi-theory models of the sandwich cantilever plate under concentrated mechanical load. Transverse displacement $w = 10^5 \times w(a, b/2, +h/2)$, electric potential $\Phi = \Phi(3a/4, b/2, +h/6)$, in-plane principal stress $\sigma_{xx} = 10^{-7} \times \sigma_{xx}(a/2, b/2, +h/2)$, transverse shear stress $\sigma_{xz} = 10^{-5} \times \sigma_{xz}(a/2, b/2, +h/6)$, transverse normal stress $\sigma_{zz} = 10^{-5} \times \sigma_{zz}(a/2, b/2, 0)$, transverse electric displacement $\mathcal{D}_z = 10^6 \times \mathcal{D}_z(a/2, b/2, +h/6)$	305

Introduction

Shell models have been developed extensively over the last several decades for structural analysis of thin and slender bodies such as panels, domes, pressure vessels, and wing stiffened panels amongst others. These models reduce the three-dimensional 3D problem into a two-dimensional 2D problem, where variables depend on the in-plane axis coordinates. 2D plate/shell theories are simpler and computationally more efficient than 3D solid models, meanwhile more accurate than 1D beam models.

Shell structures have a predominant role in a variety of engineering applications thanks to their efficient load-carrying capabilities. On the other hand, the continuous development of new structural materials, such as composite layered materials, leads to increasingly complex structural designs that require careful analysis. Anisotropy, nonlinear analysis, as well as complicating effects, such as the C_z^0 requirements (zig-zag effects in the displacements and interlaminar continuity for the stresses), the couplings between in-plane and out-of-plane strains, make the analysis of layered composite structures complicated in practice. Analytical, closed form solutions are available in very few cases. In most of the practical problems, the solution demands applications of approximated computational methods. The Finite Element Method (FEM) has a predominant role among the computational techniques implemented for the analysis of layered structures. The majority of FEM theories available in the literature are formulated by axiomatic-type theories. The conventional FEM plate model is the classical Kirchhoff-Love theory, and some examples are given in [1, 2], whose extension to laminates is known to as the Classical Lamination Theory (CLT) [3]. Another classical plate element is based on the First-order Shear Deformation Theory (FSDT), which rely on the works by Reissner [4] and Mindlin [5]. To overcome the limitations of classical theories, a large variety of plate finite element implementations of higher-order theories (HOT) have been proposed in the last years. HOT-based C^0 finite elements (C^0 means that the continuity is required only for the unknown variables and not for their derivatives) were discussed by Kant *et al.* [6] and Kant and Kommineni [7]. Many other papers are available in which HOTs have been implemented for plates, and more details can be found in the books from Reddy [8] and Palazzotto and Dennis [9]. The HOT type theories presented are Equivalent-Single-Layer (ESL) models, the variables are independent from the number of layers. Differently the Layer-Wise (LW) models permit to consider different sets of variables per each layer. A finite element implementations of Layer-Wise theories in the framework of axiomatic-type theories have been proposed by many authors, among which Noor and Burton [10], Reddy [11], Mawenya and Davies [12], Rammerstorfer et al. [13]. One of the recent contributions to plate/shell theories has been developed within the framework of the Unified Formulation by Carrera [14–16]. The main novelty of Unified Formulation models is that the order of the theory is a free parameter, or can be an input of the analysis and it can be chosen using a convergence study. Unified Formulation can also be considered as a tool to evaluate the accuracy of any structural model in a unified manner.

In aeronautics and space field such structures are subjected to several loadings: mechanical, thermal and electrical ones, this fact leads to the definition of multifield problems. Studies involving the thermo-elastic behavior using 2D classical or first-order theories are described by Kant and Khare [17] and Khdeir and Reddy [18]. In recent years, several higher-order

two-dimensional models have been developed for such problems, which consider only an assumed temperature profile through the thickness. Among these, of particular interest is the higher-order model by Whu and Chen [19]. The same temperature profile is used by Khare et alii [20] to obtain a closed-form solution for the thermomechanical analysis of laminated and sandwich shells. Khdeir [21] and Khdeir et alii [22] assume a linear or constant temperature profile through the thickness. Barut et alii [23] analyze the nonlinear thermoelastic behavior of shells using the Finite Element Method, but the assigned temperature profile is linear. In the framework of the arbitrary distribution of temperature through the thickness, Miller et alii [24] and Dumir et alii [25] are noteworthy, in the first a classical shell theory for composite shells is given, the second remarks the importance of the zig-zag form of displacements in the thermal analysis of composite shells. In the case of shells, further investigations were made by Hsu et alii [26] for both closed form and Finite Element method, and by Ding [27] for a weak formulation for the case of state equations including the boundary conditions. A satisfactory thermal stress analysis is only possible if advanced and refined computational models are developed to approximate the stiffness matrix correctly, and if a correct thermal load is recognized. Sometimes the evaluation of a correct thermal load could be mandatory on any further evaluation for the computational models. In other words, a wrong thermal load invalidates the static response of plate and shell structures even when advanced computational models are employed. In the last few years many contributions have been proposed, which are based on Unified Formulation, to investigate the thermal effects in composite structures [28–31].

The use of piezoelectric components as electro-mechanical transducers in sensor as well as in actuator applications has been continuously increasing. More recently, piezoelectrics have been considered among the most suitable materials for extending the structural capabilities beyond the purely passive load carrying one. Some examples of the most important applications of these “intelligent” structural components are given in [32–34] for vibration and noise suppression, controlled active deformation is treated in [35], and health monitoring in [36,37]. Analytical solution for general smart structural problems is a very tough task, and they exist, only, for very few specialized and idealized cases. Meanwhile, the finite element method has become the most widely used technique to model various physical processes, including piezoelectricity. The fundamentals of the modeling of piezoelectric materials have been given in many contributions, in particular in the pioneering works of Mindlin [38], EerNisse [39], Tiersten and Mindlin [40], and in the monograph of Tiersten [41]. The embedding of piezoelectric layers into plates and shells sharpens the requirements of an accurate modeling of the resulting adaptive structure due to the localized electro-mechanical coupling, see e.g. the review of Saravanos and Heyliger [42]. Therefore, within the framework of two-dimensional approaches, layerwise descriptions have been often proposed either for the electric field only (see e.g. the works of Kapuria [43] and of Ossadzow-David and Touratier [44]) or for both the mechanical and electrical unknowns (e.g. Heyliger et al. [45]). Ballhause et al. [46] showed that a fourth order assumption for the displacements leads to the correct closed form solution. They conclude that the analysis of local responses requires at least a layer-wise descriptions of the displacements, see also [47]. Benjeddou et al. [48] emphasized that a quadratic electric potential through the plate thickness satisfies the electric charge conservation law exactly. Many contributions have been proposed, which are based on Unified Formulation, to investigate the electrical effects in composite structures [49–51]

However, the high computational costs represent the drawback of refined plate/shell theories or three-dimensional analyses. In recent years considerable improvements have been obtained towards the implementation of innovative solutions for improving the analysis efficiency for a global/local scenario. In this manner, the limited computational resources can be distributed in an optimal manner to study in detail only those parts of the structure that require an accurate analysis.

Thesis objectives and outline:

The present work aims at providing a robust finite shell element for the analysis of plate and shell structures subjected to mechanical, thermal, and/or electrical loadings. A wide range of problems are considered, including static analysis, free vibration analysis, different boundary conditions and different laminations schemes, distributed pressure loads, localized pressure loads or concentrated loads are taken into account.

- Brief bibliographic surveys on classical and refined plate/shell modelling techniques for multifield problem and related solution methods are given in this introductory chapter 1.
- Chapter 2 discusses the generalized Hooke law for the definition of the constitutive equations and their extension to multifield problems through the definition of the Gibbs free-energy function. Therefore the geometrical relations for plate and shells are given for multifield problems.
- In chapter 3 the kinematics of thin structures is developed. Starting from the classical assumptions, refined plate and shell models are formulated as the natural consequences of the additions of terms within the displacement field. The Unified Formulation is introduced as an unified manner to formulate classical, higher-order and refined plate and shell theories.
- Different problems are addressed depending on the adopted Variational statement, in chapter 4. Some models are based on the principle of virtual displacements (PVD), other advanced models employ Reissner's mixed variational theorem (RMVT). Refined models for multifield problems are obtained simply by adding the thermal and electrical contributions to the well-known PVD for the pure mechanical case. In some cases, it is necessary to a priori model some variables which cannot be obtained correctly via post-processing (e.g transverse shear/normal stresses and normal electric displacement). These variational statements, which are based on RMVT, are obtained by adding opportune Lagrange multipliers to the principle of virtual displacements, and coherently rewriting the constitutive equations.
- The weak form governing equations of the generic, refined plate/shell model are developed in chapter 5. The Finite Element Method (FEM) is presented and a brief overview of the most common techniques to overcome the membrane and shear locking phenomena is given. The Mixed Interpolation of Tensorial Components (MITC) is explained for the nine-nodes shell element. By using the Principle of Virtual Displacements (PVD) or the Reissner Mixed Variational Theorem (RMVT) as variational statements, various problems are addressed by either including or excluding the virtual works due to inertial loadings and external loadings along with the virtual work of the strain energy. According to Unified Formulation, the governing equations are written in terms of the fundamental nuclei. These nuclei, given the theory order, can be automatically expanded to obtain the equations of the desired theory.
- In Chapter 6, FEM solutions are provided for plate and shell structures subjected to mechanical loadings. Attention is focused on the static problems of cross-ply laminates structures with various boundary conditions and lamination stacking sequences, although the procedure can be extended to other problems. Classical and refined Taylor polynomials, advanced Legendre polynomials and new trigonometric and exponential expansions through the thickness are employed to test the robustness of the shell element.

- In Chapter 7, plate and shell structures subjected to thermo-mechanical loadings are analyzed. The static problems of cross-ply laminates structures with various boundary conditions and lamination stacking sequences is taken into account. The importance of the temperature profile load evaluation is underlined. Results obtained with an assumed linear temperature profile are compared with those developed solving the Fourier heat conduction law.
- In Chapter 8, plate and shell structures subjected to electro-mechanical loadings are analyzed. The static problems of cross-ply laminates structures simply-supported and the free-vibration analysis of cantilevered plate with piezoelectric patches is taken into account. The robustness of the shell element is tested in Sensor and Actuator configuration, where a mechanical external load is applied and an electrical load is considered, respectively. Therefore the $RMVT - D_z$ variational theorem is taken into account to improve the transverse electric displacement description.
- The second part of the thesis is devoted to the development of an efficient shell FEM formulation. A brief overview of innovative solutions for improving the analysis efficiency for global/local scenario and the possible solutions with multi-theory models is given in chapter 9. A simultaneous multi-model is presented as Mixed ESL/LW variable kinematic method. The primary variables are described along the shell thickness selecting some plies with an ESL description and others with a LW behaviour by using the Legendre polynomials for both the assembling approaches. The efficiency of the presented multi-model is tested for mechanical, thermo-mechanical and electro-mechanical problems for various composite and sandwich plate/shell structures with different lamination schemes, various boundary conditions and external loads.
- In chapter 10 other possible solutions for improving the analysis efficiency for global/local scenario and its possible solution with multi-theory models are depicted. A new simultaneous multi-model is here presented as Node-Dependent Variable Kinematic method. The shell element with node-dependent capabilities enables one to vary the kinematic assumptions within the same finite element. The expansion order (along the shell thickness) of the shell element is, in fact, a property of the FE node in the present approach. Different kinematics can be coupled without the use of any mathematical artifice. The efficiency of the presented multi-model is tested for mechanical, and electro-mechanical problems for various composite and sandwich plate/shell structures with different lamination schemes, various boundary conditions and external loads.
- The conclusions are finally drawn in chapter 11.

Some appendices are provided for clarity and completeness.

- The fundamental nuclei obtained with the MITC method are provided in Appendix A.
- Finally, a list of publications arising from the research is provided in Appendix B.

Part I

Shell Structural Formulation

Chapter 2

Constitutive and Geometrical relations

2.1 Generalized Hooke law for mechanical case

The British physicist Robert Hooke, between 1660 and 1678 stated the law as a latin anagram as: "*ut tensio, sic vis*" ("as the extension, so the force"). The Hooke law is a physical principle that correlates the applied force to a spring or to a body with its extension or compression. An elastic body or material for which the Hooke law can be assumed is said to be linear-elastic. Hooke law is only a first-order linear approximation to the real response of elastic bodies to applied forces. If eventually the forces exceed some material limit, some permanent deformation or change of state will be appreciable. The relations that characterize the material and its reaction to applied loads are called constitutive equations. The concepts of stress and strain in a non-ambiguous and more usefull manner has to be attributed to Augustin Cauchy (1789-1857). Here, it has been considered the constitutive equations of linear elasticity for the case of infinitesimal deformations, the so called generalized Hooke law:

$$\sigma_{ij} = C_{ijkl} \epsilon_{kl} + \sigma_{ij}^0 \quad (2.1)$$

where σ_{ij} is the Cauchy stress tensor, ϵ_{kl} is the strain tensor, C_{ijkl} is called stiffness tensor and it is a fourth-order tensor of material parameters, and σ_{ij}^0 represents a residual stress state configuration term. For the sake of simplicity the residual stress term is omitted in the following discussion. In general the stiffness tensor C_{ijkl} has 81 scalar components. The number of independent components of C_{ijkl} can be reduced to 36 considering the symmetry of the stress tensor ($\sigma_{ij} = \sigma_{ji}$), strain tensor ($\epsilon_{kl} = \epsilon_{lk}$), and stiffness tensor is symmetric in the first two subscripts. If it has been assumed the material as hyperelastic, a strain energy density function $U_0(\epsilon_{ij})$ permits to have that $C_{ijkl} = C_{klij}$. This facts permits to rewrite the Eq. 2.1 using single subscripts notation for stresses and strains, and double subscript notation for the material stiffness coefficients:

$$\sigma_i = C_{ij} \epsilon_j \quad (2.2)$$

The single subscript notation for stresses and strains is called *engineering notation* or Voigt-Kelvin notation. In matrix notation the Eq. 2.2 can be written as:

$$\begin{Bmatrix} \sigma_1 \\ \sigma_2 \\ \sigma_3 \\ \sigma_4 \\ \sigma_5 \\ \sigma_6 \end{Bmatrix} = \begin{bmatrix} C_{11} & C_{12} & C_{13} & C_{14} & C_{15} & C_{16} \\ C_{21} & C_{22} & C_{23} & C_{24} & C_{25} & C_{26} \\ C_{31} & C_{32} & C_{33} & C_{34} & C_{35} & C_{36} \\ C_{41} & C_{42} & C_{43} & C_{44} & C_{45} & C_{46} \\ C_{51} & C_{52} & C_{53} & C_{54} & C_{55} & C_{56} \\ C_{61} & C_{62} & C_{63} & C_{64} & C_{65} & C_{66} \end{bmatrix} \begin{Bmatrix} \epsilon_1 \\ \epsilon_2 \\ \epsilon_3 \\ \epsilon_4 \\ \epsilon_5 \\ \epsilon_6 \end{Bmatrix} \quad (2.3)$$

where the notation for stresses and strain components is:

$$\begin{aligned} \sigma_1 &= \sigma_{11}, \quad \sigma_2 = \sigma_{22}, \quad \sigma_3 = \sigma_{33}, \quad \sigma_4 = \sigma_{23}, \quad \sigma_5 = \sigma_{13}, \quad \sigma_6 = \sigma_{12}, \\ \epsilon_1 &= \epsilon_{11}, \quad \epsilon_2 = \epsilon_{22}, \quad \epsilon_3 = \epsilon_{33}, \quad \epsilon_4 = 2\epsilon_{23}, \quad \epsilon_5 = 2\epsilon_{13}, \quad \epsilon_6 = 2\epsilon_{12} \end{aligned}$$

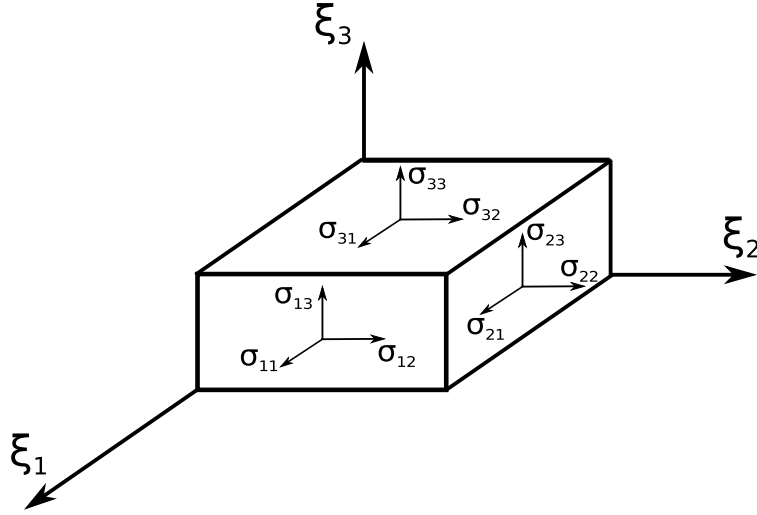


Figure 2.1: Representation of Cauchy stress tensor components in a material body.

In Figure 2.1 the meaning of the stress tensor components is clearly represented in the case of the six stress components expressed in material reference system. Therefore, the matrix coefficients C_{ij} in Eq. 2.3 are symmetric ($C_{ij} = C_{ji}$) for the assumption of hyperelastic material. So, for the most general case of elastic material, it has been a reduction of the independent stiffness coefficients from 36 to 21. The number of independent material parameters can be further reduced if some *material symmetries* are taken into account.

Monoclinic materials: if the elastic coefficients at a point have the same value for every pair of coordinate systems which are the mirror images of each other with respect to a plane, the material is called a monoclinic material. Due to this symmetry hypothesis, the following elastic coefficients are equal to zero: $C_{14} = C_{15} = C_{24} = C_{25} = C_{34} = C_{35} = C_{46} = C_{56} = 0$. So the independent parameters are $21 - 8 = 13$ and the Eq. 2.3 changes in:

$$\begin{Bmatrix} \sigma_1 \\ \sigma_2 \\ \sigma_3 \\ \sigma_4 \\ \sigma_5 \\ \sigma_6 \end{Bmatrix} = \begin{bmatrix} C_{11} & C_{12} & C_{13} & 0 & 0 & C_{16} \\ C_{12} & C_{22} & C_{23} & 0 & 0 & C_{26} \\ C_{13} & C_{23} & C_{33} & 0 & 0 & C_{36} \\ 0 & 0 & 0 & C_{44} & C_{45} & 0 \\ 0 & 0 & 0 & C_{45} & C_{55} & 0 \\ C_{16} & C_{26} & C_{36} & 0 & 0 & C_{66} \end{bmatrix} \begin{Bmatrix} \epsilon_1 \\ \epsilon_2 \\ \epsilon_3 \\ \epsilon_4 \\ \epsilon_5 \\ \epsilon_6 \end{Bmatrix} \quad (2.4)$$

Orthotropic materials: if a material has three mutually orthogonal planes of symmetry it is called orthotropic material. The number of independent elastic coefficients is reduced from 13 to 9. Considering the Eq.2.4 and considering the symmetry hypothesis of orthotropic material, the stress-strain relations change in:

$$\begin{Bmatrix} \sigma_1 \\ \sigma_2 \\ \sigma_3 \\ \sigma_4 \\ \sigma_5 \\ \sigma_6 \end{Bmatrix} = \begin{bmatrix} C_{11} & C_{12} & C_{13} & 0 & 0 & 0 \\ C_{12} & C_{22} & C_{23} & 0 & 0 & 0 \\ C_{13} & C_{23} & C_{33} & 0 & 0 & 0 \\ 0 & 0 & 0 & C_{44} & 0 & 0 \\ 0 & 0 & 0 & 0 & C_{55} & 0 \\ 0 & 0 & 0 & 0 & 0 & C_{66} \end{bmatrix} \begin{Bmatrix} \epsilon_1 \\ \epsilon_2 \\ \epsilon_3 \\ \epsilon_4 \\ \epsilon_5 \\ \epsilon_6 \end{Bmatrix} \quad (2.5)$$

The material properties are usually determined in a laboratory in terms of the engineering constants such as Young's modulus, shear modulus and Poisson's ratios. The 9 independent material coefficients in Eq. 2.5 can be expressed by 9 independent material engineering constants: $E_1, E_2, E_3, G_{12}, G_{13}, G_{23}, \nu_{12}, \nu_{13}, \nu_{23}$. The relations between material

coefficients and engineering constants are:

$$\begin{aligned}
 C_{11} &= \frac{1 - \nu_{23}\nu_{32}}{E_2 E_3 \Delta} & ; & & C_{12} &= \frac{\nu_{21} + \nu_{31}\nu_{23}}{E_2 E_3 \Delta} = \frac{\nu_{12} + \nu_{32}\nu_{13}}{E_1 E_3 \Delta} \\
 C_{13} &= \frac{\nu_{31} + \nu_{21}\nu_{32}}{E_2 E_3 \Delta} = \frac{\nu_{13} + \nu_{12}\nu_{23}}{E_1 E_2 \Delta} & ; & & C_{22} &= \frac{1 - \nu_{13}\nu_{31}}{E_1 E_3 \Delta} \\
 C_{23} &= \frac{\nu_{32} + \nu_{12}\nu_{31}}{E_1 E_3 \Delta} = \frac{\nu_{23} + \nu_{21}\nu_{13}}{E_1 E_2 \Delta} & ; & & C_{33} &= \frac{1 - \nu_{12}\nu_{21}}{E_1 E_2 \Delta} \\
 C_{44} &= G_{23} & ; & & C_{55} &= G_{13} & ; & & C_{66} &= G_{12} \\
 \Delta &= \frac{1 - \nu_{12}\nu_{21} - \nu_{23}\nu_{32} - \nu_{31}\nu_{13} - 2\nu_{21}\nu_{32}\nu_{13}}{E_1 E_2 E_3}
 \end{aligned}$$

For the Poisson coefficients the following ratios relation is valid:

$$\frac{\nu_{ij}}{E_i} = \frac{\nu_{ji}}{E_j} \quad (\text{no sum on } i, j)$$

Most simple mechanical property characterization tests are performed with a known load or stress. Hence, it is convenient to write the inverse relations of Equation 2.5. The strain-stress relations of an orthotropic material are given by:

$$\begin{Bmatrix} \epsilon_1 \\ \epsilon_2 \\ \epsilon_3 \\ \epsilon_4 \\ \epsilon_5 \\ \epsilon_6 \end{Bmatrix} = \begin{bmatrix} S_{11} & S_{12} & S_{13} & 0 & 0 & 0 \\ S_{12} & S_{22} & S_{23} & 0 & 0 & 0 \\ S_{13} & S_{23} & S_{33} & 0 & 0 & 0 \\ 0 & 0 & 0 & S_{44} & 0 & 0 \\ 0 & 0 & 0 & 0 & S_{55} & 0 \\ 0 & 0 & 0 & 0 & 0 & S_{66} \end{bmatrix} \begin{Bmatrix} \sigma_1 \\ \sigma_2 \\ \sigma_3 \\ \sigma_4 \\ \sigma_5 \\ \sigma_6 \end{Bmatrix} \quad (2.6)$$

where S_{ij} are the *compliance coefficients* $[C] = [S]^{-1}$

$$\begin{aligned}
 C_{11} &= \frac{S_{22}S_{33} - S_{23}^2}{S} & ; & & C_{12} &= \frac{S_{13}S_{23} - S_{12}S_{33}}{S} \\
 C_{22} &= \frac{S_{33}S_{11} - S_{13}^2}{S} & ; & & C_{13} &= \frac{S_{12}S_{23} - S_{13}S_{22}}{S} \\
 C_{33} &= \frac{S_{11}S_{22} - S_{12}^2}{S} & ; & & C_{23} &= \frac{S_{12}S_{13} - S_{23}S_{11}}{S} \\
 C_{44} &= \frac{1}{S_{44}} & ; & & C_{55} &= \frac{1}{S_{55}} & ; & & C_{66} &= \frac{1}{S_{66}} \\
 S &= S_{11}S_{22}S_{33} - S_{11}S_{23}^2 - S_{22}S_{13}^2 - S_{33}S_{12}^2 + 2S_{12}S_{23}S_{13}
 \end{aligned}$$

The relations between the *compliance coefficients* S_{ij} and engineering constants are the following:

$$\begin{aligned}
 S_{11} &= \frac{1}{E_1} & ; & & S_{12} &= -\frac{\nu_{12}}{E_1} & ; & & S_{13} &= -\frac{\nu_{13}}{E_1} \\
 S_{22} &= \frac{1}{E_2} & ; & & S_{23} &= -\frac{\nu_{23}}{E_2} & ; & & S_{33} &= \frac{1}{E_3} \\
 S_{44} &= \frac{1}{G_{23}} & ; & & S_{55} &= \frac{1}{G_{13}} & ; & & S_{66} &= \frac{1}{G_{12}}
 \end{aligned}$$

The constitutive relations for an orthotropic material in Eq. 2.2 are written in terms of stress and strain components that are referred to the material coordinate system (1, 2, 3). In a composite laminates each layer has its material coordinate system, and these have different orientations with respect to the most general laminate coordinates called problem

coordinate system (x, y, z) . For the orthotropic material case, Figure 2.2 shows that the material reference system is supposed to be aligned with the fibers in an unidirectionally reinforced lamina which lies in the 1–2 plane. In other words, axis 1 is the fiber longitudinal direction L, axis 2 is aligned with the fiber transversal in-plane direction T (in the plane of the lamina) and 3 is the transversal out-of-plane direction z . According to Figure 2.2, material axes 1 and 2 are rotated by a positive counterclockwise angle θ about the z axis, coincident to axis 3, from physical x and y axes.

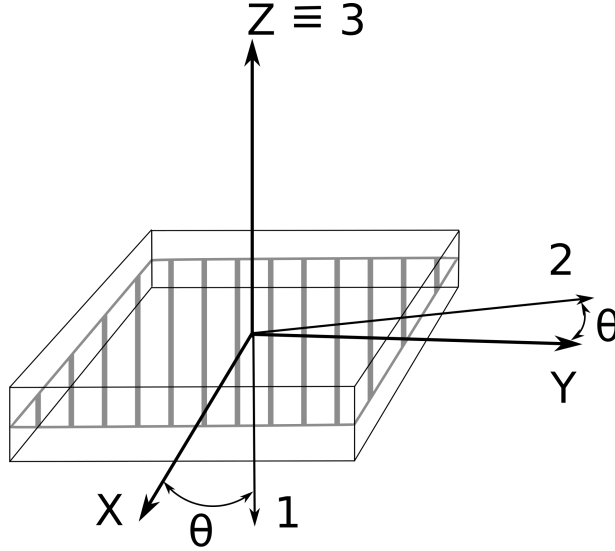


Figure 2.2: General problem coordinate system and material reference system of an unidirectionally reinforced lamina.

The relations between the two reference systems are:

$$\begin{Bmatrix} 1 \\ 2 \\ 3 \end{Bmatrix} = \begin{bmatrix} \cos \theta & \sin \theta & 0 \\ -\sin \theta & \cos \theta & 0 \\ 0 & 0 & 1 \end{bmatrix} \begin{Bmatrix} x \\ y \\ z \end{Bmatrix} = [L] \begin{Bmatrix} x \\ y \\ z \end{Bmatrix} \quad (2.7)$$

The inverse of Eq. 2.7 is:

$$\begin{Bmatrix} x \\ y \\ z \end{Bmatrix} = \begin{bmatrix} \cos \theta & -\sin \theta & 0 \\ \sin \theta & \cos \theta & 0 \\ 0 & 0 & 1 \end{bmatrix} \begin{Bmatrix} 1 \\ 2 \\ 3 \end{Bmatrix} = [L]^T \begin{Bmatrix} 1 \\ 2 \\ 3 \end{Bmatrix} \quad (2.8)$$

The inverse of $[L]$ is equal to its transpose: $[L]^{-1} = [L]^T$. The relationship between the components of stress in general problem σ and material σ_m coordinate systems is considered:

$$[\sigma_m] = [L] [\sigma] [L]^T \quad [\sigma] = [L]^T [\sigma_m] [L] \quad (2.9)$$

where

$$[\sigma] = \begin{bmatrix} \sigma_{xx} & \sigma_{xy} & \sigma_{xz} \\ \sigma_{xy} & \sigma_{yy} & \sigma_{yz} \\ \sigma_{xz} & \sigma_{yz} & \sigma_{zz} \end{bmatrix} \quad [\sigma_m] = \begin{bmatrix} \sigma_{11} & \sigma_{12} & \sigma_{13} \\ \sigma_{12} & \sigma_{22} & \sigma_{23} \\ \sigma_{13} & \sigma_{23} & \sigma_{33} \end{bmatrix} \quad (2.10)$$

Their relationships via matrices $[L]$ and $[L]^T$ derive from the transformations between second-order tensors, more details can be found in [8]. Carrying out the matrix multiplications

in Eq. 2.9 and rearranging in terms of single-subscript stress components:

$$\begin{Bmatrix} \sigma_{xx} \\ \sigma_{yy} \\ \sigma_{zz} \\ \sigma_{yz} \\ \sigma_{xz} \\ \sigma_{xy} \end{Bmatrix} = \begin{bmatrix} \cos^2 \theta & \sin^2 \theta & 0 & 0 & 0 & -\sin 2\theta \\ \sin^2 \theta & \cos^2 \theta & 0 & 0 & 0 & \sin 2\theta \\ 0 & 0 & 1 & 0 & 0 & 0 \\ 0 & 0 & 0 & \cos \theta & \sin \theta & 0 \\ 0 & 0 & 0 & -\sin \theta & \cos \theta & 0 \\ \sin \theta \cos \theta & -\sin \theta \cos \theta & 0 & 0 & 0 & \cos^2 \theta - \sin^2 \theta \end{bmatrix} \begin{Bmatrix} \sigma_{11} \\ \sigma_{22} \\ \sigma_{33} \\ \sigma_{23} \\ \sigma_{13} \\ \sigma_{12} \end{Bmatrix}. \quad (2.11)$$

in vectorial form: $[\sigma] = [T][\sigma_m]$, and

$$\begin{Bmatrix} \sigma_{11} \\ \sigma_{22} \\ \sigma_{33} \\ \sigma_{23} \\ \sigma_{13} \\ \sigma_{12} \end{Bmatrix} = \begin{bmatrix} \cos^2 \theta & \sin^2 \theta & 0 & 0 & 0 & \sin 2\theta \\ \sin^2 \theta & \cos^2 \theta & 0 & 0 & 0 & -\sin 2\theta \\ 0 & 0 & 1 & 0 & 0 & 0 \\ 0 & 0 & 0 & \cos \theta & -\sin \theta & 0 \\ 0 & 0 & 0 & \sin \theta & \cos \theta & 0 \\ -\sin \theta \cos \theta & \sin \theta \cos \theta & 0 & 0 & 0 & \cos^2 \theta - \sin^2 \theta \end{bmatrix} \begin{Bmatrix} \sigma_{xx} \\ \sigma_{yy} \\ \sigma_{zz} \\ \sigma_{yz} \\ \sigma_{xz} \\ \sigma_{xy} \end{Bmatrix}. \quad (2.12)$$

in vectorial form: $[\sigma_m] = [T]^T[\sigma]$. Similarly it is possible to relate the components of the strain vector referred to the material system in terms of the general problem system as follows:

$$[\epsilon_m] = [T]^T[\epsilon] \quad (2.13)$$

Substituting Eq. 2.2, for the material system, and Eq. 2.13 in $[\sigma] = [T][\sigma_m]$, a transformed material stiffness matrix is therefore introduced as follows:

$$[\sigma] = [T][\sigma_m] = [T][C_m][\epsilon_m] = [T][C_m][T]^T[\epsilon] = [\tilde{C}][\epsilon] \quad (2.14)$$

The transformed material stiffness matrix contains the elastic coefficients referred to the general problem coordinate system:

$$[\tilde{C}] = [T][C_m][T]^T \quad (2.15)$$

The stress-strain relations of Eq. 2.14 referred to the general coordinate system can be rewritten in terms of in-plane components $\boldsymbol{\sigma}_p = \{\sigma_{xx}, \sigma_{yy}, \sigma_{xy}\}$, $\boldsymbol{\epsilon}_p = \{\epsilon_{xx}, \epsilon_{yy}, \epsilon_{xy}\}$ related to the plate/shell reference plane, and in terms of out-of-plane components $\boldsymbol{\sigma}_n = \{\sigma_{xz}, \sigma_{yz}, \sigma_{zz}\}$, $\boldsymbol{\epsilon}_n = \{\epsilon_{xz}, \epsilon_{yz}, \epsilon_{zz}\}$ related to the thickness direction of the plate/shell, as follows:

$$\begin{aligned} \boldsymbol{\sigma}_p &= \tilde{C}_{pp} \boldsymbol{\epsilon}_p + \tilde{C}_{pn} \boldsymbol{\epsilon}_n \\ \boldsymbol{\sigma}_n &= \tilde{C}_{np} \boldsymbol{\epsilon}_p + \tilde{C}_{nn} \boldsymbol{\epsilon}_n \end{aligned} \quad (2.16)$$

where matrices \tilde{C}_{pp} , \tilde{C}_{pn} , \tilde{C}_{np} , \tilde{C}_{nn} derive from matrix \tilde{C} :

$$\begin{aligned} \tilde{C}_{pp} &= \begin{bmatrix} \tilde{C}_{11} & \tilde{C}_{12} & \tilde{C}_{16} \\ \tilde{C}_{12} & \tilde{C}_{22} & \tilde{C}_{26} \\ \tilde{C}_{16} & \tilde{C}_{26} & \tilde{C}_{66} \end{bmatrix} & \tilde{C}_{pn} &= \begin{bmatrix} 0 & 0 & \tilde{C}_{13} \\ 0 & 0 & \tilde{C}_{23} \\ 0 & 0 & \tilde{C}_{36} \end{bmatrix} \\ \tilde{C}_{np} &= \begin{bmatrix} 0 & 0 & 0 \\ 0 & 0 & 0 \\ \tilde{C}_{13} & \tilde{C}_{23} & \tilde{C}_{36} \end{bmatrix} & \tilde{C}_{nn} &= \begin{bmatrix} \tilde{C}_{55} & \tilde{C}_{45} & 0 \\ \tilde{C}_{45} & \tilde{C}_{44} & 0 \\ 0 & 0 & \tilde{C}_{33} \end{bmatrix} \end{aligned} \quad (2.17)$$

Poisson's locking phenomena:

The thickness locking mechanism, also known as Poisson's locking (PL) phenomena, affects

the plate/shell analysis [52], [53]. The PL doesn't permit to an equivalent single layer theory with transverse displacement w constant or linear through the thickness (that means transverse strain ϵ_{zz} zero or constant) to lead to the 3D solution in thin plate/shell problems. A known technique to contrast PL consists in modifying the elastic stiffness coefficients by forcing the 'contradictory' condition of transverse normal stress equal to zero: $\sigma_{zz} = 0$. By imposing this condition in the constitutive equations 2.16, the modified stiffness coefficients in material reference system (reduced stiffness coefficients) can be obtained:

$$\hat{C}_{11} = \frac{E_1}{1 - \nu_{12}\nu_{21}} \quad \hat{C}_{22} = \frac{E_2}{1 - \nu_{12}\nu_{21}} \quad \hat{C}_{12} = \frac{\nu_{12}E_2}{1 - \nu_{12}\nu_{21}} \quad (2.18)$$

In order to avoid the PL, these coefficients must be used in $[C_m]$ in the place of C_{11} , C_{22} , C_{12} and then rotated according to Eq. 2.15.

2.2 Constitutive equations for multifield problems

Constitutive equations for the electro-thermo-mechanical problem are obtained in this section in according with that reported in [54] and [50]; then three particular cases are discussed: coupled electro-mechanical problem, uncoupled thermo-mechanical problem, mixed coupled electro-mechanical problem. The coupling between the mechanical, thermal and electrical fields can be determined by using thermodynamical principles and Maxwell's relations [41, 55–57]. For this aim, it is necessary to define a Gibbs free-energy function G and a thermopiezoelectric enthalpy density H [58, 59]:

$$\begin{aligned} G(\epsilon_{ij}, \mathcal{E}_i, \theta) &= \sigma_{ij}\epsilon_{ij} + \mathcal{E}_i\mathcal{D}_i + \eta\theta \\ H(\epsilon_{ij}, \mathcal{E}_i, \theta, \vartheta_i) &= G(\epsilon_{ij}, \mathcal{E}_i, \theta) - F(\vartheta_i) \end{aligned} \quad (2.19)$$

where σ_{ij} and ϵ_{ij} are the stress and strain components, \mathcal{E}_i is the electric field vector, \mathcal{D}_i is the electric displacement vector. η is the variation of entropy per unit of volume and θ the temperature considered with respect to a reference temperature. The function $F(\vartheta_i)$ is the dissipation function, it depends by the spatial temperature gradient ϑ_i .

Thermo-mechanical problem:

In case of thermo-mechanical problem, two physical fields interact, no electrical loads are applied on the structure. The couplings between mechanical and electrical fields, and between electrical and thermal fields are not considered. If a partial coupling is considered in the structure and the temperature is only seen as an external load, the considered constitutive equations are derived from the solution of Eq.2.19:

$$\begin{aligned} \sigma_p &= C_{pp}\epsilon_p + C_{pn}\epsilon_n - \lambda_p\theta \\ \sigma_n &= C_{np}\epsilon_p + C_{nn}\epsilon_n - \lambda_n\theta \end{aligned} \quad (2.20)$$

where matrices λ_p , λ_n represents the thermo-mechanical coupling coefficients: $\lambda = C\alpha$, α vector contains the thermal expansion coefficients.

$$\alpha_p = [\alpha_1 \quad \alpha_2 \quad 0] \quad \alpha_n = [0 \quad 0 \quad \alpha_3] \quad (2.21)$$

$$\lambda_p = [\lambda_1 \quad \lambda_2 \quad \lambda_6] \quad \lambda_n = [0 \quad 0 \quad \lambda_3]$$

Electro-mechanical problem:

In case of electro-mechanical problem, two physical fields interact, no thermal loads and

spatial temperature gradients are applied on the structure. The couplings between mechanical and thermal fields, and between electrical and thermal fields are not considered. The solution of Eq.2.19 degenerates in:

$$\begin{aligned}
 \sigma_p &= C_{pp} \epsilon_p + C_{pn} \epsilon_n - e_{pp} \mathcal{E}_p - e_{pn} \mathcal{E}_n \\
 \sigma_n &= C_{np} \epsilon_p + C_{nn} \epsilon_n - e_{np} \mathcal{E}_p - e_{nn} \mathcal{E}_n \\
 \mathcal{D}_p &= e_{pp} \epsilon_p + e_{pn} \epsilon_n + \epsilon_{pp} \mathcal{E}_p + \epsilon_{pn} \mathcal{E}_n \\
 \mathcal{D}_n &= e_{np} \epsilon_p + e_{nn} \epsilon_n + \epsilon_{np} \mathcal{E}_p + \epsilon_{nn} \mathcal{E}_n
 \end{aligned} \tag{2.22}$$

where matrices e_{pp} , e_{pn} , e_{np} , e_{nn} represent the piezoelectric coupling coefficients: $e = C\mathbf{d}$, where \mathbf{d} matrix contains the piezoelectric coefficients. Matrices ϵ_{pp} , ϵ_{pn} , ϵ_{np} , ϵ_{nn} represent the permittivity coefficients ϵ_{ij} :

$$\begin{aligned}
 e_{pp} &= \begin{bmatrix} e_{11} & e_{12} & e_{16} \\ e_{21} & e_{22} & e_{26} \end{bmatrix} & e_{pn} &= \begin{bmatrix} e_{15} & e_{14} & e_{13} \\ e_{25} & e_{24} & e_{23} \end{bmatrix} \\
 e_{np} &= \begin{bmatrix} e_{31} & e_{32} & e_{36} \end{bmatrix} & e_{nn} &= \begin{bmatrix} e_{35} & e_{34} & e_{33} \end{bmatrix}
 \end{aligned} \tag{2.23}$$

$$\begin{aligned}
 \epsilon_{pp} &= \begin{bmatrix} \epsilon_{11} & \epsilon_{12} \\ \epsilon_{12} & \epsilon_{22} \end{bmatrix} & \epsilon_{pn} &= \begin{bmatrix} 0 \\ 0 \end{bmatrix} \\
 \epsilon_{np} &= \begin{bmatrix} 0 & 0 \end{bmatrix} & \epsilon_{nn} &= \begin{bmatrix} \epsilon_{33} \end{bmatrix}
 \end{aligned} \tag{2.24}$$

Actuation modes

The piezoelectric effect are made available in polarisable crystalline materials through the application of an intense electric field which imparts a net polarisation of the crystal cells. Depending on the mutual direction of the polarisation and of the applied loading, two important actuation modes are taken into account in this work.

Actuation in 3-1 mode

Transverse extension mode (3-1 mode), the applied electric field is aligned with the polarisation axis but the major deformation occurs in the transverse plane due to the thinness of the piezoelectric sheet, see Figure 2.3. The piezoelectric coefficients for the 3-1 mode are defined as follows:

$$\begin{aligned}
 d_{pp} &= \begin{bmatrix} 0 & 0 & 0 \\ 0 & 0 & 0 \end{bmatrix} & d_{pn} &= \begin{bmatrix} d_{15} & 0 & 0 \\ 0 & d_{24} & 0 \end{bmatrix} \\
 d_{np} &= \begin{bmatrix} d_{31} & d_{32} & 0 \end{bmatrix} & d_{nn} &= \begin{bmatrix} 0 & 0 & d_{33} \end{bmatrix}
 \end{aligned} \tag{2.25}$$

$$\begin{aligned}
 e_{pp} &= \begin{bmatrix} 0 & 0 & 0 \\ 0 & 0 & 0 \end{bmatrix} & e_{pn} &= \begin{bmatrix} e_{15} & e_{14} & 0 \\ e_{25} & e_{24} & 0 \end{bmatrix} \\
 e_{np} &= \begin{bmatrix} e_{31} & e_{32} & e_{36} \end{bmatrix} & e_{nn} &= \begin{bmatrix} 0 & 0 & e_{33} \end{bmatrix}
 \end{aligned} \tag{2.26}$$

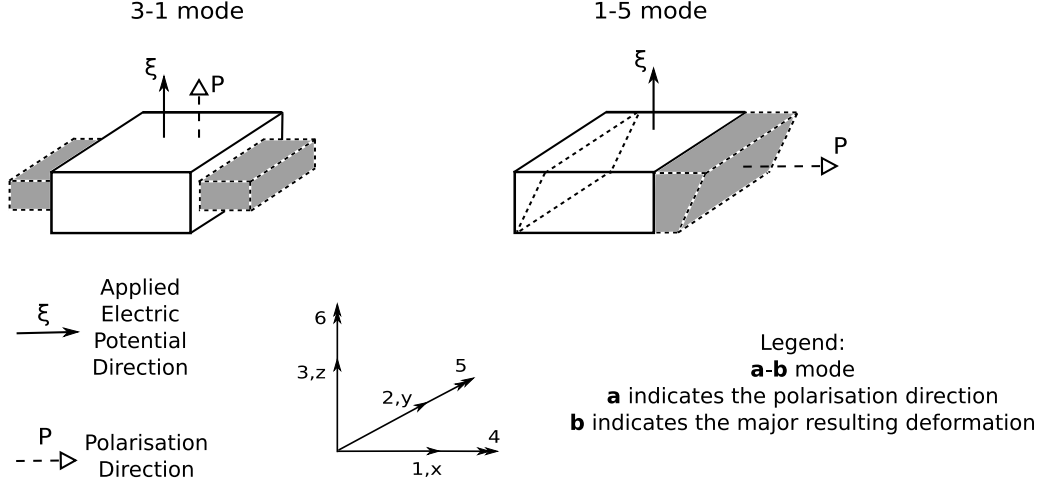


Figure 2.3: Representation of piezoelectric actuation modes taken into account. Transverse extension mode (3-1 mode), and the shear mode (1-5 mode)

Actuation in 1-5 mode

Shear mode (1-5 mode), the applied electric field is perpendicular to the polarisation direction and the principal mechanical effect is associated to a shear deformation, see Figure 2.3. The piezoelectric coefficients for the 1-5 mode are defined as follows:

$$\begin{aligned} \mathbf{d}_{pp} &= \begin{bmatrix} d_{11} & d_{12} & 0 \\ 0 & 0 & d_{26} \end{bmatrix} & \mathbf{d}_{pn} &= \begin{bmatrix} 0 & 0 & d_{13} \\ 0 & 0 & 0 \end{bmatrix} \\ \mathbf{d}_{np} &= \begin{bmatrix} 0 & 0 & 0 \end{bmatrix} & \mathbf{d}_{nn} &= \begin{bmatrix} d_{35} & 0 & 0 \end{bmatrix} \end{aligned} \quad (2.27)$$

$$\begin{aligned} \mathbf{e}_{pp} &= \begin{bmatrix} e_{11} & e_{12} & e_{16} \\ e_{21} & e_{22} & e_{26} \end{bmatrix} & \mathbf{e}_{pn} &= \begin{bmatrix} 0 & 0 & e_{13} \\ 0 & 0 & e_{23} \end{bmatrix} \\ \mathbf{e}_{np} &= \begin{bmatrix} 0 & 0 & 0 \end{bmatrix} & \mathbf{e}_{nn} &= \begin{bmatrix} e_{35} & e_{34} & 0 \end{bmatrix} \end{aligned} \quad (2.28)$$

Electro-mechanical problem using the Reissner Mixed Variational Theorem:

The Reissner Mixed Variational Theorem (RMVT) permits to add a new set of extensive variables and to model them a priori in the thickness direction. In this work, for the case of electro-mechanical problems, a particular extension of the RMVT is used: the transverse normal electric displacement \mathcal{D}_z as extensive variable without the modelization of the transverse mechanical stresses, here called *RMVT - \mathcal{D}_z* . The constitutive equations 2.22 can be written in matrix form after the following vectors are defined as:

$$\Xi_a = \{\epsilon_p, \epsilon_n, \mathcal{E}_p\}, \quad \Xi_b = \{\mathcal{E}_n\}, \quad \Sigma_a = \{\sigma_p, \sigma_n, \mathcal{D}_p\}, \quad \Sigma_b = \{\mathcal{D}_n\}$$

and the following matrix coefficients are defined as:

$$\mathbf{H}_{aa}^{(8 \times 8)} = \begin{bmatrix} \mathbf{C}_{pp} & \mathbf{C}_{pn} & -\mathbf{e}_{pp} \\ \mathbf{C}_{np} & \mathbf{C}_{nn} & -\mathbf{e}_{pn} \\ \mathbf{e}_{pp} & \mathbf{e}_{pn} & \boldsymbol{\varepsilon}_{pp} \end{bmatrix} \quad \mathbf{H}_{ab}^{(8 \times 1)} = \begin{bmatrix} -\mathbf{e}_{np} \\ -\mathbf{e}_{nn} \\ \boldsymbol{\varepsilon}_{pn} \end{bmatrix} \quad \mathbf{H}_{ba}^{(1 \times 8)} = [\mathbf{e}_{np} \quad \mathbf{e}_{nn} \quad \boldsymbol{\varepsilon}_{np}] \quad \mathbf{H}_{bb}^{(1 \times 1)} = [\boldsymbol{\varepsilon}_{nn}]$$

$$\mathbf{H}_{aa}^{(8 \times 8)} = \begin{bmatrix} C_{11} & C_{12} & C_{16} & 0 & 0 & C_{13} & 0 & 0 \\ C_{12} & C_{22} & C_{26} & 0 & 0 & C_{23} & 0 & 0 \\ C_{16} & C_{26} & C_{66} & 0 & 0 & C_{36} & 0 & 0 \\ 0 & 0 & 0 & C_{55} & C_{45} & 0 & -e_{15} & -e_{25} \\ 0 & 0 & 0 & C_{45} & C_{44} & 0 & -e_{14} & -e_{24} \\ C_{13} & C_{23} & C_{36} & 0 & 0 & C_{33} & 0 & 0 \\ 0 & 0 & 0 & e_{15} & e_{14} & 0 & \varepsilon_{11} & \varepsilon_{12} \\ 0 & 0 & 0 & e_{25} & e_{24} & 0 & \varepsilon_{12} & \varepsilon_{22} \end{bmatrix} \quad \mathbf{H}_{ab}^{(8 \times 1)} = \begin{bmatrix} -e_{31} \\ -e_{32} \\ -e_{36} \\ 0 \\ 0 \\ -e_{33} \\ 0 \\ 0 \end{bmatrix}$$

In compact form:

$$\begin{aligned} \Sigma_a &= H_{aa} \Xi_a + H_{ab} \Xi_b \\ \Sigma_b &= H_{ba} \Xi_a + H_{bb} \Xi_b \end{aligned} \quad (2.29)$$

The aim of this work is to permit the transverse electric displacement to be a priori modeled, so the constitutive equations are rewritten as follows:

$$\begin{aligned} \Sigma_a &= \tilde{H}_{aa} \Xi_a + \tilde{H}_{ab} \Sigma_b \\ \Xi_b &= \tilde{H}_{ba} \Xi_a + \tilde{H}_{bb} \Sigma_b \end{aligned} \quad (2.30)$$

where the new matrix coefficients are obtained as follows:

$$\tilde{H}_{aa} = H_{aa} - \frac{H_{ab}H_{ba}}{H_{bb}}, \quad \tilde{H}_{ab} = \frac{H_{ab}}{H_{bb}}, \quad \tilde{H}_{ba} = -\frac{H_{ba}}{H_{bb}}, \quad \tilde{H}_{bb} = \frac{1}{H_{bb}}$$

$$\tilde{\mathbf{H}}_{aa}^{(8 \times 8)} = \begin{bmatrix} C_{11} + \frac{e_{31}^2}{\varepsilon_{33}} & C_{12} + \frac{e_{31}e_{32}}{\varepsilon_{33}} & C_{16} + \frac{e_{31}e_{36}}{\varepsilon_{33}} & 0 & 0 & C_{13} + \frac{e_{31}e_{33}}{\varepsilon_{33}} & 0 & 0 \\ C_{12} + \frac{e_{31}e_{32}}{\varepsilon_{33}} & C_{22} + \frac{e_{32}^2}{\varepsilon_{33}} & C_{26} + \frac{e_{32}e_{36}}{\varepsilon_{33}} & 0 & 0 & C_{23} + \frac{e_{32}e_{33}}{\varepsilon_{33}} & 0 & 0 \\ C_{16} + \frac{e_{31}e_{36}}{\varepsilon_{33}} & C_{26} + \frac{e_{32}e_{36}}{\varepsilon_{33}} & C_{66} + \frac{e_{36}^2}{\varepsilon_{33}} & 0 & 0 & C_{36} + \frac{e_{33}e_{36}}{\varepsilon_{33}} & 0 & 0 \\ 0 & 0 & 0 & C_{55} & C_{45} & 0 & -e_{15} & -e_{25} \\ 0 & 0 & 0 & C_{45} & C_{44} & 0 & -e_{14} & -e_{24} \\ C_{13} + \frac{e_{31}e_{33}}{\varepsilon_{33}} & C_{23} + \frac{e_{32}e_{33}}{\varepsilon_{33}} & C_{36} + \frac{e_{33}e_{36}}{\varepsilon_{33}} & 0 & 0 & C_{33} + \frac{e_{33}^2}{\varepsilon_{33}} & 0 & 0 \\ 0 & 0 & 0 & e_{15} & e_{14} & 0 & \varepsilon_{11} & \varepsilon_{12} \\ 0 & 0 & 0 & e_{25} & e_{24} & 0 & \varepsilon_{12} & \varepsilon_{22} \end{bmatrix}$$

$$\widetilde{\mathbf{H}}_{ab}^{(8 \times 1)} = \begin{bmatrix} \frac{-e_{31}}{\varepsilon_{33}} \\ \varepsilon_{33} \\ \frac{-e_{32}}{\varepsilon_{33}} \\ \varepsilon_{33} \\ \frac{-e_{36}}{\varepsilon_{33}} \\ \varepsilon_{33} \\ 0 \\ 0 \\ \frac{-e_{33}}{\varepsilon_{33}} \\ \varepsilon_{33} \\ 0 \\ 0 \end{bmatrix} \quad \widetilde{\mathbf{H}}_{ba}^{(1 \times 8)} = \begin{bmatrix} \frac{-e_{31}}{\varepsilon_{33}} & \frac{-e_{32}}{\varepsilon_{33}} & \frac{-e_{36}}{\varepsilon_{33}} & 0 & 0 & \frac{-e_{33}}{\varepsilon_{33}} & 0 & 0 \end{bmatrix} \quad \widetilde{\mathbf{H}}_{bb}^{(1 \times 1)} = \begin{bmatrix} \frac{1}{\varepsilon_{33}} \end{bmatrix}$$

The new constitutive equations are:

$$\begin{aligned}
 \sigma_{pC} &= \widetilde{H}_{aa}^{(1;3;1;3)} \epsilon_{pG} + \widetilde{H}_{aa}^{(1;3;4;6)} \epsilon_{nG} + \widetilde{H}_{aa}^{(1;3;7;8)} \mathcal{E}_{pG} + \widetilde{H}_{ab}^{(1;3;1)} \mathcal{D}_{nM} \\
 \sigma_{nC} &= \widetilde{H}_{aa}^{(4;6;1;3)} \epsilon_{pG} + \widetilde{H}_{aa}^{(4;6;4;6)} \epsilon_{nG} + \widetilde{H}_{aa}^{(4;6;7;8)} \mathcal{E}_{pG} + \widetilde{H}_{ab}^{(4;6;1)} \mathcal{D}_{nM} \\
 \mathcal{D}_{pC} &= \widetilde{H}_{aa}^{(7;8;1;3)} \epsilon_{pG} + \widetilde{H}_{aa}^{(7;8;4;6)} \epsilon_{nG} + \widetilde{H}_{aa}^{(7;8;7;8)} \mathcal{E}_{pG} + \widetilde{H}_{ab}^{(7;8;1)} \mathcal{D}_{nM} \\
 \mathcal{E}_{nC} &= \widetilde{H}_{ba}^{(1;1;3)} \epsilon_{pG} + \widetilde{H}_{ba}^{(1;4;6)} \epsilon_{nG} + \widetilde{H}_{ba}^{(1;7;8)} \mathcal{E}_{pG} + \widetilde{H}_{bb}^{(1;1)} \mathcal{D}_{nM}
 \end{aligned} \tag{2.31}$$

$$\begin{bmatrix} \sigma_p \\ \sigma_n \\ \mathcal{D}_p \\ \mathcal{E}_n \end{bmatrix} = \begin{bmatrix} \boxed{\widetilde{H}_{aa}} & \boxed{\widetilde{H}_{ab}} \\ \boxed{\widetilde{H}_{ba}} & \boxed{\widetilde{H}_{bb}} \end{bmatrix} \begin{bmatrix} \epsilon_p \\ \epsilon_n \\ \mathcal{E}_p \\ \mathcal{D}_n \end{bmatrix}$$

2.3 Geometry of the shell

A thin shell as a three-dimensional body is bounded by two closely spaced curved surfaces, the distance between the two surfaces must be small in comparison with the other dimensions. The middle surface of the shell is the locus of points which lie midway between these surfaces. The distance between the surfaces measured along the normal to the middle surface is the thickness of the shell at that point [60]. Shells may be seen as generalizations of a flat plate [61]; conversely, a flat plate is a special case of a shell having no curvature. In this section the fundamental equations of thin shell theory are presented in order to obtain the geometrical relations for multifield problems. Geometrical relations for plates are seen as particular case of those for shells. The material is assumed to be linearly elastic and homogeneous, displacements are assumed to be small, thereby yielding linear equations; shear deformation and rotary inertia effects are neglected, and the thickness is taken to be small. The deformation of a thin shell is completely determined by the displacements of its middle surface [60]. The equation of the undeformed middle surface is given, in terms of two independent parameters α and β , by the radius vector:

$$\vec{r} = \vec{r}(\alpha, \beta) \quad (2.32)$$

Eq.2.32 determines a space curve on the surface. Such curves are called β curves and α curves, see Figure 2.4.

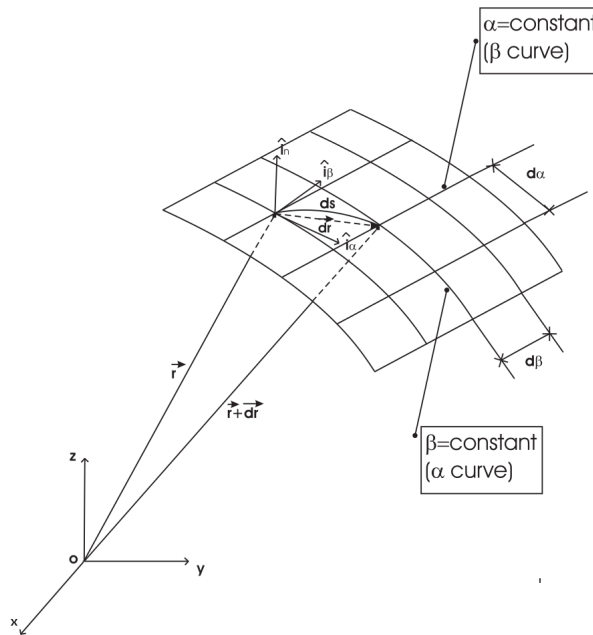


Figure 2.4: Displacements on the shell reference surface.

It is possible to assume that the parameters α and β always vary within a definite region, and that a one-to-one correspondence exists between the points on this region and points on the portion of the surface of interest:

$$\vec{r}_{,\alpha} = \frac{\delta \vec{r}}{\delta \alpha} \quad ; \quad \vec{r}_{,\beta} = \frac{\delta \vec{r}}{\delta \beta} \quad (2.33)$$

The vectors $\vec{r}_{,\alpha}$ and $\vec{r}_{,\beta}$ are tangent to the α and β curves, respectively. Their length is:

$$|\vec{r}_{,\alpha}| = A \quad ; \quad |\vec{r}_{,\beta}| = B \quad (2.34)$$

Consequently $\frac{\vec{r}',\alpha}{A}$ and $\frac{\vec{r}',\beta}{B}$ are unit vectors tangent to the coordinate curves. The angle between the coordinate curves is χ :

$$\frac{\vec{r}',\alpha}{A} \cdot \frac{\vec{r}',\beta}{B} = \cos \chi \quad (2.35)$$

where

$$\frac{\vec{r}',\alpha}{A} = \hat{i}_\alpha \quad ; \quad \frac{\vec{r}',\beta}{B} = \hat{i}_\beta \quad ; \quad \hat{i}_n = \frac{\hat{i}_\alpha \cdot \hat{i}_\beta}{\sin \chi} \quad (2.36)$$

\hat{i}_n is the unit vector of the normal to the surface and is orthogonal to the vectors \hat{i}_α and \hat{i}_β . The unit vectors \hat{i}_α , \hat{i}_β and \hat{i}_n are usually called the basic vectors of the surface [60].

First quadratic form

If we consider two points (α, β) and $(\alpha + d\alpha, \beta + d\beta)$ arbitrarily near to each other and both lying on the surface, the increment of the vector \vec{r}' in moving from the first point to the second one is:

$$d\vec{r}' = \vec{r}',\alpha d\alpha + \vec{r}',\beta d\beta \quad (2.37)$$

By considering Eqs.2.34,2.35,2.36 and 2.37, we can obtain the square of the differential of the arc length on the surface:

$$d\vec{r}' \cdot d\vec{r}' = ds^2 = A^2 d\alpha^2 + 2AB \cos \chi d\alpha d\beta + B^2 d\beta^2 \quad (2.38)$$

The right-hand side of Eq.2.38 is the first quadratic form of the surface. This form determines the infinitesimal lengths, the angle between the curves, and the area on the surface: the intrinsic geometry of the surface. However, it does not determine a surface by itself. The terms A^2 , $AB \cos \chi$, and B^2 are called first fundamental quantities.

Second quadratic form

The problem of finding the curvature of a curve which lies on the surface, can be solved by considering the second quadratic form of the surface. $\vec{r}' = \vec{r}'(s)$ is the vectorial equation of a curve on the surface (s is the arc length from a certain origin). $\hat{\tau}$ is the unit vector along the tangent to the curve:

$$\hat{\tau} = \frac{d\vec{r}'}{ds} = \vec{r}',\alpha \frac{d\alpha}{ds} + \vec{r}',\beta \frac{d\beta}{ds} \quad (2.39)$$

According to Frenet's formula [62], the derivative of this vector is:

$$\frac{d\hat{\tau}}{ds} = \frac{\hat{N}}{\rho} \quad (2.40)$$

where $\frac{1}{\rho}$ is the curvature of the curve, and \hat{N} is the unit vector of the principal normal to the curve. By omitting the middle passages, detailed described in [60], is possible to obtain the expression for the second quadratic form: $Ld\alpha^2 + 2Md\alpha d\beta + Nd\beta^2$. L, M and N are the coefficients of the form. The second quadratic form is thus related to the curvatures of the curves on the surface. The curvatures of the α curves and the β curves take $\beta = \text{constant}$ and $\alpha = \text{constant}$, respectively:

$$\frac{1}{R_\alpha} = -\frac{L}{A^2} \quad ; \quad \frac{1}{R_\beta} = -\frac{N}{B^2} \quad (2.41)$$

When A, B, R_α and R_β are given, they determine a surface uniquely, except to position and orientation in space [60]. R_α and R_β are the radii of curvature.

Strain-displacement equations

To describe the location of an arbitrary point in the space occupied by a thin shell, the position vector is defined as:

$$\vec{R}(\alpha, \beta, z) = \vec{r}(\alpha, \beta) + z\hat{i}_n \quad (2.42)$$

where z measures the distance of the point from the corresponding point on the middle surface along \hat{i}_n and varies over the thickness $\left(-\frac{h}{2} \leq z \leq \frac{h}{2}\right)$. The magnitude of an arbitrary infinitesimal change in the vector $\vec{R}(\alpha, \beta, z)$ is determined by:

$$(ds)^2 = d\vec{R} \cdot d\vec{R} = (d\vec{r} + zd\hat{i}_n + \hat{i}_n dz) \cdot (d\vec{r} + zd\hat{i}_n + \hat{i}_n dz) \quad (2.43)$$

Remembering the orthogonality of the coordinate system and the chain rule:

$$d\hat{i}_n = \frac{\partial \hat{i}_n}{\partial \alpha} d\alpha + \frac{\partial \hat{i}_n}{\partial \beta} d\beta \quad (2.44)$$

one obtains:

$$(ds)^2 = g_1 d\alpha^2 + g_2 d\beta^2 + g_3 dz^2 \quad (2.45)$$

where

$$g_1 = \left[A \left(1 + \frac{z}{R_\alpha} \right) \right]^2 ; \quad g_2 = \left[B \left(1 + \frac{z}{R_\beta} \right) \right]^2 ; \quad g_3 = 1 \quad (2.46)$$

The quantities $g_1, g_2, g_3, A, B, R_\alpha, R_\beta$ are connected by the equations of Lamb [63], since the three-dimensional space (the space in which the three independent variables α, β, z) is an Euclidean space. The fundamental shell element is the differential element bounded by two surfaces dz apart at a distance z from the middle surface, and four ruled surfaces whose generators are the normals to the middle surface along the parametric curves $\alpha = \alpha_0$, $\alpha = \alpha_0 + d\alpha$, $\beta = \beta_0$ and $\beta = \beta_0 + d\beta$ [60]. The lengths of the edges of this fundamental element are (see Figure 2.5):

$$\begin{aligned} ds_\alpha(z) &= A \left(1 + \frac{z}{R_\alpha} \right) d\alpha \\ ds_\beta(z) &= B \left(1 + \frac{z}{R_\beta} \right) d\beta \end{aligned} \quad (2.47)$$

the differential areas of the edge faces of the fundamental element are (see Figure 2.5):

$$\begin{aligned} dA_\alpha(z) &= A \left(1 + \frac{z}{R_\alpha} \right) d\alpha dz \\ dA_\beta(z) &= B \left(1 + \frac{z}{R_\beta} \right) d\beta dz \end{aligned} \quad (2.48)$$

while the volume of the fundamental element is:

$$dV(z) = \left[A \left(1 + \frac{z}{R_\alpha} \right) \right] \left[B \left(1 + \frac{z}{R_\beta} \right) \right] d\alpha d\beta dz \quad (2.49)$$

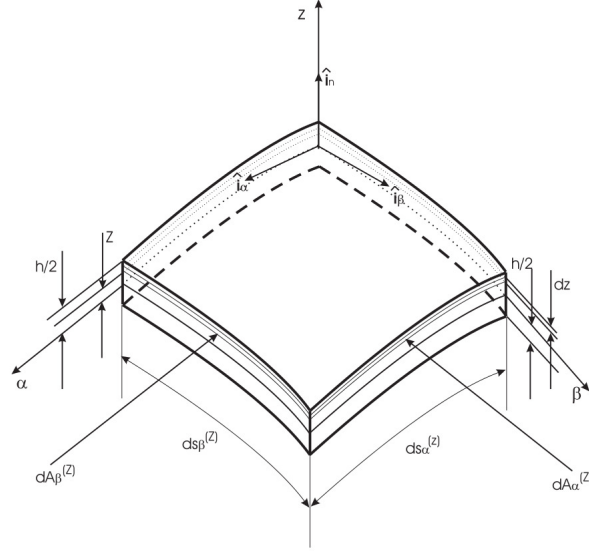


Figure 2.5: General reference system and notations for shells.

The well-known strain-displacement equations of three-dimensional theory of elasticity in orthogonal curvilinear coordinates have been obtained in [64]

$$\epsilon_i = \frac{\partial}{\partial \alpha_i} \left(\frac{U_i}{\sqrt{g_i}} \right) + \frac{1}{2g_i} \sum_{k=1}^3 \frac{\partial g_i}{\partial \alpha_k} \frac{U_k}{\sqrt{g_k}} \quad , \quad i = 1, 2, 3 \quad (2.50)$$

$$\gamma_{ij} = \frac{1}{\sqrt{g_i g_j}} \left[g_i \frac{\partial}{\partial \alpha_j} \left(\frac{U_i}{\sqrt{g_i}} \right) + g_j \frac{\partial}{\partial \alpha_i} \left(\frac{U_j}{\sqrt{g_j}} \right) \right] \quad , \quad i, j = 1, 2, 3 \quad i \neq j \quad (2.51)$$

where ϵ_i , γ_{ij} and U_i are normal strains, shear strains, and displacement components, respectively, at an arbitrary point. In the shell coordinates the indices 1, 2 and 3 are replaced by α , β and z , respectively, except for the displacements U_1 , U_2 and U_3 , which are replaced by u , v and w , respectively. Coefficients of the metric tensor are given by Eq. 2.46, thus

yielding:

$$\epsilon_{\alpha} = \frac{1}{\left(1 + \frac{z}{R_{\alpha}}\right)} \left(\frac{1}{A} \frac{\partial u}{\partial \alpha} + \frac{v}{AB} \frac{\partial A}{\partial \beta} + \frac{w}{R_{\alpha}} \right) \quad (2.52)$$

$$\epsilon_{\beta} = \frac{1}{\left(1 + \frac{z}{R_{\beta}}\right)} \left(\frac{1}{B} \frac{\partial v}{\partial \beta} + \frac{u}{AB} \frac{\partial B}{\partial \alpha} + \frac{w}{R_{\beta}} \right) \quad (2.53)$$

$$\epsilon_z = \frac{\partial w}{\partial z} \quad (2.54)$$

$$\gamma_{\alpha\beta} = \frac{A \left(1 + \frac{z}{R_{\alpha}}\right)}{B \left(1 + \frac{z}{R_{\beta}}\right)} \frac{\partial}{\partial \beta} \left[\frac{u}{A \left(1 + \frac{z}{R_{\alpha}}\right)} \right] + \frac{B \left(1 + \frac{z}{R_{\beta}}\right)}{A \left(1 + \frac{z}{R_{\alpha}}\right)} \frac{\partial}{\partial \alpha} \left[\frac{v}{B \left(1 + \frac{z}{R_{\beta}}\right)} \right] \quad (2.55)$$

$$\gamma_{\alpha z} = \frac{1}{A \left(1 + \frac{z}{R_{\alpha}}\right)} \frac{\partial w}{\partial \alpha} + A \left(1 + \frac{z}{R_{\alpha}}\right) \frac{\partial}{\partial z} \left[\frac{u}{A \left(1 + \frac{z}{R_{\alpha}}\right)} \right] \quad (2.56)$$

$$\gamma_{\beta z} = \frac{1}{B \left(1 + \frac{z}{R_{\beta}}\right)} \frac{\partial w}{\partial \beta} + B \left(1 + \frac{z}{R_{\beta}}\right) \frac{\partial}{\partial z} \left[\frac{v}{B \left(1 + \frac{z}{R_{\beta}}\right)} \right] \quad (2.57)$$

2.4 Geometrical shell relations for multifield problems

By considering Eqs.2.52-2.57, in case of shells with constant radii of curvature, the coefficients A and B are equal to 1. In this section geometrical relations are written in matrix form. The separation in in-plane (p) and out-plane (n) components of the mechanical strains is considered too:

$$\begin{aligned} \boldsymbol{\epsilon}_p &= [\epsilon_{\alpha\alpha}, \epsilon_{\beta\beta}, \epsilon_{\alpha\beta}] = (\mathbf{D}_p + \mathbf{A}_p) \mathbf{u} \\ \boldsymbol{\epsilon}_n &= [\epsilon_{\alpha z}, \epsilon_{\beta z}, \epsilon_{zz}] = (\mathbf{D}_{np} + \mathbf{D}_{nz} - \mathbf{A}_n) \mathbf{u} \end{aligned} \quad (2.58)$$

where the vector of displacement components is $\mathbf{u} = (u, v, w)$. The explicit form of the introduced arrays follows:

$$\mathbf{D}_p = \begin{bmatrix} \frac{\partial_{\alpha}}{H_{\alpha}} & 0 & 0 \\ 0 & \frac{\partial_{\beta}}{H_{\beta}} & 0 \\ \frac{\partial_{\beta}}{H_{\beta}} & \frac{\partial_{\alpha}}{H_{\alpha}} & 0 \end{bmatrix} \quad \mathbf{D}_{np} = \begin{bmatrix} 0 & 0 & \frac{\partial_{\alpha}}{H_{\alpha}} \\ 0 & 0 & \frac{\partial_{\beta}}{H_{\beta}} \\ 0 & 0 & 0 \end{bmatrix} \quad \mathbf{D}_{nz} = \begin{bmatrix} \partial_z & 0 & 0 \\ 0 & \partial_z & 0 \\ 0 & 0 & \partial_z \end{bmatrix} \quad (2.59)$$

$$\mathbf{A}_p = \begin{bmatrix} 0 & 0 & \frac{1}{H_{\alpha} R_{\alpha}} \\ 0 & 0 & \frac{1}{H_{\beta} R_{\beta}} \\ 0 & 0 & 0 \end{bmatrix} \quad \mathbf{A}_n = \begin{bmatrix} \frac{1}{H_{\alpha} R_{\alpha}} & 0 & 0 \\ 0 & \frac{1}{H_{\beta} R_{\beta}} & 0 \\ 0 & 0 & 0 \end{bmatrix}$$

In the proposed differential arrays the symbols ∂_{α} , ∂_{β} and ∂_z indicate the partial derivatives $\frac{\partial}{\partial \alpha}$, $\frac{\partial}{\partial \beta}$, and $\frac{\partial}{\partial z}$, respectively. The parameters H_{α} and H_{β} are the shell metrics, and they are defined as: $H_{\alpha} = \left(1 + \frac{z}{R_{\alpha}}\right)$, $H_{\beta} = \left(1 + \frac{z}{R_{\beta}}\right)$. Details on Eqs.2.58-2.59 are given in [65].

In [65] geometrical relations, which link the electrical field \mathcal{E} with the electric potential Φ , are also given:

$$\begin{aligned}\mathcal{E}_p &= [\mathcal{E}_\alpha, \mathcal{E}_\beta] = -D_{ep} \Phi \\ \mathcal{E}_n &= [\mathcal{E}_z] = -D_{en} \Phi\end{aligned}\tag{2.60}$$

where the meaning of introduced arrays is:

$$D_{ep} = \begin{bmatrix} \frac{\partial_\alpha}{H_\alpha} \\ \frac{\partial_\beta}{H_\beta} \end{bmatrix} \quad D_{en} = [\partial_z]\tag{2.61}$$

Chapter 3

Classical, refined and hierarchical theories

Plates and shells are bi-dimensional structures in which one dimension (in general the thickness in the z direction) is negligible with respect to the other two dimensions. A brief overview of classical and higher-order plate/shell theories is given below. Then the Unified Formulation is introduced to describe the displacement field, in the thickness direction, by arbitrary functions at any desired expansion order.

3.1 Classical and refined theories

Kirchoff's hypothesis: The simplest plate/shell theory is based on the Kirchoff's hypotheses, and, when applied to composite laminates, it is usually referred to as Classical Lamination Theory (CLT) [1–3]. In CLT, both transverse shear strains and transverse normal strains are discarded, in usual applications being negligible with respect to the in-plane ones. The displacement field of CLT is represented in Eq. 3.1 and its geometrical representation is shown in Figure 3.1.

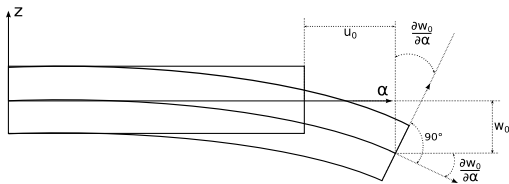


Figure 3.1: Geometrical representation of the Kirchoff's assumptions.

$$\begin{aligned} u(\alpha, \beta, z) &= u_0(\alpha, \beta) - z \frac{\partial w_0}{\partial \alpha} \\ v(\alpha, \beta, z) &= v_0(\alpha, \beta) - z \frac{\partial w_0}{\partial \beta} \end{aligned} \quad (3.1)$$

$$w(\alpha, \beta, z) = w_0(\alpha, \beta)$$

Reissner-Mindlin theory: Based on the works by Reissner [4] and Mindlin [5], the inclusion of transverse shear strains leads to the plate theory best known as the First-order Shear Deformation Theory (FSDT). The displacement field of the FSDT is represented in Eq. 3.2 and its geometrical representation is depicted in Figure 3.2.

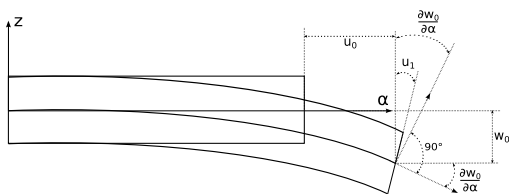
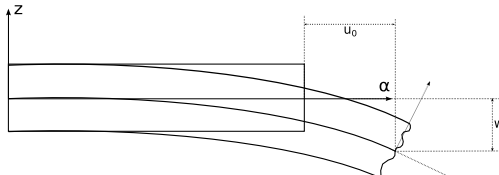


Figure 3.2: Geometrical representation of the Reissner-Mindlin theory.

$$\begin{aligned} u(\alpha, \beta, z) &= u_0(\alpha, \beta) + z u_1(\alpha, \beta) \\ v(\alpha, \beta, z) &= v_0(\alpha, \beta) + z v_1(\alpha, \beta) \\ w(\alpha, \beta, z) &= w_0(\alpha, \beta) \end{aligned} \quad (3.2)$$

Due to the inconsistency demanded by discarding the transverse normal stress in the material constitutive equations, both CLT and FSDT are no reliable when 3D local effects play a fundamental role, and the correct analysis of the stress field within the structure is needed. To completely remove the inconsistencies of classical plate/shell theories, higher-order expansions of the unknowns with respect to the z coordinate can be employed.

Higher Order Theories: Classical plate/shell models grant good results when small thickness, homogeneous structures are considered. On the other hand, the analysis of thick plates/shells and multilayered structures may require more sophisticated theories to achieve sufficiently accurate results. As a general guideline, it is clear that the richer the kinematics of the theory, the more accurate the 2D model becomes. In order to overcome the limitations of classical theories, a large variety of plate/shell higher-order theories (HOT) have been proposed in the past and recent literature. Eventually, higher-order theories can be expressed by making use of Taylor-like expansions of the generalized unknowns along the thickness. In the case of generic expansions of N terms, HOT displacement field can be expressed as in Eq. 3.3. Figure 3.3 pictorially shows the capabilities of HOT models, which can address complex kinematics in the thickness direction.



$$\begin{aligned}
 u(\alpha, \beta, z) &= u_0(\alpha, \beta) + z u_1(\alpha, \beta) + \dots + z^N u_N(\alpha, \beta) \\
 v(\alpha, \beta, z) &= v_0(\alpha, \beta) + z v_1(\alpha, \beta) + \dots + z^N v_N(\alpha, \beta) \\
 w(\alpha, \beta, z) &= w_0(\alpha, \beta) + z w_1(\alpha, \beta) + \dots + z^N w_N(\alpha, \beta)
 \end{aligned}
 \tag{3.3}$$

Figure 3.3: Geometrical representation of the Higher Order Theories.

The classical models, CLT and FSDT kinematics, are particular cases of the full linear expansion, obtained from Eq. 3.3 imposing $N = 1$. Starting from the full linear expansion $N = 1$, two possible techniques can be used to obtain FSDT, Eq. 3.2 the rearranging of rows and columns of the stiffness matrix; the penalization of the stiffness terms related to w_1 term. Therefore, CLT model, Eq. 3.1, can be obtained through the penalization of $\gamma_{\alpha z}$ and $\gamma_{\beta z}$. The condition can be imposed using a penalty value χ in the constitutive equations:

$$\begin{aligned}
 \tau_{\alpha z} &= \chi C_{55} \gamma_{\alpha z} \\
 \tau_{\beta z} &= \chi C_{44} \gamma_{\beta z}
 \end{aligned}$$

For more details see [66]. Therefore, it is well known in literature that linear models are affected by the problem of the Poisson Locking (PL) phenomena. The remedy for the Poisson locking, except to use higher-order theories, is to modify the Elastic Coefficients of the material, see Eq. 2.18. The PL phenomena originates from constitutive laws which state the intrinsic coupling between in- and out-of-plane strain components. Classical plate/shell theories correct the locking phenomena by imposing that the out-of-plane normal stress is zero. This hypothesis yields reduced material stiffness coefficients which have to be accounted in the Hooke law. Therefore, in literature, the correction of the material coefficients does not have a consistent theoretical proof. This means that the adoption of reduced material coefficients does not necessarily lead to the exact 3D solution, as shown in [52]. For the sake of clarity and simplicity of the present method explanation, the results presented in this work, with the full linear expansion kinematics, are not corrected for the PL phenomena.

3.2 Unified Formulation

According to Unified Formulation [15,66–68], refined models can be formulated in a straightforward manner by assuming an expansion of each of the primary variables by arbitrary functions in the thickness direction. Thus, each variable can be treated independently from the others, according to the required accuracy. In a displacement-based formulation, in fact, the three-dimensional displacement field is the combination of through-the-thickness functions weighted by the generalized unknown variables:

$$\begin{aligned} u(\alpha, \beta, z) &= F_0(z) u_0(\alpha, \beta) + F_1(z) u_1(\alpha, \beta) + \dots + F_N(z) u_N(\alpha, \beta) \\ v(\alpha, \beta, z) &= F_0(z) v_0(\alpha, \beta) + F_1(z) v_1(\alpha, \beta) + \dots + F_N(z) v_N(\alpha, \beta) \\ w(\alpha, \beta, z) &= F_0(z) w_0(\alpha, \beta) + F_1(z) w_1(\alpha, \beta) + \dots + F_N(z) w_N(\alpha, \beta) \end{aligned} \quad (3.4)$$

Similarly, in a compact form one has:

$$\mathbf{u}(\alpha, \beta, z) = F_s(z) \mathbf{u}_s(\alpha, \beta) \quad s = 0, 1, \dots, N \quad (3.5)$$

where $\mathbf{u}(\alpha, \beta, z)$ is the three-dimensional displacement vector defined in a general curvilinear orthogonal reference system; F_s are the thickness functions depending only on z ; \mathbf{u}_s is the generalized displacement vector of the variables; s is a sum index; and N is the number of terms of the theory expansion. Depending on the choice of the thickness functions, F_s , and the number of terms in the plate/shell kinematics, N , various theories can be implemented.

Taylor Higher-order Theories:

Classical shell models that are usually utilized in the literature and in commercial finite element tools are based on Taylor expansions of the primary variables along the thickness direction. As previously discussed, many attempts have been made to improve classical shell models. Refined theories, in general, make use of second- to higher-order polynomials for approximating the three-dimensional kinematic field along the shell thickness. Accordingly, Unified Formulation models based on Taylor polynomials express the unknown variables in terms of arbitrarily rich functions of the midplane position of the shell. This class of models are particularly efficient for thin and homogeneous structures.

In this work, Taylor-based higher-order shell models are expressed as:

$$\mathbf{u} = F_0 \mathbf{u}_0 + F_1 \mathbf{u}_1 + \dots + F_N \mathbf{u}_N = F_s \mathbf{u}_s, \quad s = 0, 1, \dots, N. \quad (3.6)$$

$$F_0 = z^0 = 1, \quad F_1 = z^1 = z, \quad \dots, \quad F_N = z^N. \quad (3.7)$$

This class of models is denoted to as ETN , where E stands for Equivalent-Single-Layer (ESL), T stands for Taylor expansions, and N denotes the number of terms of the expansion and the polynomial order, which is arbitrary in the Unified Formulation. For example, the $ET2$ model corresponds to a second-order shell model with the following kinematics:

$$\mathbf{u}(\alpha, \beta, z) = \mathbf{u}_0(\alpha, \beta) + z \mathbf{u}_1(\alpha, \beta) + z^2 \mathbf{u}_2(\alpha, \beta) \quad (3.8)$$

Classical models, such as the CLT and FSDT, can be obtained as a particular case of an Equivalent-Single-Layer (ESL) theory with $N = 1$. Or, in other words, classical shell models are degenerated cases of the $ET1$ model.

Legendre-like polynomial expansions:

Expanding the unknown variables as functions of the shell midplane position can result in inaccurate results, especially when thick composite structures are addressed. A possible

solution to this drawback can be expanding the displacement field in *non-local* sense through-the-thickness by means, for example, of Legendre-like polynomials. These polynomial set, if formulated opportunely, can allow one to express the unknown variables in function of the top and bottom position of a given sub-domain of the shell thickness (i.e., each single layer or group of layers). In the case of Legendre-like polynomial expansion models, the displacement is defined as follows:

$$\mathbf{u} = F_0 \mathbf{u}_0 + F_1 \mathbf{u}_1 + F_r \mathbf{u}_r = F_s \mathbf{u}_s, \quad s = 0, 1, r, \quad r = 2, \dots, N. \quad (3.9)$$

$$F_0 = \frac{P_0 + P_1}{2}, \quad F_1 = \frac{P_0 - P_1}{2}, \quad F_r = P_r - P_{r-2}. \quad (3.10)$$

in which $P_j = P_j(\zeta)$ is the Legendre polynomial of j -order defined in the ζ -domain: $-1 \leq \zeta \leq 1$. $P_0 = 1$, $P_1 = \zeta$, $P_2 = (3\zeta^2 - 1)/2$, $P_3 = (5\zeta^3 - 3\zeta)/2$, $P_4 = (35\zeta^4 - 30\zeta^2 + 3)/8$.

For the Layer-Wise (LW) models, the Legendre polynomials and the relative top and bottom position are defined for each layer.

Refined polynomials with Zig-Zag Function:

Due to the intrinsic anisotropy of multilayered structures, the first derivative of the displacement variables in the z -direction is discontinuous. It is possible to reproduce the zig-zag effect in the framework of the ESL description by employing the Murakami theory. According to [69], a zig-zag term can be introduced into Eq. 3.6 as follows:

$$\mathbf{u} = F_0(z) \mathbf{u}_0 + \dots + F_{N-1}(z) \mathbf{u}_{N-1} + (-1)^k \zeta_k \mathbf{u}_N. \quad (3.11)$$

Equivalently, the zig-zag function can be introduced also into Eq. 3.9 for a further enhancement of the Legendre polynomial expansions, if used in an Equivalent-Single-Layer approach:

$$\mathbf{u} = F_0 \mathbf{u}_0 + F_1 \mathbf{u}_1 + F_r \mathbf{u}_r + (-1)^k \zeta_k \mathbf{u}_N. \quad (3.12)$$

$$0 = \text{top}, \quad 1 = \text{bottom}, \quad r = 2, \dots, N - 1$$

The models outlined in Eqs. 3.11 and 3.12 are called zig-zag theories. The zig-zag function is defined in each layer k , where the non-dimensional term ζ_k takes value 1 and -1 at the top and the bottom of each layer, respectively.

Advanced Trigonometric and Exponential expansion Theories:

The definition of new kinematic models using different or unconventional functions, to improve the description of the displacement field along the thickness of the shell, is not a difficult task in the framework of Unified Formulation. If a trigonometric sine series plus a constant contribution is adopted, the displacement variables can be written as follows:

$$\mathbf{u} = \mathbf{u}_0 + \sin\left(\frac{\pi z}{h}\right) \mathbf{u}_1 + \dots + \sin\left(\frac{n\pi z}{h}\right) \mathbf{u}_N \quad (3.13)$$

where h is the whole thickness dimension and n is the half-waves number. If the linear contribution is considered, the displacement expression is:

$$\mathbf{u} = \mathbf{u}_0 + z \mathbf{u}_1 + \sin\left(\frac{\pi z}{h}\right) \mathbf{u}_2 + \dots + \sin\left(\frac{n\pi z}{h}\right) \mathbf{u}_{N+1} \quad (3.14)$$

A similar description can be provided using a trigonometric cosine series:

$$\mathbf{u} = \mathbf{u}_0 + \cos\left(\frac{\pi z}{h}\right) \mathbf{u}_1 + \dots + \cos\left(\frac{n\pi z}{h}\right) \mathbf{u}_N \quad (3.15)$$

and with the linear contribution:

$$\mathbf{u} = \mathbf{u}_0 + z \mathbf{u}_1 + \cos\left(\frac{\pi z}{h}\right) \mathbf{u}_2 + \dots + \cos\left(\frac{n\pi z}{h}\right) \mathbf{u}_{N+1} \quad (3.16)$$

A complete trigonometric series becomes:

$$\begin{aligned} \mathbf{u} = & \mathbf{u}_0 + \sin\left(\frac{\pi z}{h}\right) \mathbf{u}_1 + \cos\left(\frac{\pi z}{h}\right) \mathbf{u}_2 + \dots + \sin\left(\frac{n\pi z}{h}\right) \mathbf{u}_{2N-1} + \\ & + \cos\left(\frac{n\pi z}{h}\right) \mathbf{u}_{2N} \end{aligned} \quad (3.17)$$

If the linear contribution is considered:

$$\begin{aligned} \mathbf{u} = & \mathbf{u}_0 + z \mathbf{u}_1 + \sin\left(\frac{\pi z}{h}\right) \mathbf{u}_2 + \cos\left(\frac{\pi z}{h}\right) \mathbf{u}_3 + \dots + \\ & + \sin\left(\frac{n\pi z}{h}\right) \mathbf{u}_{2N} + \cos\left(\frac{n\pi z}{h}\right) \mathbf{u}_{2N+1} \end{aligned} \quad (3.18)$$

If an exponential expansion is employed the displacement field is:

$$\mathbf{u} = \mathbf{u}_0 + e^{(z/h)} \mathbf{u}_1 + \dots + e^{(nz/h)} \mathbf{u}_N \quad (3.19)$$

and adding the linear contribution:

$$\mathbf{u} = \mathbf{u}_0 + z \mathbf{u}_1 + e^{(z/h)} \mathbf{u}_2 + \dots + e^{(nz/h)} \mathbf{u}_{N+1} \quad (3.20)$$

Equivalently, the zig-zag function, Eq. 3.11, can be introduced also into trigonometric or exponential polynomials for a further enhancement of the displacement field description. For example, the theory *ET1S2Z* refers to the following displacement field:

$$\begin{aligned} \mathbf{u}(\alpha, \beta, z) = & \mathbf{u}_0(\alpha, \beta) + z \mathbf{u}_1(\alpha, \beta) + \sin\left(\frac{1\pi z}{h}\right) \mathbf{u}_2(\alpha, \beta) + \\ & + \sin\left(\frac{2\pi z}{h}\right) \mathbf{u}_3(\alpha, \beta) + (-1)^k \zeta_k \mathbf{u}_{4z}(\alpha, \beta) \end{aligned} \quad (3.21)$$

Multifield Formulation:

Unified Formulation becomes extremely useful when multifield problems are investigated such as thermoelastic problems, and electroelastic applications of piezoelectric structures [70–73]. In a displacement-based formulation for **mechanical problems** employing the Principle of Virtual Displacement (PVD), see Sec. 4.2, the three-dimensional displacement field is an approximation of the thickness functions weighted by the generalized unknown variables expanded with N terms:

$$\begin{aligned} u(\alpha, \beta, z) &= F_0(z) u_0(\alpha, \beta) + F_1(z) u_1(\alpha, \beta) + \dots + F_N(z) u_N(\alpha, \beta) \\ v(\alpha, \beta, z) &= F_0(z) v_0(\alpha, \beta) + F_1(z) v_1(\alpha, \beta) + \dots + F_N(z) v_N(\alpha, \beta) \\ w(\alpha, \beta, z) &= F_0(z) w_0(\alpha, \beta) + F_1(z) w_1(\alpha, \beta) + \dots + F_N(z) w_N(\alpha, \beta) \end{aligned} \quad (3.22)$$

In a displacement-based formulation for **partially coupled thermo-mechanical problems** employing the Principle of Virtual Displacement (PVD), see Sec. 4.3, the primary variables are only the three mechanical displacements (u, v, w) as the pure mechanical case, see Eq. 3.22. The temperature profile $\theta(\alpha, \beta, z)$ is an input of the uncoupled thermoelastic analysis.

In a displacement-based formulation for **coupled electro-mechanical problems** employing the Principle of Virtual Displacement (PVD), see Sec. 4.4, the primary variables are the three mechanical displacements (u, v, w) and the electric potential Φ :

$$\begin{aligned} u(\alpha, \beta, z) &= F_0(z) u_0(\alpha, \beta) + F_1(z) u_1(\alpha, \beta) + \dots + F_N(z) u_N(\alpha, \beta) \\ v(\alpha, \beta, z) &= F_0(z) v_0(\alpha, \beta) + F_1(z) v_1(\alpha, \beta) + \dots + F_N(z) v_N(\alpha, \beta) \\ w(\alpha, \beta, z) &= F_0(z) w_0(\alpha, \beta) + F_1(z) w_1(\alpha, \beta) + \dots + F_N(z) w_N(\alpha, \beta) \end{aligned} \quad (3.23)$$

$$\Phi(\alpha, \beta, z) = F_0(z) \Phi_0(\alpha, \beta) + F_1(z) \Phi_1(\alpha, \beta) + \dots + F_N(z) \Phi_N(\alpha, \beta)$$

In a mixed formulation for **mechanical problems** employing the Reissner Mixed Variational Theorem (RMVT), see Sec. 4.6, the primary variables are the three mechanical displacements (u, v, w) , and in addition a new set of extensive variables: the transverse stresses σ_n . Three possible extensions of the PVD for mechanical problems are possible: the three mechanical displacements (u, v, w) plus the transverse shear stresses $\sigma_{\alpha z}$ and $\sigma_{\beta z}$:

$$\begin{aligned} u(\alpha, \beta, z) &= F_0(z) u_0(\alpha, \beta) + F_1(z) u_1(\alpha, \beta) + \dots + F_N(z) u_N(\alpha, \beta) \\ v(\alpha, \beta, z) &= F_0(z) v_0(\alpha, \beta) + F_1(z) v_1(\alpha, \beta) + \dots + F_N(z) v_N(\alpha, \beta) \\ w(\alpha, \beta, z) &= F_0(z) w_0(\alpha, \beta) + F_1(z) w_1(\alpha, \beta) + \dots + F_N(z) w_N(\alpha, \beta) \end{aligned} \quad (3.24)$$

$$\begin{aligned} \sigma_{\alpha z}(\alpha, \beta, z) &= F_0(z) \sigma_{\alpha z_0}(\alpha, \beta) + F_1(z) \sigma_{\alpha z_1}(\alpha, \beta) + \dots + F_N(z) \sigma_{\alpha z_N}(\alpha, \beta) \\ \sigma_{\beta z}(\alpha, \beta, z) &= F_0(z) \sigma_{\beta z_0}(\alpha, \beta) + F_1(z) \sigma_{\beta z_1}(\alpha, \beta) + \dots + F_N(z) \sigma_{\beta z_N}(\alpha, \beta) \end{aligned}$$

The second possibility is the three mechanical displacements (u, v, w) plus the transverse normal stress σ_{zz} :

$$\begin{aligned} u(\alpha, \beta, z) &= F_0(z) u_0(\alpha, \beta) + F_1(z) u_1(\alpha, \beta) + \dots + F_N(z) u_N(\alpha, \beta) \\ v(\alpha, \beta, z) &= F_0(z) v_0(\alpha, \beta) + F_1(z) v_1(\alpha, \beta) + \dots + F_N(z) v_N(\alpha, \beta) \\ w(\alpha, \beta, z) &= F_0(z) w_0(\alpha, \beta) + F_1(z) w_1(\alpha, \beta) + \dots + F_N(z) w_N(\alpha, \beta) \end{aligned} \quad (3.25)$$

$$\sigma_{zz}(\alpha, \beta, z) = F_0(z) \sigma_{zz_0}(\alpha, \beta) + F_1(z) \sigma_{zz_1}(\alpha, \beta) + \dots + F_N(z) \sigma_{zz_N}(\alpha, \beta)$$

The last extension is the three mechanical displacements (u, v, w) plus all the transverse stresses $\sigma_{\alpha z}$, $\sigma_{\beta z}$ and σ_{zz} :

$$\begin{aligned} u(\alpha, \beta, z) &= F_0(z) u_0(\alpha, \beta) + F_1(z) u_1(\alpha, \beta) + \dots + F_N(z) u_N(\alpha, \beta) \\ v(\alpha, \beta, z) &= F_0(z) v_0(\alpha, \beta) + F_1(z) v_1(\alpha, \beta) + \dots + F_N(z) v_N(\alpha, \beta) \\ w(\alpha, \beta, z) &= F_0(z) w_0(\alpha, \beta) + F_1(z) w_1(\alpha, \beta) + \dots + F_N(z) w_N(\alpha, \beta) \end{aligned} \quad (3.26)$$

$$\begin{aligned} \sigma_{\alpha z}(\alpha, \beta, z) &= F_0(z) \sigma_{\alpha z_0}(\alpha, \beta) + F_1(z) \sigma_{\alpha z_1}(\alpha, \beta) + \dots + F_N(z) \sigma_{\alpha z_N}(\alpha, \beta) \\ \sigma_{\beta z}(\alpha, \beta, z) &= F_0(z) \sigma_{\beta z_0}(\alpha, \beta) + F_1(z) \sigma_{\beta z_1}(\alpha, \beta) + \dots + F_N(z) \sigma_{\beta z_N}(\alpha, \beta) \\ \sigma_{zz}(\alpha, \beta, z) &= F_0(z) \sigma_{zz_0}(\alpha, \beta) + F_1(z) \sigma_{zz_1}(\alpha, \beta) + \dots + F_N(z) \sigma_{zz_N}(\alpha, \beta) \end{aligned}$$

In a mixed formulation for **coupled electro-mechanical problems** employing the Reissner Mixed Variational Theorem (RMVT), see Sec. 4.7, the primary variables are the three mechanical displacements (u, v, w) , and in addition two new set of extensive variables: the mechanical transverse stresses σ_n , and the electric transverse displacement \mathcal{D}_z . As previously discussed for the RMVT for mechanical case, several combinations of the extensive

variables are possible. In this work the attention is focused only on the use of the electric extensive variable, the electric transverse displacement \mathcal{D}_z . The primary variables are the three mechanical displacements (u, v, w) and the electric transverse displacement \mathcal{D}_z :

$$\begin{aligned}
 u(\alpha, \beta, z) &= F_0(z) u_0(\alpha, \beta) + F_1(z) u_1(\alpha, \beta) + \dots + F_N(z) u_N(\alpha, \beta) \\
 v(\alpha, \beta, z) &= F_0(z) v_0(\alpha, \beta) + F_1(z) v_1(\alpha, \beta) + \dots + F_N(z) v_N(\alpha, \beta) \\
 w(\alpha, \beta, z) &= F_0(z) w_0(\alpha, \beta) + F_1(z) w_1(\alpha, \beta) + \dots + F_N(z) w_N(\alpha, \beta) \\
 \mathcal{D}_z(\alpha, \beta, z) &= F_0(z) \mathcal{D}_{z_0}(\alpha, \beta) + F_1(z) \mathcal{D}_{z_1}(\alpha, \beta) + \dots + F_N(z) \mathcal{D}_{z_N}(\alpha, \beta)
 \end{aligned} \tag{3.27}$$

Acronyms

A system of acronyms is given to denote the considered kinematic models. The first letters indicate the used approach, the Equivalent Single Layer is denoted by the letter E , differently if the layer-wise approach is used, the first letters become LW . For the Equivalent Single Layer approaches, the second letter indicates the kind of employed function, T for Taylor polynomials, L for Legendre polynomials, S for sines expansions, C for cosines expansions, and Exp for the exponential polynomials. The number N indicates the number of the expansion terms (except the constant term) used in the thickness direction. The last letter Z is added if the zig-zag term is considered. If the Navier analytical method is employed the subscript (a) is used.

3.3 Modelling Approaches

Two different types of modelling approaches are usually adopted in the literature for the formulation of composite structure theories; i.e., ESL and LW. Nevertheless, it is important to mention that choice of the modelling approach (i.e., ESL, LW) is independent of the type of the polynomials employed in the theory expansion within Unified Formulation.

ESL models

In an ESL model, the stiffness matrices of each layer are homogenized by simply summing the various contributions through the thickness. This approach leads to a model that has a set of variables that is assumed for the whole multilayer, and thus is independent of the number of layers. In this work, ESL models that make use of both Taylor and Legendre-like polynomials are used. For illustrative purposes, the general behaviour of the primary mechanical variables along the thickness of the structure in the case of ESL is depicted in Figure 3.4.

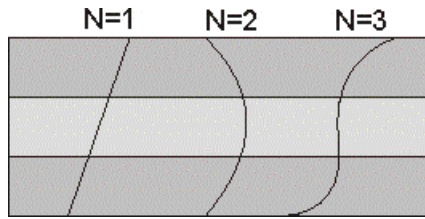


Figure 3.4: Equivalent-Single-Layer behaviour of the primary variables along the thickness of the shell.

LW models

In the case of LW, different sets of variables are assumed per each layer and the continuity of the displacements is imposed at the layer interface. The LW capability of describing correctly the discontinuous behaviour of the derivatives of the primary unknowns is graphically shown in Figure 3.5. In this work, LW models are implemented by using Legendre-like polynomial sets. In particular, the kinematic expansion is made by using Lagrange and Legendre polynomials, see Eq. 3.9. The Lagrange polynomials F_0 and F_1 , in fact, are necessary for interpolating the displacements at the top (t) and bottom (b) position of the layer, respectively. Hence, the unknown variables at the top (t) and bottom (b) position are used to impose the following compatibility conditions:

$$\mathbf{u}_t^k = \mathbf{u}_b^{k+1}, \quad k = 1, N_l - 1. \quad (3.28)$$

where k indicates the layer, and N_l is the number of layers.

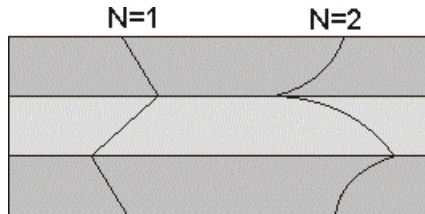


Figure 3.5: Layer-Wise behaviour of the primary variables along the thickness of the shell.

Chapter 4

Variational Principles

Thermo-electro-mechanical problems for multilayered structures had a growing interest in recent years [74]. For this reason several three-dimensional solutions are available in literature [75–77] for problems considering three different involved physical fields. Other interesting reference solutions are those related to the electro-mechanical problem [78–82], and those for thermo-mechanical coupling [83–86]. However, by considering the introduction of new materials in aerospace field, i.e. composites, sandwiches and functionally graded materials, the pure mechanical problem remains a fundamental topic, as illustrated in several works about the three-dimensional analysis of plates and shells [87–89]. The possibility of treating in a unified manner the refined and advanced two-dimensional models for multifield problems could represent a fundamental topic in the structural analysis. In this chapter the refined models are obtained by means of the Principle of Virtual Displacement (PVD) and its extensions to multifield problems. The most general case is the PVD written for the thermo-electro-mechanical case, the other PVD applications (thermo-mechanical case, electro-mechanical case, and so on) can be considered as particular cases of the most general thermo-electro-mechanical application [50]. Reissner’s Mixed Variational Theorem (RMVT) [90] extended to thermo-electro-mechanical problems gives several advanced two-dimensional models, where some transverse variables such as the transverse shear/normal stresses [91] and/or transverse normal electrical displacement are a priori modelled: in the PVD case these variables are obtained with an opportune post-processing via constitutive equations. The variables obtained a priori satisfy the Interlaminar Continuity (IC). The extension of RMVT to thermo-electro-mechanical problems is not so intuitive as the PVD case; problems such as the thermo-mechanical or the electro-mechanical ones, are not always particular cases of the most general thermo-electro-mechanical RMVT extension. In order to clarify these aspects, PVD and RMVT extensions for multifield problems are discussed in this chapter for each possible combination (one, two or three involved physical fields). Governing equations are written in a general form in order to simplify the relationships between general and particular cases.

4.1 Principle of Virtual Displacements for multifield problems

In the recent past, several two-dimensional approaches have been successfully extended to multifield problems [92–94]. Refined models, obtained via the extension of the Principle of Virtual Displacements (PVD) to thermo-electro-mechanical case and employing the Unified Formulation, give the possibility to choose the order of expansion in the thickness direction and the multilayer description (Equivalent Single Layer (ESL) or Layer Wise (LW)). The PVD for a thermo-electro-elastic medium can be derived from the Hamilton’s principle as indicated in [50] and [54]:

$$\delta \int_{t_0}^t (E_c - E_p) dt = 0 \quad \Rightarrow \quad \delta \int_{t_0}^t E_p dt = \delta \int_{t_0}^t E_c dt \quad (4.1)$$

where E_c and E_p are the kinetic and potential energy, respectively. δ is the variational symbol, t_0 the initial time and t a generic instant [54]. The variation of the kinetic energy E_c is the well-known relation [54], [50]:

$$\delta \int_{t_0}^t E_c dt = \delta \int_{t_0}^t \left[\frac{1}{2} \rho \dot{u}_i \dot{u}_i dV \right] dt = - \int_{t_0}^t \int_V \rho \ddot{u}_i \delta u_i dV dt = - \int_{t_0}^t \delta L_{in} dt \quad (4.2)$$

where V is the volume, ρ is the mass density, \dot{u}_i and \ddot{u}_i are the first and the second temporal derivative of displacement u_i , respectively. δL_{in} is the virtual variation of the work done by the inertial loads. The total potential energy E_p includes the thermopiezoelectric enthalpy density H as described in Eq.2.19 and the work done by surface tractions \bar{t}_j , and electric charge \bar{Q} on the displacements u_j , and the electric potential Φ , respectively:

$$E_p = \int_V H dV - \int_V (\bar{t}_i u_i - \bar{Q} \Phi) dV \quad (4.3)$$

The variation of the potential energy E_p can be rewritten in according to Eq 4.3:

$$\delta \int_{t_0}^t E_p dt = \delta \int_{t_0}^t \left[\int_V H dV - \int_V (\bar{t}_i u_i - \bar{Q} \Phi) dV \right] dt \quad (4.4)$$

The contribution given by the structure stiffness is the virtual variation of the internal work:

$$\delta L_i = \int_V H dV \quad (4.5)$$

The contribution given by the external loads is the virtual variation of the external work:

$$\delta L_e = \int_V (\delta u_i \bar{t}_i - \delta \Phi \bar{Q}) dV \quad (4.6)$$

Rewriting the Hamilton principle of Eq. 4.1 in terms of work variations:

$$\int_{t_0}^t \delta L_i dt = \int_{t_0}^t \delta L_e dt - \int_{t_0}^t \delta L_{in} dt \quad (4.7)$$

By discarding the dependency by the time t and introducing the vectorial form of Eqs.2.20, 2.22, Eq.4.7 can be rewritten as:

$$\int_V [\delta \epsilon_{ij} (\sigma_{ij} - \sigma_T) - \delta \mathcal{E}_i \mathcal{D}_i] dV = \int_V (\delta u_i \bar{t}_i - \delta \Phi \bar{Q}) dV - \int_V \rho \ddot{u}_i \delta u_i dV \quad (4.8)$$

where the array σ_T is the partially thermo-mechanical coupling $\sigma_T = \lambda \theta$. Therefore, splitting the in-plane (p) and out-plane (n) components, Eq. 4.8 becomes:

$$\begin{aligned} & \int_V \left[\delta \epsilon_{pG}^T (\sigma_{pC} - \sigma_{pT}) + \delta \epsilon_{nG}^T (\sigma_{nC} - \sigma_{nT}) - \delta \mathcal{E}_{pG}^T \mathcal{D}_{pC} - \delta \mathcal{E}_{nG}^T \mathcal{D}_{nC} \right] dV = \\ & = \int_V (\delta u_i \bar{t}_i - \delta \Phi \bar{Q}) dV - \int_V \rho \ddot{u}_i \delta u_i dV \end{aligned} \quad (4.9)$$

where the upscript T means the transpose of a vector. Subscript C and G suggest the substitution of constitutive and geometrical relations, respectively. The general form of governing equations of the PVD for thermo-electro-mechanical problems is:

$$\begin{aligned} \mathbf{K}_{uu} \mathbf{u} + \mathbf{K}_{u\Phi} \Phi &= \mathbf{P}_u + \mathbf{P}_\theta - \mathbf{M}_{uu} \ddot{\mathbf{u}} \\ \mathbf{K}_{\Phi u} \mathbf{u} + \mathbf{K}_{\Phi\Phi} \Phi &= \mathbf{P}_\Phi \end{aligned} \quad (4.10)$$

The stiffness matrices \mathbf{K} represent the contributions of the internal work variation, where the subscripts uu , $\Phi\Phi$, $u\Phi$ and Φu indicate the mechanical part, the electrical part and couplings of the mechanical and electrical parts respectively. The vectors contain the degrees

of freedom for the displacement u , and the electric potential Φ . M_{uu} is the inertial matrix and $\ddot{\mathbf{u}}$ is the second temporal derivative of the displacement vector. \mathbf{P}_u and \mathbf{P}_Φ are the mechanical and electrical load vectors respectively, due to the variation of the external work. \mathbf{P}_θ is the thermal load vector due to the partial thermo-mechanical coupling of the internal work. The extension of PVD, as illustrated in Eqs.4.9, 4.10, has some particular cases which are discussed in the following sections.

4.2 PVD for mechanical problems

In the case of pure mechanical problems the PVD has only the displacement u as primary variable. The variational statement, the constitutive equations and the governing equations can be considered as particular cases of the most general case of PVD for multifield problems. From Eq. 4.9, the variational statement is simplified by discarding the thermal and electrical works:

$$\int_V \left(\delta \epsilon_{pG}^T \sigma_{pC} + \delta \epsilon_{nG}^T \sigma_{nC} \right) dV = \delta L_e - \delta L_{in} \quad (4.11)$$

the governing equation for the pure mechanical case is:

$$\mathbf{K}_{uu} \mathbf{u} = \mathbf{P}_u - M_{uu} \ddot{\mathbf{u}} \quad (4.12)$$

It is important to notice that Eq. 4.12 can be obtained in a simpler way by delating in Eq. 4.10 the second line and the second column of the stiffness matrix, in fact the matrix \mathbf{K}_{uu} is the same of the general PVD for multifield problems of Eq. 4.10.

4.3 PVD for partially coupled thermo-mechanical problems

A possibility to study the thermal loads applied to elastic structures [20–22, 28, 95–99] is to consider the stress components as an algebraic summation of mechanical stresses and thermal ones as given in Eq. 2.20. The variational statement, the constitutive equations and the governing equations can be considered as particular cases of the most general case of PVD for multifield problems. From Eq. 4.9, the variational statement is simplified by discarding the electrical works:

$$\begin{aligned} & \int_V \left[\delta \epsilon_{pG}^T (\sigma_{pC} - \sigma_{pT}) + \delta \epsilon_{nG}^T (\sigma_{nC} - \sigma_{nT}) \right] dV = \delta L_e - \delta L_{in} \Rightarrow \\ & \Rightarrow \int_V \left(\delta \epsilon_{pG}^T \sigma_{pC} + \delta \epsilon_{nG}^T \sigma_{nC} \right) dV = \left[\delta L_e + \int_V \left(\delta \epsilon_{pG}^T \sigma_{pT} + \delta \epsilon_{nG}^T \sigma_{nT} \right) dV \right] - \delta L_{in} \end{aligned} \quad (4.13)$$

the governing equation for the partially coupled thermo-mechanical case is:

$$\mathbf{K}_{uu} \mathbf{u} = \mathbf{P}_u + \mathbf{P}_\theta - M_{uu} \ddot{\mathbf{u}} \quad (4.14)$$

where the external thermal load vector is $\mathbf{P}_\theta = \mathbf{K}_{u\theta} \boldsymbol{\theta}$. In the case of partially coupled thermo-mechanical problems the PVD has only the displacement u as primary variable. The thermal load can be determined by considering a temperature profile $\boldsymbol{\theta}$ through the thickness direction imposed a priori [100] or calculated by solving Fourier's heat conduction equation [101], [28]. The two cases of assumed temperature profile (T_a) and calculated temperature profile (T_c) are discussed in Sec. 7.1.

4.4 PVD for electro-mechanical problems

In the case of electro-mechanical coupling, for example the use of piezoelectric materials and/or the application of an electrical load [39, 42, 45, 102–109], the relative PVD can be simply obtained by discarding the thermal work in Eq. 4.9:

$$\int_V \left(\delta \epsilon_{pG}^T \sigma_{pC} + \delta \epsilon_{nG}^T \sigma_{nC} - \delta \mathcal{E}_{pG}^T \mathcal{D}_{pC} - \delta \mathcal{E}_{nG}^T \mathcal{D}_{nC} \right) dV = \delta L_e - \delta L_{in} \quad (4.15)$$

the governing equation for the electro-mechanical case is:

$$\begin{aligned} \mathbf{K}_{uu} \mathbf{u} + \mathbf{K}_{u\Phi} \Phi &= \mathbf{P}_u - M_{uu} \ddot{\mathbf{u}} \\ \mathbf{K}_{\Phi u} \mathbf{u} + \mathbf{K}_{\Phi\Phi} \Phi &= \mathbf{P}_\Phi \end{aligned} \quad (4.16)$$

In the case of electro-mechanical problems the PVD has the displacement u and the electric potential Φ as primary variables. The variational statement, the constitutive equations and the governing equations can be considered as particular cases of the most general case of PVD for multifield problems.

4.5 Reissner Mixed Variational Theorem for multifield problems

The Reissner Mixed Variational Theorem (RMVT) [90] permits to assume two independent sets of variables: a set of primary unknowns as the PVD case, and a set of extensive variables which are modelled a priori in the thickness direction. The main advantage of using the RMVT is a priori and complete fulfillment of the C_z^0 -requirements for the modelled extensive variables [91]. In literature different extensions of RMVT are given by starting from the PVD: transverse shear stresses σ_{xz} , σ_{yz} as extensive variables, transverse normal stress σ_{zz} as extensive variable, and both transverse shear and normal stresses as extensive variables. The way to obtain these cases is to add a Lagrange multiplier. When a new Lagrange multiplier is added [90], the constitutive equations must be rearranged in order to explicit the modelled variables.

In the case of multifield problems [110], [111] the RMVT can be extended in a general way. In particular starting from the PVD for electro-mechanical problems different extensions are possible: transverse shear stresses σ_{xz} , σ_{yz} , and transverse normal electric displacement \mathcal{D}_z as extensive variables, transverse normal stress σ_{zz} , and transverse normal electric displacement \mathcal{D}_z as extensive variables, and both transverse shear and normal stresses, and transverse normal electric displacement \mathcal{D}_z as extensive variables, and the last possibility is the transverse normal electric displacement \mathcal{D}_z as extensive variable. The way to obtain these cases is to add two different kinds of Lagrange multipliers, one for the transverse mechanical stresses, and another one for the transverse electric displacement.

4.6 RMVT for mechanical problems

By considering the variational statement in Eq. 4.12 for the PVD of mechanical problems, the RMVT is obtained modelling a priori the transverse shear/normal stresses σ_{nM} (the new subscript M is introduced to remark that the transverse stresses are now modelled and not obtained via constitutive equations). The added Lagrange multiplier is $\delta \sigma_{nM}^T (\epsilon_{nG} - \epsilon_{nC})$. The condition to add this multiplier is that the transverse strains ϵ_n calculated by means of

geometrical relations (G) and by using the constitutive equations (C) must be the same or almost the same. In this way the balance of the internal work does not change or remains almost the same.

$$\int_V \left[\delta \epsilon_{pG}^T \sigma_{pC} + \delta \epsilon_{nG}^T \sigma_{nM} + \delta \sigma_{nM}^T (\epsilon_{nG} - \epsilon_{nC}) \right] dV = \delta L_e - \delta L_{in} \quad (4.17)$$

The relative constitutive equations are obtained from Eq. 2.16 considering in them the transverse stresses σ_n as modelled (M) and the transverse strains ϵ_n as obtained from constitutive equations (C).

$$\begin{aligned} \sigma_p &= \hat{C}_{\sigma_p \epsilon_p} \epsilon_{pG} + \hat{C}_{\sigma_p \sigma_n} \sigma_{nM} \\ \epsilon_n &= \hat{C}_{\epsilon_n \epsilon_p} \epsilon_{pG} + \hat{C}_{\epsilon_n \sigma_n} \sigma_{nM} \end{aligned} \quad (4.18)$$

The coefficients in the proposed constitutive equations are rearranged as follows:

$$\begin{aligned} \hat{C}_{\sigma_p \epsilon_p} &= \tilde{C}_{pp} - \tilde{C}_{pn} \tilde{C}_{nn}^{-1} \tilde{C}_{np} \quad ; \quad \hat{C}_{\sigma_p \sigma_n} = \tilde{C}_{pn} \tilde{C}_{nn}^{-1} \\ \hat{C}_{\epsilon_n \epsilon_p} &= -\tilde{C}_{nn}^{-1} \tilde{C}_{np} \quad ; \quad \hat{C}_{\epsilon_n \sigma_n} = \tilde{C}_{nn}^{-1} \end{aligned} \quad (4.19)$$

The governing equations can be obtained by using the Eqs. 4.17, 4.18 [201], [202]:

$$\begin{aligned} \mathbf{K}_{uu} \mathbf{u} + \mathbf{K}_{u\sigma_n} \sigma_n &= \mathbf{P}_u - \mathbf{M}_{uu} \ddot{\mathbf{u}} \\ \mathbf{K}_{\sigma_n u} \mathbf{u} + \mathbf{K}_{\sigma_n \sigma_n} \sigma_n &= 0 \end{aligned} \quad (4.20)$$

The matrix \mathbf{K}_{uu} is completely different from that in Eq. 4.12 for the PVD because of the introduction of a Lagrange multiplier and the consequently rearrangement of constitutive equations.

4.7 RMVT for electro-mechanical problems

For piezo-laminated structures among the various variables, the evaluation of the transverse normal electric displacement is of particular interest. The \mathcal{D}_z is, in fact, closely related to the electrical charge:

$$Q = \int_{\Omega} \mathcal{D}_z d\Omega$$

where Ω is the plate/shell surface. The charge consists of a fundamental input/output in a closed-loop control of a smart structure. Faster and accurate evaluation of Q is a key point in the development of an efficient and reliable closed-loop control algorithm. However, \mathcal{D}_z , in classical applications, is only given a posteriori via post-processing of the primary variables (the mechanical displacements and the electrical potential). An extended RMVT application, with \mathcal{D}_z assumed as primary variable, has been employed in this work, which has been called *RMVT - \mathcal{D}_z* . By considering the variational statement in Eq. 4.15 for the PVD of electro-mechanical problems, the RMVT is obtained modelling a priori the transverse normal electric displacement \mathcal{D}_{nM} (the new subscript M is introduced to remark that the transverse normal electric displacement is now modelled and not obtained via constitutive equations). The added Lagrange multiplier is $\delta \mathcal{D}_{nM}^T (\mathcal{E}_{nG} - \mathcal{E}_{nC})$.

$$\int_V \left[\delta \epsilon_{pG}^T \sigma_{pC} + \delta \epsilon_{nG}^T \sigma_{nC} - \delta \mathcal{E}_{pG}^T \mathcal{D}_{pC} - \delta \mathcal{E}_{nG}^T \mathcal{D}_{nM} - \delta \mathcal{D}_{nM}^T (\mathcal{E}_{nG} - \mathcal{E}_{nC}) \right] dV = \delta L_e - \delta L_{in} \quad (4.21)$$

Substituting in Eq. 4.21 the rearranged constitutive Eq. 2.31 for the *RMVT - \mathcal{D}_z* , the governing equations for the electro-mechanical case are:

$$\begin{aligned} \mathbf{K}_{uu} \mathbf{u} + \mathbf{K}_{u\Phi} \Phi + \mathbf{K}_{u\mathcal{D}_n} \mathcal{D}_n &= \mathbf{P}_u - \mathbf{M}_{uu} \ddot{\mathbf{u}} \\ \mathbf{K}_{\Phi u} \mathbf{u} + \mathbf{K}_{\Phi\Phi} \Phi + \mathbf{K}_{\Phi\mathcal{D}_n} \mathcal{D}_n &= \mathbf{P}_{\Phi} \\ \mathbf{K}_{\mathcal{D}_n u} \mathbf{u} + \mathbf{K}_{\mathcal{D}_n\Phi} \Phi + \mathbf{K}_{\mathcal{D}_n\mathcal{D}_n} \mathcal{D}_n &= 0 \end{aligned} \quad (4.22)$$

The matrices \mathbf{K}_{uu} , $\mathbf{K}_{u\Phi}$, $\mathbf{K}_{\Phi u}$, $\mathbf{K}_{\Phi\Phi}$ are completely different from that in Eq. 4.16 for the PVD because of the introduction of a Lagrange multiplier and the consequently rearrangement of constitutive equations.

Chapter 5

Weak formulation for shell problems

The Finite Element Methods are based on a weak approximation of the structural problem. In other words, some considerations on the solution error are introduced, the error has an integral meaning over the whole finite element. For this reason the balance of an element is reached only in an integral sense, the element is globally in equilibrium, but locally it should be out of balance. A simple proof is when the stresses are evaluated in a shared point between more than one elements, the stresses should be different depending on the finite element considered for the evaluation postprocess cycle. The formulations that take into account the satisfaction of the balance at both global and local level are called strong formulations.

5.1 Finite Element Method

A Finite Element Method (FEM) [6,112–114] approximation can be formulated independently from the choice of the thickness functions adopted. According to FEM, the generalized displacements can be expressed as a linear combinations of the shape functions, in compact form, as follows:

$$\mathbf{u} = \mathbf{N}_j \mathbf{u}_j \quad \delta \mathbf{u} = \mathbf{N}_i \delta \mathbf{u}_i \quad \text{with } i, j = 1, \dots, (n^\circ \text{ nodes}) \quad (5.1)$$

where \mathbf{u}_j and $\delta \mathbf{u}_i$ are the nodal displacements and their virtual variations. Introducing in Eq. 5.1 the Unified Formulation, Eq. 3.5, with the thickness functions, one has:

$$\mathbf{u}_s = \mathbf{F}_s \mathbf{N}_j \mathbf{u}_{s_j} \quad \delta \mathbf{u}_\tau = \mathbf{F}_\tau \mathbf{N}_i \delta \mathbf{u}_{\tau_i} \quad (5.2)$$

with $i, j = 1, \dots, (n^\circ \text{ nodes})$ and $\tau, s = 1, \dots, N$ (*expansion order*)

In this work, a 9-node finite plate/shell element is employed and Lagrangian shape functions N_i, N_j are used to interpolate the primary variables. These Lagrangian shape functions are expressed in a local reference system of the finite element (ξ, η) , see Figure 5.1, where N_i assume value 1 in i -nodes and value 0 in the other nodes.

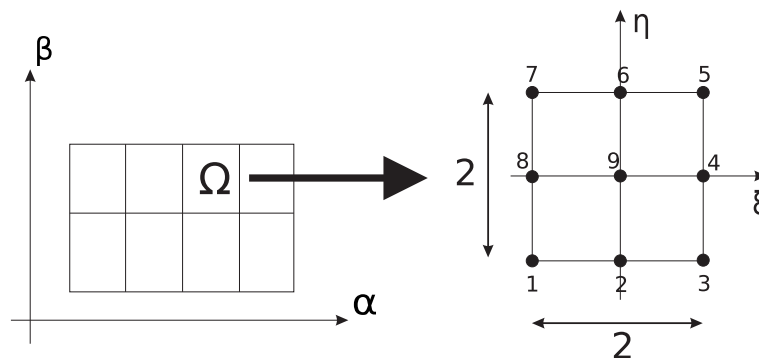


Figure 5.1: 9-node element, local reference system.

where the lagrangian shape functions for a 9-node element are the following:

$$\begin{aligned}
 N_1 &= \frac{1}{4}(\xi^2 - \xi) \begin{pmatrix} \eta^2 - \eta \\ \eta^2 - \eta \end{pmatrix} & N_2 &= \frac{1}{2}(1 - \xi^2) \begin{pmatrix} \eta^2 - \eta \\ \eta^2 - \eta \end{pmatrix} \\
 N_3 &= \frac{1}{4}(\xi^2 + \xi) \begin{pmatrix} \eta^2 - \eta \\ \eta^2 - \eta \end{pmatrix} & N_4 &= \frac{1}{2}(\xi^2 + \xi) \begin{pmatrix} 1 - \eta^2 \\ 1 - \eta^2 \end{pmatrix} \\
 N_5 &= \frac{1}{4}(\xi^2 + \xi) \begin{pmatrix} \eta^2 + \eta \\ \eta^2 + \eta \end{pmatrix} & N_6 &= \frac{1}{2}(1 - \xi^2) \begin{pmatrix} \eta^2 + \eta \\ \eta^2 + \eta \end{pmatrix} \\
 N_7 &= \frac{1}{4}(\xi^2 - \xi) \begin{pmatrix} \eta^2 + \eta \\ \eta^2 + \eta \end{pmatrix} & N_8 &= \frac{1}{2}(\xi^2 - \xi) \begin{pmatrix} 1 - \eta^2 \\ 1 - \eta^2 \end{pmatrix} \\
 N_9 &= (1 - \xi^2) \begin{pmatrix} 1 - \eta^2 \\ 1 - \eta^2 \end{pmatrix}
 \end{aligned} \tag{5.3}$$

In classical FEM techniques, the strain components are computed from displacements by using geometrical relations Eq. 2.58. In particular, by substituting Unified Formulation Eq. 3.5 and FEM approximation Eq. 5.1 into Eq. 2.58, one has:

$$\begin{aligned}
 \epsilon_p &= F_\tau (\mathbf{D}_p + \mathbf{A}_p) (N_i \mathbf{I}) \mathbf{u}_{\tau_i}, \\
 \epsilon_n &= F_\tau (\mathbf{D}_{np} - \mathbf{A}_n) (N_i \mathbf{I}) \mathbf{u}_{\tau_i} + F_{\tau,z} \mathbf{D}_{nz} (N_i \mathbf{I}) \mathbf{u}_{\tau_i},
 \end{aligned} \tag{5.4}$$

where \mathbf{I} is the 3×3 identity matrix. This procedure may result in some numerical problems related to the shear and membrane lockings. The Shear Locking Phenomena, in classical FEM analysis, lead to a “blocking effect” by the shear, in other words, the stiffness due to the shear contributions becomes too relevant. The Shear Locking is a convergence problem, and it is a pure numerical problem. The locking effect grows proportionally to the decreasing of the plate/shell thickness, the structure becomes infinitely stiff to the shear for $h \rightarrow 0$. A possible way to contrast the shear locking is to increase the mesh, but if the structure becomes thinner, the number of elements needed to contrast the locking phenomena increases exponentially. This solution is not practicable for the analysis of thin plate/shell structure. In literature many methods were developed to contrast the shear locking phenomena [115], the most commons are based on a modification of the Gauss quadrature numerical integration method, a brief overview is given below:

Reduced Integration:

If the shell thickness decrease $h \rightarrow 0$, the shear strain energy grows, and the finite element becomes too stiff. This locking problem implies that the shear strain conditions $\epsilon_{\alpha z} = 0$ and $\epsilon_{\beta z} = 0$ are not satisfied. A possible solution is to calculate the integrals, on the shell surface with the Gauss quadrature method, only in the points where it is more probable to satisfy the shear strain conditions $\epsilon_{\alpha z} = 0$ and $\epsilon_{\beta z} = 0$. The number of integration points is less than the nodes element number, this leads to underestimate the shear strain integrals, and it contrast the shear locking phenomena, this is the main idea of the Reduced Integration method [116–118]. For example, for a 4-node element the reduced integration point is only 1, for a 9-node element the reduced integration points are 4.

The Reduced Integration method could lead to some singularities $[K_{reduced}] = 0$, the presence of spurious modes, and for dynamical analysis the presence of some negative harmonic solutions $\omega < 0$.

Selective reduced Integration:

The variation of the internal work can be splitted into the bending contribution and the shear contribution as follows:

$$\delta L_{i_{bending}} + \delta L_{i_{shear}} \Rightarrow [K_{bending}] + [K_{shear}]$$

To avoid the shear locking phenomena the reduced integration have to be used for the shear contribution, but it is not necessary for the bending contribution. Consequently, it is possible

to use full integration for the bending contribution, one has:

$$\begin{aligned} [K_{bending}] &\rightarrow \text{Full integration} \\ [K_{shear}] &\rightarrow \text{Reduced integration} \end{aligned}$$

Throughout this splitted integration [119, 120], it is possible: to avoid the singularities in the major part of the possible structural cases, and the elimination of the negative harmonic solutions $\omega < 0$ in dynamic analysis. It is not possible to completely avoid the spurious modes that are still present.

A different approach to the shear locking problem is the Assumed Shear Strain Field Concept, or well known Mixed Interpolation of Tensorial Components (MITC) method. The key of the MITC method is the evaluation, by a new re-interpolation process, of the shear strains in the element points where the shear strain conditions $\epsilon_{\alpha z} = 0$ and $\epsilon_{\beta z} = 0$ could be probably satisfied.

In this work a 9-nodes shell finite element with the MITC method is employed for the multifield analysis, and its implementation is described below in Sec. 5.2.

5.2 MITC9 Finite Shell Element

In this work, a MITC technique [107, 121–124] is used to overcome the shear locking problem. According to the MITC method, the strain components are re-interpolated employing a new set of Lagrangian shape function \bar{N} :

$$\begin{aligned} \bar{\epsilon}_p &= \bar{N}_m \epsilon_{p_m} \\ \bar{\epsilon}_n &= \bar{N}_m \epsilon_{n_m} \end{aligned} \quad (5.5)$$

where m indicates summation over the new set of points called *tying points*; ϵ_{p_m} and ϵ_{n_m} are the strain vectors evaluated at the tying point m ; and \bar{N}_m are the assumed interpolation functions satisfying

$$\bar{N}_m^n = \delta_m^n, \quad \delta_m^n = \begin{cases} 1 & \text{if } m = n \\ 0 & \text{otherwise} \end{cases} \quad (5.6)$$

where m and n go from 1 to the number of tying points within the element. It should be underlined that the position and the number of tying points are different for each strain component, see Figure 5.2. Moreover, the normal transverse strain ϵ_{zz} is excluded from this procedure, and it is directly calculated from the displacements.

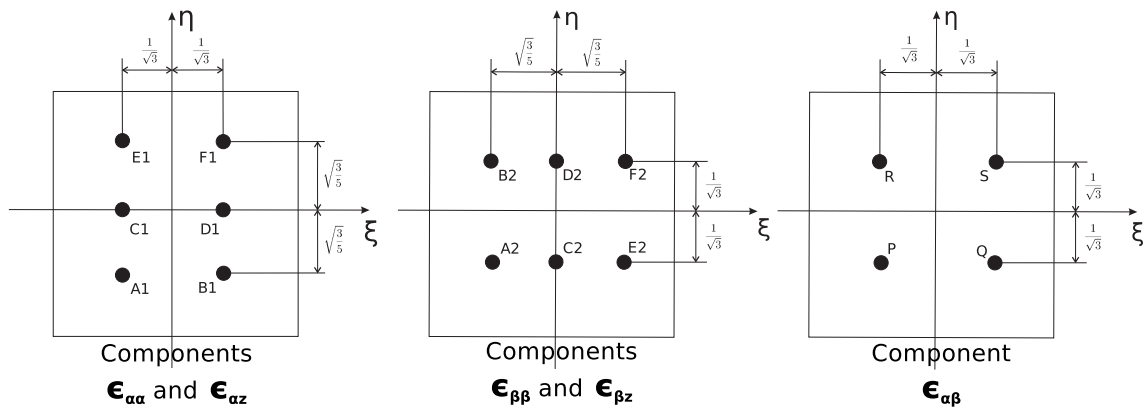


Figure 5.2: Tying points location for the MITC9 *shell* element.

The stress components $\epsilon_{\alpha\alpha}$ and $\epsilon_{\alpha z}$ are interpolated in the tying points named: $A1, B1, C1, D1, E1, F1$, see Figure 5.2, by the following new lagrangian functions:

$$\begin{aligned}\bar{N}_{A1} &= \frac{5\sqrt{3}}{12}\eta\left(\eta - \sqrt{\frac{3}{5}}\right)\left(\frac{1}{\sqrt{3}} - \xi\right) & \bar{N}_{B1} &= \frac{5\sqrt{3}}{12}\eta\left(\eta - \sqrt{\frac{3}{5}}\right)\left(\frac{1}{\sqrt{3}} + \xi\right) \\ \bar{N}_{C1} &= -\frac{5\sqrt{3}}{6}\left(\eta + \sqrt{\frac{3}{5}}\right)\left(\eta - \sqrt{\frac{3}{5}}\right)\left(\frac{1}{\sqrt{3}} - \xi\right) & \bar{N}_{D1} &= -\frac{5\sqrt{3}}{6}\left(\eta + \sqrt{\frac{3}{5}}\right)\left(\eta - \sqrt{\frac{3}{5}}\right)\left(\frac{1}{\sqrt{3}} + \xi\right) \\ \bar{N}_{E1} &= \frac{5\sqrt{3}}{12}\left(\eta + \sqrt{\frac{3}{5}}\right)\eta\left(\frac{1}{\sqrt{3}} - \xi\right) & \bar{N}_{F1} &= \frac{5\sqrt{3}}{12}\left(\eta + \sqrt{\frac{3}{5}}\right)\eta\left(\frac{1}{\sqrt{3}} + \xi\right)\end{aligned}\tag{5.7}$$

For the stress components $\epsilon_{\beta\beta}$ and $\epsilon_{\beta z}$, the interpolation functions defined in the tying points $A2, B2, C2, D2, E2, F2$, see Figure 5.2, are the following:

$$\begin{aligned}\bar{N}_{A2} &= \frac{5\sqrt{3}}{12}\xi\left(\xi - \sqrt{\frac{3}{5}}\right)\left(\frac{1}{\sqrt{3}} - \eta\right) & \bar{N}_{B2} &= \frac{5\sqrt{3}}{12}\xi\left(\xi - \sqrt{\frac{3}{5}}\right)\left(\frac{1}{\sqrt{3}} + \eta\right) \\ \bar{N}_{C2} &= -\frac{5\sqrt{3}}{6}\left(\xi + \sqrt{\frac{3}{5}}\right)\left(\xi - \sqrt{\frac{3}{5}}\right)\left(\frac{1}{\sqrt{3}} - \eta\right) & \bar{N}_{D2} &= -\frac{5\sqrt{3}}{6}\left(\xi + \sqrt{\frac{3}{5}}\right)\left(\xi - \sqrt{\frac{3}{5}}\right)\left(\frac{1}{\sqrt{3}} + \eta\right) \\ \bar{N}_{E2} &= \frac{5\sqrt{3}}{12}\left(\xi + \sqrt{\frac{3}{5}}\right)\xi\left(\frac{1}{\sqrt{3}} - \eta\right) & \bar{N}_{F2} &= \frac{5\sqrt{3}}{12}\left(\xi + \sqrt{\frac{3}{5}}\right)\xi\left(\frac{1}{\sqrt{3}} + \eta\right)\end{aligned}\tag{5.8}$$

The functions defined in the points P, Q, R, S , see Figure 5.2, for the interpolation of the strain $\epsilon_{\alpha\beta}$, are the following:

$$\begin{aligned}\bar{N}_P &= \frac{3}{4}\left(\frac{1}{\sqrt{3}} - \xi\right)\left(\frac{1}{\sqrt{3}} - \eta\right) & \bar{N}_Q &= \frac{3}{4}\left(\frac{1}{\sqrt{3}} + \xi\right)\left(\frac{1}{\sqrt{3}} - \eta\right) \\ \bar{N}_R &= \frac{3}{4}\left(\frac{1}{\sqrt{3}} - \xi\right)\left(\frac{1}{\sqrt{3}} + \eta\right) & \bar{N}_S &= \frac{3}{4}\left(\frac{1}{\sqrt{3}} + \xi\right)\left(\frac{1}{\sqrt{3}} + \eta\right)\end{aligned}\tag{5.9}$$

The strain components ϵ_{zz} is computed directly from the displacements.

For the sake of convenience, the interpolating functions are organized in the following vectors:

$$\begin{aligned}\bar{\mathbf{N}}_{m1} &= [\bar{N}_{A1}, \bar{N}_{B1}, \bar{N}_{C1}, \bar{N}_{D1}, \bar{N}_{E1}, \bar{N}_{F1}] \\ \bar{\mathbf{N}}_{m2} &= [\bar{N}_{A2}, \bar{N}_{B2}, \bar{N}_{C2}, \bar{N}_{D2}, \bar{N}_{E2}, \bar{N}_{F2}] \\ \bar{\mathbf{N}}_{m3} &= [\bar{N}_P, \bar{N}_Q, \bar{N}_R, \bar{N}_S]\end{aligned}\tag{5.10}$$

According to the MITC method Eq. 5.5, for example, the strain components $\epsilon_{\alpha\alpha}$ are defined as:

$$\begin{aligned}\bar{\epsilon}_{\alpha\alpha} &= \bar{N}_{A1}\epsilon_{\alpha\alpha}(\xi_{A1}, \eta_{A1}) + \bar{N}_{B1}\epsilon_{\alpha\alpha}(\xi_{B1}, \eta_{B1}) + \bar{N}_{C1}\epsilon_{\alpha\alpha}(\xi_{C1}, \eta_{C1}) + \bar{N}_{D1}\epsilon_{\alpha\alpha}(\xi_{D1}, \eta_{D1}) + \\ &+ \bar{N}_{E1}\epsilon_{\alpha\alpha}(\xi_{E1}, \eta_{E1}) + \bar{N}_{F1}\epsilon_{\alpha\alpha}(\xi_{F1}, \eta_{F1})\end{aligned}\tag{5.11}$$

Equivalently, in compact form in according of Eq. 5.5, one has:

$$\bar{\epsilon}_{\alpha\alpha} = \bar{\mathbf{N}}_{m1}\epsilon_{\alpha\alpha}(\xi_{m1}, \eta_{m1})\tag{5.12}$$

The reinterpolation of the strain components have to be taken into account also in the constitutive equations of the post-processed stresses.

5.3 Governing Equations for shell weak formulation

Governing equations for shell weak formulation are developed in terms of some few basic elements called fundamental nuclei. Expanding them by means of opportune indexes and loops, it is possible to obtain the stiffness matrices of the considered multilayered structures. The use of such nuclei permits to obtain in a unified manner several refined and advanced models which differ for the chosen order of expansion in the thickness direction, for the choice of the modelled multifield variables, and for the multilayer approach description: equivalent single layer (ESL) or layer wise (LW). Some of the proposed variational statements in the previous chapter are here developed to obtain the governing equations for the analysis which will be proposed in the next three chapters. Both plate and shell geometries are considered.

5.3.1 PVD for mechanical problems

The variational statement in the case of PVD for pure mechanical problems in Eq. 4.11, is written in terms of the integrals in the reference plane Ω and the integrals along the thickness of the shell A :

$$\int_{\Omega} \int_A \left(\delta \epsilon_{pG}^T \sigma_{pC} + \delta \epsilon_{nG}^T \sigma_{nC} \right) H_{\alpha} H_{\beta} d\alpha d\beta dz = \delta L_e - \delta L_{in} \quad (5.13)$$

By considering a laminate of N_l layers, and the integral on the volume V of each layer k as an integral on the in plane domain Ω_k plus the integral in the thickness-direction domain A_k , it is possible to write:

$$\sum_{k=1}^{N_l} \int_{\Omega_k} \int_{A_k} \left(\delta \epsilon_{pG}^{kT} \sigma_{pC}^k + \delta \epsilon_{nG}^{kT} \sigma_{nC}^k \right) H_{\alpha}^k H_{\beta}^k d\alpha^k d\beta^k dz^k = \sum_{k=1}^{N_l} \delta L_e^k - \sum_{k=1}^{N_l} \delta L_{in}^k \quad (5.14)$$

Substituting the constitutive equations for pure mechanical problems Eq. 2.16, the strain components computed from displacements by using geometrical relations Eq. 2.58, applying the Unified Formulation Eq. 3.5 and the FEM approximation Eq. 5.1, one obtains the following governing equations in compact form:

$$\delta u_{\tau_i} : \mathbf{K}_{uu}^{k\tau s i j} u^{k s j} = \mathbf{P}_u^{k\tau i} - \mathbf{M}_{uu}^{k\tau s i j} \ddot{u}^{k s j} \quad (5.15)$$

where $\mathbf{K}_{uu}^{k\tau s i j}$ is a 3×3 matrix, called fundamental nucleus of the mechanical stiffness matrix. The nucleus is the basic element from which the stiffness matrix of the whole structure is computed. The fundamental nucleus is expanded on the indexes τ and s to obtain the stiffness matrix of each layer k . Then, the matrixes of each layer are assembled at the multi-layer level depending on the approach considered, see Sec. 3.3. The fundamental nucleus of the mass matrix, $\mathbf{M}_{uu}^{k\tau s i j}$ a 3×3 matrix, has the main diagonal components different from zero. $\mathbf{P}_u^{k\tau i}$ is a 3×1 matrix, called fundamental nucleus of the external load. The explicit expression of the stiffness matrix and external load nuclei are given below with classical FEM method, and in Appendix A for mechanical nuclei with the reinterpolation of the strain components via the MITC method Eq. 5.5. The stiffness matrix $\mathbf{K}_{uu}^{k\tau s i j}$ nucleus is defined as follows:

$$\mathbf{K}_{uu}^{k\tau s i j} = \begin{bmatrix} K_{uu\alpha\alpha} & K_{uu\alpha\beta} & K_{uu\alpha z} \\ K_{uu\beta\alpha} & K_{uu\beta\beta} & K_{uu\beta z} \\ K_{uu z\alpha} & K_{uu z\beta} & K_{uu z z} \end{bmatrix}^{k\tau s i j} \quad (5.16)$$

$$\begin{aligned}
 K_{uu_{\alpha\alpha}}^{k\tau sij} &= \tilde{C}_{55}^k \int_{\Omega^k} N_i N_j d\alpha^k d\beta^k \int_{A^k} F_{\tau,z} F_{s,z} H_{\alpha}^k H_{\beta}^k dz^k + \tilde{C}_{66}^k \int_{\Omega^k} N_{i,\beta} N_{j,\beta} d\alpha^k d\beta^k \int_{A^k} F_{\tau} F_s \frac{H_{\alpha}^k}{H_{\beta}^k} dz^k + \\
 &+ \tilde{C}_{16}^k \int_{\Omega^k} N_{i,\alpha} N_{j,\beta} d\alpha^k d\beta^k \int_{A^k} F_{\tau} F_s dz^k + \tilde{C}_{16}^k \int_{\Omega^k} N_{i,\beta} N_{j,\alpha} d\alpha^k d\beta^k \int_{A^k} F_{\tau} F_s dz^k + \\
 &+ \tilde{C}_{11}^k \int_{\Omega^k} N_{i,\alpha} N_{j,\alpha} d\alpha^k d\beta^k \int_{A^k} F_{\tau} F_s \frac{H_{\beta}^k}{H_{\alpha}^k} dz^k - \frac{\tilde{C}_{55}^k}{R_{\alpha}^k} \int_{\Omega^k} N_i N_j d\alpha^k d\beta^k \int_{A^k} F_{\tau,z} F_s H_{\beta}^k dz^k - \\
 &- \frac{\tilde{C}_{55}^k}{R_{\alpha}^k} \int_{\Omega^k} N_i N_j d\alpha^k d\beta^k \int_{A^k} F_{\tau} F_{s,z} H_{\beta}^k dz^k - \frac{\tilde{C}_{55}^k}{(R_{\alpha}^k)^2} \int_{\Omega^k} N_i N_j d\alpha^k d\beta^k \int_{A^k} F_{\tau} F_s \frac{H_{\beta}^k}{H_{\alpha}^k} dz^k
 \end{aligned}$$

$$\begin{aligned}
 K_{uu_{\alpha\beta}}^{k\tau sij} &= \tilde{C}_{45}^k \int_{\Omega^k} N_i N_j d\alpha^k d\beta^k \int_{A^k} F_{\tau,z} F_{s,z} H_{\alpha}^k H_{\beta}^k dz^k + \tilde{C}_{26}^k \int_{\Omega^k} N_{i,\beta} N_{j,\beta} d\alpha^k d\beta^k \int_{A^k} F_{\tau} F_s \frac{H_{\alpha}^k}{H_{\beta}^k} dz^k + \\
 &+ \tilde{C}_{12}^k \int_{\Omega^k} N_{i,\alpha} N_{j,\beta} d\alpha^k d\beta^k \int_{A^k} F_{\tau} F_s dz^k + \tilde{C}_{66}^k \int_{\Omega^k} N_{i,\beta} N_{j,\alpha} d\alpha^k d\beta^k \int_{A^k} F_{\tau} F_s dz^k + \\
 &+ \tilde{C}_{16}^k \int_{\Omega^k} N_{i,\alpha} N_{j,\alpha} d\alpha^k d\beta^k \int_{A^k} F_{\tau} F_s \frac{H_{\beta}^k}{H_{\alpha}^k} dz^k - \frac{\tilde{C}_{45}^k}{R_{\beta}^k} \int_{\Omega^k} N_i N_j d\alpha^k d\beta^k \int_{A^k} F_{\tau,z} F_s H_{\beta}^k dz^k - \\
 &- \frac{\tilde{C}_{45}^k}{R_{\alpha}^k} \int_{\Omega^k} N_i N_j d\alpha^k d\beta^k \int_{A^k} F_{\tau} F_{s,z} H_{\beta}^k dz^k - \frac{\tilde{C}_{45}^k}{R_{\alpha}^k R_{\beta}^k} \int_{\Omega^k} N_i N_j d\alpha^k d\beta^k \int_{A^k} F_{\tau} F_s \frac{H_{\beta}^k}{H_{\alpha}^k} dz^k
 \end{aligned}$$

$$\begin{aligned}
 K_{uu_{\alpha z}}^{k\tau sij} &= \tilde{C}_{45}^k \int_{\Omega^k} N_i N_{j,\beta} d\alpha^k d\beta^k \int_{A^k} F_{\tau,z} F_s H_{\alpha}^k dz^k + \tilde{C}_{55}^k \int_{\Omega^k} N_i N_{j,\alpha} d\alpha^k d\beta^k \int_{A^k} F_{\tau,z} F_s H_{\beta}^k dz^k + \\
 &+ \tilde{C}_{36}^k \int_{\Omega^k} N_{i,\beta} N_j d\alpha^k d\beta^k \int_{A^k} F_{\tau} F_{s,z} H_{\alpha}^k dz^k + \tilde{C}_{13}^k \int_{\Omega^k} N_{i,\alpha} N_j d\alpha^k d\beta^k \int_{A^k} F_{\tau} F_{s,z} H_{\beta}^k dz^k - \\
 &- \frac{\tilde{C}_{45}^k}{R_{\alpha}^k} \int_{\Omega^k} N_i N_{j,\beta} d\alpha^k d\beta^k \int_{A^k} F_{\tau} F_s dz^k - \frac{\tilde{C}_{55}^k}{R_{\alpha}^k} \int_{\Omega^k} N_i N_{j,\alpha} d\alpha^k d\beta^k \int_{A^k} F_{\tau} F_s \frac{H_{\beta}^k}{H_{\alpha}^k} dz^k + \\
 &+ \frac{\tilde{C}_{26}^k}{R_{\beta}^k} \int_{\Omega^k} N_{i,\beta} N_j d\alpha^k d\beta^k \int_{A^k} F_{\tau} F_s \frac{H_{\alpha}^k}{H_{\beta}^k} dz^k + \frac{\tilde{C}_{16}^k}{R_{\alpha}^k} \int_{\Omega^k} N_{i,\beta} N_j d\alpha^k d\beta^k \int_{A^k} F_{\tau} F_s dz^k + \\
 &+ \frac{\tilde{C}_{12}^k}{R_{\beta}^k} \int_{\Omega^k} N_{i,\alpha} N_j d\alpha^k d\beta^k \int_{A^k} F_{\tau} F_s dz^k + \frac{\tilde{C}_{11}^k}{R_{\alpha}^k} \int_{\Omega^k} N_{i,\alpha} N_j d\alpha^k d\beta^k \int_{A^k} F_{\tau} F_s \frac{H_{\beta}^k}{H_{\alpha}^k} dz^k
 \end{aligned}$$

$$\begin{aligned}
 K_{uu_{\beta\alpha}}^{k\tau sij} &= \tilde{C}_{45}^k \int_{\Omega^k} N_i N_j d\alpha^k d\beta^k \int_{A^k} F_{\tau,z} F_{s,z} H_{\alpha}^k H_{\beta}^k dz^k + \tilde{C}_{26}^k \int_{\Omega^k} N_{i,\beta} N_{j,\beta} d\alpha^k d\beta^k \int_{A^k} F_{\tau} F_s \frac{H_{\alpha}^k}{H_{\beta}^k} dz^k + \\
 &+ \tilde{C}_{66}^k \int_{\Omega^k} N_{i,\alpha} N_{j,\beta} d\alpha^k d\beta^k \int_{A^k} F_{\tau} F_s dz^k + \tilde{C}_{12}^k \int_{\Omega^k} N_{i,\beta} N_{j,\alpha} d\alpha^k d\beta^k \int_{A^k} F_{\tau} F_s dz^k + \\
 &+ \tilde{C}_{16}^k \int_{\Omega^k} N_{i,\alpha} N_{j,\alpha} d\alpha^k d\beta^k \int_{A^k} F_{\tau} F_s \frac{H_{\beta}^k}{H_{\alpha}^k} dz^k - \frac{\tilde{C}_{45}^k}{R_{\alpha}^k} \int_{\Omega^k} N_i N_j d\alpha^k d\beta^k \int_{A^k} F_{\tau,z} F_s H_{\beta}^k dz^k - \\
 &- \frac{\tilde{C}_{45}^k}{R_{\beta}^k} \int_{\Omega^k} N_i N_j d\alpha^k d\beta^k \int_{A^k} F_{\tau} F_{s,z} H_{\alpha}^k dz^k + \frac{\tilde{C}_{45}^k}{R_{\alpha}^k R_{\beta}^k} \int_{\Omega^k} N_i N_j d\alpha^k d\beta^k \int_{A^k} F_{\tau} F_s dz^k
 \end{aligned}$$

$$\begin{aligned}
 K_{uu_{\beta\beta}}^{k\tau sij} &= \tilde{C}_{44}^k \int_{\Omega^k} N_i N_j d\alpha^k d\beta^k \int_{A^k} F_{\tau,z} F_{s,z} H_\alpha^k H_\beta^k dz^k + \tilde{C}_{22}^k \int_{\Omega^k} N_{i,\beta} N_{j,\beta} d\alpha^k d\beta^k \int_{A^k} F_\tau F_s \frac{H_\alpha^k}{H_\beta^k} dz^k + \\
 &+ \tilde{C}_{26}^k \int_{\Omega^k} N_{i,\alpha} N_{j,\beta} d\alpha^k d\beta^k \int_{A^k} F_\tau F_s dz^k + \tilde{C}_{26}^k \int_{\Omega^k} N_{i,\beta} N_{j,\alpha} d\alpha^k d\beta^k \int_{A^k} F_\tau F_s dz^k + \\
 &+ \tilde{C}_{66}^k \int_{\Omega^k} N_{i,\alpha} N_{j,\alpha} d\alpha^k d\beta^k \int_{A^k} F_\tau F_s \frac{H_\beta^k}{H_\alpha^k} dz^k - \frac{\tilde{C}_{44}^k}{R_\beta^k} \int_{\Omega^k} N_i N_j d\alpha^k d\beta^k \int_{A^k} F_{\tau,z} F_s H_\alpha^k dz^k - \\
 &- \frac{\tilde{C}_{44}^k}{R_\beta^k} \int_{\Omega^k} N_i N_j d\alpha^k d\beta^k \int_{A^k} F_\tau F_{s,z} H_\alpha^k dz^k + \frac{\tilde{C}_{44}^k}{(R_\beta^k)^2} \int_{\Omega^k} N_i N_j d\alpha^k d\beta^k \int_{A^k} F_\tau F_s \frac{H_\alpha^k}{H_\beta^k} dz^k
 \end{aligned}$$

$$\begin{aligned}
 K_{uu_{\beta z}}^{k\tau sij} &= \tilde{C}_{44}^k \int_{\Omega^k} N_i N_{j,\beta} d\alpha^k d\beta^k \int_{A^k} F_{\tau,z} F_s H_\alpha^k dz^k + \tilde{C}_{45}^k \int_{\Omega^k} N_i N_{j,\alpha} d\alpha^k d\beta^k \int_{A^k} F_{\tau,z} F_s H_\beta^k dz^k + \\
 &+ \tilde{C}_{23}^k \int_{\Omega^k} N_{i,\beta} N_j d\alpha^k d\beta^k \int_{A^k} F_\tau F_{s,z} H_\alpha^k dz^k + \tilde{C}_{36}^k \int_{\Omega^k} N_{i,\alpha} N_j d\alpha^k d\beta^k \int_{A^k} F_\tau F_{s,z} H_\beta^k dz^k - \\
 &- \frac{\tilde{C}_{44}^k}{R_\beta^k} \int_{\Omega^k} N_i N_{j,\beta} d\alpha^k d\beta^k \int_{A^k} F_\tau F_s \frac{H_\alpha^k}{H_\beta^k} dz^k - \frac{\tilde{C}_{45}^k}{R_\beta^k} \int_{\Omega^k} N_i N_{j,\alpha} d\alpha^k d\beta^k \int_{A^k} F_\tau F_s dz^k + \\
 &+ \frac{\tilde{C}_{22}^k}{R_\beta^k} \int_{\Omega^k} N_{i,\beta} N_j d\alpha^k d\beta^k \int_{A^k} F_\tau F_s \frac{H_\alpha^k}{H_\beta^k} dz^k + \frac{\tilde{C}_{12}^k}{R_\alpha^k} \int_{\Omega^k} N_{i,\beta} N_j d\alpha^k d\beta^k \int_{A^k} F_\tau F_s dz^k + \\
 &+ \frac{\tilde{C}_{26}^k}{R_\beta^k} \int_{\Omega^k} N_{i,\alpha} N_j d\alpha^k d\beta^k \int_{A^k} F_\tau F_s dz^k + \frac{\tilde{C}_{16}^k}{R_\alpha^k} \int_{\Omega^k} N_{i,\alpha} N_j d\alpha^k d\beta^k \int_{A^k} F_\tau F_s \frac{H_\beta^k}{H_\alpha^k} dz^k
 \end{aligned}$$

$$\begin{aligned}
 K_{uu_{z\alpha}}^{k\tau sij} &= \tilde{C}_{36}^k \int_{\Omega^k} N_i N_{j,\beta} d\alpha^k d\beta^k \int_{A^k} F_{\tau,z} F_s H_\alpha^k dz^k + \tilde{C}_{13}^k \int_{\Omega^k} N_i N_{j,\alpha} d\alpha^k d\beta^k \int_{A^k} F_{\tau,z} F_s H_\beta^k dz^k + \\
 &+ \tilde{C}_{45}^k \int_{\Omega^k} N_{i,\beta} N_j d\alpha^k d\beta^k \int_{A^k} F_\tau F_{s,z} H_\alpha^k dz^k + \tilde{C}_{55}^k \int_{\Omega^k} N_{i,\alpha} N_j d\alpha^k d\beta^k \int_{A^k} F_\tau F_{s,z} H_\beta^k dz^k + \\
 &+ \frac{\tilde{C}_{26}^k}{R_\beta^k} \int_{\Omega^k} N_i N_{j,\beta} d\alpha^k d\beta^k \int_{A^k} F_\tau F_s \frac{H_\alpha^k}{H_\beta^k} dz^k + \frac{\tilde{C}_{16}^k}{R_\alpha^k} \int_{\Omega^k} N_i N_{j,\beta} d\alpha^k d\beta^k \int_{A^k} F_\tau F_s dz^k + \\
 &+ \frac{\tilde{C}_{12}^k}{R_\beta^k} \int_{\Omega^k} N_i N_{j,\alpha} d\alpha^k d\beta^k \int_{A^k} F_\tau F_s dz^k + \frac{\tilde{C}_{11}^k}{R_\alpha^k} \int_{\Omega^k} N_i N_{j,\alpha} d\alpha^k d\beta^k \int_{A^k} F_\tau F_s \frac{H_\beta^k}{H_\alpha^k} dz^k - \\
 &- \frac{\tilde{C}_{45}^k}{R_\alpha^k} \int_{\Omega^k} N_{i,\beta} N_j d\alpha^k d\beta^k \int_{A^k} F_\tau F_s dz^k - \frac{\tilde{C}_{55}^k}{R_\alpha^k} \int_{\Omega^k} N_{i,\alpha} N_j d\alpha^k d\beta^k \int_{A^k} F_\tau F_s \frac{H_\beta^k}{H_\alpha^k} dz^k
 \end{aligned}$$

$$\begin{aligned}
 K_{uu_{z\beta}}^{k\tau sij} &= \tilde{C}_{23}^k \int_{\Omega^k} N_i N_{j,\beta} d\alpha^k d\beta^k \int_{A^k} F_{\tau,z} F_s H_\alpha^k dz^k + \tilde{C}_{36}^k \int_{\Omega^k} N_i N_{j,\alpha} d\alpha^k d\beta^k \int_{A^k} F_{\tau,z} F_s H_\beta^k dz^k + \\
 &+ \tilde{C}_{44}^k \int_{\Omega^k} N_{i,\beta} N_j d\alpha^k d\beta^k \int_{A^k} F_\tau F_{s,z} H_\alpha^k dz^k + \tilde{C}_{45}^k \int_{\Omega^k} N_{i,\alpha} N_j d\alpha^k d\beta^k \int_{A^k} F_\tau F_{s,z} H_\beta^k dz^k + \\
 &+ \frac{\tilde{C}_{22}^k}{R_\beta^k} \int_{\Omega^k} N_i N_{j,\beta} d\alpha^k d\beta^k \int_{A^k} F_\tau F_s \frac{H_\alpha^k}{H_\beta^k} dz^k + \frac{\tilde{C}_{12}^k}{R_\alpha^k} \int_{\Omega^k} N_i N_{j,\beta} d\alpha^k d\beta^k \int_{A^k} F_\tau F_s dz^k + \\
 &+ \frac{\tilde{C}_{26}^k}{R_\beta^k} \int_{\Omega^k} N_i N_{j,\alpha} d\alpha^k d\beta^k \int_{A^k} F_\tau F_s dz^k + \frac{\tilde{C}_{16}^k}{R_\alpha^k} \int_{\Omega^k} N_i N_{j,\alpha} d\alpha^k d\beta^k \int_{A^k} F_\tau F_s \frac{H_\beta^k}{H_\alpha^k} dz^k - \\
 &- \frac{\tilde{C}_{44}^k}{R_\beta^k} \int_{\Omega^k} N_{i,\beta} N_j d\alpha^k d\beta^k \int_{A^k} F_\tau F_s \frac{H_\alpha^k}{H_\beta^k} dz^k - \frac{\tilde{C}_{45}^k}{R_\beta^k} \int_{\Omega^k} N_{i,\alpha} N_j d\alpha^k d\beta^k \int_{A^k} F_\tau F_s dz^k
 \end{aligned}$$

$$\begin{aligned}
 K_{uu_{zz}}^{k\tau sij} = & \tilde{C}_{33}^k \int_{\Omega^k} N_i N_j d\alpha^k d\beta^k \int_{A^k} F_{\tau,z} F_{s,z} H_\alpha^k H_\beta^k dz^k + \tilde{C}_{44}^k \int_{\Omega^k} N_{i,\beta} N_{j,\beta} d\alpha^k d\beta^k \int_{A^k} F_\tau F_s \frac{H_\alpha^k}{H_\beta^k} dz^k + \\
 & + \tilde{C}_{45}^k \int_{\Omega^k} N_{i,\alpha} N_{j,\beta} d\alpha^k d\beta^k \int_{A^k} F_\tau F_s dz^k + \tilde{C}_{45}^k \int_{\Omega^k} N_{i,\beta} N_{j,\alpha} d\alpha^k d\beta^k \int_{A^k} F_\tau F_s dz^k + \\
 & + \tilde{C}_{55}^k \int_{\Omega^k} N_{i,\alpha} N_{j,\alpha} d\alpha^k d\beta^k \int_{A^k} F_\tau F_s \frac{H_\beta^k}{H_\alpha^k} dz^k + \frac{\tilde{C}_{23}^k}{R_\beta^k} \int_{\Omega^k} N_i N_j d\alpha^k d\beta^k \int_{A^k} F_{\tau,z} F_s H_\alpha^k dz^k + \\
 & + \frac{\tilde{C}_{13}^k}{R_\alpha^k} \int_{\Omega^k} N_i N_j d\alpha^k d\beta^k \int_{A^k} F_{\tau,z} F_s H_\beta^k dz^k + \frac{\tilde{C}_{23}^k}{R_\beta^k} \int_{\Omega^k} N_i N_j d\alpha^k d\beta^k \int_{A^k} F_\tau F_{s,z} H_\alpha^k dz^k + \\
 & + \frac{\tilde{C}_{13}^k}{R_\alpha^k} \int_{\Omega^k} N_i N_j d\alpha^k d\beta^k \int_{A^k} F_\tau F_{s,z} H_\beta^k dz^k + \frac{2\tilde{C}_{12}^k}{R_\alpha^k R_\beta^k} \int_{\Omega^k} N_i N_j d\alpha^k d\beta^k \int_{A^k} F_\tau F_s dz^k + \\
 & + \frac{\tilde{C}_{22}^k}{(R_\beta^k)^2} \int_{\Omega^k} N_i N_j d\alpha^k d\beta^k \int_{A^k} F_\tau F_s \frac{H_\alpha^k}{H_\beta^k} dz^k + \frac{\tilde{C}_{11}^k}{(R_\alpha^k)^2} \int_{\Omega^k} N_i N_j d\alpha^k d\beta^k \int_{A^k} F_\tau F_s \frac{H_\beta^k}{H_\alpha^k} dz^k
 \end{aligned}$$

In the proposed nucleus components the symbols $(N_{i,\alpha}, N_{j,\alpha}, N_{i,\beta}, N_{j,\beta})$ and $(F_{\tau,z}, F_{s,z})$, where comma denote partial derivatives, indicate the following shape and thickness functions derivatives respectively:

$$\left(\frac{\partial N_i}{\partial \alpha}, \frac{\partial N_j}{\partial \alpha}, \frac{\partial N_i}{\partial \beta}, \frac{\partial N_j}{\partial \beta} \right) \text{ and } \left(\frac{\partial F_\tau}{\partial z}, \frac{\partial F_s}{\partial z} \right).$$

The mass matrix $M_{uu}^{k\tau sij}$ nucleus is defined as follows:

$$M_{uu}^{k\tau sij} = \begin{bmatrix} M_{uu_{\alpha\alpha}} & 0 & 0 \\ 0 & M_{uu_{\beta\beta}} & 0 \\ 0 & 0 & M_{uu_{zz}} \end{bmatrix}^{k\tau sij} \quad (5.17)$$

$$M_{uu_{\alpha\alpha}}^{k\tau sij} = M_{uu_{\beta\beta}}^{k\tau sij} = M_{uu_{zz}}^{k\tau sij} = \rho^k \int_{\Omega^k} N_i N_j d\alpha^k d\beta^k \int_{A^k} F_\tau F_s H_\alpha^k H_\beta^k dz^k$$

where ρ^k is the material density of the k^{th} lamina of the multilayer. The external load vector $P_u^{k\tau i}$ nucleus is defined as follows:

$$P_u^{k\tau i} = \begin{bmatrix} P_{u_\alpha} \\ P_{u_\beta} \\ P_{u_z} \end{bmatrix}^{k\tau i} \quad (5.18)$$

If, for example, the external load is a transverse pressure to the reference shell plane, one has:

$$P_{u_\alpha}^{k\tau i} = P_{u_\beta}^{k\tau i} = 0 \quad P_{u_z}^{k\tau i} = P^k(\alpha, \beta) H_\alpha^k H_\beta^k F_\tau \int_{\Omega^k} N_i d\alpha^k d\beta^k$$

where $P^k(\alpha, \beta)$ is the pressure behaviour in the shell reference in-plane directions. If, for example, the external load is a concentrated in-plane load in β direction, one has:

$$P_{u_\alpha}^{k\tau i} = P_{u_z}^{k\tau i} = 0 \quad P_{u_\beta}^{k\tau i} = P^k H_\alpha^k H_\beta^k F_\tau N_i$$

where P^k is the concentrated load magnitude.

5.3.2 PVD for partially coupled thermo-mechanical problems

The variational statement in the case of PVD for partially coupled thermo-mechanical problems in Eq. 4.13, is written in terms of the integrals in the reference plane Ω and the integrals along the thickness of the shell A :

$$\begin{aligned} & \int_{\Omega} \int_A \left(\delta \epsilon_{pG}^T \sigma_{pC} + \delta \epsilon_{nG}^T \sigma_{nC} \right) H_{\alpha} H_{\beta} d\alpha d\beta dz = [\delta L_e + \\ & + \int_{\Omega} \int_A \left(\delta \epsilon_{pG}^T \sigma_{pT} + \delta \epsilon_{nG}^T \sigma_{nT} \right) H_{\alpha} H_{\beta} d\alpha d\beta dz] - \delta L_{in} \end{aligned} \quad (5.19)$$

By considering a laminate of N_l layers, and the integral on the volume V of each layer k as an integral on the in plane domain Ω_k plus the integral in the thickness-direction domain A_k , it is possible to write:

$$\begin{aligned} & \sum_{k=1}^{N_l} \int_{\Omega_k} \int_{A_k} \left(\delta \epsilon_{pG}^{kT} \sigma_{pC}^k + \delta \epsilon_{nG}^{kT} \sigma_{nC}^k \right) H_{\alpha}^k H_{\beta}^k d\alpha^k d\beta^k dz^k = \sum_{k=1}^{N_l} \delta L_e^k + \\ & + \sum_{k=1}^{N_l} \int_{\Omega_k} \int_{A_k} \left(\delta \epsilon_{pG}^{kT} \sigma_{pT}^k + \delta \epsilon_{nG}^{kT} \sigma_{nT}^k \right) H_{\alpha}^k H_{\beta}^k d\alpha^k d\beta^k dz^k - \sum_{k=1}^{N_l} \delta L_{in}^k \end{aligned} \quad (5.20)$$

Substituting the constitutive equations for partially coupled thermo-mechanical problems Eq. 2.20, the strain components computed from displacements by using geometrical relations Eq. 2.58, applying the Unified Formulation Eq. 3.5 and the FEM approximation Eq. 5.1, one obtains the following governing equations in compact form:

$$\delta u_{\tau_i} : \mathbf{K}_{uu}^{k\tau sij} u^{ksj} = \mathbf{P}_u^{k\tau i} + \mathbf{P}_{\theta}^{k\tau i} - \mathbf{M}_{uu}^{k\tau sij} \ddot{u}^{ksj} \quad (5.21)$$

where the stiffness matrix nucleus $\mathbf{K}_{uu}^{k\tau sij}$, the mass matrix nucleus $\mathbf{M}_{uu}^{k\tau sij}$, and the mechanical external load vector nucleus $\mathbf{P}_u^{k\tau i}$ are the same defined for the pure mechanical problems in the previous subsection 5.3.1. The external thermal load vector is $\mathbf{P}_{\theta}^{k\tau i} = \mathbf{K}_{u\theta}^{k\tau i} \theta^{k\tau i}$. In the case of partially coupled thermo-mechanical problems the PVD has only the displacement u as primary variable. The thermal load can be determined by considering a temperature profile θ through the thickness direction imposed a priori [100] or calculated by solving Fourier's heat conduction equation [101], [28]. The two cases of assumed temperature profile (T_a) and calculated temperature profile (T_c) are discussed in Sec. 7.1.

The thermal load matrix $\mathbf{K}_{u\theta}^{k\tau i}$ nucleus is defined as follows:

$$\mathbf{K}_{u\theta}^{k\tau i} = \begin{bmatrix} K_{u\theta_{\alpha}} \\ K_{u\theta_{\beta}} \\ K_{u\theta_z} \end{bmatrix}^{k\tau i} \quad (5.22)$$

$$K_{u\theta_{\alpha}}^{k\tau i} = \tilde{\lambda}_6^k \int_{\Omega^k} N_{i,\beta} d\alpha^k d\beta^k \int_{A^k} F_{\tau} H_{\alpha}^k dz^k + \tilde{\lambda}_1^k \int_{\Omega^k} N_{i,\alpha} d\alpha^k d\beta^k \int_{A^k} F_{\tau} H_{\beta}^k dz^k$$

$$K_{u\theta_{\beta}}^{k\tau i} = \tilde{\lambda}_2^k \int_{\Omega^k} N_{i,\beta} d\alpha^k d\beta^k \int_{A^k} F_{\tau} H_{\alpha}^k dz^k + \tilde{\lambda}_6^k \int_{\Omega^k} N_{i,\alpha} d\alpha^k d\beta^k \int_{A^k} F_{\tau} H_{\beta}^k dz^k$$

$$\begin{aligned}
 K_{u\theta_z}^{k\tau i} = & \tilde{\lambda}_3^k \int_{\Omega^k} N_i d\alpha^k d\beta^k \int_{A^k} F_{\tau,z} H_\alpha^k H_\beta^k dz^k + \frac{\tilde{\lambda}_2^k}{R_\beta^k} \int_{\Omega^k} N_i d\alpha^k d\beta^k \int_{A^k} F_\tau H_\alpha^k dz^k + \\
 & + \frac{\tilde{\lambda}_1^k}{R_\alpha^k} \int_{\Omega^k} N_i d\alpha^k d\beta^k \int_{A^k} F_\tau H_\beta^k dz^k
 \end{aligned}$$

5.3.3 PVD for electro-mechanical problems

The variational statement in the case of PVD for coupled electro-mechanical problems in Eq. 4.15, is written in terms of the integrals in the reference plane Ω and the integrals along the thickness of the shell A :

$$\int_{\Omega} \int_A \left(\delta \epsilon_{pG}^T \sigma_{pC} + \delta \epsilon_{nG}^T \sigma_{nC} - \delta \mathcal{E}_{pG}^T \mathcal{D}_{pC} - \delta \mathcal{E}_{nG}^T \mathcal{D}_{nC} \right) H_\alpha H_\beta d\alpha d\beta dz = \delta L_e - \delta L_{in} \quad (5.23)$$

By considering a laminate of N_l layers, and the integral on the volume V of each layer k as an integral on the in plane domain Ω_k plus the integral in the thickness-direction domain A_k , it is possible to write:

$$\begin{aligned}
 & \sum_{k=1}^{N_l} \int_{\Omega_k} \int_{A_k} \left(\delta \epsilon_{pG}^{kT} \sigma_{pC}^k + \delta \epsilon_{nG}^{kT} \sigma_{nC}^k - \delta \mathcal{E}_{pG}^{kT} \mathcal{D}_{pC}^k - \delta \mathcal{E}_{nG}^{kT} \mathcal{D}_{nC}^k \right) H_\alpha^k H_\beta^k d\alpha^k d\beta^k dz^k = \\
 & = \sum_{k=1}^{N_l} \delta L_e^k - \sum_{k=1}^{N_l} \delta L_{in}^k
 \end{aligned} \quad (5.24)$$

Substituting the constitutive equations for coupled electro-mechanical problems Eq. 2.22, the strain components computed from displacements by using geometrical relations Eq. 2.58, the electric field computed from the electric potential by using electric geometrical relations Eq. 2.60, applying the Unified Formulation Eq. 3.5 and the FEM approximation Eq. 5.1, one obtains the following governing equations in compact form:

$$\begin{aligned}
 \delta u_{\tau_i} : & \mathbf{K}_{uu}^{k\tau sij} \mathbf{u}^{ksj} + \mathbf{K}_{u\Phi}^{k\tau sij} \Phi^{ksj} = \mathbf{P}_u^{k\tau i} - \mathbf{M}_{uu}^{k\tau sij} \ddot{\mathbf{u}}^{ksj} \\
 \delta \Phi_{\tau_i} : & \mathbf{K}_{\Phi u}^{k\tau sij} \mathbf{u}^{ksj} + \mathbf{K}_{\Phi\Phi}^{k\tau sij} \Phi^{ksj} = \mathbf{P}_{\Phi}^{k\tau i}
 \end{aligned} \quad (5.25)$$

where the stiffness matrix nucleus $\mathbf{K}_{uu}^{k\tau sij}$, the mass matrix nucleus $\mathbf{M}_{uu}^{k\tau sij}$, and the mechanical external load vector nucleus $\mathbf{P}_u^{k\tau i}$ are the same defined for the pure mechanical problems in the previous subsection 5.3.1. $\mathbf{K}_{u\Phi}^{k\tau sij}$ and $\mathbf{K}_{\Phi u}^{k\tau sij}$ are a 3×1 and 1×3 matrices, called fundamental nuclei of the electro-mechanical coupling, therefore $\mathbf{K}_{\Phi\Phi}^{k\tau sij}$ is the fundamental nucleus of the pure electric contribution. The explicit expression of the stiffness electro-mechanical coupling matrices and the pure electric nucleus are given below with classical FEM method, and in Appendix A for electro-mechanical nuclei with the reinterpolation of the strain components via the MITC method Eq. 5.5. The pure electric contribution is defined as follows:

$$\begin{aligned}
 \mathbf{K}_{\Phi\Phi}^{k\tau sij} = & -\tilde{\epsilon}_{33}^k \int_{\Omega^k} N_i N_j d\alpha^k d\beta^k \int_{A^k} F_{\tau,z} F_{s,z} H_\alpha^k H_\beta^k dz^k - \tilde{\epsilon}_{22}^k \int_{\Omega^k} N_{i,\beta} N_{j,\beta} d\alpha^k d\beta^k \int_{A^k} F_\tau F_s \frac{H_\alpha^k}{H_\beta^k} dz^k - \\
 & - \tilde{\epsilon}_{12}^k \int_{\Omega^k} N_{i,\alpha} N_{j,\beta} d\alpha^k d\beta^k \int_{A^k} F_\tau F_s dz^k - \tilde{\epsilon}_{12}^k \int_{\Omega^k} N_{i,\beta} N_{j,\alpha} d\alpha^k d\beta^k \int_{A^k} F_\tau F_s dz^k - \\
 & - \tilde{\epsilon}_{11}^k \int_{\Omega^k} N_{i,\alpha} N_{j,\alpha} d\alpha^k d\beta^k \int_{A^k} F_\tau F_s \frac{H_\beta^k}{H_\alpha^k} dz^k
 \end{aligned}$$

The stiffness electro-mechanical coupling matrices $\mathbf{K}_{u\Phi}^{k\tau sij}$ and $\mathbf{K}_{\Phi u}^{k\tau sij}$ are defined as follows:

$$\mathbf{K}_{u\Phi}^{k\tau sij} = \begin{bmatrix} K_{u\Phi_\alpha} \\ K_{u\Phi_\beta} \\ K_{u\Phi_z} \end{bmatrix}^{k\tau sij} \quad (5.26)$$

$$\mathbf{K}_{\Phi u}^{k\tau sij} = [K_{\Phi u_\alpha} \quad K_{\Phi u_\beta} \quad K_{\Phi u_z}]^{k\tau sij} \quad (5.27)$$

Actuation in 3-1 mode

$$\begin{aligned} K_{u\Phi_\alpha}^{k\tau sij} = & \tilde{e}_{25}^k \int_{\Omega^k} N_i N_{j,\beta} d\alpha^k d\beta^k \int_{A^k} F_{\tau,z} F_s H_\alpha^k dz^k + \tilde{e}_{15}^k \int_{\Omega^k} N_i N_{j,\alpha} d\alpha^k d\beta^k \int_{A^k} F_{\tau,z} F_s H_\beta^k dz^k + \\ & + \tilde{e}_{36}^k \int_{\Omega^k} N_{i,\beta} N_j d\alpha^k d\beta^k \int_{A^k} F_\tau F_{s,z} H_\alpha^k dz^k + \tilde{e}_{31}^k \int_{\Omega^k} N_{i,\alpha} N_j d\alpha^k d\beta^k \int_{A^k} F_\tau F_{s,z} H_\beta^k dz^k - \\ & - \frac{\tilde{e}_{25}^k}{R_\alpha^k} \int_{\Omega^k} N_i N_{j,\beta} d\alpha^k d\beta^k \int_{A^k} F_\tau F_s dz^k - \frac{\tilde{e}_{15}^k}{R_\alpha^k} \int_{\Omega^k} N_i N_{j,\alpha} d\alpha^k d\beta^k \int_{A^k} F_\tau F_s \frac{H_\beta^k}{H_\alpha^k} dz^k \end{aligned}$$

$$\begin{aligned} K_{u\Phi_\beta}^{k\tau sij} = & \tilde{e}_{24}^k \int_{\Omega^k} N_i N_{j,\beta} d\alpha^k d\beta^k \int_{A^k} F_{\tau,z} F_s H_\alpha^k dz^k + \tilde{e}_{14}^k \int_{\Omega^k} N_i N_{j,\alpha} d\alpha^k d\beta^k \int_{A^k} F_{\tau,z} F_s H_\beta^k dz^k + \\ & + \tilde{e}_{32}^k \int_{\Omega^k} N_{i,\beta} N_j d\alpha^k d\beta^k \int_{A^k} F_\tau F_{s,z} H_\alpha^k dz^k + \tilde{e}_{36}^k \int_{\Omega^k} N_{i,\alpha} N_j d\alpha^k d\beta^k \int_{A^k} F_\tau F_{s,z} H_\beta^k dz^k - \\ & - \frac{\tilde{e}_{24}^k}{R_\beta^k} \int_{\Omega^k} N_i N_{j,\beta} d\alpha^k d\beta^k \int_{A^k} F_\tau F_s \frac{H_\alpha^k}{H_\beta^k} dz^k - \frac{\tilde{e}_{14}^k}{R_\beta^k} \int_{\Omega^k} N_i N_{j,\alpha} d\alpha^k d\beta^k \int_{A^k} F_\tau F_s dz^k \end{aligned}$$

$$\begin{aligned} K_{u\Phi_z}^{k\tau sij} = & \tilde{e}_{33}^k \int_{\Omega^k} N_i N_j d\alpha^k d\beta^k \int_{A^k} F_{\tau,z} F_{s,z} H_\alpha^k H_\beta^k dz^k + \frac{\tilde{e}_{32}^k}{R_\beta^k} \int_{\Omega^k} N_i N_j d\alpha^k d\beta^k \int_{A^k} F_\tau F_{s,z} H_\alpha^k dz^k + \\ & + \frac{\tilde{e}_{31}^k}{R_\alpha^k} \int_{\Omega^k} N_i N_j d\alpha^k d\beta^k \int_{A^k} F_\tau F_{s,z} H_\beta^k dz^k + \tilde{e}_{24}^k \int_{\Omega^k} N_{i,\beta} N_{j,\beta} d\alpha^k d\beta^k \int_{A^k} F_\tau F_s \frac{H_\alpha^k}{H_\beta^k} dz^k + \\ & + \tilde{e}_{25}^k \int_{\Omega^k} N_{i,\alpha} N_{j,\beta} d\alpha^k d\beta^k \int_{A^k} F_\tau F_s dz^k + \tilde{e}_{14}^k \int_{\Omega^k} N_{i,\beta} N_{j,\alpha} d\alpha^k d\beta^k \int_{A^k} F_\tau F_s dz^k + \\ & + \tilde{e}_{15}^k \int_{\Omega^k} N_{i,\alpha} N_{j,\alpha} d\alpha^k d\beta^k \int_{A^k} F_\tau F_s \frac{H_\beta^k}{H_\alpha^k} dz^k \end{aligned}$$

$$\begin{aligned} K_{\Phi u_\alpha}^{k\tau sij} = & \tilde{e}_{36}^k \int_{\Omega^k} N_i N_{j,\beta} d\alpha^k d\beta^k \int_{A^k} F_{\tau,z} F_s H_\alpha^k dz^k + \tilde{e}_{31}^k \int_{\Omega^k} N_i N_{j,\alpha} d\alpha^k d\beta^k \int_{A^k} F_{\tau,z} F_s H_\beta^k dz^k + \\ & + \tilde{e}_{25}^k \int_{\Omega^k} N_{i,\beta} N_j d\alpha^k d\beta^k \int_{A^k} F_\tau F_{s,z} H_\alpha^k dz^k + \tilde{e}_{15}^k \int_{\Omega^k} N_{i,\alpha} N_j d\alpha^k d\beta^k \int_{A^k} F_\tau F_{s,z} H_\beta^k dz^k - \\ & - \frac{\tilde{e}_{25}^k}{R_\alpha^k} \int_{\Omega^k} N_{i,\beta} N_j d\alpha^k d\beta^k \int_{A^k} F_\tau F_s dz^k - \frac{\tilde{e}_{15}^k}{R_\alpha^k} \int_{\Omega^k} N_{i,\alpha} N_j d\alpha^k d\beta^k \int_{A^k} F_\tau F_s \frac{H_\beta^k}{H_\alpha^k} dz^k \end{aligned}$$

$$\begin{aligned}
 K_{\Phi u_\beta}^{k\tau sij} &= \tilde{e}_{32}^k \int_{\Omega^k} N_i N_{j,\beta} d\alpha^k d\beta^k \int_{A^k} F_{\tau,z} F_s H_\alpha^k dz^k + \tilde{e}_{36}^k \int_{\Omega^k} N_i N_{j,\alpha} d\alpha^k d\beta^k \int_{A^k} F_{\tau,z} F_s H_\beta^k dz^k + \\
 &+ \tilde{e}_{24}^k \int_{\Omega^k} N_{i,\beta} N_j d\alpha^k d\beta^k \int_{A^k} F_\tau F_{s,z} H_\alpha^k dz^k + \tilde{e}_{14}^k \int_{\Omega^k} N_{i,\alpha} N_j d\alpha^k d\beta^k \int_{A^k} F_\tau F_{s,z} H_\beta^k dz^k - \\
 &- \frac{\tilde{e}_{24}^k}{R_\beta^k} \int_{\Omega^k} N_{i,\beta} N_j d\alpha^k d\beta^k \int_{A^k} F_\tau F_s \frac{H_\alpha^k}{H_\beta^k} dz^k - \frac{\tilde{e}_{14}^k}{R_\beta^k} \int_{\Omega^k} N_{i,\alpha} N_j d\alpha^k d\beta^k \int_{A^k} F_\tau F_s dz^k
 \end{aligned}$$

$$\begin{aligned}
 K_{\Phi u_z}^{k\tau sij} &= \tilde{e}_{33}^k \int_{\Omega^k} N_i N_j d\alpha^k d\beta^k \int_{A^k} F_{\tau,z} F_{s,z} H_\alpha^k H_\beta^k dz^k + \frac{\tilde{e}_{32}^k}{R_\beta^k} \int_{\Omega^k} N_i N_j d\alpha^k d\beta^k \int_{A^k} F_{\tau,z} F_s H_\alpha^k dz^k + \\
 &+ \frac{\tilde{e}_{31}^k}{R_\alpha^k} \int_{\Omega^k} N_i N_j d\alpha^k d\beta^k \int_{A^k} F_{\tau,z} F_s H_\beta^k dz^k + \tilde{e}_{24}^k \int_{\Omega^k} N_{i,\beta} N_{j,\beta} d\alpha^k d\beta^k \int_{A^k} F_\tau F_s \frac{H_\alpha^k}{H_\beta^k} dz^k + \\
 &+ \tilde{e}_{14}^k \int_{\Omega^k} N_{i,\alpha} N_{j,\beta} d\alpha^k d\beta^k \int_{A^k} F_\tau F_s dz^k + \tilde{e}_{25}^k \int_{\Omega^k} N_{i,\beta} N_{j,\alpha} d\alpha^k d\beta^k \int_{A^k} F_\tau F_s dz^k + \\
 &+ \tilde{e}_{15}^k \int_{\Omega^k} N_{i,\alpha} N_{j,\alpha} d\alpha^k d\beta^k \int_{A^k} F_\tau F_s \frac{H_\beta^k}{H_\alpha^k} dz^k
 \end{aligned}$$

Actuation in 1-5 mode

$$\begin{aligned}
 K_{u\Phi_\alpha}^{k\tau sij} &= \tilde{e}_{35}^k \int_{\Omega^k} N_i N_j d\alpha^k d\beta^k \int_{A^k} F_{\tau,z} F_{s,z} H_\alpha^k H_\beta^k dz^k - \frac{\tilde{e}_{35}^k}{R_\alpha^k} \int_{\Omega^k} N_i N_j d\alpha^k d\beta^k \int_{A^k} F_\tau F_{s,z} H_\beta^k dz^k + \\
 &+ \tilde{e}_{26}^k \int_{\Omega^k} N_{i,\beta} N_{j,\beta} d\alpha^k d\beta^k \int_{A^k} F_\tau F_s \frac{H_\alpha^k}{H_\beta^k} dz^k + \tilde{e}_{21}^k \int_{\Omega^k} N_{i,\alpha} N_{j,\beta} d\alpha^k d\beta^k \int_{A^k} F_\tau F_s dz^k + \\
 &+ \tilde{e}_{16}^k \int_{\Omega^k} N_{i,\beta} N_{j,\alpha} d\alpha^k d\beta^k \int_{A^k} F_\tau F_s dz^k + \tilde{e}_{11}^k \int_{\Omega^k} N_{i,\alpha} N_{j,\alpha} d\alpha^k d\beta^k \int_{A^k} F_\tau F_s \frac{H_\beta^k}{H_\alpha^k} dz^k
 \end{aligned}$$

$$\begin{aligned}
 K_{u\Phi_\beta}^{k\tau sij} &= \tilde{e}_{34}^k \int_{\Omega^k} N_i N_j d\alpha^k d\beta^k \int_{A^k} F_{\tau,z} F_{s,z} H_\alpha^k H_\beta^k dz^k - \frac{\tilde{e}_{34}^k}{R_\beta^k} \int_{\Omega^k} N_i N_j d\alpha^k d\beta^k \int_{A^k} F_\tau F_{s,z} H_\alpha^k dz^k + \\
 &+ \tilde{e}_{22}^k \int_{\Omega^k} N_{i,\beta} N_{j,\beta} d\alpha^k d\beta^k \int_{A^k} F_\tau F_s \frac{H_\alpha^k}{H_\beta^k} dz^k + \tilde{e}_{26}^k \int_{\Omega^k} N_{i,\alpha} N_{j,\beta} d\alpha^k d\beta^k \int_{A^k} F_\tau F_s dz^k + \\
 &+ \tilde{e}_{12}^k \int_{\Omega^k} N_{i,\beta} N_{j,\alpha} d\alpha^k d\beta^k \int_{A^k} F_\tau F_s dz^k + \tilde{e}_{16}^k \int_{\Omega^k} N_{i,\alpha} N_{j,\alpha} d\alpha^k d\beta^k \int_{A^k} F_\tau F_s \frac{H_\beta^k}{H_\alpha^k} dz^k
 \end{aligned}$$

$$\begin{aligned}
 K_{u\Phi_z}^{k\tau sij} &= \tilde{e}_{23}^k \int_{\Omega^k} N_i N_{j,\beta} d\alpha^k d\beta^k \int_{A^k} F_{\tau,z} F_s H_\alpha^k dz^k + \tilde{e}_{13}^k \int_{\Omega^k} N_i N_{j,\alpha} d\alpha^k d\beta^k \int_{A^k} F_{\tau,z} F_s H_\beta^k dz^k + \\
 &+ \tilde{e}_{34}^k \int_{\Omega^k} N_{i,\beta} N_j d\alpha^k d\beta^k \int_{A^k} F_\tau F_{s,z} H_\alpha^k dz^k + \tilde{e}_{35}^k \int_{\Omega^k} N_{i,\alpha} N_j d\alpha^k d\beta^k \int_{A^k} F_\tau F_{s,z} H_\beta^k dz^k + \\
 &+ \frac{\tilde{e}_{22}^k}{R_\beta^k} \int_{\Omega^k} N_i N_{j,\beta} d\alpha^k d\beta^k \int_{A^k} F_\tau F_s \frac{H_\alpha^k}{H_\beta^k} dz^k + \frac{\tilde{e}_{21}^k}{R_\alpha^k} \int_{\Omega^k} N_i N_{j,\beta} d\alpha^k d\beta^k \int_{A^k} F_\tau F_s dz^k + \\
 &+ \frac{\tilde{e}_{12}^k}{R_\beta^k} \int_{\Omega^k} N_i N_{j,\alpha} d\alpha^k d\beta^k \int_{A^k} F_\tau F_s dz^k + \frac{\tilde{e}_{11}^k}{R_\alpha^k} \int_{\Omega^k} N_i N_{j,\alpha} d\alpha^k d\beta^k \int_{A^k} F_\tau F_s \frac{H_\beta^k}{H_\alpha^k} dz^k
 \end{aligned}$$

$$\begin{aligned}
 K_{\Phi u_\alpha}^{k\tau s i j} &= \tilde{e}_{35}^k \int_{\Omega^k} N_i N_j d\alpha^k d\beta^k \int_{A^k} F_{\tau,z} F_{s,z} H_\alpha^k H_\beta^k dz^k - \frac{\tilde{e}_{35}^k}{R_\alpha^k} \int_{\Omega^k} N_i N_j d\alpha^k d\beta^k \int_{A^k} F_{\tau,z} F_s H_\beta^k dz^k + \\
 &+ \tilde{e}_{26}^k \int_{\Omega^k} N_{i,\beta} N_{j,\beta} d\alpha^k d\beta^k \int_{A^k} F_\tau F_s \frac{H_\alpha^k}{H_\beta^k} dz^k + \tilde{e}_{16}^k \int_{\Omega^k} N_{i,\alpha} N_{j,\beta} d\alpha^k d\beta^k \int_{A^k} F_\tau F_s dz^k + \\
 &+ \tilde{e}_{21}^k \int_{\Omega^k} N_{i,\beta} N_{j,\alpha} d\alpha^k d\beta^k \int_{A^k} F_\tau F_s dz^k + \tilde{e}_{11}^k \int_{\Omega^k} N_{i,\alpha} N_{j,\alpha} d\alpha^k d\beta^k \int_{A^k} F_\tau F_s \frac{H_\beta^k}{H_\alpha^k} dz^k
 \end{aligned}$$

$$\begin{aligned}
 K_{\Phi u_\beta}^{k\tau s i j} &= \tilde{e}_{34}^k \int_{\Omega^k} N_i N_j d\alpha^k d\beta^k \int_{A^k} F_{\tau,z} F_{s,z} H_\alpha^k H_\beta^k dz^k - \frac{\tilde{e}_{34}^k}{R_\beta^k} \int_{\Omega^k} N_i N_j d\alpha^k d\beta^k \int_{A^k} F_{\tau,z} F_s H_\alpha^k dz^k + \\
 &+ \tilde{e}_{22}^k \int_{\Omega^k} N_{i,\beta} N_{j,\beta} d\alpha^k d\beta^k \int_{A^k} F_\tau F_s \frac{H_\alpha^k}{H_\beta^k} dz^k + \tilde{e}_{12}^k \int_{\Omega^k} N_{i,\alpha} N_{j,\beta} d\alpha^k d\beta^k \int_{A^k} F_\tau F_s dz^k + \\
 &+ \tilde{e}_{26}^k \int_{\Omega^k} N_{i,\beta} N_{j,\alpha} d\alpha^k d\beta^k \int_{A^k} F_\tau F_s dz^k + \tilde{e}_{16}^k \int_{\Omega^k} N_{i,\alpha} N_{j,\alpha} d\alpha^k d\beta^k \int_{A^k} F_\tau F_s \frac{H_\beta^k}{H_\alpha^k} dz^k
 \end{aligned}$$

$$\begin{aligned}
 K_{\Phi u_z}^{k\tau s i j} &= \tilde{e}_{34}^k \int_{\Omega^k} N_i N_{j,\beta} d\alpha^k d\beta^k \int_{A^k} F_{\tau,z} F_s H_\alpha^k dz^k + \tilde{e}_{35}^k \int_{\Omega^k} N_i N_{j,\alpha} d\alpha^k d\beta^k \int_{A^k} F_{\tau,z} F_s H_\beta^k dz^k + \\
 &+ \tilde{e}_{23}^k \int_{\Omega^k} N_{i,\beta} N_j d\alpha^k d\beta^k \int_{A^k} F_\tau F_{s,z} H_\alpha^k dz^k + \tilde{e}_{13}^k \int_{\Omega^k} N_{i,\alpha} N_j d\alpha^k d\beta^k \int_{A^k} F_\tau F_{s,z} H_\beta^k dz^k + \\
 &+ \frac{\tilde{e}_{22}^k}{R_\beta^k} \int_{\Omega^k} N_{i,\beta} N_j d\alpha^k d\beta^k \int_{A^k} F_\tau F_s \frac{H_\alpha^k}{H_\beta^k} dz^k + \frac{\tilde{e}_{21}^k}{R_\alpha^k} \int_{\Omega^k} N_{i,\beta} N_j d\alpha^k d\beta^k \int_{A^k} F_\tau F_s dz^k + \\
 &+ \frac{\tilde{e}_{12}^k}{R_\beta^k} \int_{\Omega^k} N_{i,\alpha} N_j d\alpha^k d\beta^k \int_{A^k} F_\tau F_s dz^k + \frac{\tilde{e}_{11}^k}{R_\alpha^k} \int_{\Omega^k} N_{i,\alpha} N_j d\alpha^k d\beta^k \int_{A^k} F_\tau F_s \frac{H_\beta^k}{H_\alpha^k} dz^k
 \end{aligned}$$

Chapter 6

Results on Mechanical Problems

This chapter discusses the results for the pure mechanical analysis of multilayered composite and sandwich plates/shells. First, some preliminary assessments are given in order to demonstrate the capability of the refined and advanced models to obtain the quasi-3D results. Then, some new benchmarks are proposed. Therefore different polynomials for the thickness function are employed, as trigonometric, exponential and miscellaneous polynomials.

6.1 Doubly-Curved Shell

6.1.1 Assessment

In order to assess the robustness of the present shell element and show its efficiency in the analysis of laminated composites, some numerical results for simply-supported cross-ply square shells are presented. These are compared with the 3D solutions given in [125] and the solutions of the higher-order shell theory (HSDT₁) discussed in [126]. The analytical solution $LW4_a$ is also provided as reference solution. This is obtained using the $LW4$ theory and the Navier's method to solve the governing equations in closed form. In [127], it was demonstrated that the $LW4_a$ solutions can be considered quasi-3D.

Being a the length of the edge and $R = R_\alpha = R_\beta$ the curvature radius, deep ($R/a = 1, 2$) and shallow ($R/a = 5$) shells are examined. The lamination schemes ($0^\circ, 90^\circ \dots$) are of symmetric and anti-symmetric type with number of layers $N_l = 3, 5$ and $N_l = 4$, respectively. The shell is subjected to a bi-sinusoidal pressure applied at the top surface $p_z^+ = \hat{p}_z^+ \sin(\pi\alpha/a)\sin(\pi\beta/a)$, where m, n are the numbers of half-waves. The lamina material properties and the load parameters are given in Table 6.1.

Table 6.1: Elastic and Geometrical properties

<i>Spherical panel</i>	
E_{11}/E_{22}	25
$G_{12}/E_{22} = G_{13}/E_{22}$	0.5
G_{23}/E_{22}	0.2
$\nu_{12} = \nu_{13} = \nu_{23}$	0.25
\hat{p}_z^+	1
m, n	1,1

The following nondimensionalized deflections and stresses are considered:

$$\begin{aligned} \bar{w} = w(a/2, a/2) \frac{100 E_{22} h^3}{a^4 \hat{p}_z^+} ; \quad \bar{\sigma}_{\alpha\alpha} = \sigma_{\alpha\alpha}(a/2, a/2) \frac{h^2}{a^2 \hat{p}_z^+} \\ \bar{\sigma}_{\alpha z} = \sigma_{\alpha z}(0, a/2) \frac{h}{a \hat{p}_z^+} ; \quad \bar{\sigma}_{zz} = \sigma_{zz}(a/2, a/2) \frac{1}{\hat{p}_z^+} \end{aligned} \quad (6.1)$$

For brevity reasons, the convergence study is here omitted, but it has been verified that a mesh (9×9) permits the convergence solution to be reached. All the results are calculated using this mesh. Tables 6.2-6.4 present results in terms of transversal displacement \bar{w} for the three lamination cases. Different thickness ratios a/h and curvature ratios R/a are considered and various theories contained in the Unified Formulation are used. One can note that, in thin shells ($a/h = 100$), all the theories, comprising CLT and FSDT, match the reference solutions (3D, $HSDT_1$ and $LW4_a$). While, increasing the thickness, higher-order models are required. In particular, higher-order zig-zag models work better than ESL ones and LW better than zig-zag. The $LW4$ theory is able to reproduce the reference solutions in all the cases considered. There are no differences in the behavior of the element between deep and shallow shells because, in the formulation of the models, no assumptions have been made about the curvature. The same considerations can be made considering both symmetric and anti-symmetric laminations.

Table 6.2: Transversal displacement $\bar{w}(z = 0)$. Three-layered shell, symmetric lamination ($0^\circ, 90^\circ, 0^\circ$).

	$R/a = 1$			$R/a = 2$			$R/a = 5$		
	5	10	100	5	10	100	5	10	100
3D [125]	—	—	—	1.482	0.6087	—	1.549	0.7325	—
$HSDT_1$ [126]	1.208	0.3761	—	1.482	0.6090	—	1.546	0.7340	—
$LW4_a$	1.2081	0.3766	0.0054	1.4824	0.6087	0.0208	1.5494	0.7325	0.1036
a/h	5	10	100	5	10	100	5	10	100
LW4	1.2081	0.3767	0.0054	1.4824	0.6087	0.0208	1.5494	0.7325	0.1036
LW1	1.1839	0.3732	0.0054	1.4413	0.5990	0.0208	1.5019	0.7179	0.1036
ET3Z	1.2015	0.3760	0.0054	1.4772	0.6081	0.0208	1.5452	0.7322	0.1036
ET4	1.1656	0.3693	0.0054	1.4038	0.5858	0.0208	1.4564	0.6974	0.1036
ET2	1.0342	0.3504	0.0054	1.1776	0.5315	0.0208	1.1961	0.6174	0.1036
FSDT	1.0491	0.3507	0.0054	1.1968	0.5326	0.0208	1.2129	0.6191	0.1036
CLT	0.5148	0.2947	0.0054	0.4748	0.3934	0.0208	0.4487	0.4295	0.1034

Table 6.3: Transversal displacement $\bar{w}(z = 0)$. Four-layered shell, antisymmetric lamination ($0^\circ, 90^\circ, 0^\circ, 90^\circ$).

	$R/a = 1$			$R/a = 2$			$R/a = 5$		
3D [125]	–	–	–	1.434	0.6128	–	1.495	0.7408	–
$HSDT_1$ [126]	1.179	0.3748	–	1.433	0.6085	–	1.488	0.7345	–
$LW4_a$	1.1768	0.3763	0.0054	1.4344	0.6128	0.0208	1.4951	0.7408	0.1067
a/h	5	10	100	5	10	100	5	10	100
LW4	1.1769	0.3763	0.0054	1.4343	0.6128	0.0208	1.4951	0.7408	0.1067
ET3Z	1.1650	0.3746	0.0054	1.4152	0.6079	0.0208	1.4733	0.7333	0.1067
ET4	1.1190	0.3689	0.0054	1.3295	0.5899	0.0208	1.3719	0.7054	0.1067
FSDT	0.9943	0.3543	0.0054	1.1096	0.5452	0.0208	1.1154	0.6383	0.1067
CLT	0.5823	0.3173	0.0054	0.5522	0.4478	0.0208	0.5261	0.5016	0.1066

Table 6.4: Transversal displacement $\bar{w}(z = 0)$. Five-layered shell, symmetric lamination ($0^\circ, 90^\circ, 0^\circ, 90^\circ, 0^\circ$).

	$R/a = 1$			$R/a = 2$			$R/a = 5$		
3D [125]	–	–	–	1.376	0.5671	–	1.417	0.6707	–
$HSDT_1$ [126]	1.151	0.3615	–	1.379	0.5670	–	1.425	0.6708	–
$LW4_a$	1.1397	0.3617	0.0054	1.3674	0.5671	0.0207	1.4165	0.6707	0.1032
a/h	5	10	100	5	10	100	5	10	100
LW4	1.1397	0.3617	0.0054	1.3674	0.5671	0.0207	1.4165	0.6706	0.1032
ET3Z	1.1315	0.3608	0.0054	1.3543	0.5647	0.0207	1.4017	0.6672	0.1032
ET4	1.0476	0.3504	0.0054	1.2052	0.5341	0.0207	1.2286	0.6219	0.1032
FSDT	0.9794	0.3413	0.0054	1.0873	0.5090	0.0207	1.0910	0.5862	0.1032
CLT	0.5133	0.2937	0.0054	0.4744	0.3929	0.0207	0.4486	0.4294	0.1031

In the symmetric case with $N_l = 3$, the normal stress $\bar{\sigma}_{\alpha\alpha}$ is also evaluated (see Table 6.5). The behavior of the element is the same. Higher-order models are necessary in the analysis of thick shells. The $LW4$ theory doesn't match perfectly the reference solutions but provides very good results. The shear stress $\bar{\sigma}_{\alpha z}$ is reported in Table 6.6 for the different laminations and considering $R/a = 2$. Good results are obtained also in this case using higher-order layer-wise theories, especially for thick shells. A slightly higher error can be observed only in the case of antisymmetric lamination. Figures 6.1a-6.2b and 6.3a-6.4b show the distributions along the thickness of the shear stress $\bar{\sigma}_{\alpha z}$ and the normal stress $\bar{\sigma}_{zz}$ for different combinations of R/a and a/h in the symmetric $N_l = 3$ and the antisymmetric $N_l = 4$ case. In all the cases, one can note that only the layer-wise model is able to fulfill the continuity conditions of the transverse stresses at the interface between layers.

Table 6.5: In-plane stress $\bar{\sigma}_{\alpha\alpha}(z = -h/2)$. Three-layered shell, symmetric lamination $(0^\circ, 90^\circ, 0^\circ)$.

	$R/a = 1$			$R/a = 2$			$R/a = 5$		
HSDT ₁ [126]	-0.4699	–	–	-0.6706	–	–	-0.7399	–	–
$LW4_a$	-0.5080	-0.2362	0.0012	-0.6740	-0.4433	-0.0112	-0.7128	-0.5616	-0.1003
a/h	5	10	100	5	10	100	5	10	100
LW4	-0.5055	-0.2351	0.0012	-0.6706	-0.4411	-0.0112	-0.7092	-0.5588	-0.0999
LW1	-0.4579	-0.2300	0.0012	-0.6079	-0.4291	-0.0112	-0.6432	-0.5415	-0.1001
ET3Z	-0.5042	-0.2355	0.0012	-0.6692	-0.4415	-0.0112	-0.7080	-0.5593	-0.0999
ET4	-0.5144	-0.2418	0.0012	-0.6661	-0.4433	-0.0112	-0.6972	-0.5543	-0.0999
ET2	-0.3464	-0.2306	0.0012	-0.4446	-0.4048	-0.0112	-0.4644	-0.4938	-0.1000
FSDT	-0.3592	-0.2293	0.0012	-0.4569	-0.4037	-0.0112	-0.4769	-0.4941	-0.1000
CLT	-0.6317	-0.3149	0.0012	-0.6031	-0.4681	-0.0114	-0.5659	-0.5281	-0.1005

Table 6.6: Shear stress $\bar{\sigma}_{\alpha z}$ evaluated in $(z = 0)$ for $N_l = 3, 5$ and $(z = -h/8)$ for $N_l = 4$. Curvature ratio $R/a = 2$.

	$N_l = 3$			$N_l = 4$			$N_l = 5$		
$LW4_a$	0.2744	0.2821	0.0184	0.2380	0.2090	0.0077	0.2654	0.2378	0.0145
a/h	5	10	100	5	10	100	5	10	100
LW4	0.2771	0.2849	0.0186	0.2168	0.1663	0.0112	0.2681	0.2401	0.0146
LW1	0.2791	0.2863	0.0186	0.1972	0.1557	0.0107	0.2590	0.2351	0.0143
ET3Z	0.2787	0.2881	0.0188	0.2005	0.1587	0.0113	0.2729	0.2487	0.0153
ET4	0.2175	0.2114	0.0132	0.2508	0.2040	0.0146	0.4335	0.4570	0.1176
ET2	0.1266	0.1145	0.0067	0.2211	0.1826	0.0138	0.2740	0.2509	0.0148
FSDT	0.1270	0.1141	0.0067	0.2363	0.1977	0.0141	0.2752	0.2502	0.0147

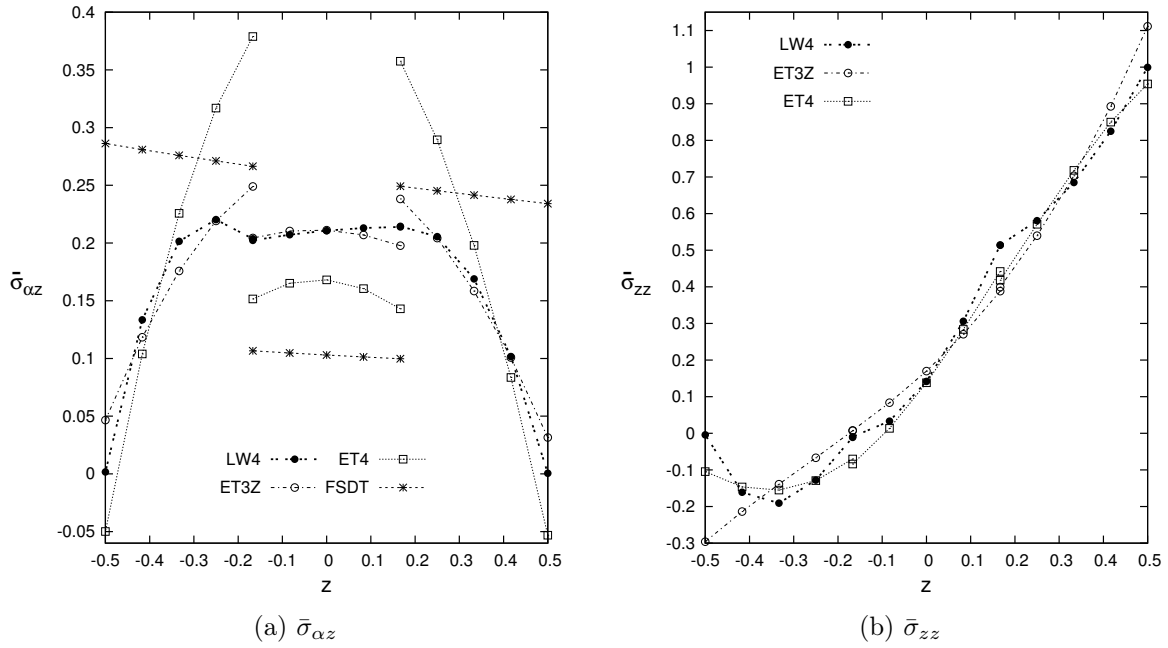


Figure 6.1: Three-layered shell, symmetric lamination, $R/a = 1$ and $a/h = 5$. Transverse shear and normal stresses $\bar{\sigma}_{\alpha z}$, $\bar{\sigma}_{zz}$.

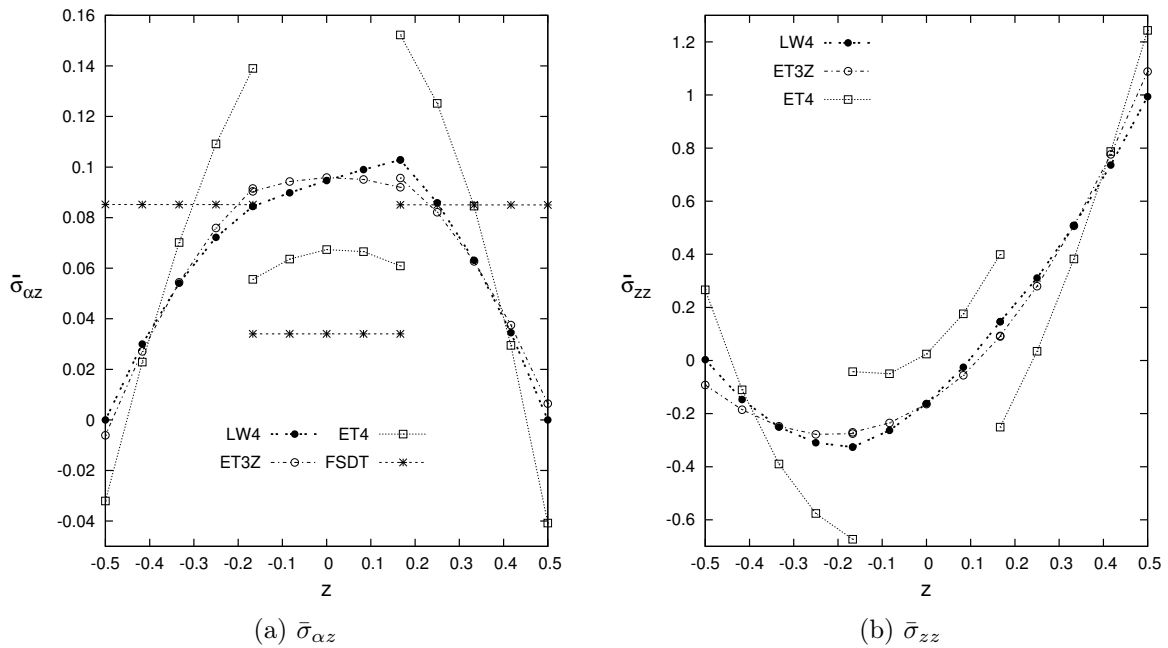


Figure 6.2: Three-layered shell, symmetric lamination, $R/a = 5$ and $a/h = 100$. Transverse shear and normal stresses $\bar{\sigma}_{\alpha z}$, $\bar{\sigma}_{zz}$.

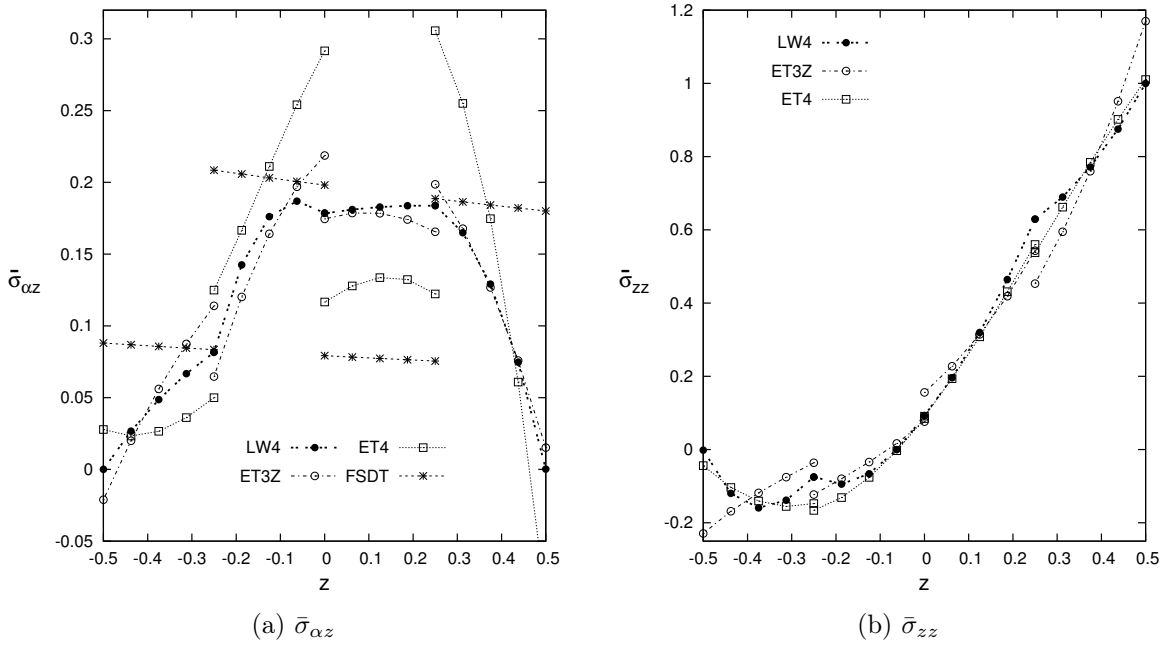


Figure 6.3: Four-layered shell, symmetric lamination, $R/a = 1$ and $a/h = 5$. Transverse shear and normal stresses $\bar{\sigma}_{\alpha z}$, $\bar{\sigma}_{zz}$.

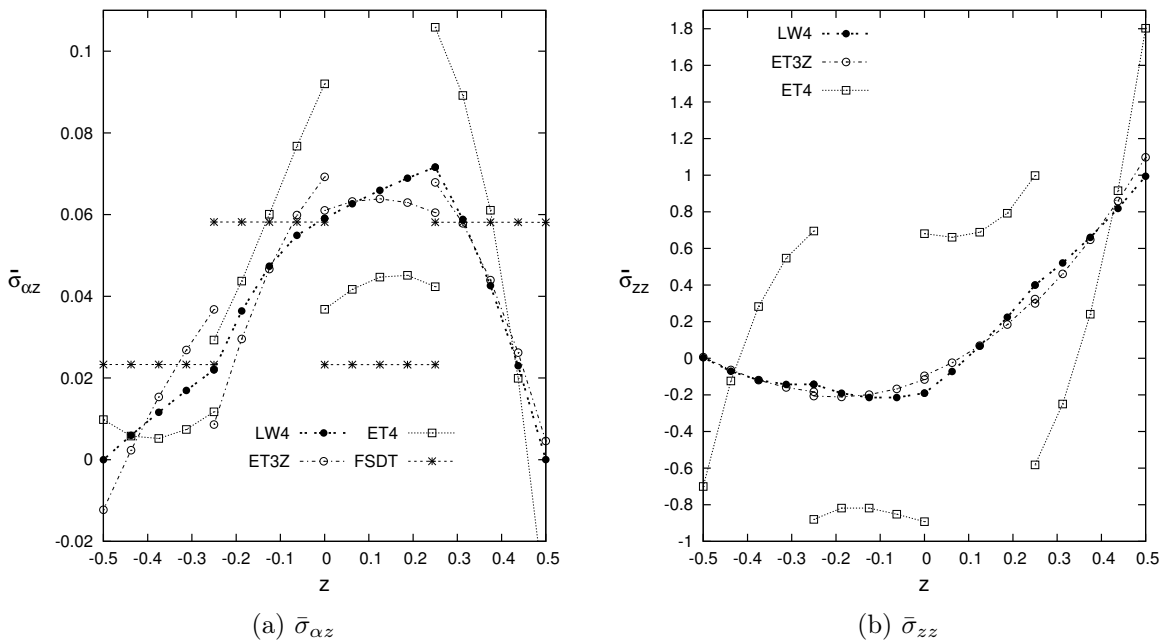


Figure 6.4: Four-layered shell, symmetric lamination, $R/a = 5$ and $a/h = 100$. Transverse shear and normal stresses $\bar{\sigma}_{\alpha z}$, $\bar{\sigma}_{zz}$.

6.1.2 FEM benchmark solutions

Similar spherical shells are analyzed, considering three new problems that have not reference analytical solutions:

1. Shell with anti-symmetric lamination ($45^\circ / -45^\circ$) under bi-sinusoidal load and simply-supported boundary conditions.
2. Shell with clamped-free boundary conditions: edges parallel to β -direction clamped

and those parallel to α -direction free. The lamination is $(0^\circ, 90^\circ, 0^\circ)$ and the load is bi-sinusoidal.

3. Shell subjected to a concentrated load (intensity $P = a^2$), applied in the central point at the top surface, with $(0^\circ, 90^\circ, 0^\circ)$ lamination and simply-supported boundary conditions.

The material properties and load parameters are given in Table 6.1. The solutions are calculated using a (9×9) mesh and the LW4 model. In order to get more accurate results, two fictitious layers are considered per each layer.

In Tables 6.7-6.9, the results are given in terms of w , $\sigma_{\alpha\alpha}$, $\sigma_{\beta\beta}$, $\sigma_{\alpha\beta}$, $\sigma_{\alpha z}$, $\sigma_{\beta z}$ and σ_{zz} for different thickness ratios a/h and curvature ratios R/a . Depending on the problem analyzed, these quantities are evaluated in different points. For problem 1, one has:

$$\begin{aligned}
 w &\rightarrow (a/2, a/2, 0) \\
 \sigma_{\alpha\alpha}, \sigma_{\beta\beta} &\rightarrow (a/2, a/2, \pm h/2) \\
 \sigma_{\alpha\beta} &\rightarrow (0, 0, \pm h/2) \\
 \sigma_{\alpha z} &\rightarrow (0, a/2, -h/12) \\
 \sigma_{\beta z} &\rightarrow (a/2, 0, h/12) \\
 \sigma_{zz} &\rightarrow (a/2, a/2, h/12)
 \end{aligned} \tag{6.2}$$

for problem 2:

$$\begin{aligned}
 w &\rightarrow (a/2, a/2, 0) \\
 \sigma_{\alpha\alpha}, \sigma_{\beta\beta} &\rightarrow (a/2, a/2, \pm h/2) \\
 \sigma_{\alpha\beta} &\rightarrow (0, 0, \pm h/2) \\
 \sigma_{\alpha z} &\rightarrow (0, a/2, -h/4) \\
 \sigma_{\beta z} &\rightarrow (a/2, 0, h/4) \\
 \sigma_{zz} &\rightarrow (a/2, a/2, h/4)
 \end{aligned} \tag{6.3}$$

and for problem 3:

$$\begin{aligned}
 w &\rightarrow (a/2, a/2, 0) \\
 \sigma_{\alpha\alpha}, \sigma_{\beta\beta} &\rightarrow (a/2, a/2, \pm h/2) \\
 \sigma_{\alpha\beta} &\rightarrow (0, 0, \pm h/2) \\
 \sigma_{\alpha z} &\rightarrow (0, a/2, -h/4) \\
 \sigma_{\beta z} &\rightarrow (a/2, 0, h/4) \\
 \sigma_{zz} &\rightarrow (a/2, a/2, h/4)
 \end{aligned} \tag{6.4}$$

Figures 6.5a-6.6b and 6.7a-6.8b show the distributions along the thickness of the shear stress $\sigma_{\alpha z}$ and the normal stress σ_{zz} for different combinations of thickness ratio a/h and curvature ratio R/a for problem 1 and 2, respectively. For comparison purposes, also the ET3Z solution is represented. As in the assessment analysis, the ET3Z model is not able to satisfy the continuity conditions of transverse stresses at the interface between layers. In some cases, neither the LW4 model is efficient in this sense. This fact suggests the use of mixed models based on Reissner's Mixed Variational Theorem, in which the trasverse stresses are modelled a-priori (see the works [67], [68]) and future companion works can be devoted to this subject. Finally, figures 6.9a-6.10b show the distributions of the shear stress $\sigma_{\alpha z}$ and the normal stress σ_{zz} by varying a/h for $R/a = 2$ and R/a for $a/h = 10$, in the case of concentrated load (problem 3).

Table 6.7: Antisymmetric lamination ($45^\circ/-45^\circ$) with simply-supported boundary conditions and bi-sinusoidal load. Theory LW4.

a/h	$R/a = 1$			$R/a = 2$			$R/a = 5$		
	5	10	100	5	10	100	5	10	100
w	0.4476	0.1115	0.0009	0.8614	0.3017	0.0036	1.1633	0.5738	0.0236
$\sigma_{\alpha\alpha}$	0.1917	0.0819	0.0051	0.2881	0.1693	0.0101	0.3256	0.2547	0.0308
	0.0025	0.0238	0.0047	-0.1040	-0.0260	0.0086	-0.2190	-0.1443	0.0164
$\sigma_{\beta\beta}$	0.1917	0.0819	0.0051	0.2881	0.1693	0.0101	0.3256	0.2547	0.0308
	0.0025	0.0238	0.0047	-0.1040	-0.0260	0.0086	-0.2190	-0.1443	0.0164
$\sigma_{\alpha\beta}$	-0.0154	-0.0120	-0.0017	-0.0473	-0.0415	-0.0115	-0.0722	-0.0723	-0.0476
	1.0585	0.5024	0.0308	1.3171	0.7804	0.0726	1.1315	0.8170	0.2007
$\sigma_{\alpha z}$	0.1074	0.0766	0.0081	0.1761	0.1628	0.0207	0.2220	0.2727	0.0780
$\sigma_{\beta z}$	0.0967	0.0641	0.0019	0.1651	0.1427	0.0052	0.2168	0.2563	0.0290
σ_{zz}	0.5515	0.5720	0.6319	0.5061	0.4884	0.7049	0.5296	0.4886	0.9962

Table 6.8: Symmetric lamination ($0^\circ/90^\circ/0^\circ$) with clamped-free boundary conditions and bi-sinusoidal load. Theory LW4.

a/h	$R/a = 1$			$R/a = 2$			$R/a = 5$		
	5	10	100	5	10	100	5	10	100
w	0.3119	0.0819	0.0013	0.6495	0.1936	0.0042	1.0508	0.3618	0.0190
$\sigma_{\alpha\alpha}$	0.3731	0.1748	0.0166	0.5077	0.2787	0.0359	0.5627	0.3530	0.0929
	0.0531	0.0326	0.0069	-0.0206	-0.0032	0.0099	-0.2283	-0.1378	0.0058
$\sigma_{\beta\beta}$	0.0252	0.0082	0.0004	0.0353	0.0138	0.0008	0.0434	0.0206	0.0022
	-0.0084	-0.0024	0.0002	-0.0192	-0.0077	0.0001	-0.0296	-0.0155	-0.0006
$\sigma_{\alpha\beta}$	0.0020	0.0006	-0.0003	0.0007	0.0007	0.0000	-0.0049	-0.0021	0.0006
	0.0090	0.0029	-0.0002	0.0155	0.0065	0.0002	0.0170	0.0085	0.0009
$\sigma_{\alpha z}$	-0.0015	-0.0188	-0.0618	0.1363	0.1078	-0.0681	0.2923	0.2986	-0.0126
$\sigma_{\beta z}$	-0.0009	-0.0025	-0.0020	0.0011	-0.0008	-0.0019	0.0033	0.0014	-0.0016
σ_{zz}	0.6672	0.6347	0.6140	0.6986	0.6565	0.5755	0.7532	0.7381	0.5398

Table 6.9: Symmetric lamination ($90^\circ/0^\circ/90^\circ$) with simply-supported boundary conditions and concentrated load. Theory LW4.

a/h	$R/a = 1$			$R/a = 2$			$R/a = 5$		
	5	10	100	5	10	100	5	10	100
w	35.5844	3.2329	0.0012	43.3005	4.5602	0.0027	46.4546	5.3029	0.0083
$\sigma_{\alpha\alpha}$	24.6050 -2.8433	1.9587 -0.5929	0.0016 -0.0012	26.7568 -3.4302	2.1125 -0.7221	0.0023 -0.0018	28.0121 -3.6722	2.1866 -0.7921	0.0034 -0.0029
$\sigma_{\beta\beta}$	129.4768 -22.2940	11.3214 -4.5605	0.0186 -0.0108	138.6554 -26.8411	12.4595 -5.8998	0.0243 -0.0153	143.2570 -28.5773	12.9911 -6.6941	0.0334 -0.0239
$\sigma_{\alpha\beta}$	0.2677 1.1584	0.0688 0.1536	0.0001 0.0001	-0.0895 1.0927	0.0261 0.1823	0.0002 0.0003	-0.4274 0.8786	-0.0471 0.1542	0.0005 0.0007
$\sigma_{\alpha z}$	0.8085	0.0831	0.0003	0.7397	0.0770	0.0004	0.5528	0.0449	0.0004
$\sigma_{\beta z}$	1.9680	0.2951	-0.0013	3.2534	0.7891	-0.0037	3.7429	1.0684	-0.0017
σ_{zz}	4.7550	2.0643	0.0255	4.9643	2.1359	0.0262	5.1002	2.1881	0.0268

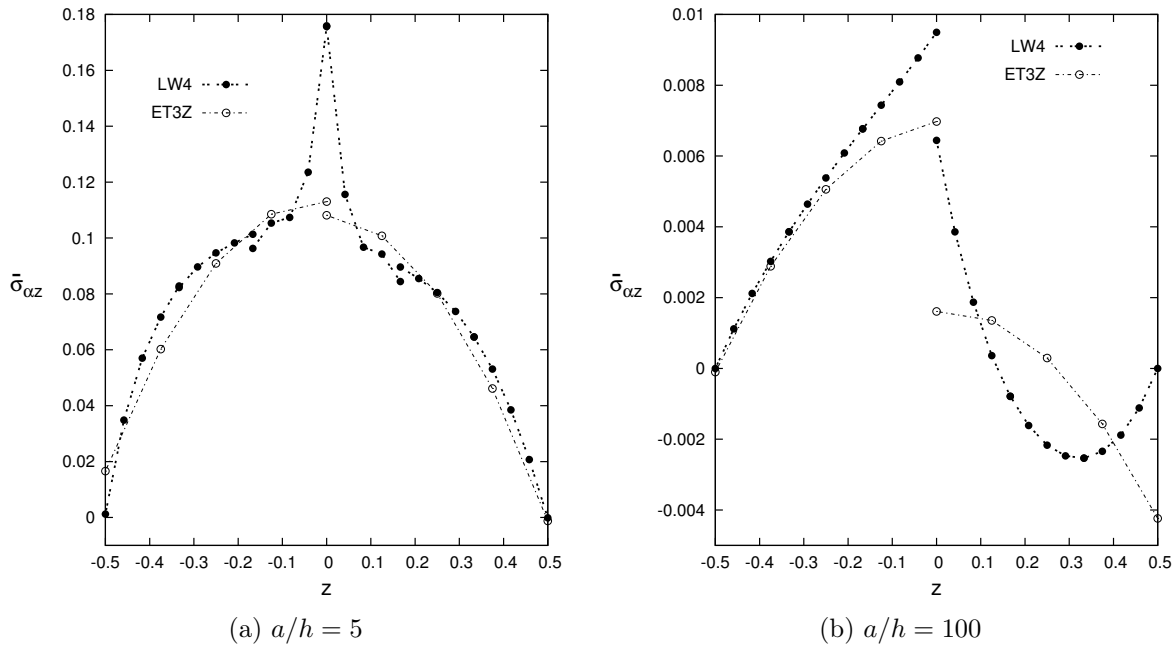


Figure 6.5: Two-layered shell, lamination ($45^\circ, -45^\circ$), $R/a = 1$. Transverse shear stress $\bar{\sigma}_{\alpha z}$ for aspect ratios $a/h = 5$ and $a/h = 100$.

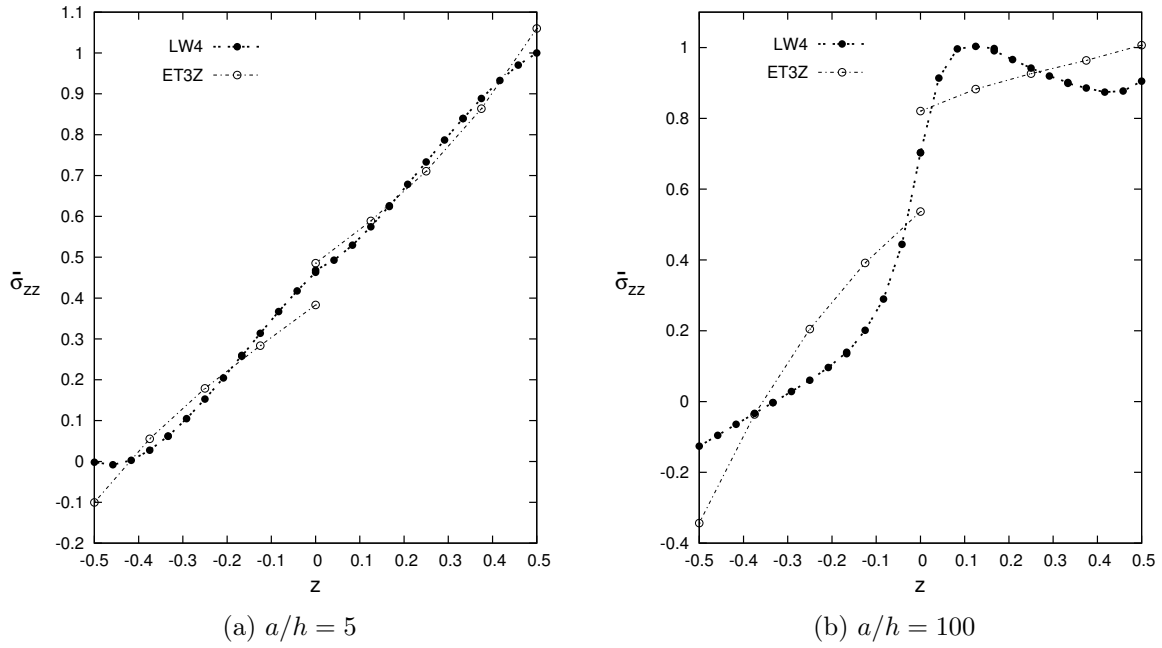


Figure 6.6: Two-layered shell, lamination $(45^\circ, -45^\circ)$, $R/a = 5$. Transverse normal stress $\bar{\sigma}_{zz}$ for aspect ratios $a/h = 5$ and $a/h = 100$.

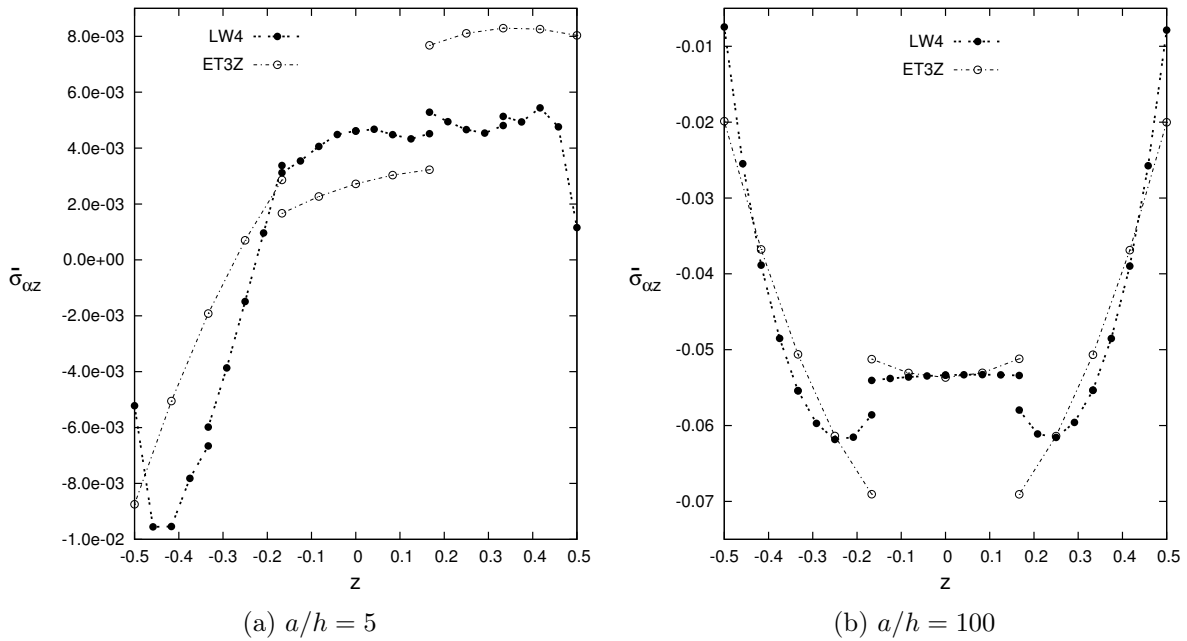


Figure 6.7: Three-layered shell, clamped-free boundary conditions, $R/a = 1$. Transverse shear stress $\bar{\sigma}_{\alpha z}$ for aspect ratios $a/h = 5$ and $a/h = 100$.

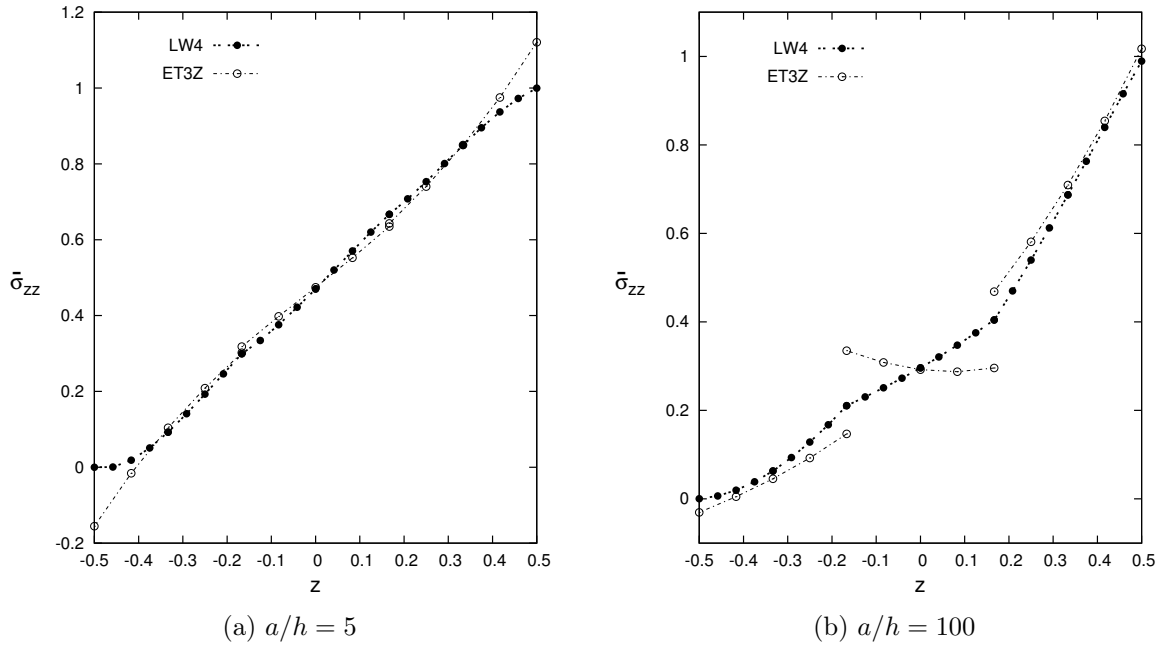


Figure 6.8: Three-layered shell, clamped-free boundary conditions, $R/a = 5$. Transverse normal stress $\bar{\sigma}_{zz}$ for aspect ratios $a/h = 5$ and $a/h = 100$.

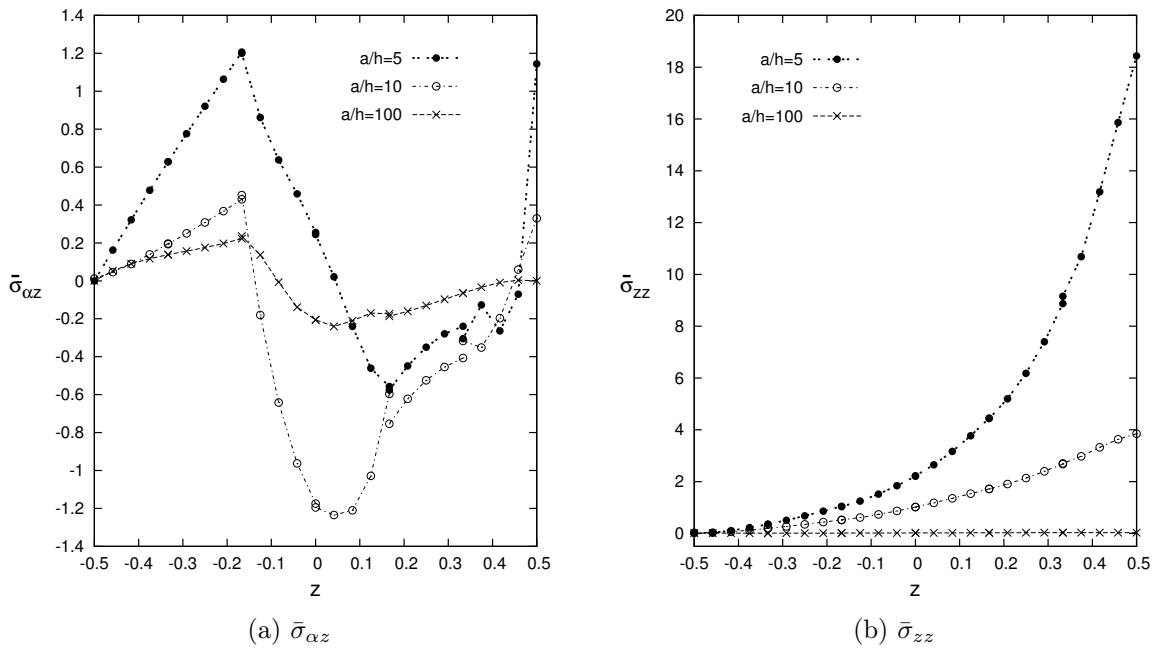


Figure 6.9: Three-layered shell, concentrated load, by varying a/h for $R/a = 2$. Transverse shear and normal stresses $\bar{\sigma}_{\alpha z}$ and $\bar{\sigma}_{zz}$.

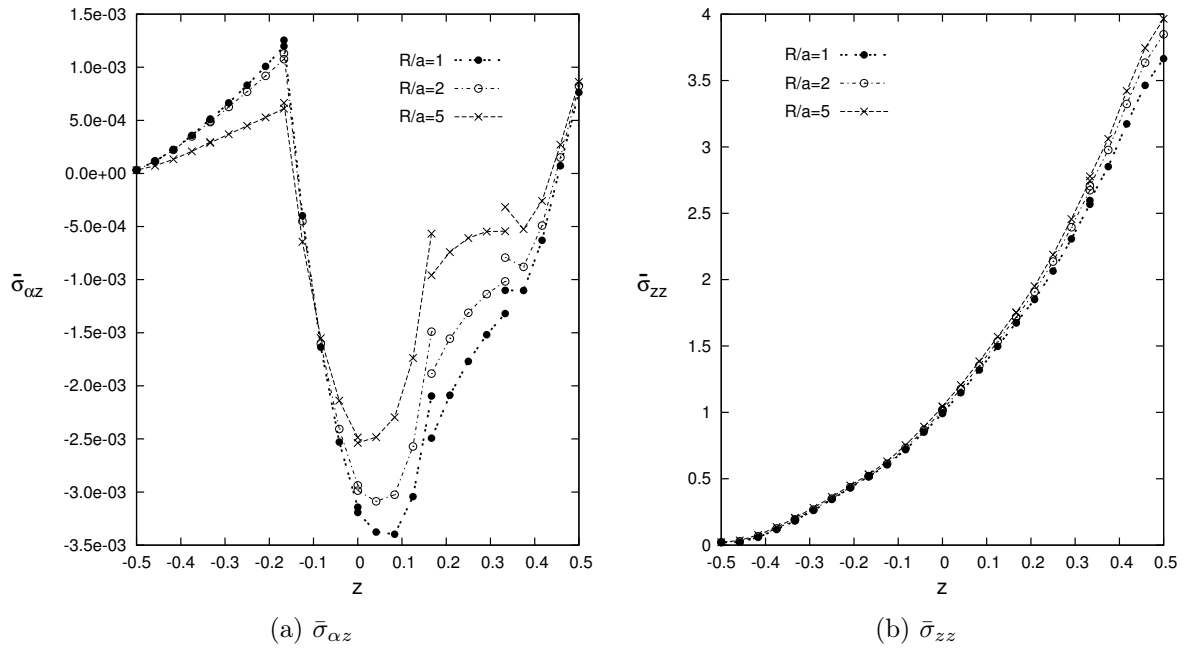


Figure 6.10: Three-layered shell, concentrated load, by varying R/a for $a/h = 10$. Transverse shear and normal stresses $\bar{\sigma}_{\alpha z}$ and $\bar{\sigma}_{zz}$.

6.2 Trigonometric and Exponential Thickness Functions

To assess the trigonometric and the exponential polynomial expansions the following reference problems have been considered in this section:

- A three-layer cross-ply square plate with lamination (0°/90°/0°)
- A two-layer cross-ply square plate with lamination (0°/90°)
- A four-layer cross-ply square plate with lamination (0°/90°/90°/0°)
- A three-layer rectangular sandwich plate

A system of acronyms is given in section 3.2 to denote the considered kinematic models. For the present numerical section, the considered expansion are summarized in Table 6.10.

Table 6.10: Expansion terms of the proposed theories.

N =	<i>cost</i>				z^N	$(-1)^k \zeta_k$	$\sin\left(N\frac{z\pi}{h}\right)$					$\cos\left(N\frac{z\pi}{h}\right)$				$e^{\left(N\frac{z}{h}\right)}$					
	1	2	3	4			1	2	3	4	5	1	2	3	4	1	2	3	4	5	6
ET4	✓	✓	✓	✓	✓	
ES5	✓	✓	✓	✓	✓	✓	
ET1S1	✓	✓	✓	
ET1C1	✓	✓	✓	
EEexp3	✓	✓	✓	✓	.	.	.	
ET1Exp2	✓	✓	✓	✓	✓	.	.	.	
EEexp4	✓	✓	✓	✓	✓	.	.	
ET1Exp3	✓	✓	✓	✓	✓	.	.	.	
ES3C3	✓	✓	✓	✓	.	.	✓	✓	✓	
ES4C4	✓	✓	✓	✓	✓	.	✓	✓	✓	✓	
ET1S1C1	✓	✓	✓	✓	
ET1S2C2	✓	✓	✓	✓	.	.	.	✓	✓	
ET3Z	✓	✓	✓	✓	✓	✓	
ES4Z	✓	✓	✓	✓	✓	✓	
ES5Z	✓	✓	✓	✓	✓	✓	✓	
ET1S2Z	✓	✓	.	.	.	✓	✓	✓	
ET1S3Z	✓	✓	.	.	.	✓	✓	✓	✓	
ET1C2Z	✓	✓	.	.	.	✓	✓	✓	
EEexp5Z	✓	✓	✓	✓	✓	✓	✓	✓	
EEexp6Z	✓	✓	✓	✓	✓	✓	✓	✓	
ET1Exp4Z	✓	✓	.	.	.	✓	✓	✓	✓	✓	✓	✓	
ET1Exp5Z	✓	✓	.	.	.	✓	✓	✓	✓	✓	✓	✓	
ES4C4Z	✓	✓	✓	✓	✓	.	✓	✓	✓	✓	
ET1S3C3Z	✓	✓	.	.	.	✓	✓	✓	✓	.	✓	✓	✓	

6.2.1 Three-layer cross-ply square plate (0°/90°/0°)

A three layered cross-ply square plate with lamination (0°/90°/0°) and simply-supported boundary condition is considered. The applied load is:

$$p(x, y, z_{top}) = \hat{p} \sin\left(\frac{m\pi x}{a}\right) \sin\left(\frac{n\pi y}{b}\right) \quad (6.5)$$

where $m = n = 1$, see Figure 6.11. The mechanical properties of the material are: $E_L/E_T = 25$; $G_{LT}/E_T = 0,5$; $G_{TT}/E_T = 0,2$; $\nu_{LT} = \nu_{TT} = 0,25$. The geometrical dimensions are: $a = b = 1.0$. The mechanical load amplitude at the top position is: $\hat{p} = 1.0$. The results are presented for different thickness ratios $a/h = 4, 10, 100$, and reported in non-dimensional form:

$$\hat{w} = \frac{100wE_T h^3}{\hat{p} a^4} \quad ; \quad \hat{\sigma}_{xx} = \frac{\sigma_{xx}}{\hat{p} \left(\frac{a}{h}\right)^2} \quad ; \quad \hat{\sigma}_{xz/yz} = \frac{\sigma_{xz/yz}}{\hat{p} \left(\frac{a}{h}\right)} \quad (6.6)$$

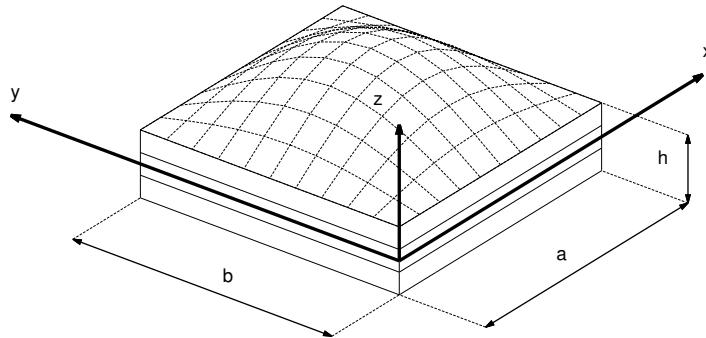


Figure 6.11: Reference system of the plate with a bi-sinusoidal loading.

Convergence and locking study

First of all, a convergence study on the plate element has been performed. A composite plate with thickness ratio $a/h = 100$, is evaluated. The Navier-type solution with a Taylor polynomials expansion of the 4th order has been taken as reference solution. It can be noticed that, evaluating the transverse displacement w and transverse shear stress σ_{xz} , the convergence is not depending on the different kinds of employed polynomials, see Table 6.11. A mesh grid of 10×10 elements ensures the convergence. Then a locking study has been performed evaluating different types of integration methods [115] for the same plate structure to prove that the element is locking free, see Table 6.12. The plate element with the MITC9 method leads to accurate results in terms of both transverse displacement and shear stress.

Table 6.11: Convergence study. Plate with lamination $[0^\circ/90^\circ/0^\circ]$ and with thickness ratio $a/h = 100$.

	Mesh	4×4	6×6	8×8	10×10	$ET4_a$	$LW4$	$3D \text{ Exact Elasticity [128]}$
$ET4$	w	0.4344	0.4343	0.4342	0.4342	0.4342	0.4347	-
	σ_{xz}	0.295	0.287	0.284	0.282	0.281	0.398	0.395
$ET1S1$	w	0.4294	0.4292	0.4292	0.4292			
	σ_{xz}	0.308	0.300	0.297	0.295			
$ET1Exp3$	w	0.4345	0.4343	0.4343	0.4343			
	σ_{xz}	0.315	0.307	0.304	0.302			
$ET3Z$	w	0.420	0.4347	0.4347	0.4347			
	σ_{xz}	0.4349	0.409	0.405	0.403			
$ET1C2Z$	w	0.4347	0.4346	0.4345	0.4345			
	σ_{xz}	0.414	0.403	0.399	0.397			

Table 6.12: Locking study. Plate with lamination $[0^\circ/90^\circ/0^\circ]$ and with thickness ratio $a/h = 100$. All the cases are computed with a mesh of 10×10 elements.

		<i>Reduced</i>	<i>Selective</i>	<i>MITC9</i>	<i>ET4_a</i>	<i>LW4</i>	<i>3D Exact Elasticity</i> [128]
<i>ET4</i>	<i>w</i>	0.4342	0.4334	0.4342	0.4342	0.4347	-
	σ_{xz}	0.501	0.510	0.282	0.281	0.398	0.395
<i>ET1S1</i>	<i>w</i>	0.4292	0.4284	0.4292			
	σ_{xz}	0.511	0.526	0.295			
<i>ET1Exp3</i>	<i>w</i>	0.4343	0.4335	0.4343			
	σ_{xz}	0.521	0.538	0.302			
<i>ET3Z</i>	<i>w</i>	0.4347	0.4339	0.4347			
	σ_{xz}	0.621	0.673	0.403			
<i>ET1C2Z</i>	<i>w</i>	0.4345	0.4337	0.4345			
	σ_{xz}	0.614	0.675	0.397			

For thick and thin plates $a/h = 4, 100$ the results are presented in Table 6.13 for various expansions. The values of the transversal displacement w , in-plane stress σ_{xx} and transverse shear stresses σ_{xz} and σ_{yz} are compared with the exact 3D elasticity solution [128], the analytical solution calculated with a Taylor's polynomial expansion of the 4th order (*ET4_a*), and the FEM solution obtained with a Layer-Wise approach using a Legendre expansion of the 4th order (*LW4*).

Table 6.13: Plate with lamination $[0^\circ/90^\circ/0^\circ]$. Transverse displacement $\hat{w} = \hat{w}(a/2, b/2, +h/2)$, in-plane principal stress $\hat{\sigma}_{xx} = \hat{\sigma}_{xx}(a/2, b/2, \pm h/2)$, transverse shear stress $\hat{\sigma}_{xz} = \hat{\sigma}_{xz}(a, b/2, 0)$ and $\hat{\sigma}_{yz} = \hat{\sigma}_{yz}(a/2, b, 0)$.

	$a/h = 4$					$a/h = 100$					DOFs
	\hat{w}	$\hat{\sigma}_{xx}$		$\hat{\sigma}_{xz}$	$\hat{\sigma}_{yz}$	\hat{w}	$\hat{\sigma}_{xx}$		$\hat{\sigma}_{xz}$	$\hat{\sigma}_{yz}$	
		top	bottom				top	bottom			
3D Exact Elasticity [128]	-	0.801	-0.755	0.256	0.2172	-	0.539	-0.539	0.395	0.0828	
LW4	2.1216	0.807	-0.761	0.258	0.2197	0.4347	0.544	-0.544	0.398	0.0836	17199
ET4 _a	2.0083	0.786	-0.740	0.205	0.1830	0.4342	0.539	-0.539	0.281	0.0734	
ET4	2.0082	0.793	-0.746	0.207	0.1845	0.4342	0.543	-0.543	0.283	0.0742	6615
ES5	2.0765	0.774	-0.779	0.293	0.2110	0.4294	0.541	-0.541	0.413	0.0451	7938
ET1S1	2.0089	0.772	-0.776	0.214	0.1857	0.4292	0.541	-0.541	0.295	0.0771	3969
ET1C1	1.6497	0.470	-0.426	0.122	0.1257	0.4332	0.543	-0.543	0.144	0.0605	3969
EExp3	1.9105	0.777	-0.604	0.177	0.1657	0.3945	0.497	-0.495	-0.303	-0.547	5292
ET1Exp2	1.9794	0.801	-0.696	0.198	0.1801	0.4341	0.544	-0.544	0.265	0.0731	5292
EExp4	2.0266	0.785	-0.747	0.223	0.1860	0.4323	0.541	-0.541	0.414	0.1664	6615
ET1Exp3	2.0199	0.785	-0.757	0.215	0.1850	0.4343	0.544	-0.544	0.302	0.0743	6615
ES3C3	2.0416	0.777	-0.732	0.245	0.1760	0.3781	0.474	-0.474	-0.435	-0.840	9261
ES4C4	2.0841	0.798	-0.752	0.287	0.1994	0.4324	0.541	-0.541	0.605	0.281	11907
ET1S1C1	2.0176	0.796	-0.752	0.213	0.1868	0.4342	0.544	-0.544	0.296	0.0747	5292
ET1S2C2	2.0448	0.788	-0.742	0.241	0.1821	0.4345	0.544	-0.544	0.376	0.0712	7938
ET3Z	2.1078	0.802	-0.756	0.259	0.1856	0.4347	0.544	-0.544	0.403	0.0709	6615
ES4Z	2.1116	0.783	-0.788	0.257	0.2209	0.4274	0.538	-0.538	0.586	0.2283	7938
ES5Z	2.1117	0.783	-0.788	0.257	0.2233	0.4295	0.541	-0.541	0.370	0.0591	9261
ET1S2Z	2.1084	0.782	-0.787	0.253	0.1975	0.4296	0.541	-0.541	0.401	0.0775	6615
ET1S3Z	2.1110	0.783	-0.788	0.255	0.2167	0.4296	0.541	-0.541	0.399	0.0843	7938
ET1C2Z	2.0461	0.709	-0.663	0.259	0.1741	0.4345	0.544	-0.544	0.397	0.0673	6615
EExp5Z	2.1134	0.805	-0.755	0.259	0.1899	0.4346	0.544	-0.544	0.426	0.1229	9261
EExp6Z	2.1180	0.805	-0.759	0.253	0.2032	0.4347	0.544	-0.544	0.403	0.0791	10584
ET1Exp4Z	2.1152	0.805	-0.758	0.257	0.1897	0.4347	0.544	-0.544	0.403	0.0725	9261
ET1Exp5Z	2.1186	0.806	-0.760	0.253	0.2023	0.4347	0.544	-0.544	0.402	0.0772	10584
ES4C4Z	2.1211	0.807	-0.761	0.257	0.2213	0.4324	0.541	-0.541	0.590	0.2283	13230
ET1S3C3Z	2.1206	0.807	-0.761	0.254	0.2172	0.4347	0.544	-0.544	0.401	0.0826	11907

For thin plates, $a/h = 100$, the following considerations are drawn:

- Regarding the transverse displacement w the exponential function (*EExp4*), the cosine expansion (*ET1C1*) and its combinations with series of sine functions (*ES4C4*) are more accurate than sine functions (*ES5*), see Figure 6.12a. It can be noticed that the use of the linear term (*ET1Exp3*, *ET1S2C2*) determines a significant improvement of the results with a lower number of degrees of freedom (DOFs). The addition of the zig-zag term improves the accuracy even if for the sine function (*ES5Z*, *ET1S3Z*), and its combination with cosine (*ES4C4Z*) the improvement is lower, see Figure 6.12b.
- The in-plane stress σ_{xx} is accurately described by all functions with or without the zig-zag term.
- For the transverse shear stress σ_{xz} the sine and the exponential functions, with the linear contribution, are close to the Taylor polynomial series of the 4th order, but at interfaces the continuity is not fulfilled. To overcome this problem, it has been employed the zig-zag function, see Figure 6.13. As expected the zig-zag term improves the results, this is true excepting for the cosine function, the sine, and their combination.
- The transverse normal stress σ_{zz} is accurately described by the cosine function and its combination with the sine series, see Figure 6.14. It can be noticed that the sine series and its combination with the linear contribution lead to a completely wrong description of the transverse normal stress.

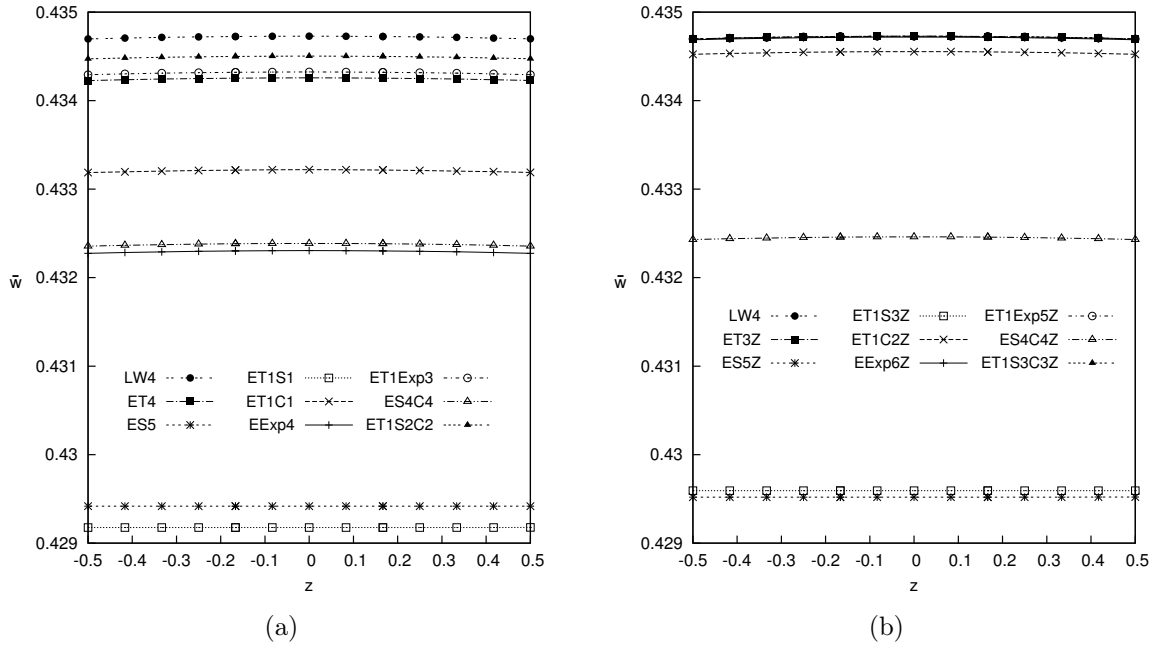


Figure 6.12: Three-layered plate, transverse displacement w along the thickness, with thickness ratio $(a/h) = 100$.

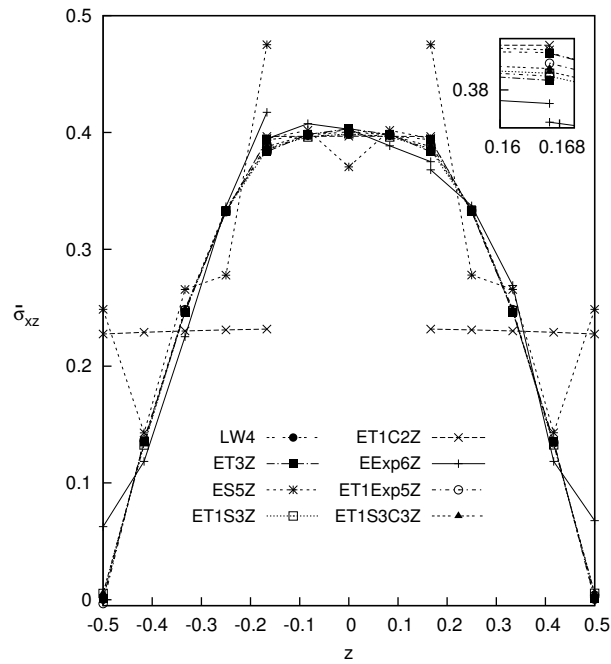


Figure 6.13: Three-layered plate, transverse shear stress σ_{xz} along the thickness, with thickness ratio $(a/h) = 100$.

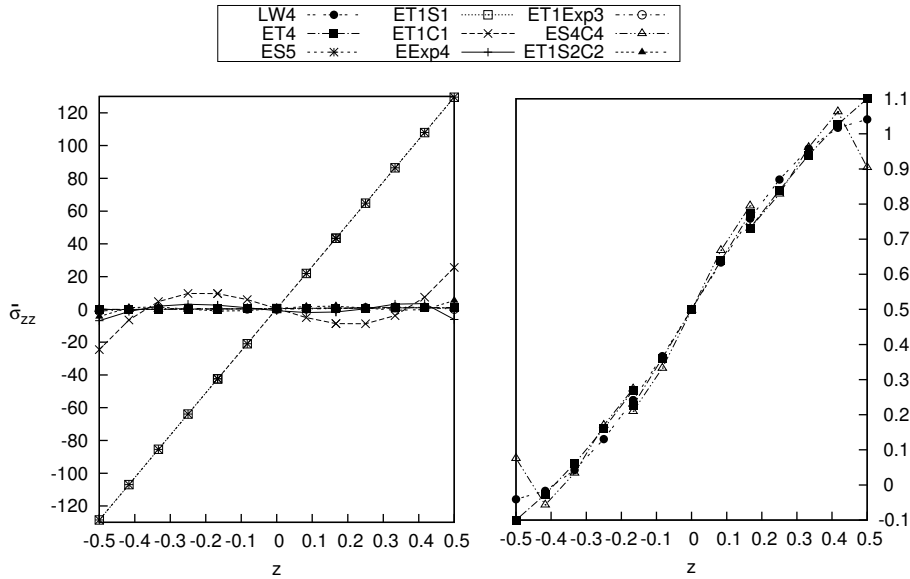


Figure 6.14: Three-layered plate, transverse normal stress σ_{zz} along the thickness, with thickness ratio $(a/h) = 100$.

For thick plates, $a/h = 4$, the following considerations are drawn:

- Regarding the transverse displacement w , the increase of the performance of exponential series, and the sine function instead of cosine ones is more evident than the thin case. Furthermore using the zig-zag term the results are very close to the exact solution, except for the cosine ($ET1C2Z$), see Figure 6.15. Moreover, it can be observed that the sine series ($ES5Z$, $ET1S3Z$) predict a linear displacement profile, while the exponential expansion is the best approximation of the solution.
- The in-plane stress σ_{xx} is not accurately described by the cosine function ($ET1C1$), see Figure 6.16a. It can be noticed that the Taylor results at the lower interface give a minor discontinuity. Only adding the zig-zag function the results strongly agree with the solution, see Figure 6.16b.
- For the transverse shear stress σ_{xz} at interfaces the continuity is not fulfilled, see Figure 6.17a. Also in this case only the addition of the zig-zag term is able to improve the results, see Figure 6.17b. Except for the cosine series, all the employed functions can lead to good results. The discontinuity is very reduced and it is smaller than ones obtained by using Taylor polynomials.
- The transverse normal stress σ_{zz} , unlike the previous case $a/h = 100$, can be described correctly by the sine series too, see Figure 6.18a. Adding the zig-zag term the results are closer to the exact solution, especially the exponential expansion and the sine and cosine combination lead to very accurate results, see Figure 6.18b.

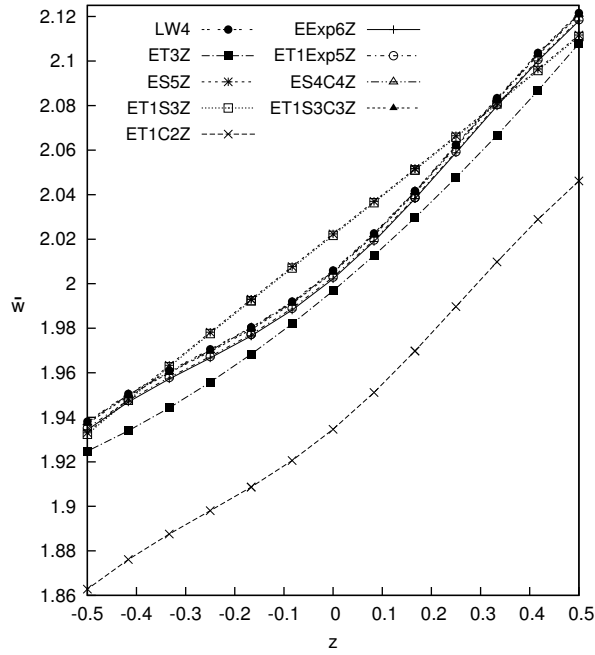


Figure 6.15: Three-layered plate, transverse displacement w along the thickness, with thickness ratio $(a/h) = 4$.

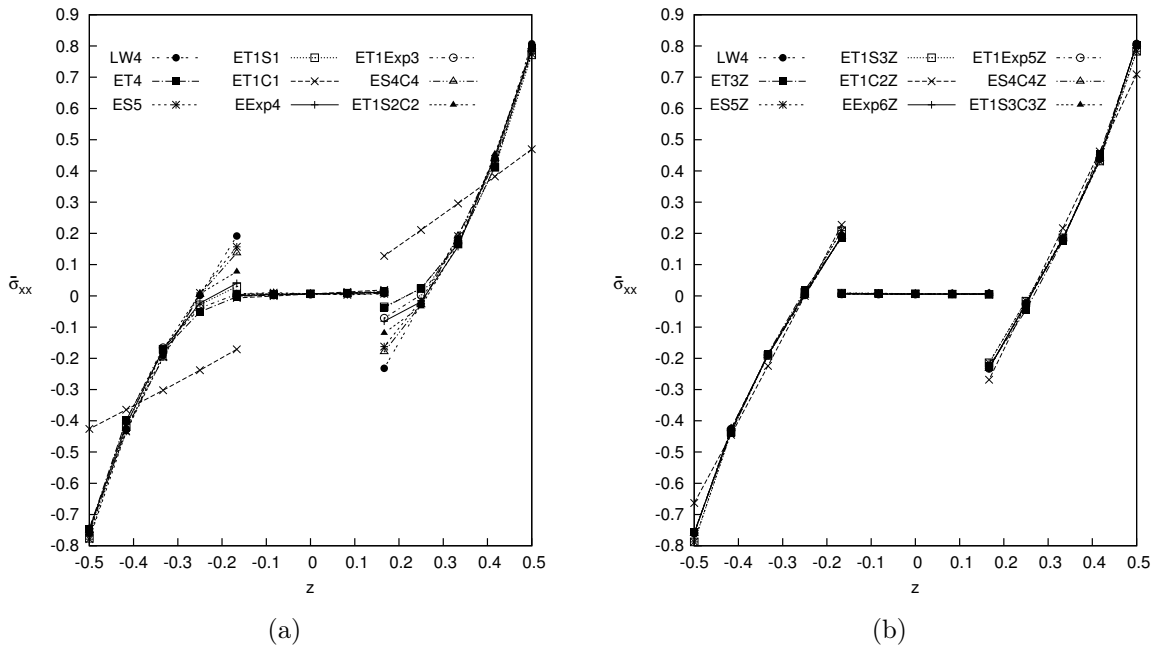


Figure 6.16: Three-layered plate, in-plane stress σ_{xx} along the thickness, with thickness ratio $(a/h) = 4$.

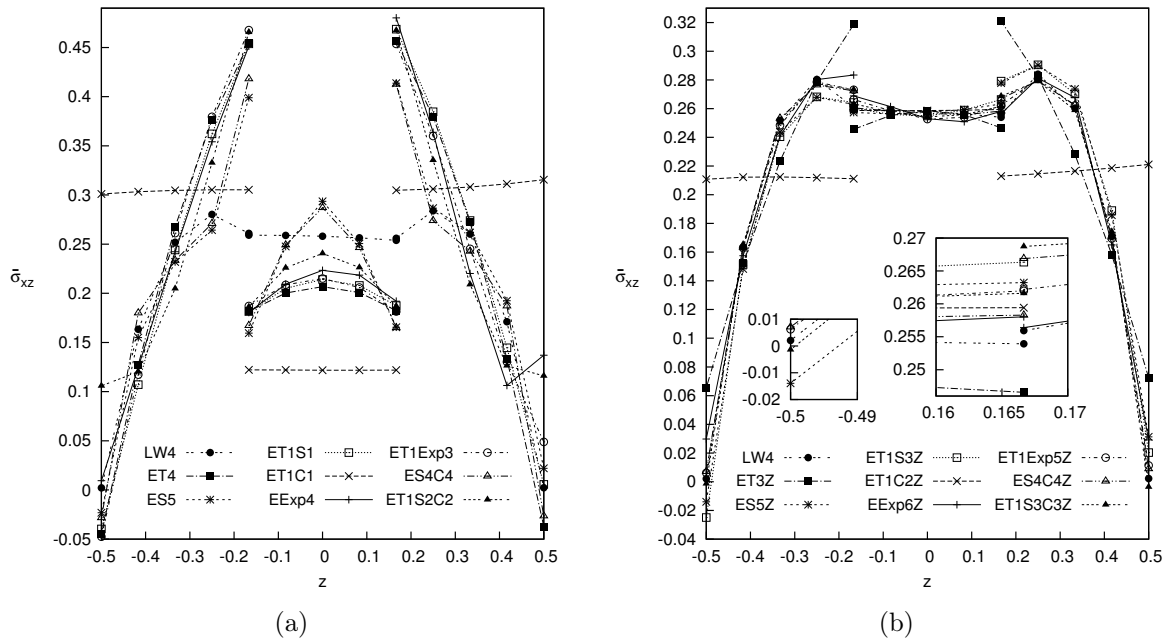


Figure 6.17: Three-layered plate, transverse shear stress σ_{xz} along the thickness, with thickness ratio $(a/h) = 4$.

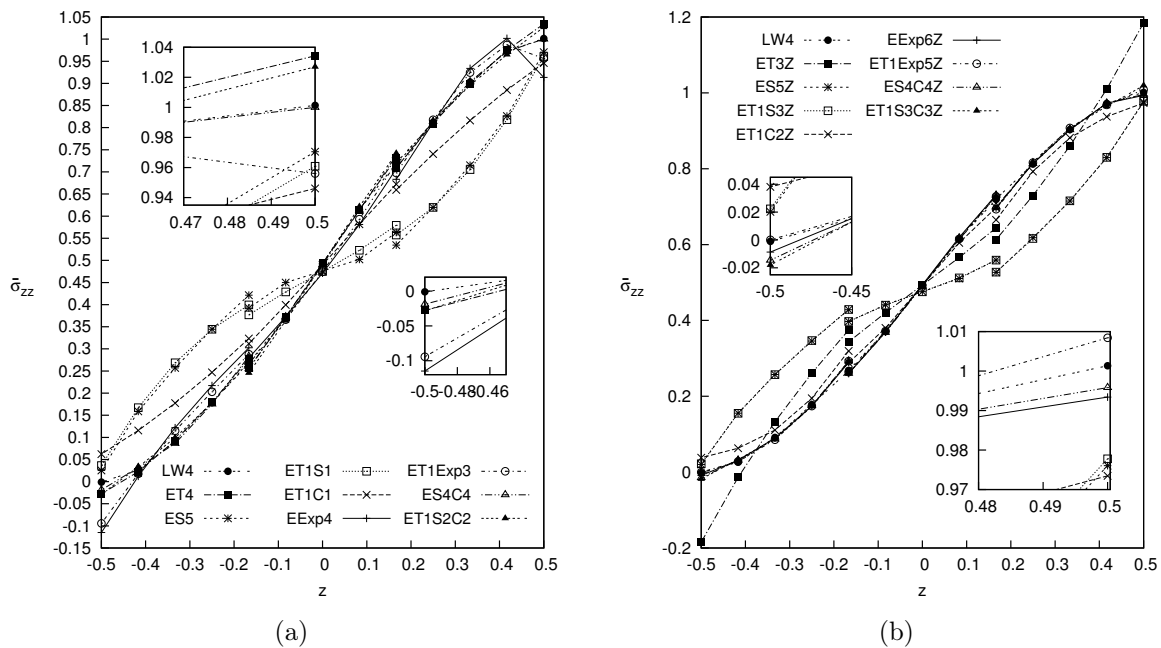


Figure 6.18: Three-layered plate, transverse normal stress σ_{zz} along the thickness, with thickness ratio $(a/h) = 4$.

For the thickness ratio $a/h = 10$ the results are presented in Table 6.14. The values of the transversal displacement w , in-plane stress σ_{xx} and transverse shear stresses σ_{xz} and σ_{yz} are compared with the exact 3D elasticity solution and with different reference solutions taken in the literature. For moderately thin plate, the following considerations are drawn:

- Regarding the transverse displacement w , the exponential series, and in particular the sine functions are more efficient than the cosine series. Furthermore, using the zig-zag term, except the cosine ($ET1C2Z$) and the sine series ($ES5Z$, $ET1S3Z$), the results are closer to the exact solution.

- The in-plane stress σ_{xx} is not correctly described as for thin plate $a/h = 100$, moreover the cosine function (*ET1C1*) does not match the solution. Only adding the zig-zag function the results match the exact solution.
- For the transverse shear stress σ_{xz} , also in this case, the addition of the zig-zag term to functions series is able to improve the results and to reduce the discontinuity. Except for the cosine series, all the functions employed can lead to accurate results.
- The transverse normal stress σ_{zz} is not accurately described by sine functions, see Figure 6.19, but this problem is reduced compared to the thin plate $a/h = 100$.

Table 6.14: Plate with lamination $[0^\circ/90^\circ/0^\circ]$ and thickness ratio $a/h = 10$. Transverse displacement $\hat{w} = \hat{w}(a/2, b/2, 0)$, in-plane principal stress $\hat{\sigma}_{xx} = \hat{\sigma}_{xx}(a/2, b/2, \pm h/2)$, transverse shear stress $\hat{\sigma}_{xz} = \hat{\sigma}_{xz}(a, b/2, 0)$ and $\hat{\sigma}_{yz} = \hat{\sigma}_{yz}(a/2, b, 0)$.

	\hat{w}	$\hat{\sigma}_{xx}$		$\hat{\sigma}_{xz}$	$\hat{\sigma}_{yz}$	DOFs
		<i>top</i>	<i>bottom</i>			
<i>3D Exact Elasticity</i> [129]	0.7530	0.590	-0.590	0.357	0.1228	
<i>L&S</i> [130]	0.7546	0.580	-0.580	0.367	0.127	
<i>Moriya</i> [131]	0.7512	0.5759	-0.5785	0.3993	0.1296	
<i>R - H</i> [132]	0.7125	0.5684	-	0.1033	-	
<i>H&L</i> [133]	0.7531	0.5884	-0.5879	0.3627	0.1284	
<i>ET4(IS)</i> [129]	0.7268	0.5776	-0.5753	0.2948	0.1464	
<i>LW4</i>	0.7530	0.595	-0.595	0.3602	0.1238	17199
<i>ET4</i>	0.7151	0.588	-0.587	0.2639	0.1038	6615
<i>ES5</i>	0.7380	0.591	-0.592	0.4038	0.1194	7938
<i>ET1S1</i>	0.7142	0.588	-0.589	0.2746	0.1066	3969
<i>ET1C1</i>	0.6294	0.521	-0.521	0.1387	0.0759	3969
<i>EExp3</i>	0.6817	0.577	-0.550	0.2104	0.0852	5292
<i>ET1Exp2</i>	0.7066	0.588	-0.577	0.2484	0.1013	5292
<i>EExp4</i>	0.7254	0.589	-0.591	0.2993	0.1066	6615
<i>ET1Exp3</i>	0.7203	0.588	-0.591	0.2804	0.1046	6615
<i>ES3C3</i>	0.7310	0.586	-0.586	0.3434	0.0860	9261
<i>ES4C4</i>	0.7430	0.593	-0.592	0.4015	0.1149	11907
<i>ET1S1C1</i>	0.7192	0.591	-0.590	0.2754	0.1051	5292
<i>ET1S2C2</i>	0.7338	0.591	-0.590	0.3400	0.1030	7938
<i>ET3Z</i>	0.7528	0.596	-0.595	0.3646	0.1038	6615
<i>ES4Z</i>	0.7478	0.594	-0.594	0.3624	0.1273	7938
<i>ES5Z</i>	0.7478	0.594	-0.594	0.3583	0.1265	9261
<i>ET1S2Z</i>	0.7477	0.594	-0.594	0.3607	0.1122	6615
<i>ET1S3Z</i>	0.7478	0.594	-0.594	0.3598	0.1230	7938
<i>ET1C2Z</i>	0.7381	0.575	-0.575	0.3606	0.0973	6615
<i>EExp5Z</i>	0.7527	0.595	-0.594	0.3662	0.1072	9261
<i>EExp6Z</i>	0.7529	0.595	-0.594	0.3622	0.1142	10584
<i>ET1Exp4Z</i>	0.7528	0.595	-0.594	0.3642	0.1062	9261
<i>ET1Exp5Z</i>	0.7529	0.595	-0.594	0.3620	0.1136	10584
<i>ES4C4Z</i>	0.7530	0.595	-0.595	0.3636	0.1265	13230
<i>ET1S3C3Z</i>	0.7530	0.595	-0.595	0.3611	0.1222	11907

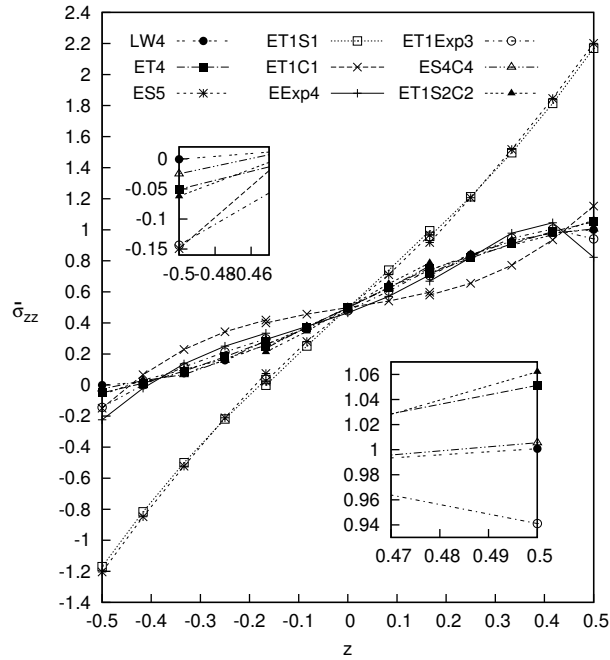


Figure 6.19: Three-layered plate, transverse normal stress σ_{zz} along the thickness, with thickness ratio $(a/h) = 10$.

6.2.2 Two-layer ($0^\circ/90^\circ$) and four-layer ($0^\circ/90^\circ/90^\circ/0^\circ$) cross-ply square plate

The plates are simply-supported and different thickness ratios are studied. The geometrical and material properties are the same of the previous three-layer plate. The plate structures are loaded by the same bi-sinusoidal load pressure applied at the top surface.

For the 2 layered plate the results are listed in Table 6.15. As expected, for thin plates, $a/h = 100$, all the functions lead to accurate results. Despite the transverse displacement w and the in-plane principal stress σ_{xx} match the exact solution, the shear stresses σ_{xz} and σ_{yz} are not correctly described. For thick plates $a/h = 4$, the *ET4* expansion underestimates the transverse displacement and the in-plane stress compared to the reference solution given by a layer-wise approach. All the results obtained by the proposed trigonometric and exponential expansions are close to the layer-wise solution more than the Taylor polynomial one. Furthermore, adding the zig-zag term to the expansion series, all the FE results achieve significant accuracy, also in terms of shear stresses. For the 4 layered plate the results are listed in Table 6.16. The values of the transversal displacement w are compared with the exact 3D elasticity solution and with different reference solutions available in the literature. It is clear that for thin plate all the FE results are close to the exact solution, conversely for thick plates the results match the exact solution only by adding the zig-zag function. It can be noticed that the zig-zag function strongly improves the solution, especially for thick plates. The reduction of computational costs is particularly relevant in some cases compared to the layer-wise solution.

Table 6.15: Plate with lamination $[0^\circ/90^\circ]$. Transverse displacement $\hat{w} = \hat{w}(a/2, b/2, +h/2)$, in-plane principal stress $\hat{\sigma}_{xx} = \hat{\sigma}_{xx}(a/2, b/2, \pm h/2)$, transverse shear stress $\hat{\sigma}_{xz} = \hat{\sigma}_{xz}(a, b/2, 0)$ and $\hat{\sigma}_{yz} = \hat{\sigma}_{yz}(a/2, b, 0)$.

	$a/h = 4$					$a/h = 100$				
	\hat{w}	$\hat{\sigma}_{xx}$		$\hat{\sigma}_{xz}$	$\hat{\sigma}_{yz}$	\hat{w}	$\hat{\sigma}_{xx}$		$\hat{\sigma}_{xz}$	$\hat{\sigma}_{yz}$
		<i>top</i>	<i>bottom</i>				<i>top</i>	<i>bottom</i>		
<i>LW4</i>	2.1699	0.1106	-0.7960	0.1451	0.1215	1.0652	0.0851	-0.7217	0.1234	0.1234
<i>ET4_a</i>	2.1282	0.1093	-0.7708	0.2878	0.1091	1.0651	0.0842	-0.7157	0.2800	0.1120
<i>ET4</i>	2.1281	0.1100	-0.7770	0.2901	0.1100	1.0651	0.0849	-0.7215	0.2829	0.1132
<i>ES5</i>	2.1376	0.1031	-0.8334	0.2259	0.0831	1.0388	0.0905	-0.7124	0.1279	0.0511
<i>ET1S1</i>	2.0924	0.0990	-0.8109	0.3007	0.1149	1.0388	0.0905	-0.7124	0.3046	0.1218
<i>ET1C1</i>	2.0403	0.1025	-0.6585	0.2255	0.0871	1.0643	0.0867	-0.7231	0.2229	0.0891
<i>EExp3</i>	2.1144	0.1095	-0.7249	0.2846	0.1022	0.8801	0.0713	-0.5948	-0.8887	-0.9132
<i>ET1Exp2</i>	2.1204	0.1101	-0.7544	0.2965	0.1109	1.0650	0.0854	-0.7222	0.2924	0.1155
<i>EExp4</i>	2.1228	0.1080	-0.7546	0.3036	0.1012	1.0508	0.0832	-0.7125	0.9537	0.0877
<i>ET1Exp3</i>	2.1279	0.1090	-0.7683	0.3003	0.1041	1.0651	0.0848	-0.7218	0.2974	0.1070
<i>ES3C3</i>	2.1569	0.1101	-0.7917	0.2452	0.0902	0.8020	0.0640	-0.5429	-1.9729	-0.7892
<i>ES4C4</i>	2.1574	0.1104	-0.7911	0.2500	0.0917	1.0508	0.0838	-0.7119	0.7852	0.3141
<i>ET1S1C1</i>	2.1170	0.1109	-0.7657	0.2961	0.1142	1.0644	0.0867	-0.7233	0.2956	0.1182
<i>ET1S2C2</i>	2.1515	0.1119	-0.7897	0.2537	0.0940	1.0651	0.0852	-0.7219	0.2400	0.0960
<i>ET3Z</i>	2.1261	0.1095	-0.7674	0.2648	0.1293	1.0651	0.0851	-0.7217	0.2752	0.1351
<i>ES4Z</i>	2.1425	0.1087	-0.8103	0.2551	0.0824	1.0418	0.0872	-0.7109	0.9506	0.3623
<i>ES5Z</i>	2.1445	0.1090	-0.8112	0.2438	0.0777	1.0573	0.0885	-0.7214	0.1370	0.0352
<i>ET1S2Z</i>	2.1408	0.1088	-0.8102	0.2678	0.0879	1.0573	0.0885	-0.7214	0.2616	0.0850
<i>ET1S3Z</i>	2.1430	0.1089	-0.8106	0.2555	0.0827	1.0573	0.0885	-0.7214	0.2427	0.0775
<i>ET1C2Z</i>	2.0789	0.1042	-0.6984	0.1437	0.1207	1.0650	0.0853	-0.7219	0.1360	0.1233
<i>EExp5Z</i>	2.1595	0.1105	-0.7883	0.1770	0.1481	1.0642	0.0851	-0.7212	0.1654	0.2802
<i>EExp6Z</i>	2.1672	0.1098	-0.7960	0.1702	0.1352	1.0651	0.0850	-0.7217	0.0912	0.1205
<i>ET1Exp4Z</i>	2.1638	0.1107	-0.7940	0.1735	0.1443	1.0652	0.0851	-0.7217	0.1668	0.1499
<i>ET1Exp5Z</i>	2.1675	0.1099	-0.7963	0.1814	0.1358	1.0652	0.0851	-0.7217	0.1739	0.1399
<i>ES4C4Z</i>	2.1686	0.1103	-0.7957	0.1622	0.1386	1.0519	0.0840	-0.7127	0.1466	0.7019
<i>ET1S3C3Z</i>	2.1685	0.1105	-0.7956	0.1725	0.1352	1.0652	0.0851	-0.7218	0.1594	0.1382

Table 6.16: Plate of 4 layers $[0^\circ/90^\circ/90^\circ/0^\circ]$ with various thickness ratios a/h . Transverse displacement $\hat{w} = \hat{w}(a/2, b/2, 0)$.

a/h	4	10	20	100	$DOFs$
<i>3D Exact Elasticity</i> [129]	1.937	0.737	0.513	0.435	
<i>R – H</i> [132]	1.8937	0.7147	0.5060	0.4343	
<i>R – C</i> [134]	1.7100	0.6628	0.4912	0.4337	
<i>P&K</i> [135]	1.8744	0.7185	-	0.4346	
<i>D&R</i> [136]	1.9530	0.7377	0.5122	0.4333	
<i>A&S</i> [137]	-	0.6693	-	-	
<i>LH&X</i> [138]	1.7095	0.6627	0.4912	0.4337	
<i>ET4(IS)</i> [129]	1.9506	0.7272	0.5112	0.4366	
<i>LW4</i>	1.9367	0.7370	0.5130	0.4346	22491
<i>ET4</i>	1.8708	0.7179	0.5073	0.4344	6615
<i>ES5</i>	1.9333	0.7267	0.5062	0.4294	7938
<i>ET1S1</i>	1.8995	0.7167	0.5032	0.4293	3969
<i>ET1C1</i>	1.4894	0.6244	0.4811	0.4332	3969
<i>EExp3</i>	1.7668	0.6844	0.4919	0.3953	5292
<i>ET1Exp2</i>	1.8435	0.7098	0.5050	0.4343	5292
<i>EExp4</i>	1.8905	0.7252	0.5095	0.4324	6615
<i>ET1Exp3</i>	1.8826	0.7218	0.5085	0.4344	6615
<i>ES3C3</i>	1.8956	0.7258	0.5074	0.3825	9261
<i>ES4C4</i>	1.9013	0.7273	0.5097	0.4318	11907
<i>ET1S1C1</i>	1.8818	0.7210	0.5082	0.4343	5292
<i>ET1S2C2</i>	1.8977	0.7271	0.5101	0.4345	7938
<i>ET3Z</i>	1.8715	0.7179	0.5073	0.4344	6615
<i>ES4Z</i>	1.9207	0.7235	0.5055	0.4277	7938
<i>ES5Z</i>	1.9336	0.7273	0.5070	0.4303	9261
<i>ET1S2Z</i>	1.9171	0.7233	0.5058	0.4303	6615
<i>ET1S3Z</i>	1.9214	0.7237	0.5059	0.4303	7938
<i>ET1C2Z</i>	1.4912	0.6244	0.4811	0.4332	6615
<i>EExp5Z</i>	1.8908	0.7254	0.5097	0.4344	9261
<i>EExp6Z</i>	1.9013	0.7275	0.5102	0.4345	10584
<i>ET1Exp4Z</i>	1.8912	0.7257	0.5097	0.4345	9261
<i>ET1Exp5Z</i>	1.9004	0.7274	0.5102	0.4345	10584
<i>ES4C4Z</i>	1.9014	0.7273	0.5097	0.4318	13230
<i>ET1S3C3Z</i>	1.9022	0.7275	0.5102	0.4345	11907

6.2.3 Three-layer rectangular sandwich plate

A 3 layered, unsymmetrically laminated, rectangular sandwich plate has been analyzed. The plate is loaded by a constant uniform pressure $P_z^{top} = -0.1 MPa$ applied to the whole top surface. The geometrical dimensions are: $a = 100 mm$, $b = 200 mm$, $h = 12 mm$. The faces have different thickness: $h_{top} = 0.1 mm$, $h_{bottom} = 0.5 mm$, and the core thickness is $h_{core} = 11.4 mm$. The two faces have the following material data: $E_1 = 70000 MPa$, $E_2 = 71000 MPa$, $E_3 = 69000 MPa$, $G_{12} = G_{13} = G_{23} = 26000 MPa$, $\nu_{12} = \nu_{13} = \nu_{23} = 0.3$. The core made of metallic foam has the following data: $E_1 = E_2 = 3 MPa$, $E_3 = 2.8 MPa$, $G_{12} = G_{13} = G_{23} = 1 MPa$, $\nu_{12} = \nu_{13} = \nu_{23} = 0.25$.

The results of local values at top and bottom surfaces are listed in Table 6.17. It can be observed that although moderately thick plates are considered $a/h = (100/12)$, lower order theories as $ET1_a$ lead to completely wrong results. Very accurate models are required to

capture the stress distribution in the two faces, and the importance of the zig-zag term has to be underlined for this type of layered structure.

Table 6.17: Sandwich rectangular plate. Transverse displacement $w = w(a/2, b/2, \pm h/2)$, in-plane principal stresses $\sigma_{xx} = \sigma_{xx}(a/2, b/2)$ and $\sigma_{yy} = \sigma_{yy}(a/2, b/2)$.

	w		σ_{xx}				σ_{yy}			
	<i>top</i>	<i>bottom</i>	Top Skin		Bottom Skin		Top Skin		Bottom Skin	
			<i>top</i>	<i>bottom</i>	<i>top</i>	<i>bottom</i>	<i>top</i>	<i>bottom</i>	<i>top</i>	<i>bottom</i>
<i>LW4_a</i> [139]	-9.142	-8.968	-112.4	-48.435	-133.21	166.27	-52.824	-23.320	-54.327	69.915
<i>LW4</i>	-9.140	-8.968	-110.7	-51.073	-132.85	166.10	-50.519	-25.617	-53.664	69.254
<i>ET1_a</i> [139]	-0.1022	-0.1020	-89.63	-88.715	15.508	20.008	-51.453	-50.932	8.4375	11.041
<i>ET4</i>	-6.138	-6.031	-83.62	-81.92	-84.42	114.60	-28.265	-50.032	-35.270	46.817
<i>ES5</i>	-7.305	-7.286	-112.7	-56.801	-105.96	158.63	-66.121	-38.325	-42.071	81.605
<i>ET1S1</i>	-1.731	-1.638	-85.10	-85.295	-47.978	84.448	-35.870	-42.617	-43.629	58.979
<i>ET1C1</i>	-0.127	-0.129	-88.45	-87.420	14.642	20.492	-41.521	-40.932	6.314	9.564
<i>EExp3</i>	-4.371	-4.323	-92.47	-78.557	-76.505	113.58	-39.169	-41.849	-44.857	62.113
<i>ET1Exp2</i>	-2.765	-2.730	-90.87	-79.453	-45.443	82.566	-40.886	-39.775	-29.510	46.796
<i>EExp4</i>	-4.497	-4.434	-64.32	-104.42	-63.669	99.959	-11.174	-68.260	-30.944	47.640
<i>ET1Exp3</i>	-4.835	-4.756	-68.21	-98.110	-64.585	98.892	-15.117	-63.323	-28.370	43.578
<i>ES3C3</i>	-7.167	-7.043	-86.88	-82.210	-100.75	132.40	-28.679	-51.200	-41.649	54.757
<i>ES4C4</i>	-7.725	-7.584	-100.2	-64.880	-108.01	143.89	-42.273	-36.314	-43.099	60.993
<i>ET1S1C1</i>	-1.873	-1.859	-92.42	-80.000	-24.335	61.361	-43.735	-38.237	-16.651	34.028
<i>ET1S2C2</i>	-6.630	-6.513	-87.24	-78.839	-90.690	124.87	-30.876	-47.612	-36.754	52.577
<i>ET3Z</i>	-7.402	-7.273	-124.6	-35.263	-106.73	140.18	-68.284	-7.0972	-44.822	59.631
<i>ES4Z</i>	-7.362	-7.184	-123.1	-42.628	-114.88	126.33	-65.387	-12.490	-54.109	47.247
<i>ES5Z</i>	-7.482	-7.303	-119.7	-45.595	-110.17	135.74	-61.693	-15.638	-48.151	55.481
<i>ET1S2Z</i>	-6.334	-6.166	-115.7	-51.880	-92.06	116.54	-59.280	-18.998	-41.748	47.515
<i>ET1S3Z</i>	-7.142	-6.968	-124.3	-42.770	-113.80	119.94	-66.762	-11.918	-55.304	42.962
<i>ET1C2Z</i>	-7.650	-7.516	-105.2	-54.839	-109.73	143.35	-48.303	-27.188	-45.287	60.373
<i>EExp5Z</i>	-7.606	-7.473	-108.1	-52.184	-108.58	142.57	-51.282	-24.240	-44.719	60.114
<i>EExp6Z</i>	-8.278	-8.126	-107.1	-52.842	-119.37	150.98	-48.835	-26.058	-48.859	62.350
<i>ET1Exp4Z</i>	-7.805	-7.665	-107.7	-52.359	-111.53	144.39	-50.512	-24.802	-45.700	60.124
<i>ET1Exp5Z</i>	-8.379	-8.225	-107.7	-52.612	-121.51	152.06	-49.329	-25.945	-50.000	62.425
<i>ES4C4Z</i>	-8.561	-8.403	-107.9	-52.185	-123.22	156.43	-49.162	-25.942	-49.863	65.144
<i>ET1S3C3Z</i>	-8.508	-8.351	-108.7	-51.973	-121.82	156.16	-49.995	-25.507	-49.019	65.342

Chapter 7

Results on Thermo-Mechanical Problems

This chapter considers the thermal stress analysis of multilayered composite plates and shells. In order to determine the thermal load two different cases are considered: - the temperature distribution in the thickness direction is assumed linear; - the temperature distribution in the thickness direction is calculated via Fourier's heat conduction equation. Some results are given in order to demonstrate the capability of the refined and advanced models to obtain the quasi-3D results.

7.1 Heat conduction problem in layered structures

The heat conduction problem is investigated by solving the Fourier heat conduction equation as described in [83] for the plate case. Here the solution is given for the shell case as proposed in [31]. If the values of the temperature are known at the top and bottom surface of the shell, the temperature profile through the thickness can be considered in two different ways. The first method introduces an assumed profile $\hat{\theta}(z)$ that varies linearly from the top to the bottom as follows:

$$\hat{\theta}(z) = \theta_{bottom} + \frac{\theta_{top} - \theta_{bottom}}{h} * \left(z + \frac{h}{2} \right) \quad z \in \left[\frac{-h}{2}; \frac{h}{2} \right] \quad (7.1)$$

Independently by the number of considered layers the linear profile is always the same. The second one computes $\hat{\theta}(z)$ by solving the Fourier heat conduction equation. In case of multi-layered structures, in general for the k^{th} homogeneous orthotropic layer, the differential Fourier equation of heat conduction reads:

$$\left(\frac{\mathcal{K}_1^k}{(H_\alpha^k)^2} \right) \frac{\delta^2 \theta}{\delta \alpha^2} + \left(\frac{\mathcal{K}_2^k}{(H_\beta^k)^2} \right) \frac{\delta^2 \theta}{\delta \beta^2} + \left(\mathcal{K}_3^k \right) \frac{\delta^2 \theta}{\delta z^2} = 0 \quad (7.2)$$

where $\mathcal{K}_1^k, \mathcal{K}_2^k, \mathcal{K}_3^k$ are the thermal conductivities coefficients in material coordinates (1, 2, 3) for each orthotropic layer k and then rotated in the general curvilinear reference system (α, β, z) . In case of multi-layered structures, continuity conditions for the temperature θ and the transverse normal heat flux q_z hold in the thickness direction at each k^{th} layer interface, reading:

$$\theta_t^k = \theta_b^{k+1} \quad q_{zt}^k = q_{zb}^{k+1} \quad for \ k = 1, \dots, N_l - 1 \quad (7.3)$$

where N_l is the number of layers in the considered structure. The relationship between the transverse heat flux and the temperature is given as:

$$q_z^k = \mathcal{K}_3^k \frac{\delta \theta}{\delta z} \quad (7.4)$$

For the k^{th} layer of the shell structure it is supposed that $\mathcal{K}_1^k, \mathcal{K}_2^k, \mathcal{K}_3^k$ are constant because in each layer H_α^k, H_β^k are calculated. For each layer both governing equations and boundary conditions are satisfied by assuming the following temperature field:

$$\theta(\alpha, \beta, z) = f(z) \sin\left(\frac{m\pi\alpha}{a}\right) \sin\left(\frac{n\pi\beta}{b}\right) \quad (7.5)$$

where $f(z)$ is assumed as:

$$f(z) = \theta_0 \exp\left(s^k z\right) \quad (7.6)$$

where θ_0 is a constant and s^k a parameter. Substituting 7.5 in 7.2 and solving for s^k :

$$s_{1,2}^k = \pm \sqrt{\frac{\frac{\mathcal{K}_1^k}{(H_\alpha^k)^2} \left(\frac{m\pi}{a}\right)^2 + \frac{\mathcal{K}_2^k}{(H_\beta^k)^2} \left(\frac{n\pi}{b}\right)^2}{\mathcal{K}_3^k}} \quad (7.7)$$

Therefore:

$$\begin{aligned} f(z) &= \theta_{01}^k \exp\left(s_1^k z\right) + \theta_{02}^k \exp\left(s_2^k z\right) \text{ or} \\ f(z) &= C_1^k \cosh\left(s_1^k z\right) + C_2^k \sinh\left(s_1^k z\right) \end{aligned} \quad (7.8)$$

The solution for a layer k can be written as:

$$\theta_c(\alpha, \beta, z) = \theta^k = \left[C_1^k \cosh\left(s_1^k z\right) + C_2^k \sinh\left(s_1^k z\right) \right] \sin\left(\frac{m\pi\alpha}{a}\right) \sin\left(\frac{n\pi\beta}{b}\right) \quad (7.9)$$

wherein the coefficients C_1^k and C_2^k are constant for each layer k. In 7.8 for each layer k two unknowns (C_1^k and C_2^k) remain. Therefore, if the number of layers is N_l , the number of unknowns is $(2N_l)$ and $(2N_l)$ equations to determine the unknowns are needed. The first two conditions are given by the temperature at the top and the bottom of the shell structure:

$$\begin{aligned} f(z_{bottom}) &= \hat{\theta}_{bottom} = C_1^1 \cosh\left(s_1^1 z_{bottom}\right) + C_2^1 \sinh\left(s_1^1 z_{bottom}\right) \\ f(z_{top}) &= \hat{\theta}_{top} = C_1^{N_l} \cosh\left(s_1^{N_l} z_{top}\right) + C_2^{N_l} \sinh\left(s_1^{N_l} z_{top}\right) \end{aligned} \quad (7.10)$$

Another $(N_l - 1)$ equations can be obtained from the continuity of temperature at each layer interface as follows:

$$C_1^k \cosh\left(s_1^k z_t^k\right) + C_2^k \sinh\left(s_1^k z_t^k\right) - C_1^{k+1} \cosh\left(s_1^{k+1} z_b^{k+1}\right) - C_2^{k+1} \sinh\left(s_1^{k+1} z_b^{k+1}\right) = 0 \quad (7.11)$$

and another $(N_l - 1)$ equations can be obtained from the continuity of heat flux through the interfaces as follows:

$$\begin{aligned} s_1^k \mathcal{K}_3^k \left[C_1^k \sinh\left(s_1^k z_t^k\right) + C_2^k \cosh\left(s_1^k z_t^k\right) \right] - s_1^{k+1} \mathcal{K}_3^{k+1} \left[C_1^{k+1} \sinh\left(s_1^{k+1} z_b^{k+1}\right) + \right. \\ \left. + C_2^{k+1} \cosh\left(s_1^{k+1} z_b^{k+1}\right) \right] = 0 \end{aligned} \quad (7.12)$$

In 7.11 and 7.12 subscripts t and b indicate the top and bottom of each layer. Solving the system given by 7.10, 7.11 and 7.12 the $(2N_l)$ coefficients C_1^k and C_2^k are obtained. The temperature amplitude in the thickness shell direction is given by:

$$\hat{\theta}_c(z) = \hat{\theta}^k = C_1^k \cosh\left(s_1^k z\right) + C_2^k \sinh\left(s_1^k z\right) \quad \text{for } k = 1, \dots, N_l \quad (7.13)$$

7.2 Thermal Profile Assumed Linear

To assess the robustness of this shell element three reference problems are considered: the first is a cross-ply square multilayered plate with lamination $(0^\circ/90^\circ/0^\circ)$ and simply-supported boundary conditions, compared with the ones obtained with the 3D elasticity approach by Bhaskar et al. [96]. The second is a cylindrical panel, analytically analyzed, with three different layout configurations: 1 isotropic layer of Aluminium, 2 isotropic layer of Titanium and Aluminium, 2 composite layer with lamination $(0^\circ/90^\circ)$. The third is a square, spherical panel, analytically analyzed, made of 2 composite layers with lamination $(0^\circ/90^\circ)$. The boundary condition is simply-supported. Both of them are evaluated applying a temperature distribution with a bi-sinusoidal in-plane behavior:

$$\theta(\alpha, \beta, z) = \hat{\theta}(z) \sin\left(\frac{m\pi\alpha}{a}\right) \sin\left(\frac{n\pi\beta}{b}\right) \quad (7.14)$$

where $m = n = 1$ and an assumed linear behavior through the thickness:

$$\hat{\theta}(z) = \theta_{bottom} + \frac{\theta_{top} - \theta_{bottom}}{h} * \left(z + \frac{h}{2}\right) \quad z \in \left[\frac{-h}{2}; \frac{h}{2}\right] \quad (7.15)$$

The three problems are briefly described in the following sections.

7.2.1 Multilayered plate

The structure analyzed by Bhaskar et al. [96] (see Figure 7.1) is a composite multilayered square plate with lamination $(0^\circ/90^\circ/0^\circ)$. The physical properties of the material of the plate, Composite, are given in Table 7.1. The geometrical dimensions are: $a = b = 1.0$. The temperature boundary conditions are: $\theta_{top} = +1.0$, $\theta_{bottom} = -1.0$. The results are presented for different thickness ratios $a/h = 2, 10, 50, 100$. A mesh grid of 10×10 elements is taken to ensure the convergence of the solution.

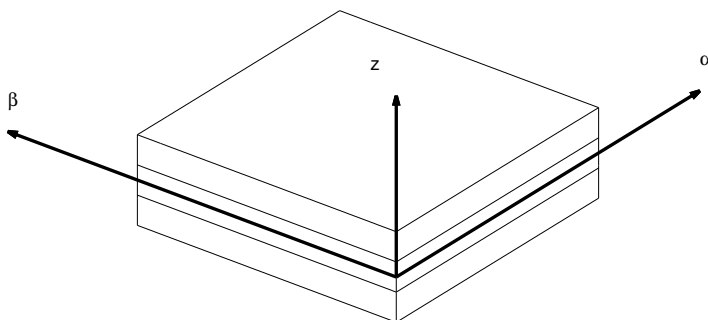


Figure 7.1: Reference system of the plate.

Material	Composite	Aluminium	Titanium	Carbon
E_{11}	25.0	70.3 $E9$	110.0 $E9$	25.0
E_{22}	1.0	70.3 $E9$	110.0 $E9$	1.0
E_{33}	1.0	70.3 $E9$	110.0 $E9$	1.0
ν_{12}	0.25	0.33	0.32	0.25
ν_{13}	0.25	0.33	0.32	0.25
ν_{23}	0.25	0.33	0.32	0.25
G_{12}	0.5	26.429 $E9$	41.667 $E9$	0.5
G_{13}	0.5	26.429 $E9$	41.667 $E9$	0.5
G_{23}	0.2	26.429 $E9$	41.667 $E9$	0.2
α_1	1.0	24.0 $E - 6$	8.6 $E - 6$	1.0
α_2	1125.0	24.0 $E - 6$	8.6 $E - 6$	3.0
α_3	1125.0	24.0 $E - 6$	8.6 $E - 6$	3.0

Table 7.1: Material data for multilayered plate, cylindrical and spherical shell.

The values of the transversal displacement w , the principal in-plane stress $\sigma_{\alpha\alpha}$ and the transverse shear stress $\sigma_{\alpha z}$ are listed in Table 7.2 for the assumed linear temperature profile. Other results in terms of transverse shear stress and transverse principal stress are shown in Figures 7.2a-7.3b. All the FEs lead to accurate results with respect to the 3D [96] and analytical solutions for all the thickness ratios except for $FSDT$. In fact, plate elements that present a constant transverse normal strain such as $FSDT$ lead to inaccurate results for both thick and thin plates. It is confirmed what found in [28]: at least a parabolic expansion for the displacements (u, v, w) is required to capture the linear thermal strains that are related to a linear through-the-thickness temperature distribution. In general, LW theories work better than ESLZ theories, and these last perform better than ESL ones and often also with a lower-order expansion of the unknowns. Equivalent single layer analyses are quite satisfactory only for the transverse displacement or in-plane stresses if applied to thin plates $a/h = 100$, but not for the solution of the transverse normal and shear stresses, as shown in Figures 7.2a-7.3b. On the other hand, higher-order theories lead to better results but computationally more expensive.

Table 7.2: Plate with lamination ($0^\circ/90^\circ/0^\circ$). Transverse displacement $w = w(a/2, b/2) * h_{tot}$ and principal in-plane stress $\sigma_{\alpha\alpha} = \sigma_{\alpha\alpha}(a/2, b/2)$, evaluated at $z = \pm h/2$. Transverse shear stress $\sigma_{\alpha z} = \sigma_{\alpha z}(a, b/2)$, evaluated at $z = +h/6$.

	a/h	2	10	50	100
w	3D [96]	96.79	17.39	10.50	10.26
$\sigma_{\alpha\alpha}$	3D [96]	1390	1026	967.5	965.4
$\sigma_{\alpha z}$	3D [96]	63.92	60.54	14.07	7.073
w	$LW4_a$	96.78	17.39	10.50	10.26
	$LW4$	96.77	17.39	10.50	10.26
	$LW1$	89.23	17.62	11.14	10.91
	$ET3Z$	94.85	17.37	10.50	10.26
	$ET4_a$	98.21	16.90	10.47	10.25
	$ET4$	98.20	16.90	10.47	10.25
	$ET2$	83.45	14.96	10.38	10.23
	$FSDT$	41.27	18.33	15.17	15.06
$\sigma_{\alpha\alpha}$	$LW4$	1392	1029	970.1	968.0
	$LW1$	641.5	906.7	896.2	895.7
	$ET3Z$	1281	1028	970.1	968.0
	$ET4$	1338	1022	969.7	967.9
	$ET2$	189.1	870.3	963.0	966.2
	$FSDT$	161.8	1065	1190	1194
$\sigma_{\alpha z}$	$LW4_a$	63.82	60.54	14.07	7.073
	$LW4$	63.93	60.66	14.10	7.088
	$LW1$	42.54	58.78	13.69	6.883
	$ET3Z$	27.42	52.61	12.45	6.263
	$ET4_a$	37.25	36.33	8.251	4.143
	$ET4$	37.30	36.41	8.268	4.152
	$ET2$	11.58	16.21	3.624	1.819
	$FSDT$	44.48	28.00	6.127	3.073

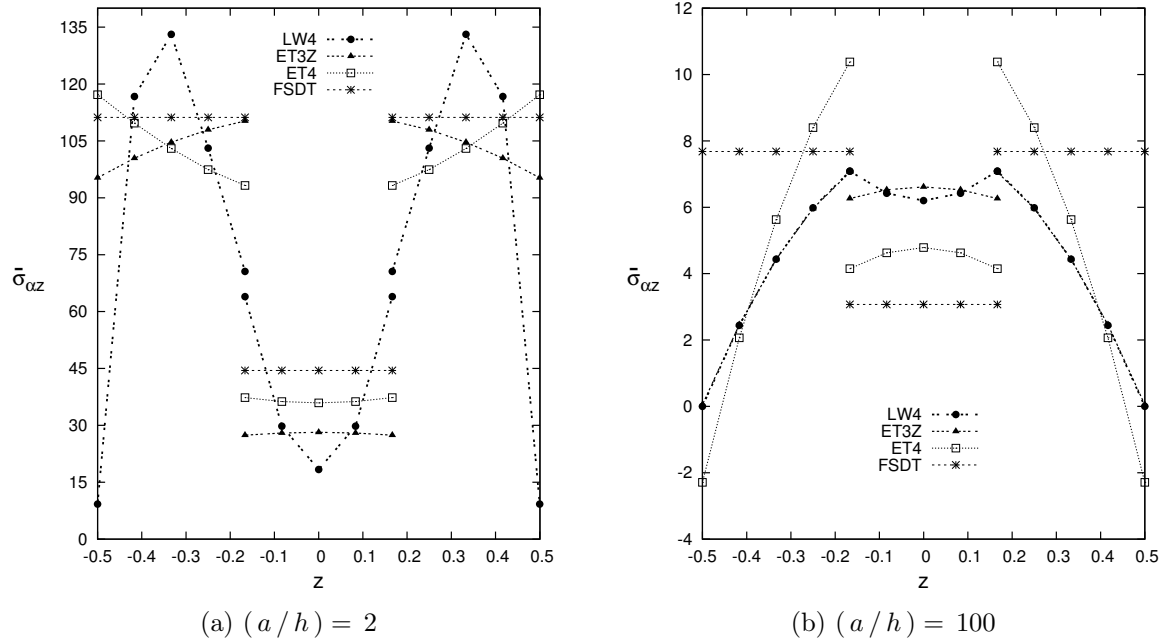


Figure 7.2: Three-layered plate, by varying a/h . Transverse shear stress $\bar{\sigma}_{\alpha z}$.

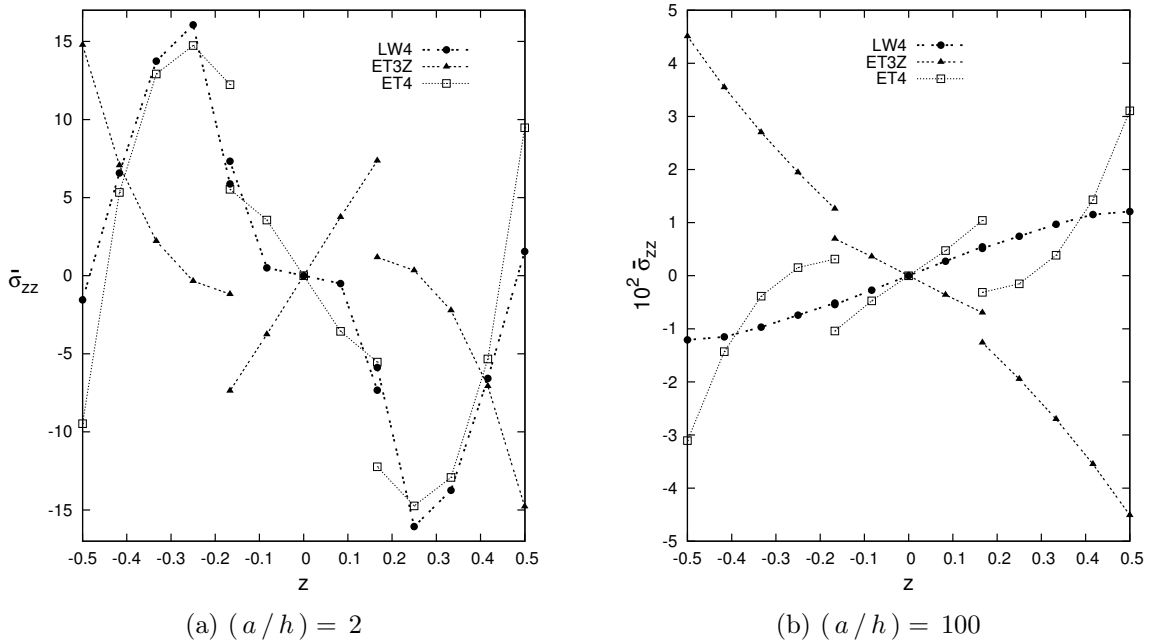


Figure 7.3: Three-layered plate, by varying a/h . Transverse normal stress $\bar{\sigma}_{zz}$.

The same structure is analyzed with a thermal load with the same bi-sinusoidal in-plane behavior and a constant temperature profile $\hat{\theta}(z) = +1.0$. The results are presented for different thickness ratios $a/h = 10, 100$. The values of the transversal displacement w , the principal in-plane stress $\sigma_{\alpha\alpha}$, the transverse shear stress $\sigma_{\alpha z}$ and the transverse normal stress σ_{zz} are listed in Table 7.3 for the constant temperature profile case.

Table 7.3: Constant thermal profile. Plate with lamination ($0^\circ/90^\circ/0^\circ$) and cylindrical and spherical panel with lamination ($0^\circ/90^\circ$), transverse displacement $w = w(a/2, b/2)$, in-plane stress $\sigma_{\alpha\alpha} = \sigma_{\alpha\alpha}(a/2, b/2)$, transverse shear stress $\sigma_{\alpha z} = \sigma_{\alpha z}(a, b/2)$, transverse normal stress $\sigma_{zz} = \sigma_{zz}(a/2, b/2)$. Only for the cylindrical and spherical panel the transverse displacement $w = w 10$, transverse shear stress $\sigma_{\alpha z} = \sigma_{\alpha z} 10^2$, transverse normal stress $\sigma_{zz} = \sigma_{zz} 10^2$.

		<i>Plate</i>		<i>Cylindrical</i>			<i>Spherical</i>		
		a/h	10	100	R/h	10	100	10	100
		$z = +h/2$		$z = +h/2$			$z = +h/2$		
w	$LW4_a$	68.754	6.8879	4.9843	1.4408	4.6505	1.9888		
	$LW4$	68.753	6.8876	4.9846	1.4409	4.6505	1.9890		
	$LW1$	68.783	6.8877	4.8907	1.4232	4.5876	1.9551		
	$ET3Z$	68.839	6.8877	4.9628	1.4366	4.6369	1.9805		
	$ET4_a$	68.777	6.8879	4.9593	1.4366	4.6312	1.9804		
	$ET4$	68.777	6.8877	4.9596	1.4367	4.6313	1.9806		
	$ET2$	68.839	6.8877	4.9015	1.4273	4.5873	1.9618		
	$FSDT$	0.0000	0.0000	4.9736	0.6770	4.4581	1.3244		
		$z = +h/2$		$z = 0^-$		$z = 0^-$			
$\sigma_{\alpha\alpha}$	$LW4$	612.81	454.01	2.5036	0.2558	3.4327	0.6358		
	$LW1$	567.69	453.56	2.3516	0.1301	3.2901	0.5051		
	$ET3Z$	593.28	453.82	2.7386	0.4523	3.7287	0.8255		
	$ET4$	609.56	454.48	2.5096	0.2868	3.4389	0.6595		
	$ET2$	595.93	453.54	2.5005	0.2623	3.4476	0.6400		
	$FSDT$	553.43	553.43	3.6316	0.9261	3.6614	1.2794		
		$z = +h/3$		$z = 0^+$		$z = 0^+$			
$\sigma_{\alpha z}$	$LW4_a$	30.066	2.6696	6.1495	6.5682	7.5142	5.9752		
	$LW4$	30.128	2.6752	6.1582	6.5773	7.5241	5.9833		
	$LW1$	29.251	2.6743	5.0680	5.8966	5.6191	5.5013		
	$ET3Z$	26.748	2.4338	4.2012	5.4270	5.0108	4.7507		
	$ET4_a$	44.361	4.2101	1.6141	3.2464	1.8457	2.6573		
	$ET4$	44.452	4.2188	1.6161	3.2508	1.8478	2.6607		
	$ET2$	26.728	2.4298	0.4314	2.0210	0.3309	1.5369		
	$FSDT$	0.0000	0.0000	0.5730	2.7948	1.7815	2.3323		
		$z = 0$		$z = 0^+$		$z = -h/4$			
σ_{zz}	$LW4$	3.2666	0.0558	-4.2134	-0.2811	-4.9017	-0.1503		
	$LW1$	1.2709	0.0361	-11.732	-2.0980	-3.8270	-0.3264		
	$ET3Z$	2.4211	0.0481	-5.1615	0.1098	-3.2337	0.1982		
	$ET4$	3.0754	1.1539	-5.4135	-0.3486	-3.9658	-0.1466		
	$ET2$	-0.9299	2.4817	-4.3722	-0.7267	-3.3934	-0.1670		

7.2.2 Multilayered cylindrical panel

In this section, a cylindrical panel is analysed (see Figure 7.4). Three different layout configuration are considered:

- 1 layered isotropic cylindrical panel made of Aluminium.
- 2 layered isotropic cylindrical panel made of Titanium and Aluminium.
- 2 layered composite cylindrical panel with lamination ($0^\circ/90^\circ$).

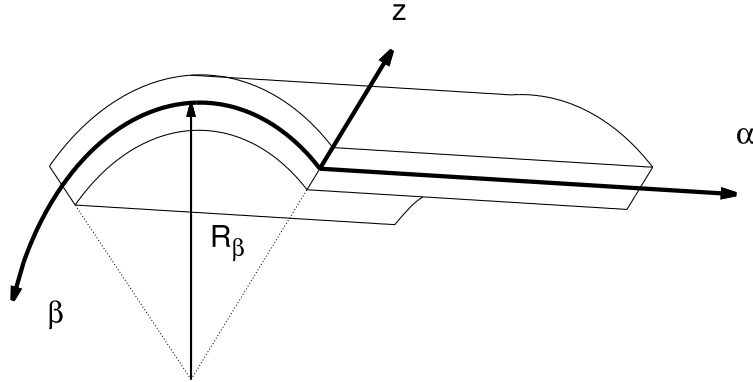


Figure 7.4: Reference system of the cylindrical shell.

The temperature boundary conditions are: $\theta_{top} = +0.5$, $\theta_{bottom} = -0.5$ for all the cases. The results are compared with the correspondent closed form solution. A mesh grid of 10×10 elements is taken to ensure the convergence of the solution. For the 1 and 2 layered isotropic cylindrical panel the geometrical dimensions are: $a = 1.0$ and $b = \frac{\pi}{3}R_\beta = 10.47197551$, curvature radii $R_\alpha = \infty$ and $R_\beta = 10$. The results are presented for different radius to thickness ratios $R_\beta/h_{tot} = (4; 10; 100; 1000)$ with the corresponding thicknesses $h_{tot} = (2.5; 1.0; 0.1; 0.01)$. For the 2 layered isotropic case the bottom layer is made of Aluminium and the top layer is made of Titanium. The physical properties of the Aluminium and Titanium are given in Table 7.1. The values of the transversal displacement w are listed in Table 7.4 for the assumed linear temperature profile. All the FEs lead to accurate results with respect to the analytical solutions for all the thickness ratios except for *LW1*, *ET1*, *FSDT* elements. For the 2 layered composite cylindrical panel the geometrical dimensions are: $a = 1.0$ and $b = 1.0$, global thickness $h_{tot} = 0.1$, curvature radius $R_\alpha = \infty$. The physical properties of the Carbon are given in Table 7.1. The results are presented for different radius to thickness ratios $R_\beta/h_{tot} = (10; 50; 100; 500)$ with the corresponding curvature radius $R_\beta = (1.0; 5.0; 10.0; 50.0)$. The lamination angle is 0° for the bottom layer and 90° for the top layer. The values of the transversal displacement w , the principal in-plane stress $\sigma_{\alpha\alpha}$, the transverse shear stress $\sigma_{\alpha z}$ and the transverse normal stress σ_{zz} are listed in Table 7.5 for the assumed linear temperature profile.

Table 7.4: Cylindrical panel with 1 layer made of isotropic materials Aluminum, $N_l = 1$. Transverse displacement $w = w(a/2, b/2) * 10 h_{tot} / \alpha_{Al} a^2 \Delta T$, evaluated along the thickness in $z = 0$. Cylindrical panel with 2 layers made of isotropic materials Aluminum-Titanium, $N_l = 2$. Transverse displacement $w = w(a/2, b/2) * 10 h_{tot} / \alpha_{Al} a^2 \Delta T$, evaluated along the thickness in $z = +h/4$.

N_l	R_β/h	4	10	100	1000
1	<i>ET4_a</i>	-1.0091	0.9468	1.2007	0.1151
	<i>ET4</i>	-1.0091	0.9468	1.2008	0.1151
	<i>ET3</i>	-0.9787	0.9603	1.2008	0.1151
	<i>ET2</i>	-1.0679	1.9784	1.1995	0.1151
	<i>ET1</i>	1.9502	1.9784	1.8359	0.2189
	<i>FSDT</i>	1.9838	1.9818	1.7943	0.1715
	2	<i>LW4_a</i>	0.4002	0.7472	0.7468
<i>LW4</i>		0.4001	0.7472	0.7468	0.0326
<i>LW3</i>		0.4242	0.7487	0.7468	0.0326
<i>LW2</i>		0.3998	0.7355	0.7468	0.0326
<i>LW1</i>		0.3512	0.7318	0.8630	0.0487
<i>ET4_a</i>		0.4053	0.7386	0.7469	0.0325
<i>ET4</i>		0.4054	0.7386	0.7469	0.0326
<i>ET3</i>		0.4142	0.7405	0.7471	0.0326
<i>ET2</i>		-0.2781	0.5087	0.7466	0.0327
<i>ET1</i>		1.1306	1.1949	1.1524	0.0957
<i>FSDT</i>		1.2350	1.2673	1.1056	0.0463

Table 7.5: Cylindrical panel with lamination ($0^\circ/90^\circ$). Transverse displacement $w = w(a/2, b/2)$, in-plane stress $\sigma_{\alpha\alpha} = \sigma_{\alpha\alpha}(a/2, b/2) * 10$, transverse shear stress $\sigma_{\alpha z} = \sigma_{\alpha z}(a, b/2) * 10^2$, transverse normal stress $\sigma_{zz} = \sigma_{zz}(a/2, b/2) * 10^3$. The variables are evaluated at $z = 0$.

	R_β/h	10	50	100	500
w	$LW4_a$	0.7450	1.1192	1.1359	1.1412
	$LW4$	0.7450	1.1192	1.1359	1.1412
	$LW1$	0.7712	1.1538	1.1706	1.1759
	$ET3Z$	0.7454	1.1177	1.1342	1.1396
	$ET4_a$	0.7461	1.1194	1.1360	1.1413
	$ET4$	0.7461	1.1194	1.1360	1.1413
	$ET2$	0.7455	1.1152	1.1316	1.1369
	$FSDT$	0.8745	1.2781	1.2941	1.2979
$\sigma_{\alpha\alpha}$	$LW4_a$	0.1802 ⁺	0.4204 ⁺	0.3855 ⁺	0.3446 ⁺
	$LW4$	0.1805 ⁺	0.4213 ⁺	0.3864 ⁺	0.3454 ⁺
	$LW1$	2.6963 ⁺	2.7995 ⁺	2.7627 ⁺	2.7235 ⁺
	$ET3Z$	0.3280 ⁺	0.4736 ⁺	0.4290 ⁺	0.3807 ⁺
	$ET4_a$	0.2305 ⁺	0.4192 ⁺	0.3823 ⁺	0.3404 ⁺
	$ET4$	0.2309 ⁺	0.4200 ⁺	0.3831 ⁺	0.3411 ⁺
	$ET2$	0.2010 ⁺	0.4247 ⁺	0.3911 ⁺	0.3519 ⁺
	$FSDT$	0.4683 ⁺	0.7037 ⁺	0.6587 ⁺	0.6086 ⁺
$\sigma_{\alpha z}$	$LW4_a$	-10.901 ⁺	-3.7541 ⁺	-2.8789 ⁺	-2.2428 ⁺
	$LW4$	-10.923 ⁺	-3.7615 ⁺	-2.8845 ⁺	-2.2471 ⁺
	$LW1$	-8.3115 ⁺	-4.0011 ⁺	-3.5188 ⁺	-3.1781 ⁺
	$ET3Z$	-10.522 ⁺	-3.5686 ⁺	-2.7832 ⁺	-2.2277 ⁺
	$ET4_a$	-6.8978 ⁺	-1.7276 ⁺	-1.2097 ⁺	-0.8599 ⁺
	$ET4$	-6.9120 ⁺	-1.7309 ⁺	-1.2120 ⁺	-0.8614 ⁺
	$ET2$	-5.6195 ⁺	-1.7814 ⁺	-1.4294 ⁺	-1.2006 ⁺
	$FSDT$	-4.8037 ⁺	-0.6032 ⁺	-0.2571 ⁺	-0.0436 ⁺
σ_{zz}	$LW4_a$	16.981 ⁺	3.5138 ⁺	1.9186 ⁺	0.4215 ⁺
	$LW4$	17.007 ⁺	3.5359 ⁺	1.9369 ⁺	0.4370 ⁺
	$LW1$	991.25 ⁺	913.40 ⁺	910.39 ⁺	909.18 ⁺
	$ET3Z$	28.853 ⁺	2.5312 ⁺	1.3325 ⁺	0.2854 ⁺
	$ET4_a$	26.667 ⁺	0.1818 ⁺	-1.3515 ⁺	-2.5631 ⁺
	$ET4$	26.682 ⁺	0.1809 ⁺	-1.3563 ⁺	-2.5703 ⁺
	$ET2$	17.342 ⁺	-1.3994 ⁺	-2.2390 ⁺	-2.8356 ⁺
	$FSDT$				

Other results in terms of transverse shear stress and transverse principal stress are shown in Figures 7.5a-7.6b. All the FEs lead to accurate results with respect to the analytical solutions for all the thickness ratios except for $FSDT$ elements. In general, LW theories work better than ESLZ theories, and these last perform better than ESL ones and often also with a lower-order expansion of the unknowns. Equivalent single layer analyses are quite satisfactory only for the transverse displacement also for lower radii to thickness ratios $R/h = 10$, but not for the solutions of the stresses, as shown in Figures 7.5a-7.6b.

The same composite cylindrical panel is analyzed with a thermal load with the same bi-sinusoidal in-plane behavior and a constant temperature profile $\hat{\theta}(z) = +0.5$. The results are presented for different thickness ratios $R/h = 10, 100$. The values of the transversal displacement w , the principal in-plane stress $\sigma_{\alpha\alpha}$, the transverse shear stress $\sigma_{\alpha z}$ and the transverse normal stress σ_{zz} are listed in Table 7.3 for the constant temperature profile case.

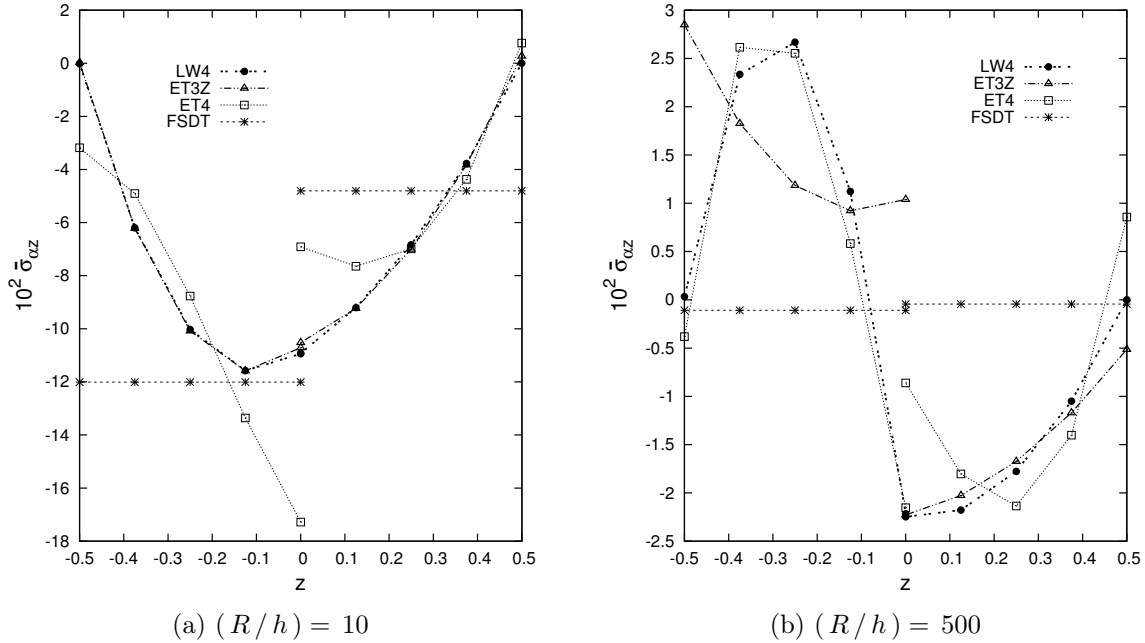


Figure 7.5: Two-layered cylindrical shell, by varying R/h . Transverse shear stress $\bar{\sigma}_{\alpha z}$.

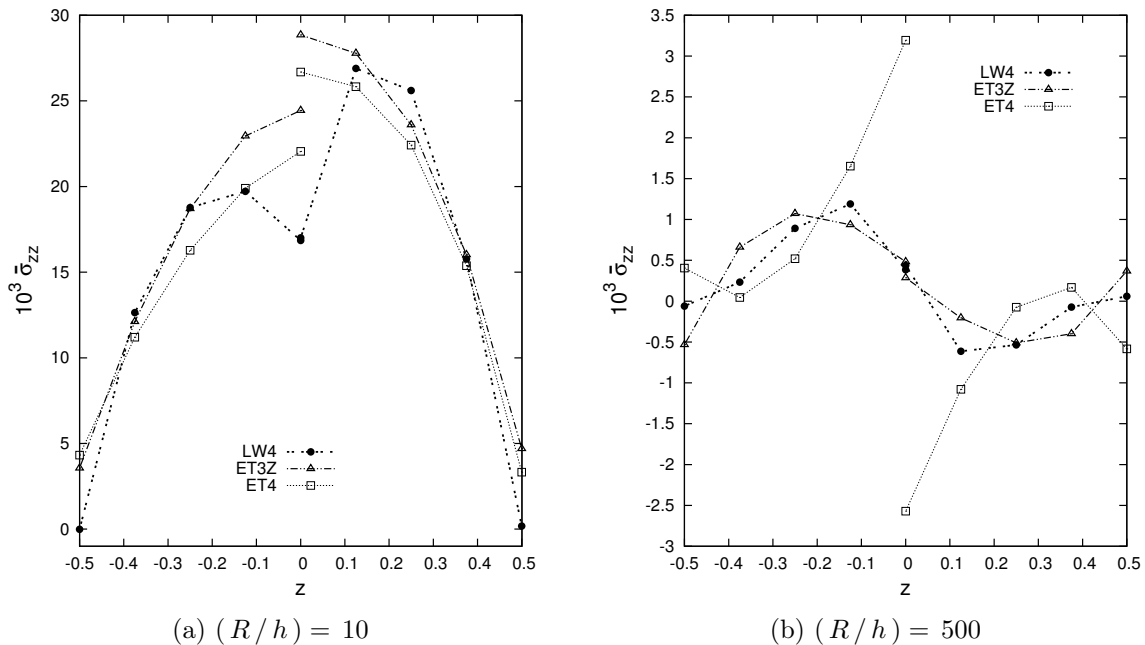


Figure 7.6: Two-layered cylindrical shell, by varying R/h . Transverse normal stress $\bar{\sigma}_{zz}$.

7.2.3 Multilayered spherical panel

In this section, a square, spherical panel is analysed (see Figure 7.7). The temperature boundary conditions are: $\theta_{top} = +0.5$, $\theta_{bottom} = -0.5$ for all the cases. The results are

compared with an analytical solution. A mesh grid of 10×10 elements is taken to ensure the convergence of the solution. The geometrical dimensions are: $a = 1.0$ and $b = 1.0$, global thickness $h_{tot} = 0.1$, curvature radii $R_\alpha = R_\beta = R$. The physical properties of the Carbon are given in Table 7.1.

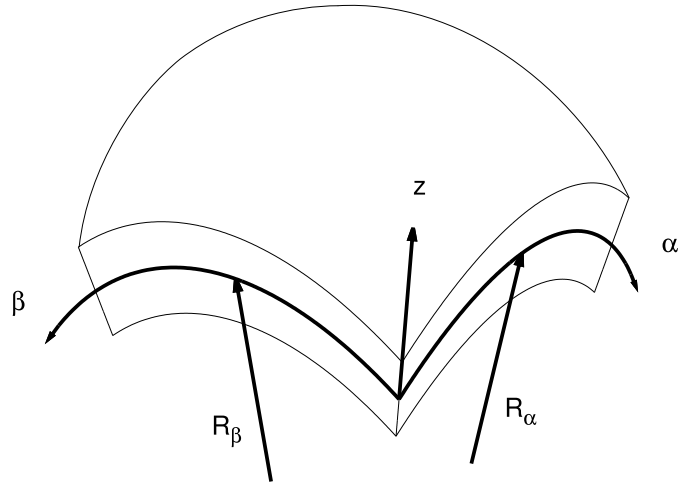


Figure 7.7: Reference system of the spherical shell.

The results are presented for different radius to thickness ratios $R/h_{tot} = (10; 50; 100; 500)$ with the corresponding curvature radius $R = (1.0; 5.0; 10.0; 50.0)$. The lamination angle is 0° for the bottom layer and 90° for the top layer. The values of the transversal displacement w , the principal in-plane stress $\sigma_{\alpha\alpha}$, the transverse shear stress $\sigma_{\alpha z}$ and the transverse normal stress σ_{zz} are listed in Table 7.6 for the assumed linear temperature profile. Other results in terms of transverse shear stress and transverse principal stress are shown in Figures 7.8a-7.9b. All the FEs lead to accurate results with respect to the analytical solutions for all the thickness ratios except for *FSDT* elements. In general, LW theories work better than ESLZ theories, and these last perform better than ESL ones and often also with a lower-order expansion of the unknowns. Equivalent single layer analyses are quite satisfactory only for the transverse displacement also for lower radii to thickness ratios $R/h = 10$, but not for the solutions of the stresses, as shown in Figures 7.8a-7.9b.

The same composite spherical panel is analyzed with a thermal load with the same bi-sinusoidal in-plane behavior and a constant temperature profile $\hat{\theta}(z) = +0.5$. The results are presented for different thickness ratios $R/h = 10, 100$. The values of the transversal displacement w , the principal in-plane stress $\sigma_{\alpha\alpha}$, the transverse shear stress $\sigma_{\alpha z}$ and the transverse normal stress σ_{zz} are listed in Table 7.3 for the constant temperature profile case.

Table 7.6: Spherical panel with lamination ($0^\circ/90^\circ$). Transverse displacement $w = w(a/2, b/2)$, in-plane stress $\sigma_{\alpha\alpha} = \sigma_{\alpha\alpha}(a/2, b/2) * 10$ and transverse normal stress $\sigma_{zz} = \sigma_{zz}(a/2, b/2) * 10^3$ evaluated at $z = 0$, transverse shear stress $\sigma_{\alpha z} = \sigma_{\alpha z}(a, b/2) * 10^2$ evaluated at $z = -h/4$.

	R/h	10	50	100	500
w	$LW4_a$	0.3299	1.0507	1.1174	1.1404
	$LW4$	0.3299	1.0507	1.1174	1.1405
	$LW1$	0.3386	1.0836	1.1516	1.1751
	$ET3Z$	0.3306	1.0496	1.1159	1.1388
	$ET4_a$	0.3309	1.0511	1.1176	1.1406
	$ET4$	0.3309	1.0511	1.1176	1.1406
	$ET2$	0.3315	1.0477	1.1134	1.1361
	$FSDT$	0.3927	1.1967	1.2709	1.2965
$\sigma_{\alpha\alpha}$	$LW4_a$	-25.208 ⁻	10.291 ⁻	11.875 ⁻	11.363 ⁻
	$LW4$	-25.244 ⁻	10.305 ⁻	11.892 ⁻	11.379 ⁻
	$LW1$	-29.322 ⁻	9.5416 ⁻	11.413 ⁻	11.072 ⁻
	$ET3Z$	-21.884 ⁻	12.316 ⁻	13.447 ⁻	12.579 ⁻
	$ET4_a$	-24.080 ⁻	10.619 ⁻	12.076 ⁻	11.486 ⁻
	$ET4$	-24.114 ⁻	10.634 ⁻	12.093 ⁻	11.502 ⁻
	$ET2$	-25.115 ⁻	10.823 ⁻	12.399 ⁻	11.876 ⁻
	$FSDT$	-17.466 ⁻	19.697 ⁻	21.054 ⁻	20.123 ⁻
$\sigma_{\alpha z}$	$LW4_a$	24.096	1.1199	-1.3854	-2.5674
	$LW4$	24.131	1.1212	-1.3877	-2.5714
	$LW1$	19.500	1.5598	-0.5309	-1.5931
	$ET3Z$	21.061	2.4154	0.1275	-1.0771
	$ET4_a$	21.281	0.8662	-1.3842	-2.4603
	$ET4$	21.312	0.8673	-1.3865	-2.4641
	$ET2$	20.284	3.0723	0.9925	-0.0983
	$FSDT$	21.845	3.9515	1.5581	0.2307
σ_{zz}	$LW4_a$	76.657 ⁺	9.2085 ⁺	4.3230 ⁺	0.8525 ⁺
	$LW4$	76.652 ⁺	9.2360 ⁺	4.3451 ⁺	0.8698 ⁺
	$LW1$	1100.7 ⁺	928.03 ⁺	915.09 ⁺	909.73 ⁺
	$ET3Z$	98.145 ⁺	8.8651 ⁺	3.9948 ⁺	0.7759 ⁺
	$ET4_a$	111.83 ⁺	6.3462 ⁺	0.8566 ⁺	-2.2210 ⁺
	$ET4$	111.83 ⁺	6.3530 ⁺	0.8569 ⁺	-2.2255 ⁺
	$ET2$	76.502 ⁺	2.4683 ⁺	-0.9816 ⁺	-2.6625 ⁺

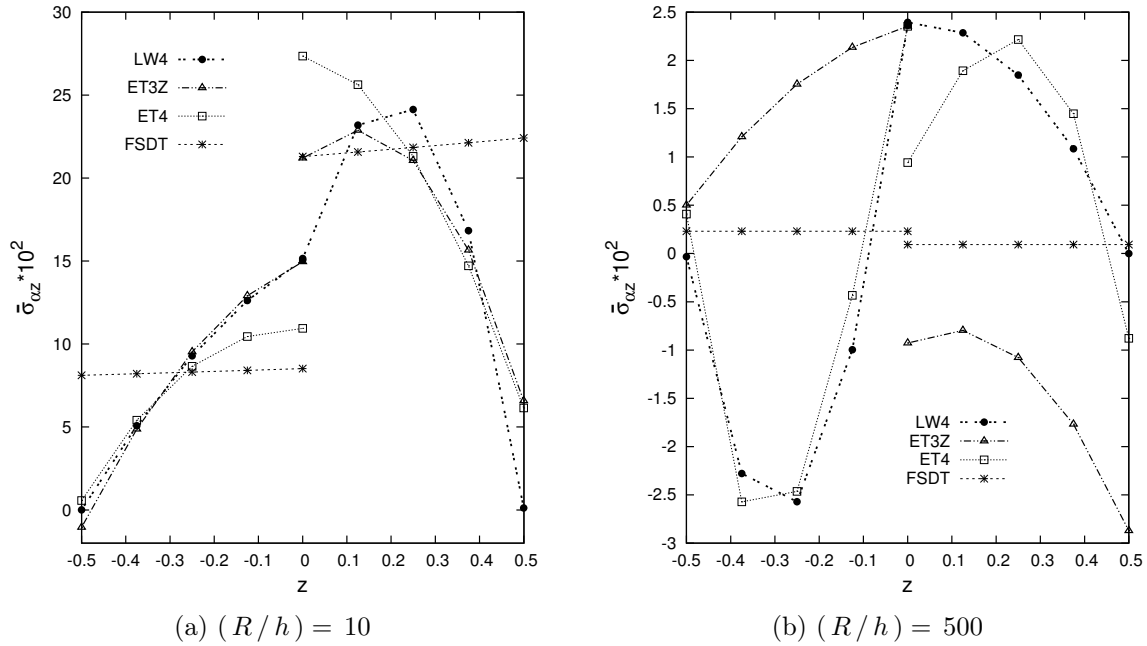


Figure 7.8: Two-layered spherical shell, by varying R/h . Transverse shear stress $\bar{\sigma}_{\alpha z}$.

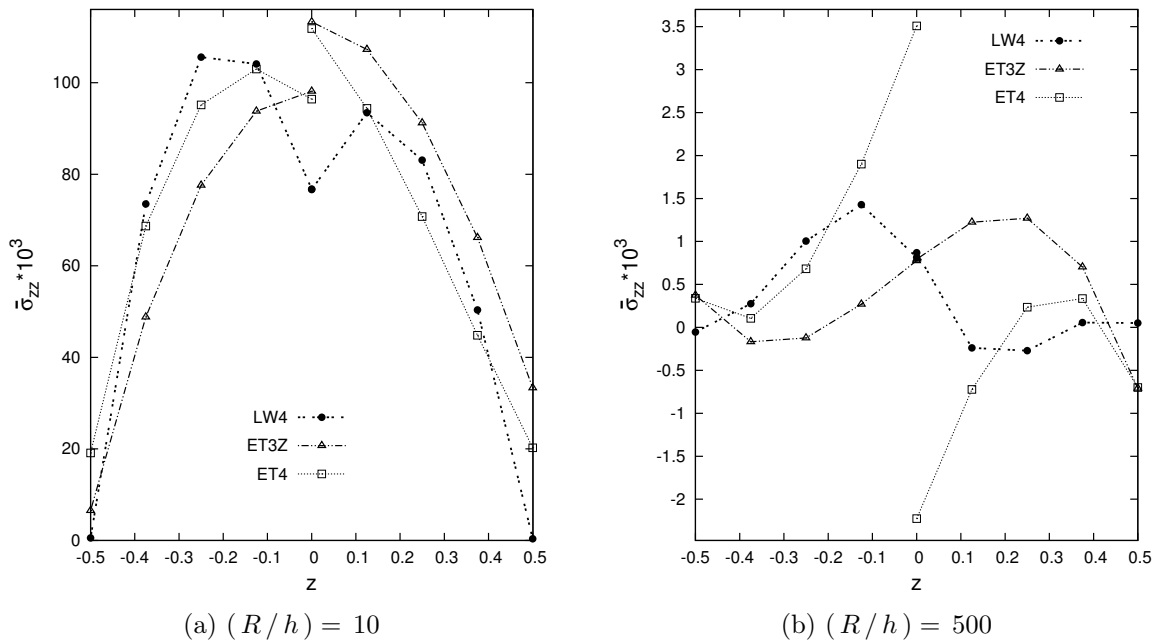


Figure 7.9: Two-layered spherical shell, by varying R/h . Transverse normal stress $\bar{\sigma}_{zz}$.

7.3 Calculated Thermal Profile

This section is composed of two parts. The first one is devoted to the assessment of the shell element based on the Unified Formulation by the static analysis of simply supported plates, cylindrical shells and spherical shells. Both of them are evaluated applying a thermal load with a bi-sinusoidal in-plane behavior. Before the assessment results of the static analysis a briefly discussion about the evaluation of the temperature profile is given. Using the theory that provides the most accurate results, the second part presents some benchmark solutions relative to plates, cylindrical shells and spherical shells with particular lamination and boundary conditions.

In the following numerical section, the results obtained with an assumed linear temperature profile are indicated with the letters T_a , otherwise if the Fourier heat conduction law is used, the results are marked with the letters T_c .

7.3.1 Temperature profile evaluation

The temperature profile along the thickness direction, for the plate structure and the cylindrical shell panel, is evaluated for both the assumed linear profile and the calculated temperature profile via Fourier heat conduction law. For the three layered composite plate structure, see Figure 7.10, the calculated profile is plotted for different thickness ratios a/h . It is evident that for thin plates the temperature profile can be assumed almost linear, conversely for thick plates the temperature behavior is very far from the linear ones, and large errors computing the thermal load can be committed if the temperature profile is assumed as linear.

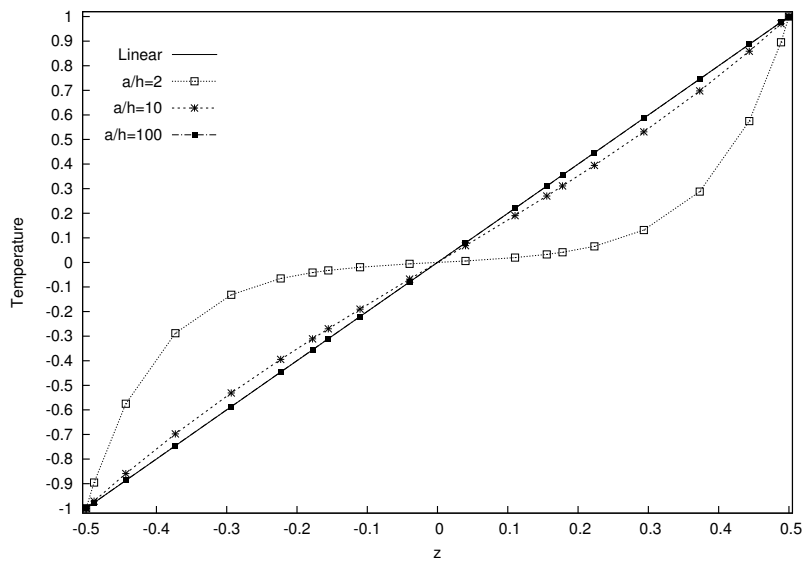


Figure 7.10: Temperature Profiles for different thickness ratios (a/h). Composite plate.

For the two layered composite cylindrical shell panel, see Figure 7.11, the calculated profile is plotted for different thickness to radius ratios R/h and all for the same thickness ratio $a/h = 10$. It is evident that the effect of the curvature is negligible for the approximation of the temperature profile and the difference respect to the linear profile is due only to the thickness ratio $a/h = 10$.

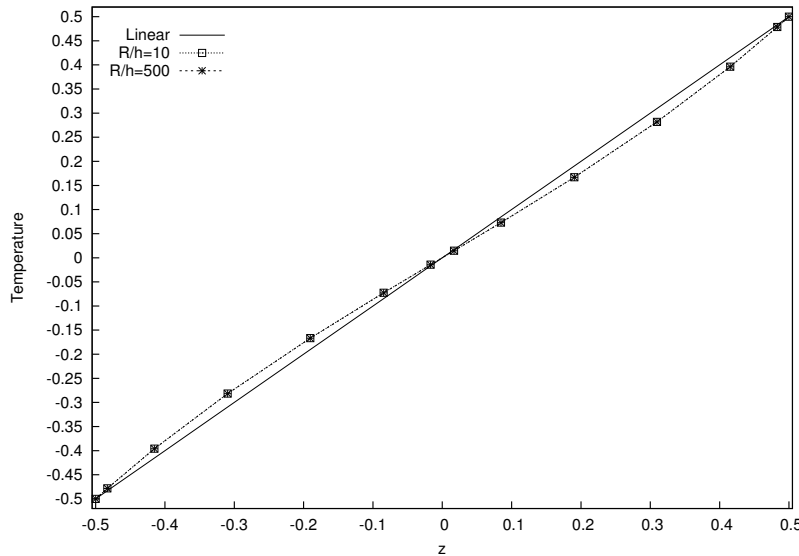


Figure 7.11: Temperature Profiles for different radius to thickness ratios (R/h). Composite cylinder.

The proposed temperature profile evaluations clarify the importance of a calculated temperature profile for thick plates and shells to avoid large errors for the approximation of thermal load.

7.3.2 Assessment

To assess the robustness of this shell element three reference problems are considered: the first is a cross-ply square multilayered plate with lamination ($0^\circ/90^\circ/0^\circ$) and simply-supported boundary condition, compared with the ones obtained with the 3D elasticity approach by Bhaskar et al. [96]. The second is a square cylindrical panel, analytically analyzed, with lamination ($0^\circ/90^\circ$) and simply-supported boundary condition. The third is a square spherical panel, analytically analyzed, with lamination ($0^\circ/90^\circ$). The boundary condition is simply-supported. Both of them are evaluated applying a thermal load with a bi-sinusoidal in-plane behavior:

$$\theta(\alpha, \beta, z) = \hat{\theta}(z) \sin\left(\frac{m\pi\alpha}{a}\right) \sin\left(\frac{n\pi\beta}{b}\right) \quad (7.16)$$

where $m = n = 1$. The three problems are briefly described in the following sections.

Multilayered plate

The structure analyzed by Bhaskar et al. [96] is a composite multilayered square plate with lamination ($0^\circ/90^\circ/0^\circ$). The physical properties of the material of the plate, Composite, are given in Table 7.7. The geometrical dimensions are: $a = b = 1.0$. The temperature boundary conditions are: $\hat{\theta}_{top} = +1.0$, $\hat{\theta}_{bottom} = -1.0$.

Table 7.7: Physical data for multilayered plate, cylindrical and spherical shell.

Material	E_{11}	E_{22}	E_{33}	ν_{12}	ν_{13}	ν_{23}	G_{12}	G_{13}	G_{23}	α_1	α_2	α_3	\mathcal{K}_1	\mathcal{K}_2	\mathcal{K}_3
Composite	25.0	1.0	1.0	0.25	0.25	0.25	0.5	0.5	0.2	1.0	1125.0	1125.0	36.42	0.96	0.96
Carbon	25.0	1.0	1.0	0.25	0.25	0.25	0.5	0.5	0.2	1.0	3.0	3.0	36.42	0.96	0.96

The results are presented for different thickness ratios $a/h = 2, 10, 50, 100$. A mesh grid of 10×10 elements is taken to ensure the convergence of the solution, see Table 7.8. The accuracy of the shell element is tested and compared with different type of integration methods [115] for a thin plate to prove that the element is locking free, see Table 7.9.

Table 7.8: Convergence study. Plate with thickness ratio $a/h = 100$, cylindrical panel and spherical panel with radius to thickness ratio $R/h = 500$. All the cases are computed for the calculated temperature profile T_c and with a *LW4* theory.

	Mesh	4×4	6×6	8×8	10×10	<i>Analytical</i>
<i>Plate</i>	w	10.27	10.26	10.25	10.25	10.25
	$\sigma_{\alpha z}$	7.466	7.213	7.102	7.084	7.069
<i>Cylindrical</i>	w	1.0966	1.0955	1.0953	1.0952	1.0953
	$\sigma_{\alpha z}$	-1.7090	-1.7131	-1.7093	-1.6983	-1.6957
<i>Spherical</i>	w	1.0958	1.0948	1.0946	1.0945	1.0945
	$\sigma_{\alpha z}$	-2.2848	-2.2065	-2.1562	-2.1461	-2.1403

Table 7.9: Locking study. Plate with thickness ratio $a/h = 100$. All the cases are computed for the calculated temperature profile T_c , with a mesh of 10×10 elements.

		<i>Reduced</i>	<i>Selective</i>	<i>MITC9</i>
<i>LW4</i>	w	10.1368	10.2515	10.2532
	$\sigma_{\alpha z}$	10.512	8.737	7.084
<i>ET4</i>	w	10.2273	10.2446	10.2464
	$\sigma_{\alpha z}$	5.554	5.489	4.149

The values of the transversal displacement w and the transverse shear stress $\sigma_{\alpha z}$ are listed in Table 7.10 for the temperature profile calculated solving the Fourier heat conduction equation and compared with the assumed linear temperature profile. Other results in terms of transverse shear stress and transversal displacement are shown in Figures 7.12a-7.13b.

Table 7.10: Plate with lamination (0°/90°/0°). Transverse displacement $w = w(a/2, b/2) * h_{tot}$, evaluated at $z = \pm h/2$. Transverse shear stress $\sigma_{\alpha z} = \sigma_{\alpha z}(a, 0)$, evaluated at $z = +h/6$.

		a/h	2	10	50	100	
w	3D [96]		96.79	17.39	10.50	10.26	
$\sigma_{\alpha z}$	3D [96]		63.92	60.54	14.07	7.073	
w	$LW4_a$	T_a	96.78	17.39	10.50	10.26	
		T_c	49.09	16.39	10.47	10.25	
	$LW4$	T_a	96.77	17.39	10.50	10.26	
		T_c	48.85	16.39	10.47	10.25	
	$LW1$	T_a	89.23	17.62	11.14	10.91	
		T_c	44.17	16.69	11.11	10.91	
	$ET3Z$	T_a	94.85	17.37	10.50	10.26	
		T_c	50.08	16.41	10.47	10.25	
	$ET4_a$	T_a	98.21	16.90	10.47	10.25	
		T_c	49.55	15.93	10.44	10.25	
	$ET4$	T_a	98.20	16.90	10.47	10.25	
		T_c	49.29	15.93	10.44	10.25	
	$ET2$	T_a	83.45	14.96	10.38	10.23	
		T_c	40.87	14.09	10.35	10.22	
	$FSDT$	T_a	41.27	18.33	15.17	15.06	
		T_c	20.35	17.26	15.13	15.05	
	$\sigma_{\alpha z}$	$LW4_a$	T_a	63.82	60.54	14.07	7.073
			T_c	30.11	57.07	14.04	7.069
$LW4$		T_a	63.93	60.66	14.10	7.088	
		T_c	30.00	57.18	14.07	7.084	
$LW1$		T_a	42.54	58.78	13.69	6.883	
		T_c	31.69	56.35	13.21	6.879	
$ET3Z$		T_a	27.42	52.61	12.45	6.263	
		T_c	23.42	50.43	12.43	6.260	
$ET4_a$		T_a	37.25	36.33	8.251	4.143	
		T_c	24.04	34.47	8.232	4.140	
$ET4$		T_a	37.30	36.41	8.268	4.152	
		T_c	23.96	34.55	8.250	4.149	
$ET2$		T_a	11.58	16.21	3.624	1.819	
		T_c	6.065	15.31	3.616	1.818	
$FSDT$		T_a	44.48	28.00	6.127	3.073	
		T_c	22.09	26.41	6.112	3.071	

All the FEs, with an assumed linear temperature profile, lead to accurate results with respect to the 3D [96], that makes use of the same linear profile assumption, and analytical

solutions for all the thickness ratios except for *FSDT*. In fact, plate elements that present a constant transverse normal strain such as *FSDT* lead to inaccurate results for both thick and thin plates. It is confirmed what found in [28]: at least a parabolic expansion for the displacements (u, v, w) is required to capture the linear thermal strains that are related to a linear through-the-thickness temperature distribution. The results obtained with the calculated temperature profile are close to them of the assumed linear profile for plates with thickness ratios $a/h = 50, 100$, instead for plates with thickness ratios $a/h = 2, 10$ the thermal profile behavior is clearly non linear and results are different respect to linear profile cases even if the variables are approximated in a refined way.

In general, LW theories perform better than ESL ones and often also with a lower-order expansion of the unknowns. Equivalent single layer analyses are quite satisfactory only for the transverse displacement if applied to thin plates $a/h = 100$, but not for the solution of the transverse shear stresses, as shown in Figures 7.12a-7.13b. On the other hand, higher-order theories lead to better results but computationally more expensive.

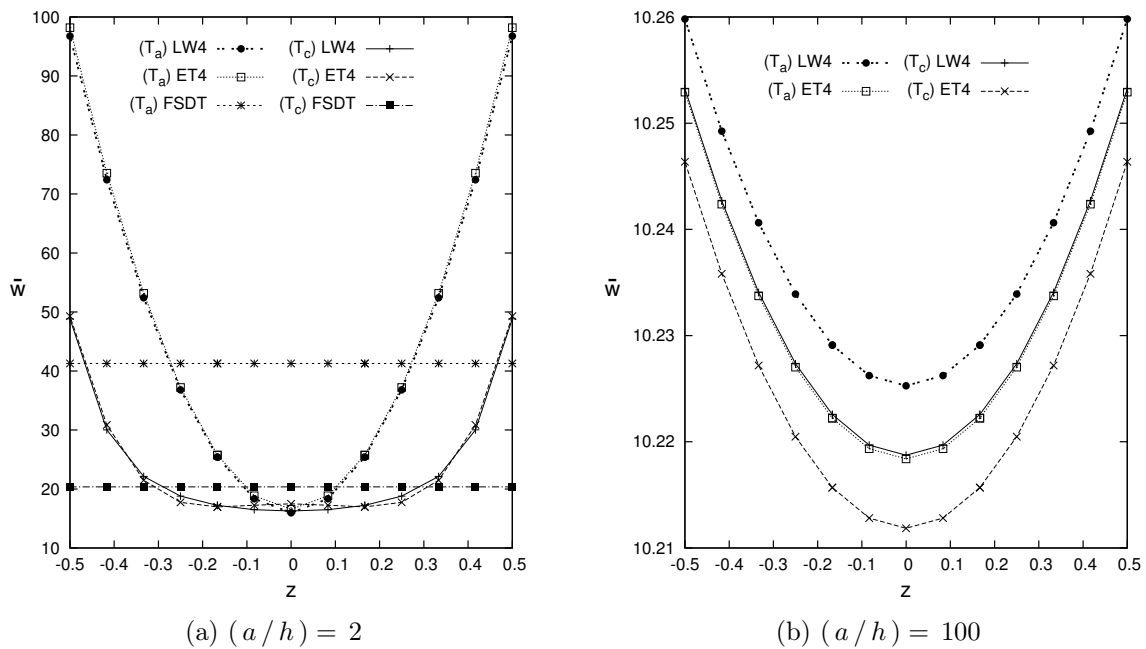


Figure 7.12: Three-layered plate, by varying a/h . Transverse displacement w .

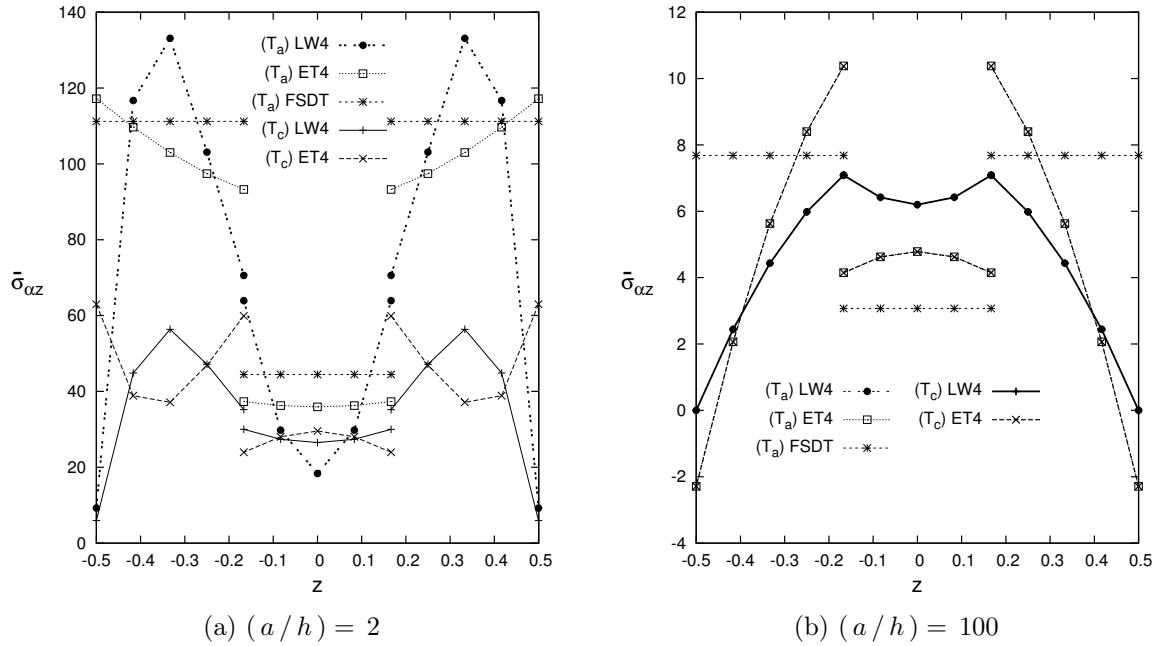


Figure 7.13: Three-layered plate, by varying a/h . Transverse shear stress $\sigma_{\alpha z}$.

Multilayered cylindrical panel

In this section, a cylindrical composite panel with lamination $(0^\circ/90^\circ)$ is analysed. The lamination angle is 0° for the bottom layer and 90° for the top layer. The geometrical dimensions are: $a = 1.0$ and $b = 1.0$, global thickness $h_{tot} = 0.1$, curvature radius $R_\alpha = \infty$. The physical properties of the Carbon are given in Table 7.7. The temperature boundary conditions are: $\hat{\theta}_{top} = +0.5$, $\hat{\theta}_{bottom} = -0.5$ for all the cases. The results are compared with the correspondent closed form solution and they are presented for different radius to thickness ratios $R_\beta/h_{tot} = (10; 50; 100; 500)$ with the corresponding curvature radius $R_\beta = (1.0; 5.0; 10.0; 50.0)$. A mesh grid of 10×10 elements is taken to ensure the convergence of the solution, see Table 7.8. The values of the transversal displacement w and the transverse shear stress $\sigma_{\alpha z}$ are listed in Table 7.11 for the temperature profile calculated solving the Fourier heat conduction equation and compared with the assumed linear temperature profile. Other results in terms of transverse shear stress and transversal displacement are shown in Figures 7.14a-7.15b.

Table 7.11: Cylindrical panel with lamination ($0^\circ/90^\circ$). Transverse displacement $w = w(a/2, b/2)$, transverse shear stress $\sigma_{\alpha z} = \sigma_{\alpha z}(a, 0) * 10^2$, evaluated at $z = 0$.

R_β/h		10	50	100	500		
w	$LW4_a$	T_a	0.7450	1.1192	1.1359	1.1412	
		T_c	0.7188	1.0748	1.0904	1.0953	
	$LW4$	T_a	0.7450	1.1192	1.1359	1.1412	
		T_c	0.7158	1.0743	1.0902	1.0952	
	$LW1$	T_a	0.7712	1.1538	1.1706	1.1759	
		T_c	0.7412	1.1082	1.1243	1.1293	
	$ET3Z$	T_a	0.7454	1.1177	1.1342	1.1396	
		T_c	0.7147	1.0717	1.0875	1.0926	
	$ET4_a$	T_a	0.7461	1.1194	1.1360	1.1413	
		T_c	0.7199	1.0751	1.0907	1.0955	
	$ET4$	T_a	0.7461	1.1194	1.1360	1.1413	
		T_c	0.7170	1.0746	1.0904	1.0955	
	$ET2$	T_a	0.7455	1.1152	1.1316	1.1369	
		T_c	0.7150	1.0695	1.0852	1.0902	
	$FSDT$	T_a	0.8745	1.2781	1.2941	1.2979	
		T_c	0.8367	1.2229	1.2382	1.2419	
	$\sigma_{\alpha z}$	$LW4_a$	T_a	-10.901 ⁺	-3.7541 ⁺	-2.8789 ⁺	-2.2428 ⁺
			T_c	-10.051	-3.1516	-2.3086	-1.6957
$LW4$		T_a	-10.923 ⁺	-3.7615 ⁺	-2.8845 ⁺	-2.2471 ⁺	
		T_c	-10.011 ⁺	-3.1485 ⁺	-2.3086 ⁺	-1.6983 ⁺	
$LW1$		T_a	-8.3115 ⁺	-4.0011 ⁺	-3.5188 ⁺	-3.1781 ⁺	
		T_c	-7.7544 ⁺	-3.6140 ⁺	-3.1507 ⁺	-2.8235 ⁺	
$ET3Z$		T_a	-10.522 ⁺	-3.5686 ⁺	-2.7832 ⁺	-2.2277 ⁺	
		T_c	-9.7816 ⁺	-3.1176 ⁺	-2.3651 ⁺	-1.8329 ⁺	
$ET4_a$		T_a	-6.8978 ⁺	-1.7276 ⁺	-1.2097 ⁺	-0.8599 ⁺	
		T_c	-6.3568	-1.3735	-0.8747	-0.5374	
$ET4$		T_a	-6.9120 ⁺	-1.7309 ⁺	-1.2120 ⁺	-0.8614 ⁺	
		T_c	-6.3345 ⁺	-1.3701 ⁺	-0.8732 ⁺	-0.5377 ⁺	
$ET2$		T_a	-5.6195 ⁺	-1.7814 ⁺	-1.4294 ⁺	-1.2006 ⁺	
		T_c	-5.3090 ⁺	-1.6296 ⁺	-1.2921 ⁺	-1.0727 ⁺	
$FSDT$		T_a	-4.8037 ⁺	-0.6032 ⁺	-0.2571 ⁺	-0.0436 ⁺	
		T_c	-4.5916 ⁺	-0.5767 ⁺	-0.2457 ⁺	-0.0418 ⁺	

All the FEs, both the calculated profile and the assumed linear ones, lead to accurate results with respect to the analytical solutions for all the thickness ratios except for *FSDT* elements. The difference between the calculated temperature profile solutions and the assumed linear profile ones is constant and it is not affected by the thickness to radii ratio R_β/h , this difference is due to the thickness ratio which is $a/h = 10$ for all the shell cases. In general, LW theories perform better than ESL ones and often also with a lower-order expansion of the unknowns. Equivalent single layer analyses are quite satisfactory only for the transverse

displacement also for lower radii to thickness ratios $R/h = 10$, but not for the solutions of the transverse shear stress, as shown in Figures 7.14a-7.15b.

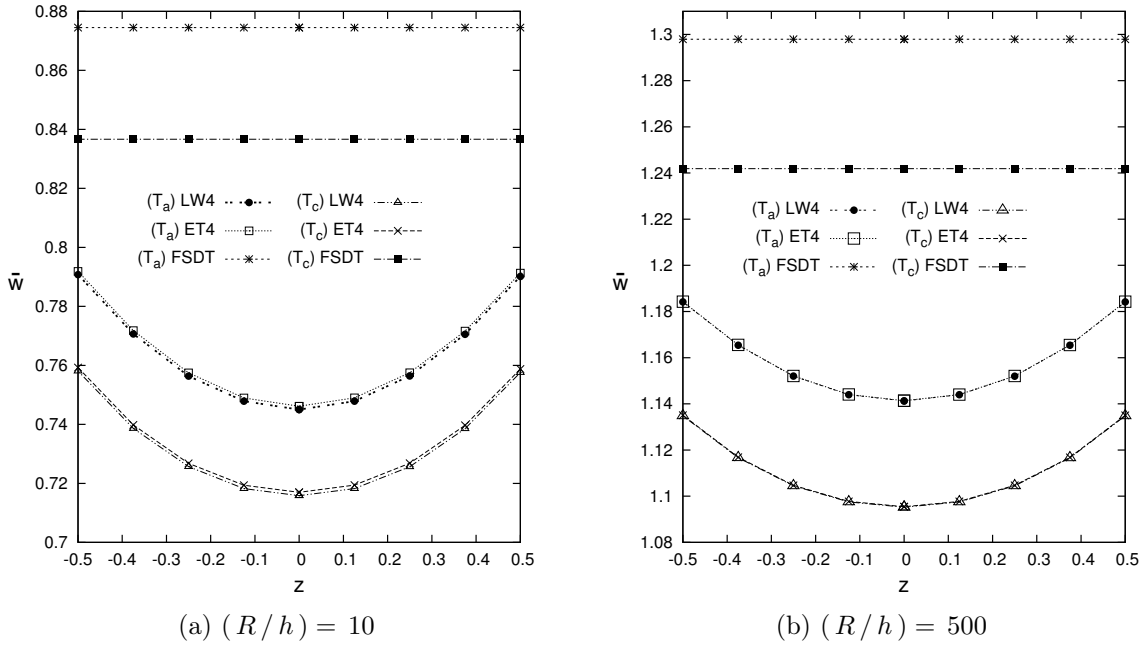


Figure 7.14: Cylindrical panel, by varying R/h . Transverse displacement w .

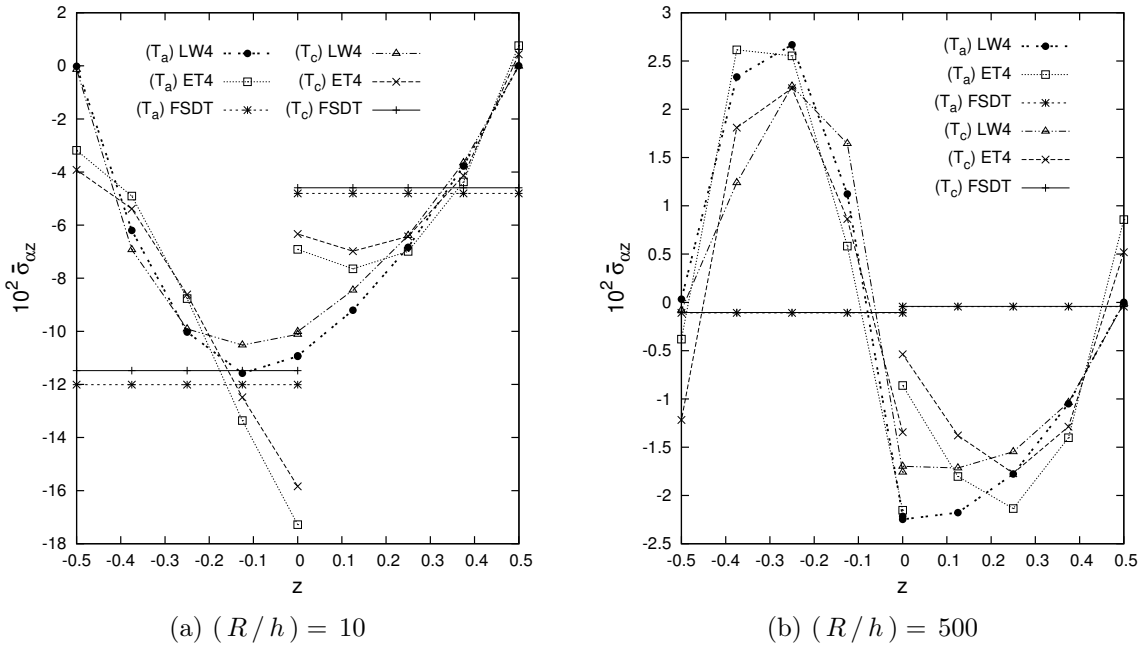


Figure 7.15: Cylindrical panel, by varying R/h . Transverse shear stress $\sigma_{\alpha z}$.

Multilayered spherical panel

In this section, a square, spherical panel is analysed. The temperature boundary conditions are: $\theta_{top} = +0.5$, $\theta_{bottom} = -0.5$ for all the cases. The results are compared with an analytical solution. A mesh grid of 10×10 elements is taken to ensure the convergence of the solution, see Table 7.8. The geometrical dimensions are: $a = 1.0$ and $b = 1.0$, global thickness $h_{tot} = 0.1$, curvature radii $R_\alpha = R_\beta = R$. The physical properties of the Carbon are given in Table 7.7.

The results are presented for different radius to thickness ratios $R/h_{tot} = (10; 50; 100; 500)$ with the corresponding curvature radius $R = (1.0; 5.0; 10.0; 50.0)$. The lamination angle is 0° for the bottom layer and 90° for the top layer. The values of the transversal displacement w and the transverse shear stress $\sigma_{\alpha z}$ are listed in Table 7.12 for the temperature profile calculated solving the Fourier heat conduction equation and compared with the assumed linear temperature profile. Other results in terms of transverse shear stress and transversal displacement are shown in Figures 7.16a-7.17b.

Table 7.12: Spherical panel with lamination ($0^\circ/90^\circ$). Transverse displacement $w = w(a/2, b/2)$, evaluated at $z = 0$, transverse shear stress $\sigma_{\alpha z} = \sigma_{\alpha z}(a, 0) * 10^2$ evaluated at $z = -h/4$.

R/h		10	50	100	500		
w	$LW4_a$	T_a	0.3299	1.0507	1.1174	1.1404	
		T_c	0.3203	1.0087	1.0725	1.0945	
	$LW4$	T_a	0.3299	1.0507	1.1174	1.1405	
		T_c	0.3240	1.0091	1.0726	1.0945	
	$LW1$	T_a	0.3386	1.0836	1.1516	1.1751	
		T_c	0.3325	1.0414	1.1062	1.1285	
	$ET3Z$	T_a	0.3306	1.0496	1.1159	1.1388	
		T_c	0.3235	1.0071	1.0701	1.0918	
	$ET4_a$	T_a	0.3309	1.0511	1.1176	1.1406	
		T_c	0.3213	1.0093	1.0728	1.0947	
	$ET4$	T_a	0.3309	1.0511	1.1176	1.1406	
		T_c	0.3250	1.0096	1.0729	1.0947	
	$ET2$	T_a	0.3315	1.0477	1.1134	1.1361	
		T_c	0.3248	1.0054	1.0679	1.0895	
	$FSDT$	T_a	0.3927	1.1967	1.2709	1.2965	
		T_c	0.3837	1.1459	1.2163	1.2406	
	$\sigma_{\alpha z}$	$LW4_a$	T_a	24.096	1.1199	-1.3854	-2.5674
			T_c	23.379	1.3972	-1.0041	-2.1403
$LW4$		T_a	24.131	1.1212	-1.3877	-2.5714	
		T_c	23.289	1.3831	-1.0122	-2.1461	
$LW1$		T_a	19.500	1.5598	-0.5309	-1.5931	
		T_c	18.818	1.6718	-0.3315	-1.3536	
$ET3Z$		T_a	21.061	2.4154	0.1275	-1.0771	
		T_c	20.328	2.5096	0.3181	-0.8407	
$ET4_a$		T_a	21.281	0.8662	-1.3842	-2.4603	
		T_c	20.593	1.0635	-1.0932	-2.1270	
$ET4$		T_a	21.312	0.8673	-1.3865	-2.4641	
		T_c	20.521	1.0521	-1.1000	-2.1325	
$ET2$		T_a	20.284	3.0723	0.9925	-0.0983	
		T_c	19.598	3.1406	1.1473	0.0970	
$FSDT$		T_a	21.845	3.9515	1.5581	0.2307	
		T_c	21.011	3.8024	1.5047	0.2240	

All the FEs, both the calculated profile and the assumed linear ones, lead to accurate results with respect to the analytical solutions for all the thickness ratios except for $FSDT$ elements. The difference between the calculated temperature profile solutions and the assumed linear profile ones is constant and it is not affected by the thickness to radii ratio R_β/h , this difference is due to the thickness ratio which is $a/h = 10$ for all the shell cases. In general, LW theories perform better than ESL ones and often also with a lower-order expansion of

the unknowns. Equivalent single layer analyses are quite satisfactory only for the transverse displacement also for lower radii to thickness ratios $R/h = 10$, but not for the solutions of the transverse shear stress, as shown in Figures 7.16a-7.17b.

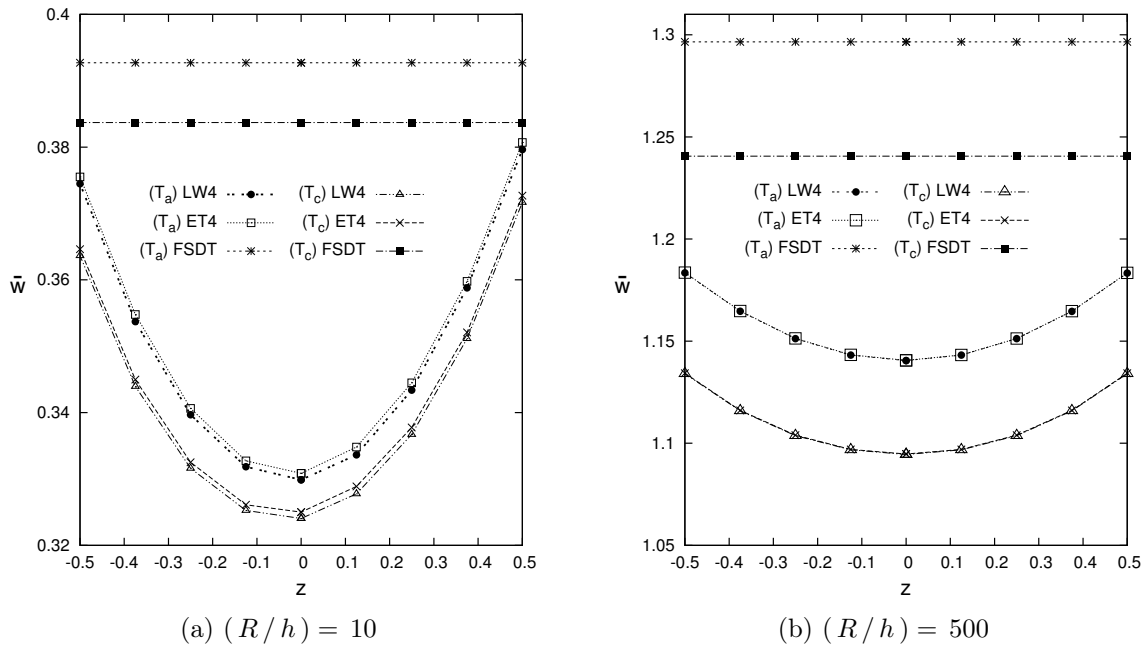


Figure 7.16: Spherical panel, by varying R/h . Transverse displacement w .

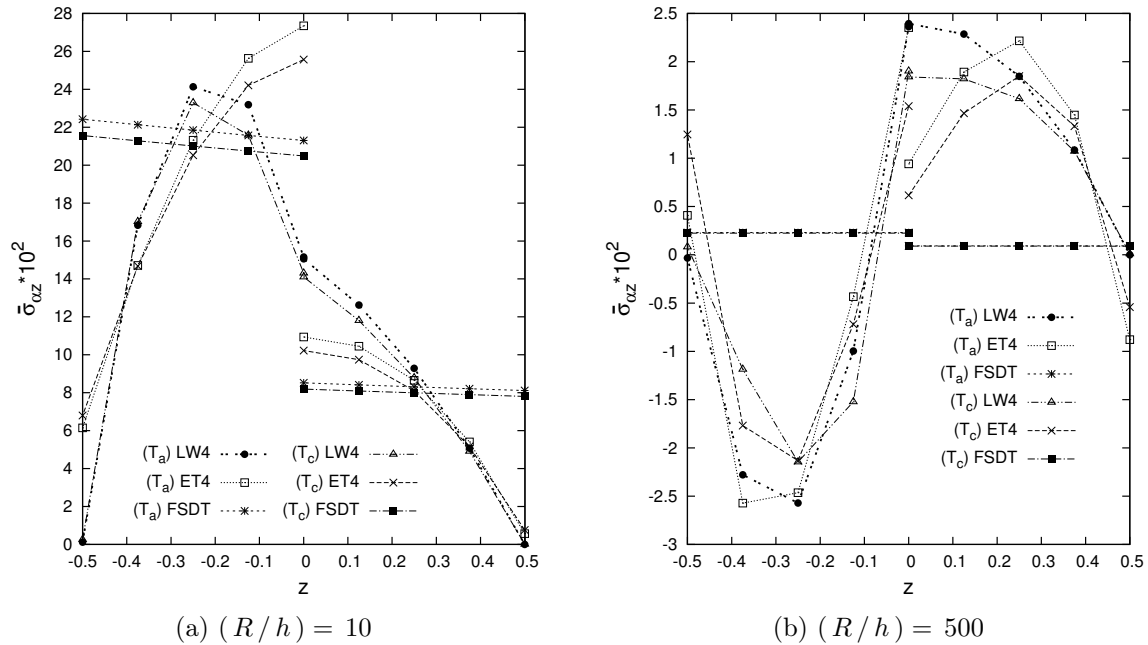


Figure 7.17: Spherical panel, by varying R/h . Transverse shear stress $\sigma_{\alpha z}$.

7.3.3 FEM benchmark solutions

Similar plates, cylindrical shells and spherical shells are analyzed, considering two new problems that have not reference analytical solutions:

1. Structures with anti-symmetric lamination $\pm 45^\circ$ under bi-sinusoidal load and simply-

supported boundary conditions.

2. Structures with clamped-free boundary conditions: edges parallel to β -direction clamped and those parallel to α -direction free. The lamination is equal to the assessment cases.

Anti-symmetric lamination $\pm 45^\circ$

The first structure analyzed is a composite multilayered square plate with lamination $(-45^\circ / 45^\circ / -45^\circ)$. The physical properties of the material, the geometrical data and the temperature boundary conditions are the same of the assessment cases. The structure is simply supported. The results are presented for different thickness ratios $a/h = 10, 100$. The same mesh grid of 10×10 elements of the assessment cases is taken to ensure the convergence of the solution. The values of the transversal displacement w and the transverse shear stress $\sigma_{\alpha z}$ are listed in Table 7.13.

Table 7.13: Benchmark problems. Case 1 with anti-symmetric lamination $\pm 45^\circ$. Plate, cylindrical and spherical panel, transverse displacement $w = 10 w(a/2, b/2, +h/2)$ and transverse shear stress $\sigma_{\alpha z} = 10^2 \sigma_{\alpha z}(a, b/2, 0)$.

		<i>Plate</i>		<i>Cylindrical</i>			<i>Spherical</i>		
		<i>a/h</i>	10	100	<i>R/h</i>	10	100	10	100
<i>w</i>	<i>LW4</i>	<i>T_a</i>	1375.4	4607.8	4.8796	7.4058	2.6295	7.4971	
		<i>T_c</i>	1293.5	4604.7	4.5741	7.0165	2.5533	7.1029	
	<i>LW1</i>	<i>T_a</i>	1274.3	4895.2	4.7358	7.5077	2.4930	7.6005	
		<i>T_c</i>	1203.2	4892.2	4.4477	7.1343	2.4305	7.2202	
	<i>ET3Z</i>	<i>T_a</i>	1307.7	4586.4	4.7120	7.3351	2.5257	7.4200	
		<i>T_c</i>	1232.7	4583.4	4.4154	6.9528	2.4542	7.0325	
	<i>ET4</i>	<i>T_a</i>	1250.8	4550.1	4.7274	7.3978	2.5388	7.4776	
		<i>T_c</i>	1177.8	4547.1	4.4239	7.0045	2.4615	7.0793	
	<i>ET2</i>	<i>T_a</i>	1164.1	4501.7	4.7187	7.2171	2.5756	7.3229	
		<i>T_c</i>	1096.3	4498.8	4.4192	6.8330	2.5029	6.9316	
	<i>FSDT</i>	<i>T_a</i>	1294.9	7222.5	5.0729	7.5539	2.6941	7.6548	
		<i>T_c</i>	1219.4	7217.9	4.8079	7.2151	2.6483	7.3099	
$\sigma_{\alpha z}$	<i>LW4</i>	<i>T_a</i>	-85.932	-56.181	15.624	2.4665	24.592	3.7828	
		<i>T_c</i>	-81.708	-56.148	14.483	1.9577	22.964	3.2169	
	<i>LW1</i>	<i>T_a</i>	-98.335	-56.066	17.223	5.5156	23.450	6.7916	
		<i>T_c</i>	-93.436	-56.033	16.299	5.1621	22.161	6.3780	
	<i>ET3Z</i>	<i>T_a</i>	-97.289	-55.800	17.350	2.6837	26.823	4.0857	
		<i>T_c</i>	-92.420	-55.767	16.512	2.5503	25.369	3.8853	
	<i>ET4</i>	<i>T_a</i>	-80.357	-52.295	16.651	0.3544	27.067	1.8573	
		<i>T_c</i>	-76.298	-52.264	15.711	0.2248	25.347	1.6474	
	<i>ET2</i>	<i>T_a</i>	-61.532	-37.094	15.936	2.8891	23.900	4.2028	
		<i>T_c</i>	-58.089	-37.072	15.343	2.9668	22.689	4.2054	
	<i>FSDT</i>	<i>T_a</i>	-92.857	-45.626	12.861	2.2035	20.014	3.2885	
		<i>T_c</i>	-87.595	-45.598	12.219	2.0645	18.994	3.0974	

The second structure analyzed is a composite square cylindrical panel with lamination $(-45^\circ/45^\circ)$. The lamination angle is -45° for the bottom layer and 45° for the top layer. The physical properties of the material, the geometrical data and the temperature boundary conditions are the same of the assessment cases. The structure is simply supported. The results are presented for different radius to thickness ratios $R/h = 10, 100$. The same mesh grid of 10×10 elements of the assessment cases is taken to ensure the convergence of the solution. The values of the transversal displacement w and the transverse shear stress $\sigma_{\alpha z}$ are listed in Table 7.13.

The last structure analyzed is a composite square spherical panel with lamination $(-45^\circ/45^\circ)$. The lamination angle is -45° for the bottom layer and 45° for the top layer. The physical properties of the material, the geometrical data and the temperature boundary conditions

are the same of the assessment cases. The structure is simply supported. The results are presented for different radius to thickness ratios $R/h = 10, 100$. The same mesh grid of 10×10 elements of the assessment cases is taken to ensure the convergence of the solution. The values of the transversal displacement w and the transverse shear stress $\sigma_{\alpha z}$ are listed in Table 7.13.

Clamped-free boundary conditions

In this part the structures are considered with clamped-free boundary conditions: edges parallel to β -direction clamped and those parallel to α -direction free.

The first structure analyzed is a composite multilayered square plate. The physical properties of the material, the lamination angle, the geometrical data and the temperature boundary conditions are the same of the assessment cases. The results are presented for different thickness ratios $a/h = 10, 100$. The same mesh grid of 10×10 elements of the assessment cases is taken to ensure the convergence of the solution. The values of the transversal displacement w and the transverse shear stress $\sigma_{\alpha z}$ are listed in Table 7.14.

The second structure analyzed is a composite square cylindrical panel. The physical properties of the material, the lamination angle, the geometrical data and the temperature boundary conditions are the same of the assessment cases. The results are presented for different radius to thickness ratios $R/h = 10, 100$. The same mesh grid of 10×10 elements of the assessment cases is taken to ensure the convergence of the solution. The values of the transversal displacement w and the transverse shear stress $\sigma_{\alpha z}$ are listed in Table 7.14.

The last structure analyzed is a composite square spherical panel. The physical properties of the material, the lamination angle, the geometrical data and the temperature boundary conditions are the same of the assessment cases. The results are presented for different radius to thickness ratios $R/h = 10, 100$. The same mesh grid of 10×10 elements of the assessment cases is taken to ensure the convergence of the solution. The values of the transversal displacement w and the transverse shear stress $\sigma_{\alpha z}$ are listed in Table 7.14.

Table 7.14: Benchmark problems. Case 2 with clamped-free boundary condition. Plate, cylindrical and spherical panel, transverse displacement $w = 10 w(a/2, b/2, +h/2)$ and transverse shear stress $\sigma_{\alpha z} = 10^2 \sigma_{\alpha z}(a, b/2, 0)$.

		<i>Plate</i>			<i>Cylindrical</i>			<i>Spherical</i>	
		a/h	10	100	R/h	10	100	10	100
w	<i>LW4</i>	T_a	1226.8	3096.9	4.5476	5.3307	-0.3479	3.7373	
		T_c	1157.7	3094.9	4.3447	5.1018	-0.1750	3.6265	
	<i>LW1</i>	T_a	1210.9	3274.4	4.6164	5.3874	-0.3642	3.8575	
		T_c	1145.2	3272.3	4.4100	5.1571	-0.1923	3.7404	
	<i>ET3Z</i>	T_a	1222.0	3096.8	4.5239	5.2945	-0.3407	3.7334	
		T_c	1155.2	3094.9	4.3237	5.0705	-0.1681	3.6250	
	<i>ET4</i>	T_a	1183.3	3083.9	4.5479	5.3215	-0.3423	3.7477	
		T_c	1116.2	3081.9	4.3460	5.0941	-0.1696	3.6368	
	<i>ET2</i>	T_a	986.40	3048.6	4.5152	5.2473	-0.3369	3.7263	
		T_c	929.51	3046.7	4.3093	5.0195	-0.1652	3.6119	
	<i>FSDT</i>	T_a	1039.7	4356.4	4.7747	5.5564	-0.5836	3.9916	
		T_c	979.72	4353.6	4.5553	5.3129	-0.4107	3.8624	
$\sigma_{\alpha z}$	<i>LW4</i>	T_a	-2619.8	-522.26	-3.9875	-5.1179	15.086	0.2373	
		T_c	-2519.9	-522.01	-3.9154	-5.0207	13.754	-0.0535	
	<i>LW1</i>	T_a	-2655.5	-579.97	-1.5318	-2.3709	14.765	1.8361	
		T_c	-2520.6	-579.67	-1.5150	-2.3397	13.594	1.5630	
	<i>ET3Z</i>	T_a	-2436.3	-537.18	-2.9825	-3.9052	14.614	0.8821	
		T_c	-2303.2	-536.90	-2.8354	-3.7432	13.481	0.6988	
	<i>ET4</i>	T_a	-2695.3	-465.54	-3.3266	-4.2840	14.134	0.4614	
		T_c	-2582.7	-465.30	-3.2708	-4.2082	12.905	0.1929	
	<i>ET2</i>	T_a	-2287.1	-240.08	-2.8190	-3.6334	13.936	0.7940	
		T_c	-2159.2	-239.94	-2.7079	-3.5120	12.809	0.5937	
	<i>FSDT</i>	T_a	-4195.5	-446.19	-6.0953	-6.9657	13.570	-2.0926	
		T_c	-3955.6	-445.91	-5.7896	-6.6468	12.506	-2.1219	

Chapter 8

Results on Electro-Mechanical Problems

In case of smart structures, obtained by the inclusion of some piezoelectric layers, the electro-mechanical analysis is a fundamental aspect in their design. In this chapter refined and advanced models are validated in case of multilayered smart structures, and applied to investigate their physical behavior. In the proposed cases both sensor and actuator configurations are analyzed. The use of advanced mixed models permits to obtain a priori the transverse normal electric displacement, with the possibility of imposing its continuity at interfaces.

8.1 Static piezo-composite plates and shells

The model introduced, unlike 3-D degenerate approach, does not involve an approximation of the geometry of the shell and it describes accurately the curvature of the shell. However, the locking phenomenon is still present. In this work, such a model is combined with a simple displacement formulation for the analysis of composite structures. In electro-mechanical problems it is necessary to impose the value of the electric potential variable at top and bottom position. To obtain this, Layer-Wise models with Legendre polynomials are employed. The efficiency of Layer-Wise models is tested with the finite element scheme, and the numerical results are compared with the ones obtained with the 3D elasticity approach. In this direction, two kind of reference problems are considered: the composite square plate embedding piezoelectric layers at top and bottom position, analytically analyzed in [46], and single and multilayered cylinders embedding piezoelectric layers, analytically analyzed. Both of them are evaluated in sensor and actuator configuration. For the sensor case, a bi-sinusoidal transverse normal pressure is applied at the top surface for the plate and at the bottom surface for the shells:

$$p_z^\pm = \hat{p}_z^\pm \sin(m\pi\alpha/a)\sin(n\pi\beta/b) \quad (8.1)$$

with amplitude $\hat{p}_z^\pm = 1$ and wave numbers $m = 1$, $n = 1$ for the plate and $n = 8$ for the shell. The potential at top and bottom position is imposed $\Phi_t = \Phi_b = 0$.

For the actuator case, a bi-sinusoidal electric potential is imposed at top surface:

$$\Phi^+ = \hat{\phi}_z^+ \sin(m\pi\alpha/a)\sin(n\pi\beta/b) \quad (8.2)$$

with amplitude $\hat{\phi}_z^+ = 1$ and wave numbers $m = 1$, $n = 1$ for the plate and $n = 8$ for the shell. The potential at bottom position is imposed $\Phi_b = 0$. No mechanical load is applied. The two problems are briefly described in the following sections.

8.1.1 Multilayered plate

The assessment is based on the plate structure analyzed in [46] (see Figure 8.1). It has been considered a composite square plate embedding piezoelectric layers made globally of four layers, a core in Gr/Ep composite material by two orthotropic layers with lamination ($0^\circ/90^\circ$), and the skins in PZT-4 by two piezoelectric layers. In respect to the total thickness, a single piezoelectric skin is thick $h_p = 0.1h_{tot}$, while the single core layer is thick $h_c = 0.4h_{tot}$. The physical properties of the shell are given in Table 8.1.

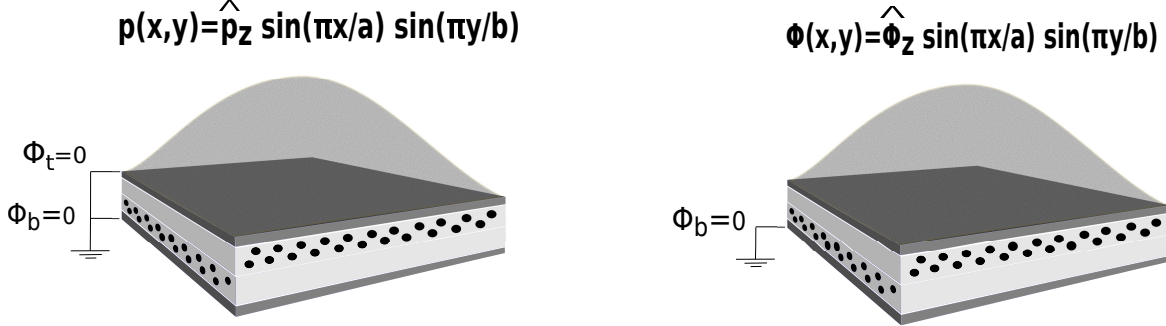


Figure 8.1: Multilayered plate structure. Sensor Case, and Actuator Case configuration.

Properties	PZT-4	Gr/EP
E_{11} [GPa]	81.3	132.38
E_{22} [GPa]	81.3	10.756
E_{33} [GPa]	64.5	10.756
ν_{12} [-]	0.329	0.24
ν_{13} [-]	0.432	0.24
ν_{23} [-]	0.432	0.49
G_{44} [GPa]	25.6	3.606
G_{55} [GPa]	25.6	5.6537
G_{66} [GPa]	30.6	5.6537
e_{15} [C/m ²]	12.72	0
e_{24} [C/m ²]	12.72	0
e_{31} [C/m ²]	-5.20	0
e_{32} [C/m ²]	-5.20	0
e_{33} [C/m ²]	15.08	0
$\tilde{\epsilon}_{11}/\epsilon_0$ [-]	1475	3.5
$\tilde{\epsilon}_{22}/\epsilon_0$ [-]	1475	3.0
$\tilde{\epsilon}_{33}/\epsilon_0$ [-]	1300	3.0
ϵ_0 [C/Vm]	$8.85 * 10^{-12}$	$8.85 * 10^{-12}$

Table 8.1: Physical data for multilayered plate and cylindrical shell.

Due to the symmetry of both the geometry and the load, a quarter of plate is analysed and the following symmetry and boundary conditions (simply-supported) are applied:

$$\begin{aligned}
 u_\tau(0, y) &= 0 \\
 v_\tau(x, 0) &= 0 \\
 w_\tau(x, b/2) &= 0 \\
 w_\tau(a/2, y) &= 0 \\
 u_\tau(x, b/2) &= 0 \\
 v_\tau(a/2, y) &= 0
 \end{aligned}
 \tag{8.3}$$

with $\tau = 0, 1, \dots, N$.

The results are presented for different thickness ratios $a/h = 2, 4, 10, 100$.

A mesh grid of 12×12 elements is taken to ensure the convergence of the solution. In general the results approach to the exact solution by increasing the order of expansion N for the various thickness ratios, see Tables 8.2, 8.3 . One can note that the element doesn't suffer the locking phenomenon even when the plate is very thin ($a/h = 100$), see Tables 8.4, 8.5. Only the LW4 model is able to exactly reproduce the analytical solution in the case of thick shell.

		a/h	2	4	10	100
	w	$LW4_a$	4.9113	30.029	582.06	4675300
		$FSDT_a$	2.8575	18.488	423.29	3668700
Ref. [46]	Φ	$LW4_a$	0.9103	6.1084	44.471	4580.2
		$FSDT_a$	0.78657	2.6580	15.044	1470.3
	\mathcal{D}_z	$LW4_a$	0.0256	0.0161	0.0139	0.0136
		$FSDT_a$	0.0615	0.0401	-0.1174	-18.729
w		LW4	4.9112	30.0286	582.1298	4675118.5
		LW3	4.9112	30.0285	582.1298	4675118.5
		LW2	4.8954	29.9812	581.8951	4675095.5
		LW1	4.8087	29.8512	579.2426	4647075.5
Φ		LW4	0.9106	6.1107	44.4934	4586.8311
		LW3	0.9103	6.1102	44.4920	4586.8311
		LW2	0.8948	6.0899	44.4760	4586.7891
		LW1	0.8599	6.0320	44.1802	4559.1191
\mathcal{D}_z		LW4	0.0252	0.0140	0.0051	-0.0140
		LW3	0.0255	0.0142	0.0054	-0.0144
		LW2	0.0271	0.0156	0.0064	-0.0205
		LW1	-0.0665	-0.0890	-0.2905	-23.8867

Table 8.2: Transverse normal displacement $w * 10^{11}$ evaluated along the thickness in ($z = 0$). Electric potential $\Phi * 10^3$ evaluated along the thickness in ($z = 0$). Transverse normal electric displacement $\mathcal{D}_z * 10^9$ evaluated along the thickness at *top* ($z = +h/2$). Plate with 4 layers. Sensor case.

		a/h	2	4	10	100
	w	$LW4_a$	-1.7475	-1.4707	-1.3697	-1.3493
		$FSDT_a$	-13.923	-14.107	-14.159	-14.169
<i>Ref.</i> [46]	Φ	$LW4_a$	0.3330	0.4477	0.4910	0.4999
		$FSDT_a$	0.3219	0.4461	0.4908	0.4999
	\mathcal{D}_z	$LW4_a$	-9.4085	-2.4184	-0.4168	-0.0370
		$FSDT_a$	-3.6667	-0.9566	-0.1816	-0.0347
w	LW4	-1.7476	-1.4708	-1.3697	-1.3494	
	LW3	-1.7476	-1.4707	-1.3697	-1.3494	
	LW2	-1.7291	-1.4663	-1.3691	-1.3493	
	LW1	-2.1030	-1.5963	-1.4297	-1.3971	
Φ	LW4	0.3330	0.4477	0.4910	0.4999	
	LW3	0.3330	0.4477	0.4910	0.4999	
	LW2	0.3331	0.4477	0.4910	0.4999	
	LW1	0.3241	0.4468	0.4910	0.4999	
\mathcal{D}_z	LW4	-9.4104	-2.4185	-0.4167	-0.0370	
	LW3	-9.4047	-2.4182	-0.4167	-0.0370	
	LW2	-9.3822	-2.4167	-0.4166	-0.0370	
	LW1	-5.2969	-1.3815	-0.2504	-0.0353	

Table 8.3: Transverse normal displacement $w * 10^{11}$ evaluated along the thickness in ($z = 0$). Electric potential Φ evaluated along the thickness in ($z = 0$). Transverse normal electric displacement $\mathcal{D}_z * 10^9$ evaluated along the thickness at *top* ($z = +h/2$). Plate with 4 layers. Actuator case.

		a/h	2	4	10	100
Ref. [46]	$\sigma_{\alpha\alpha}$	$LW4_a$	3.2207	6.5642	32.771	3142.1
	$\sigma_{\alpha z}$	$LW4_a$	-0.26995	-0.68720	-1.8540	-18.832
		LW4	3.2240	6.5710	32.8145	3146.8381
	$\sigma_{\alpha\alpha}$	LW3	3.2263	6.5719	32.8153	3146.8376
		LW2	3.2088	6.5659	32.8137	3146.8433
		LW1	3.5228	7.0093	34.3028	3271.7583
		LW4	-0.2758	-0.6902	-1.8576	-18.8640
	$\sigma_{\alpha z}$	LW3	-0.2697	-0.6862	-1.8560	-18.8638
		LW2	-0.3620	-0.8157	-2.1371	-21.6073
		LW1	-0.3165	-0.7094	-1.8693	-18.9304
		LW4	1.0001	1.0001	1.0001	0.9955
	σ_{zz}	LW3	1.0052	1.0015	1.0008	0.9957
		LW2	1.0334	1.0268	1.0270	1.0757
		LW1	2.1237	2.3562	5.1631	342.3075

Table 8.4: Principal stresses $\sigma_{\alpha\alpha}$, σ_{zz} evaluated along the thickness at *top* ($z = +h/2$) and shear stress $\sigma_{\alpha z}$ evaluated along the thickness in ($z = 0$). Plate with 4 layers. Sensor case.

	a/h	2	4	10	100	
Ref. [46]	$\sigma_{\alpha\alpha}$	LW4 _a	3.8162	1.1180	0.1680	-0.0246
	$\sigma_{\alpha z}$	LW4 _a	0.0864	0.0239	0.0020	0.0000
		LW4	3.8404	1.1249	0.1693	-0.0246
	$\sigma_{\alpha\alpha}$	LW3	3.8618	1.1262	0.1693	-0.0246
		LW2	3.9439	1.1312	0.1695	-0.0246
		LW1	12.4636	3.3532	0.5272	-0.0210
		LW4	0.0929	0.0241	0.0020	0.0000
	$\sigma_{\alpha z}$	LW3	0.0651	0.0227	0.0020	0.0000
		LW2	0.1824	0.0359	0.0028	0.0000
		LW1	0.0215	0.0029	0.0004	0.0000
		LW4	0.0006	0.0001	0.0000	0.0000
	σ_{zz}	LW3	0.0271	0.0019	0.0001	0.0000
		LW2	0.0547	0.0045	0.0001	0.0000
		LW1	8.1925	2.1772	0.3540	0.0036

Table 8.5: Principal stresses $\sigma_{\alpha\alpha}$, σ_{zz} evaluated along the thickness at *top* ($z = +h/2$) and shear stress $\sigma_{\alpha z}$ evaluated along the thickness in ($z = 0$). Plate with 4 layers. Actuator case.

The behavior of transverse shear and normal stresses $\sigma_{\alpha z}$, σ_{zz} is non-linear along the thickness of the plate. The continuity conditions are reached only by increasing the order of expansion N , see Figures 8.2a-8.3b. For the description of the electric potential Φ it is necessary to use higher-order models to describe the non-linear behavior in thick plates ($a/h = 2$), see Figures 8.4a, 8.4b. On the other hand for thin plates ($a/h = 100$) a layer-wise description of lower order is sufficient. The electric displacement \mathcal{D}_z has a non-linear behavior in the sensor case, it is necessary an higher-order model to obtain the continuity interface, see Figure 8.5a. For the actuator case, due to its linear behavior, the electric displacement can be described by lower-order layer-wise model, see Figure 8.5b.

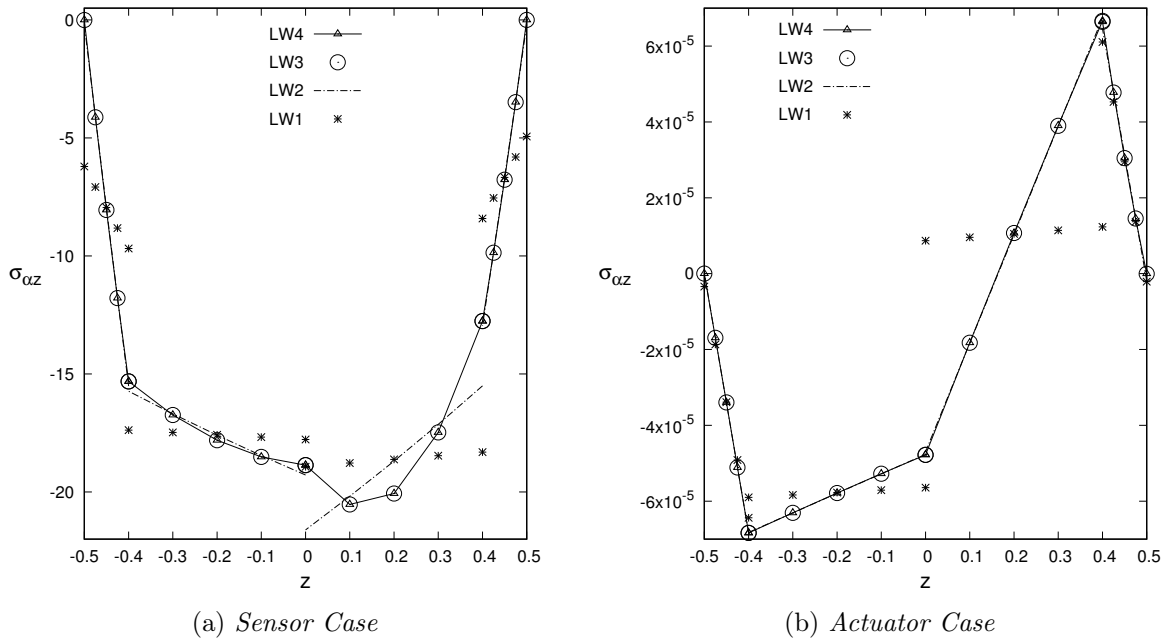


Figure 8.2: Four-layered plate, with thickness ratio $(a/h) = 100$. Transverse shear stress σ_{oz} .

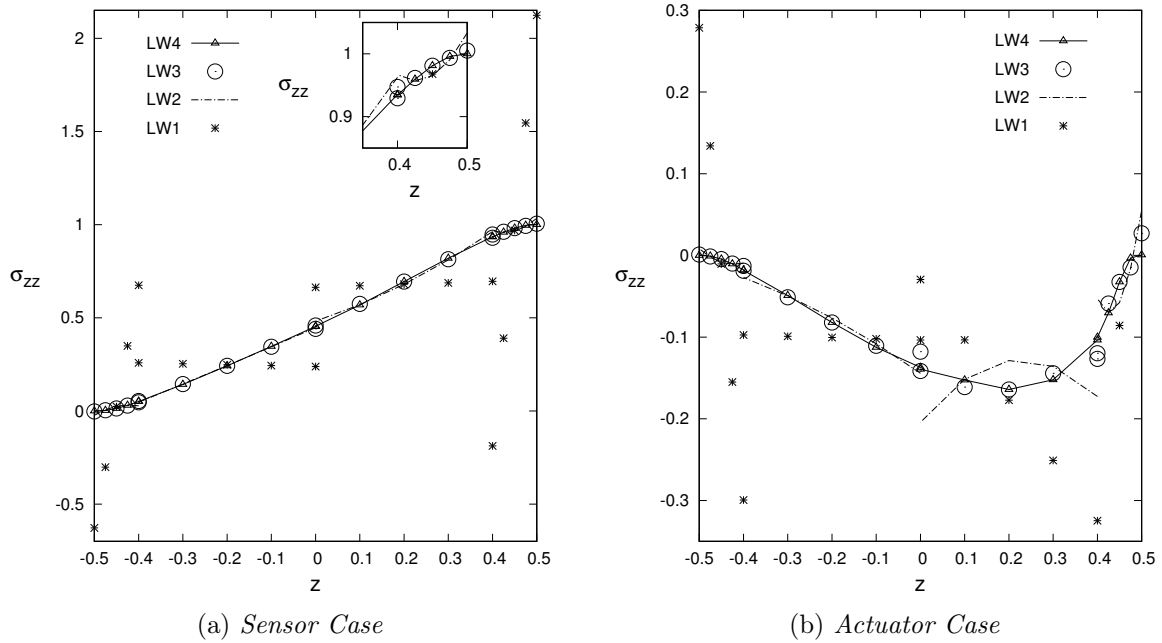


Figure 8.3: Four-layered plate, with thickness ratio $(a/h) = 2$. Transverse normal stress σ_{zz} .

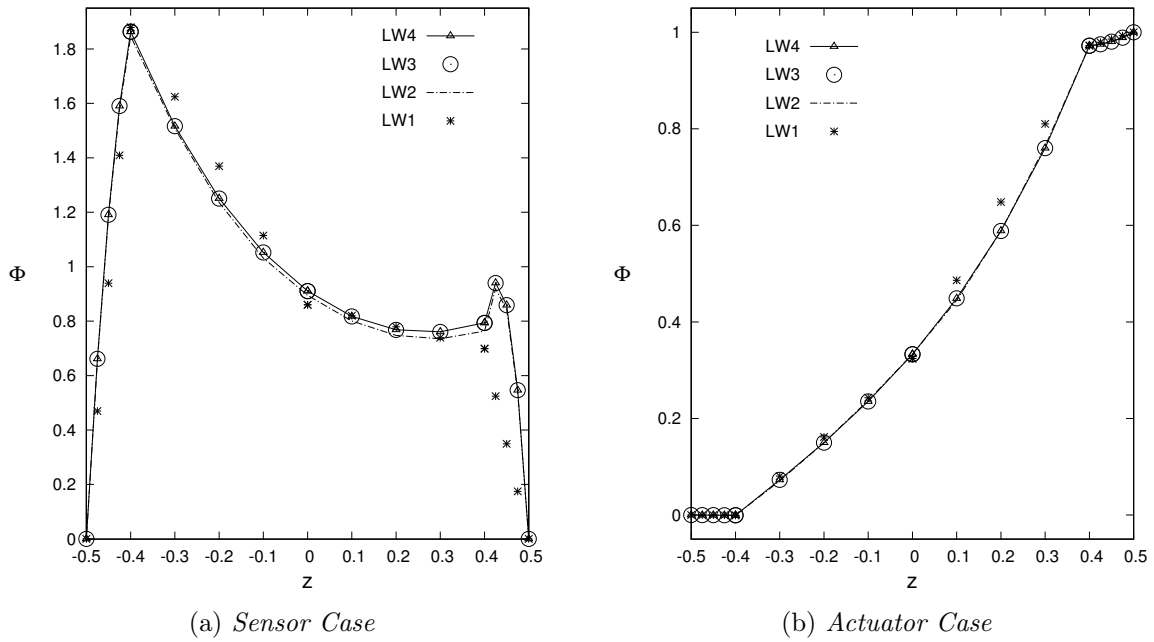


Figure 8.4: Four-layered plate, with thickness ratio $(a/h) = 2$. Electric potential Φ .

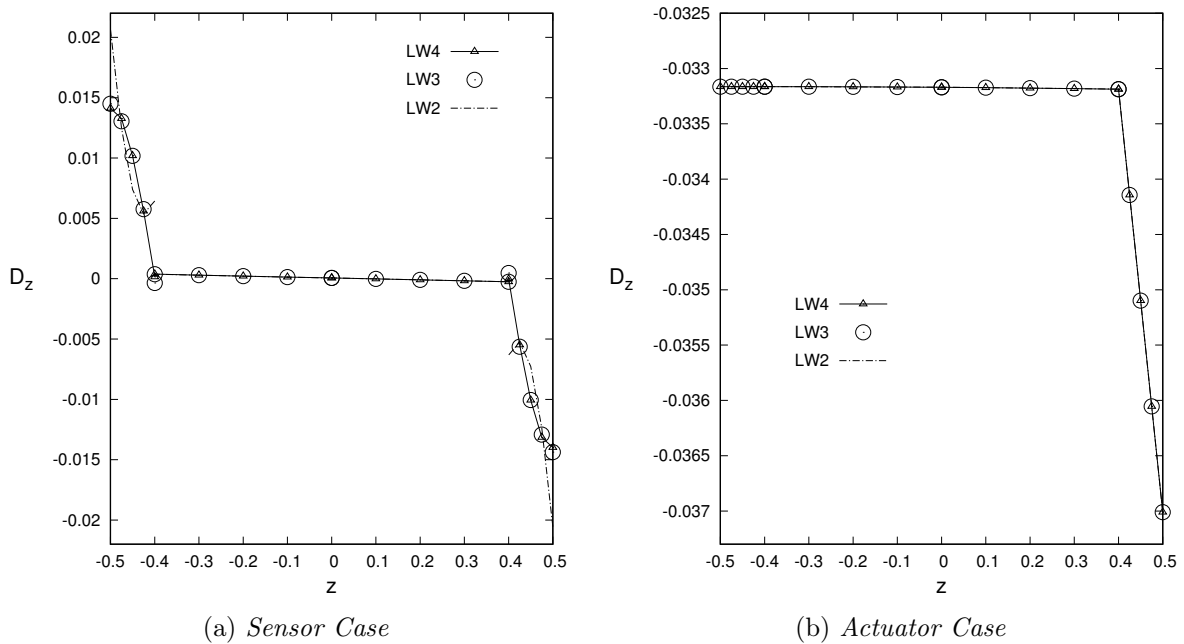


Figure 8.5: Four-layered plate, with thickness ratio $(a/h) = 100$. Electric displacement D_z .

8.1.2 Multilayered piezoelectric cylinder.

The shell structure considered is taken from [140] (see Figure 8.6). The first assessment is a mono-layered piezoelectric cylinder, with the same material properties of the previous plate example, given in Table 8.1. Moreover a 3 layer configuration cylinder with the core in Gr/Ep composite material is analyzed. For multilayered cases, reference solutions are evaluated with an analytical Layer-Wise Full Mixed approach (LWFM). With the LWFM it is possible to impose the interface continuity of both mechanical transverse stresses and normal electric displacement.

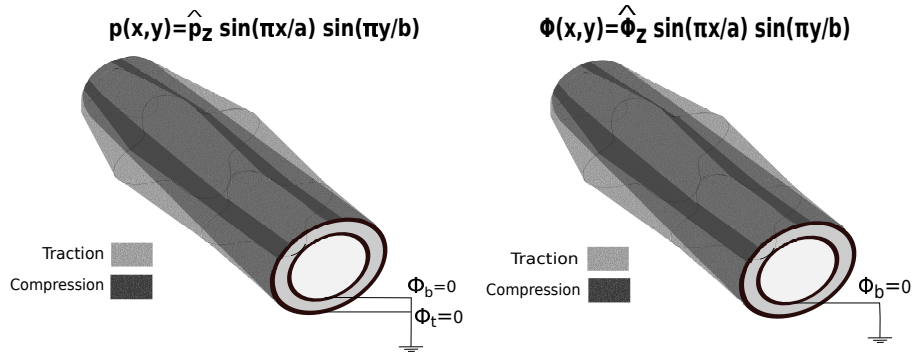


Figure 8.6: Multilayered cylindrical shell. Sensor Case, and Actuator Case configuration.

The geometrical parameters of the considered cylinder are: $a = 40$, $b = 2\pi R_\beta$, $R_\beta = 10$. Due to the symmetry of both the geometry and the load, an octave of the cylinder is studied (1/2 in the axial direction and 1/4 in the hoop direction). The following symmetry conditions are applied:

$$\begin{aligned} v_\tau(\alpha, 0) &= 0 \\ u_\tau(0, \beta) &= 0 \\ v_\tau(\alpha, R_\beta\pi/2) &= 0 \end{aligned} \tag{8.4}$$

and the following boundary conditions are prescribed:

$$v_\tau(a/2, \beta) = w_\tau(a/2, \beta) = 0 \tag{8.5}$$

with $\tau = 0, 1, \dots, N$. The results are presented for these cases for different thickness ratios $R/h = 2, 4, 10, 100$. A mesh grid of 12×12 elements is taken to ensure the convergence of the solution. The results are presented in tabular form for the mono-layered cylinder, and the three-layered shell in Tables 8.6-8.7, and 8.8-8.9 respectively. The following considerations, similar to the comments made for the plate case, can be drawn: the solution converges to the exact solution by increasing the order of expansion N ; the LW models are able to give good results. If one considers the stresses the behavior is the same: higher-order layer wise models are necessary to match the reference solution in the thick shells. In this case, the use of the LW4 model becomes preferable.

R/h		2	4	10	100	
<i>Ref.</i> [140]	$w (10^9)$	<i>LWFM4_a</i>	0.0566	0.3332	4.5483	3016.6
	σ_{zz}	<i>LWFM4_a</i>	-1.1392	-1.0671	-1.0269	-1.0018
	Φ	<i>LWFM4_a</i>	0.0153	0.0355	0.0942	0.6513
	$\mathcal{D}_z (10^9)$	<i>LWFM4_a</i>	0.0095	0.0028	-0.1646	-111.76
$w (10^9)$	LW4	0.0566	0.3331	4.5473	3017.2876	
$\sigma_{\alpha\alpha}$	LW4	0.4332 -1.4003	2.3837 -3.3497	17.5910 -17.0300	2055.6587 -316.7597	
$\sigma_{\beta\beta}$	LW4	0.9068 -2.0590	4.9006 -6.5066	35.0550 -38.7790	2567.2803 -2542.8062	
$\sigma_{\alpha\beta}$	LW4	0.0008 -0.0008	0.0039 -0.0040	0.0291 -0.0329	1.3707 -4.0802	
$\sigma_{\alpha z}$	LW4	-0.1084	-0.2644	-0.7242	-5.1421	
$\sigma_{\beta z}$	LW4	0.0046	0.0194	0.0750	0.2104	
σ_{zz}	LW4	-0.0798 -1.1658	-0.0469 -1.0914	0.0317 -1.0992	3.2476 -5.2059	
Φ	LW4	0.0153	0.0356	0.0949	0.6696	
$\mathcal{D}_z (10^9)$	LW4	0.0054	-0.0179	-0.2668	-111.1786	

Table 8.6: Transverse normal displacement $w * 10^9$, electric potential Φ , shear stresses $\sigma_{\alpha z}$, $\sigma_{\beta z}$ evaluated along the thickness in ($z = 0$). Transverse normal electric displacement $\mathcal{D}_z * 10^9$ evaluated along the thickness at *top* ($z = +h/2$). In-plane stresses $\sigma_{\alpha\alpha}$, $\sigma_{\beta\beta}$, $\sigma_{\alpha\beta}$ and transverse normal stress σ_{zz} evaluated along the thickness at ($z = \pm h/2$). Shell mono-layered piezoelectric cylinder. *Mesh* (10×10). Sensor case.

R/h		2	4	10	100	
<i>Ref.</i> [140]	$w (10^{11})$	$LWFM4_a$	-9.6220	-11.285	6.4540	11277
	σ_{zz}	$LWFM4_a$	0.0431	0.0114	0.0004	-0.0001
	Φ	$LWFM4_a$	0.3431	0.4611	0.5037	0.5254
	$\mathcal{D}_z (10^{11})$	$LWFM4_a$	-584.80	-783.99	-1615.6	-16266
$w (10^{11})$	LW4	-9.6219	-11.2852	6.4451	11275.3779	
$\sigma_{\alpha\alpha}$	LW4	-3.2642 -0.9616	-4.4933 -3.5544	-8.9704 -10.3507	-18.4390 -106.9489	
$\sigma_{\beta\beta}$	LW4	0.3518 0.4177	0.3624 0.0395	1.3358 -1.4200	94.4157 -94.1954	
$\sigma_{\alpha\beta}$	LW4	0.0036 0.0005	0.0042 0.0019	0.0082 0.0054	0.1075 -0.0114	
$\sigma_{\alpha z}$	LW4	-0.0207	-0.0207	-0.0324	-0.1905	
$\sigma_{\beta z}$	LW4	0.0023	0.0027	0.0014	0.0072	
σ_{zz}	LW4	0.0731 0.1009	0.0311 0.0371	0.0090 0.0047	0.1865 0.0454	
Φ	LW4	0.3432	0.4611	0.5037	0.5259	
$\mathcal{D}_z (10^{11})$	LW4	-586.0881	-786.2541	-1621.7268	-16310.8350	

Table 8.7: Transverse normal displacement $w * 10^{11}$, electric potential Φ , shear stresses $\sigma_{\alpha z}$, $\sigma_{\beta z}$ evaluated along the thickness in ($z = 0$). Transverse normal electric displacement $\mathcal{D}_z * 10^{11}$ evaluated along the thickness at *top* ($z = +h/2$). In-plane stresses $\sigma_{\alpha\alpha}$, $\sigma_{\beta\beta}$, $\sigma_{\alpha\beta}$ and transverse normal stress σ_{zz} evaluated along the thickness at ($z = \pm h/2$). Shell mono-layered piezoelectric cylinder. *Mesh* (10×10). Actuator case.

R/h		2	4	10	100
$w (10^{11})$	$LWFM4_a$	30.225	111.91	969.70	403190
$\sigma_{\alpha z}$	$LWFM4_a$	-0.1193	-0.2575	-0.6365	-3.1560
σ_{zz}	$LWFM4_a$	-0.415	-0.661	-1.150	-3.997
Φ	$LWFM4_a$	0.00497	0.0195	0.0602	0.3127
$\mathcal{D}_z (10^{11})$	$LWFM4_a$	0.752	1.104	1.325	-5.495
$w (10^{11})$	LW4	30.223	111.906	969.672	403287
	LW1	31.60	111.731	947.779	397293
$\sigma_{\alpha z}$	LW4	-0.1195	-0.2579	-0.6385	-3.2162
	LW1	-0.1144	-0.2383	-0.5845	-2.9859
σ_{zz}	LW4	-0.4129	-0.6597	-1.1529	-4.0875
	LW1	-0.4033	-0.6466	-1.1245	-3.9824
Φ	LW4	0.0050	0.0195	0.0604	0.3190
	LW1	0.0072	0.0212	0.0604	0.3143
$\mathcal{D}_z (10^{11})$	LW4	0.1516	-0.8323	-3.0984	-23.473
	LW1	-2.950	-8.7942	-36.282	-1648.83

Table 8.8: Transverse normal displacement $w * 10^{11}$, electric potential Φ , shear stress $\sigma_{\alpha z}$ and transverse normal stress σ_{zz} evaluated along the thickness in ($z = 0$). Transverse normal electric displacement $\mathcal{D}_z * 10^{11}$ evaluated along the thickness at *top* ($z = +h/2$). Shell cylinder with 3 layers. Sensor case.

R/h		2	4	10	100	
$w (10^{11})$	$LWFM4_a$	-1.306	-1.400	-1.4667	5.5418	
$\sigma_{\alpha z} (10^4)$	$LWFM4_a$	19.176	8.4776	1.5865	-0.5423	
$\sigma_{zz} (10^4)$	$LWFM4_a$	-116.36	-17.086	-0.5748	-0.5571	
Φ	$LWFM4_a$	0.4058	0.4826	0.5029	0.5009	
$\mathcal{D}_z (10^{11})$	$LWFM4_a$	-106.61	-66.035	-32.684	-36.209	
$w (10^{11})$		LW4	-1.3066	-1.4007	-1.4662	5.5418
		LW1	-1.3646	-1.4450	-1.4849	5.4331
$\sigma_{\alpha z} (10^4)$		LW4	19.250	8.5036	1.5412	-0.5538
		LW1	11.005	5.5673	0.9585	-0.5193
$\sigma_{zz} (10^4)$		LW4	-119.606	-18.605	3.309	-0.357
		LW1	-82.662	-8.323	5.147	-0.490
Φ		LW4	0.4058	0.4827	0.5029	0.5009
		LW1	0.4917	0.4975	0.4996	0.500
$\mathcal{D}_z (10^{11})$		LW4	-106.851	-66.045	-32.642	-36.201
		LW1	-62.002	-38.432	-19.998	-34.863

Table 8.9: Transverse normal displacement $w * 10^{11}$, electric potential Φ , shear stresses $\sigma_{\alpha z} * 10^4$ and transverse normal stress $\sigma_{zz} * 10^4$ evaluated along the thickness in ($z = 0$). Transverse normal electric displacement $\mathcal{D}_z * 10^{11}$ evaluated along the thickness at *top* ($z = +h/2$). Shell cylinder with 3 layers. Actuator case.

The LW4 model only is able to fulfill the continuity conditions of shear stresses $\sigma_{\alpha z}$ at the interfaces between layers, while lower-order model gives a completely wrong result, even if the shell is very thin ($R/h = 100$), see Figures 8.7a- 8.7b. The LW4 model is not able to fulfill the continuity conditions of transverse stresses σ_{zz} at the interfaces between layers, see Figures 8.8a-8.8b. To overcome this problem a mixed variational principle could be used. For the description of the electric potential Φ it is necessary to use the higher-order model, LW4, to describe the non-linear behavior of thick shell ($R/h = 2$), see Figures 8.9a-8.9b, on the other hand for thin shell ($R/h = 100$) a layer-wise description of lower order is sufficient. Concerning the electric displacement \mathcal{D}_z , for the thin cylinder ($R/h = 100$), the continuity interface cannot be reached, see Figure 8.10a. For the actuator case, in spite of its linear behavior, it is necessary an higher-order model to obtain the continuity interface of the electric displacement, see Figures 8.10b. To overcome this problem a mixed variational principle could be used.

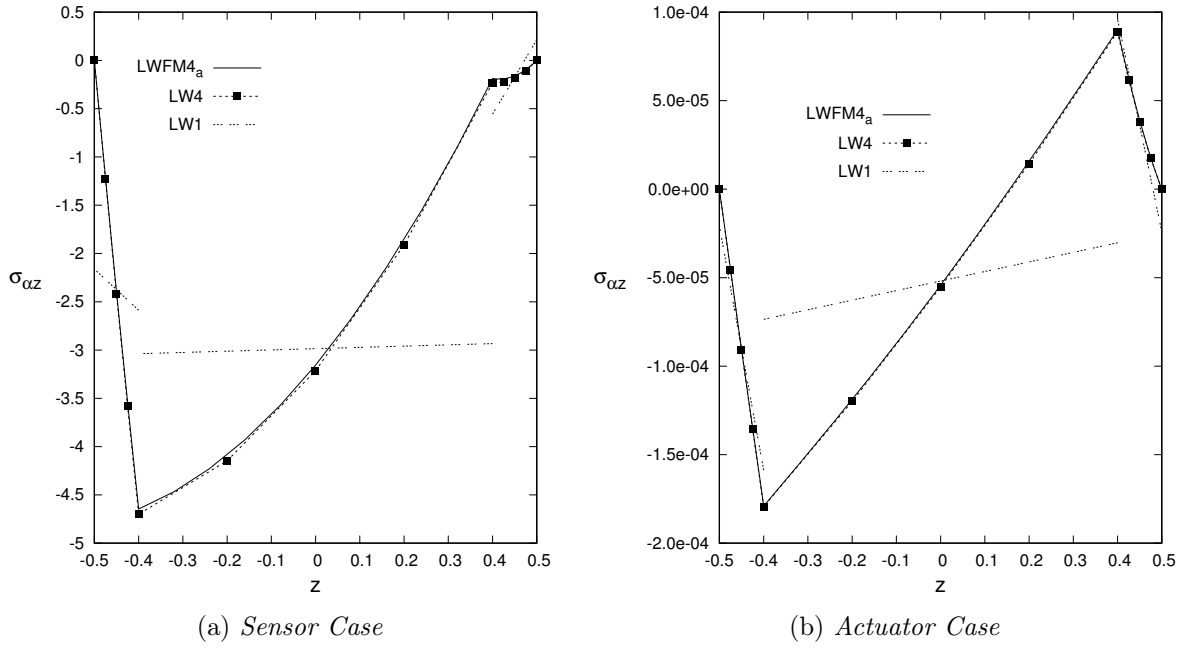


Figure 8.7: Four-layered cylinder, with radius to thickness ratio $(R/h) = 100$. Transverse shear stress $\sigma_{\alpha z}$.

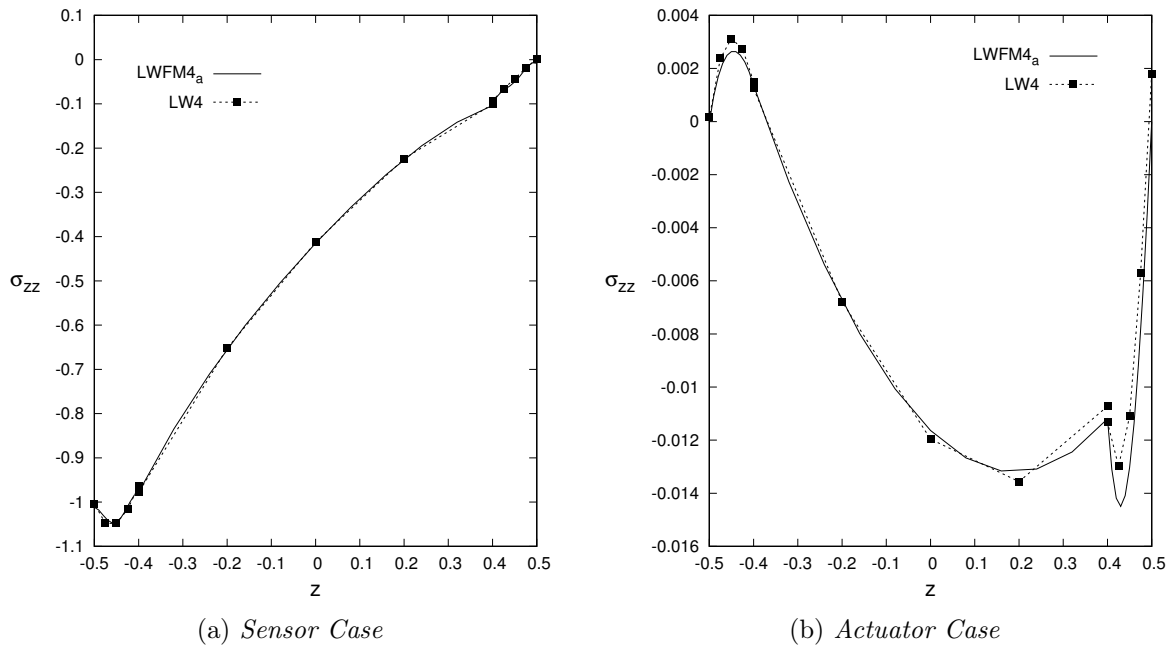


Figure 8.8: Four-layered cylinder, with radius to thickness ratio $(R/h) = 2$. Transverse normal stress σ_{zz} .

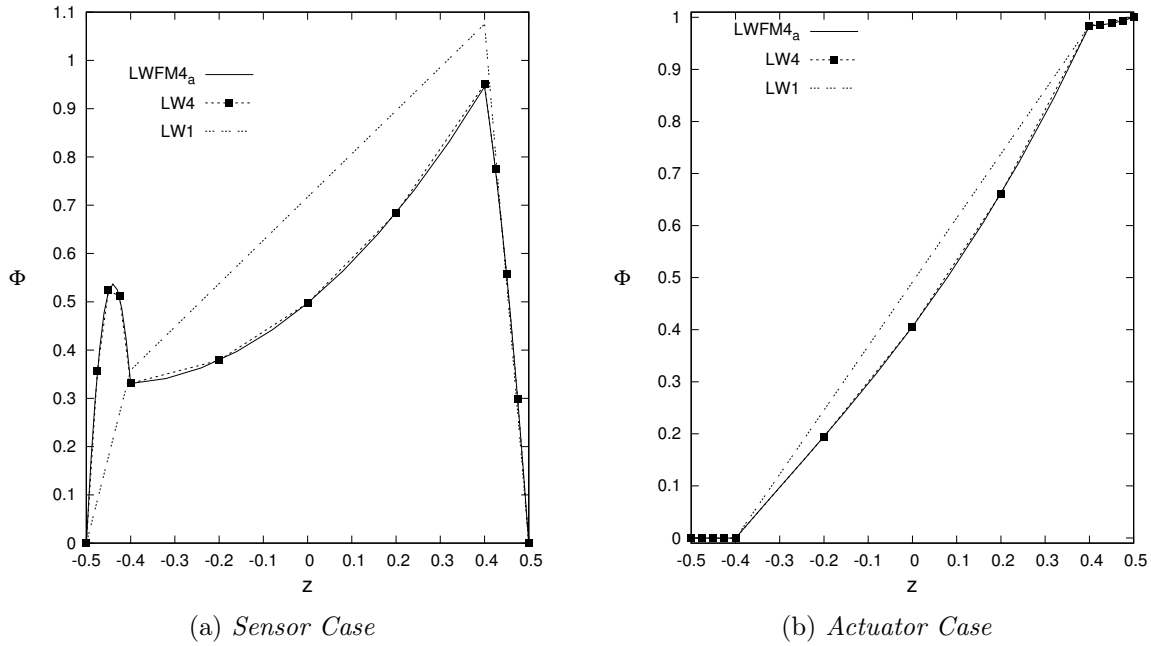


Figure 8.9: Four-layered cylinder, with radius to thickness ratio $(R/h) = 2$. Electric potential Φ .

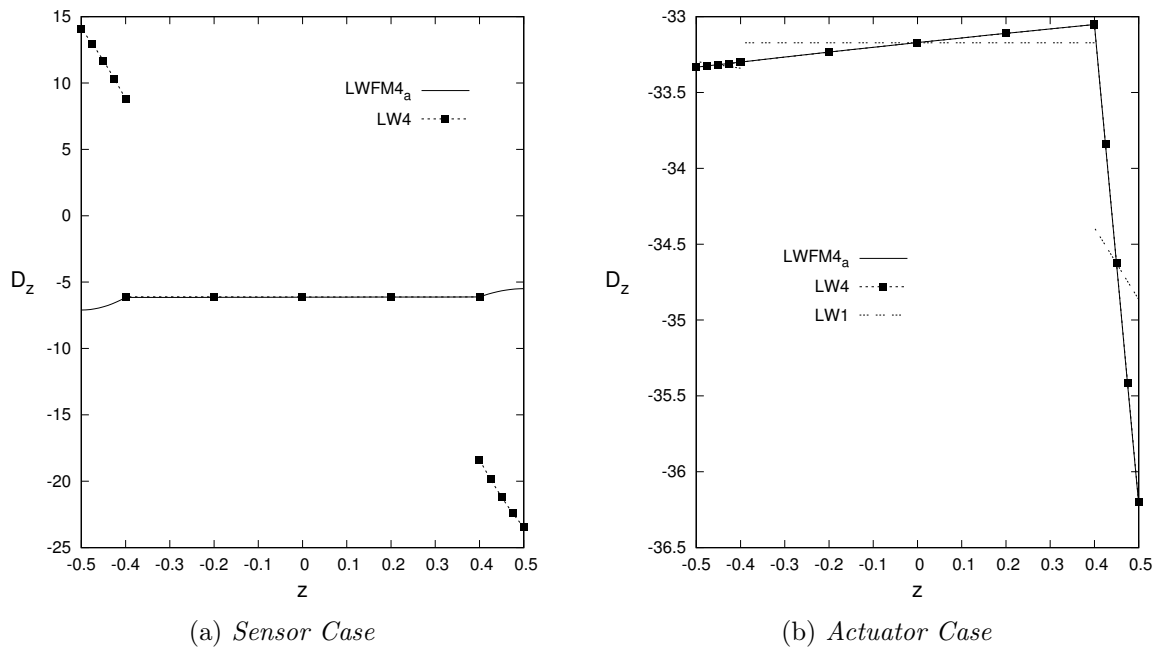


Figure 8.10: Four-layered cylinder, with radius to thickness ratio $(R/h) = 100$. Electric displacement D_z .

8.2 RMVT-Dz for shells

In the study of electro-mechanical problems, it is usually necessary to impose the values of the electric potential at top and bottom surfaces of the shell. To obtain this, a simple way is to use Layer-Wise models with Legendre polynomials. The efficiency of Layer-Wise models is tested with the finite element scheme, and the numerical results are compared with the ones obtained with the 3D elasticity approach. In this direction, the reference problem of the previous numerical section is considered: multilayered cylinders embedding piezoelectric

layers analytically evaluated in sensor and actuator configuration.

In this work the Principle of Virtual Displacements and the Reissner Mixed Variational Theorem $-Dz$ (transverse electric displacement is a priori modelled) are used, for the considered variational theorem the layer-wise models are indicated with the letters (LW) and (LWM) respectively. Reference solutions are calculated with Full Reissner Mixed Variational Theory (both transverse stresses and transverse electric displacement are a priori modelled), so the model acronyms are ($LWFM$) and subscript (a) is added if the Navier analytical method is employed.

A three layered configuration cylinder with the core in Gr/Ep composite material and the skins made of piezoelectric material PZT is analysed: the material properties are the same of the previous numerical section, and they are given in Table 8.1. The reference solutions are evaluated with an analytical Layer-Wise Full Mixed approach (LWFM). The geometrical parameters of the considered cylinder are: $a = 40$, $b = 2\pi R_\beta$, $R_\beta = 10$. In respect to the total thickness, a single piezoelectric skin is thick $h_p = 0.1h_{tot}$, while the core layer is thick $h_c = 0.8h_{tot}$. For the sensor case, a bi-sinusoidal transverse normal pressure is applied at the inner surface of the cylinder:

$$p_z^- = \hat{p}_z^- \sin(m\pi\alpha/a)\sin(n\pi\beta/b) \quad (8.6)$$

with amplitude $\hat{p}_z^- = 1$ and wave numbers $m = 1$, $n = 8$. The potential at top and bottom position is imposed: $\Phi_t = \Phi_b = 0$. For the actuator case, a bi-sinusoidal electric potential is imposed at top surface:

$$\Phi^+ = \hat{\phi}_z^+ \sin(m\pi\alpha/a)\sin(n\pi\beta/b) \quad (8.7)$$

with amplitude $\hat{\phi}_z^+ = 1$ and wave numbers $m = 1$, $n = 8$. The potential at bottom position is imposed $\Phi_b = 0$. No mechanical load is applied. Due to the symmetry of both the geometry and the load, an octave of the cylinder is studied ($1/2$ in the axial direction and $1/4$ in the hoop direction). The following symmetry conditions are applied:

$$\begin{aligned} v_\tau(\alpha, 0) &= 0 \\ u_\tau(0, \beta) &= 0 \\ v_\tau(\alpha, R_\beta\pi/2) &= 0 \end{aligned} \quad (8.8)$$

and the following boundary conditions are prescribed:

$$v_\tau(a/2, \beta) = w_\tau(a/2, \beta) = 0 \quad (8.9)$$

$$\Phi_\tau(a/2, \beta) = \mathcal{D}_{n_\tau}(a/2, \beta) = 0 \quad (8.10)$$

with $\tau = 0, 1, \dots, N$. The results are presented for different thickness ratios $R/h = 2, 4, 10, 100$. A mesh grid of 6×22 elements is taken to ensure the convergence of the solution for the mechanical displacement and stresses and the electric potential for the actuator configuration, see Table 8.10. The solution for the electric displacement is not exactly reached for the sensor case, this is due to the machine limitations, but increasing the mesh grid value a more accurate solution can be reached, see Table 8.11.

Mesh	6×6	10×10	6×10	6×14	6×18	6×20	6×22	$LWFM4_a$
$w * 10^{11}$	5.5407	5.5417	5.5417	5.5418	5.5418	5.5418	5.5419	5.5418
$\sigma_{zz} * 10^4$	1.0829	-0.2981	-0.2974	-0.3583	-0.3450	-0.3405	-0.3373	-0.5571
$\Phi * 10^2$	50.093	50.093	50.093	50.093	50.093	50.093	50.093	50.093
$\mathcal{D}_z * 10^{11}$	-36.214	-36.199	-36.199	-36.202	-36.205	-36.205	-36.206	-36.209

Table 8.10: Convergence study for transverse mechanical displacement $w * 10^{11}$, electric potential $\Phi * 10^2$ and transverse normal stress $\sigma_{zz} * 10^4$ evaluated at the midsurface ($z = 0$), and electric displacement $\mathcal{D}_z * 10^{11}$ evaluated at *top* ($z = +h/2$). All the variables are evaluated in $(\alpha = \frac{a}{2m}; \beta = \frac{b}{2n} \pm r \frac{b}{n})$, $r = 0, \dots, n - 1$. Thickness ratio $(R/h) = 100$. Actuator case.

Mesh	6×6	10×10	6×10	6×14	6×18	6×20	6×22	$LWFM4_a$
$w * 10^{11}$	30.193	30.221	30.221	30.224	30.225	30.225	30.225	30.225
$\sigma_{zz} * 10$	-4.0810	-4.1201	-4.1199	-4.1342	-4.1405	-4.1424	-4.1438	-4.1498
$\Phi * 10^4$	49.659	49.728	49.728	49.725	49.722	49.721	49.720	49.717
$\mathcal{D}_z * 10^{12}$	-3.2131	0.3878	0.3425	2.8149	4.2432	4.7330	5.1244	7.5228

Table 8.11: Convergence study for transverse mechanical displacement $w * 10^{11}$, electric potential $\Phi * 10^4$ and transverse normal stress $\sigma_{zz} * 10$ evaluated at the midsurface ($z = 0$), and electric displacement $\mathcal{D}_z * 10^{12}$ evaluated at *top* ($z = +h/2$). All the variables are evaluated in $(\alpha = \frac{a}{2m}; \beta = \frac{b}{2n} \pm r \frac{b}{n})$, $r = 0, \dots, n - 1$. Thickness ratio $(R/h) = 2$. Sensor case.

The results are presented in tabular form in terms of mechanical transverse displacement, electric potential, mechanical transverse normal stress, electric transverse displacement, see Tables 8.12-8.13. Similar comments as the previous numerical section can be drawn. For the sensor and actuator cases the results can reach an accuracy close to the exact solution by increasing the order of expansion N .

R/h		2	4	10	100
$w (10^{11})$	$LWFM4_a$	30.225	111.91	969.70	403190
	LW4	30.223	111.91	969.67	403287
$\sigma_{zz} (10)$	$LWFM4_a$	-4.1498	-6.6147	-11.496	-39.970
	LW4	-4.1289	-6.5970	-11.529	-40.875
$\Phi (10^4)$	$LWFM4_a$	49.717	195.10	601.80	3127.6
	LW4	49.727	195.16	603.92	3190.3
$w (10^{11})$	LWM4	30.225	111.91	969.72	403196
	LWM3	30.267	111.93	969.73	403196
	LWM2	30.334	111.85	969.42	403195
	LWM1	31.572	111.71	947.77	397191
$\sigma_{zz} (10)$	LWM4	-4.1438	-6.6081	-11.492	-40.191
	LWM3	-4.1248	-6.5981	-11.488	-40.190
	LWM2	-4.3702	-6.5022	-10.708	-35.511
	LWM1	-4.0397	-6.4720	-11.210	-39.152
$\Phi (10^4)$	LWM4	49.720	195.13	602.00	3146.4
	LWM3	49.543	194.94	601.63	3146.4
	LWM2	48.374	194.33	601.37	3146.4
	LWM1	83.725	218.84	606.95	3146.6

Table 8.12: Transverse normal displacement $w * 10^{11}$, electric potential $\Phi * 10^4$ and transverse normal stress $\sigma_{zz} * 10$ evaluated at the midsurface ($z = 0$). Transverse normal electric displacement $\mathcal{D}_z * 10^{12}$ evaluated at *top* ($z = +h/2$). All the variables are evaluated in $(\alpha = \frac{a}{2m}; \beta = \frac{b}{2n} \pm r \frac{b}{n})$, $r = 0, \dots, n - 1$. Sensor case. Mesh 6×22 .

R/h		2	4	10	100
$w (10^{11})$	<i>LWFM4_a</i>	-1.3062	-1.4004	-1.4667	5.5418
	LW4	-1.3065	-1.4006	-1.4662	5.5418
$\sigma_{zz} (10^4)$	<i>LWFM4_a</i>	-116.36	-17.086	-0.5748	-0.5571
	LW4	-119.60	-18.605	3.3095	-0.3576
$\Phi (10^2)$	<i>LWFM4_a</i>	40.585	48.265	50.288	50.093
	LW4	40.584	48.265	50.289	50.093
$\mathcal{D}_z (10^{11})$	<i>LWFM4_a</i>	-106.61	-66.035	-32.684	-36.209
	LW4	-106.85	-66.045	-32.642	-36.201
$w (10^{11})$	LWM4	-1.3062	-1.4004	-1.4667	5.5419
	LWM3	-1.3080	-1.4008	-1.4667	5.5418
	LWM2	-1.3127	-1.3995	-1.4661	5.5418
	LWM1	-1.3180	-1.4226	-1.4717	5.4381
$\sigma_{zz} (10^4)$	LWM4	-117.25	-17.825	-0.3725	-0.3373
	LWM3	-117.62	-17.964	-0.3700	-0.3316
	LWM2	-60.609	-12.151	-0.8932	-0.3545
	LWM1	-76.196	-8.9195	0.3516	-0.3932
$\Phi (10^2)$	LWM4	40.585	48.265	50.288	50.093
	LWM3	40.662	48.288	50.290	50.093
	LWM2	40.475	48.247	50.287	50.093
	LWM1	48.826	49.645	49.937	50.000
$\mathcal{D}_z (10^{11})$	LWM4	-106.75	-66.079	-32.676	-36.206
	LWM3	-106.74	-66.076	-32.675	-36.205
	LWM2	-106.60	-66.018	-32.649	-36.202
	LWM1	-108.43	-66.779	-32.787	-36.086

Table 8.13: Transverse normal displacement $w * 10^{11}$, electric potential $\Phi * 10^2$ and transverse normal stress $\sigma_{zz} * 10^4$ evaluated at the midsurface ($z = 0$). Transverse normal electric displacement $\mathcal{D}_z * 10^{11}$ evaluated at *top* ($z = +h/2$). All the variables are evaluated in $(\alpha = \frac{a}{2m}; \beta = \frac{b}{2n} \pm r \frac{b}{n})$, $r = 0, \dots, n - 1$. Actuator case. Mesh 6×22 .

Concerning the transverse normal stress σ_{zz} , higher-order layer wise models are necessary to match the reference solution. In this work no mechanical stresses continuity conditions are used; but imposing a transverse electric displacement continuity, a benefit for the mechanical transverse normal stress is obtained. This is evident compared to the PVD layer-wise solution, for shells with radius to thickness ratio $R/h = 100$, see Figures 8.11a-8.11b. For the thick shells with radius to thickness ratio $R/h = 2$ the necessity of higher order models is evident, see Figures 8.12a-8.12b.

For the description of the electric potential Φ it is necessary to use the higher-order model, LWM4, to describe the non-linear behavior in the thick shell ($R/h = 2$), see Figures 8.13a-8.13b; on the other hand, for thin shell ($R/h = 100$), a layer-wise description of lower order is sufficient.

The transverse electric displacement \mathcal{D}_z has a non-linear behavior in the sensor case, and PVD models are not sufficient to describe it correctly along the thickness for thick shell ($R/h = 2$), see Figure 8.14a. For the thin cylinder ($R/h = 100$) the continuity interface cannot be reached with PVD models, see Figure 8.14b. The RMVT-Dz with the transverse electric displacement continuity conditions allows to guarantee good results, but an higher mesh grid is necessary to reach to exact solution. For the actuator case, the transverse electric displacement has a linear behavior and the mesh grid employed is sufficient to reach the exact solution.

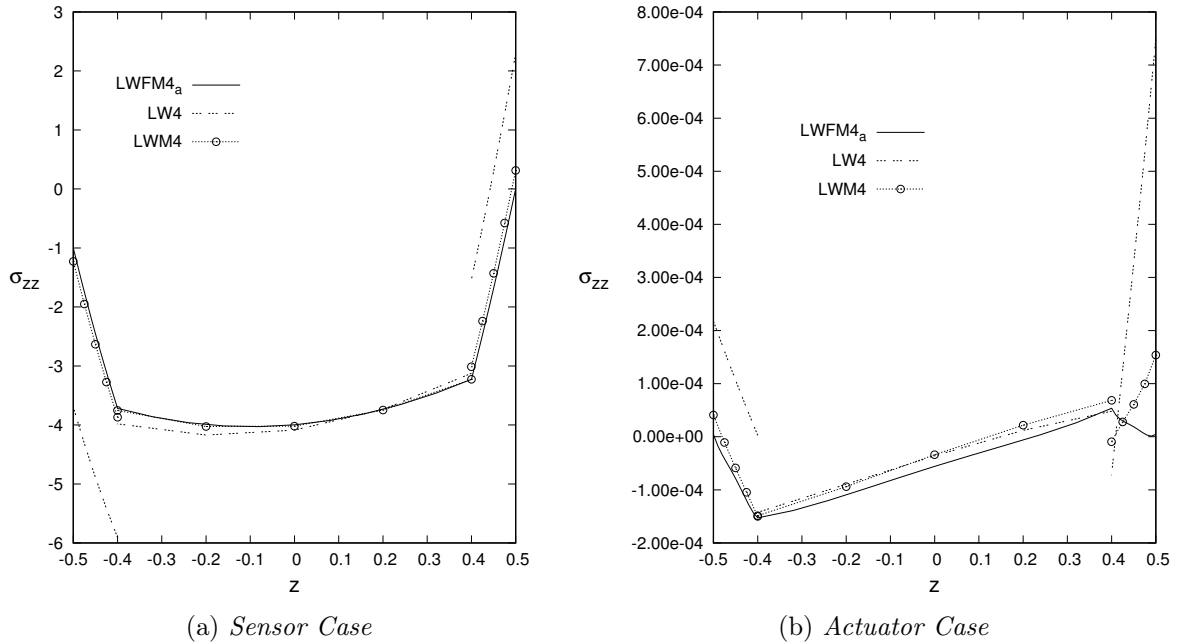


Figure 8.11: Three-layered cylinder, with radius to thickness ratio (R/h) = 100. Transverse normal stress σ_{zz} .

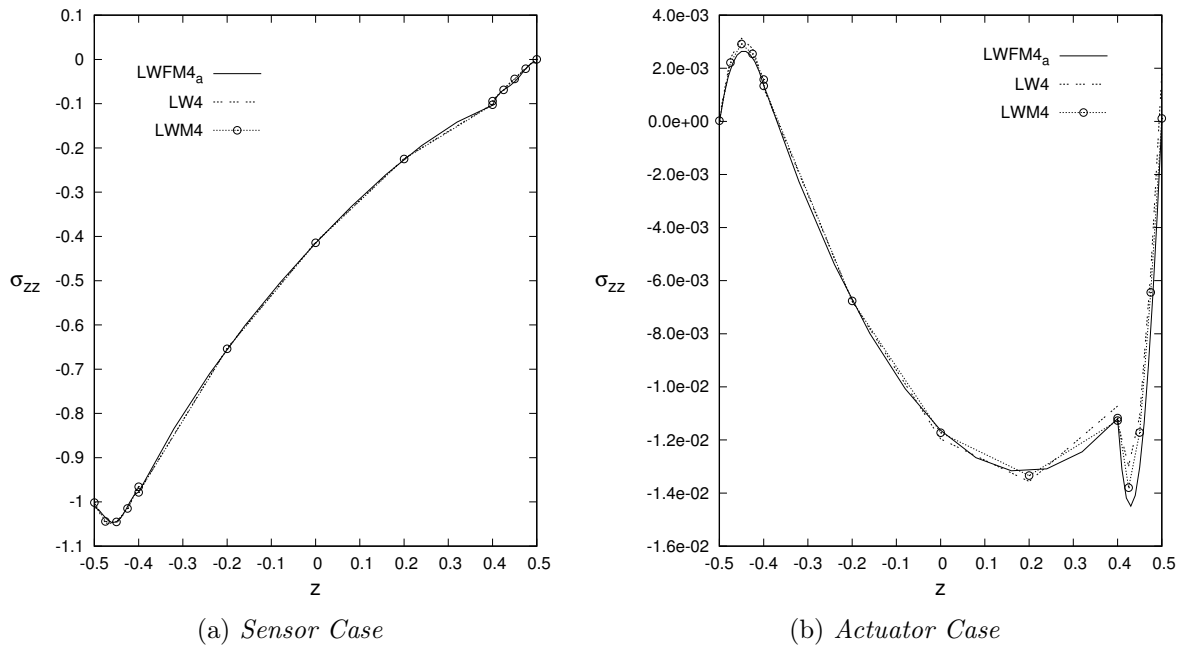


Figure 8.12: Three-layered cylinder, with radius to thickness ratio (R/h) = 2. Transverse normal stress σ_{zz} .

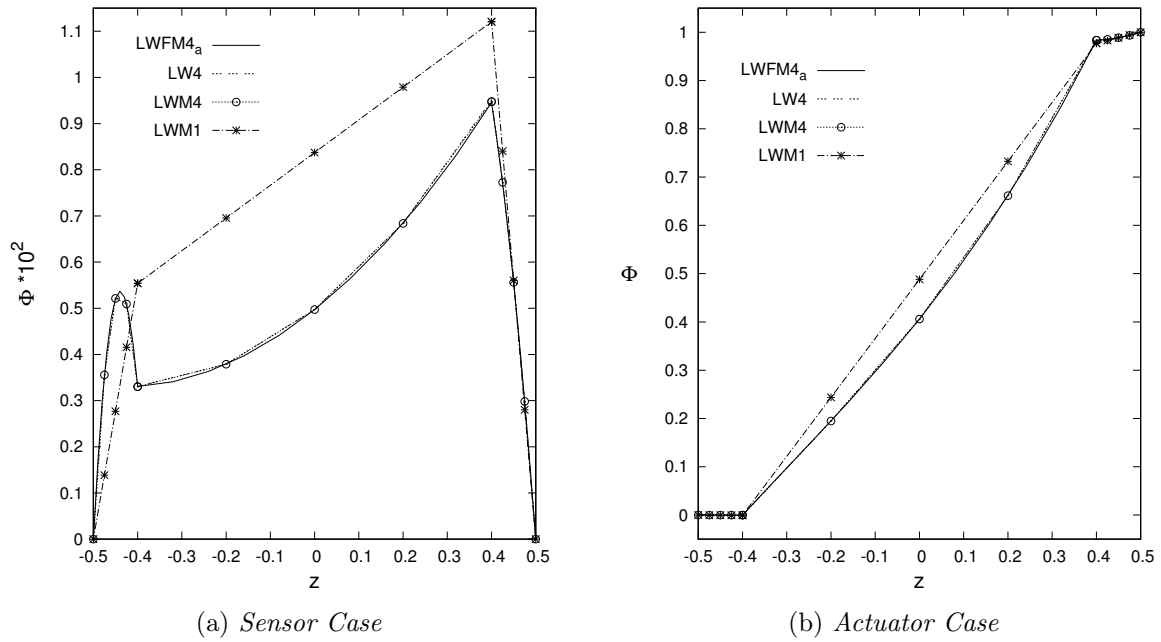


Figure 8.13: Three-layered cylinder, with radius to thickness ratio $(R/h) = 2$. Electric potential Φ .

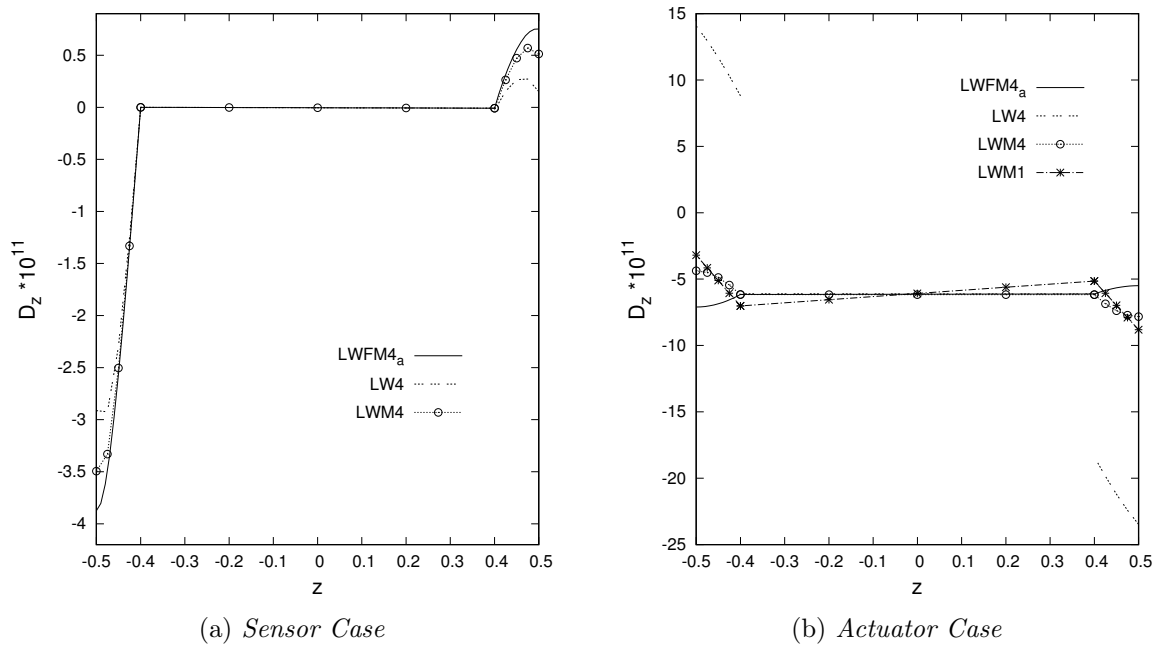


Figure 8.14: Three-layered cylinder, Sensor Case. Transverse electric displacement D_z .

8.3 Plate with piezoelectric Patches

Vibration and noise suppression, controlled active deformation and health monitoring are among the most important applications of the piezoelectric structural components. A plate finite element is presented in this section for the free-vibration analysis of isotropic plate structures with piezo-patches. In this direction, two kind of reference problems are considered: the aluminum rectangular plate with 8 piezoelectric patches, 4 on the top and 4 on the bottom surface symmetrically with patches short circuited in the first case and in open circuit mode for the second case.

8.3.1 Cantilevered plate with piezo-patches

To assess the plate element for the free-vibration analysis of plate structures with piezo-patches, it is taken into account the structure analyzed by Yasin et al. [141], see Figure 8.15. It is a cantilevered aluminum plate with 8 piezoelectric patches, 4 on the top surface and symmetrically 4 on the bottom ones. The plate is clamped on one short edge and free on the other three sides. The material and geometrical properties of the plate are given in Table 8.14. A mesh grid of 20×8 elements is adopted, see Figure 8.16, after a convergence analysis, see Table 8.15.

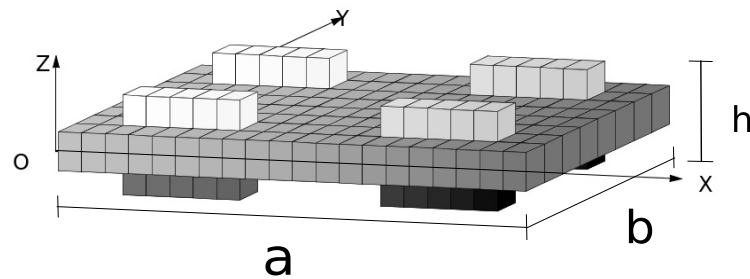


Figure 8.15: Geometry of the plate.

Material	PZT	Aluminum
a [m]	0.075	0.3
b [m]	0.025	0.2
h [m]	0.63×10^{-3}	0.8×10^{-3}
<i>Density</i> [Kg/m^3]	7600.0	2700.0
E_{11} [N/m^2]	63.0×10^9	70.0×10^9
E_{22} [N/m^2]	63.0×10^9	70.0×10^9
E_{33} [N/m^2]	63.0×10^9	70.0×10^9
ν_{12} [-]	0.28	0.32
ν_{13} [-]	0.28	0.32
ν_{23} [-]	0.28	0.32
G_{12} [N/m^2]	24.8×10^9	26.515×10^9
G_{13} [N/m^2]	24.8×10^9	26.515×10^9
G_{23} [N/m^2]	24.8×10^9	26.515×10^9
d_{15} [m/V]	670.0×10^{-12}	0
d_{24} [m/V]	670.0×10^{-12}	0
d_{31} [m/V]	-220.0×10^{-12}	0
d_{32} [m/V]	-220.0×10^{-12}	0
d_{33} [m/V]	374.0×10^{-12}	0
ϵ_{11} [F/m]	15.3×10^{-9}	30.975×10^{-12}
ϵ_{22} [F/m]	15.3×10^{-9}	26.55×10^{-12}
ϵ_{33} [F/m]	15.0×10^{-9}	26.55×10^{-12}

Table 8.14: Material and geometrical data for cantilevered plate with piezoelectric patches

Table 8.15: Frequency of cantilevered Plate with piezo-patches. Open Circuit case. Convergence study. LW4 model.

Mode	Q4	Q9
1	7.6526	7.6074
2	25.967	25.351
3	46.379	45.790
4	92.789	90.454
5	126.01	123.76
6	153.40	149.00
7	189.47	184.88
8	249.12	235.48
9	316.52	327.03
10	347.66	332.31

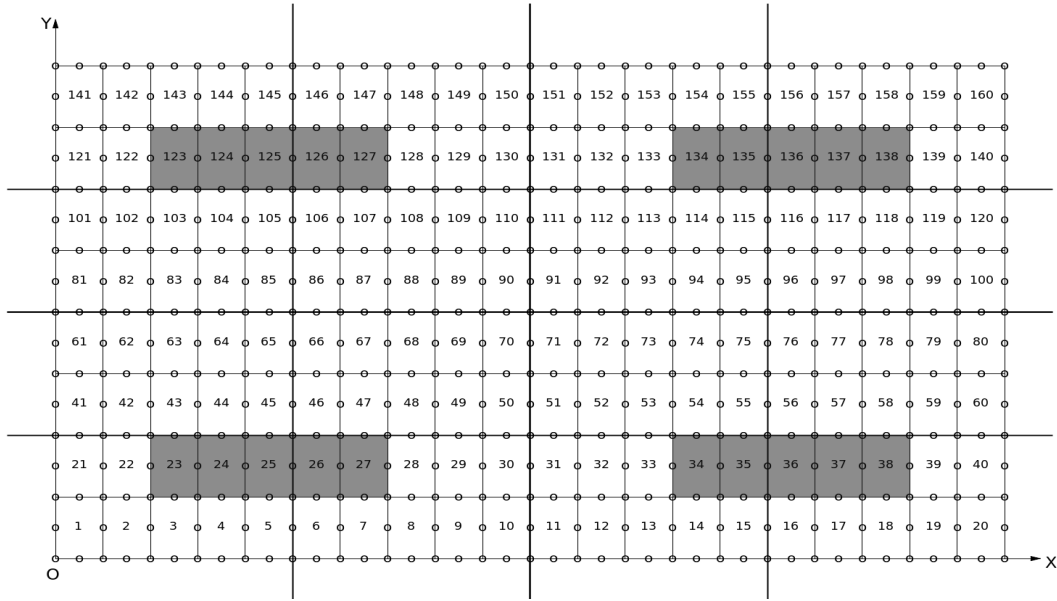


Figure 8.16: Isotropic plate with piezo patches, mesh grid representation.

Short Circuit Mode

For the first case the piezoelectric patches are short circuited thereby rendering ineffective the piezoelectric coupling effect that enhances the stiffness of otherwise passive structure. This case includes only the pure structural stiffness of the PZT patches and modal analysis, made by Yasin et al. [141], involves the solution of simplified following Eigen value problem:

$$(\mathbf{K}_{uu} - \omega_n^2 \mathbf{M}) \mathbf{q}_n = 0$$

In this work two methods are used for short circuit mode, free-vibration analysis using mechanical stiffness only as Yasin et al. [141] and free-vibration analysis with complete stiffness matrix applying penalty technique for the electrical degrees of freedom of the top and bottom surface of piezoelectric patches. One can note that the element doesn't suffer the locking phenomenon for the examined thin plate $a/h = 300$, see Table 8.16.

Table 8.16: Frequency of cantileverd Plate with piezo-patches comparing different locking correction methods. For all the cases a LW4 model is adopted.

Mode	Short Circuit			Open Circuit		
	MITC	Selective	Reduced	MITC	Selective	Reduced
1	7.6059	7.5897	7.5125	7.6074	7.5914	7.5167
2	25.346	25.306	11.955	25.351	25.313	16.443
3	45.787	45.732	12.038	45.790	45.737	16.614
4	90.446	90.250	12.110	90.454	90.274	16.854
5	123.76	123.62	12.116	123.76	123.64	17.478
6	148.93	148.23	12.133	149.00	148.28	17.739
7	184.69	184.02	25.168	184.88	184.09	17.873
8	235.50	234.94	25.451	235.48	235.01	17.994
9	328.22	327.38	25.468	327.03	327.46	25.218
10	332.49	329.79	25.549	332.31	329.96	45.375

In general the results approach to the exact solution by increasing the order of expansion N , see Table 8.17. The mechanical solution obtained by using Layer-Wise models of higher order only is able to reach the correct solution, there are few differences with the references ones due to different description of the field of displacement employed, higher in this work than the reference solution one. A three dimensional representation of the first four modes are shown in Figures 8.17-8.20. The solution with the penalty technique applied to the electrical DOFs shows few differences with the mechanical results, see Table 8.18, this is due to the higher order modeling of the electric potential along the thickness of the patches.

Table 8.17: Frequency of cantilevered Plate with piezo-patches. Pure Mechanical case.

<i>Mode</i>	<i>Ref</i> [141]	<i>LW4</i>	<i>LW3</i>	<i>LW2</i>	<i>LW1</i>
1	7.5236	7.5639	7.5640	7.5661	8.2918
2	25.195	25.312	25.324	25.356	26.324
3	45.542	45.718	45.723	45.736	50.113
4	90.215	90.236	90.277	90.386	96.301
5	123.03	123.66	123.69	123.76	133.99
6	147.62	147.08	147.09	147.18	161.14
7	183.16	182.65	182.69	182.85	194.84
8	234.05	235.40	235.51	235.76	254.69
9	326.93	325.14	325.15	325.27	347.75
10	328.04	326.98	327.13	327.52	364.35

<i>Mode</i>	<i>ESL4</i>	<i>ESL3</i>	<i>ESL2</i>	<i>ESL1</i>	<i>FSDT</i>
1	7.7235	7.7318	7.7413	7.6713	7.6882
2	25.654	25.689	25.814	25.737	25.781
3	46.004	46.035	46.072	45.830	45.855
4	91.347	91.459	91.864	91.545	91.667
5	124.78	124.87	125.05	124.75	124.87
6	152.86	153.06	153.45	152.02	152.63
7	188.45	188.61	189.26	187.96	188.51
8	240.23	240.33	241.04	239.63	240.24
9	329.53	329.71	331.25	329.07	329.19
10	343.19	346.92	347.63	342.85	345.16

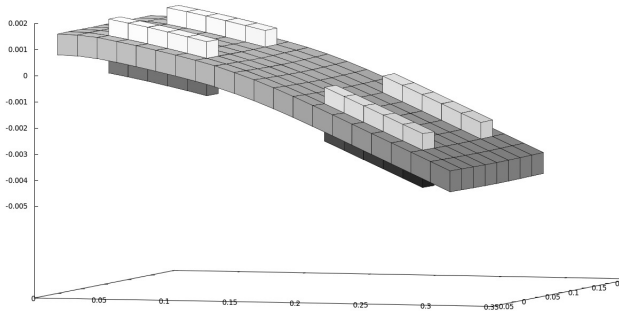


Figure 8.17: Natural frequency $7.5639 Hz$. Mode 1.

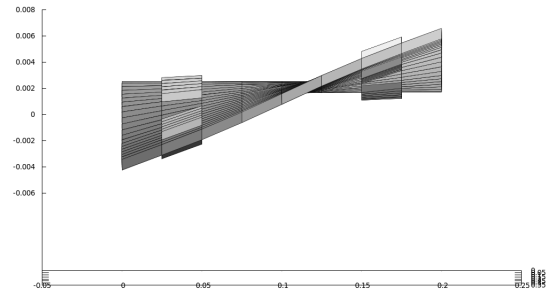


Figure 8.18: Natural frequency $25.312 Hz$. Mode 2.

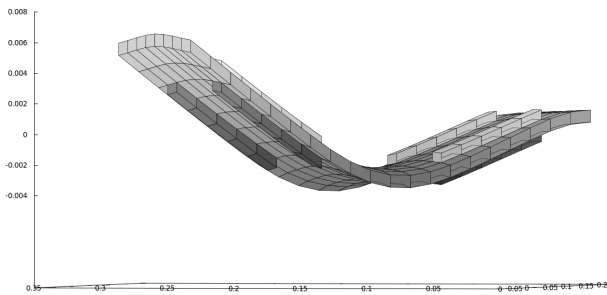


Figure 8.19: Natural frequency $45.718 Hz$. Mode 3.

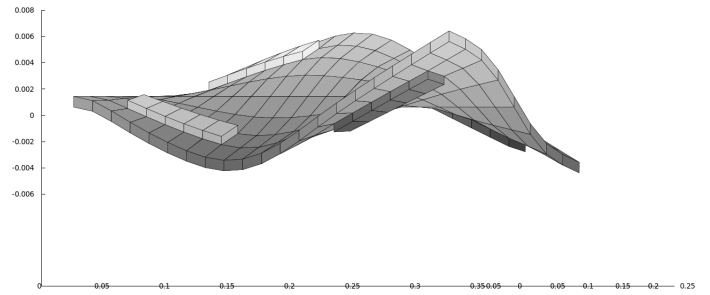


Figure 8.20: Natural frequency $90.236 Hz$. Mode 4.

Table 8.18: Frequency of cantilevered Plate with piezo-patches. Short Circuit case.

<i>Mode</i>	<i>Ref</i> [141]	<i>LW4</i>	<i>LW3</i>	<i>LW2</i>	<i>LW1</i>
1	7.5236	7.6059	7.6061	7.6083	8.3386
2	25.195	25.346	25.359	25.393	26.363
3	45.542	45.787	45.792	45.805	50.190
4	90.215	90.446	90.490	90.607	96.513
5	123.03	123.76	123.79	123.86	134.22
6	147.62	148.93	148.94	149.04	162.99
7	183.16	184.69	184.73	184.91	196.96
8	234.05	235.50	235.62	235.88	254.79
9	326.93	328.22	328.37	328.78	355.13
10	328.04	332.49	332.50	332.64	365.61

Open Circuit Mode

For the second case the piezoelectric patches are acting as sensors, so in open circuit mode no electric potential is imposed. A static condensation of the electrical DOFs is made by Yasin et al. [141]:

$$(\{ \mathbf{K}_{uu} - \mathbf{K}_{u\Phi} \mathbf{K}_{\Phi\Phi}^{-1} \mathbf{K}_{\Phi u}^T \} - \omega_n^2 \mathbf{M}) \mathbf{q}_n = 0$$

For the open circuit mode, in this work, free-vibration analysis with complete stiffness matrix is done, see Table 8.19. In general the results approach to the exact solution by increasing the order of expansion N . The Layer-Wise model of higher order only is able to reach the correct solution, there are few differences with the references ones due to different description of the field of displacement employed, higher in this work than the reference solution one.

Table 8.19: Frequency of cantilevered Plate with piezo-patches. Open Circuit case.

<i>Mode</i>	<i>Ref</i> [141]	<i>LW4</i>	<i>LW3</i>	<i>LW2</i>	<i>LW1</i>
1	7.5639	7.6074	7.6076	7.6098	8.3402
2	25.221	25.351	25.362	25.396	26.368
3	45.591	45.790	45.795	45.808	50.194
4	90.371	90.454	90.500	90.617	96.526
5	123.10	123.76	123.80	123.87	134.24
6	149.56	149.00	148.98	149.08	163.03
7	185.11	184.88	184.77	184.96	197.01
8	234.05	235.48	235.65	235.91	254.83
9	328.18	327.03	328.40	328.81	355.22
10	335.68	332.31	332.59	332.73	365.65

Part II

Efficient Shell FEM Formulation

Chapter 9

Variable Kinematic Mixed ESL/LW

Although the enormous improvements and formulations of higher-order plate/shell structural theories, considerable work has been recently directed towards the implementation of innovative solutions for improving the analysis efficiency for complex geometries and assemblies, possibly in a global/local scenario. In this manner, the limited computational resources can be distributed in an optimal manner to study in detail only those parts of the structure that require an accurate analysis. The main concept of the global/local analysis is to formulate multi-model methods, in which different subregions of the structure are analysed with different mathematical models. In general, multi-theory methods can be divided into sequential or multistep methods, and simultaneous methods. In a sequential multi-model, the global region is analysed with an adequate model with a cheap computational cost to determine the displacement or force boundary conditions for a subsequent analysis at the local level. The simultaneous multi-model methods are characterized by the analysis of the entire structural domain, where different subregions are modeled with different mathematical models and/or distinctly different levels of domain discretization, in a unique step. One of the simplest type of simultaneous multi-model methods for composite laminates analysis, is the concept of selective ply grouping or sublaminates [142–144]. In the literature, the local region (i.e., the region where accurate stress analysis is desired) is generally modeled by using 3-D finite elements in the domain of selective ply grouping method.

The concept of the present Mixed ESL/LW multi-model element, with variable kinematic through-the-thickness approximation, is to use 2-D finite elements for both local and global regions. According to the present modelling technique, in fact, the plate kinematics can vary through the thickness of the finite element. The main novelty of the present work is that Legendre-like polynomial expansions are used to indiscriminately implement ESL, LW as well as variable kinematics with combined ESL/LW capabilities. Therefore, refined approximations and layer-wise descriptions of the primary mechanical variables can be utilized only in the portion of the structure that requires a more detailed analysis. In the work by Botshekanan Dehkordi et al. [145], a variable description in the thickness direction was employed for the static analysis of sandwich plates. That model was derived from the RMVT in order to describe a-priori the transverse shear and normal stresses. The transverse stresses were described with a LW approach, whereas the displacement were approximated through a combined LW/ESL approach. The same combined LW/ESL approach with RMVT was then used in [146] for nonlinear dynamic analysis of sandwich plates with flexible core and composite faces embedded with shape memory alloy wires. As it will be clear later in following numerical sections, the variable kinematics allows to accurately capture the mechanical behaviour of selected areas of multi-layer structures with LW resolution. On the other hand, as the number of layers increases, full LW models may require a very large computational effort if compared to variable kinematics plate/shell theory, which can be extremely useful in problems where localized phenomena play an important role (e.g., delamination and low-velocity impact).

9.1 Modeling Approaches Comparison

Two different types of modeling approaches are usually used in the literature:

- The Equivalent Single Layer approach, here referred to as ESL;
- The Layer Wise approach, here referred to as LW.

In this chapter, a variable kinematic model, with combined ESL/LW capabilities, is also used. However, it is worth mentioning that the choice of the modeling approach does not depend on the type of thickness functions used in the structural theory.

9.1.1 ESL models

In an ESL model, a homogenization of the properties of each layer is conducted by summing the contributions of each layer in the stiffness matrix. This process leads to a model that has a set of variables that is assumed for the whole multilayer, see Figure 9.1. Therefore, the number of degrees of freedom does not depend on the number of layers. In this work the ESL model is employed using both Taylor and Legendre polynomials. The ESL assembly procedure of the stiffness matrix in the framework of Unified Formulation is shown in Figure 9.2.

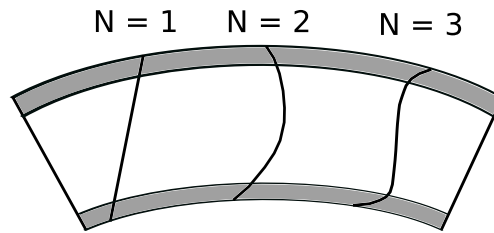


Figure 9.1: Equivalent-Single-Layer behaviour of the primary variables along the thickness of the shell.

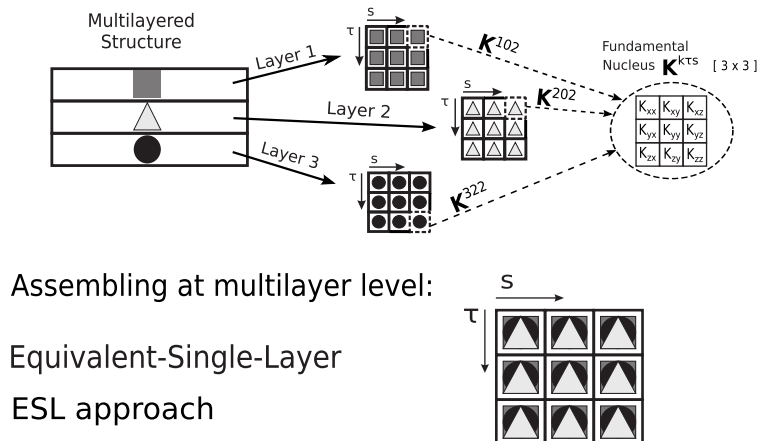


Figure 9.2: Equivalent-Single-Layer assembling scheme for a second-order ($N = 2$) plate model: The fundamental nucleus of the stiffness matrix, \mathbf{K}^{kTs} , is expanded for each layer k . The laminate stiffness matrix is then obtained by summing, term by term, the contribution of each layer. The dimension of the global matrix does not depend on the number of layers.

9.1.2 LW models

LW considers different sets of variables per each layer, and the homogenization is just conducted at the interface level, see Figure 9.3. The LW assembly procedure is presented in

Figure 9.4. In this work, the LW model is employed using the Legendre-like polynomials. The Lagrange polynomials F_0 and F_1 interpolate the displacements at the top (t) and bottom (b) position of the layer, respectively. The unknown variables at the top (t) and bottom (b) position are, thus, used to impose the following compatibility conditions:

$$\mathbf{u}_t^k = \mathbf{u}_b^{k+1}, \quad k = 1, N_l - 1. \quad (9.1)$$

where N_l is the number of layers. Refined LW models can be obtained by further expanding the displacement field according to Equation (3.9).

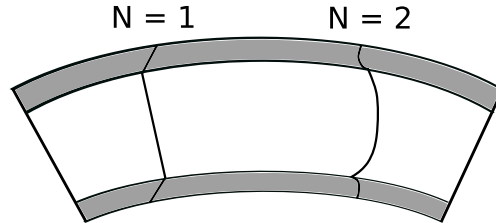


Figure 9.3: Layer-Wise behaviour of the primary variables along the thickness of the shell.

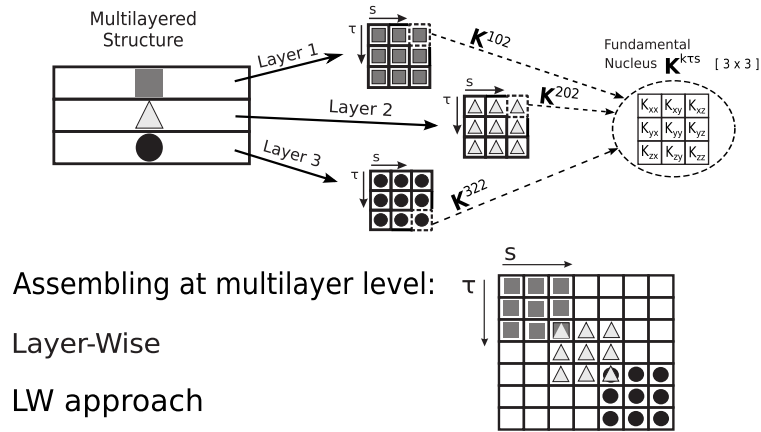


Figure 9.4: Layer-Wise assembling scheme for a second-order ($N = 2$) plate model: The fundamental nucleus of the stiffness matrix, \mathbf{K}^{kts} , is expanded for each layer k . The laminate stiffness matrix is then obtained by assembling the contribution of each layer at the layer/layer interface. The dimension of the global matrix depends on the number of layers.

9.1.3 Variable kinematics Mixed ESL/LW

In this chapter a variable kinematic approach with combined ESL/LW capabilities is also taken into account. Different sets of F_r and F_s functions can be employed through the thickness of the laminate, resulting in variable kinematic theories. Thus, advanced models combining the advantages of both ESL and LW approach can be easily obtained. In particular, in this work, ESL and LW approaches are combined by employing structural theories based on Legendre-like polynomials. In a multilayered structures some layers can be modeled with a homogenization of the properties and modeled with an ESL assembling procedure, whereas for some layers the homogenization is conducted just at the interface level, see Figure 9.5. The variable-kinematic assembling, developed in the framework of the Unified Formulation, is very simple to integrate, for example in a FORTRAN code, with few code statements. The code lines of the equations of the nucleus, in fact, are the same for both ESL, LW and for variable kinematic assembling. For clarity purposes, the variable-kinematic assembly procedure of the stiffness matrix in the framework of Unified Formulation is shown in Figure 9.6, where the two bottom layers of a three-layer structure are homogenized in an ESL sense and then assembled at the interface with the top layer.

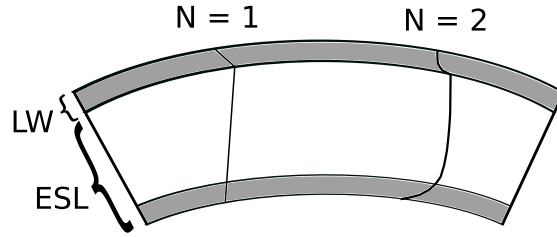


Figure 9.5: Variable-Kinematics behaviour of the primary variables along the thickness of the shell.

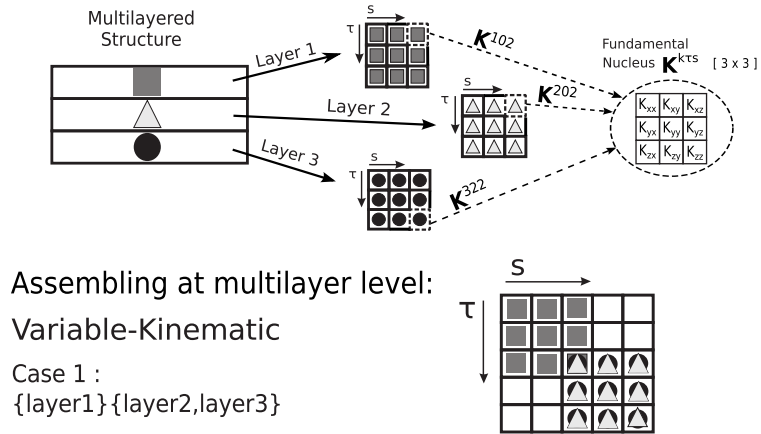


Figure 9.6: Variable-kinematic assembling scheme for a second-order ($N = 2$) plate model: The fundamental nucleus of the stiffness matrix, $\mathbf{K}^{k\tau s}$, is expanded for each layer k . Depending on the modelling choice, the laminate stiffness matrix is then obtained by adopting a combined ESL/LW approach. In this example, layers 2 and 3 are homogenized by ESL and then assembled with layer 1 by LW. The dimension of the global matrix depends on the modelling choice.

9.2 Mechanical Analysis Results

In this section, the static mechanical analysis of plate and shell structures are performed to assess the variable-kinematics mixed ESL/LW plate/shell element. To study the effectiveness of the proposed approach several reference problems were considered. The following composite multilayered plates and sandwich plate structures have been analyzed:

- A three-layer cross-ply square plate with lamination $(0^\circ/90^\circ/0^\circ)$
- An eight-layer cantilevered beam
- A three-layer rectangular sandwich plate
- A five-layer composite sandwich plate

Moreover the following reference problems have been considered for assessing the novel variable kinematic shell element:

- A three-layer simply-supported cylinder with $(90^\circ/0^\circ/90^\circ)$ lamination.
- A ten-layer simply-supported cylinder with $(90^\circ/0^\circ/90^\circ/0^\circ/90^\circ)_S$ lamination.
- A composite square simply-supported spherical panel with three-layer configuration $(0^\circ/90^\circ/0^\circ)$ and four-layer configuration $(0^\circ/90^\circ/90^\circ/0^\circ)$.
- An eleven-layer simply-supported sandwich cylindrical panel with $(0^\circ/90^\circ/0^\circ/Core/0^\circ/90^\circ/0^\circ/Core/0^\circ/90^\circ/0^\circ)$ lamination.

Wherever possible, solutions from variable-kinematic models are compared with those from higher-order ESL models, LW models, 3D elasticity solutions and analytical results.

9.2.1 Three-layer composite plate

A three-layer cross-ply $(0^\circ/90^\circ/0^\circ)$ square plate with simply-supported boundary condition is considered as the first assessment. The plate is subjected to the following load condition:

$$p(x, y, z_{top}) = \hat{p} \sin\left(\frac{\pi x}{a}\right) \sin\left(\frac{\pi y}{b}\right) \quad (9.2)$$

The load amplitude at the top position is: $\hat{p} = 1$. The mechanical properties of the material are such that: $E_L/E_T = 25$; $G_{LT}/E_T = 0,5$; $G_{TT}/E_T = 0,2$; $\nu_{LT} = \nu_{TT} = 0,25$. The geometrical dimensions are: $a = b = 1$. The results are presented for different thickness ratios, namely $a/h = 4$ and $a/h = 100$, and they are given in non-dimensional form:

$$\hat{w} = \frac{100wE_T h^3}{\hat{p}^+ a^4} \quad ; \quad \hat{\sigma}_{xx} = \frac{\sigma_{xx}}{\hat{p}^+ \left(\frac{a}{h}\right)^2} \quad ; \quad \hat{\sigma}_{xz/yz} = \frac{\sigma_{xz/yz}}{\hat{p}^+ \left(\frac{a}{h}\right)} \quad (9.3)$$

Table 9.1: Convergence study. Composite plate with lamination $[0^\circ/90^\circ/0^\circ]$ and with thickness ratio $a/h = 100$.

	Mesh	4×4	6×6	8×8	10×10
<i>LW4</i>	<i>w</i>	0.4349	0.4347	0.4347	0.4347
	σ_{xz}	0.415	0.404	0.400	0.398
<i>EL4</i>	<i>w</i>	0.4344	0.4343	0.4342	0.4342
	σ_{xz}	0.295	0.287	0.284	0.283
<i>ET4</i>	<i>w</i>	0.4344	0.4343	0.4342	0.4342
	σ_{xz}	0.295	0.287	0.284	0.282

First a convergence study versus the number of plate elements was performed by considering the case $a/h = 100$ and fourth-order ($N = 4$) ESL and LW models. As shown in Table 9.1, a mesh grid of 10×10 elements ensures the FEM convergence. Subsequently, in order to prove that the proposed element is locking free, various integrations schemes [115] were considered and the results are shown in Table 9.2.

Table 9.2: Locking study. Composite plate with lamination $[0^\circ/90^\circ/0^\circ]$ and with thickness ratio $a/h = 100$. All the cases are computed with a mesh of 10×10 elements.

		<i>Reduced</i>	<i>Selective</i>	<i>MITC9</i>	<i>Analytical</i>
3D [128]	w				-
	σ_{xz}				0.395
LW4	w	0.4347	0.4339	0.4347	0.4347
	σ_{xz}	0.616	0.664	0.398	0.395
EL4	w	0.4342	0.4334	0.4342	
	σ_{xz}	0.501	0.510	0.283	
ET4	w	0.4342	0.4334	0.4342	0.4342
	σ_{xz}	0.501	0.510	0.283	0.282

In this table, the results from the present higher-order finite elements are compared to various 2D and 3D analytical solutions. It is clear that the plate element with the MITC9 method ensures acceptable accuracy on both the transverse displacement and the shear stress.

Table 9.3: Composite plate with lamination $[0^\circ/90^\circ/0^\circ]$. Transverse displacement $\hat{w} = \hat{w}(a/2, b/2, +h/2)$, in-plane stress $\hat{\sigma}_{xx} = \hat{\sigma}_{xx}(a/2, b/2, \pm h/2)$, transverse shear stress $\hat{\sigma}_{xz} = \hat{\sigma}_{xz}(a, b/2, 0)$ and $\hat{\sigma}_{yz} = \hat{\sigma}_{yz}(a/2, b, 0)$. Taylor vs Legendre models.

	$a/h = 4$					$a/h = 100$				<i>DOFs</i>	
	\hat{w}	$\hat{\sigma}_{xx}$		$\hat{\sigma}_{xz}$	$\hat{\sigma}_{yz}$	\hat{w}	$\hat{\sigma}_{xx}$		$\hat{\sigma}_{xz}$		$\hat{\sigma}_{yz}$
		<i>top</i>	<i>bottom</i>				<i>top</i>	<i>bottom</i>			
3D [128]	-	0.801	-0.755	0.256	0.2172	-	0.539	-0.539	0.395	0.0828	
LW4 _a [147]	2.1216	0.801	-0.755	0.256	0.2180	0.4347	0.539	-0.539	0.395	0.0828	
LW4	2.1216	0.807	-0.761	0.258	0.2197	0.4347	0.544	-0.544	0.398	0.0836	17199
ET4 _a [147]	2.0083	0.786	-0.740	0.205	0.1830	0.4342	0.539	-0.539	0.281	0.0734	15
ET4	2.0082	0.7926	-0.7461	0.2067	0.1845	0.4342	0.5435	-0.5436	0.2830	0.0742	6615
ET3	2.0069	0.7940	-0.7479	0.2068	0.1845	0.4342	0.5436	-0.5436	0.2830	0.0742	5292
ET2	1.6499	0.4714	-0.4252	0.1219	0.1258	0.4333	0.5428	-0.5428	0.1436	0.0603	3969
ET1*	1.6574	0.4484	-0.4537	0.1234	0.1237	0.4333	0.5428	-0.5428	0.1428	0.0592	2646
ET1 ⁻	1.6448	0.4465	-0.4517	0.1227	0.1258	0.4282	0.5404	-0.5404	0.1421	0.0614	2646
EL4	2.0082	0.7926	-0.7461	0.2067	0.1845	0.4342	0.5435	-0.5436	0.2830	0.0742	6615
EL3	2.0069	0.7940	-0.7479	0.2068	0.1845	0.4342	0.5436	-0.5436	0.2830	0.0742	5292
EL2	1.6499	0.4714	-0.4252	0.1219	0.1258	0.4333	0.5428	-0.5428	0.1436	0.0603	3969
EL1	1.6448	0.4465	-0.4517	0.1227	0.1258	0.4282	0.5404	-0.5404	0.1421	0.0614	2646

* thickness locking correction
 - no correction

An assessment of the Legendre-like polynomial expansion theories with a full ESL approach was performed subsequently. All the results presented in Table 9.3, for thick and thin plates, show that the Legendre polynomials lead to the same results as the Taylor-based ESL

models. Regarding the Taylor linear model, if the thickness locking correction is applied, $ET1^*$, a moderate difference in the results is noticeable, with respect to the $EL1$ theory. Nevertheless, the use of either polynomials is invariant respect to the solution accuracy, see Figures 9.7 to 9.10. Therefore, Legendre polynomials are employed hereafter to implement ESL, LW and variable kinematic plates.

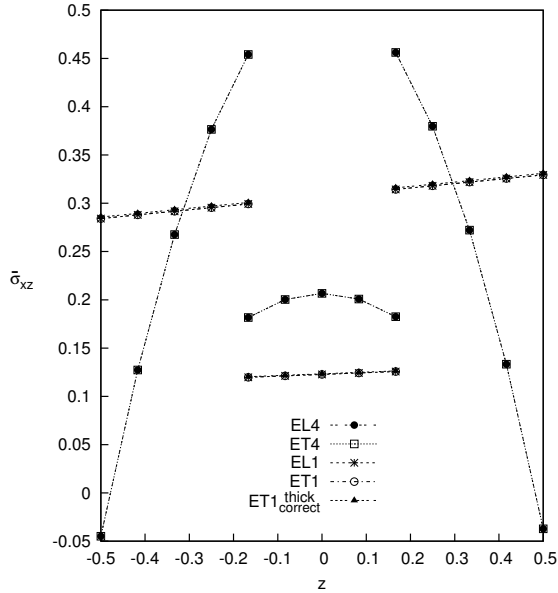


Figure 9.7: Transverse shear stress σ_{xz} along the thickness, with thickness ratio $(a/h) = 4$. Composite plate.

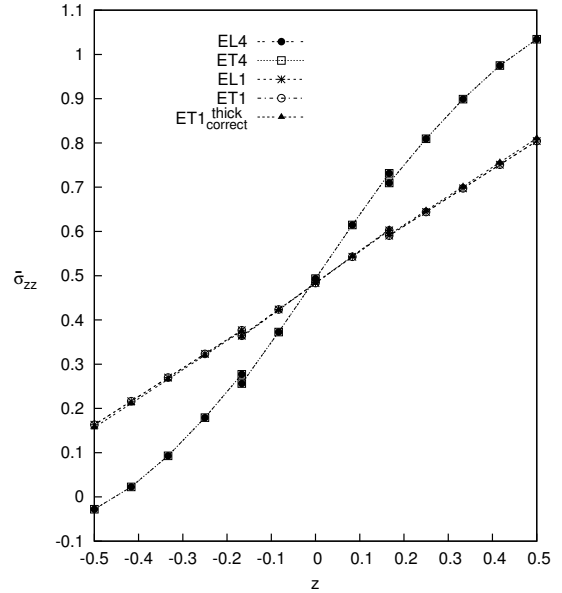


Figure 9.8: Transverse normal stress σ_{zz} along the thickness, with thickness ratio $(a/h) = 4$. Composite plate.

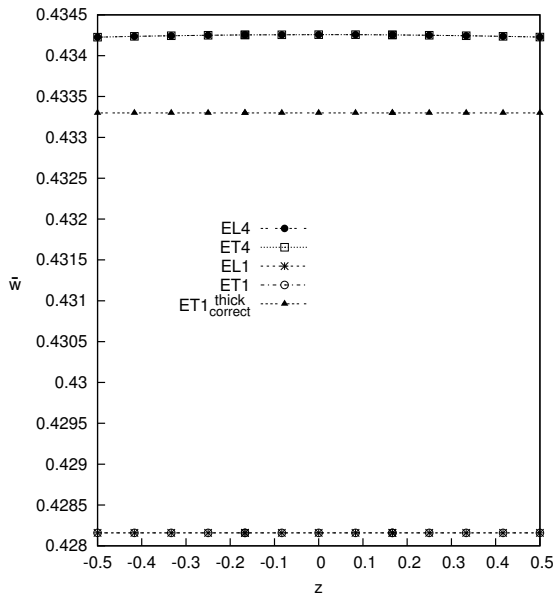


Figure 9.9: Transverse displacement w along the thickness, with thickness ratio $(a/h) = 100$. Composite plate.

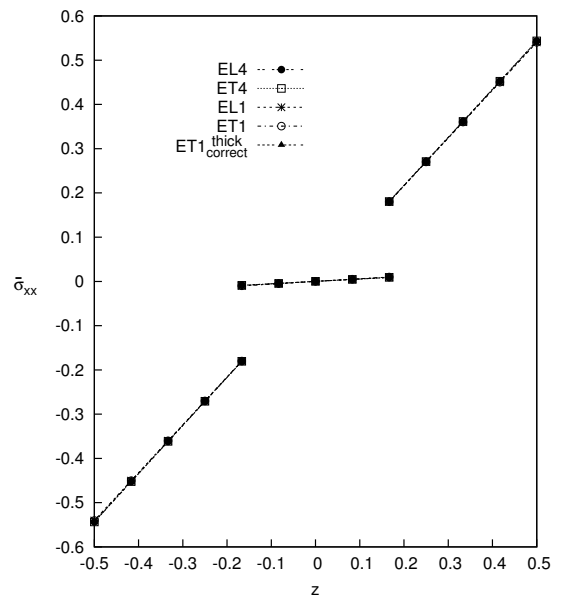


Figure 9.10: In-plane stress σ_{xx} along the thickness, with thickness ratio $(a/h) = 100$. Composite plate.

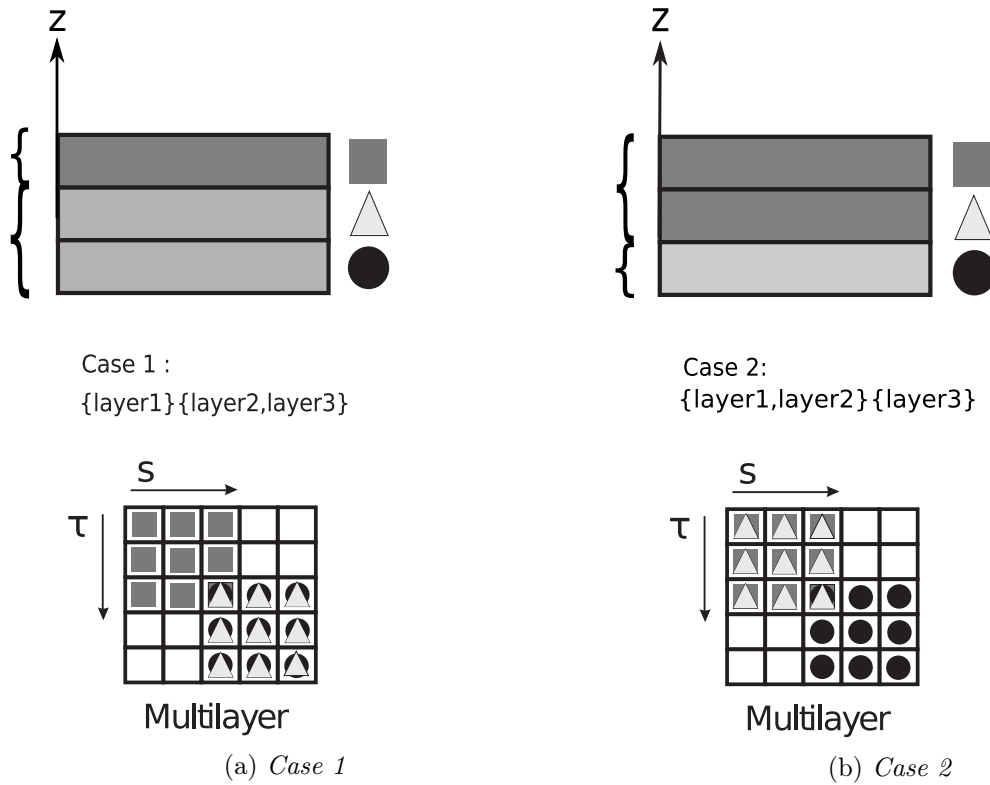


Figure 9.11: Variable Kinematic Models for the three-layer plate. Case 1 and Case 2.

Different variable kinematic models were used to perform the analysis of the plate structures, see Figures 9.11a and 9.11b. In this case, the acronyms was modified adding a subscript for clarity purposes. In particular, two different variable kinematic models of the structure under consideration are addressed:

- $Case1 = \{layer1\}\{layer2, layer3\}$
- $Case2 = \{layer1, layer2\}\{layer3\}$

In *Case1* (Figure 9.11a), the two bottom layers are homogenized and then assembled at the top layer in a LW sense. Vice versa, in *Case2* (Figure 9.11b), the two top layers are homogenized.

Table 9.4: Composite plate with lamination $[0^\circ/90^\circ/0^\circ]$. Transverse displacement $\hat{w} = \hat{w}(a/2, b/2, +h/2)$, in-plane stress $\hat{\sigma}_{xx} = \hat{\sigma}_{xx}(a/2, b/2, \pm h/2)$, transverse shear stress $\hat{\sigma}_{xz} = \hat{\sigma}_{xz}(a, b/2, 0)$ and $\hat{\sigma}_{yz} = \hat{\sigma}_{yz}(a/2, b, 0)$. Variable kinematic models.

	$a/h = 4$					$a/h = 100$					$DOFs$
	\hat{w}	$\hat{\sigma}_{xx}$		$\hat{\sigma}_{xz}$	$\hat{\sigma}_{yz}$	\hat{w}	$\hat{\sigma}_{xx}$		$\hat{\sigma}_{xz}$	$\hat{\sigma}_{yz}$	
		<i>top</i>	<i>bottom</i>				<i>top</i>	<i>bottom</i>			
3D [128]	-	0.801	-0.755	0.256	0.2172	-	0.539	-0.539	0.395	0.0828	
LW4	2.1216	0.807	-0.761	0.258	0.2197	0.4347	0.544	-0.544	0.398	0.0836	17199
<i>EL4,Case1</i>	2.0865	0.7970	-0.7524	0.2548	0.1954	0.4346	0.5436	-0.5436	0.4006	0.0750	11907
<i>EL4,Case2</i>	2.0862	0.7986	-0.7506	0.2530	0.1951	0.4346	0.5436	-0.5436	0.4006	0.0750	11907
<i>EL3,Case1</i>	2.0803	0.7962	-0.7577	0.2395	0.1858	0.4345	0.5436	-0.5436	0.3568	0.0727	9261
<i>EL3,Case2</i>	2.0818	0.8034	-0.7500	0.2398	0.1889	0.4345	0.5436	-0.5436	0.3568	0.0727	9261
<i>EL2,Case1</i>	2.0671	0.7851	-0.7431	0.2378	0.1750	0.4345	0.5436	-0.5436	0.3569	0.0679	6615
<i>EL2,Case2</i>	2.0675	0.7901	-0.7394	0.2380	0.1759	0.4345	0.5436	-0.5436	0.3569	0.0679	6615
<i>EL1,Case1</i>	1.7328	0.6288	-0.3581	0.1480	0.1386	0.4317	0.5425	-0.5430	0.1795	0.0635	3969
<i>EL1,Case2</i>	1.6925	0.3774	-0.5854	0.1411	0.1339	0.4317	0.5430	-0.5425	0.1795	0.0635	3969
<i>EL4</i>	2.0082	0.7926	-0.7461	0.2067	0.1845	0.4342	0.5435	-0.5436	0.2830	0.0742	6615
<i>EL3</i>	2.0069	0.7940	-0.7479	0.2068	0.1845	0.4342	0.5436	-0.5436	0.2830	0.0742	5292
<i>EL2</i>	1.6499	0.4714	-0.4252	0.1219	0.1258	0.4333	0.5428	-0.5428	0.1436	0.0603	3969
<i>EL1</i>	1.6448	0.4465	-0.4517	0.1227	0.1258	0.4282	0.5404	-0.5404	0.1421	0.0614	2646

The results from these variable kinematic models are listed in Table 9.4. The following considerations can be drawn:

- As far as the transverse displacement w is considered, the theories *EL4,Case1* and *EL4,Case2* lead a significant improvement of the solution respect to the *EL4*, see Figures 9.12 and 9.17.
- Regarding the σ_{xx} stress component, the theories *EL4,Case1* and *EL4,Case2* improve the results in the interface zones (see Figures 9.13 and 9.18) with respect to *EL4*.
- As shown in Figures 9.14,9.19, the variable kinematics does not improve the accuracy of the transverse normal stress σ_{zz} .
- Figures 9.15, 9.16, 9.20 and 9.21 show that, if the shear stress σ_{xz} is considered, variable kinematic models can be used to locally refine the solution in order to obtain a LW accuracy in the parts of the structure that require a more detailed analysis. Eventually, as it is clear from Table 9.4, variable kinematic models provide high accuracy with less degrees of freedom with respect to full LW models.

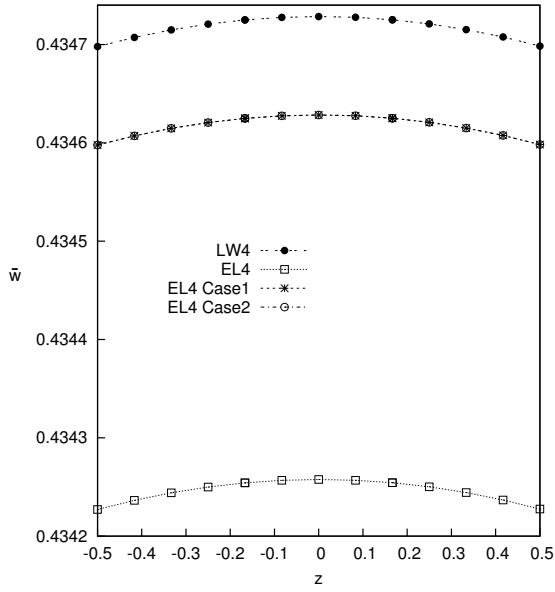


Figure 9.12: Transverse displacement w along the thickness, with thickness ratio $(a/h) = 100$. Composite plate.

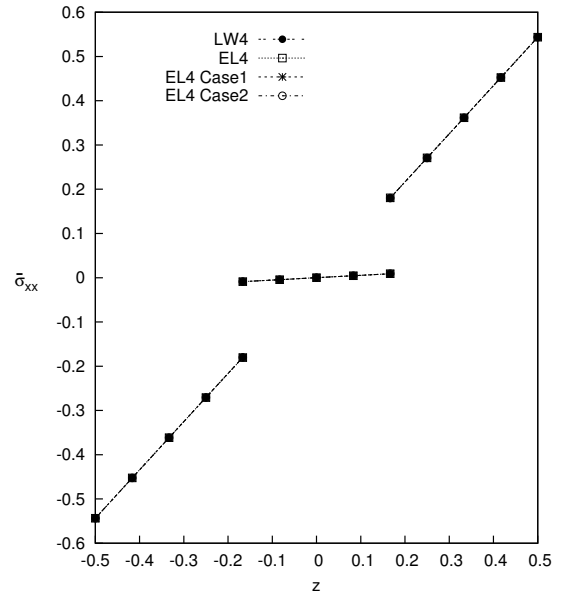


Figure 9.13: In-plane stress σ_{xx} along the thickness, with thickness ratio $(a/h) = 100$. Composite plate.

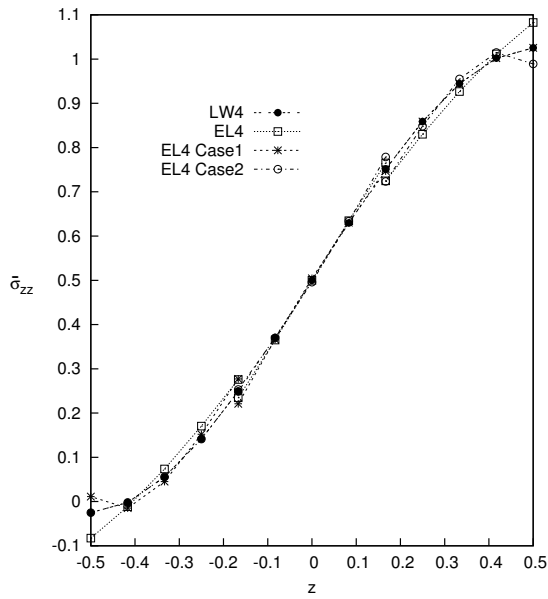


Figure 9.14: Transverse normal stress σ_{zz} along the thickness, with thickness ratio $(a/h) = 100$. Composite plate.

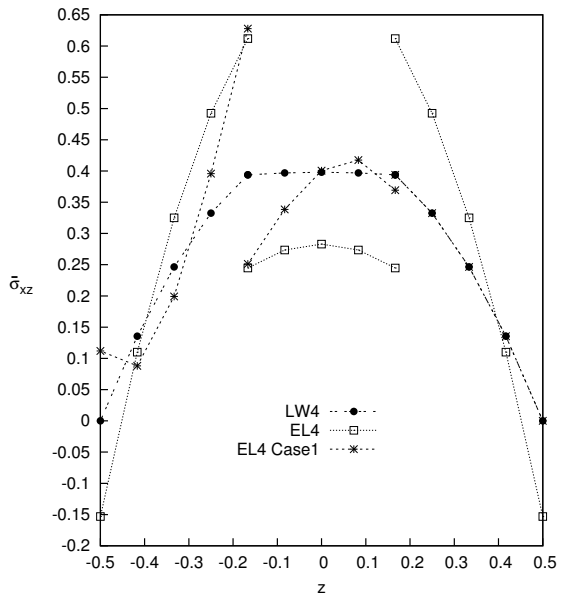


Figure 9.15: Transverse shear stress σ_{xz} along the thickness, with thickness ratio $(a/h) = 100$. Composite plate.

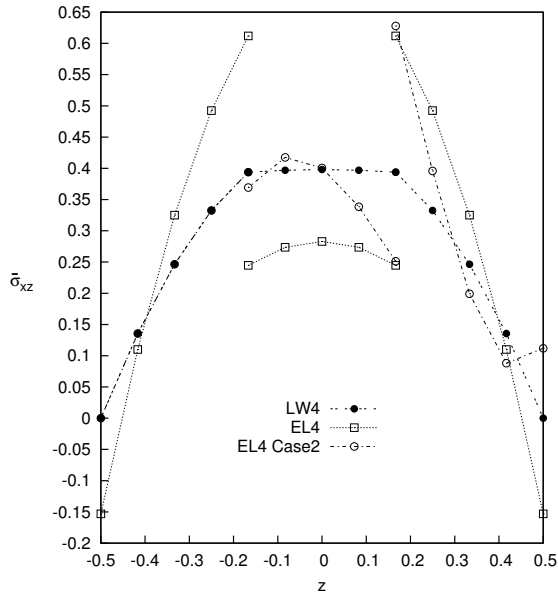


Figure 9.16: Transverse shear stress σ_{xz} along the thickness, with thickness ratio $(a/h) = 100$. Composite plate.

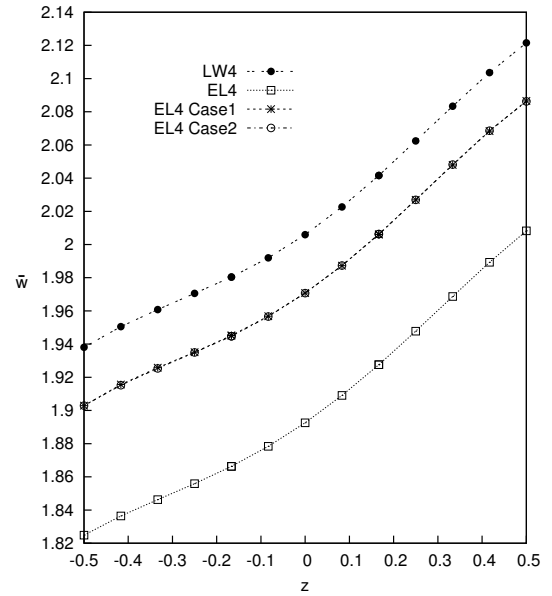


Figure 9.17: Transverse displacement w along the thickness, with thickness ratio $(a/h) = 4$. Composite plate.

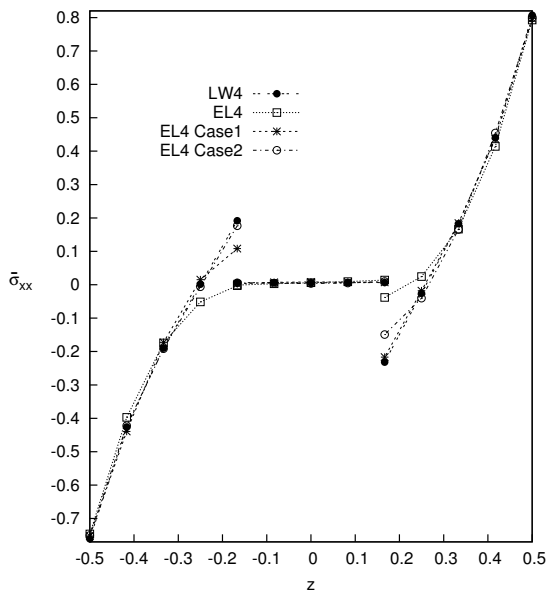


Figure 9.18: In-plane stress σ_{xx} along the thickness, with thickness ratio $(a/h) = 4$. Composite plate.

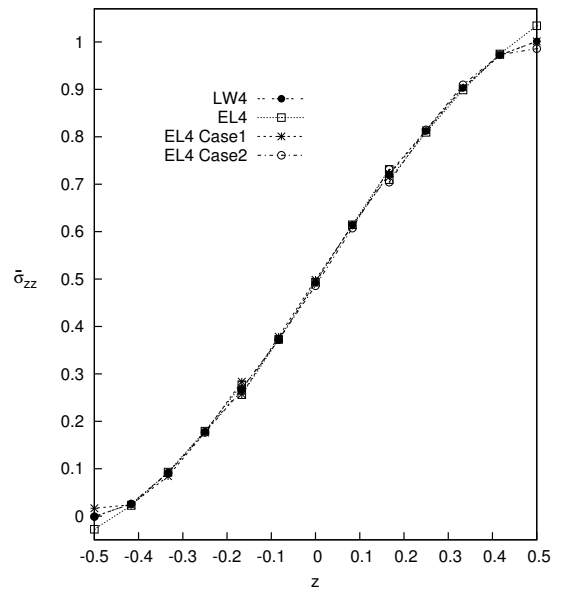


Figure 9.19: Transverse normal stress σ_{zz} along the thickness, with thickness ratio $(a/h) = 4$. Composite plate.

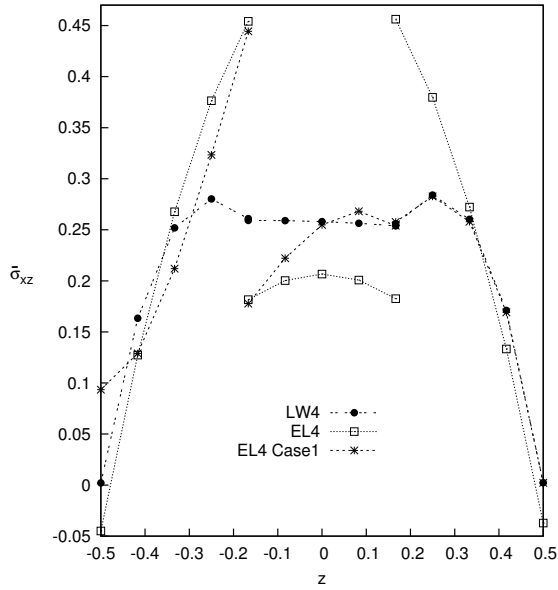


Figure 9.20: Transverse shear stress σ_{xz} along the thickness, with thickness ratio $(a/h) = 4$. Composite plate.

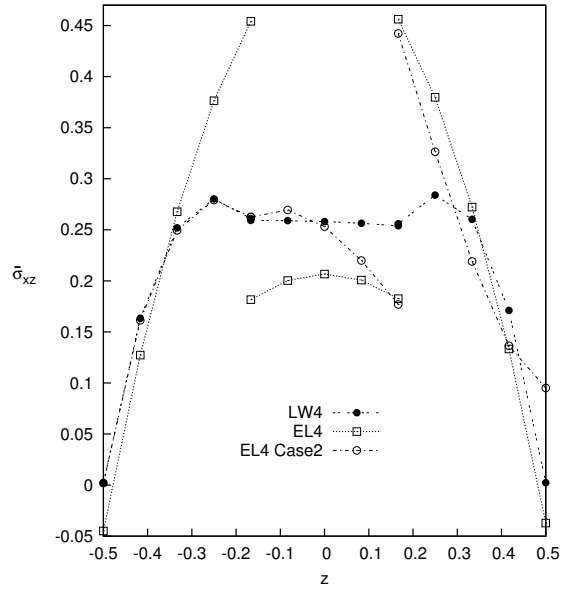


Figure 9.21: Transverse shear stress σ_{xz} along the thickness, with thickness ratio $(a/h) = 4$. Composite plate.

9.2.2 Eight-layer composite beam

The cantilever eight-layer beam shown in Figure 9.22 is analysed as the second assessment. The structure was loaded at the free end with a concentrated load equal to $P_z = -0,2N$ and it was applied at *top* position. The geometrical dimensions are: $a = 90\text{ mm}$, $b = 1\text{ mm}$, $h = 10\text{ mm}$. The mechanical properties of the material labeled with the number 1 (see Figure 9.22) are: $E_L = 30\text{ GPa}$, $E_T = 1\text{ GPa}$, $G_{LT} = G_{TT} = 0,5\text{ GPa}$, $\nu_{LT} = \nu_{TT} = 0,25$. Whereas the mechanical properties of the material labeled with the number 2 are: $E_L = 5\text{ GPa}$, $E_T = 1\text{ GPa}$, $G_{LT} = G_{TT} = 0,5\text{ GPa}$, $\nu_{LT} = \nu_{TT} = 0,25$. The material stacking sequence is $[1/2/1/2]_s$. The FEM results of the present paper are compared with some solutions from the literature, and with the analytical solution derived by theory of elasticity as presented in [148] and here referred to as *Lekhnitskii*.

First, a convergence study on the plate model was performed (see Table 9.5). It is clear that a mesh grid of 12×2 elements ensures the convergence.

Table 9.5: Convergence study. Eight-layer cantilever beam. Transverse displacement $w = -10^2 w(a, b/2, 0)$, in-plane stress $\sigma_{xx} = 10^3 \sigma_{xx}(a/2, b/2, +h/2)$, transverse shear stress $\sigma_{xz} = 10^2 \sigma_{xz}(a/2, b/2, 0)$.

	Mesh	2×2	4×2	6×2	8×2	10×2	12×2
LW4	w	3.031	3.032	3.031	3.030	3.030	3.030
	σ_{xx}	651	690	716	725	728	730
	σ_{xz}	2.991	2.797	2.792	2.791	2.790	2.789
EL4	w	3.029	3.029	3.029	3.028	3.028	3.028
	σ_{xx}	684	723	730	731	731	731
	σ_{xz}	3.054	2.829	2.821	2.822	2.822	2.822

Various variable kinematic models have then been used to perform the analysis of the

proposed plate structure, and they are summarized in the following:

- $Case1 = \{layer1\} \{layer2, layer3, layer4, layer5, layer6, layer7\} \{layer8\}$
- $Case2 = \{layer1, layer2\} \{layer3, layer4, layer5, layer6\} \{layer7, layer8\}$
- $Case3 = \{layer1\} \{layer2\} \{layer3, layer4, layer5, layer6\} \{layer7\} \{layer8\}$
- $Case4 = \{layer1, layer2, layer3\} \{layer4, layer5\} \{layer6, layer7, layer8\}$

As in the previous analysis case, the curl brackets are used to group layer that are homogenized according to an ESL approach.

Table 9.6: Eight-layer cantilever beam. Transverse displacement $w = w(a, b/2, 0)$, in-plane stress $\sigma_{xx} = \sigma_{xx}(a/2, b/2, +h/2)$, transverse shear stress $\sigma_{xz} = \sigma_{xz}(a/2, b/2, 0)$.

	$-w \times 10^2 (mm)$	$\sigma_{xx} \times 10^3 (MPa)$	$\sigma_{xz} \times 10^2 (MPa)$	$DOFs$
Nguyen and Surana [149]	3.031	720		
Davalos et al. [150]	3.029	700		
Xiaoshan [151]	3.060	750		
Vo and Thai [152]	3.024			
Lekhnitskii [148]		730	2.789	
<i>LW4</i>	3.030	730	2.789	12375
<i>EL4,Case1</i>	3.029	730	2.773	4875
<i>EL4,Case2</i>	3.029	731	2.854	4875
<i>EL4,Case3</i>	3.030	730	2.854	7875
<i>EL4,Case4</i>	3.029	731	2.788	4875
<i>EL3,Case1</i>	3.029	731	2.773	3750
<i>EL3,Case2</i>	3.029	731	2.854	3750
<i>EL3,Case3</i>	3.030	731	2.854	6000
<i>EL3,Case4</i>	3.028	731	2.788	3750
<i>EL2,Case1</i>	3.021	731	2.360	2625
<i>EL2,Case2</i>	3.025	731	2.593	2625
<i>EL2,Case3</i>	3.027	731	2.593	4125
<i>EL2,Case4</i>	3.026	731	2.775	2625
<i>EL1,Case1</i>	3.017	730	2.357	1500
<i>EL1,Case2</i>	3.012	731	2.592	1500
<i>EL1,Case3</i>	3.023	730	2.592	2250
<i>EL1,Case4</i>	2.996	731	2.774	1500
<i>EL4</i>	3.028	731	2.822	1875
<i>EL3</i>	3.027	731	2.822	1500
<i>EL2</i>	2.980	731	2.005	1125
<i>EL1</i>	2.981	729	2.000	750

Some noteworthy results are listed in Table 9.6. The conducted analysis suggests the following comments:

- As shown in Figure 9.23, the theories *EL4,Case1*, *EL4,Case2*, *EL4,Case3* and *EL4,Case4* lead a significant improvement of the solution with respect to the *EL4* if the transverse displacement w is considered.

- As far as the in-plane stress σ_{xx} is concerned, all the considered theories show exactly the same accuracy (see Figure 9.24).
- The distribution of the transverse normal stress σ_{zz} is significantly improved by $EL4_{,Case1}$ and $EL4_{,Case3}$ with respect to $EL4$. On the other hand, as depicted in Figure 9.25, although the theories $EL4_{,Case2}$ and $EL4_{,Case4}$ show an improvement of the solution in the top layer of the beam, they also introduce a discontinuity of the σ_{zz} along the thickness.
- Regarding the shear stress σ_{xz} , the $LW4$ model is able to reproduce the exact analytical solution (Lekhnitskii), see Figure 9.26(a). Conversely, the results by the present variable kinematic models accurately describe the shear stress only within the layers that are modelled via a LW approach; namely, the top and bottom layers for $EL4_{,Case1}$ (Figure 9.26(a)), the first two top layers and last two bottom layers for $EL4_{,Case3}$ (Figure 9.26(c)), the two central layers for $EL4_{,Case4}$ (Figure 9.26(d)). Contrarily, the layers that are modelled via an ESL approach present a loss of accuracy, see Figures 9.26(a,b,c,d).

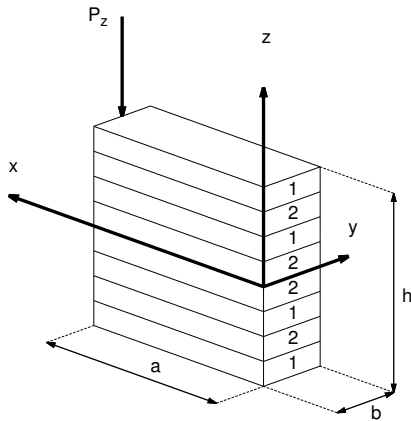


Figure 9.22: Reference system of the eight-layer beam with a concentrated load. The material lamination scheme is indicated with label 1 and label 2.

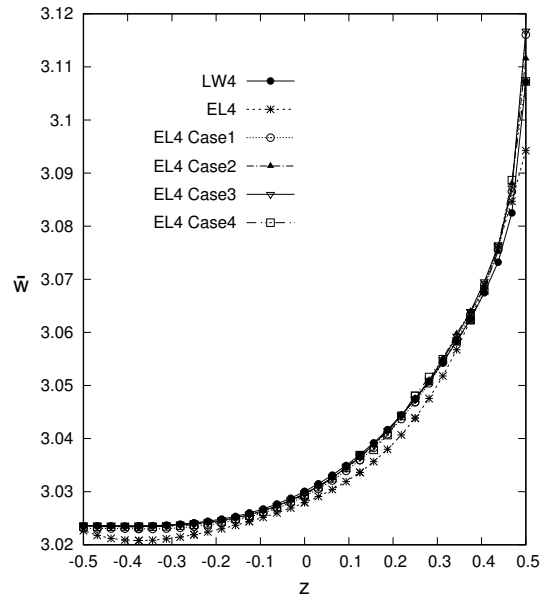


Figure 9.23: Transverse displacement w along the thickness, with thickness ratio $(a/h) = 9$. Composite beam.

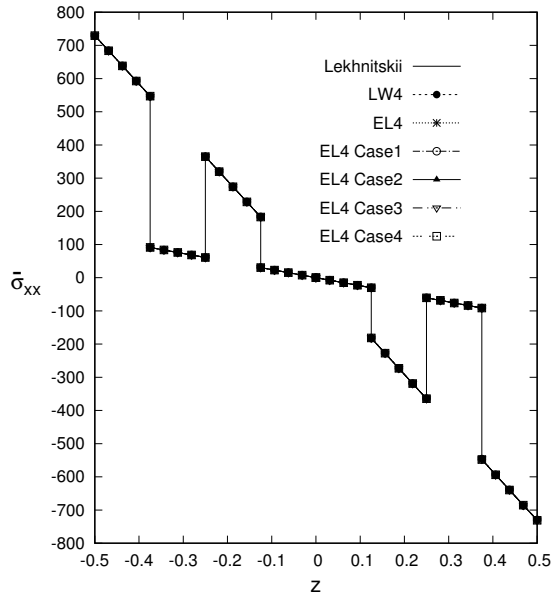


Figure 9.24: In-plane stress σ_{xx} along the thickness, with thickness ratio $(a/h) = 9$. Composite beam.

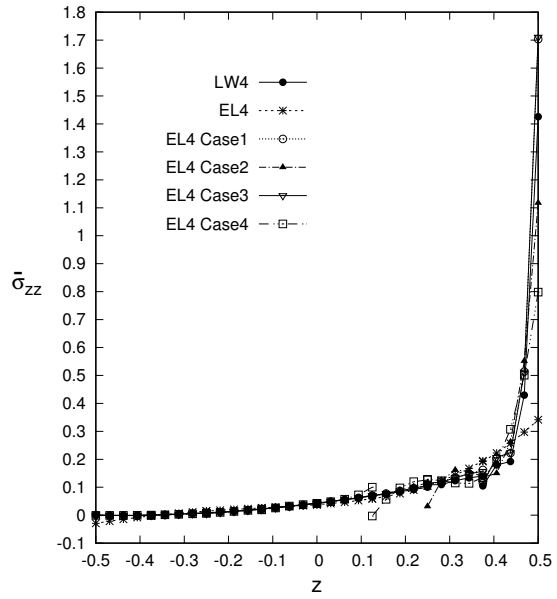


Figure 9.25: Transverse normal stress σ_{zz} along the thickness, with thickness ratio $(a/h) = 9$. Composite beam.

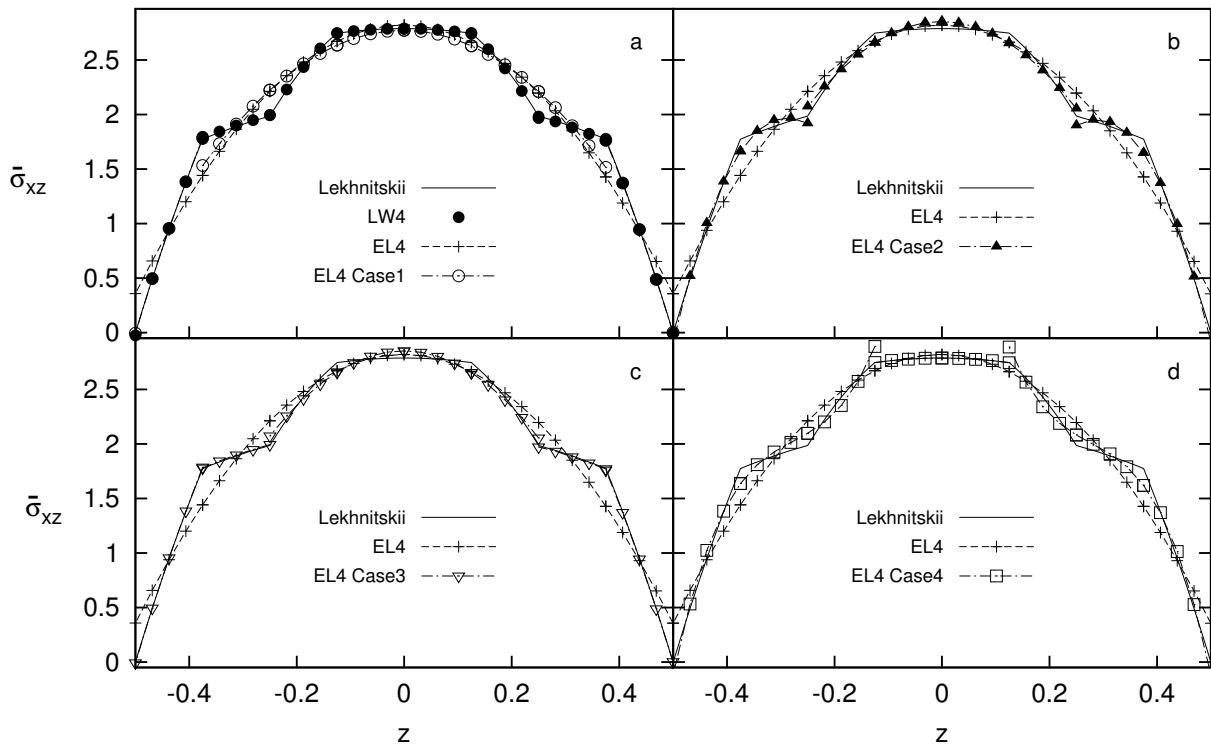


Figure 9.26: Transverse shear stress σ_{xz} along the thickness, with thickness ratio $(a/h) = 9$. Composite beam.

9.2.3 Three-layer sandwich plate

A three-layer, unsymmetrically laminated, rectangular sandwich plate was also considered. The plate is simply-supported and loaded by a constant uniform pressure $P_z^{top} = -0.1 MPa$ applied to the whole top surface. The geometrical dimensions are: $a = 100 mm$, $b = 200 mm$, $h = 12 mm$. The faces have different thicknesses, i.e. $h_{top} = 0.1 mm$ and $h_{bottom} = 0.5 mm$, and the thickness of the core is $h_{core} = 11.4 mm$. The two faces have the following orthotropic material data: $E_1 = 70000 MPa$, $E_2 = 71000 MPa$, $E_3 = 69000 MPa$, $G_{12} = G_{13} = G_{23} = 26000 MPa$, $\nu_{12} = \nu_{13} = \nu_{23} = 0.3$. The core is made of a metallic foam with the following data: $E_1 = E_2 = 3 MPa$, $E_3 = 2.8 MPa$, $G_{12} = G_{13} = G_{23} = 1 MPa$, $\nu_{12} = \nu_{13} = \nu_{23} = 0.25$. The mesh adopted in the analysis is the same of the three-layer composite plate, 10×10 elements.

Table 9.7: Sandwich rectangular plate. Transverse displacement $w = w(a/2, b/2, \pm h/2)$, in-plane stresses $\sigma_{xx} = \sigma_{xx}(a/2, b/2)$ and $\sigma_{yy} = \sigma_{yy}(a/2, b/2)$.

	w		σ_{xx}				σ_{yy}				DOFs
	<i>top</i>	<i>bottom</i>	Top Skin		Bottom Skin		Top Skin		Bottom Skin		
			<i>top</i>	<i>bottom</i>	<i>top</i>	<i>bottom</i>	<i>top</i>	<i>bottom</i>	<i>top</i>	<i>bottom</i>	
<i>LW4_a</i> [139]	-9.142	-8.968	-112.4	-48.435	-133.21	166.27	-52.824	-23.320	-54.327	69.915	17199
<i>LW4</i>	-9.140	-8.968	-110.7	-51.073	-132.85	166.10	-50.519	-25.617	-53.664	69.254	
<i>ET1_a</i> [139]	-0.1022	-0.1020	-89.63	-88.715	15.508	20.008	-51.453	-50.932	8.4375	11.041	6615
<i>ET4</i>	-6.138	-6.031	-83.621	-81.922	-84.422	114.60	-28.265	-50.032	-35.270	46.817	
<i>EL4_{,Case1}</i>	-7.0933	-6.9667	-103.84	-57.814	-100.44	131.90	-47.740	-28.419	-41.748	54.605	11907
<i>EL4_{,Case2}</i>	-8.1492	-7.9967	-88.077	-78.083	-115.99	149.22	-28.613	-49.735	-46.729	62.324	11907
<i>EL3_{,Case1}</i>	-5.6061	-5.5118	-98.957	-62.599	-77.967	112.48	-45.764	-30.385	-33.885	49.155	9261
<i>EL3_{,Case2}</i>	-8.0258	-7.8758	-97.903	-69.009	-113.98	147.20	-38.471	-40.344	-45.904	61.499	9261
<i>EL2_{,Case1}</i>	-4.7261	-4.6580	-97.159	-66.531	-86.447	123.39	-45.014	-31.995	-51.271	68.389	6615
<i>EL2_{,Case2}</i>	-6.9117	-6.7812	-109.20	-61.634	-96.204	129.19	-51.057	-30.000	-38.608	54.121	6615
<i>EL1_{,Case1}</i>	-0.1271	-0.1255	-88.364	-87.142	14.684	20.341	-40.693	-40.007	5.8738	9.0807	3969
<i>EL1_{,Case2}</i>	-0.1570	-0.1631	-88.379	-87.267	13.850	21.281	-40.930	-40.298	6.0253	10.149	3969
<i>EL4</i>	-6.1381	-6.0307	-83.621	-81.922	-84.422	114.60	-28.265	-50.032	-35.270	46.817	6615
<i>EL3</i>	-1.4379	-1.4206	-90.232	-82.528	-17.848	54.888	-42.125	-39.696	-14.416	31.674	5292
<i>EL2</i>	-0.1264	-0.1286	-88.361	-87.534	15.110	19.996	-41.420	-41.038	6.7722	9.0627	3969
<i>EL1</i>	-0.1022	-0.1019	-90.065	-89.146	15.589	20.182	-51.489	-50.967	8.4427	11.048	2646

Different variable-kinematic models have been used to perform the analysis of the sandwich. Namely,

- *Case1* = {*layer1*} {*layer2, layer3*}
- *Case2* = {*layer1, layer2*} {*layer3*}

Some results at top and bottom surfaces by the present variable kinematic models, ESL as well as LW theories are listed in Table 9.7. In the same table, also some analytical solutions are given for comparison purposes. It can be observed that, although moderately thick plates are considered ($a/h = (100/12)$), lower order theories as *ET1_a*, *EL1*, *EL2*, *EL1_{,Case1}* and *EL1_{,Case2}* lead to completely wrong results. ESL theories modelled with Taylor or Legendre polynomials, even with higher order expansions, do not allow to obtain acceptable results, see *ET4*, *EL3*, *EL4*. On the other hand, variable-kinematics models lead to some improvements starting from the second order of expansion, i.e. *EL2_{,Case1}*, *EL2_{,Case2}*, *EL3_{,Case1}*, and so on. Anyway, regardless from the theory expansion, it should be noted that the (*Case2*) among the variable kinematic models have a better approximation of the results than (*Case1*).

9.2.4 Five-layer composite sandwich plate

A five-layer composite sandwich plate was analyzed as the last assessment. The plate was simply-supported and it underwent the same bi-sinusoidal load as the three-layer composite plate, see Equation 9.2.1. The mechanical load amplitude at the top position was $\hat{p} = 1000 Pa$. A thickness ratio $a/h = 100$ was considered. The results are reported in a non-dimensional form as follows:

$$\hat{w} = \frac{100wE_T h^3}{\hat{p} a^4} \quad ; \quad \hat{\sigma}_{xx} = \frac{\sigma_{xx}}{\hat{p} \left(\frac{a}{h}\right)^2} \quad ; \quad \hat{\sigma}_{xz/yz} = \frac{\sigma_{xz/yz}}{\hat{p} \left(\frac{a}{h}\right)} \quad ; \quad \hat{\sigma}_{zz} = \frac{\sigma_{zz}}{\hat{p}} \quad (9.4)$$

The top and bottom skins of the sandwich plates are made of two orthotropic layers each. The thickness of the four sheets is $h_1 = h_2 = h_4 = h_5 = 0.5 mm$. The ply sequences of the bottom and top skins are $0^\circ/90^\circ$ and $90^\circ/0^\circ$, respectively. Their material properties are: $E_1 = 50 GPa$, $E_2 = E_3 = 10 GPa$, $G_{12} = G_{13} = G_{23} = 5 GPa$, $\nu_{12} = \nu_{13} = \nu_{23} = 0.25$. The Nomex core has thickness $h_3 = 8 mm$. The properties of the material of the core are: $E_1 = E_2 = 0.01 MPa$, $E_3 = 75.85 MPa$, $G_{12} = G_{13} = G_{23} = 22.5 MPa$, $\nu_{12} = \nu_{13} = \nu_{23} = 0.25$. The adopted mesh is the same as the one used for the three-layer composite plate in Section 9.2.1, i.e. 10×10 elements are employed.

Several variable kinematic models have been utilized in the analysis of the present sandwich structure and they are named as in the following:

- $Case1 = \{layer1\} \{layer2, layer3, layer4\} \{layer5\}$
- $Case2 = \{layer1, layer2\} \{layer3\} \{layer4, layer5\}$
- $Case3 = \{layer1\} \{layer2\} \{layer3, layer4, layer5\}$
- $Case4 = \{layer1, layer2, layer3\} \{layer4\} \{layer5\}$

The results by the proposed variable kinematic models are listed in Table 9.8 and they are compared to those from an higher-order LW model and full ESL models. Stress and through-the-thickness displacement distributions are also shown in Figures 9.27 to 9.29. Some interesting comments stem from the analysis of the composite sandwich plate.

- The adoption of higher-order variable kinematic models, i.e. $EL4_{Case1}$, $EL4_{Case2}$, $EL4_{Case3}$ and $EL4_{Case4}$, lead to a significant improvement of the out-of-plane displacement w with respect to the full ESL fourth-order model $EL4$. It is evident that $EL4_{Case2}$ is able to reproduce the exact solution reducing the computational costs in terms of DOFs with respect to the $LW4$ model.
- As shown in Figure 9.28, all the theories presented give the same degree of accuracy if the in-plane stress σ_{xx} is considered.
- For the evaluation of the transverse normal stress σ_{zz} , higher-order theories are necessary. The linear ESL model gives completely wrong results. However, even higher-order ESL models present errors ranging from approximately -1600% to $+153\%$ with respect the reference solution ($LW4$). Variable-kinematic models with higher-order terms can lead to significant benefits for the description of the σ_{zz} . The variable-kinematic theories $Case1$ and $Case3$, which are modelled with a LW approach in the top layer, can obtain noticeable improvements. The models denoted as $Case2$ show better accuracy of the results respect the ESL models. Conversely, $Case4$ models are not able to obtain an improvement of the solution of the σ_{zz} with respect to the full ESL models.
- Figure 9.29(a) shows that the present $LW4$ FEM solution perfectly match the analytical one provided by [153]. Regarding the proposed variable kinematic models, it is

interesting to note that they can provide the exact solution only in the layers that are described through a LW approach. For example, it is interesting to note that $EL4,Case3$ provide analytical accuracy in the top LW layers, whereas the solution worsens close to the bottom layers, where an ESL approach is used (see Figure 9.29(d)). Also, particular attention should be focused on the model $EL4,Case2$, which has been obtained by using an ESL approach for the top and bottom composite skins and a LW approach for assembling outer ESL sheets and the inner core. This model clearly gives the exact solution with an evident DOFs reduction with respect to the $LW4$ theory.

Table 9.8: Composite sandwich plate. Transverse displacement $\hat{w} = \hat{w}(a/2, b/2, +h/2)$, in-plane stress $\hat{\sigma}_{xx} = \hat{\sigma}_{xx}(a/2, b/2, \pm h/2)$, transverse shear stress $\hat{\sigma}_{xz} = \hat{\sigma}_{xz}(a, b/2, 0)$ and transverse normal stress $\hat{\sigma}_{zz} = \hat{\sigma}_{zz}(a/2, b/2, +h/2)$. Variable kinematic models.

	\hat{w}	$\hat{\sigma}_{xx}$		$\hat{\sigma}_{xz}$	$\hat{\sigma}_{zz}$	$DOFs$
		<i>top</i>	<i>bottom</i>			
$LW4$	3.1167	0.7805	-0.7819	0.1825	1.1715	27783
$EL4,Case1$	3.0978	0.7802	-0.7804	0.1853	1.1838	17199
$EL4,Case2$	3.1167	0.7805	-0.7819	0.1825	1.1288	17199
$EL4,Case3$	3.0842	0.7799	-0.7691	0.1923	1.1736	17199
$EL4,Case4$	3.1202	0.8007	-0.7808	0.1930	630.46	17199
$EL3,Case1$	3.0978	0.7802	-0.7804	0.1853	1.1838	13230
$EL3,Case2$	3.1167	0.7805	-0.7819	0.1825	1.2289	13230
$EL3,Case3$	3.0579	0.7793	-0.7980	0.1415	1.1790	13230
$EL3,Case4$	3.0926	0.7722	-0.7807	0.1379	-255.07	13230
$EL2,Case1$	2.9474	0.7771	-0.7773	0.0071	1.1793	9261
$EL2,Case2$	3.1167	0.7805	-0.7819	0.1859	1.2445	9261
$EL2,Case3$	3.1004	0.7803	-0.7846	0.1333	1.1840	9261
$EL2,Case4$	3.1001	0.7780	-0.7802	0.1334	-77.333	9261
$EL1,Case1$	2.8922	0.7640	-0.7641	0.0070	46.798	5292
$EL1,Case2$	3.1236	0.7837	-0.7852	0.1824	99.587	5292
$EL1,Case3$	2.9477	0.7787	-0.7799	0.0071	47.671	5292
$EL1,Case4$	2.9465	0.7798	-0.7787	0.0071	94.022	5292
$EL4$	3.0220	0.7782	-0.7795	0.0917	-18.676	6615
$EL3$	3.0220	0.7784	-0.7796	0.0917	-14.282	5292
$EL2$	2.9432	0.7771	-0.7771	0.0038	2.975	3969
$EL1$	2.8221	0.7731	-0.7732	0.0037	891.70	2646

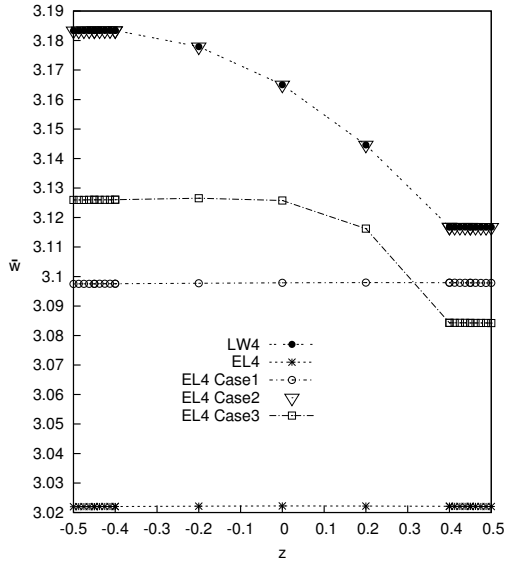


Figure 9.27: Transverse displacement w along the thickness. Composite Sandwich Plate.

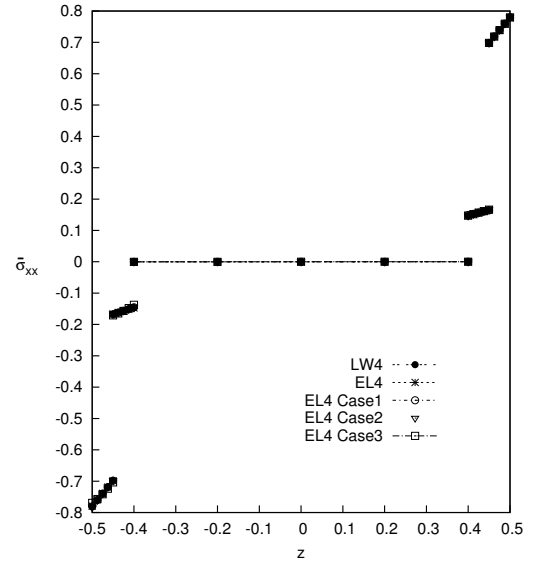


Figure 9.28: In-plane stress σ_{xx} along the thickness. Composite Sandwich Plate.

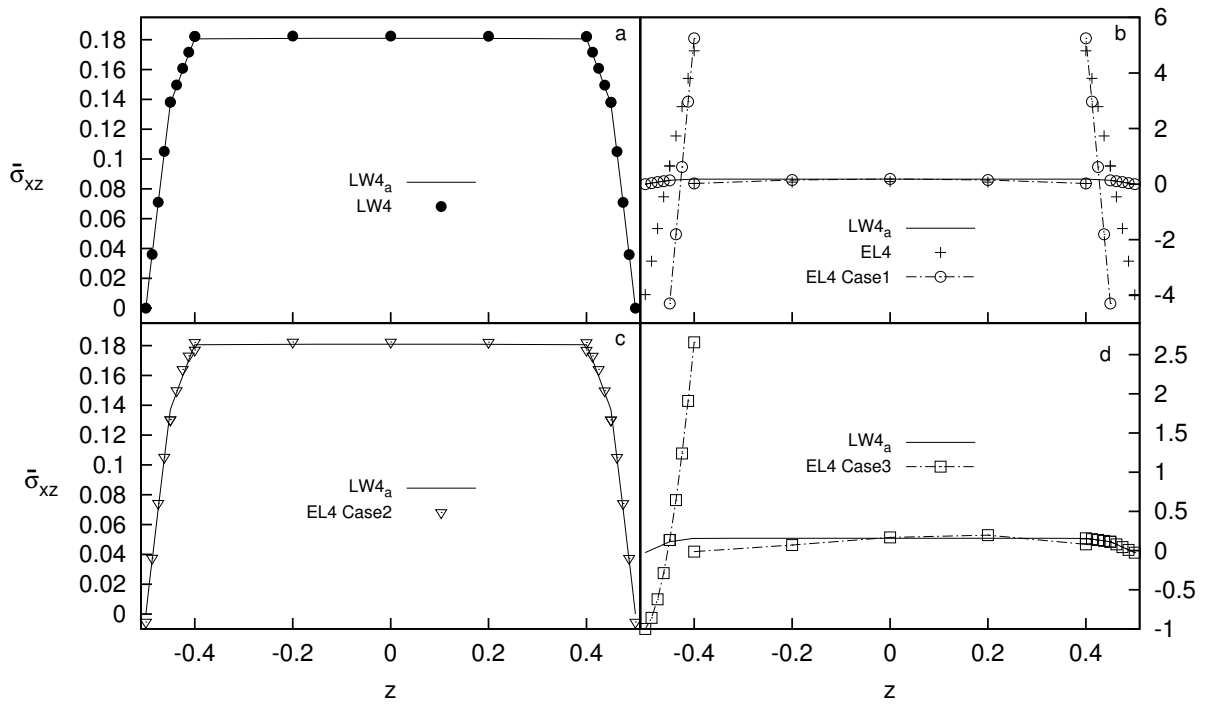


Figure 9.29: Transverse shear stress σ_{xz} along the thickness. Composite Sandwich Plate.

9.2.5 Three-layer composite cylinder

A three-layer cross-ply cylinder with lamination ($90^\circ/0^\circ/90^\circ$) and simply-supported boundary conditions is considered as the first numerical example. The applied load for the whole cylinder is a pressure applied at the inner surface of the shell, defined as follows:

$$p(\alpha, \beta, z_{bottom}) = \hat{p} \sin\left(\frac{m\pi\alpha}{a}\right) \cos\left(\frac{n\pi\beta}{b}\right) \quad (9.5)$$

where $\hat{p} = 1.0$ is the pressure amplitude; $m = 1$ and $n = 8$ are the half-waves number. Note that a is the length of the cylinder in the axial direction in this example. The mechanical properties of the material are such that $E_L/E_T = 25$; $G_{LT}/E_T = 0.5$; $G_{TT}/E_T = 0.2$; $\nu_{LT} = \nu_{TT} = 0.25$. For all the considered cases, the length-to-radius ratio is $a/R = 4$, $b = 2\pi R$. On the other hand, the layers are of equal thickness and $h_{total} = 1, 0$. The results are presented below for different radius-to-thickness ratios $R/h = 2, 4, 10, 50, 100, 500$, and reported in the following non-dimensional form:

$$\hat{w} = \frac{10wE_L}{\hat{p}h(R/h)^4} \quad \hat{\sigma}_{\alpha\alpha/\beta\beta/\alpha\beta} = \frac{10\sigma_{\alpha\alpha/\beta\beta/\alpha\beta}}{\hat{p}(R/h)^2} \quad \hat{\sigma}_{\alpha z/\beta z} = \frac{10\sigma_{\alpha z/\beta z}}{\hat{p}(R/h)} \quad \hat{\sigma}_{zz} = \frac{\sigma_{zz}}{\hat{p}}$$

Due to the geometrical symmetry of the cylinder, the symmetry of the load pressure and boundary conditions, and the symmetry of the lamination stacking sequence, only one octave of the cylinder is analysed; i.e., only one half of the cylinder along the α axis direction and one quarter along the β circumferential axis direction is considered. The applied load for an octave of the cylinder is, therefore, defined as follows:

$$p(\alpha, \beta, z_{bottom}) = \hat{p} \cos\left(\frac{m\pi\alpha}{a}\right) \cos\left(\frac{n\pi\beta}{b}\right) \quad (9.6)$$

where $m = 0, 5$ and $n = 2$. The FEM results coming from the present refined shell elements are compared with a 3D elasticity solution [88] and a layer-wise analytical model [68].

First, a convergence study on the shell element was performed. A representative composite shell with radius-to-thickness ratio $R/h = 500$ was evaluated. According to Table 9.9, a mesh grid of 8×32 elements ensures the convergence and accuracy on both the transverse displacement and the stresses. Thus, this mesh size is used in the subsequent analyses. Furthermore, in order to prove that the proposed element is locking free, various integrations schemes (see Huges *et al.* [115]) were considered and the results are shown in Table 9.10. In this table, the results from the present higher-order finite elements are compared to 3D analytical solutions. It is clear that the shell element with the MITC9 method ensures acceptable accuracy on both the transverse displacement, the transverse shear stress and the transverse normal stress. In both Tables 9.9 and 9.10, superscript + denotes that stress is measured at the layer interface and the top value is given.

Table 9.9: Convergence study. Composite cylinder with lamination $[90^\circ/0^\circ/90^\circ]$ and with radius to thickness ratio $R/h = 500$. The mesh is referred to one octave of the cylinder.

	Mesh	2×8	4×16	6×24	8×32	<i>3D Elasticity</i> [88]
<i>LW4</i>	$\hat{w}(z=0)$	0.1029	0.1027	0.1027	0.1027	0.1027
	$\hat{\sigma}_{\alpha\alpha}(z=+h/2)$	0.0586	0.0566	0.0562	0.0560	0.0559
	$\hat{\sigma}_{\beta\beta}(z=+h/2)$	0.8279	0.7994	0.7940	0.7921	0.7895
	$\hat{\sigma}_{\alpha z}(z^+ = -h/6)$	0.1107	0.1066	0.1058	0.1055	0.1051
	$\hat{\sigma}_{zz}(z=0)$	-7.15	-9.04	-9.13	-9.13	-9.12
<i>ET4</i>	$\hat{w}(z=0)$	0.1029	0.1027	0.1027	0.1027	
	$\hat{\sigma}_{\alpha\alpha}(z=+h/2)$	0.0589	0.0568	0.0564	0.0563	
	$\hat{\sigma}_{\beta\beta}(z=+h/2)$	0.8283	0.7998	0.7944	0.7925	
	$\hat{\sigma}_{\alpha z}(z^+ = -h/6)$	0.1400	0.1348	0.1338	0.1334	
	$\hat{\sigma}_{zz}(z=0)$	15.41	12.84	12.61	12.56	
<i>EL4</i>	$\hat{w}(z=0)$	0.1029	0.1027	0.1027	0.1027	
	$\hat{\sigma}_{\alpha\alpha}(z=+h/2)$	0.0589	0.0568	0.0564	0.0563	
	$\hat{\sigma}_{\beta\beta}(z=+h/2)$	0.8283	0.7998	0.7944	0.7925	
	$\hat{\sigma}_{\alpha z}(z^+ = -h/6)$	0.1400	0.1348	0.1338	0.1334	
	$\hat{\sigma}_{zz}(z=0)$	15.41	12.84	12.61	12.56	

Table 9.10: Locking study. Composite cylinder with lamination $[90^\circ/0^\circ/90^\circ]$ and with radius to thickness ratio $R/h = 500$. All the present FEM analyses are computed with a mesh of 8×32 elements.

		<i>Reduced</i>	<i>Selective</i>	<i>MITC9</i>	<i>Analytical</i>
<i>3D Elasticity</i> [88]	$w(z=0)$				0.1027
	$\sigma_{\alpha z}(z^+ = -h/6)$				0.1051
	$\sigma_{zz}(z=0)$				-9.12
<i>LW4</i>	$w(z=0)$	0.1027	0.1023	0.1027	
	$\sigma_{\alpha z}(z^+ = -h/6)$	1.2767	0.1070	0.1055	
	$\sigma_{zz}(z=0)$	-52.14	-9.70	-9.13	
<i>EL4</i>	$w(z=0)$	0.1027	0.1023	0.1027	
	$\sigma_{\alpha z}(z^+ = -h/6)$	1.3152	0.1368	0.1334	
	$\sigma_{zz}(z=0)$	-30.52	15.00	12.56	
<i>ET4</i>	$w(z=0)$	0.1027	0.1023	0.1027	
	$\sigma_{\alpha z}(z^+ = -h/6)$	1.3152	0.1368	0.1334	
	$\sigma_{zz}(z=0)$	-30.52	15.00	12.56	

An assessment of the Legendre-like and Taylor based ESL models is performed next. All the results presented in Table 9.11, for thick and thin shells, show that the Legendre polynomials lead to the same results of the Taylor polynomials. Regarding the linear expansion ESL model, e.g. *ET1*, if the thickness locking correction is applied (see [66]), a moderate difference in the results is noticeable. Nevertheless, the use of either polynomials is invariant with respect to the solution accuracy, thus, Legendre-like models are indistinctly used to implement ESL, LW as well as variable-kinematic models in the analyses below.

Table 9.11: Composite three-layered cylinder with lamination $[90^\circ/0^\circ/90^\circ]$. Taylor vs Legendre models.

$z =$	\hat{w}	$\hat{\sigma}_{\alpha\alpha}$		$\hat{\sigma}_{\beta\beta}$		$\hat{\sigma}_{\alpha\beta}$		$\hat{\sigma}_{\alpha z}$	$\hat{\sigma}_{\beta z}$	$\hat{\sigma}_{zz}$	DOFs		
	0	+h/2	-h/2	+h/2	-h/2	+h/2	-h/2	-h/6	0	0			
$R/h = 500$	3D Elasticity [88]	0.1027	0.0559	0.0379	0.7895	-0.7542	-0.0766	-0.0889	0.1051	-0.691	-9.12		
	LW4	0.1027	0.0560	0.0380	0.7921	-0.7567	-0.0771	-0.0894	0.1055	-0.693	-9.13	43095	
	EL3Z	0.1027	0.0561	0.0380	0.7921	-0.7567	-0.0771	-0.0894	0.0586	-0.703	-9.47	16575	
	EL4	0.1027	0.0563	0.0383	0.7925	-0.7563	-0.0771	-0.0894	0.1334	-0.494	12.56	16575	
	EL3	0.1027	0.0564	0.0383	0.7925	-0.7563	-0.0771	-0.0894	0.0615	-0.494	12.56	13260	
	EL2	0.1027	0.0557	0.0377	0.7918	-0.7571	-0.0771	-0.0894	0.0611	-0.250	43.39	9945	
	EL1	0.1026	0.0584	0.0349	0.7945	-0.7597	-0.0770	-0.0894	0.0106	-0.250	43.23	6630	
	ET3Z	0.1027	0.0561	0.0380	0.7921	-0.7567	-0.0771	-0.0894	0.0586	-0.703	-9.47	16575	
	ET4	0.1027	0.0563	0.0383	0.7925	-0.7563	-0.0771	-0.0894	0.1334	-0.494	12.56	16575	
	ET3	0.1027	0.0564	0.0383	0.7925	-0.7563	-0.0771	-0.0894	0.0615	-0.494	12.56	13260	
	ET2	0.1027	0.0557	0.0377	0.7918	-0.7571	-0.0771	-0.0894	0.0611	-0.250	43.39	9945	
	ET1 ⁻	0.1026	0.0584	0.0349	0.7945	-0.7597	-0.0770	-0.0894	0.0106	-0.250	43.23	6630	
	ET1*	0.1032	0.0529	0.0348	0.7971	-0.7585	-0.0770	-0.0894	0.0100	-0.250	43.42	6630	
	$R/h = 2$	3D Elasticity [88]	10.11	0.1761	-0.8428	7.168	-18.19	0.1797	-0.2922	0.3006	-1.379	-0.34	
		LW4	10.10	0.1741	-0.8730	7.179	-18.17	0.1807	-0.2934	0.3018	-1.382	-0.34	43095
		EL3Z	9.65	0.1487	-0.8951	6.848	-14.15	0.1728	-0.2653	0.2679	-1.294	-0.32	16575
		EL4	9.59	0.1425	-0.9572	6.568	-15.63	0.1775	-0.2783	0.4244	-1.219	-0.35	16575
		EL3	9.54	0.1431	-0.9179	7.048	-14.65	0.1785	-0.2706	0.3704	-1.216	-0.35	13260
EL2		8.16	0.0965	-0.6479	0.981	-5.88	0.1208	-0.2025	0.3183	-0.847	-0.43	9945	
EL1		8.82	-0.1046	-0.3218	2.441	-3.79	0.1542	-0.2152	0.2941	-0.927	-0.37	6630	
ET3Z		9.65	0.1487	-0.8951	6.848	-14.15	0.1728	-0.2653	0.2679	-1.294	-0.32	16575	
ET4		9.59	0.1425	-0.9572	6.568	-15.63	0.1775	-0.2783	0.4244	-1.219	-0.35	16575	
ET3		9.54	0.1431	-0.9179	7.048	-14.65	0.1785	-0.2706	0.3704	-1.216	-0.35	13260	
ET2		8.16	0.0965	-0.6479	0.981	-5.88	0.1208	-0.2025	0.3183	-0.847	-0.43	9945	
ET1 ⁻		8.82	-0.1046	-0.3218	2.441	-3.79	0.1542	-0.2152	0.2941	-0.927	-0.37	6630	
ET1*		8.83	-0.1193	-0.3081	2.442	-3.79	0.1556	-0.2160	0.2922	-0.927	-0.37	6630	

* thickness locking correction
 - no correction

Different variable kinematic models are used to perform the global/local analysis of the cylindrical shell structures and they are graphically depicted in Figure 9.30. Two different sublaminates groupings are considered here and they are denoted to as:

- Case 1 = {layer1} {layer2, layer3}
- Case 2 = {layer1, layer2} {layer3}

In Case 1, for example, layers number 2 and 3 are grouped in an ESL manner and then assembled to layer 1 in a LW sense, see Figure 9.30. Case 1 and Case 2 are used as subscripts together with the usual acronym notation, which also indicates the theory order N .

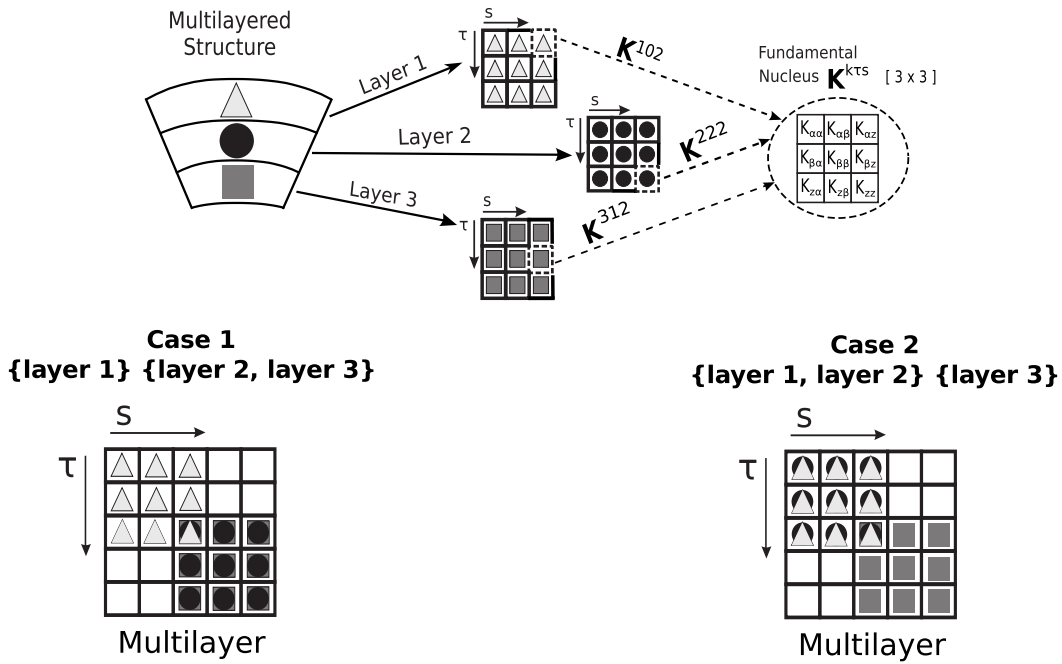


Figure 9.30: Variable-kinematic assembly schemes for the three-layered cylindrical shell.

The results from present variable kinematic models are listed in Tables 9.12 and 9.13 and Figures 9.31a to 9.34b for various radius to thickness ratios R/h . For the shell structures analysed, the following considerations can be drawn:

- Regarding the transverse displacement w , the theories $EL4_{,Case 1}$ and $EL4_{,Case 2}$ lead a significant improvement of the solution with respect to $EL4$ for large radius-to-thickness ratios $R/h = 500$, see Figure 9.31a. On the other hand, if small ratios $R/h = 2$ are considered, differences among the various models adopted are barely observable from Figure 9.31b.
- For the in-plane stress $\sigma_{\beta\beta}$, no accuracy differences are appreciable between models for ratios $R/h = 500$, see Figure 9.32a. For small ratios $R/h = 2$ the theories $EL4_{,Case 1}$ and $EL4_{,Case 2}$ improve the results with respect to the $EL4$ model, especially where a layer-wise description within the variable-kinematics is adopted; i.e., the top layer for $EL4_{,Case 1}$ and the bottom layer for $EL4_{,Case 2}$, see Figure 9.32b.
- As far as the shear stress $\sigma_{\alpha z}$ is concerned, Figures 9.33a and 9.33b show that the variable kinematic models provide exact solution accuracy for every radius-to-thickness-ratios within the layers that have a layer-wise assembling. Conversely, the remaining layers with an equivalent-single-layer assembling have a loss of accuracy.
- Regarding the transverse normal stress σ_{zz} and for large ratios $R/h = 500$, the results reach the exact solution in the layers that have a layer-wise assembling and a variable kinematic approach, see Figure 9.34a. Instead, for small ratios $R/h = 2$ the theories $EL4_{,Case 2}$ approximate very well the layer-wise solution along the thickness, see Figure 9.34b.
- For all the considered cases, the variable kinematic models have a number of degrees of freedom, and thus a computational cost, which is lower that full LW models.

Table 9.12: Composite three-layered cylinder with $[90^\circ/0^\circ/90^\circ]$ lamination. Comparison of various models for thin cylinders.

	$z =$	\dot{w} 0	$\hat{\sigma}_{\alpha\alpha}$		$\hat{\sigma}_{\beta\beta}$		$\hat{\sigma}_{\alpha\beta}$		$\hat{\sigma}_{\alpha z}$	$\hat{\sigma}_{\beta z}$	$\hat{\sigma}_{zz}$	<i>DOFs</i>
			+h/2	-h/2	+h/2	-h/2	+h/2	-h/2	-h/6	0	0	
$R/h = 500$	3D Elasticity [88]	0.1027	0.0559	0.0379	0.7895	-0.7542	-0.0766	-0.0889	0.1051	-0.691	-9.12	
	LW4	0.1027	0.0560	0.0380	0.7921	-0.7567	-0.0771	-0.0894	0.1055	-0.693	-9.13	43095
	LW1	0.1027	0.0569	0.0370	0.7931	-0.7578	-0.0771	-0.0894	0.0092	-0.692	-9.12	13260
	EL3Z	0.1027	0.0561	0.0380	0.7921	-0.7567	-0.0771	-0.0894	0.0586	-0.703	-9.47	16575
	EL4	0.1027	0.0563	0.0383	0.7925	-0.7563	-0.0771	-0.0894	0.1334	-0.494	12.56	16575
	EL1	0.1026	0.0584	0.0349	0.7945	-0.7597	-0.0770	-0.0894	0.0106	-0.250	43.23	6630
	EL4 _{Case 1}	0.1027	0.0560	0.0379	0.7921	-0.7569	-0.0771	-0.0894	0.1323	-0.698	-16.56	29835
	EL1 _{Case 1}	0.1027	0.0569	0.0357	0.7930	-0.7590	-0.0771	-0.0894	0.0445	-0.311	119.23	9945
	EL4 _{Case 2}	0.1027	0.0559	0.0380	0.7919	-0.7567	-0.0771	-0.0894	0.0965	-0.699	-11.98	29835
EL1 _{Case 2}	0.1027	0.0574	0.0370	0.7936	-0.7579	-0.0771	-0.0894	-0.0244	-0.316	-58.85	9945	
$R/h = 100$	3D Elasticity [88]	0.4715	0.0838	0.0018	3.507	-3.507	-0.0478	-0.1038	0.1223	-3.127	-8.30	
	LW2 _a [68]	0.4715	-	-	-	-	-	-	-	-3.127	-8.29	
	ESL2 _a [68]	0.4694	-	-	-	-	-	-	-	-	-	
	LW4	0.4715	0.0841	0.0018	3.518	-3.518	-0.0481	-0.1045	0.1228	-3.137	-8.32	43095
	LW1	0.4711	0.0869	-0.0034	3.518	-3.520	-0.0481	-0.1044	0.0385	-3.131	-8.31	13260
	EL3Z	0.4715	0.0842	0.0017	3.518	-3.518	-0.0481	-0.1045	0.0781	-3.183	-8.63	16575
	EL4	0.4708	0.0841	0.0021	3.517	-3.517	-0.0480	-0.1043	0.1576	-2.237	-8.00	16575
	EL1	0.4674	0.0939	-0.0121	3.512	-3.512	-0.0477	-0.1036	0.0450	-1.131	-4.32	6630
	EL4 _{Case 1}	0.4714	0.0841	0.0017	3.518	-3.518	-0.0481	-0.1044	0.1627	-3.161	-9.06	29835
EL1 _{Case 1}	0.4688	0.0866	-0.0083	3.513	-3.514	-0.0478	-0.1039	0.0732	-1.416	10.77	9945	
EL4 _{Case 2}	0.4714	0.0841	0.0018	3.518	-3.517	-0.0481	-0.1044	0.1223	-3.160	-8.23	29835	
EL1 _{Case 2}	0.4691	0.0898	-0.0035	3.513	-3.517	-0.0478	-0.1040	0.0120	-1.424	-21.35	9945	
$R/h = 50$	3D Elasticity [88]	0.5495	0.0712	-0.0225	3.930	-3.987	-0.0118	-0.0760	0.0894	-3.491	-4.85	
	LW2 _a [68]	0.5495	-	-	-	-	-	-	-	-3.492	-4.73	
	ESL2 _a [68]	0.5384	-	-	-	-	-	-	-	-	-	
	LW4	0.5495	0.0715	-0.0225	3.943	-3.999	-0.0119	-0.0765	0.0897	-3.502	-4.86	43095
	LW1	0.5479	0.0732	-0.0297	3.933	-3.995	-0.0118	-0.0763	0.0439	-3.497	-4.85	13260
	EL3Z	0.5495	0.0718	-0.0229	3.943	-4.000	-0.0119	-0.0765	0.0626	-3.554	-5.03	16575
	EL4	0.5458	0.0711	-0.0225	3.937	-3.993	-0.0117	-0.0761	0.1161	-2.501	-5.02	16575
	EL1	0.5358	0.0799	-0.0390	3.900	-3.957	-0.0115	-0.0748	0.0508	-1.265	-3.39	6630
	EL4 _{Case 1}	0.5487	0.0714	-0.0225	3.941	-3.998	-0.0119	-0.0764	0.1237	-3.529	-5.07	29835
EL1 _{Case 1}	0.5385	0.0724	-0.0348	3.916	-3.954	-0.0115	-0.0751	0.0650	-1.582	0.69	9945	
EL4 _{Case 2}	0.5488	0.0715	-0.0225	3.942	-3.998	-0.0118	-0.0764	0.0949	-3.527	-4.84	29835	
EL1 _{Case 2}	0.5391	0.0752	-0.0298	3.896	-3.979	-0.0115	-0.0752	0.0313	-1.593	-8.17	9945	

Table 9.13: Composite three-layered cylinder with $[90^\circ/0^\circ/90^\circ]$ lamination. Comparison of various models for thick cylinders.

	$z =$	\hat{w} 0	$\hat{\sigma}_{\alpha\alpha}$		$\hat{\sigma}_{\beta\beta}$		$\hat{\sigma}_{\alpha\beta}$		$\hat{\sigma}_{\alpha z}$	$\hat{\sigma}_{\beta z}$	$\hat{\sigma}_{zz}$	$DOFs$
			+h/2	-h/2	+h/2	-h/2	+h/2	-h/2	-h/6	0	0	
$R/h = 10$	3D <i>Elasticity</i> [88]	1.223	0.0739	-0.0791	4.683	-5.224	0.0374	-0.0729	0.0826	-3.264	-1.27	
	<i>LW</i> _{2a} [68]	1.223	-	-	-	-	-	-	-	-3.283	-1.24	
	<i>ESL</i> _{2a} [68]	0.944	-	-	-	-	-	-	-	-	-	
	<i>LW</i> ₄	1.223	0.0741	-0.0793	4.698	-5.240	0.0376	-0.0734	0.0829	-3.274	-1.27	43095
	<i>LW</i> ₁	1.190	0.0626	-0.0950	4.456	-4.972	0.0363	-0.0707	0.0717	-3.281	-1.27	13260
	<i>EL</i> _{3Z}	1.223	0.0791	-0.0882	4.705	-5.241	0.0376	-0.0733	0.0680	-3.321	-1.30	16575
	<i>EL</i> ₄	1.143	0.0703	-0.0820	4.578	-5.106	0.0363	-0.0692	0.1068	-2.422	-1.35	16575
	<i>EL</i> ₁	0.953	0.0448	-0.0840	3.744	-4.107	0.0303	-0.0566	0.0713	-1.262	-1.08	6630
	<i>EL</i> ₄ <i>Case</i> ₁	1.204	0.0733	-0.0784	4.660	-5.206	0.0372	-0.0725	0.1238	-3.280	-1.27	29835
	<i>EL</i> ₁ <i>Case</i> ₁	0.985	0.0534	-0.0799	4.123	-3.923	0.0324	-0.0573	0.0738	-1.534	-1.04	9945
	<i>EL</i> ₄ <i>Case</i> ₂	1.205	0.0733	-0.0788	4.673	-5.200	0.0374	-0.0723	0.0973	-3.276	-1.27	29835
	<i>EL</i> ₁ <i>Case</i> ₂	0.992	0.0387	-0.0886	3.547	-4.578	0.0301	-0.0600	0.0661	-1.584	-1.22	9945
$R/h = 4$	3D <i>Elasticity</i> [88]	4.009	0.1270	-0.2701	6.545	-9.323	0.1081	-0.1609	0.1736	-2.349	-0.62	
	<i>LW</i> _{2a} [68]	4.007	-	-	-	-	-	-	-	-2.399	-0.60	
	<i>ESL</i> _{2a} [68]	2.917	-	-	-	-	-	-	-	-	-	
	<i>LW</i> ₄	4.009	0.1271	-0.2725	6.565	-9.354	0.1088	-0.1619	0.1742	-2.356	-0.62	43095
	<i>LW</i> ₁	3.852	0.0826	-0.2772	5.585	-7.702	0.1020	-0.1491	0.1663	-2.360	-0.62	13260
	<i>EL</i> _{3Z}	3.970	0.1352	-0.3140	6.519	-9.056	0.1072	-0.1593	0.1496	-2.353	-0.62	16575
	<i>EL</i> ₄	3.772	0.1124	-0.3026	6.342	-9.094	0.1050	-0.1545	0.2332	-1.936	-0.67	16575
	<i>EL</i> ₁	3.004	-0.0052	-0.1676	3.210	-4.024	0.0787	-0.1085	0.1512	-1.147	-0.62	6630
	<i>EL</i> ₄ <i>Case</i> ₁	3.917	0.1244	-0.2796	6.434	-9.155	0.1065	-0.1594	0.2708	-2.269	-0.59	29835
	<i>EL</i> ₁ <i>Case</i> ₁	3.084	0.0549	-0.1711	4.505	-3.311	0.0839	-0.1085	0.1571	-1.272	-0.72	9945
	<i>EL</i> ₄ <i>Case</i> ₂	3.940	0.1232	-0.2706	6.475	-9.213	0.1079	-0.1588	0.2078	-2.305	-0.62	29835
	<i>EL</i> ₁ <i>Case</i> ₂	3.151	-0.0065	-0.2510	2.334	-6.233	0.0768	-0.1201	0.1484	-1.389	-0.54	9945
$R/h = 2$	3D <i>Elasticity</i> [88]	10.11	0.1761	-0.8428	7.168	-18.19	0.1797	-0.2922	0.3006	-1.379	-0.34	
	<i>LW</i> _{2a} [68]	10.33	-	-	-	-	-	-	-	-1.421	-0.33	
	<i>ESL</i> _{2a} [68]	8.95	-	-	-	-	-	-	-	-	-	
	<i>LW</i> ₄	10.10	0.1741	-0.8730	7.179	-18.17	0.1807	-0.2934	0.3018	-1.382	-0.34	43095
	<i>LW</i> ₁	9.51	0.0738	-0.6604	5.079	-10.67	0.1630	-0.2339	0.2974	-1.328	-0.33	13260
	<i>EL</i> _{3Z}	9.65	0.1487	-0.8951	6.848	-14.15	0.1728	-0.2653	0.2679	-1.294	-0.32	16575
	<i>EL</i> ₄	9.59	0.1425	-0.9572	6.568	-15.63	0.1775	-0.2783	0.4244	-1.219	-0.35	16575
	<i>EL</i> ₁	8.82	-0.1046	-0.3218	2.441	-3.79	0.1542	-0.2152	0.2941	-0.927	-0.37	6630
	<i>EL</i> ₄ <i>Case</i> ₁	9.80	0.1690	-0.9187	6.955	-16.58	0.1756	-0.2859	0.4837	-1.191	-0.30	29835
	<i>EL</i> ₁ <i>Case</i> ₁	8.48	0.0335	-0.3866	3.356	-3.10	0.1391	-0.2029	0.3104	-0.875	-0.50	9945
	<i>EL</i> ₄ <i>Case</i> ₂	9.97	0.1703	-0.8701	6.931	-17.98	0.1798	-0.2894	0.3561	-1.318	-0.34	29835
	<i>EL</i> ₁ <i>Case</i> ₂	8.71	-0.0647	-0.6301	0.711	-8.71	0.1380	-0.2087	0.2700	-1.031	-0.26	9945

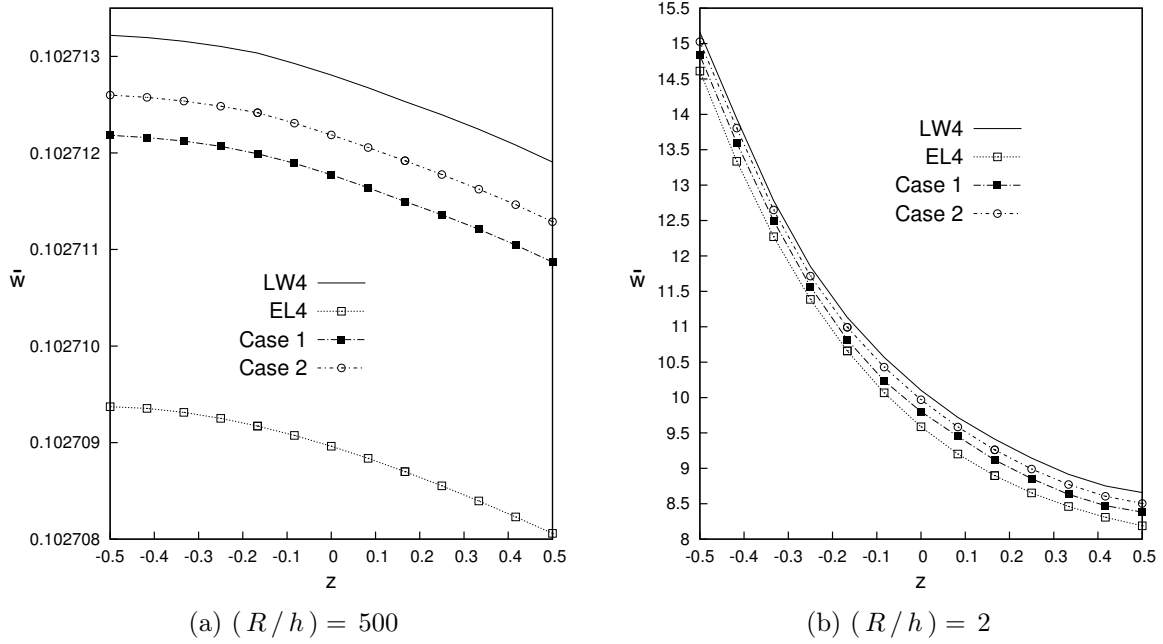


Figure 9.31: Composite three-layered cylinder, by varying R/h . Transverse displacement w .

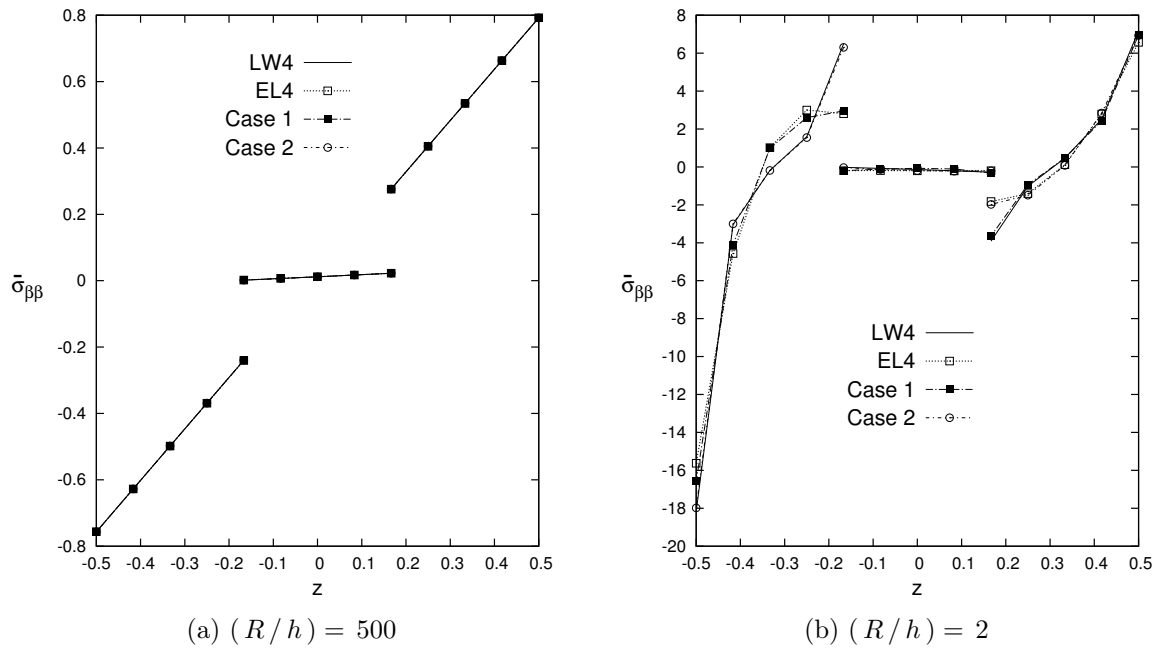


Figure 9.32: Composite three-layered cylinder, by varying R/h . In-plane stress $\sigma_{\beta\beta}$.

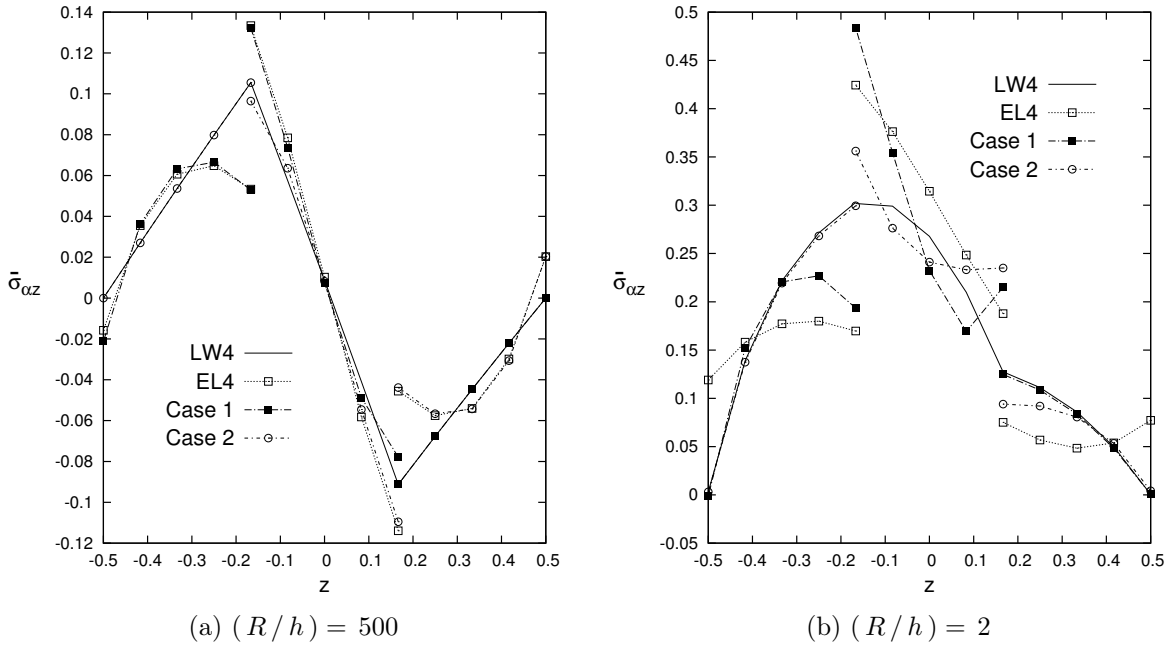


Figure 9.33: Composite three-layered cylinder, by varying R/h . Transverse shear stress $\sigma_{\alpha z}$.

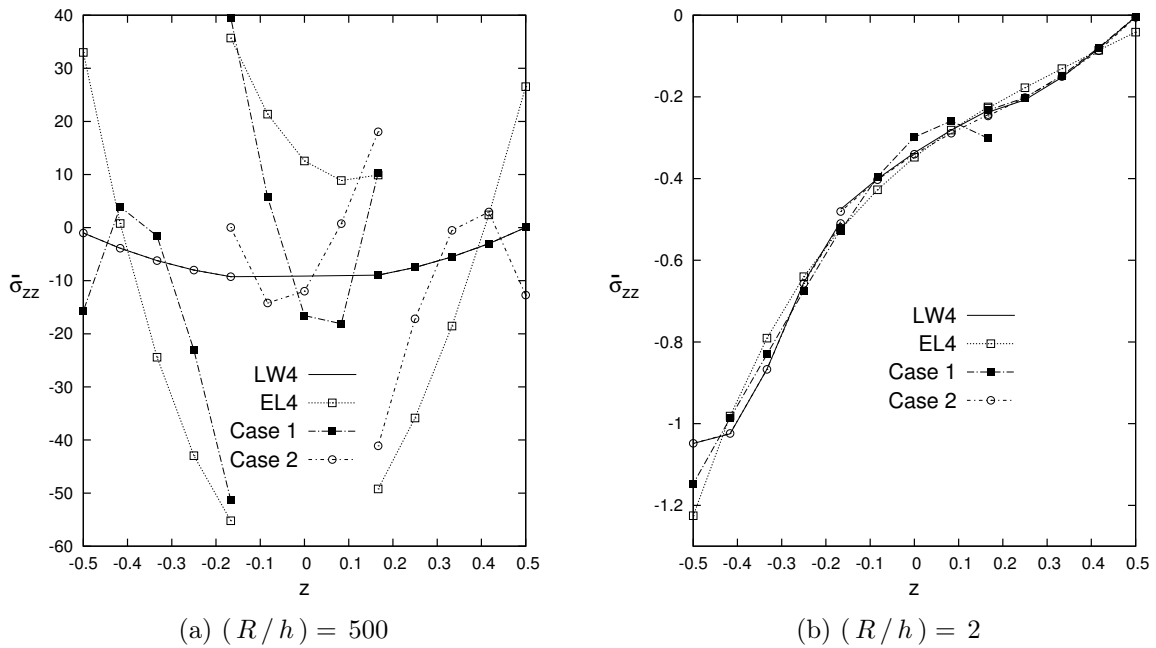


Figure 9.34: Composite three-layered cylinder, by varying R/h . Transverse normal stress σ_{zz} .

9.2.6 Ten-layer composite cylinder

As a second assessment, a ten-layer cross-ply cylinder with lamination $(90^\circ/0^\circ/90^\circ/0^\circ/90^\circ)_S$ and simply-supported boundary condition is considered. The geometrical and material data and the applied load at the inner surface of the shell are the same as those defined for the previous analysis case. Also, because of the geometrical symmetry of the cylinder, the symmetry of the load pressure and boundary condition, and the symmetry of the lamination stacking sequence, only one octave of the cylinder is analysed. A mesh grid of 8×32 elements is used, as in the case of the three-layered cylinder of the previous section.

Different variable kinematic models are employed to show the global/local capabilities of the present methodology. Depending on the sublaminates grouping, the acronyms have been modified adding a subscript to them in the case of variable kinematics. The list of subscripts is given below for the sake of completeness:

- $Case\ 1 = \{layer1\} \{layer2, layer3, layer4, layer5, layer6, layer7, layer8, layer9\} \{layer10\}$
- $Case\ 2 = \{layer1, layer2\} \{layer3, layer4, layer5, layer6, layer7, layer8\} \{layer9, layer10\}$
- $Case\ 3 = \{layer1, layer2, layer3\} \{layer4, layer5, layer6, layer7\} \{layer8, layer9, layer10\}$
- $Case\ 4 = \{layer1, layer2, layer3, layer4\} \{layer5, layer6\} \{layer7, layer8, layer9, layer10\}$
- $Case\ 5 = \{layer1\} \{layer2, layer3\} \{layer4, layer5, layer6, layer7\} \{layer8, layer9\} \{layer10\}$
- $Case\ 6 = \{layer1\} \{layer2, layer3, layer4\} \{layer5, layer6\} \{layer7, layer8, layer9\} \{layer10\}$

The results from the present models are reported in non-dimensional form, as in the previous case, and they are listed in Tables 9.14 and 9.15 and Figures 9.35b to 9.38b for various radius-to-thickness ratios R/h . The present FEM results are compared with those from 3D elasticity solution [88] and a layer-wise analytical model [68]. The following comments can be made from the analysis of the results

- Regarding the transverse displacement w , all the variable-kinematic models lead a significant improvement of the solution with respect to $EL4$ and for every radius-to-thickness ratios, see Figures 9.35a and 9.35b.
- As in the previous analysis case and according to Figure 9.36a, no accuracy differences are appreciable in terms of in-plane stress $\sigma_{\beta\beta}$ between the various models of the thin cylinders. Conversely, for small ratios $R/h = 2$, the theories $EL4, Case1$, $EL4, Case4$ and $EL4, Case6$ improve the results with respect to the global $EL4$ model, especially in the layers that have a layer-wise assembling, see Figure 9.36b.
- In the case of shear stress $\sigma_{\alpha z}$ and variable kinematic models, the results reach the exact solution in the layers that have a layer-wise assembling for both thin and thick cylinders. On the contrary, the remaining layers with an equivalent-single-layer assembling have a loss of accuracy, see Figures 9.37a and 9.37b.
- As far as the transverse normal stress σ_{zz} is concerned and for large ratios $R/h = 500$, the variable kinematics results reach the exact and full LW solutions in the layers that have a layer-wise assembling, see Figure 9.38a. On the other hand, Figure 9.38b shows that the shell theory $EL4, Case6$ approximates very well the layer-wise solution along the thickness in the case of thin structures.

Table 9.14: Composite ten-layered cylinder with $[90^\circ/0^\circ/90^\circ/0^\circ/90^\circ]_S$ lamination. Comparison of various models for thin cylinders.

$z =$	\hat{w}	$\hat{\sigma}_{\alpha\alpha}$		$\hat{\sigma}_{\beta\beta}$		$\hat{\sigma}_{\alpha\beta}$		$\hat{\sigma}_{\alpha z}$	$\hat{\sigma}_{\beta z}$	$\hat{\sigma}_{zz}$	$DOFs$	
	0	+h/2	-h/2	+h/2	-h/2	+h/2	-h/2	0	0	0		
$R/h = 500$	3D Elasticity [88]	0.1006	0.0516	0.0340	0.7770	-0.7351	-0.0829	-0.0949	0.0102	-0.4670	-6.32	
	LW4	0.1006	0.0518	0.0341	0.7795	-0.7374	-0.0834	-0.0956	0.0103	-0.4685	-6.33	135915
	LW1	0.1006	0.0520	0.0338	0.7798	-0.7378	-0.0834	-0.0956	0.0264	-0.4587	-32.36	36465
	EL3Z	0.1006	0.0517	0.0338	0.7794	-0.7377	-0.0834	-0.0956	0.0057	-0.6194	-49.00	16575
	ELA	0.1006	0.0516	0.0339	0.7793	-0.7376	-0.0834	-0.0956	0.0065	-0.6196	-37.69	16575
	EL1	0.1005	0.0541	0.0311	0.7819	-0.7404	-0.0834	-0.0955	0.0044	-0.4438	-31.93	6630
	EL4 _{Case 1}	0.1006	0.0518	0.0341	0.7795	-0.7374	-0.0834	-0.0956	0.0069	-0.5528	-24.37	43095
	EL4 _{Case 2}	0.1006	0.0517	0.0339	0.7794	-0.7376	-0.0834	-0.0956	0.0064	-0.6123	-35.38	43095
	EL4 _{Case 3}	0.1006	0.0519	0.0346	0.7797	-0.7369	-0.0834	-0.0956	0.0091	-0.4281	-8.35	43095
	EL4 _{Case 4}	0.1006	0.0520	0.0346	0.7797	-0.7368	-0.0834	-0.0956	0.0103	-0.4685	-6.33	43095
	EL4 _{Case 5}	0.1006	0.0518	0.0341	0.7795	-0.7374	-0.0834	-0.0956	0.0091	-0.4281	-8.35	69615
	EL4 _{Case 6}	0.1006	0.0518	0.0341	0.7795	-0.7374	-0.0834	-0.0956	0.0103	-0.4685	-6.33	69615
$R/h = 100$	3D Elasticity [88]	0.6261	0.1076	-0.0015	4.677	-4.670	-0.0734	-0.1479	0.0631	-2.884	-7.69	
	LW2 _a [68]	0.6261	-	-	-	-	-	-	-	-2.884	-7.69	
	ESL2 _a [68]	0.6252	-	-	-	-	-	-	-	-	-	
	LW4	0.6261	0.1080	-0.0016	4.692	-4.685	-0.0738	-0.1489	0.0634	-2.893	-7.71	135915
	LW1	0.6261	0.1090	-0.0038	4.693	-4.687	-0.0738	-0.1489	0.0831	-2.830	-13.96	36465
	EL3Z	0.6254	0.1079	-0.0027	4.693	-4.686	-0.0737	-0.1487	0.0393	-3.830	-12.10	16575
	ELA	0.6254	0.1075	-0.0022	4.692	-4.686	-0.0737	-0.1487	0.0402	-3.827	-9.29	16575
	EL1	0.6221	0.1218	-0.0195	4.689	-4.681	-0.0733	-0.1480	0.0269	-2.732	-7.02	6630
	EL4 _{Case 1}	0.6255	0.1079	-0.0016	4.692	-4.685	-0.0737	-0.1487	0.0424	-3.414	-8.53	43095
	EL4 _{Case 2}	0.6255	0.1082	-0.0021	4.692	-4.685	-0.0737	-0.1488	0.0393	-3.782	-9.19	43095
	EL4 _{Case 3}	0.6259	0.1075	-0.0002	4.692	-4.683	-0.0738	-0.1488	0.0560	-2.643	-7.67	43095
	EL4 _{Case 4}	0.6258	0.1072	-0.0003	4.692	-4.683	-0.0738	-0.1488	0.0634	-2.893	-7.71	43095
EL4 _{Case 5}	0.6260	0.1079	-0.0016	4.692	-4.685	-0.0738	-0.1488	0.0560	-2.643	-7.67	69615	
EL4 _{Case 6}	0.6259	0.1079	-0.0016	4.692	-4.685	-0.0738	-0.1488	0.0634	-2.893	-7.71	69615	
$R/h = 50$	3D Elasticity [88]	0.7622	0.0971	-0.0340	5.529	-5.606	-0.0223	-0.1120	0.0760	-3.425	-4.76	
	LW2 _a [68]	0.7622	-	-	-	-	-	-	-	-3.425	-4.76	
	ESL2 _a [68]	0.7564	-	-	-	-	-	-	-	-	-	
	LW4	0.7622	0.0974	-0.0341	5.546	-5.624	-0.0225	-0.1128	0.0763	-3.436	-4.77	135915
	LW1	0.7620	0.0980	-0.0374	5.545	-5.626	-0.0225	-0.1127	0.0880	-3.360	-6.54	36465
	EL3Z	0.7580	0.0972	-0.0358	5.544	-5.624	-0.0222	-0.1123	0.0477	-4.553	-5.86	16575
	ELA	0.7580	0.0965	-0.0351	5.543	-5.623	-0.0222	-0.1123	0.0483	-4.545	-5.02	16575
	EL1	0.7517	0.1118	-0.0563	5.524	-5.599	-0.0220	-0.1113	0.0321	-3.243	-3.77	6630
	EL4 _{Case 1}	0.7585	0.0972	-0.0342	5.543	-5.621	-0.0222	-0.1123	0.0508	-4.055	-4.86	43095
	EL4 _{Case 2}	0.7589	0.0977	-0.0346	5.543	-5.620	-0.0223	-0.1124	0.0472	-4.492	-5.01	43095
	EL4 _{Case 3}	0.7607	0.0967	-0.0327	5.546	-5.623	-0.0224	-0.1126	0.0673	-3.139	-4.70	43095
	EL4 _{Case 4}	0.7604	0.0962	-0.0330	5.546	-5.624	-0.0223	-0.1125	0.0761	-3.436	-4.77	43095
EL4 _{Case 5}	0.7614	0.0974	-0.0341	5.546	-5.623	-0.0224	-0.1127	0.0673	-3.140	-4.70	69615	
EL4 _{Case 6}	0.7611	0.0974	-0.0341	5.546	-5.624	-0.0224	-0.1126	0.0762	-3.436	-4.77	69615	

Table 9.15: Composite ten-layered cylinder with $[90^\circ/0^\circ/90^\circ/0^\circ/90^\circ]_S$ lamination. Comparison of various models for thick cylinders.

$z =$	\hat{w}	$\hat{\sigma}_{\alpha\alpha}$		$\hat{\sigma}_{\beta\beta}$		$\hat{\sigma}_{\alpha\beta}$		$\hat{\sigma}_{\alpha z}$	$\hat{\sigma}_{\beta z}$	$\hat{\sigma}_{zz}$	$DOFs$	
	0	+h/2	-h/2	+h/2	-h/2	+h/2	-h/2	0	0	0		
$R/h = 10$	3D Elasticity [88]	1.380	0.0877	-0.0927	5.875	-6.462	0.0406	-0.0869	0.1084	-3.479	-1.32	
	LW2 _a [68]	1.380	-	-	-	-	-	-	-	-3.475	-1.32	
	ESL2 _a [68]	1.200	-	-	-	-	-	-	-	-	-	
	LW4	1.380	0.0879	-0.0929	5.893	-6.483	0.0408	-0.0874	0.1087	-3.490	-1.32	135915
	LW1	1.375	0.0835	-0.1029	5.855	-6.453	0.0407	-0.0870	0.1127	-3.395	-1.32	36465
	EL3Z	1.265	0.0856	-0.1007	5.795	-6.382	0.0397	-0.0819	0.0656	-4.624	-1.37	16575
	ELA	1.265	0.0806	-0.0958	5.788	-6.380	0.0397	-0.0820	0.0656	-4.584	-1.33	16575
	EL1	1.205	0.0715	-0.1102	5.420	-5.947	0.0375	-0.0771	0.0415	-3.309	-1.09	6630
	EL4 _{Case1}	1.282	0.0849	-0.0914	5.778	-6.352	0.0397	-0.0826	0.0698	-4.095	-1.31	43095
	EL4 _{Case2}	1.293	0.0860	-0.0909	5.772	-6.339	0.0398	-0.0831	0.0650	-4.547	-1.33	43095
	EL4 _{Case3}	1.339	0.0876	-0.0913	5.895	-6.490	0.0406	-0.0857	0.0944	-3.167	-1.30	43095
	EL4 _{Case4}	1.330	0.0853	-0.0937	5.888	-6.490	0.0405	-0.0853	0.1060	-3.471	-1.32	43095
	EL4 _{Case5}	1.357	0.0873	-0.0927	5.872	-6.458	0.0407	-0.0864	0.0955	-3.179	-1.30	69615
	EL4 _{Case6}	1.351	0.0872	-0.0927	5.877	-6.467	0.0406	-0.0861	0.1074	-3.485	-1.32	69615
$R/h = 4$	3D Elasticity [88]	4.206	0.1243	-0.2674	6.635	-8.970	0.0972	-0.1652	0.2117	-3.154	-0.71	
	LW2 _a [68]	4.206	-	-	-	-	-	-	-	-3.137	-0.71	
	ESL2 _a [68]	3.240	-	-	-	-	-	-	-	-	-	
	LW4	4.206	0.1247	-0.2678	6.656	-8.998	0.0978	-0.1663	0.2124	-3.164	-0.71	135915
	LW1	4.175	0.1116	-0.2913	6.473	-8.712	0.0967	-0.1640	0.2161	-3.027	-0.65	36465
	EL3Z	3.566	0.1177	-0.2955	6.215	-8.109	0.0900	-0.1457	0.1239	-4.053	-0.70	16575
	ELA	3.563	0.0957	-0.2771	6.128	-8.231	0.0898	-0.1465	0.1236	-3.952	-0.70	16575
	EL1	3.335	0.0136	-0.1942	4.635	-5.818	0.0817	-0.1241	0.0748	-3.012	-0.63	6630
	EL4 _{Case1}	3.705	0.1150	-0.2600	6.223	-8.394	0.0917	-0.1510	0.1347	-3.578	-0.70	43095
	EL4 _{Case2}	3.768	0.1161	-0.2583	6.202	-8.358	0.0923	-0.1529	0.1256	-4.003	-0.70	43095
	EL4 _{Case3}	3.973	0.1243	-0.2700	6.635	-8.997	0.0958	-0.1602	0.1825	-2.791	-0.69	43095
	EL4 _{Case4}	3.923	0.1210	-0.2755	6.614	-8.979	0.0952	-0.1589	0.2020	-3.079	-0.70	43095
	EL4 _{Case5}	4.088	0.1227	-0.2663	6.572	-8.876	0.0968	-0.1631	0.1873	-2.842	-0.70	69615
	EL4 _{Case6}	4.052	0.1224	-0.2664	6.584	-8.893	0.0966	-0.1623	0.2082	-3.137	-0.71	69615
$R/h = 2$	3D Elasticity [88]	11.44	0.1691	-0.8532	7.202	-18.31	0.1545	-0.3363	0.3019	-2.608	-0.42	
	LW2 _a [68]	11.44	-	-	-	-	-	-	-	-2.581	-0.42	
	ESL2 _a [68]	9.39	-	-	-	-	-	-	-	-	-	
	LW4	11.44	0.1696	-0.8554	7.225	-18.37	0.1555	-0.3384	0.3029	-2.618	-0.42	135915
	LW1	11.28	0.1442	-0.8850	6.750	-16.42	0.1518	-0.3265	0.3062	-2.426	-0.36	36465
	EL3Z	9.42	0.1369	-0.8804	6.101	-11.96	0.1418	-0.2877	0.1876	-3.039	-0.39	16575
	ELA	9.39	0.0967	-0.8775	5.485	-13.08	0.1382	-0.2952	0.1874	-2.820	-0.39	16575
	EL1	9.46	-0.1091	-0.3480	3.509	-5.46	0.1368	-0.2097	0.1245	-2.449	-0.39	6630
	EL4 _{Case1}	10.13	0.1561	-0.8409	6.555	-17.04	0.1484	-0.3205	0.2095	-2.671	-0.40	43095
	EL4 _{Case2}	10.31	0.1562	-0.8490	6.528	-17.12	0.1494	-0.3243	0.1912	-3.009	-0.40	43095
	EL4 _{Case3}	10.76	0.1675	-0.8962	7.109	-18.21	0.1527	-0.3305	0.2666	-2.229	-0.40	43095
	EL4 _{Case4}	10.61	0.1667	-0.9099	7.081	-18.14	0.1524	-0.3312	0.2911	-2.484	-0.41	43095
	EL4 _{Case5}	11.11	0.1666	-0.8518	7.067	-18.03	0.1544	-0.3340	0.2739	-2.298	-0.41	69615
	EL4 _{Case6}	11.02	0.1665	-0.8519	7.072	-17.99	0.1548	-0.3351	0.3006	-2.568	-0.42	69615

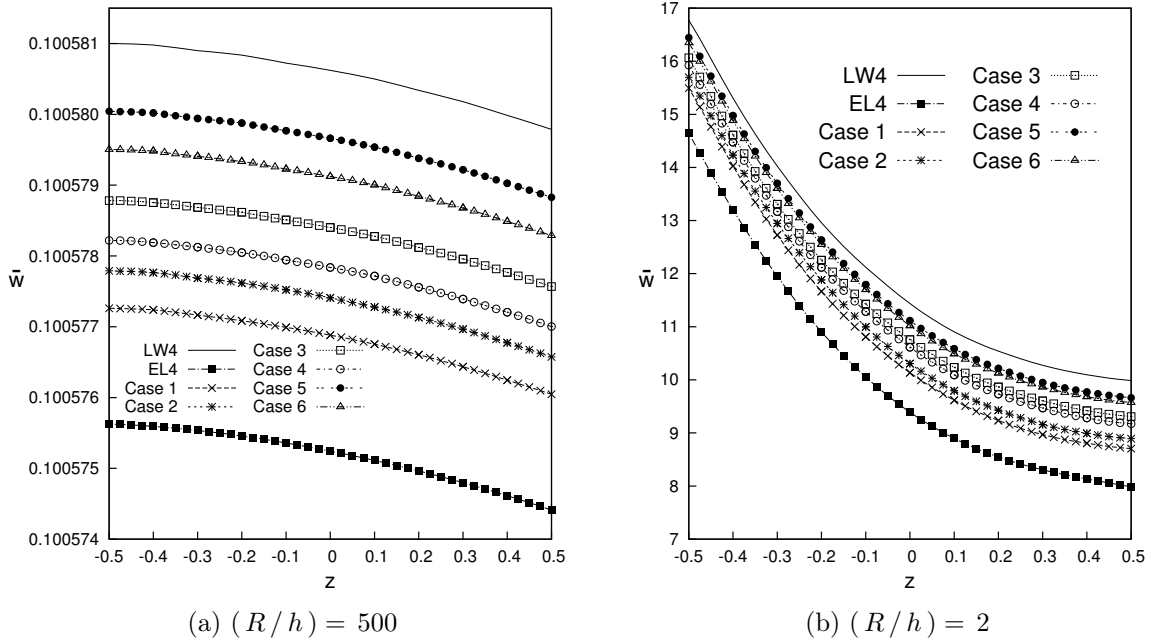


Figure 9.35: Composite ten-layered cylinder, by varying R/h . Transverse displacement w .

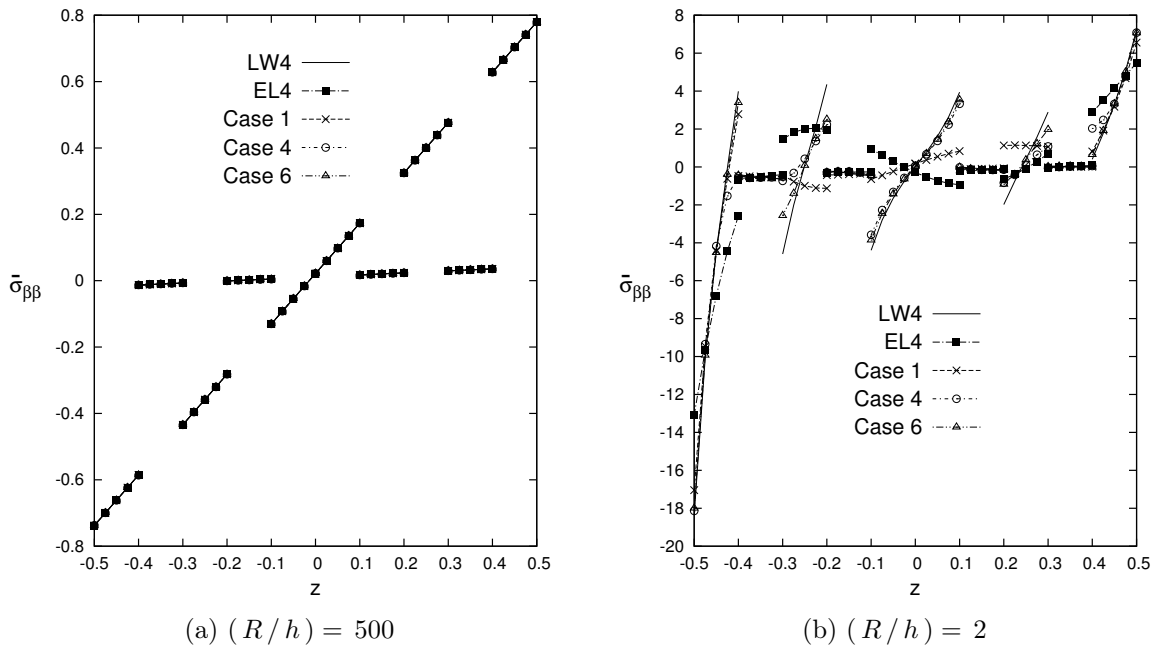
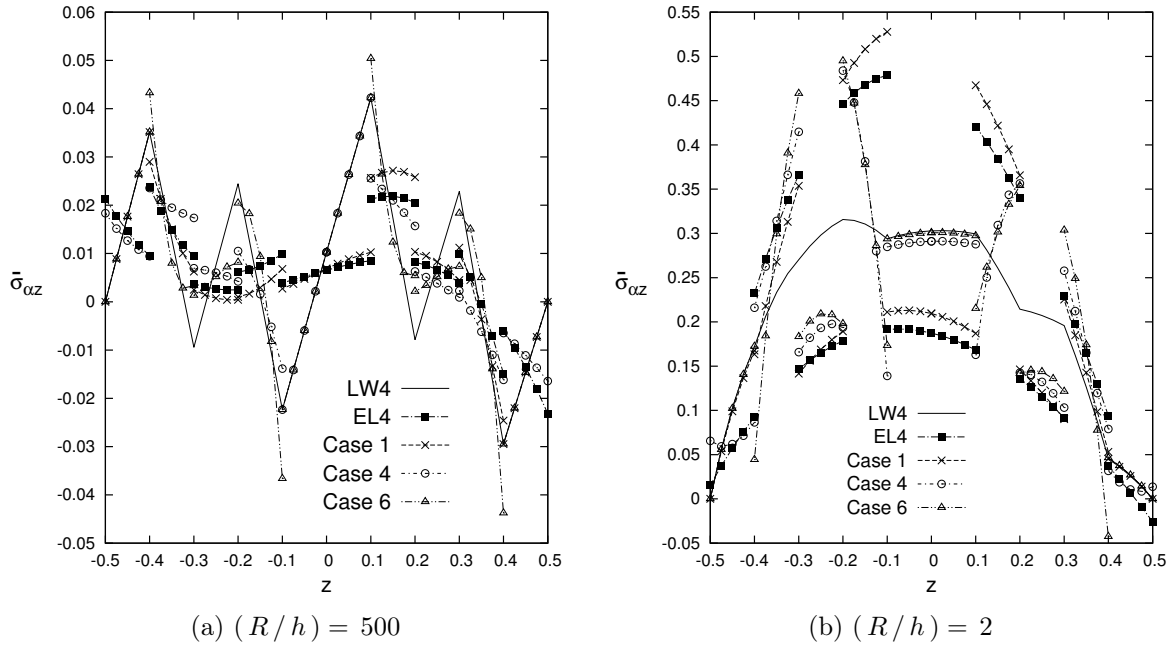
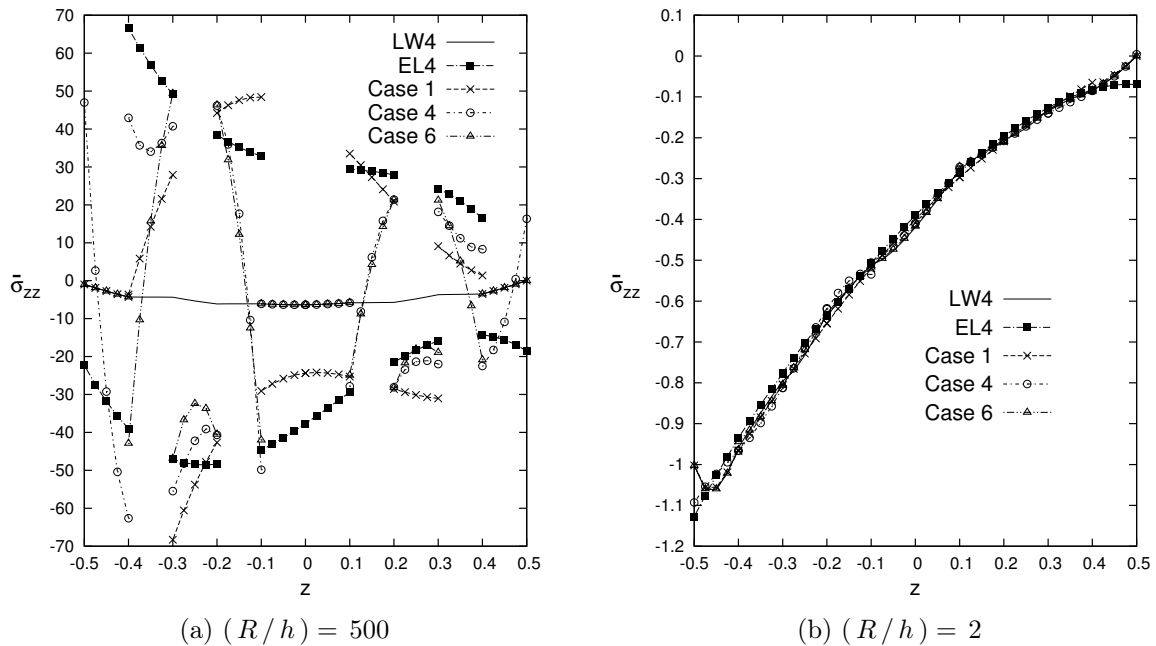


Figure 9.36: Composite ten-layered cylinder, by varying R/h . In-plane stress $\sigma_{\beta\beta}$.


 Figure 9.37: Composite ten-layered cylinder, by varying R/h . Transverse shear stress $\sigma_{\alpha z}$.

 Figure 9.38: Composite ten-layered cylinder, by varying R/h . Transverse normal stress σ_{zz} .

9.2.7 Composite spherical panel

A preliminary analysis of cross-ply spherical panels with $(0^\circ/90^\circ/0^\circ)$ and $(0^\circ/90^\circ/90^\circ/0^\circ)$ laminations and simply-supported boundary conditions are considered next. The load is a pressure applied at the outer surface of the shell and it is defined as follows:

$$p(\alpha, \beta, z_{top}) = \hat{p} \sin\left(\frac{m\pi\alpha}{a}\right) \sin\left(\frac{n\pi\beta}{b}\right) \quad (9.7)$$

where $\hat{p} = 1.0$, $m = 1$ and $n = 1$. The mechanical properties of the material are: $E_L/E_T = 25$; $G_{LT}/E_T = 0.5$; $G_{TT}/E_T = 0.2$; $\nu_{LT} = \nu_{TT} = 0.25$. Different radius-to-side length

ratios $R/a = 5, 10, 50, 100$ and different side length-to-thickness ratios $a/h = 10, 100$ are considered. The panel is square such that $a/b = 1$ and $R_\alpha/R_\beta = 1$. The layers are of equal thickness and $h_{total} = 1.0$. The results are given in terms of transverse displacements and reported in non-dimensional form as follows:

$$\hat{w} = -\frac{10^3 w E_T h^3}{\hat{p} a^4} \quad \hat{\sigma}_{\alpha z} = \frac{10^4 \sigma_{\alpha z}}{\hat{p}(R/h)} \quad \hat{\sigma}_{zz} = \frac{\sigma_{zz}}{\hat{p}}$$

Even for this analysis case, different variable kinematic models are used to perform the analysis of the shell structures. Usual acronyms are enriched with the following subscripts which indicate the sublaminates grouping. For the three-layered spherical shell we consider

- *Case1* = {*layer1*} {*layer2, layer3*}
- *Case2* = {*layer1, layer2*} {*layer3*}

On the other hand, for the four-layered shell we have

- *Case1* = {*layer1*} {*layer2, layer3, layer4*}
- *Case2* = {*layer1, layer2, layer3*} {*layer4*}
- *Case3* = {*layer1, layer2*} {*layer3, layer4*}
- *Case4* = {*layer1*} {*layer2, layer3*} {*layer4*}

First, a convergence study on the shell element was performed. A composite shell with radius to side length ratio $R/a = 10$ and side length to thickness ratio $a/h = 10$ is considered for this purpose. As demonstrated in Table 9.16 in the case of a full LW model, a mesh grid of 12×12 elements ensures the convergence. The results from the other full kinematic and variable kinematic models are reported in non-dimensional form for the transverse displacement in Table 9.17, and for the transverse shear and normal stresses in Table 9.18 for different thickness ratios a/h and radius-to-side length ratio R/a . The present FEM results are compared with higher-order models from the literature, i.e. [154] and [155], and a layer-wise analytical model by Carrera [68]. It can be observed that changing the R/a ratio, the transverse displacement variation is higher for thin shells with ratio $a/h = 100$ than for thick shells with ratio $a/h = 10$. Therefore it can be seen that the best approximation compromise is given by the theory $EL4_{Case1}$, where the loaded layer is described by a layer-wise model and the remaining layers are described by equivalent single layer approach. For the four-layered shell, the theory $EL4_{Case4}$ is more accurate than $EL4_{Case1}$ model. This is due only to the fact that a symmetric lamination scheme is considered.

Table 9.16: Convergence study. Composite spherical panel with lamination $[0^\circ/90^\circ/0^\circ]$. Radius-to-side length ratio $R/a = 10$ and side length-to-thickness ratio $a/h = 10$.

Mesh	4×4	6×6	8×8	10×10	12×12
<i>LW4</i> $\hat{w}(z=0)$	7.5175	7.5129	7.5121	7.5118	7.5117

Table 9.17: Composite spherical panel with $[0^\circ/90^\circ/0^\circ]$ and $[0^\circ/90^\circ/90^\circ/0^\circ]$ laminations. Transverse displacement $\hat{w} = \hat{w}(a/2, b/2, 0)$. Results presented for different R/a and a/h ratios.

		$a/h = 10$				$a/h = 100$				$DOFs$
R/a		5	10	50	100	5	10	50	100	
3 Layers	$HS DT^1$ [154]	6.7688	7.0325	7.1212	7.1240	1.0321	2.4099	4.2071	4.3074	
	$HS DT^2$ [155]	6.8201	7.0459	7.1213	7.1237	1.0321	2.4020	4.1249	4.2603	
	$LW2_a$ [68]	7.121	7.392		7.504					
	$LW4$	7.3252	7.5117	7.5408	7.5365	1.0364	2.4166	4.2132	4.3131	24375
	$LW1$	7.1793	7.3568	7.3835	7.3792	1.0360	2.4143	4.2061	4.3057	7500
	$EL3Z$	7.3219	7.5089	7.5382	7.5339	1.0364	2.4166	4.2132	4.3131	9375
	$EL4$	6.9739	7.1376	7.1606	7.1564	1.0362	2.4152	4.2087	4.3085	9375
	$EL1$	6.1234	6.2381	6.2489	6.2450	1.0327	2.3962	4.1514	4.2485	3750
	$EL4_{Case 1}$	7.2331	7.4092	7.4327	7.4279	1.0364	2.4163	4.2121	4.3120	16875
	$EL4_{Case 2}$	7.2309	7.4080	7.4324	7.4278	1.0364	2.4163	4.2121	4.3120	16875
4 Layers	$HS DT^1$ [154]	6.7865	7.0536	7.1436	7.1464	1.0264	2.4024	4.2071	4.3082	
	$HS DT^2$ [155]	6.8380	7.0670	7.1436	7.1459	1.0254	2.3866	4.1284	4.2418	
	$LW4$	7.1738	7.3528	7.3801	7.3758	1.0306	2.4083	4.2111	4.3117	31875
	$LW1$	7.0820	7.2554	7.2811	7.2769	1.0303	2.4070	4.2071	4.3075	9375
	$EL3Z$	6.9973	7.1651	7.1894	7.1852	1.0304	2.4076	4.2088	4.3093	9375
	$EL4$	6.9971	7.1648	7.1891	7.1849	1.0304	2.4076	4.2088	4.3093	9375
	$EL1$	6.0771	6.1912	6.2020	6.1982	1.0269	2.3884	4.1503	4.2480	3750
	$EL4_{Case 1}$	7.1141	7.2877	7.3127	7.3083	1.0305	2.4081	4.2103	4.3108	16875
	$EL4_{Case 2}$	7.1086	7.2850	7.3124	7.3083	1.0305	2.4080	4.2102	4.3108	16875
	$EL4_{Case 3}$	7.0925	7.2663	7.2921	7.2879	1.0305	2.4080	4.2100	4.3106	16875
$EL4_{Case 4}$	7.1738	7.3528	7.3801	7.3758	1.0306	2.4083	4.2111	4.3117	24375	

Table 9.18: Composite spherical panel with $[0^\circ/90^\circ/0^\circ]$ and $[0^\circ/90^\circ/90^\circ/0^\circ]$ laminations. Transverse shear stress $\hat{\sigma}_{\alpha z} = \hat{\sigma}_{\alpha z}(a/2, b/2, 0)$, and transverse normal stress $\hat{\sigma}_{zz} = \hat{\sigma}_{\alpha z}(a/2, b/2, +h/2)$. Results presented for different R/a and a/h ratios.

		$a/h = 10$				$a/h = 100$				$DOFs$
R/a		$\hat{\sigma}_{\alpha z}$		$\hat{\sigma}_{zz}$		$\hat{\sigma}_{\alpha z}$		$\hat{\sigma}_{zz}$		
		5	100	5	100	5	100	5	100	
3 Layers	$LW4$	-0.4909	-0.0254	-1.0003	-1.0005	-0.1270	-0.0308	-1.0041	-1.0125	24375
	$LW1$	-0.5225	-0.0270	-1.3539	-1.5057	-0.1295	-0.0312	-10.839	-43.924	7500
	$EL3Z$	-0.5328	-0.0276	-1.2200	-1.2358	-0.1350	-0.0323	-1.0997	-1.2631	9375
	$EL4$	-0.3635	-0.0188	-1.0383	-1.0505	-0.0911	-0.0231	-1.2561	-1.1229	9375
	$EL1$	-0.1581	-0.0081	-1.7265	-1.9412	-0.0215	-0.0082	-30.651	-127.85	3750
	$EL4_{Case 1}$	-0.4928	-0.0255	-1.0003	-1.0005	-0.1297	-0.0320	-1.0041	-1.0125	16875
$EL4_{Case 2}$	-0.4946	-0.0255	-0.9581	-0.9690	-0.1387	-0.0321	-0.8627	-0.9513	16875	
4 Layers	$LW4$	-0.4156	-0.0215	-1.0003	-1.0003	-0.1014	-0.0263	-1.0041	-1.0127	31875
	$LW1$	-0.4250	-0.0217	-1.2889	-1.4107	-0.1204	-0.0277	-8.3048	-33.237	9375
	$EL3Z$	-0.4070	-0.0209	-1.2260	-1.2282	-0.1043	-0.0254	-1.0603	-1.2434	9375
	$EL4$	-0.3942	-0.0204	-1.0547	-1.0545	-0.0979	-0.0255	-1.0206	-1.0782	9375
	$EL1$	-0.1616	-0.0083	-1.6803	-1.8929	-0.0202	-0.0086	-30.687	-127.84	3750
	$EL4_{Case 1}$	-0.4406	-0.0228	-1.0003	-1.0003	-0.1093	-0.0288	-1.0041	-1.0127	16875
	$EL4_{Case 2}$	-0.4433	-0.0228	-0.9935	-1.0043	-0.1192	-0.0289	-1.0082	-1.0272	16875
	$EL4_{Case 3}$	-0.3894	-0.0202	-0.9690	-0.9760	-0.0647	-0.0222	-0.9956	-0.9831	16875
$EL4_{Case 4}$	-0.4157	-0.0215	-1.0003	-1.0003	-0.1011	-0.0262	-1.0041	-1.0127	24375	

9.2.8 Eleven-layer sandwich cylindrical panel

An eleven-layer simply-supported sandwich cylindrical panel with $(0^\circ/90^\circ/0^\circ/Core/0^\circ/90^\circ/0^\circ/Core/0^\circ/90^\circ/0^\circ)$ lamination and simply-supported boundary condition is considered. The load is a pressure applied at the outer surface of the shell, and it is defined as follows:

$$p(\alpha, \beta, z_{top}) = \hat{p} \sin\left(\frac{m\pi\alpha}{a}\right) \sin\left(\frac{n\pi\beta}{b}\right) \quad (9.8)$$

where $m = 1$ and $n = 1$, whereas $\hat{p} = 1.0$. Different axis length-to-circumferential length ratios $b/a = 1, 2$ and circumferential length-to-thickness ratios $a/h = 5, 10$ are considered. The radius-to-circumferential length ratio is fixed for all the cases and it is assumed to be equal to $R_\alpha/a = 2$. Each face sheet of the shell has a thickness of $0.015 \times h_{total}$ and is made of composite material with the following properties: $E_1 = 172.5 \text{ GPa}$, $E_2 = E_3 = 6.9 \text{ GPa}$, $G_{12} = G_{13} = 3.45 \text{ GPa}$, $G_{23} = 2.76 \text{ GPa}$, $\nu_{12} = \nu_{13} = \nu_{23} = 0.25$. On the other hand, each core has a thickness of $0.4325 \times h_{total}$ and the material properties are the following: $E_1 = E_2 = 0.276 \text{ GPa}$, $E_3 = 3.45 \text{ GPa}$, $G_{12} = 0.1104 \text{ GPa}$, $G_{13} = G_{23} = 0.414 \text{ GPa}$, $\nu_{12} = 0.25$, $\nu_{13} = \nu_{23} = 0.02$. The total thickness is assumed to be $h_{total} = 1.0$. As in the previous analysis cases, the results are reported in non-dimensional form:

$$\hat{w} = \frac{10^2 w E_{2(\text{face sheets})} h^3}{\hat{p} a^4} \quad (\hat{\sigma}_{\alpha\alpha}, \hat{\sigma}_{\beta\beta}, \hat{\sigma}_{\alpha\beta}) = \frac{(\sigma_{\alpha\alpha}, \sigma_{\beta\beta}, \sigma_{\alpha\beta}) h^2}{\hat{p} a^2} \quad \hat{\sigma}_{\alpha z} = \frac{\sigma_{\alpha z} h}{\hat{p} a}$$

Different variable kinematic models have been used to perform the analyses of the shell structures. These models make use of various sublaminar groupings, which are summarized in the following by using the usual notation:

- $Case1 = \{layer1\} \{layer2, layer3, layer4, layer5, layer6, layer7, layer8, layer9, layer10\} \{layer11\}$
- $Case2 = \{layer1\} \{layer2\} \{layer3, layer4, layer5, layer6, layer7, layer8, layer9\} \{layer10\} \{layer11\}$
- $Case3 = \{layer1\} \{layer2\} \{layer3\} \{layer4, layer5, layer6, layer7, layer8\} \{layer9\} \{layer10\} \{layer11\}$
- $Case4 = \{layer1, layer2, layer3\} \{layer4, layer5, layer6, layer7, layer8\} \{layer9, layer10, layer11\}$
- $Case5 = \{layer1, layer2, layer3\} \{layer4\} \{layer5, layer6, layer7\} \{layer8\} \{layer9, layer10, layer11\}$
- $Case6 = \{layer1, layer2, layer3, layer4\} \{layer5, layer6, layer7\} \{layer8, layer9, layer10, layer11\}$
- $Case7 = \{layer1, layer2, layer3, layer4\} \{layer5\} \{layer6\} \{layer7\} \{layer8, layer9, layer10, layer11\}$

First a convergence study on the shell element was performed and it is shown in Table 9.19. For this analysis case, a composite sandwich cylindrical panel with circumferential length to thickness ratio $a/h = 5$ and side length ratio $b/a = 1$ is considered. Clearly, a mesh grid of 12×12 elements ensures the convergence in terms of both transverse displacement and the stresses. This mesh size is, thus, utilized for the remaining analyses.

Table 9.19: Convergence study. Composite sandwich cylindrical panel with circumferential length-to-thickness ratio $a/h = 5$ and side length ratio $b/a = 1$.

	Mesh	4 × 4	6 × 6	8 × 8	10 × 10	12 × 12	ZIGT _a [25]	3D Elasticity [156]
LW4	$\hat{w}(z=0)$	5.2621	5.2593	5.2588	5.2587	5.2586	5.2616	5.2824
	$\hat{\sigma}_{\alpha\alpha}(z=-h/2)$	-2.1441	-2.0947	-2.0758	-2.0668	-2.0618	-2.1337	-2.0731
	$10 \times \hat{\sigma}_{\beta\beta}(z=+h/2)$	1.5573	1.5216	1.5086	1.5024	1.4990	1.4423	1.5395
	$\hat{\sigma}_{\alpha\beta}(z=-h/2)$	1.7780	1.6917	1.6603	1.6456	1.6375	1.6588	1.6409
	$\hat{\sigma}_{\alpha z}(z=0)$	0.2140	0.2081	0.2061	0.2051	0.2046	0.2170	0.2001

The results from the variable kinematic models and from complete ESL and LW models are listed in Table 9.20 for various axis length-to-circumferential length ratios b/a and different circumferential length-to-thickness ratios a/h . In this table, the present FEM results are compared with a 3D elasticity solution [156] and a layer-wise theory, called the zigzag theory (ZIGT). In particular, both analytical [25] and FEM [157] ZIGT solutions are given for comparison purposes. For the sake of completeness, the through-the-thickness behaviour of the stress components are also illustrated in Figures 9.39 to 9.43. The behaviour of the variables along the thickness is invariant with respect to the b/a or a/h ratios. Thus, the case $b/a = 1$ and $a/h = 10$ is taken into account to plot the variables behaviour along the thickness in those figures. For the shell structures analysed in this section, the following considerations can be drawn:

- In terms of transverse displacement w , variable kinematic models with combined ESL/LW assumptions (i.e., $EL4_{,Case1}$, $EL4_{,Case2}$, $EL4_{,Case3}$, and $EL4_{,Case4}$) provide better accuracy with respect to the full ESL models, such as $EL4$, see Figure 9.39. However, the best accuracy is reached assembling the sandwich cores with a layer-wise scheme while keeping the face composite sheets as ESL, i.e. $EL4_{,Case5}$. In this case, it is possible to reduce the computational costs in terms of degrees of freedom as high as 53.33% with respect to a full LW reference solution. Variable kinematic models $EL4_{,Case6}$ and $EL4_{,Case7}$ still provide an improvement of the solution accuracy with respect to $EL4_{,Case1}$ to $EL4_{,Case4}$. Moreover, it is interesting to note that the $EL4_{,Case4}$ model has the same accuracy of the $EL4_{,Case3}$ model but with a DOFs reduction of 55.17%. Equivalently, $EL4_{,Case6}$ model has the same accuracy of the $EL4_{,Case7}$ model with a DOFs reduction of 38.09%.
- Figures 9.40 to 9.42 show that very small differences in terms of accuracy of $\sigma_{\alpha\alpha}$, $\sigma_{\beta\beta}$ and $\sigma_{\alpha\beta}$ distributions are visible in the composite sheets layers if $EL4_{,Case1}$ and $EL4_{,Case2}$ models are compared to $EL4_{,Case5}$, and $EL4_{,Case6}$ models. Nevertheless, $EL4_{,Case5}$, and $EL4_{,Case6}$ models provide the same solution of full refined LW model with a considerable reduction of the computational costs. For these stress components, the distribution within the core is roughly the same for all the models considered.
- As far as the shear stress $\sigma_{\alpha z}$ distribution is considered, Figure 9.43 shows that all the variable-kinematic models provide results as accurate as the reference solutions in those layers that are approximated with a LW accuracy. This allows the analyst to choose the approximation accuracy in each thickness subdomain independently and save, eventually, computational costs but still having accurate solution in localized zones. For the analysis case under consideration, however, the best compromise between an accurate solution and an huge reduction of computational cost in terms of DOFs with respect to the full layer-wise solution, is obtained with the $EL4_{,Case5}$ model, whose DOFs reduction is 53.33%.

Table 9.20: Sandwich eleven-layered cylinder. Transverse displacement $\hat{w}(\alpha, \beta) = \hat{w}(a/2, b/2)$, in-plane stresses $\hat{\sigma}_{\alpha\alpha}(\alpha, \beta) = \hat{\sigma}_{\alpha\alpha}(a/2, b/2)$, $\hat{\sigma}_{\beta\beta}(\alpha, \beta) = \hat{\sigma}_{\beta\beta}(a/2, b/2)$, in-plane shear stress $\hat{\sigma}_{\alpha\beta}(\alpha, \beta) = \hat{\sigma}_{\alpha\beta}(0, 0)$ and transverse shear stress $\hat{\sigma}_{\alpha z}(\alpha, \beta) = \hat{\sigma}_{\alpha z}(0, b/2)$.

		$a/h = 5$					$a/h = 10$					$DOFs$	
$z =$	\hat{w}	$\hat{\sigma}_{\alpha\alpha}$	$10 \times \hat{\sigma}_{\beta\beta}$	$10 \times \hat{\sigma}_{\alpha\beta}$	$\hat{\sigma}_{\alpha z}$	\hat{w}	$\hat{\sigma}_{\alpha\alpha}$	$10 \times \hat{\sigma}_{\beta\beta}$	$10 \times \hat{\sigma}_{\alpha\beta}$	$\hat{\sigma}_{\alpha z}$			
	0	$-h/2$	$h/2$	$-h/2$	0	0	$-h/2$	$h/2$	$-h/2$	0			
$b/a = 1$	<i>3D Elasticity</i> [156]	5.2824	-2.0731	1.5395	1.6409	0.2001	2.5850	-1.9675	1.2612	1.4885	0.2021		
	<i>ZIGT_a</i> [25]	5.2616	-2.1337	1.4423	1.6588	0.2170	2.5762	-1.9776	1.2377	1.4893	0.2245		
	<i>ZIGT_{FE}</i> [157]	5.1264	-1.9903	1.4540	1.5745	0.2171	2.5024	-1.9228	1.2255	1.4369	0.2240		
	<i>LW4</i>	5.2824	-2.0848	1.5476	1.6595	0.2012	2.5850	-1.9786	1.2682	1.5055	0.2033	84375	
	<i>LW1</i>	5.2775	-2.0858	1.5488	1.6588	0.2012	2.5847	-1.9790	1.2690	1.5053	0.2033	22500	
	<i>EL3Z</i>	4.1624	-2.0624	1.5618	1.4801	1.2367	2.3091	-2.0089	1.3025	1.4260	1.2688	9375	
	<i>EL4</i>	4.0764	-2.0717	1.4538	1.4712	0.9815	2.2918	-2.0163	1.2346	1.4239	1.0007	9375	
	<i>EL1</i>	3.7660	-2.0435	1.4769	1.4030	0.6698	2.2028	-2.0122	1.3150	1.3891	0.6781	3750	
	<i>EL4_{Case1}</i>	4.1405	-2.0819	1.4495	1.4870	0.9513	2.3072	-2.0153	1.2267	1.4295	0.9705	24375	
	<i>EL4_{Case2}</i>	4.2709	-2.1075	1.4603	1.5093	0.9156	2.3379	-2.0199	1.2302	1.4384	0.9316	39375	
	<i>EL4_{Case3}</i>	4.7676	-2.0863	1.5096	1.5837	0.7458	2.4609	-1.9976	1.2517	1.4728	0.7653	54375	
	<i>EL4_{Case4}</i>	4.7675	-2.0865	1.5127	1.5837	0.7458	2.4609	-1.9977	1.2534	1.4728	0.7653	24375	
	<i>EL4_{Case5}</i>	5.2822	-2.0850	1.5510	1.6595	0.1875	2.5849	-1.9786	1.2700	1.5054	0.1892	39375	
	<i>EL4_{Case6}</i>	5.1562	-2.0918	1.5091	1.6422	0.1881	2.5525	-1.9821	1.2429	1.4962	0.1897	24375	
	<i>EL4_{Case7}</i>	5.1564	-2.0918	1.5091	1.6423	0.2019	2.5525	-1.9821	1.2429	1.4962	0.2038	39375	
	$b/a = 2$	<i>3D Elasticity</i> [156]	9.0416	-3.7989	1.3594	1.6680	0.3348	4.3974	-3.5216	0.9654	1.2841	0.3294	
		<i>ZIGT_a</i> [25]	9.0141	-3.9003	1.2524	1.6723	0.3650	4.3762	-3.5377	0.9380	1.2818	0.3667	
<i>ZIGT_{FE}</i> [157]		8.6267	-3.5873	1.2445	1.5549	0.3585	4.1713	-3.3774	0.9154	1.2156	0.3590		
<i>LW4</i>		9.0785	-3.8203	1.3665	1.6870	0.3367	4.3975	-3.5415	0.9707	1.2987	0.3313	84375	
<i>LW1</i>		9.0726	-3.8213	1.3658	1.6867	0.3368	4.3971	-3.5421	0.9706	1.2987	0.3313	22500	
<i>EL3Z</i>		7.1160	-3.7190	1.3297	1.4529	2.0518	3.8967	-3.5301	0.9950	1.2013	2.0438	9375	
<i>EL4</i>		6.9062	-3.6954	1.2053	1.4248	1.6129	3.8490	-3.5263	0.9191	1.1924	1.6043	9375	
<i>EL1</i>		6.3528	-3.6156	1.2343	1.3430	1.0941	3.6956	-3.5017	1.0058	1.1577	1.0835	3750	
<i>EL4_{Case1}</i>		7.0208	-3.7166	1.2043	1.4423	1.5647	3.8776	-3.5284	0.9102	1.1988	1.5572	24375	
<i>EL4_{Case2}</i>		7.2117	-3.7496	1.2193	1.4645	1.5003	3.9252	-3.5355	0.9157	1.2079	1.4938	39375	
<i>EL4_{Case3}</i>		8.1588	-3.7862	1.3000	1.5821	1.2388	4.1655	-3.5411	0.9450	1.2553	1.2380	54375	
<i>EL4_{Case4}</i>		8.1586	-3.7855	1.2983	1.5821	1.2388	4.1654	-3.5401	0.9408	1.2553	1.2380	24375	
<i>EL4_{Case5}</i>		9.0781	-3.8197	1.3652	1.6870	0.3139	4.3973	-3.5406	0.9667	1.2987	0.3085	39375	
<i>EL4_{Case6}</i>		8.8374	-3.8187	1.3192	1.6594	0.3140	4.3345	-3.5398	0.9465	1.2864	0.3086	24375	
<i>EL4_{Case7}</i>		8.8377	-3.8188	1.3193	1.6595	0.3369	4.3346	-3.5398	0.9465	1.2865	0.3314	39375	

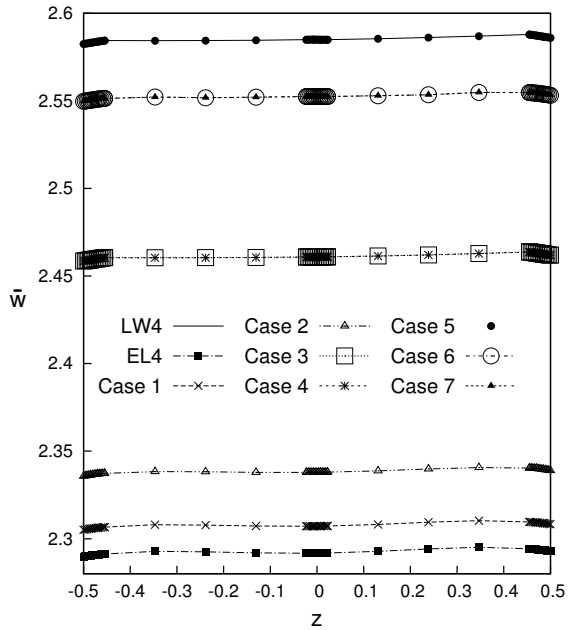


Figure 9.39: Sandwich eleven-layered cylinder. Transverse displacement w along the thickness, with axis length to circumferential length ratio $b/a = 1$ and circumferential length to thickness ratios $a/h = 10$.

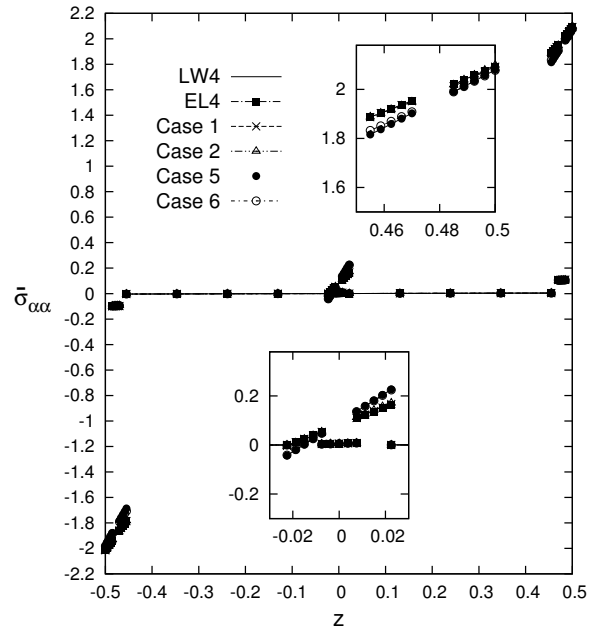


Figure 9.40: Sandwich eleven-layered cylinder. In-plane stress $\sigma_{\alpha\alpha}$ along the thickness, with axis length to circumferential length ratio $b/a = 1$ and circumferential length to thickness ratios $a/h = 10$.

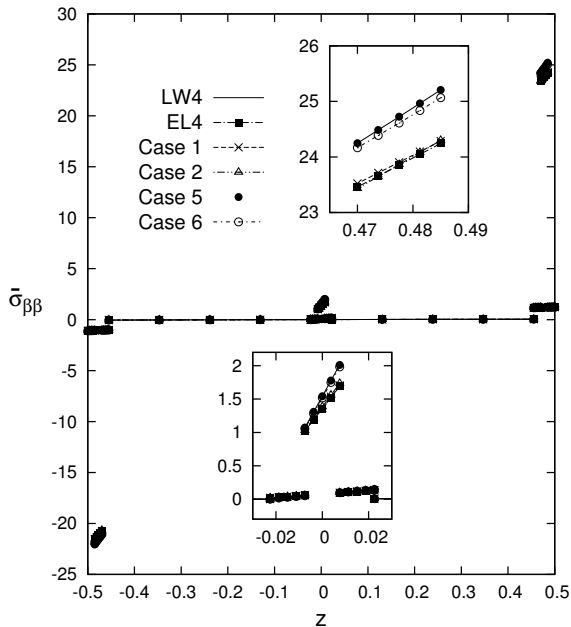


Figure 9.41: Sandwich eleven-layered cylinder. In-plane stress $\sigma_{\beta\beta}$ along the thickness, with axis length to circumferential length ratio $b/a = 1$ and circumferential length to thickness ratios $a/h = 10$.

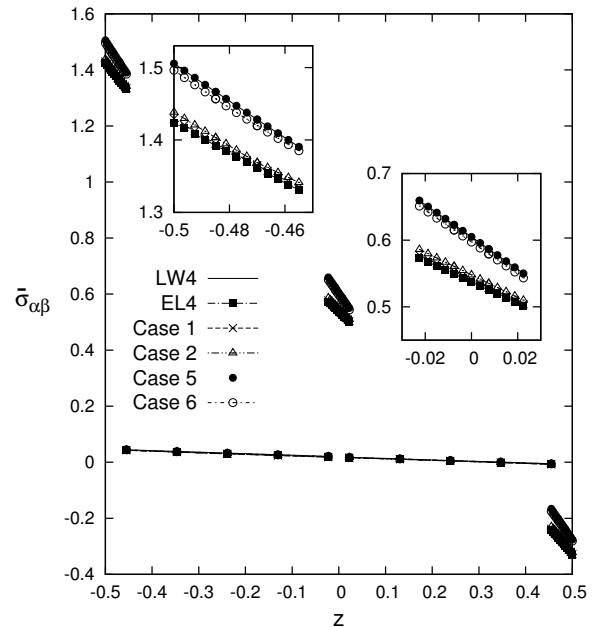


Figure 9.42: Sandwich eleven-layered cylinder. In-plane shear stress $\sigma_{\alpha\beta}$ along the thickness, with axis length to circumferential length ratio $b/a = 1$ and circumferential length to thickness ratios $a/h = 10$.

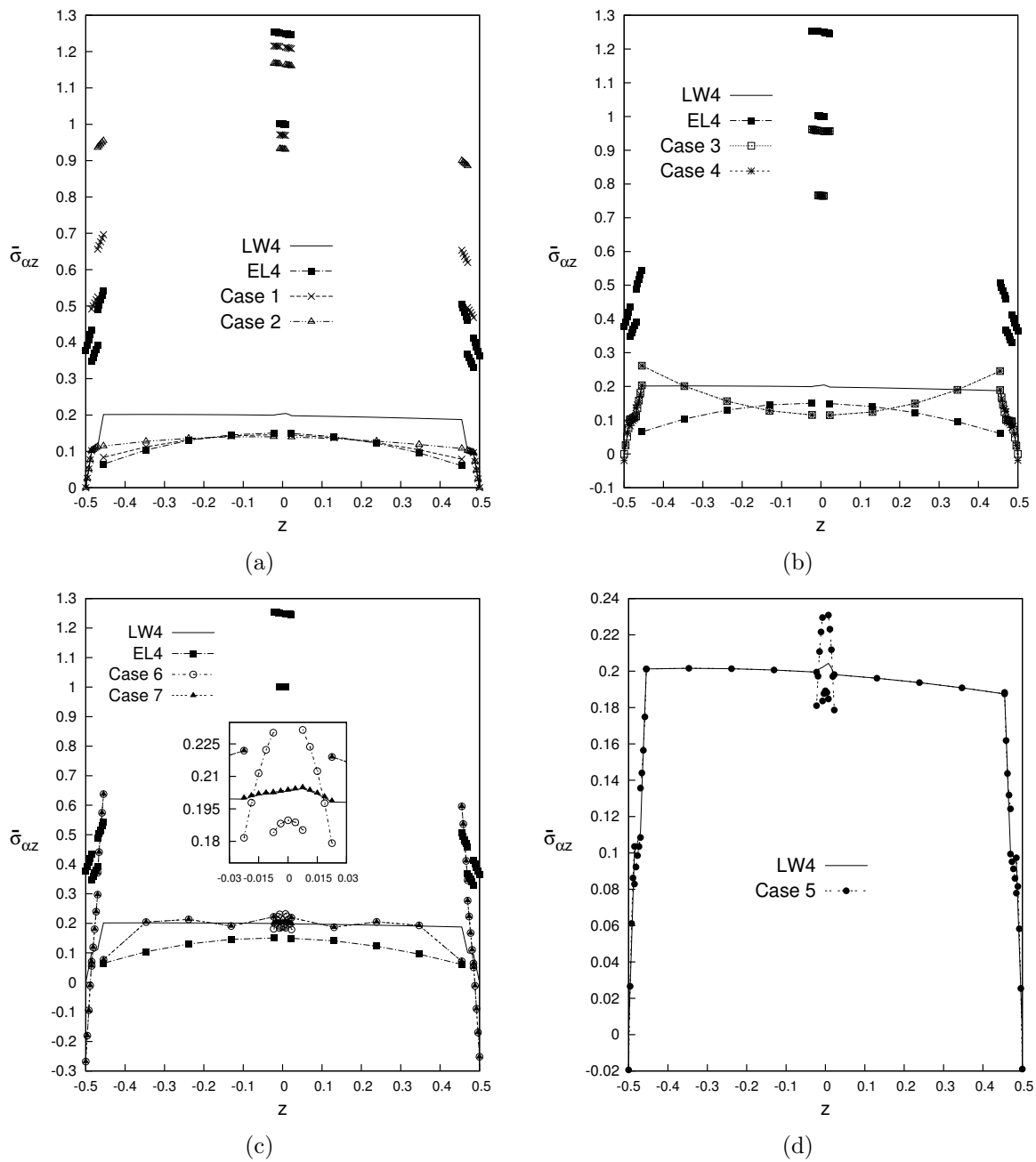


Figure 9.43: Sandwich eleven-layered cylinder. Transverse shear stress $\sigma_{\alpha z}$ along the thickness, with axis length to circumferential length ratio $b/a = 1$ and circumferential length to thickness ratios $a/h = 10$.

9.3 Thermo-Mechanical Analysis Results

In this section, the static thermo-mechanical analysis of plate and shell structures are performed to assess the variable-kinematics mixed ESL/LW plate/shell element. To study the effectiveness of the proposed approach, the following composite multilayered plates, cylindrical shells, and spherical sandwich shell structures have been analyzed:

- A three-layer square plate with lamination $[0^\circ/90^\circ/0^\circ]$
- A ten-layer cylindrical shell panel with lamination $[0^\circ/90^\circ]_5$
- A sandwich composite spherical panel with lamination $[0^\circ/90^\circ/Core/90^\circ/0^\circ]$

Both of them are evaluated applying a thermal load with a bi-sinusoidal in-plane behavior:

$$\theta(\alpha, \beta, z) = \hat{\theta}(z) \sin\left(\frac{m\pi\alpha}{a}\right) \sin\left(\frac{n\pi\beta}{b}\right) \quad (9.9)$$

where $m = n = 1$. Solutions with the assumed linear thermal profile $\hat{\theta}(z)$, and/or with the calculated thermal profile obtained via the Fourier heat conduction law are given. Wherever possible, solutions from variable-kinematic models are compared with those from higher-order ESL models, LW models, 3D elasticity solutions and analytical results.

9.3.1 Three-layer plate

A three-layer cross-ply square plate, see Figure 9.44, with cross-ply composite layers with lamination $[0^\circ/90^\circ/0^\circ]$ and simply-supported boundary condition is considered.

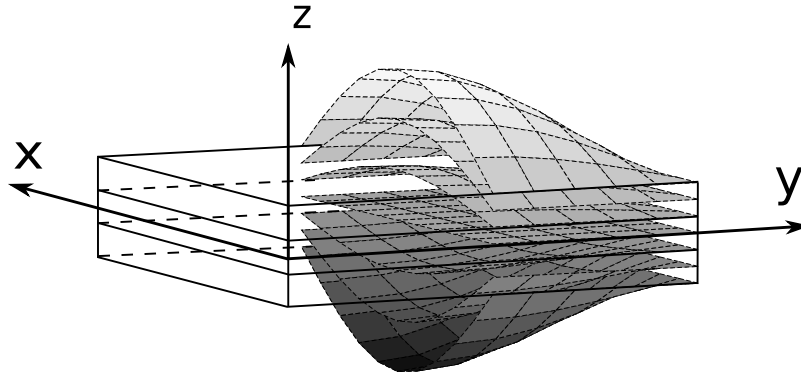


Figure 9.44: Reference system of the composite plate with section of thermal load applied.

The Carbon-Epoxy material constants of the plate are taken from [70, 96], the values are expressed in terms of ratios of the longitudinal and transversal fiber directional properties: $E_L/E_T = 25$; $G_{LT}/E_T = 0,5$; $G_{TT}/E_T = 0,2$; $\nu_{LT} = \nu_{TT} = 0,25$; $\frac{\alpha_T}{\alpha_L} = 1125,0$; $\frac{\kappa_L}{\kappa_T} = \frac{36,42}{0,96}$. The geometrical dimensions are: $a = b = 1,0$. The temperature boundary conditions are: $\hat{\theta}_{top} = +1,0$, $\hat{\theta}_{bottom} = -1,0$. The results are presented for different thickness ratios $a/h = 2; 100$, and the deflections and stresses are presented in the following dimensionless forms:

$$\hat{w} = \frac{w}{h\alpha_L\theta_0\left(\frac{a}{h}\right)^2} \quad \hat{\sigma}_{i,j} = \frac{\sigma_{i,j}}{E_T\alpha_L\theta_0}$$

where the temperature gradient is $\theta_0 = 1$. A mesh grid of 32×32 elements is taken to ensure the convergence of the solution, see Table 9.21. The rate of convergence is invariant respect to the temperature profile.

Table 9.21: Convergence study. Composite three layered plate with thickness ratio $a/h = 100$. All the cases are computed with a *LW4* model.

	Mesh	4×4	8×8	12×12	16×16	20×20	24×24	28×28	32×32	<i>3DExact</i> [96]
T_a	\hat{w}	10.274	10.261	10.260	10.260	10.260	10.260	10.260	10.260	10.26
	$\hat{\sigma}_{xx}$	1030.5	981.69	972.63	969.45	967.98	967.18	966.70	966.39	965.4
	$\hat{\sigma}_{xz}$	7.4509	7.1665	7.1150	7.0968	7.0883	7.0837	7.0809	7.0791	7.073
	$\hat{\sigma}_{zz}$	2.3686	0.1772	0.0379	0.0126	0.0056	0.0030	0.0019	0.0014	-0.1738×10^{-5}
T_c	\hat{w}	10.268	10.254	10.253	10.253	10.253	10.253	10.253	10.253	
	$\hat{\sigma}_{xx}$	1029.7	980.87	971.81	968.64	967.17	966.37	965.89	965.57	
	$\hat{\sigma}_{xz}$	7.4463	7.1621	7.1106	7.0924	7.0839	7.0793	7.0765	7.0747	
	$\hat{\sigma}_{zz}$	2.3652	0.1777	0.0378	0.0126	0.0055	0.0030	0.0019	0.0014	

Therefore a locking study has been performed evaluating different types of integration methods [115] for the same plate structure to prove that the element is locking free, see Table 9.22. The plate element with the MITC9 method ensures accuracy on both the transverse displacement and the stresses variables.

Table 9.22: Locking study. Composite three layered plate with thickness ratio $a/h = 100$. The *Temperature Assumed Linear* and the *Temperature Calculated* cases are computed with a mesh of 32×32 elements and with a *LW4* model.

		<i>Reduced</i>	<i>Selective</i>	<i>MITC9</i>	<i>3DExact</i> [96]
T_a	\hat{w}	10.257	10.259	10.260	10.26
	$\hat{\sigma}_{xx}$	815.55	966.12	966.39	965.4
	$\hat{\sigma}_{xz}$	10.929	7.8184	7.0791	7.073
	$\hat{\sigma}_{zz}$	14.431	-0.0071	0.0014	-0.1738×10^{-5}
T_c	\hat{w}	10.251	10.253	10.253	
	$\hat{\sigma}_{xx}$	814.74	965.30	965.57	
	$\hat{\sigma}_{xz}$	10.924	7.8135	7.0747	
	$\hat{\sigma}_{zz}$	14.456	-0.0071	0.0014	

The description of the temperature profile along the thickness of the multilayered plate is given in Figure 9.45 for different aspect ratios a/h . It has to be noticed that for thin plates the temperature profile is almost linear or very close to it; differently for thick plates it is very important to use the calculated profile solving the Fourier heat conduction equation, the linear profile leads to relevant errors in the approximation of the temperature load, the temperature load is overestimated.

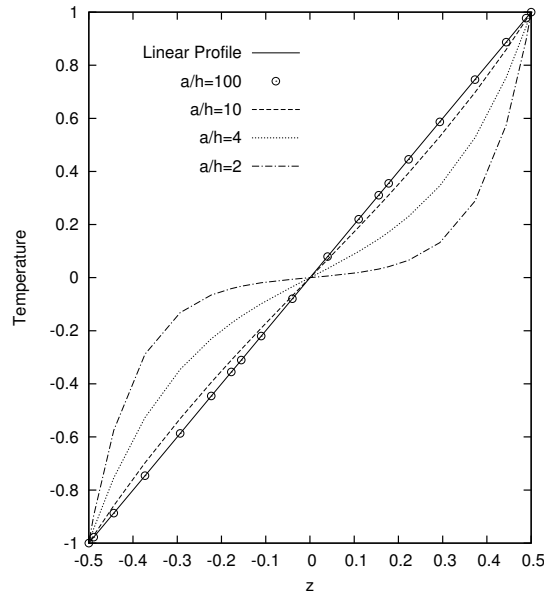


Figure 9.45: Three-layered plate. Temperature Profiles Comparison.

An assessment of the Legendre polynomials with a full ESL approach has been performed for the pure mechanical case in [158] for plates and in [159] for shells. All the results presented in [158,159], for thick and thin plates and shells, show that the Legendre polynomials lead to the same results of the Taylor polynomials. The use of either polynomials is invariant respect to the solution accuracy.

Hereafter Legendre polynomials have been employed for the structure analyzes. Different Variable Kinematic models have been used to perform the analysis of the plate structures, see Figure 9.46. The acronyms have been modified adding a subscript to them, for the sake of clarity the list of subscripts is given below:

- $Case1 = \{layer1\} \{layer2, layer3\}$
- $Case2 = \{layer1, layer2\} \{layer3\}$

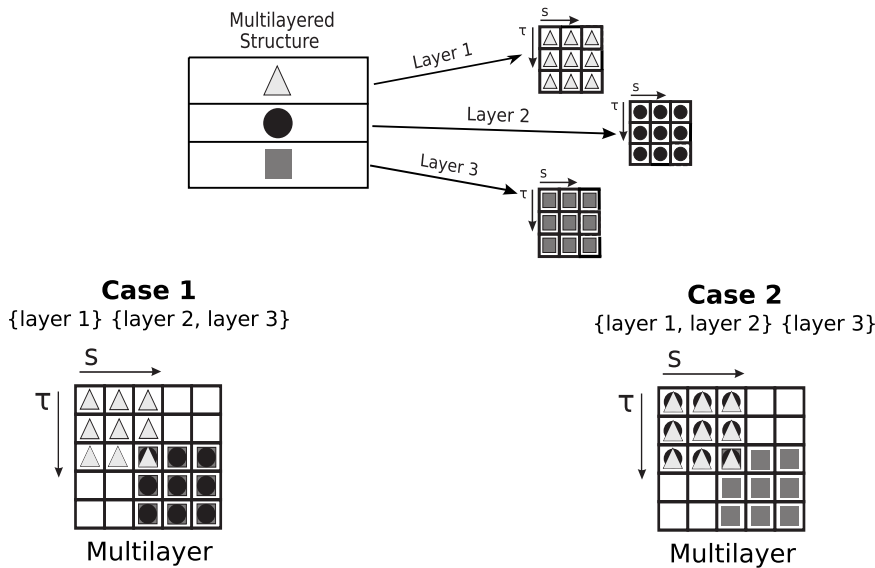


Figure 9.46: Variable Kinematic Cases. Compact example of assembling scheme.

The results are listed in Table 9.23. For the plate structures analysed the following considerations can be drawn:

- Regarding the transverse displacement w , for thin plates $a/h = 100$, the theories $EL4,Case1$ and $EL4,Case2$ lead a relevant improvement of the solution respect to the $EL4$ showing the same accuracy, see Figure 9.47a. The same comments can be drawn for both the temperature assumed linear cases T_a and for the temperature calculated via the Fourier heat conduction law T_c . For thick plates $a/h = 2$, the variable kinematic theories have the same accuracy of the full layer-wise and full equivalent-single-layer solutions, see Figure 9.47b. The maximum transverse displacement T_c case value is 49.53% smaller than the T_a case, this relevant difference is due to temperature calculated profile T_c that permits to better describe the temperature load.
- For both the transverse shear stress σ_{xz} , see Figure 9.48a, and the transverse normal stress, see Figure 9.48b, the theories $EL4,Case1$ and $EL4,Case2$ improve the results respect to the $EL4$ theory only in the layer with a layer-wise description. It has to be noticed that no differences can be appreciated between the temperature assumed linear cases T_a and the temperature calculated via the Fourier heat conduction law T_c cases.
- For the in-plane stress σ_{xx} , see Figures 9.49a, 9.49b, noticeable differences of the stress amplitude are present between the temperature assumed linear cases T_a and the temperature calculated profile T_c cases. The variable kinematic theories $EL4,Case1$ and $EL4,Case2$ improve the results respect to the $EL4$ theory only in the layer with a layer-wise description. It has to be noticed that the interlaminar continuity of the stress is reached in the temperature assumed cases T_a , but not in the calculated profile cases T_c .

Table 9.23: Three-layer composite plate with lamination $[0^\circ/90^\circ/0^\circ]$. Mechanical variables described by Mono-models and Variable kinematic models for various aspect ratios a/h . Evaluation position for transverse displacement $\hat{w}(x, y, z) = \hat{w}(a/2, b/2, +h/2)$, in-plane stress $\hat{\sigma}_{xx}(x, y, z) = \hat{\sigma}_{xx}(a/2, b/2, +h/2)$, transverse shear stress $\hat{\sigma}_{xz}(x, y, z) = \hat{\sigma}_{xz}(0, b/2, +h/6)$, transverse normal stress $\hat{\sigma}_{zz}(x, y, z) = \hat{\sigma}_{zz}(a/2, b/2, +h/6)$.

T_a (Assumed Linear)									
	$a/h = 100$				$a/h = 2$				$DOFs$
	\hat{w}	$\hat{\sigma}_{xx}$	$\hat{\sigma}_{xz}$	$\hat{\sigma}_{zz}$	\hat{w}	$\hat{\sigma}_{xx}$	$\hat{\sigma}_{xz}$	$\hat{\sigma}_{zz}$	
<i>3DE</i> <i>exact</i> [96]	10.26	965.4	7.073	-0.1738×10^{-5}	96.79	1390	63.92	-7.391	
<i>LW</i> 4_a [70]	10.26	-	7.073	-	96.78	-	63.82	-	
<i>LW</i> 4	10.260	966.39	7.0791	0.0014	96.783	1391.0	70.532	-5.9366	164775
<i>LW</i> 1	10.915	893.99	1.8031	492.56	89.252	640.39	-3.9613	417.76	50700
<i>EL</i> 3 <i>Z</i>	10.260	966.39	7.0489	-0.0346	94.871	1279.6	110.16	-31.218	63375
<i>EL</i> 4	10.253	966.28	10.365	-0.0074	98.215	1336.5	93.196	-12.266	63375
<i>EL</i> 3	10.253	966.29	10.365	-0.0122	98.150	1335.3	93.208	-19.536	50700
<i>EL</i> 2	10.231	964.60	4.5411	-0.0108	83.471	188.71	28.967	-17.038	38025
<i>EL</i> 1	16.093	1240.6	7.9964	-487.39	42.714	164.03	114.24	-459.25	25350
<i>EL</i> 4 <i>Case</i> 1	10.258	966.36	7.0794	0.0014	96.679	1389.3	71.700	-5.9661	114075
<i>EL</i> 4 <i>Case</i> 2	10.258	966.38	10.466	-0.0063	97.009	1389.5	89.699	-11.812	114075
<i>EL</i> 3 <i>Case</i> 1	10.258	966.34	7.0789	0.0013	96.338	1376.4	43.807	-11.728	88725
<i>EL</i> 3 <i>Case</i> 2	10.258	966.37	9.9672	-0.0077	97.122	1331.9	99.761	-10.802	88725
<i>EL</i> 2 <i>Case</i> 1	10.258	966.33	8.0746	0.0031	94.629	1224.0	121.26	-11.109	63375
<i>EL</i> 2 <i>Case</i> 2	10.258	966.29	9.0002	-0.0176	95.508	1029.8	55.725	-20.599	63375
<i>EL</i> 1 <i>Case</i> 1	12.203	1042.9	2.4285	491.28	72.269	211.32	-12.328	435.51	38025
<i>EL</i> 1 <i>Case</i> 2	12.203	918.14	7.6641	0.0229	68.305	44.865	97.018	-40.574	38025

T_c (Calculated via Fourier Heat conduction Law)									
	$a/h = 100$				$a/h = 2$				$DOFs$
	\hat{w}	$\hat{\sigma}_{xx}$	$\hat{\sigma}_{xz}$	$\hat{\sigma}_{zz}$	\hat{w}	$\hat{\sigma}_{xx}$	$\hat{\sigma}_{xz}$	$\hat{\sigma}_{zz}$	
<i>LW</i> 4_a [70]	10.25	-	7.069	-	49.09	-	30.11	-	
<i>LW</i> 4	10.253	965.58	7.0747	0.0014	48.851	486.92	35.171	-13.392	164775
<i>LW</i> 1	10.908	892.94	1.8018	492.57	44.174	33.733	-0.5026	344.19	50700
<i>EL</i> 3 <i>Z</i>	10.253	965.27	7.0443	0.3590	50.086	403.89	55.696	172.60	63375
<i>EL</i> 4	10.246	965.47	10.360	-0.0074	49.301	410.42	59.850	-47.521	63375
<i>EL</i> 3	10.246	965.17	10.360	0.3815	51.328	446.81	59.474	179.54	50700
<i>EL</i> 2	10.224	963.49	4.5384	0.3829	40.880	-317.44	15.166	181.62	38025
<i>EL</i> 1	16.083	1239.3	7.9915	-486.69	21.047	-329.45	56.660	-33.581	25350
<i>EL</i> 4 <i>Case</i> 1	10.252	965.55	7.0750	0.0014	48.741	484.86	35.799	-13.346	114075
<i>EL</i> 4 <i>Case</i> 2	10.252	965.56	10.460	-0.0064	48.830	446.19	59.176	-30.492	114075
<i>EL</i> 3 <i>Case</i> 1	10.251	965.51	7.0744	0.0371	48.805	454.55	17.787	85.001	88725
<i>EL</i> 3 <i>Case</i> 2	10.251	965.46	9.9617	-0.0077	49.179	395.76	62.223	-29.540	88725
<i>EL</i> 2 <i>Case</i> 1	10.251	965.39	8.0701	-0.3191	48.785	328.05	72.670	-224.56	63375
<i>EL</i> 2 <i>Case</i> 2	10.251	965.16	8.9953	0.3402	48.871	258.99	37.141	156.37	63375
<i>EL</i> 1 <i>Case</i> 1	12.195	1041.7	2.4268	491.28	34.834	-208.92	-3.5914	353.85	38025
<i>EL</i> 1 <i>Case</i> 2	12.195	917.08	7.6599	0.3808	32.350	-426.20	53.745	144.06	38025

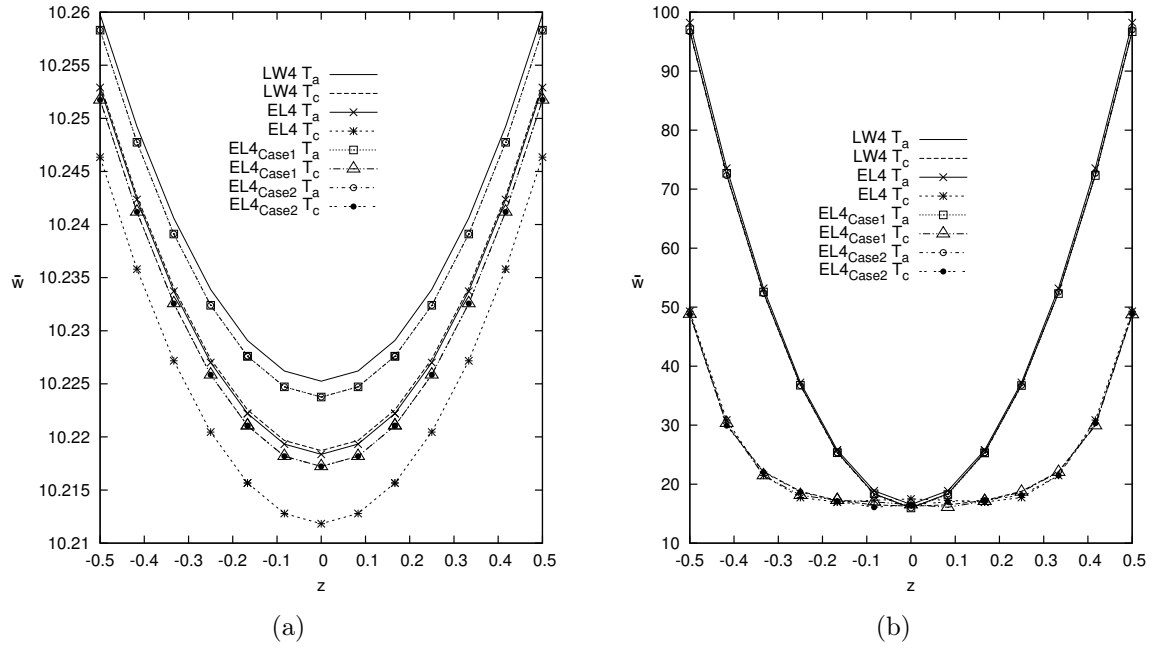


Figure 9.47: Three-layered plate, transverse mechanical displacement \hat{w} , $a/h = 100$ (a), $a/h = 2$ (b).

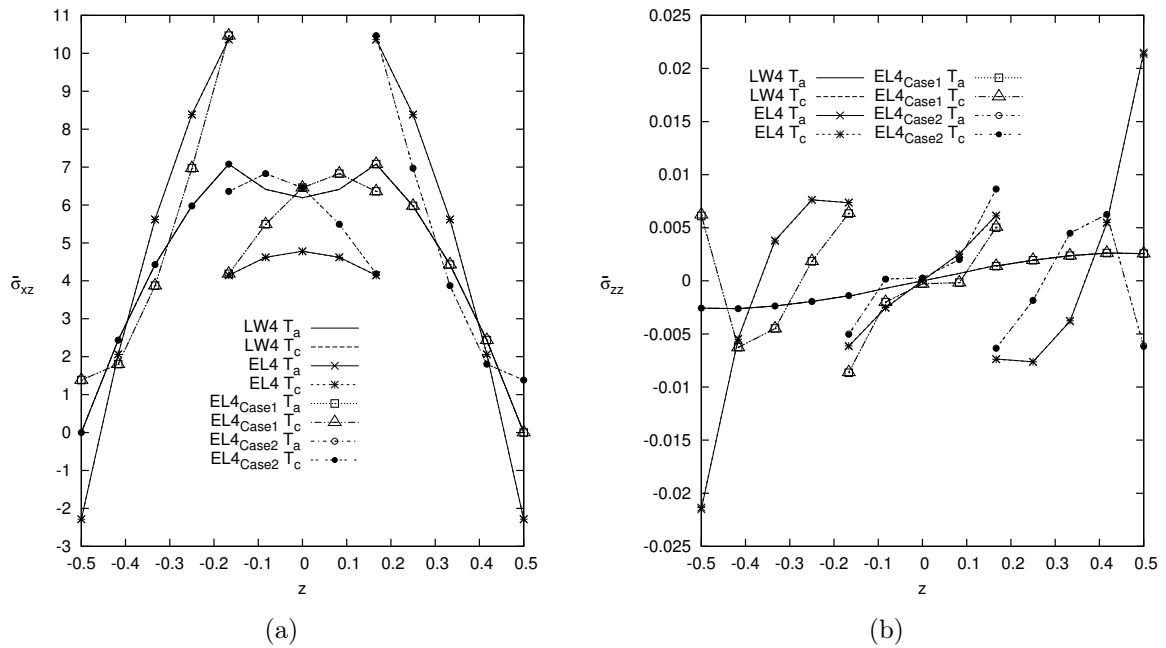


Figure 9.48: Three-layered thin plates $a/h = 100$, transverse shear and normal stresses, $\hat{\sigma}_{xz}$ (a), $\hat{\sigma}_{zz}$ (b).

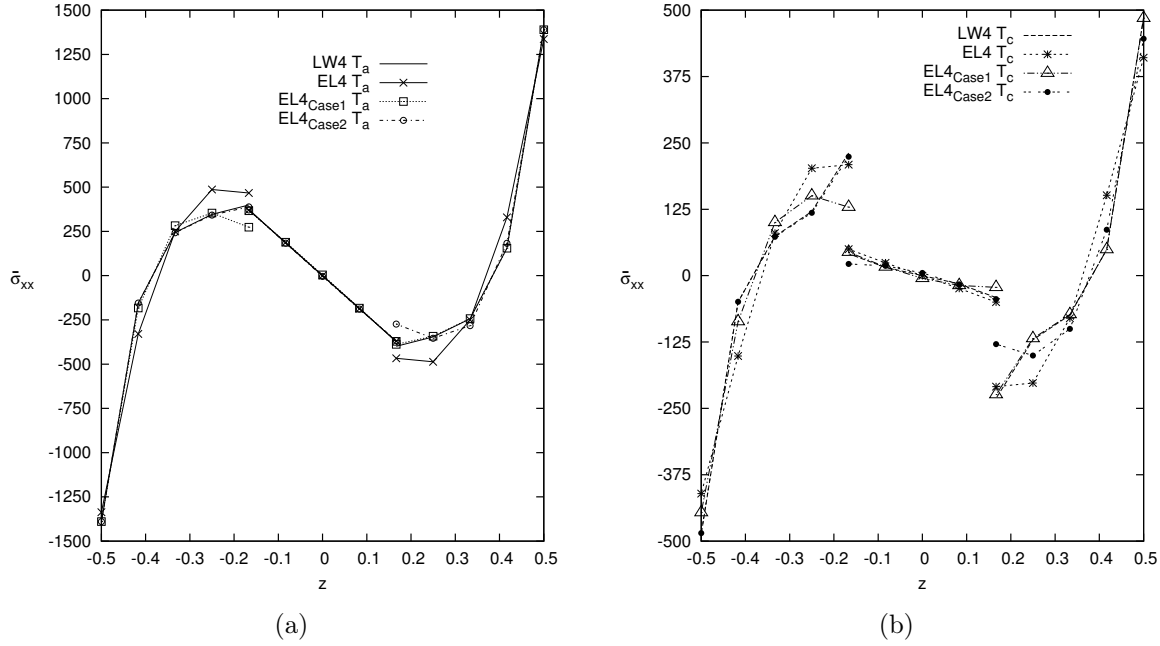


Figure 9.49: Three-layered thick plates $a/h = 2$, in-plane stress $\hat{\sigma}_{xx}$, T_a assumed linear (a), T_c calculated via Fourier heat law (b).

9.3.2 Ten-layer cylindrical panel

A ten-layer cross-ply cylindrical shell panel with cross-ply composite layers with lamination $[0^\circ/90^\circ]_5$ and simply-supported boundary condition is considered. The Carbon-Epoxy material constants of the shell panel are taken from [20, 22], the values are expressed in terms of ratios of the longitudinal and transversal fiber directional properties : $\frac{E_1}{E_2} = 25, 0$; $E_2 = E_3$; $\frac{G_{12}}{E_2} = 0, 5$; $\frac{G_{23}}{E_2} = 0, 2$; $G_{12} = G_{13}$; $\nu_{12} = \nu_{13} = \nu_{23} = 0, 25$; $\frac{\alpha_2}{\alpha_1} = 3, 0$; $\alpha_1 = \alpha_3$; $\frac{\mathcal{K}_1}{\mathcal{K}_2} = \frac{36,42}{0,96}$; $\mathcal{K}_2 = \mathcal{K}_3$. The geometrical dimensions are: $a = b = 1, 0$ and $h_{total} = 0, 1$. The temperature boundary conditions are: $\hat{\theta}_{top} = +0, 5$, $\hat{\theta}_{bottom} = -0, 5$. The results are presented for different radius to length side ratios $R/a = 5; 10; 50$. The deflections and stresses are presented in the following dimensionless forms:

$$\hat{w} = \frac{w}{\alpha_1 \theta_1 b^2} \quad \hat{\sigma}_{i,j} = \frac{\sigma_{i,j}}{E_2 \alpha_1 \theta_1}$$

where $\theta_1 = 1$. The adopted mesh is the same of the previous numerical example. Due to the symmetry of both the geometry and load, a quarter of the cylindrical shell panel is analyzed, see Figure 9.50, with a corresponding mesh grid of 16×16 elements. The corresponding thermal load, using the symmetry conditions, is defined as follows:

$$\theta(\alpha, \beta, z) = \hat{\theta}(z) \cos\left(\frac{m\pi\alpha}{a}\right) \cos\left(\frac{n\pi\beta}{b}\right) \quad (9.10)$$

where $m = n = 0, 5$. The symmetry conditions and the boundary conditions are defined as follows:

$$\begin{aligned} u_\tau(\alpha, \beta) &= u_\tau(a/2, \beta) = 0 \\ v_\tau(\alpha, \beta) &= v_\tau(\alpha, b/2) = 0 \\ u_\tau(\alpha, \beta) &= u_\tau(\alpha, b) = 0 \\ v_\tau(\alpha, \beta) &= v_\tau(a, \beta) = 0 \\ w_\tau(\alpha, \beta) &= w_\tau(\alpha, b) = 0 \\ w_\tau(\alpha, \beta) &= w_\tau(a, \beta) = 0 \end{aligned} \quad (9.11)$$

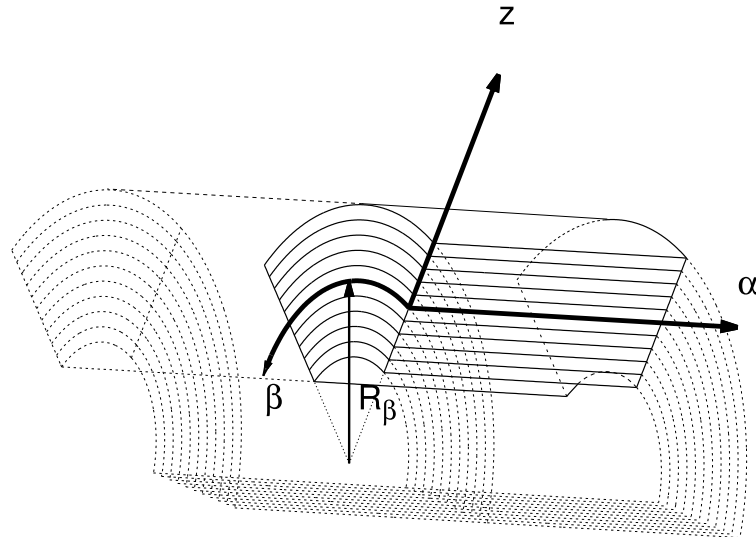


Figure 9.50: Reference system of the quarter of the composite cylindrical shell panel with symmetry condition applied.

The effect of the shell curvature on the temperature profile along the thickness of the multilayered cylindrical panel is given in Figure 9.51 for different radius to length ratios R/a . It has to be noticed that the curvature radius has no relevant influence on the approximation of the temperature load; as mentioned about the plate temperature profile discussion, the aspect ratio a/h shows the principal effect. It is preferable to use a calculated temperature profile to avoid to overestimate the temperature load.

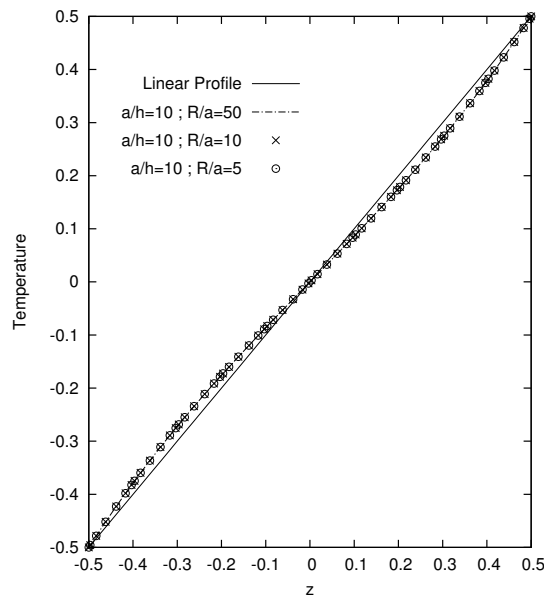


Figure 9.51: Ten-layered cylindrical shell panel. Temperature Profiles Comparison.

Different Variable Kinematic models, via the Legendre polynomials, have been used to perform the analysis of the shell structures. The acronyms have been modified adding a subscript to them, for the sake of clarity the list of subscripts is given below:

- $Case1 = \{layer1\} \{layer2, layer3, layer4, layer5, layer6, layer7, layer8, layer9\} \{layer10\}$
- $Case2 = \{layer1\} \{layer2\} \{layer3, layer4, layer5, layer6, layer7, layer8\} \{layer9\} \{layer10\}$
- $Case3 = \{layer1\} \{layer2\} \{layer3, layer4\} \{layer5, layer6\} \{layer7, layer8\} \{layer9\} \{layer10\}$

- $Case4 = \{layer1\} \{layer2, layer3\} \{layer4\} \{layer5, layer6\} \{layer7\} \{layer8, layer9\} \{layer10\}$

The results are listed in Table 9.24 for various radius to length side ratios R/a , and the degrees of freedom $DOFs$ are indicated for a quarter of the considered structure. The present FEs results are compared with an equivalent single layer model with cubic expansion in the z direction named *HOST12* [20], and with an higher order shear deformation theory named *HSDT* [22]. The transverse displacement \hat{w} and the in-plane stress $\hat{\sigma}_{\alpha\alpha}$ show small accuracy differences for the considered cases R/a , see Table 9.24, this is due to the fixed aspect ratio $a/h = 10$. The difference of the variables magnitude is due to the different description of the temperature profile, assumed linear profile for the upper part of the table results T_a and calculated solving the Fourier heat conduction equations for the lower part of the table results T_c .

The behavior of the transverse shear stress $\hat{\sigma}_{\alpha z}$ along the thickness is not simple to well describe; for example for the assumed linear temperature profile T_a , the full equivalent-single-layer model *EL4* is not able to perform the discontinuous nature of the shear stress along the thickness, see Figure 9.52a. The Variable-Kinematic model $EL4_{Case2}$ and $EL4_{Case3}$ show different level of accuracy respect to the full layer-wise solution *LW4*, meanwhile the model $EL4_{Case4}$ seems to describe well the shear stress along the thickness with small loss of accuracy in the layers with an *ESL* description and with a regardable $-29, 27\%$ $DOFs$ reduction respect to the full layer-wise solution *LW4*, see Figure 9.52b.

As already mentioned for the shear stress, the description of the transverse normal stress $\hat{\sigma}_{zz}$ is not simple to perform too. For example, for the calculated temperature profile T_c , see Figure 9.53a, the full equivalent-single-layer *EL4* model is not sufficient to correctly describe the stress profile along the thickness. Relevant improvements of the solution accuracy are shown by the Variable-Kinematic model $EL4_{Case2}$ and $EL4_{Case3}$. These Variable-Kinematic models permit to have noticeable reduction of the computational cost in terms of degrees of freedom; for example a $-29, 27\%$ $DOFs$ reduction respect to the full layer-wise solution *LW4* is obtained by the model $EL4_{Case4}$, see Figure 9.53b, with very small loss in the solution accuracy in the layers with an *ESL* description.

Table 9.24: Ten-layer composite cylindrical shell panel with lamination $[0^\circ/90^\circ]_5$. Mechanical variables described by Mono-models and Variable kinematic models for various radius to length side ratios R/a . Evaluation position for transverse displacement $\hat{w}(x, y, z) = \hat{w}(a/2, b/2, 0)$, in-plane stress $\hat{\sigma}_{\alpha\alpha}(x, y, z) = \hat{\sigma}_{\alpha\alpha}(a/2, b/2, +h/2)$, transverse shear stress $\hat{\sigma}_{\alpha z}(x, y, z) = 10 \times \hat{\sigma}_{\alpha z}(a, b/2, +\frac{2}{5}h)$, transverse normal stress $\hat{\sigma}_{zz}(x, y, z) = 10^2 \times \hat{\sigma}_{zz}(a/2, b/2, 0)$.

T_a (Assumed Linear)									
	$R/a = 50$				$R/a = 5$				$DOFs$
	\hat{w}	$\hat{\sigma}_{\alpha\alpha}$	$\hat{\sigma}_{\alpha z}$	$\hat{\sigma}_{zz}$	\hat{w}	$\hat{\sigma}_{\alpha\alpha}$	$\hat{\sigma}_{\alpha z}$	$\hat{\sigma}_{zz}$	
<i>HOST12</i> [20]	1.0325	-	-	-	1.0224	-	-	-	
<i>HSDT</i> [22]	1.0332	-	-	-	1.0216	-	-	-	
<i>LW4</i>	1.0306	-0.9823	0.1368	0.0263	1.0207	-0.9789	0.1651	0.2817	133947
<i>LW1</i>	1.0306	-1.0023	0.0188	8.0403	1.0207	-0.9990	0.0448	8.3176	35937
<i>EL3Z</i>	1.0302	-0.9825	0.1123	0.0190	1.0205	-0.9792	0.1226	0.2852	16335
<i>EL4</i>	1.0301	-0.9827	0.1064	0.0038	1.0210	-0.9794	0.1383	0.2660	16335
<i>EL3</i>	1.0301	-0.9825	0.1079	0.0037	1.0210	-0.9792	0.1386	0.2660	13068
<i>EL2</i>	1.0271	-0.9851	-0.0207	-0.0037	1.0186	-0.9810	0.0275	0.1826	9801
<i>EL1</i>	1.0656	-1.1649	0.0016	0.0162	1.0575	-1.1611	0.0481	0.4828	6534
<i>EL4_{Case 1}</i>	1.0303	-0.9825	0.0974	0.0033	1.0211	-0.9790	0.1116	0.2677	42471
<i>EL4_{Case 2}</i>	1.0304	-0.9824	0.1369	0.0042	1.0211	-0.9789	0.1651	0.2669	68607
<i>EL4_{Case 3}</i>	1.0306	-0.9823	0.1368	0.0042	1.0208	-0.9789	0.1651	0.2650	94743
<i>EL4_{Case 4}</i>	1.0306	-0.9823	0.1500	0.0043	1.0208	-0.9789	0.1883	0.2651	94743
<i>EL1_{Case 1}</i>	1.0499	-0.9934	0.0050	0.0108	1.0413	-0.9899	0.0577	0.4065	13068
<i>EL1_{Case 2}</i>	1.0402	-0.9990	0.0075	0.0101	1.0311	-0.9956	0.0337	0.3525	19602
<i>EL1_{Case 3}</i>	1.0314	-1.0023	0.0190	0.0048	1.0222	-0.9989	0.0451	0.2773	26136
<i>EL1_{Case 4}</i>	1.0315	-1.0019	0.0111	0.0049	1.0222	-0.9985	0.0555	0.2766	26136

T_c (Calculated via Fourier Heat conduction Law)									
	$R/a = 50$				$R/a = 5$				$DOFs$
	\hat{w}	$\hat{\sigma}_{\alpha\alpha}$	$\hat{\sigma}_{\alpha z}$	$\hat{\sigma}_{zz}$	\hat{w}	$\hat{\sigma}_{\alpha\alpha}$	$\hat{\sigma}_{\alpha z}$	$\hat{\sigma}_{zz}$	
<i>LW4</i>	0.9706	-1.0226	0.1443	0.0198	0.9613	-1.0194	0.1708	0.2155	133947
<i>LW1</i>	0.9707	-1.0498	0.0343	6.6928	0.9613	-1.0465	0.0588	6.9191	35937
<i>EL3Z</i>	0.9698	-1.0377	0.1231	0.6375	0.9606	-1.0344	0.1329	0.8491	16335
<i>EL4</i>	0.9699	-1.0231	0.1288	0.0141	0.9613	-1.0198	0.1587	0.2372	16335
<i>EL3</i>	0.9697	-1.0388	0.1198	0.0137	0.9611	-1.0355	0.1489	0.2223	13068
<i>EL2</i>	0.9654	-1.0428	-0.0702	0.0105	0.9573	-1.0388	-0.0246	0.1826	9801
<i>EL1</i>	1.0018	-1.2114	0.0015	0.0311	0.9941	-1.2078	0.0451	0.4673	6534
<i>EL4_{Case 1}</i>	0.9698	-1.0228	0.1254	0.0130	0.9611	-1.0195	0.1386	0.2269	42471
<i>EL4_{Case 2}</i>	0.9698	-1.0228	0.1444	0.0130	0.9610	-1.0195	0.1709	0.2197	68607
<i>EL4_{Case 3}</i>	0.9705	-1.0226	0.1443	0.0112	0.9613	-1.0194	0.1709	0.2128	94743
<i>EL4_{Case 4}</i>	0.9706	-1.0226	0.1582	0.0113	0.9613	-1.0194	0.1942	0.2130	94743
<i>EL1_{Case 1}</i>	0.9869	-1.0420	-0.0098	0.0247	0.9787	-1.0386	0.0398	0.3828	13068
<i>EL1_{Case 2}</i>	0.9780	-1.0471	0.0249	0.0212	0.9694	-1.0438	0.0494	0.3176	19602
<i>EL1_{Case 3}</i>	0.9705	-1.0500	0.0349	0.0133	0.9618	-1.0467	0.0594	0.2287	26136
<i>EL1_{Case 4}</i>	0.9712	-1.0494	0.0185	0.0145	0.9624	-1.0461	0.0603	0.2287	26136

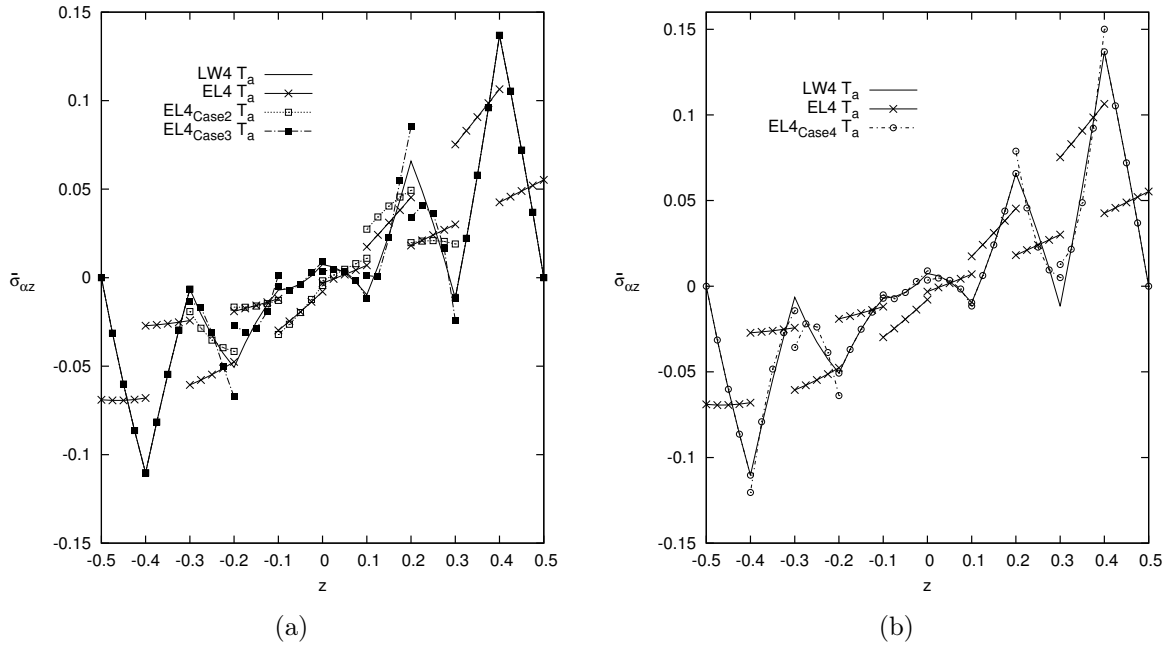


Figure 9.52: Ten-layered cylindrical shell panel $R/a = 50$, transverse shear stress $\hat{\sigma}_{\alpha z}$, T_a assumed linear.

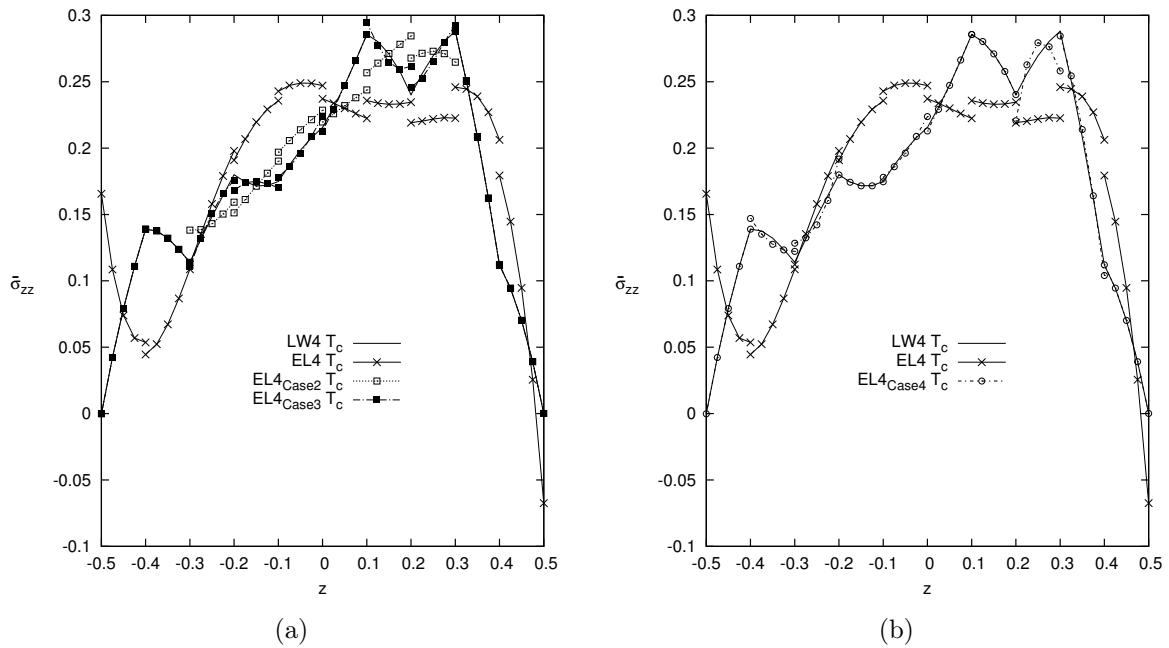


Figure 9.53: Ten-layered cylindrical shell panel $R/a = 5$, transverse normal stress $\hat{\sigma}_{zz}$, T_c calculate via Fourier heat conduction law.

9.3.3 Sandwich composite spherical panel

A sandwich spherical shell panel with cross-ply composite skins with lamination $[0^\circ/90^\circ/\text{Core}/90^\circ/0^\circ]$ and simply-supported boundary condition is considered. The physical properties of the sandwich spherical panel are taken from [20, 100]. The material constants of the Carbon-Epoxy skins are: $E_1 = 172,37 \text{ GPa}$; $E_2 = E_3 = 6,89 \text{ GPa}$; $G_{12} = G_{13} = 3,45 \text{ GPa}$; $G_{23} = 1,38 \text{ GPa}$; $\nu_{12} = \nu_{13} = \nu_{23} = 0,25$; $\alpha_1 = \alpha_3 = 0,1 \times 10^{-5} \frac{1}{^\circ\text{C}}$; $\alpha_2 = 2,0 \times 10^{-5} \frac{1}{^\circ\text{C}}$; $\mathcal{K}_1 = 36,42 \text{ W}/(m^\circ\text{C})$; $\mathcal{K}_2 = \mathcal{K}_3 = 0,96 \text{ W}/(m^\circ\text{C})$. The mate-

rial properties of the Honeycomb soft core are: $E_1 = E_2 = 0,28 \text{ GPa}$; $E_3 = 3,45 \text{ GPa}$; $G_{12} = 0,11 \text{ GPa}$; $G_{13} = G_{23} = 0,41 \text{ GPa}$; $\nu_{12} = \nu_{13} = \nu_{23} = 0,02$; $\alpha_1 = \alpha_3 = 0,1 \times 10^{-6} \frac{1}{^\circ\text{C}}$; $\alpha_2 = 2,0 \times 10^{-6} \frac{1}{^\circ\text{C}}$; $\mathcal{K}_1 = 3,642 \text{ W}/(m^\circ\text{C})$; $\mathcal{K}_2 = \mathcal{K}_3 = 0,096 \text{ W}/(m^\circ\text{C})$. The geometrical dimensions are: $a = b = 1,0$; the core thickness is $h_{core} = 0,8 \times h_{total}$ and each skin is $h_{skin} = 0,05 \times h_{total}$. The temperature boundary conditions are: $\hat{\theta}_{top} = +0,5$, $\hat{\theta}_{bottom} = -0,5$. The results are presented for different radius to length side ratios $R/a = 5; 20$ and different aspect ratios $a/h = 4; 100$. The deflections and stresses are presented in the following dimensionless forms:

$$\hat{w} = \frac{w}{\alpha_1 \theta_1 b^2} \quad \hat{\sigma}_{i,j} = \frac{\sigma_{i,j}}{E_2 \alpha_1 \theta_1}$$

where $\theta_1 = 1$, E_2 and α_1 are the properties of the composite skins. The adopted mesh is the same of the previous numerical example. Due to the symmetry of both the geometry and load, a quarter of the spherical shell panel is analyzed, see Figure 9.54, with a corresponding mesh grid of 16×16 elements. The corresponding thermal load and boundary conditions are the same of previous numerical example.

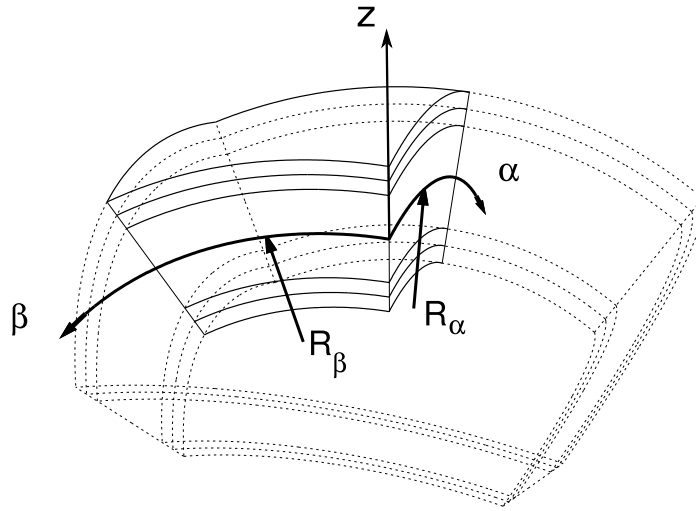


Figure 9.54: Reference system of the quarter of the sandwich spherical shell panel with symmetry condition applied.

The description of the temperature profile along the thickness of the sandwich spherical panel is discussed for different radius to length ratios R/a and aspect ratios a/h . It has to be noticed that for thin shells, see Figure 9.55a, the calculated temperature profile is far from the linear one, and differently from the previous numerical example the linear profile is underestimating the temperature load. For thick shells, see Figure 9.55b, the calculated profile has a non-linear behavior along the thickness direction, the linear profile is both underestimating and overestimating the temperature load in different part of the multilayered structure. Looking at the results of the thick sandwich spherical shells, the global effect is that the linear profile is underestimating the temperature load. For both the thin and thick shells the radius to length ratios R/a is not showing any relevant effect on the calculated temperature profiles.

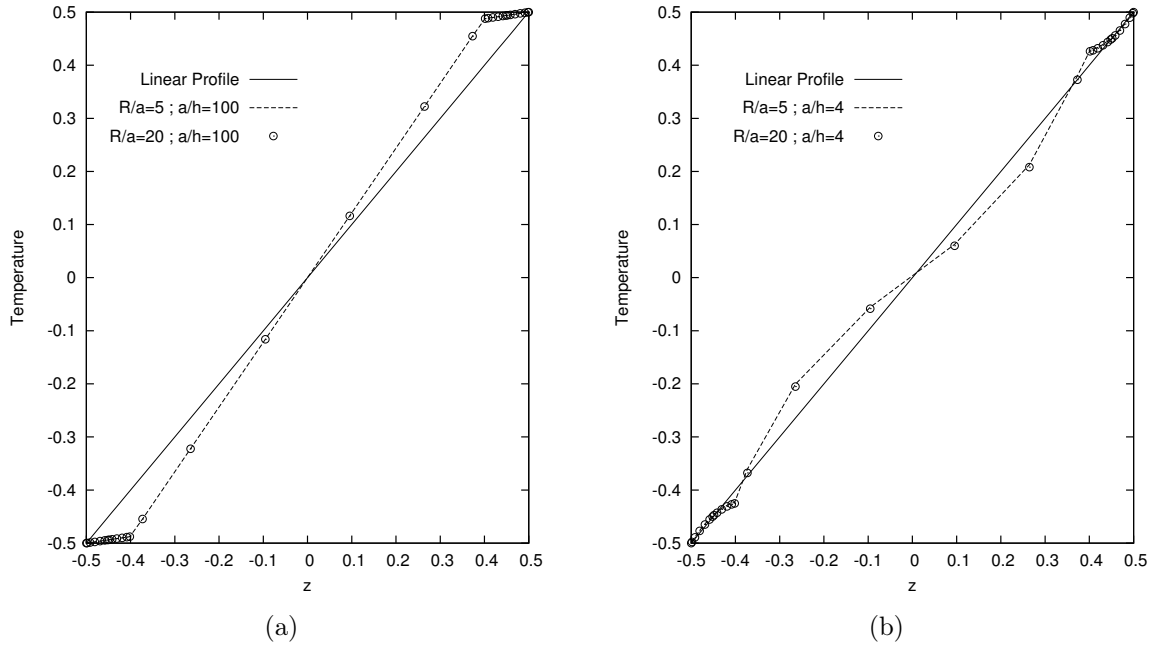


Figure 9.55: Five-layered sandwich spherical shell panel. Temperature Profiles Comparison. $a/h = 100$ (a), $a/h = 4$ (b)

Different Variable Kinematic models, via the Legendre polynomials, have been used to perform the analysis of the shell structures. The acronyms have been modified adding a subscript to them, for the sake of clarity the list of subscripts is given below:

- $Case1 = \{layer1\} \{layer2, layer3, layer4\} \{layer5\}$
- $Case2 = \{layer1, layer2\} \{layer3, layer4, layer5\}$
- $Case3 = \{layer1, layer2\} \{layer3\} \{layer4, layer5\}$

The results are listed in Table 9.25 with a temperature profile assumed linear T_a for various radius to length side ratios R/a and various aspect ratios a/h , and the degrees of freedom $DOFs$ are indicated for a quarter of the considered structure. The present FEs results are compared with an equivalent single layer model with cubic expansion in the z direction named $HOST12$ [20], and with two analytical models, a layer-wise theory of the fourth order named $LW4_a$ [100] and an equivalent-single-layer theory of the fourth order with Taylor polynomials named $ET4_a$ [100]. Therefore the temperature profile calculated solving the Fourier heat conduction equations T_c is evaluated and the results are presented in Table 9.26 for various radius to length side ratios R/a and various aspect ratios a/h . The following considerations can be drawn:

- Regarding the transverse displacement w , for thin plates $a/h = 100$, the theories $EL4_{Case1}$ and $EL4_{Case2}$ lead an improvement of the solution respect to the $EL4$, and the model $EL4_{Case3}$ show the same accuracy of the full layer-wise solution $LW4$ with a reduction of $-38,1\%$ $DOFs$ respect the $LW4$ theory, see Figure 9.56a. The same comments can be drawn for both the temperature assumed linear cases T_a and for the temperature calculated via the Fourier heat conduction law T_c . For thick plates $a/h = 2$, the description of the transverse displacement is well drawn only by $EL4_{Case3}$ that show an accuracy very close to the full layer-wise solution $LW4$, see Figure 9.56b.
- For the in-plane stress $\sigma_{\alpha\alpha}$ no relevant differences can be appreciated between all the presented models.

- Regarding the transverse shear stress $\sigma_{\alpha z}$, the variable kinematic model $EL4,Case1$ improves the results respect to the $EL4$ theory only in the layer with a layer-wise description, see Figure 9.57a. The theories $EL4,Case3$ can improve the results along the whole thickness with some errors in the description of the composite skins, see Figure 9.57b.
- For the transverse normal stress σ_{zz} , the variable kinematic model $EL4,Case1$ improves the results respect to the $EL4$ theory only in the layer with a layer-wise description, see Figure 9.58a. The theories $EL4,Case3$ has the same accuracy of the full layer-wise solution along the whole thickness of the spherical sandwich panel, see Figure 9.58b.

Table 9.25: Five-layer sandwich spherical shell panel with lamination $[0^\circ/90^\circ/Core/90^\circ/0^\circ]$. Mechanical variables described by Mono-models and Variable kinematic models for various radius to length side ratios R/a and various aspect ratios a/h . Evaluation position for transverse displacement $\hat{w}(x, y, z) = \hat{w}(a/2, b/2, 0)$, in-plane stress $\hat{\sigma}_{\alpha\alpha}(x, y, z) = \hat{\sigma}_{\alpha\alpha}(a/2, b/2, +h/2)$, transverse shear stress $\hat{\sigma}_{\alpha z}(x, y, z) = 10 \times \hat{\sigma}_{\alpha z}(a, b/2, +\frac{9}{20}h)$, transverse normal stress $\hat{\sigma}_{zz}(x, y, z) = 10^2 \times \hat{\sigma}_{zz}(a/2, b/2, 0)$. The temperature profile is assumed linear T_a .

$a/h = 100$									
	$R/a = 20$				$R/a = 5$				$DOFs$
	\hat{w}	$\hat{\sigma}_{\alpha\alpha}$	$\hat{\sigma}_{\alpha z}$	$\hat{\sigma}_{zz}$	\hat{w}	$\hat{\sigma}_{\alpha\alpha}$	$\hat{\sigma}_{\alpha z}$	$\hat{\sigma}_{zz}$	
<i>HOST12</i> [20]	1.6614	-	-	-	0.7332	-	-	-	
<i>LW4</i>	1.6296	6.9442	-0.1049	0.0165	0.7178	-3.1483	0.0603	0.2818	68607
<i>LW1</i>	1.6298	6.9005	-0.0431	0.0172	0.7179	-3.1968	0.0419	0.2837	19602
<i>EL3Z</i>	1.6619	7.0796	-0.0209	0.3365	0.7333	-3.2259	0.2987	0.8667	16335
<i>EL4</i>	1.6387	7.2355	-0.0405	0.3199	0.7223	-2.8967	0.3029	0.8617	16335
<i>EL3</i>	1.6620	7.0788	-0.0424	0.3135	0.7334	-3.2272	0.3057	0.8269	13068
<i>EL2</i>	1.6623	7.0792	-0.0015	-0.5764	0.7349	-3.2468	0.7680	-0.8356	9801
<i>EL1</i>	1.7362	7.4627	0.0282	-0.5819	0.7711	-3.3300	0.8482	-0.7890	6534
<i>EL4_{Case 1}</i>	1.6378	7.0512	-0.1065	0.2951	0.7219	-3.0907	0.0596	0.8051	42471
<i>EL4_{Case 2}</i>	1.6345	6.9486	-0.1335	6.8462	0.7195	-3.1891	0.1277	7.7908	29403
<i>EL4_{Case 3}</i>	1.6296	6.9443	-0.1335	0.0165	0.7178	-3.1483	0.1265	0.2819	42471
<i>EL1_{Case 1}</i>	1.6775	7.5348	-0.0480	-0.3343	0.7418	-2.8316	0.0394	-0.3409	13068
<i>EL1_{Case 2}</i>	1.6696	6.9080	-0.0639	-26.156	0.7337	-3.5591	0.1289	-28.658	9801
<i>EL1_{Case 3}</i>	1.6301	6.8592	-0.0639	0.0172	0.7181	-3.2449	0.1224	0.2837	13068

$a/h = 4$									
	$R/a = 20$				$R/a = 5$				$DOFs$
	\hat{w}	$\hat{\sigma}_{\alpha\alpha}$	$\hat{\sigma}_{\alpha z}$	$\hat{\sigma}_{zz}$	\hat{w}	$\hat{\sigma}_{\alpha\alpha}$	$\hat{\sigma}_{\alpha z}$	$\hat{\sigma}_{zz}$	
<i>HOST12</i> [20]	1.7959	-	-	-	1.7738	-	-	-	
<i>LW4_a</i> [100]	1.8259	-	-	-	1.8059	-	-	-	
<i>ET4_a</i> [100]	1.8370	-	-	-	1.8125	-	-	-	
<i>LW4</i>	1.8254	6.5416	-2.7197	0.1938	1.8052	6.6884	-2.6941	0.7940	68607
<i>LW1</i>	1.8241	6.4558	-1.1339	0.2070	1.8038	6.6040	-1.1245	0.8482	19602
<i>EL3Z</i>	1.7897	6.6392	-1.0356	-0.0284	1.7700	6.7748	-1.0097	-0.0901	16335
<i>EL4</i>	1.8371	6.7068	-1.5927	0.2405	1.8184	6.8654	-1.5633	0.9855	16335
<i>EL3</i>	1.7954	6.6231	-1.6543	-0.0264	1.7759	6.7600	-1.6257	-0.0820	13068
<i>EL2</i>	1.6641	6.2299	-1.1041	0.1285	1.6548	6.3836	-1.0617	0.5291	9801
<i>EL1</i>	1.9033	6.5229	-0.7331	0.5996	1.8922	6.6269	-0.7111	2.4134	6534
<i>EL4_{Case 1}</i>	1.8503	6.6151	-2.7443	0.2290	1.8314	6.7656	-2.7192	0.9378	42471
<i>EL4_{Case 2}</i>	1.8408	6.5387	-3.5575	6.8849	1.8224	6.6884	-3.5236	7.6024	29403
<i>EL4_{Case 3}</i>	1.8236	6.5457	-3.5647	0.1936	1.8034	6.6922	-3.5297	0.7932	42471
<i>EL1_{Case 1}</i>	1.8601	6.7508	-1.2004	0.4221	1.8458	6.9087	-1.1911	1.7059	13068
<i>EL1_{Case 2}</i>	1.7971	6.0653	-1.7360	-24.504	1.7960	6.2311	-1.7219	-23.352	9801
<i>EL1_{Case 3}</i>	1.8109	6.3652	-1.8325	0.2061	1.7910	6.5116	-1.8116	0.8445	13068

Table 9.26: Five-layer sandwich spherical shell panel with lamination $[0^\circ/90^\circ/Core/90^\circ/0^\circ]$. Mechanical variables described by Mono-models and Variable kinematic models for various radius to length side ratios R/a and various aspect ratios a/h . Evaluation position for transverse displacement $\hat{w}(x, y, z) = \hat{w}(a/2, b/2, 0)$, in-plane stress $\hat{\sigma}_{\alpha\alpha}(x, y, z) = \hat{\sigma}_{\alpha\alpha}(a/2, b/2, +h/2)$, transverse shear stress $\hat{\sigma}_{\alpha z}(x, y, z) = 10 \times \hat{\sigma}_{\alpha z}(a, b/2, +\frac{9}{20}h)$, transverse normal stress $\hat{\sigma}_{zz}(x, y, z) = 10^2 \times \hat{\sigma}_{zz}(a/2, b/2, 0)$. The temperature profile is calculated via Fourier heat conduction equation T_c .

$a/h = 100$									
	$R/a = 20$				$R/a = 5$				$DOFs$
	\hat{w}	$\hat{\sigma}_{\alpha\alpha}$	$\hat{\sigma}_{\alpha z}$	$\hat{\sigma}_{zz}$	\hat{w}	$\hat{\sigma}_{\alpha\alpha}$	$\hat{\sigma}_{\alpha z}$	$\hat{\sigma}_{zz}$	
<i>LW4</i>	1.7822	9.0011	-0.1253	0.0185	0.7850	-2.0364	0.0553	0.3101	68607
<i>LW1</i>	1.7823	9.0037	-0.0550	0.0193	0.7850	-2.0383	0.0379	0.3123	19602
<i>EL3Z</i>	1.8174	9.2487	-0.0317	0.3689	0.8019	-2.0210	0.3178	0.9518	16335
<i>EL4</i>	1.7932	9.4104	-0.0564	0.3509	0.7905	-1.6778	0.3194	0.9461	16335
<i>EL3</i>	1.8174	9.2478	-0.0584	0.3442	0.8020	-2.0224	0.3223	0.9098	13068
<i>EL2</i>	1.8178	9.2492	-0.0167	-0.6303	0.8036	-2.0431	0.8248	-0.9137	9801
<i>EL1</i>	1.8987	9.6691	0.0158	-0.6364	0.8433	-2.1342	0.9125	-0.8628	6534
<i>EL4_{Case 1}</i>	1.7919	9.1278	-0.1272	0.3235	0.7898	-1.9682	0.0544	0.8835	42471
<i>EL4_{Case 2}</i>	1.7879	9.0075	-0.1632	7.3768	0.7870	-2.0835	0.1225	8.4112	29403
<i>EL4_{Case 3}</i>	1.7822	9.0011	-0.1633	0.0185	0.7850	-2.0364	0.1211	0.3101	42471
<i>EL1_{Case 1}</i>	1.8379	9.7435	-0.0607	-0.3653	0.8128	-1.6140	0.0350	-0.3695	13068
<i>EL1_{Case 2}</i>	1.8256	9.0597	-0.0814	-28.720	0.8023	-2.3859	0.1295	-31.455	9801
<i>EL1_{Case 3}</i>	1.7822	9.0053	-0.0813	0.0193	0.7851	-2.0416	0.1224	0.3123	13068

$a/h = 4$									
	$R/a = 20$				$R/a = 5$				$DOFs$
	\hat{w}	$\hat{\sigma}_{\alpha\alpha}$	$\hat{\sigma}_{\alpha z}$	$\hat{\sigma}_{zz}$	\hat{w}	$\hat{\sigma}_{\alpha\alpha}$	$\hat{\sigma}_{\alpha z}$	$\hat{\sigma}_{zz}$	
<i>LW4</i>	1.8301	6.6442	-2.7929	0.1954	1.8102	6.8325	-2.7774	0.7999	68607
<i>LW1</i>	1.8278	6.5515	-1.1718	0.2127	1.8078	6.7420	-1.1679	0.8704	19602
<i>EL3Z</i>	1.7951	6.7499	-1.0524	-0.0426	1.7756	6.9282	-1.0335	-0.1473	16335
<i>EL4</i>	1.8426	6.8165	-1.6421	0.2351	1.8242	7.0193	-1.6195	0.9630	16335
<i>EL3</i>	1.8010	6.7329	-1.7036	-0.0317	1.7817	6.9141	-1.6818	-0.1037	13068
<i>EL2</i>	1.6760	6.3515	-1.1377	0.1692	1.6667	6.5495	-1.1031	0.6915	9801
<i>EL1</i>	1.9164	6.6461	-0.7640	0.6424	1.9053	6.7943	-0.7475	2.5840	6534
<i>EL4_{Case 1}</i>	1.8572	6.7241	-2.8195	0.2096	1.8385	6.9166	-2.8046	0.8598	42471
<i>EL4_{Case 2}</i>	1.8457	6.6422	-3.6752	6.8694	1.8276	6.8335	-3.6549	7.5752	29403
<i>EL4_{Case 3}</i>	1.8282	6.6485	-3.6822	0.1952	1.8083	6.8365	-3.6608	0.7991	42471
<i>EL1_{Case 1}</i>	1.8723	6.8700	-1.2427	0.4647	1.8580	7.0716	-1.2390	1.8761	13068
<i>EL1_{Case 2}</i>	1.8064	6.1758	-1.8030	-24.714	1.8053	6.3862	-1.7970	-23.479	9801
<i>EL1_{Case 3}</i>	1.8135	6.4685	-1.8977	0.2119	1.7940	6.6587	-1.8846	0.8669	13068

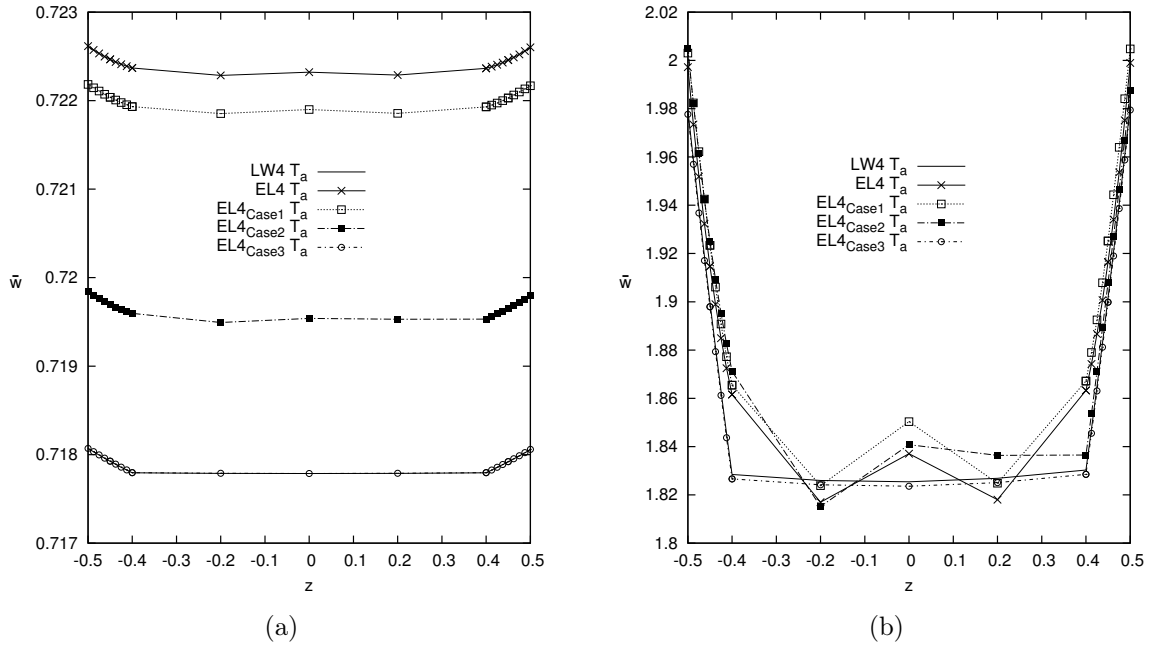


Figure 9.56: Five-layered sandwich spherical panel transverse displacement \hat{w} with an assumed linear temperature profile T_a , $R/a = 5$ and $a/h = 100$ (a), $R/a = 20$ and $a/h = 4$ (b)

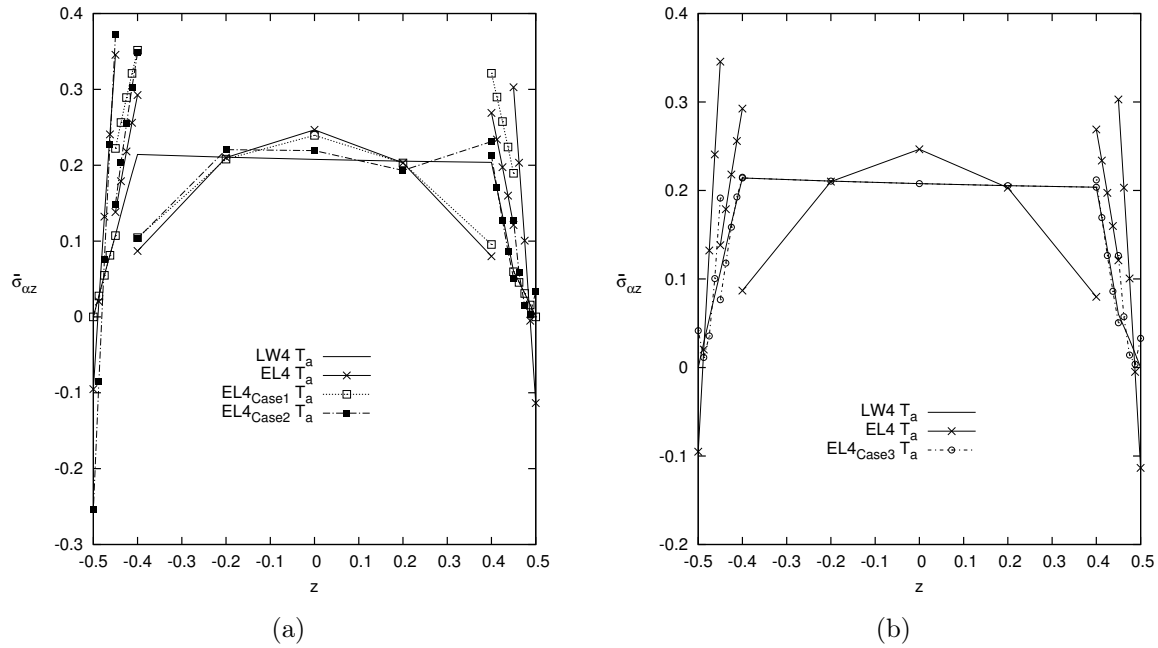


Figure 9.57: Five-layered sandwich spherical panel transverse shear stress $\hat{\sigma}_{\alpha z}$ with an assumed linear temperature profile T_a , $R/a = 5$ and $a/h = 100$.

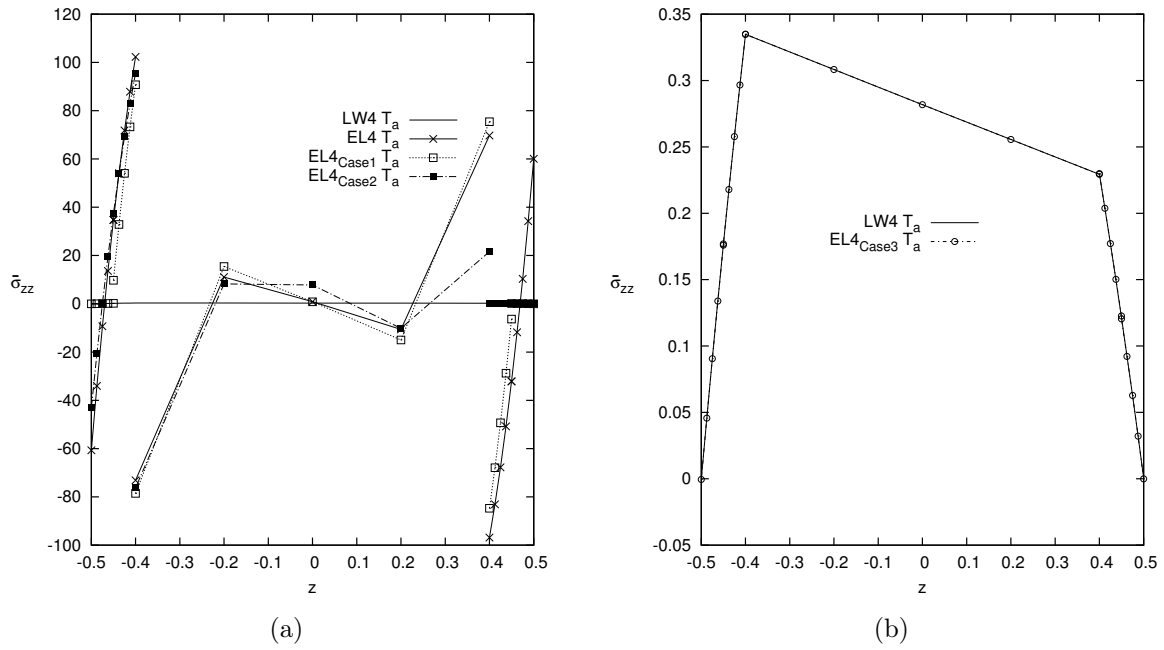


Figure 9.58: Five-layered sandwich spherical panel transverse normal stress $\hat{\sigma}_{zz}$ with an assumed linear temperature profile T_a , $R/a = 5$ and $a/h = 100$.

9.4 Electro-Mechanical Analysis Results

In this section, the static electro-mechanical analysis of plate and shell structures are performed to assess the variable-kinematics mixed ESL/LW plate/shell element. To study the effectiveness of the proposed approach some reference problems were considered. The following composite multilayered plates and shell with piezoelectric skins have been analyzed:

- A four-layer square plate with a cross-ply composite core $[0^\circ/90^\circ]$ and piezoelectric external skins
- A three-layer cylindrical shell with a composite core and piezoelectric external skins
- A four-layer cylindrical shell with a cross-ply composite core $[90^\circ/0^\circ]$ and piezoelectric external skins

Wherever possible, solutions from variable-kinematic models are compared with those from higher-order ESL models, LW models, and analytical results.

9.4.1 Four-layer plate

A four-layer cross-ply square plate, see Figure 9.59, with a cross-ply Gr/Ep composite core $[0^\circ/90^\circ]$ and PZT-4 piezoelectric external skins, simply-supported boundary condition is considered. The static analysis of the plate structure is evaluated in sensor and actuator configuration.

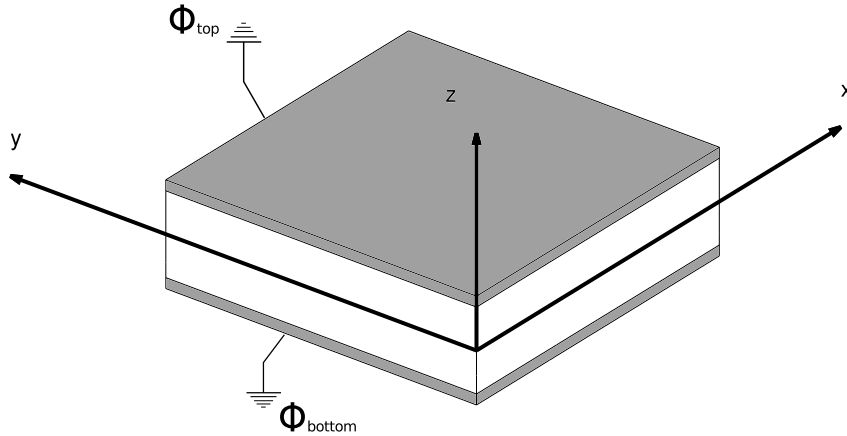


Figure 9.59: Reference system of the composite plate with piezoelectric skins.

For the sensor case, a bi-sinusoidal transverse normal pressure is applied to the top surface of the plate:

$$p(x, y, z_{top}) = p_z^o \sin(m\pi x/a) \sin(n\pi y/b) \quad (9.12)$$

with amplitude $p_z^o = 1$ and wave numbers $m = 1$, $n = 1$. The potential at top and bottom position is imposed $\Phi_t = \Phi_b = 0$.

For the actuator case, a bi-sinusoidal electric potential is imposed at top surface:

$$\Phi(x, y, z_{top}) = \phi_z^o \sin(m\pi x/a) \sin(n\pi y/b) \quad (9.13)$$

with amplitude $\phi_z^o = 1$ and wave numbers $m = 1$, $n = 1$. The potential at bottom position is imposed $\Phi_b = 0$. No mechanical load is applied.

In respect to the total thickness, a single piezoelectric skin is thick $h_p = 0.1h_{tot}$, while the

single core layer is thick $h_c = 0.4h_{tot}$. The material properties of the plate are given in Table 9.27.

Table 9.27: Material data for multilayered plate and shell.

Properties	PZT-4	Gr/EP
E_{11} [GPa]	81.3	132.38
E_{22} [GPa]	81.3	10.756
E_{33} [GPa]	64.5	10.756
ν_{12} [-]	0.329	0.24
ν_{13} [-]	0.432	0.24
ν_{23} [-]	0.432	0.49
G_{12} [GPa]	30.6	5.6537
G_{13} [GPa]	25.6	5.6537
G_{23} [GPa]	25.6	3.606
e_{15} [C/m ²]	12.72	0
e_{24} [C/m ²]	12.72	0
e_{31} [C/m ²]	-5.20	0
e_{32} [C/m ²]	-5.20	0
e_{33} [C/m ²]	15.08	0
$\tilde{\epsilon}_{11}/\epsilon_0$ [-]	1475	3.5
$\tilde{\epsilon}_{22}/\epsilon_0$ [-]	1475	3.0
$\tilde{\epsilon}_{33}/\epsilon_0$ [-]	1300	3.0
ϵ_0 [C/Vm]	$8.85 * 10^{-12}$	$8.85 * 10^{-12}$

The results are calculated for different thickness ratios $a/h = 2, 100$, and they are evaluated in the following positions with the following form for the sensor cases:

$$\begin{aligned} \hat{w}(x, y, z) &= w(a/2, b/2, 0) * 10^{11} & , & & \hat{\sigma}_{xx}(x, y, z) &= \sigma_{xx}(a/2, b/2, +h/2) \\ \hat{\sigma}_{xz}(x, y, z) &= \sigma_{xz}(a, b/2, 0) & , & & \hat{\sigma}_{zz}(x, y, z) &= \sigma_{zz}(a/2, b/2, +h/2) \\ \hat{\Phi}(x, y, z) &= \Phi(a/2, b/2, 0) * 10^3 & , & & \hat{\mathcal{D}}_z(x, y, z) &= \mathcal{D}_z(a/2, b/2, +h/2) * 10^9 \end{aligned}$$

For the actuator cases the variables are evaluated in the same way as the sensor cases, except for the electric potential:

$$\hat{\Phi}(x, y, z) = \Phi(a/2, b/2, 0)$$

First, a convergence study on the plate element was performed. A composite plate with thickness ratios $a/h = 100$ is evaluated. For the sensor case a mesh grid of 40×40 elements ensures the convergence of both the mechanical and electrical variables except for the transverse electric displacement \mathcal{D}_z that has a very slow convergence rate. For the actuator case a mesh grid of 24×24 elements ensures the convergence for all the variables, see Table 9.28.

Table 9.28: Convergence study. Composite four layered plate with thickness ratio $a/h = 100$.

Sensor Case												
Mesh	4×4	8×8	12×12	16×16	20×20	24×24	28×28	32×32	36×36	40×40	Analytical [46]	
LW4	\hat{w}	4678433	4675324	4675148	4675117	4675109	4675106	4675104	4675104	4675104	4675103	4675300
	$\hat{\sigma}_{xx}$	3302.4	3182.6	3160.1	3152.3	3148.7	3146.7	3145.5	3144.7	3144.2	3143.8	3142.1
	$\hat{\sigma}_{xz}$	-20.154	-19.167	-18.975	-18.909	-18.879	-18.863	-18.854	-18.849	-18.845	-18.842	-18.832
	$\hat{\sigma}_{zz}$	18.210	2.306	1.284	1.101	1.047	1.025	1.015	1.009	1.006	1.003	-
	$\hat{\Phi}$	4780.7	4636.5	4605.7	4594.6	4589.5	4586.7	4585.1	4584.1	4583.5	4583.0	4580.2
	\hat{D}_z	-1.2691	-0.1006	-0.0307	-0.0193	-0.0165	-0.0154	-0.0149	-0.0144	-0.0140	-0.0136	0.0136
Actuator Case												
Mesh	4×4	8×8	12×12	16×16	20×20	24×24					Analytical [46]	
LW4	\hat{w}	-1.3486	-1.3492	-1.3493	-1.3493	-1.3493	-1.3493					-1.3493
	$\hat{\sigma}_{xx}$	-0.0238	-0.0244	-0.0245	-0.0245	-0.0246	-0.0246					-0.0246
	$\hat{\sigma}_{xz}$	0.0000	0.0000	0.0000	0.0000	0.0000	0.0000					0.0000
	$\hat{\sigma}_{zz}$	0.0002	0.0000	0.0000	0.0000	0.0000	0.0000					-
	$\hat{\Phi}$	0.4999	0.4999	0.4999	0.4999	0.4999	0.4999					0.4999
	\hat{D}_z	-0.0370	-0.0370	-0.0370	-0.0370	-0.0370	-0.0370					-0.0370

Therefore a locking study has been performed evaluating different types of integration methods [115] for the same plate structure to prove that the element is locking free, see Table 9.29. The plate element with the MITC9 method ensures accuracy on both the transverse displacement and the shear stress.

Table 9.29: Locking study. Composite four layered plate with thickness ratio $a/h = 100$. The Sensor cases are computed with a mesh of 40×40 elements, the Actuator cases are computed with a mesh of 24×24 elements.

Sensor Case					Actuator Case				
	Reduced	Selective	MITC9	Analytical [46]	Reduced	Selective	MITC9	Analytical [46]	
LW4	\hat{w}	4675103	4675003	4675103	4675300	-1.3493	-1.3496	-1.3493	-1.3493
	$\hat{\sigma}_{xz}$	-23.096	-22.018	-18.842	-18.832	0.0000	0.0000	0.0000	0.0000
	$\hat{\Phi}$	4581.9	4582.7	4583.0	4580.2	0.4999	0.4999	0.4999	0.4999
	\hat{D}_z	-0.1511	0.0340	-0.0136	0.0136	-0.0366	-0.0370	-0.0370	-0.0370

An assessment of the Legendre polynomials with a full ESL approach has been performed for the pure mechanical case in [158] for plates and in [159] for shells. All the results presented in [158, 159], for thick and thin plates and shells, show that the Legendre polynomials lead to the same results of the Taylor polynomials. The use of either polynomial is invariant respect to the solution accuracy.

Hereafter Legendre polynomials have been employed for the structure analyzes. Different Variable Kinematic models have been used to perform the analysis of the plate structures, see Figure 9.60. The acronyms have been modified adding a subscript to them, for the sake of clarity the list of subscripts is given below:

- $Case1 = \{layer1\} \{layer2, layer3, layer4\}$
- $Case2 = \{layer1, layer2, layer3\} \{layer4\}$
- $Case3 = \{layer1\} \{layer2, layer3\} \{layer4\}$

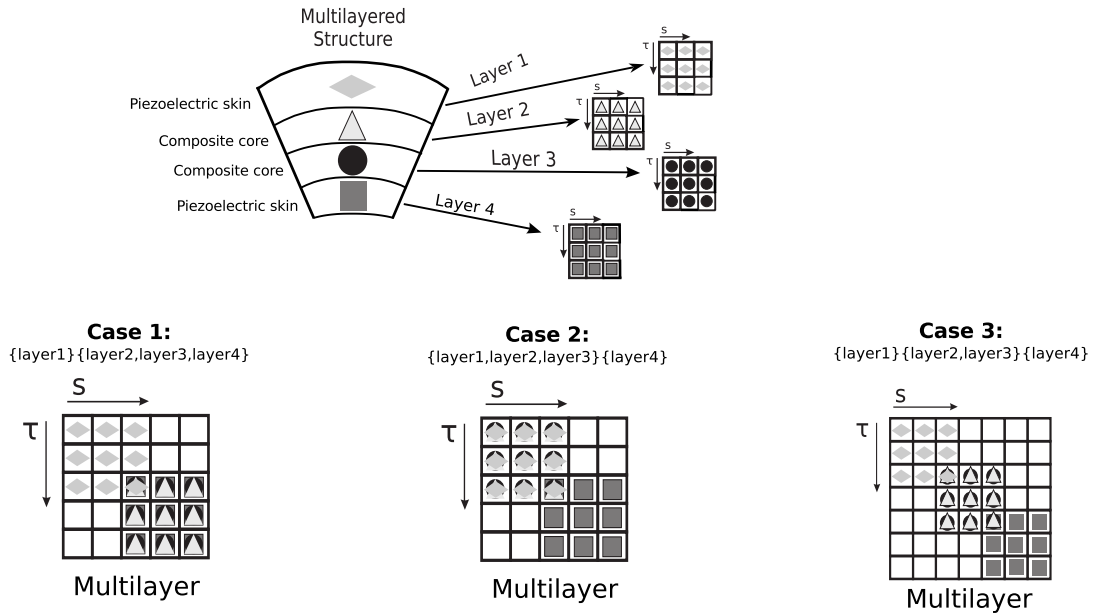


Figure 9.60: Variable Kinematic Cases. Compact example of assembling scheme.

The results are listed in Table 9.30 for the sensor case, and in Table 9.31 for the actuator case. For the plate structures analysed the following considerations can be drawn for the sensor cases:

- Regarding the transverse displacement w , for thin plates $a/h = 100$, the theories $EL4_{,Case1}$, $EL4_{,Case2}$ and $EL4_{,Case3}$ lead an improvement of the solution respect to the $EL4$ without appreciable differences within them, see Figure 9.61a. For thick plates $a/h = 2$, the variable kinematic theories show different levels of accuracy. The $EL4_{,Case3}$ theory is able to approximate very well the full layer-wise reference solution $LW4$. It has to be noticed that the $EL4_{,Case1}$ theory has a better behaviour than the $EL4_{,Case2}$ theory due to the layer-wise approximation of the upper loaded layer, see Figure 9.61b.
- For both the transverse shear stress σ_{xz} , see Figure 9.62a, and the transverse normal stress, see Figure 9.62b, the theories $EL4_{,Case1}$ and $EL4_{,Case2}$ improve the results respect to the $EL4$ theory only in the layer with a layer-wise description. The $EL4_{,Case3}$ theory is able to approximate very well along the entire thickness of the plate the full layer-wise reference solution $LW4$.
- Regarding the electric potential Φ , for thin plates $a/h = 100$, the theories $EL4_{,Case1}$, $EL4_{,Case2}$ and $EL4$ theories overestimate the reference solution, see Figure 9.63a. For thick plates $a/h = 2$, the variable kinematic theories can underestimate and overestimate the solution, see Figure 9.63b. For both thin and thick plates only the $EL4_{,Case3}$ theory is able to approximate very well the full layer-wise reference solution $LW4$.
- For the electric transverse displacement \mathcal{D}_z , for both thin plates $a/h = 100$, see Figure 9.64a, and thick plates $a/h = 2$, see Figure 9.64b, the theories $EL4_{,Case1}$ and $EL4_{,Case2}$ improve the results respect to the $EL4$ theory only in the layer with a layer-wise description. The $EL4_{,Case3}$ theory is the best approximating theory respect to the full layer-wise reference solution $LW4$.

For the plate structures analysed in actuator configuration, the following considerations can be drawn:

- Regarding the transverse displacement w , for thin plates $a/h = 100$, the variable kinematic theories show different levels of accuracy, see Figure 9.65a, the $EL4,Case3$ solution is closer than $EL4,Case1$ and $EL4,Case2$ theories to the full layer-wise reference solution $LW4$. For thick plates $a/h = 2$ the $EL4,Case1$ and $EL4,Case3$ theories are able to approximate very well the full layer-wise reference solution $LW4$, see Figure 9.65b.
- For both the transverse shear stress σ_{xz} , see Figure 9.66a, and the transverse normal stress, see Figure 9.66b, the same considerations as the sensor cases can be depicted. The theories $EL4,Case1$ and $EL4,Case2$ improve the results respect to the $EL4$ theory only in the layer with a layer-wise description. The $EL4,Case3$ theory is able to approximate very well along the entire thickness of the plate the full layer-wise reference solution $LW4$.
- Regarding the electric potential Φ , for thin plates $a/h = 100$, see Figure 9.67a, the theories $EL4,Case1$, $EL4,Case2$ and $EL4$ theories can underestimate and overestimate the solution in the central composite layers. The $EL4,Case3$ theory is able to approximate very well the full layer-wise reference solution $LW4$.
- For the electric transverse displacement \mathcal{D}_z , for thick plates $a/h = 2$, see Figure 9.67b, the theories $EL4,Case1$ and $EL4,Case2$ improve the results respect to the $EL4$ theory only in the layer with a layer-wise description. The $EL4,Case3$ theory is the best approximating theory respect to the full layer-wise reference solution $LW4$.

Therefore, the euclidean norm of the error of primary variables (mechanical displacements, and electric potential), and secondary variables (mechanical stresses, and electric displacements), is evaluated along the plate thickness by mono-models and variable-kinematic models, respect to the adopted reference solution $ref = LW4$. The euclidean norm of the error $\|f_E\|_2$ is calculated for a generic mechanical or electric variables f along the plate thickness z as follows:

$$\|f_E\|_2 = \sqrt{\int_{z_1}^{z_2} (f_{ref}(z) - f(z))^2 dz} \quad (9.14)$$

for a multilayered structure, the integral is splitted, along the thickness direction z , in the integral sum of each layer k . Equation 9.14 changes into:

$$\|f_E\|_2 = \sqrt{\sum_{k=1}^{N_{layers}} \int_{z_1^k}^{z_2^k} (f_{ref}^k(z) - f^k(z))^2 dz^k} \quad (9.15)$$

The euclidean norms are listed in Table 9.32 for various aspect ratios, and both sensor and actuator case are taken into account. Here, the norm is a global indicator of the solution accuracy along the multilayer thickness, it is not distinguishing the local layer approximation. For the Sensor case (mechanical load applied), the mechanical variables have almost the same solution accuracy independently of the used kinematic model. The variable-kinematic model *Case 3*, where the piezoelectric skins have to be modeled by a layer-wise description, permits to have an huge reduction of the error ($10^3 : 10^4$ times) respect to the others mono-models and variable-kinematic models, for the description of the electric potential Φ , and for the electric transverse displacement \mathcal{D}_z . For the Actuator case (electrical load applied), the variable-kinematic model *Case 3*, where the piezoelectric skins have to be modeled by a layer-wise description, permits to have better results for both mechanical and electrical variables. The mechanical variables show an error reduction of ($10^3 : 10^5$ times) respect to the other kinematic models. The accuracy of the electric variables is improved more than mechanical ones, the error is ($10^3 : 10^8$ times) lower than the other kinematic models. For the multilayered plate structures, in conclusion, it is clear that to have more accurate results, the piezoelectric skins have to be modeled by a layer-wise description. The Variable-Kinematic model permits to improve globally the results, and at the same time permits

to reduce the computational cost of the analysis, assembling the composite core with an equivalent-single-layer model.

Table 9.30: Four-layer square plate with a cross-ply composite core $[0^\circ/90^\circ]$ and piezoelectric external skins. Mechanical and electrical variables described by Mono-models and Variable kinematic models for various aspect ratios a/h . Sensor case.

	$a/h = 100$						$DOFs$
	\hat{w}	$\hat{\sigma}_{xx}$	$\hat{\sigma}_{xz}$	$\hat{\sigma}_{zz}$	$\hat{\Phi}$	\hat{D}_z	
$LW4_a$ [46]	4675300	3142.1	-18.832	-	4580.2	0.0136	
$LW4$	4675103	3143.8	-18.842	1.004	4583.0	-0.0136	446148
$LW1$	4647068	3268.7	-18.909	342.0	4555.3	-23.863	131220
$EL3Z$	4674435	3142.2	-26.188	43.85	6967.9	-21.051	131220
$EL4$	4674758	3133.9	-27.238	-37.15	12122	7.9569	131220
$EL3$	4674453	3153.0	-26.719	23.08	12658	-1.5890	104976
$EL2$	4669551	3152.5	-10.677	23.56	12660	-1.0612	78732
$EL1$	3719168	3657.9	-10.203	2727	0.0000	-190.38	52488
$EL4_{Case1}$	4674882	3143.9	-25.668	1.004	9320.7	0.2112	236196
$EL4_{Case2}$	4674874	3141.3	-25.386	-19.59	9308.7	6.5076	236196
$EL4_{Case3}$	4674870	3143.8	-24.713	1.004	4582.9	-0.0135	341172
$EL3_{Case1}$	4674914	3144.0	-26.972	1.004	10412	0.3304	183708
$EL3_{Case2}$	4674905	3151.0	-25.839	-38.11	10396	23.176	183708
$EL3_{Case3}$	4674740	3143.8	-24.463	1.004	4582.8	-0.0135	262440
$EL2_{Case1}$	4673789	3143.2	-17.418	1.029	12620	0.3017	131220
$EL2_{Case2}$	4673770	3159.6	-21.524	38.19	12613	-2.8657	131220
$EL2_{Case3}$	4674702	3143.8	-23.057	1.029	4582.7	-0.0139	183708
$EL1_{Case1}$	4405952	3105.1	-14.014	324.3	2521.9	14.873	78732
$EL1_{Case2}$	4405007	3483.4	-14.290	1742	2522.2	-360.17	78732
$EL1_{Case3}$	4560604	3214.1	-22.118	335.6	4472.9	-23.419	104976

	$a/h = 2$						$DOFs$
	\hat{w}	$\hat{\sigma}_{xx}$	$\hat{\sigma}_{xz}$	$\hat{\sigma}_{zz}$	$\hat{\Phi}$	\hat{D}_z	
$LW4_a$ [46]	4.9113	3.2207	-0.26995	-	0.9103	0.0256	
$LW4$	4.9112	3.2220	-0.27556	1.0002	0.9106	0.0257	446148
$LW1$	4.8087	3.5198	-0.31619	2.1220	0.8600	-0.0663	131220
$EL3Z$	4.3973	3.3894	-0.45298	1.5681	23.803	-0.0579	131220
$EL4$	4.5038	2.3684	-0.46102	-0.3149	-6.0143	-0.0938	131220
$EL3$	4.6282	3.1386	-0.45210	1.6818	2.9967	-0.1295	104976
$EL2$	2.9334	2.3985	-0.19243	2.1722	4.1979	0.3281	78732
$EL1$	2.8907	2.1141	-0.19247	2.4231	0.0000	0.1730	52488
$EL4_{Case1}$	4.6885	3.1302	-0.42763	1.0002	2.4015	0.0252	236196
$EL4_{Case2}$	4.7123	2.4890	-0.40574	-0.4832	-9.0305	0.0531	236196
$EL4_{Case3}$	4.8731	3.2003	-0.40012	1.0002	0.9037	0.0256	341172
$EL3_{Case1}$	4.6374	3.1506	-0.45238	1.0048	4.1069	0.0255	183708
$EL3_{Case2}$	4.6556	3.0310	-0.44481	0.8657	-10.643	-0.0182	183708
$EL3_{Case3}$	4.8779	3.1923	-0.40117	1.0050	0.9049	0.0258	262440
$EL2_{Case1}$	4.1357	2.5720	-0.30963	1.0249	6.9886	0.0227	131220
$EL2_{Case2}$	4.1730	3.0466	-0.32652	2.2611	1.8004	0.0260	131220
$EL2_{Case3}$	4.8895	3.1797	-0.39916	1.0325	0.8674	0.0272	183708
$EL1_{Case1}$	4.2378	3.1781	-0.29120	1.8672	0.8329	0.0204	78732
$EL1_{Case2}$	3.2987	1.8259	-0.24482	2.0088	1.0888	0.1602	78732
$EL1_{Case3}$	5.0470	3.2388	-0.40237	2.0573	1.4450	-0.0620	104976

Table 9.31: Four-layer square plate with a cross-ply composite core $[0^\circ/90^\circ]$ and piezoelectric external skins. Mechanical and electrical variables described by Mono-models and Variable kinematic models for various aspect ratios a/h . Actuator case.

	$a/h = 100$						$DOFs$
	\hat{w}	$\hat{\sigma}_{xx}$	$\hat{\sigma}_{xz}$	$\hat{\sigma}_{zz}$	$\hat{\Phi}$	\hat{D}_z	
$LW4_a$ [46]	-1.3493	-0.0246	0.0000	-	0.4999	-0.0370	
$LW4$	-1.3493	-0.0246	0.0000	0.0000	0.4999	-0.0370	163268
$LW1$	-1.3970	-0.0210	0.0000	0.0035	0.4999	-0.0353	48020
$EL3Z$	-3.6123	1.8546	-0.0154	-4.8765	0.4969	3.7228	48020
$EL4$	-3.2153	1.8587	-0.0087	-4.8932	0.5000	3.7332	48020
$EL3$	-3.1556	1.8607	-0.0117	-4.8929	0.5000	3.7340	38416
$EL2$	-13.288	-8.2308	0.0186	5.4440	0.5000	-13.546	28812
$EL1$	-14.415	-8.2361	0.0198	5.4391	0.5000	-13.544	19208
$EL4_{Case 1}$	-23.806	-0.0362	-0.0002	0.0000	0.3220	-0.0452	86436
$EL4_{Case 2}$	19.359	0.0934	-0.0046	-0.0148	0.6780	0.0516	86436
$EL4_{Case 3}$	-1.3493	-0.0246	0.0000	0.0000	0.4999	-0.0370	124852
$EL3_{Case 1}$	35.698	-0.0417	-0.0002	0.0000	0.2554	-0.0525	67228
$EL3_{Case 2}$	30.710	0.5397	-0.0140	-1.4381	0.7445	1.0801	67228
$EL3_{Case 3}$	-1.3492	-0.0246	0.0000	0.0000	0.4999	-0.0370	96040
$EL2_{Case 1}$	-32.853	-0.0398	-0.0001	0.0000	0.2810	-0.0529	48020
$EL2_{Case 2}$	23.714	0.6197	0.0102	-1.9831	0.7190	1.3987	48020
$EL2_{Case 3}$	-1.3492	-0.0246	0.0000	0.0000	0.4999	-0.0370	67228
$EL1_{Case 1}$	-3744.8	-2.0834	-0.0001	-0.2717	0.5487	-1.6144	28812
$EL1_{Case 2}$	3725.0	-6.0577	0.0262	10.138	0.4513	-14.470	28812
$EL1_{Case 3}$	-1.3711	-0.0210	0.0000	0.0035	0.5000	-0.0353	38416

	$a/h = 2$						$DOFs$
	\hat{w}	$\hat{\sigma}_{xx}$	$\hat{\sigma}_{xz}$	$\hat{\sigma}_{zz}$	$\hat{\Phi}$	\hat{D}_z	
$LW4_a$ [46]	-1.7475	3.8162	0.0864	-	0.3330	-9.4085	
$LW4$	-1.7475	3.8329	0.0928	0.0006	0.3330	-9.4093	163268
$LW1$	-2.1030	12.452	0.0215	8.1858	0.3241	-5.2964	48020
$EL3Z$	-1.4360	5.9403	-0.4065	10.264	-1.5893	-8.2244	48020
$EL4$	-4.4070	10.954	-0.1212	-0.2279	0.5118	-4.0866	48020
$EL3$	-4.0468	13.687	-0.1547	-0.5378	0.4615	-2.0398	38416
$EL2$	-12.428	-3.0088	1.0887	7.3130	0.4674	-16.882	28812
$EL1$	-14.415	-11.286	1.1108	0.6048	0.5000	-14.549	19208
$EL4_{Case 1}$	-1.6859	3.8635	0.1467	0.0006	0.2387	-9.4124	86436
$EL4_{Case 2}$	-4.2234	8.0541	0.0733	4.8358	0.6467	-8.9133	86436
$EL4_{Case 3}$	-1.7323	3.8406	0.1339	0.0006	0.3330	-9.4092	124852
$EL3_{Case 1}$	-1.7082	3.8931	0.1402	0.0269	0.2076	-9.4088	67228
$EL3_{Case 2}$	-5.3533	10.947	-0.4043	4.5420	0.7964	-6.1619	67228
$EL3_{Case 3}$	-1.7510	3.8810	0.1413	0.0268	0.3310	-9.4034	96040
$EL2_{Case 1}$	-1.2439	4.4452	0.0248	0.0604	0.2687	-9.3855	48020
$EL2_{Case 2}$	-10.423	7.5934	1.0047	-0.9364	0.6714	-3.6157	48020
$EL2_{Case 3}$	-1.7733	4.0563	0.0847	0.0549	0.3311	-9.3809	67228
$EL1_{Case 1}$	-5.3835	8.8014	0.2170	6.9842	0.5340	-6.7681	28812
$EL1_{Case 2}$	-13.537	-7.9884	1.3111	5.4393	0.4493	-15.734	28812
$EL1_{Case 3}$	-2.0311	12.943	0.1103	8.1694	0.4858	-5.2979	38416

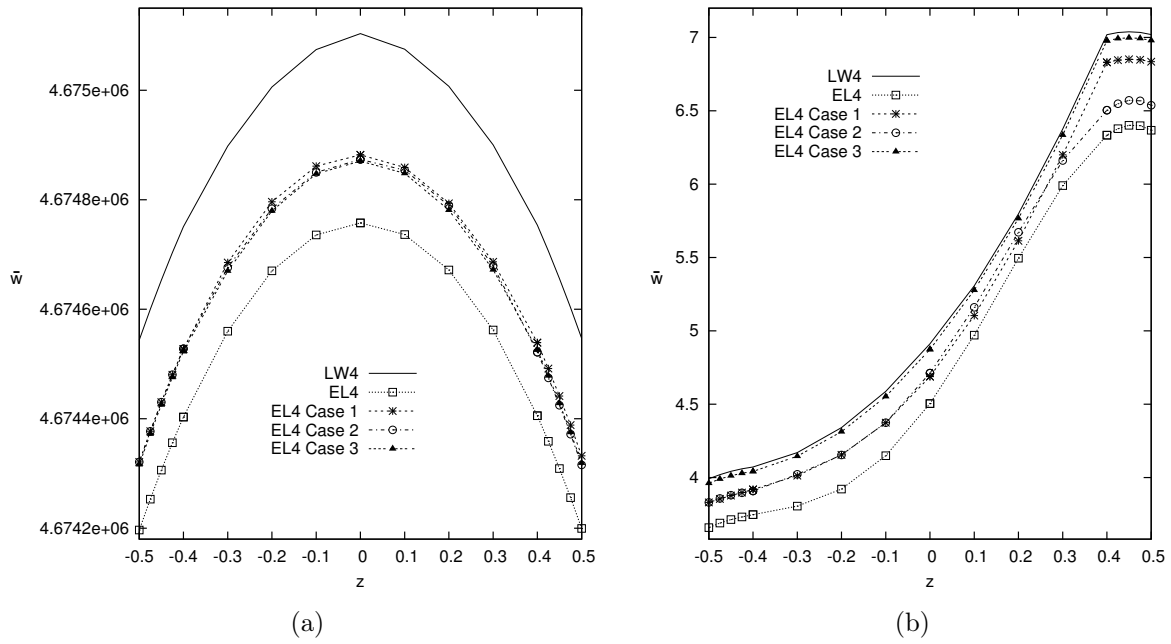


Figure 9.61: Four-layered plate, Sensor case, transverse mechanical displacement \hat{w} , $a/h = 100$ (a), $a/h = 2$ (b).

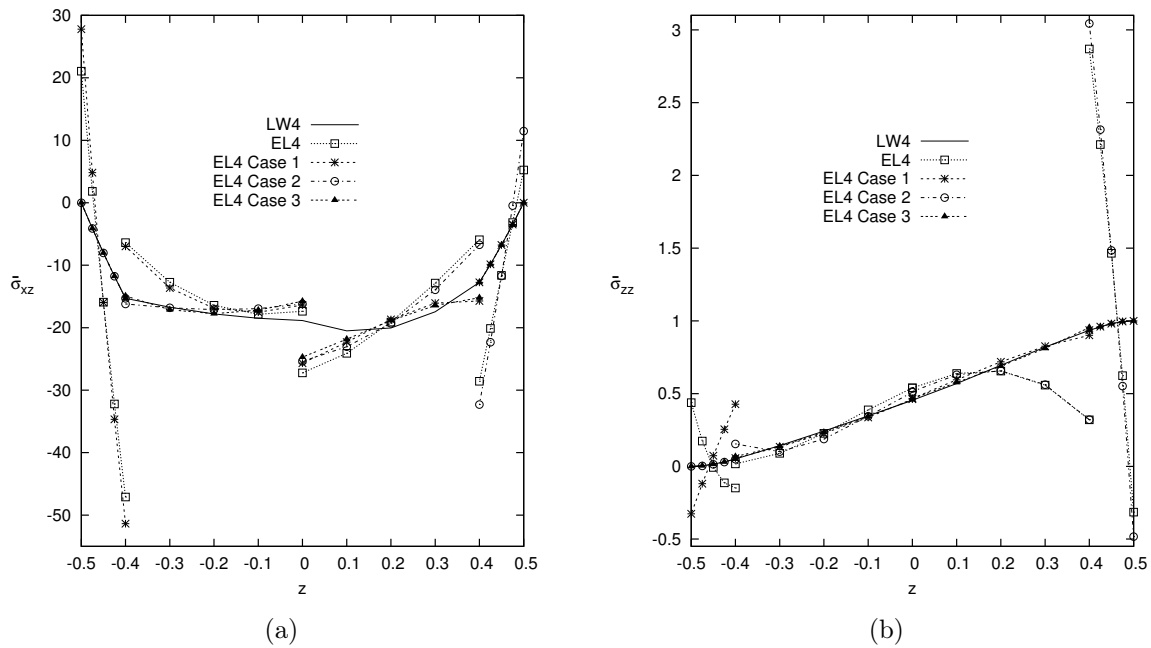


Figure 9.62: Four-layered plate, Sensor case, transverse mechanical stresses, $\hat{\sigma}_{xz}$ for $a/h = 100$ ratio (a), $\hat{\sigma}_{zz}$ for $a/h = 2$ ratio (b).

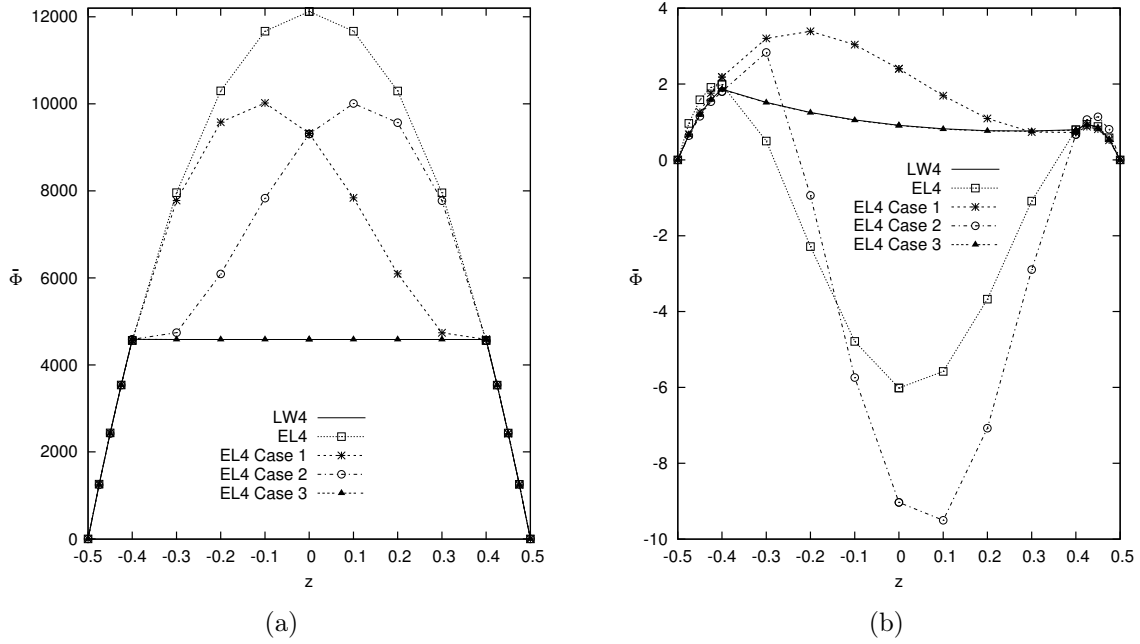


Figure 9.63: Four-layered plate, Sensor case, Electric Potential $\hat{\Phi}$, $a/h = 100$ (a), $a/h = 2$ (b).

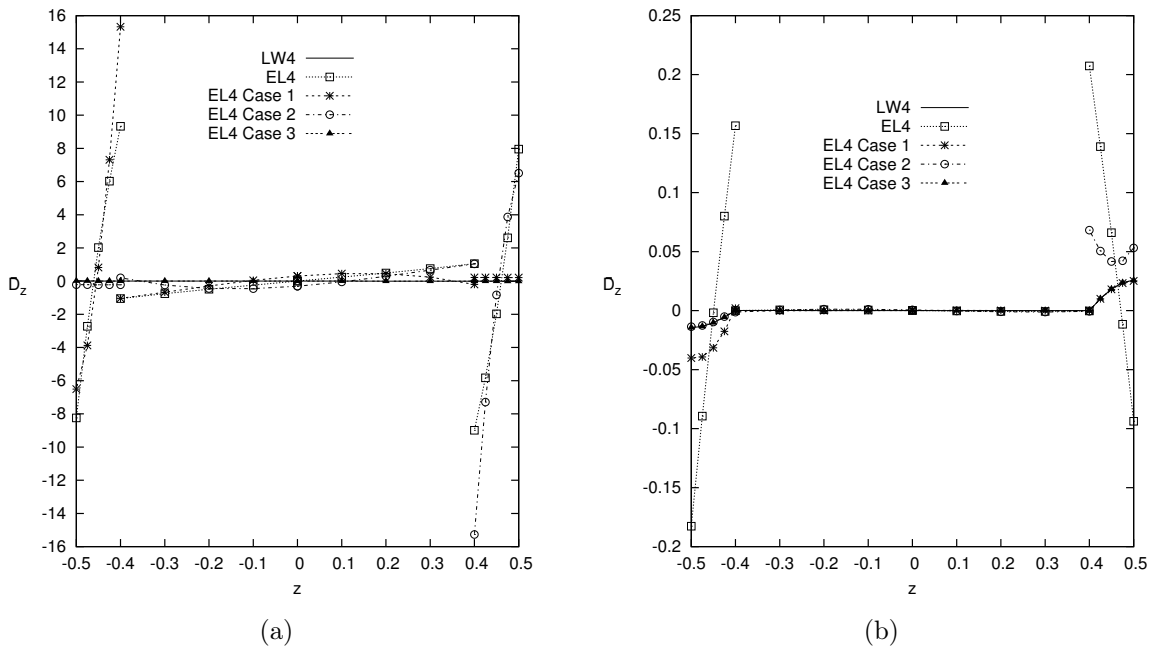


Figure 9.64: Four-layered plate, Sensor case, transverse electric displacement \hat{D}_z , $a/h = 100$ (a), $a/h = 2$ (b).

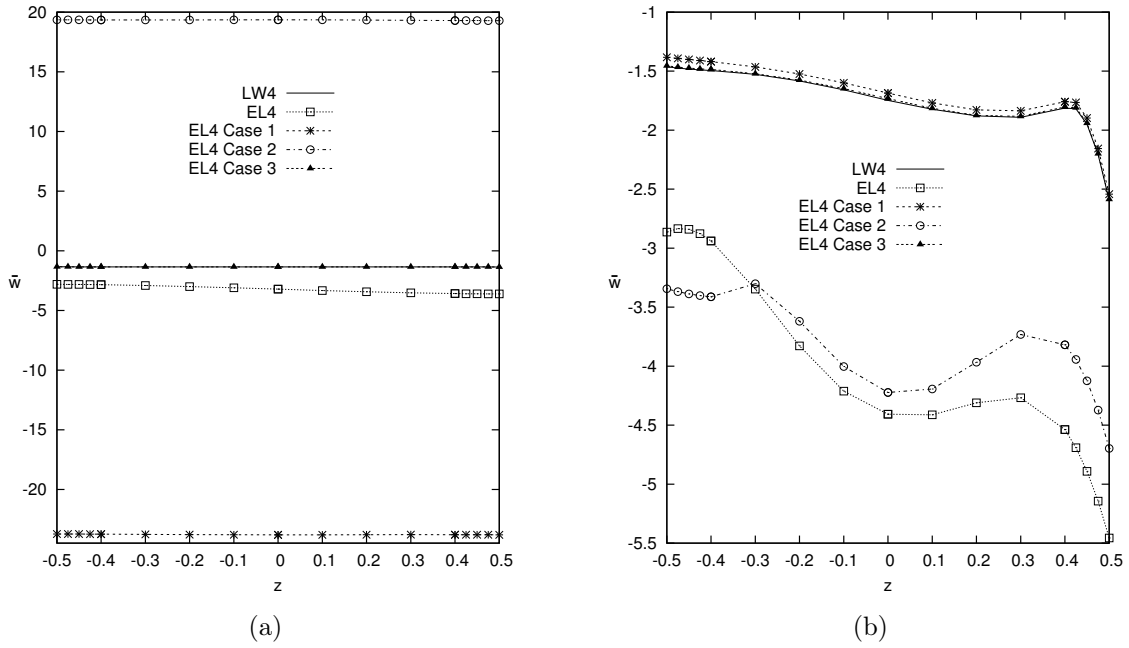


Figure 9.65: Four-layered plate, Actuator case, transverse mechanical displacement \hat{w} , $a/h = 100$ (a), $a/h = 2$ (b).

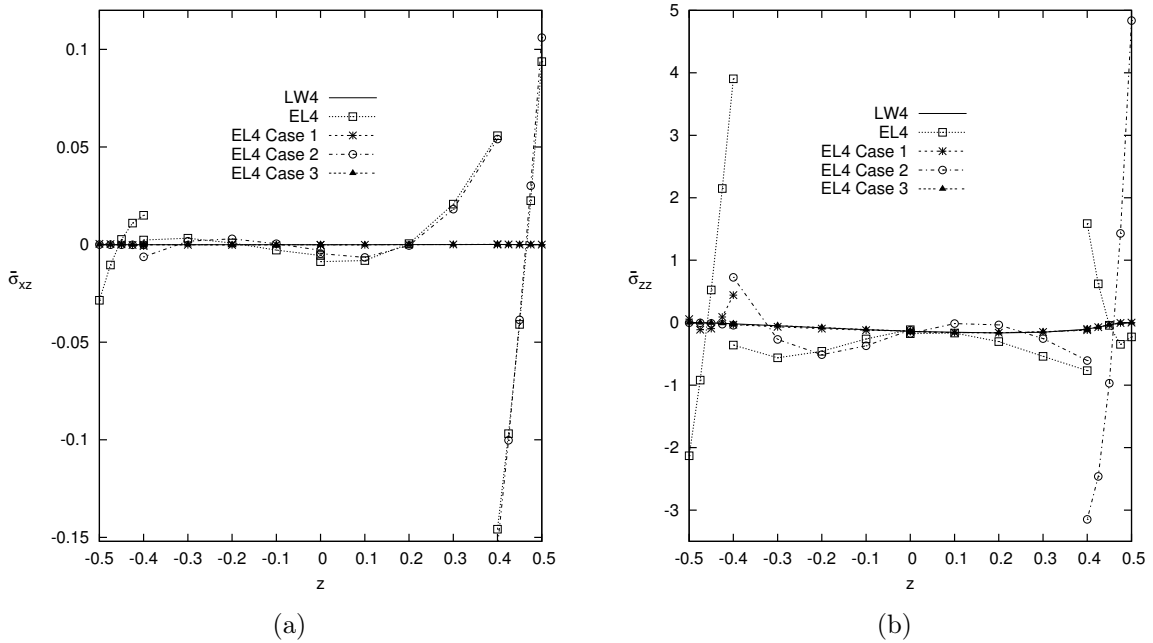


Figure 9.66: Four-layered plate, Actuator case, transverse mechanical stresses, $\hat{\sigma}_{xz}$ for $a/h = 100$ ratio (a), $\hat{\sigma}_{zz}$ for $a/h = 2$ ratio (b).

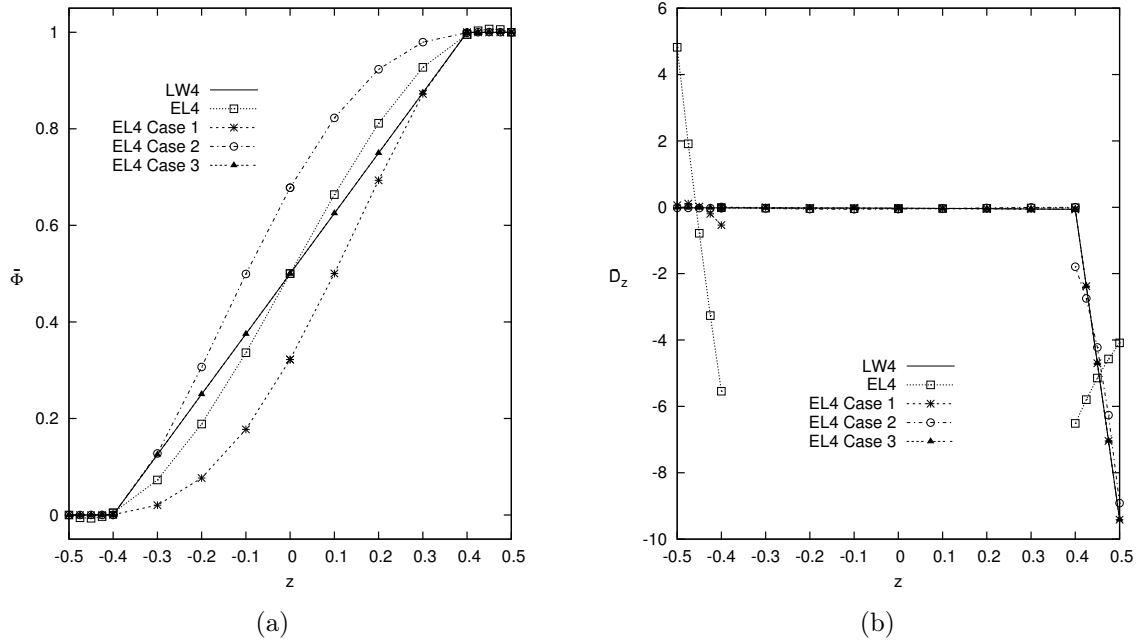


Figure 9.67: Four-layered plate, Actuator case, electric potential and electric transverse displacement, $\hat{\Phi}$ for $a/h = 100$ ratio (a), \hat{D}_z for $a/h = 2$ ratio (b).

Table 9.32: Four-layer square plate with a cross-ply composite core $[0^\circ/90^\circ]$ and piezoelectric external skins. Euclidean norm of the error respect to the reference solution *LW4* for mechanical and electrical variables described by Mono-models and Variable kinematic models for various aspect ratios a/h . Sensor and Actuator cases.

<i>Sensor Case</i>							
a/h		\hat{w}	$\hat{\Phi}$	$\hat{\sigma}_{xx}$	$\hat{\sigma}_{xz}$	$\hat{\sigma}_{zz}$	\hat{D}_z
100	<i>ELA</i>	0.3410 E+03	0.4954 E+04	0.5481 E+01	0.6929 E+01	0.1552 E+02	0.2390 E+01
	<i>ELACase1</i>	0.2155 E+03	0.3164 E+04	0.3934 E+01	0.6697 E+01	0.1039 E+02	0.2182 E+01
	<i>ELACase2</i>	0.2238 E+03	0.3157 E+04	0.3399 E+01	0.3995 E+01	0.1078 E+02	0.2177 E+01
	<i>ELACase3</i>	0.2278 E+03	0.1310 E+00	0.1955 E+01	0.1513 E+01	0.4410 E+01	0.2100 E-04
2	<i>ELA</i>	0.4228 E+00	0.3996 E+01	0.2865 E+00	0.1367 E+00	0.3652 E+00	0.4461 E-01
	<i>ELACase1</i>	0.1870 E+00	0.1211 E+01	0.7011 E-01	0.1131 E+00	0.6709 E-01	0.6323 E-02
	<i>ELACase2</i>	0.2424 E+00	0.5773 E+01	0.2423 E+00	0.1136 E+00	0.3874 E+00	0.1095 E-01
	<i>ELACase3</i>	0.3376 E-01	0.7868 E-02	0.4050 E-01	0.2977 E-01	0.6621 E-02	0.2712 E-04
<i>Actuator Case</i>							
a/h		\hat{w}	$\hat{\Phi}$	$\hat{\sigma}_{xx}$	$\hat{\sigma}_{xz}$	$\hat{\sigma}_{zz}$	\hat{D}_z
100	<i>ELA</i>	0.1886 E+01	0.4020 E-01	0.5294 E+00	0.2824 E-01	0.1361 E+01	0.1099 E+01
	<i>ELACase1</i>	0.2244 E+02	0.1142 E+00	0.5039 E-01	0.1077 E-03	0.9711 E-01	0.8997 E-01
	<i>ELACase2</i>	0.2069 E+02	0.1143 E+00	0.4999 E-01	0.2882 E-01	0.9694 E-01	0.9004 E-01
	<i>ELACase3</i>	0.4251 E-04	0.1880 E-08	0.5106 E-06	0.3669 E-05	0.1276 E-05	0.6322 E-08
2	<i>ELA</i>	0.2345 E+01	0.1261 E+00	0.1669 E+01	0.1458 E+01	0.6965 E+00	0.1454 E+01
	<i>ELACase1</i>	0.6071 E-01	0.6160 E-01	0.5113 E-01	0.3643 E-01	0.5155 E-01	0.6265 E-01
	<i>ELACase2</i>	0.2097 E+01	0.2057 E+00	0.1147 E+01	0.1469 E+01	0.7718 E+00	0.2346 E+00
	<i>ELACase3</i>	0.8899 E-02	0.1470 E-03	0.2288 E-01	0.1462 E-01	0.4666 E-02	0.6206 E-04

9.4.2 Three-layer cylindrical shell

A three-layer composite cylindrical shell, see Figure 9.68, with a Gr/Ep composite core and PZT-4 piezoelectric external skins, simply-supported boundary condition is considered. The static analysis of the shell structure is evaluated in sensor and actuator configuration.

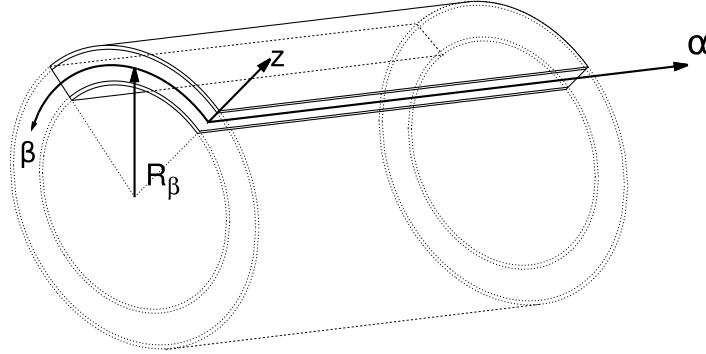


Figure 9.68: Reference system of the composite cylinder with piezoelectric skins.

For the sensor case a mechanical load pressure is applied, for the whole cylinder, at the inner surface of the shell, defined as follows:

$$p(\alpha, \beta, z_{bottom}) = p^o \sin\left(\frac{m\pi\alpha}{a}\right) \cos\left(\frac{n\pi\beta}{b}\right) \quad (9.16)$$

with amplitude $p^o = 1$ and wave numbers $m = 1$ and $n = 8$. The potential at top and bottom position is imposed $\Phi_t = \Phi_b = 0$.

For the actuator case a bi-sinusoidal electric potential, for the whole cylinder, is imposed at outer surface:

$$\Phi(\alpha, \beta, z_{top}) = \phi^o \sin\left(\frac{m\pi\alpha}{a}\right) \cos\left(\frac{n\pi\beta}{b}\right) \quad (9.17)$$

with amplitude $\phi^o = 1$ and wave numbers $m = 1$, $n = 8$. The potential at bottom position is imposed $\Phi_b = 0$. No mechanical load is applied.

The material properties of the cylinder are given in Table 9.27. For all the cases the geometrical data are $a = 40$, $b = 2\pi R_\beta$, $R_\beta = 10$. In respect to the total thickness, a single piezoelectric skin is thick $h_p = 0.1h_{tot}$, while the single core layer is thick $h_c = 0.8h_{tot}$. The results are presented for different radius to thickness ratios $R_\beta/h = 2, 4, 10, 100$. Due to the geometrical symmetry of the cylinder, the symmetry of the load pressure and boundary condition, and the symmetry of the lamination stacking sequence, an octave of the cylinder is analyzed, half cylinder along the α axis direction and a quarter along the β circumferential axis direction. The applied mechanical load for an octave of the cylinder is defined as follows:

$$p(\alpha, \beta, z_{bottom}) = p^o \cos\left(\frac{m\pi\alpha}{a}\right) \cos\left(\frac{n\pi\beta}{b}\right) \quad (9.18)$$

and the electric load for an octave of the cylinder is defined as follows:

$$\Phi(\alpha, \beta, z_{top}) = \phi^o \cos\left(\frac{m\pi\alpha}{a}\right) \cos\left(\frac{n\pi\beta}{b}\right) \quad (9.19)$$

where $m = 0, 5$ and $n = 2$. The results are calculated in the following positions with the following form for the sensor cases:

$$\begin{aligned} \hat{w}(\alpha, \beta, z) &= w(a/2, 0, 0) * 10^{11} & , & \quad \hat{\sigma}_{\alpha\alpha}(\alpha, \beta, z) = \sigma_{\alpha\alpha}(a/2, 0, +h/2) \\ \hat{\sigma}_{\alpha z}(\alpha, \beta, z) &= \sigma_{\alpha z}(a, 0, 0) & , & \quad \hat{\sigma}_{zz}(\alpha, \beta, z) = \sigma_{zz}(a/2, 0, 0) \\ \hat{\Phi}(\alpha, \beta, z) &= \Phi(a/2, 0, 0) & , & \quad \hat{\mathcal{D}}_z(\alpha, \beta, z) = \mathcal{D}_z(a/2, 0, +h/2) * 10^{11} \end{aligned}$$

For the actuator cases the variables are evaluated in the following form:

$$\begin{aligned}\hat{w}(\alpha, \beta, z) &= w(a/2, 0, 0) * 10^{11} & , & \quad \hat{\sigma}_{\alpha\alpha}(\alpha, \beta, z) = \sigma_{\alpha\alpha}(a/2, 0, +h/2) \\ \hat{\sigma}_{\alpha z}(\alpha, \beta, z) &= \sigma_{\alpha z}(a, 0, 0) * 10^4 & , & \quad \hat{\sigma}_{zz}(\alpha, \beta, z) = \sigma_{zz}(a/2, 0, 0) * 10^4 \\ \hat{\Phi}(\alpha, \beta, z) &= \Phi(a/2, 0, 0) & , & \quad \hat{\mathcal{D}}_z(\alpha, \beta, z) = \mathcal{D}_z(a/2, 0, +h/2) * 10^{11}\end{aligned}$$

First a convergence study on the shell element was performed. A composite shell with radius to thickness ratio $R_\beta/h = 100$ is evaluated. For the sensor case a mesh grid of 20×80 elements ensures the convergence of both the mechanical and electrical variables except for the transverse electric displacement \mathcal{D}_z that has a very slow convergence rate. For the actuator case a mesh grid of 14×56 elements ensures the convergence for all the variables, see Table 9.33.

Table 9.33: Convergence study. Composite three layered cylindrical shell with radius to thickness ratio $R_\beta/h = 100$.

Sensor Case												
	Mesh	2 × 8	4 × 16	6 × 24	8 × 32	10 × 40	12 × 48	14 × 56	16 × 64	18 × 72	20 × 80	Analytical [72]
LW4	\hat{w}	403698	403225	403194	403188	403187	403186	403186	403186	403186	403186	403190
	$\hat{\sigma}_{\alpha\alpha}$	2706.1	2612.6	2594.4	2587.9	2585.0	2583.4	2582.4	2581.7	2581.3	2581.0	-
	$\hat{\sigma}_{\alpha z}$	-3.5070	-3.2390	-3.1880	-3.1722	-3.1656	-3.1622	-3.1604	-3.1592	-3.1585	-3.1579	-3.1560
	$\hat{\sigma}_{zz}$	-3.9198	-4.0225	-4.0154	-4.0109	-4.0082	-4.0063	-4.0048	-4.0035	-4.0024	-4.0016	-3.997
	$\hat{\Phi}$	0.3263	0.3164	0.3143	0.3136	0.3132	0.3131	0.3129	0.3129	0.3128	0.3128	0.3127
	$\hat{\mathcal{D}}_z$	-121.54	-16.278	-9.6342	-8.5184	-8.2038	-8.0807	-8.0178	-7.9754	-7.9386	-7.9020	-5.495
Actuator Case												
	Mesh	2 × 8	4 × 16	6 × 24	8 × 32	10 × 40	12 × 48	14 × 56				Analytical [72]
LW4	\hat{w}	5.5422	5.5420	5.5419	5.5418	5.5418	5.5418	5.5418				5.5418
	$\hat{\sigma}_{\alpha\alpha}$	-0.2048	-0.2119	-0.2132	-0.2137	-0.2140	-0.2141	-0.2141				-
	$\hat{\sigma}_{\alpha z}$	-0.6069	-0.5559	-0.5466	-0.5439	-0.5427	-0.5422	-0.5419				-0.5423
	$\hat{\sigma}_{zz}$	0.0390	-0.3508	-0.3370	-0.3438	-0.3742	-0.4104	-0.4417				-0.5571
	$\hat{\Phi}$	0.5009	0.5009	0.5009	0.5009	0.5009	0.5009	0.5009				0.5009
	$\hat{\mathcal{D}}_z$	-36.201	-36.203	-36.207	-36.208	-36.209	-36.209	-36.209				-36.209

Different Variable Kinematic models have been used to perform the analysis of the shell structures. The acronyms have been modified adding a subscript to them, for the sake of clarity the list of subscripts is given below:

- $Case1 = \{layer1\} \{layer2, layer3\}$
- $Case2 = \{layer1, layer2\} \{layer3\}$

The results are listed in Table 9.34 for the sensor case, and in Table 9.35 for the actuator case. For the plate structures analyzed the following considerations can be drawn for the sensor cases and actuator cases. For both mechanical and electrical variables the variable kinematic configurations $EL4_{Case1}$, $EL4_{Case2}$ show an improvement of the solutions respect to the full equivalent single layer theory $EL4$. As demonstrated in the previous numerical example, it is preferable to model the piezoelectric skins of a multilayered structure with a layer-wise approach to obtain more accurate results. For this numerical example, the two possible variable kinematic theories $Case1$ and $Case2$ cannot be as accurate as the configuration with the piezoelectric skins modeled with a layer-wise approach, that for this three-layered structure is coincident with the full-layer wise model. The more accurate variable kinematic configuration is that which takes into account the layer-wise description of the layer subject to the mechanical or electrical load. For the sensor cases the $Case2$ configuration is more accurate, for the actuator cases the $Case1$ configuration is more close to the reference solution.

Table 9.34: Three-layer cylinder with a composite core and piezoelectric external skins. Mechanical and electrical variables described by Mono-models and Variable kinematic models for various radius to thickness ratios R/h . Sensor case.

	$R/h = 100$						$DOFs$
	\hat{w}	$\hat{\sigma}_{\alpha\alpha}$	$\hat{\sigma}_{\alpha z}$	$\hat{\sigma}_{zz}$	$\hat{\Phi}$	\hat{D}_z	
$LW4_a$ [72]	403190	-	-3.1560	-3.997	0.3127	-5.495	
$LW4$	403185	2581.0	-3.1579	-4.0016	0.3128	-7.9020	343252
$LW1$	397196	2638.2	-2.9309	-3.8980	0.3081	-1600.8	105616
$EL3Z$	403237	2582.2	-3.1637	-3.9975	0.8662	-112.76	132020
$EL4$	403251	2580.8	-3.5091	-2.5532	0.8378	3648.5	132020
$EL3$	403251	2581.7	-3.5069	-2.5495	0.8664	3003.5	105616
$EL2$	405108	2546.2	-1.5952	-27.979	0.8724	-12631	79212
$EL1$	355114	3094.8	-1.6844	-25.846	0.0000	-25607	52808
$EL4_{Case1}$	403170	2580.9	-3.4019	-3.1394	0.4913	0.6731	237636
$EL4_{Case2}$	403214	2561.5	-3.1384	-2.7264	0.7887	513.47	237636
$EL3_{Case1}$	403164	2580.9	-3.7731	-2.1040	0.5107	3.0502	184828
$EL3_{Case2}$	403235	2580.9	-3.0706	-1.9132	0.9247	2531.1	184828
$EL2_{Case1}$	403131	2580.7	-2.2146	-6.0200	0.6671	0.3341	132020
$EL2_{Case2}$	403186	2592.1	-2.8999	-7.3777	1.0618	972.84	132020
$EL1_{Case1}$	388319	2575.6	-2.1355	102.05	0.2198	-213.08	79212
$EL1_{Case2}$	393626	2843.8	-2.0230	-147.95	0.1272	-38700	79212

	$R/h = 2$						$DOFs$
	\hat{w}	$\hat{\sigma}_{\alpha\alpha}$	$\hat{\sigma}_{\alpha z}$	$\hat{\sigma}_{zz}$	$\hat{\Phi}$	\hat{D}_z	
$LW4_a$ [72]	30.225	-	-0.1193	-0.415	0.00497	0.752	
$LW4$	30.225	1.2065	-0.1194	-0.4150	0.00497	0.7348	343252
$LW1$	31.598	1.4335	-0.1143	-0.4047	0.00714	-2.5374	105616
$EL3Z$	30.162	1.4929	-0.1163	-0.3957	0.01110	-9.9503	132020
$EL4$	27.653	1.0410	-0.1275	-0.5243	-0.02601	16.025	132020
$EL3$	27.839	1.9639	-0.1246	-0.4625	0.01396	13.033	105616
$EL2$	16.090	0.3806	-0.0500	-0.1429	0.02323	-12.100	79212
$EL1$	16.373	0.5292	-0.0506	-0.1539	0.00000	-31.931	52808
$EL4_{Case1}$	28.508	1.1485	-0.1211	-0.4757	-0.0577	0.6670	237636
$EL4_{Case2}$	29.402	1.3944	-0.1208	-0.4218	0.0165	2.2707	237636
$EL3_{Case1}$	27.943	1.0920	-0.1256	-0.5498	-0.0586	0.6076	184828
$EL3_{Case2}$	29.292	1.4955	-0.1248	-0.4048	0.0246	3.9826	184828
$EL2_{Case1}$	24.031	0.8845	-0.0835	-0.1615	0.0035	0.5862	132020
$EL2_{Case2}$	27.241	1.4981	-0.0956	-0.4982	0.0320	8.6203	132020
$EL1_{Case1}$	18.060	1.0674	-0.0632	-0.1374	0.0050	-1.5134	79212
$EL1_{Case2}$	25.976	0.0759	-0.0801	-0.3057	0.0046	-55.425	79212

Table 9.35: Three-layer cylinder with a composite core and piezoelectric external skins. Mechanical and electrical variables described by Mono-models and Variable kinematic models for various radius to thickness ratios R/h . Actuator case.

	$R/h = 100$						$DOFs$
	\hat{w}	$\hat{\sigma}_{\alpha\alpha}$	$\hat{\sigma}_{\alpha z}$	$\hat{\sigma}_{zz}$	$\hat{\Phi}$	\hat{D}_z	
$LW4_a$ [72]	5.5418	-	-0.5423	-0.5571	0.5009	-36.209	
$LW4$	5.5418	-0.2141	-0.5419	-0.4417	0.5009	-36.209	170404
$LW1$	5.4331	-0.1833	-0.5080	-0.4459	0.5000	-34.865	52432
$EL3Z$	1.8837	-0.9776	-0.4124	830.44	0.5000	-141.81	65540
$EL4$	92.747	19.424	-202.29	-15334	0.5010	3724.6	65540
$EL3$	92.691	19.534	-203.24	-15337	0.5002	3745.2	52432
$EL2$	2520.2	-64.432	486.90	-141817	0.5066	-14300	39324
$EL1$	2250.4	-61.527	483.72	-141707	0.5000	-14451	26216
$EL4_{Case1}$	-3.1798	-0.2202	-2.6406	-1.6166	0.3224	-44.401	117972
$EL4_{Case2}$	26.953	0.9671	-124.78	15.979	0.6785	50.273	117972
$EL3_{Case1}$	-5.6162	-0.1922	-4.0188	-2987.5	0.2561	-51.697	91756
$EL3_{Case2}$	41.196	5.4375	-293.32	-2943.7	0.7453	1073.7	91756
$EL2_{Case1}$	-2.4141	-0.1676	-3.1852	-1083.3	0.2810	-52.076	65540
$EL2_{Case2}$	37.439	6.2793	337.58	-1117.0	0.7191	1400.4	65540
$EL1_{Case1}$	-1364.0	0.6154	-72.913	-113980	0.5516	-1636.7	39324
$EL1_{Case2}$	4140.8	-59.763	736.08	-125596	0.4490	-15022	39324

	$R/h = 2$						$DOFs$
	\hat{w}	$\hat{\sigma}_{\alpha\alpha}$	$\hat{\sigma}_{\alpha z}$	$\hat{\sigma}_{zz}$	$\hat{\Phi}$	\hat{D}_z	
$LW4_a$ [72]	-1.306	-	19.176	-116.36	0.4058	-106.61	
$LW4$	-1.306	-0.1759	19.208	-116.49	0.4058	-106.64	170404
$LW1$	-1.366	0.8046	11.078	-79.83	0.4916	-61.79	52432
$EL3Z$	-0.425	-0.5514	12.571	1044.0	0.4675	-211.86	65540
$EL4$	-3.137	0.5679	-156.43	-255.73	0.5486	-36.31	65540
$EL3$	-1.861	1.0151	-217.99	-622.17	0.4778	3.62	52432
$EL2$	-12.84	-0.9158	571.77	-3914.7	0.5395	-254.03	39324
$EL1$	-12.62	-1.9369	606.79	-3745.8	0.5000	-301.24	26216
$EL4_{Case1}$	-1.249	-0.1742	19.120	-116.75	0.2831	-106.72	117972
$EL4_{Case2}$	-3.281	0.1703	-73.019	-136.42	0.6549	-103.57	117972
$EL3_{Case1}$	-1.199	-0.1714	18.647	-155.50	0.2518	-106.74	91756
$EL3_{Case2}$	-3.728	0.5372	-279.71	174.84	0.7918	-69.74	91756
$EL2_{Case1}$	-0.949	-0.1750	-6.798	-106.46	0.2743	-107.49	65540
$EL2_{Case2}$	-7.025	0.6781	346.93	-1318.3	0.6902	-33.85	65540
$EL1_{Case1}$	-5.393	0.5046	104.25	-2031.9	0.5432	-80.87	39324
$EL1_{Case2}$	-11.69	-1.6581	643.28	-3892.4	0.4521	-319.48	39324

9.4.3 Four-layer cylindrical shell

A four-layer composite cylindrical shell with a Gr/Ep composite core $[90^\circ/0^\circ]$ and PZT-4 piezoelectric external skins, see Figure 9.68, simply-supported boundary condition is considered. The static analysis of the shell structure is evaluated in sensor and actuator configuration. The material properties of the cylinder are given in Table 9.27. For all the cases the

geometrical data are the same of the previous numerical subsection. In respect to the total thickness, a single piezoelectric skin is thick $h_p = 0.1h_{tot}$, while the single composite core layer is thick $h_c = 0.4h_{tot}$. The results are presented for different radius to thickness ratios $R_\beta/h = 2, 4, 10, 100$. The applied load is the same of the previous numerical example, due to the geometrical symmetry of the cylinder, the symmetry of the load pressure and boundary condition, an octave of the cylinder is analyzed, half cylinder along the α axis direction and a quarter along the β circumferential axis direction. For the sensor case a mesh grid of 20×80 , and for the actuator case a mesh grid of 14×56 elements are employed as the previous example of the three-layered cylinder.

The results are calculated in the following positions with the following form for the sensor cases:

$$\begin{aligned} \hat{w}(\alpha, \beta, z) &= w(a/2, 0, 0) * 10^9 & , & \quad \hat{\sigma}_{\alpha\alpha}(\alpha, \beta, z) = \sigma_{\alpha\alpha}(a/2, 0, +h/2) \\ \hat{\sigma}_{\alpha z}(\alpha, \beta, z) &= \sigma_{\alpha z}(a, 0, 0^-) & , & \quad \hat{\sigma}_{zz}(\alpha, \beta, z) = \sigma_{zz}(a/2, 0, -h/2) \\ \hat{\Phi}(\alpha, \beta, z) &= \Phi(a/2, 0, 0) & , & \quad \hat{\mathcal{D}}_z(\alpha, \beta, z) = \mathcal{D}_z(a/2, 0, +h/2) * 10^{11} \end{aligned}$$

For the actuator cases the variables are evaluated in the following form:

$$\begin{aligned} \hat{w}(\alpha, \beta, z) &= w(a/2, 0, 0) * 10^{11} & , & \quad \hat{\sigma}_{\alpha\alpha}(\alpha, \beta, z) = \sigma_{\alpha\alpha}(a/2, 0, +h/2) \\ \hat{\sigma}_{\alpha z}(\alpha, \beta, z) &= \sigma_{\alpha z}(a, 0, 0^-) & , & \quad \hat{\sigma}_{zz}(\alpha, \beta, z) = \sigma_{zz}(a/2, 0, +h/2) \\ \hat{\Phi}(\alpha, \beta, z) &= \Phi(a/2, 0, 0) & , & \quad \hat{\mathcal{D}}_z(\alpha, \beta, z) = \mathcal{D}_z(a/2, 0, +h/2) * 10^9 \end{aligned}$$

Different Variable Kinematic models have been used to perform the analysis of the shell structures. The acronyms have been modified adding a subscript to them, for the sake of clarity the list of subscripts is given below:

- $Case1 = \{layer1\} \{layer2, layer3, layer4\}$
- $Case2 = \{layer1, layer2, layer3\} \{layer4\}$
- $Case3 = \{layer1\} \{layer2, layer3\} \{layer4\}$

The results are listed in Table 9.36 for the sensor case, and in Table 9.37 for the actuator case. For the cylindrical shell structures analysed the following considerations can be drawn for the sensor cases:

- For big radius to thickness ratios $R/h = 100$ regarding the transverse displacement w , the theories $EL4_{Case1}$, $EL4_{Case2}$ and $EL4_{Case3}$ lead an improvement of the solution respect to the $EL4$ with different levels of accuracy, see Figure 9.69a. For small radius to thickness ratios $R/h = 2$, the in-plane stress $\sigma_{\alpha\alpha}$ is well described along the thickness, except from the $EL4_{Case1}$ and the full equivalent-single-layer theory $EL4$, those theories have a loss in accuracy for the description of the loaded lower layer, see Figure 9.69b.
- For both the transverse shear stress $\sigma_{\alpha z}$, see Figure 9.70a, and the transverse normal stress σ_{zz} , see Figure 9.70b, the theories $EL4_{Case1}$ and $EL4_{Case2}$ improve the results respect to the $EL4$ theory only in the layer with a layer-wise description. The $EL4_{Case3}$ theory is able to approximate very well along the entire thickness of the plate the full layer-wise reference solution $LW4$.
- Regarding the electric potential Φ , for big radius to thickness ratios $R/h = 100$, the theories $EL4_{Case1}$, $EL4_{Case2}$ and $EL4$ theories overestimate the reference solution, see Figure 9.71a. For the electric transverse displacement \mathcal{D}_z , for small radius to thickness ratios $R/h = 2$, see Figures 9.71b, the theories $EL4_{Case1}$ and $EL4_{Case2}$ improve the results respect to the $EL4$ theory only in the layer with a layer-wise description. The $EL4_{Case3}$ theory is the best approximating theory respect to the full layer-wise reference solution $LW4$.

For the cylindrical shell structures analysed in actuator configuration, the following considerations can be drawn:

- Regarding the transverse displacement w , for big radius to thickness ratios $R/h = 100$, the variable kinematic theories show different levels of accuracy, see Figure 9.72a, the $EL4,Case3$ solution is closer than $EL4,Case1$ and $EL4,Case2$ theories to the full layer-wise reference solution $LW4$. For small radius to thickness ratios $R/h = 2$ the in-plane stress $\sigma_{\alpha\alpha}$ is well described along the thickness only from the $EL4,Case3$ theory, the other theories have a loss in accuracy especially in loaded upper layer, see Figure 9.72b.
- For both the transverse shear stress $\sigma_{\alpha z}$, see Figure 9.73a, and the transverse normal stress σ_{zz} , see Figure 9.73b, the same considerations as the sensor cases can be depicted. The theories $EL4,Case1$ and $EL4,Case2$ improve the results respect to the $EL4$ theory only in the layer with a layer-wise description. The $EL4,Case3$ theory is able to approximate very well along the entire thickness of the plate the full layer-wise reference solution $LW4$.
- Regarding the electric potential Φ , for big radius to thickness ratios $R/h = 100$, see Figure 9.74a, the theories $EL4,Case1$, $EL4,Case2$ and $EL4$ theories can underestimate and overestimate the solution in the central composite layers. The $EL4,Case3$ theory is able to approximate very well the full layer-wise reference solution $LW4$.
- For the electric transverse displacement \mathcal{D}_z , for small radius to thickness ratios $R/h = 2$, see Figures 9.74b, the theories $EL4,Case1$ and $EL4,Case2$ improve the results respect to the $EL4$ theory only in the layer with a layer-wise description. The $EL4,Case3$ theory is the best approximating theory respect to the full layer-wise reference solution $LW4$.

The euclidean norm, as defined in equation 9.15, is a global indicator of the solution accuracy, it can be related to the reduction of degrees of freedom (dofs) of the structure model, in other words the euclidean norm can be related to the computational cost of the used models. In Figure 9.75 various mono-models and variable-kinematic models with different expansion order are related to the reduction dofs % respect to the adopted reference solution $LW4$ with the following definition:

$$reduction\ dofs\ \% = \frac{100 (DOFS_{LW4} - DOFS)}{DOFS_{LW4}} \quad (9.20)$$

It is taken into account the error norm of the transverse mechanical displacement \hat{w} for the actuator case of the shell with $R/h = 2$ ratio. It is evident, from Figure 9.75, that as expected the solution accuracy grows with the increasing of the polynomial order with a convergence to the fourth-order. The ESL mono-models have the biggest dofs reduction coupled with large solution errors. Differently LW models have the biggest solution accuracy coupled with low dofs reductions. It is noticeable that variable-kinematic Case 1 models are able to have reduced solution errors because they are describing with layer-wise approach the loaded top layer. Differently variable-kinematic Case 2 models represent the worst solution for both accuracy and dofs reduction. Therefore, variable-kinematic Case 3 models describe very accurate results comparable with the LW models, with noticeable dofs reduction.

Table 9.36: Four-layer cylinder with a composite core and piezoelectric external skins. Mechanical and electrical variables described by Mono-models and Variable kinematic models for various radius to thickness ratios R/h . Sensor case.

	$R/h = 100$						$DOFs$
	\hat{w}	$\hat{\sigma}_{\alpha\alpha}$	$\hat{\sigma}_{\alpha z}$	$\hat{\sigma}_{zz}$	$\hat{\Phi}$	\hat{D}_z	
$LW4_a$ [140]	4403.2	-	-	-32549	0.3414	227910	
$LW4M_a$ [140]	4403.2	-	-	-1.0000	0.3414	227910	
$LW4FM_a$ [140]	4403.2	-	-	-0.9999	0.3414	-2.4676	
$LW4$	4403.1	2716.7	-0.6654	-0.9985	0.3416	-4.0092	448868
$LW1$	4387.1	2812.3	-2.5224	-260.44	0.3403	-1764.8	132020
$EL3Z$	4401.8	2710.2	-2.3028	-46.243	0.5404	-154.76	132020
$EL4$	4402.1	2741.2	-2.1376	-57.284	0.9333	2141.3	132020
$EL3$	4401.9	2715.0	-2.2215	-20.875	0.9488	1407.3	105616
$EL2$	4403.5	2684.2	-1.1480	55.766	0.9506	-5722.9	79212
$EL1$	3813.1	3256.8	-1.3543	-2176.7	0.0000	-20590	52808
$EL4_{Case1}$	4402.2	2716.3	-1.6024	-89.931	0.6519	10.560	237636
$EL4_{Case2}$	4402.4	2725.2	-1.5633	-0.9991	0.7804	522.82	237636
$EL4_{Case3}$	4402.6	2716.4	-1.3976	-0.9987	0.3415	-4.0166	343252
$EL3_{Case1}$	4401.4	2715.9	-2.2183	24.322	0.6849	15.898	184828
$EL3_{Case2}$	4402.6	2734.7	-1.7344	-0.9988	0.8974	2304.4	184828
$EL3_{Case3}$	4402.2	2716.3	-1.3883	-0.9986	0.3415	-4.0260	264040
$EL2_{Case1}$	4400.6	2715.2	-1.7809	7.2858	0.8519	13.417	132020
$EL2_{Case2}$	4402.3	2712.3	-1.9502	-1.2046	1.0438	315.94	132020
$EL2_{Case3}$	4401.8	2715.9	-2.0836	-1.2042	0.3415	-3.5428	184828
$EL1_{Case1}$	4226.9	2724.1	-1.6474	-1249.3	0.2146	478.46	79212
$EL1_{Case2}$	4246.2	2975.9	-1.5025	-252.10	0.1699	-33077	79212
$EL1_{Case3}$	4323.2	2773.2	-2.2237	-256.67	0.3354	-1739.1	105616
	$R/h = 2$						$DOFs$
	\hat{w}	$\hat{\sigma}_{\alpha\alpha}$	$\hat{\sigma}_{\alpha z}$	$\hat{\sigma}_{zz}$	$\hat{\Phi}$	\hat{D}_z	
$LW4_a$ [140]	0.2633	-	-	-2.2444	0.0039	9.8912	
$LW4M_a$ [140]	0.2633	-	-	-1.0013	0.0039	9.8858	
$LW4FM_a$ [140]	0.2633	-	-	-1.0013	0.0039	0.6092	
$LW4$	0.2633	1.0152	-0.0765	-1.0010	0.0038	0.5929	448868
$LW1$	0.2582	1.1101	-0.0706	-2.6056	0.0035	-2.4079	132020
$EL3Z$	0.2369	1.8632	-0.1103	-2.1548	0.1037	22.094	132020
$EL4$	0.2415	0.8268	-0.1152	-0.3013	-0.0269	14.010	132020
$EL3$	0.2371	1.6585	-0.1075	-2.1536	0.0107	8.5755	105616
$EL2$	0.1416	0.1893	-0.0385	-2.2960	0.0147	-5.8960	79212
$EL1$	0.1468	0.0882	-0.0391	-2.3340	0.0000	-22.409	52808
$EL4_{Case1}$	0.2471	0.9560	-0.1028	0.2054	-0.0547	0.5236	237636
$EL4_{Case2}$	0.2569	1.1699	-0.1071	-1.0010	0.0129	1.6966	237636
$EL4_{Case3}$	0.2617	1.0081	-0.1010	-1.0010	0.0038	0.5880	343252
$EL3_{Case1}$	0.2377	0.9327	-0.1044	-1.4773	-0.0512	0.5090	184828
$EL3_{Case2}$	0.2577	1.2839	-0.1177	-1.0131	0.0196	2.9519	184828
$EL3_{Case3}$	0.2622	1.0222	-0.1010	-1.0133	0.0039	0.6057	264040
$EL2_{Case1}$	0.1860	0.5272	-0.0664	-2.4012	0.0079	0.2537	132020
$EL2_{Case2}$	0.2448	1.2798	-0.0804	-1.0996	0.0234	7.6853	132020
$EL2_{Case3}$	0.2631	0.9789	-0.0974	-1.1102	0.0035	0.6479	184828
$EL1_{Case1}$	0.1631	0.8048	-0.0544	-2.1771	0.0031	-1.4746	79212
$EL1_{Case2}$	0.2167	-0.4708	-0.0564	-2.1445	0.0050	-36.727	79212
$EL1_{Case3}$	0.2702	1.0339	-0.0951	-2.5063	0.0054	-2.2854	105616

Table 9.37: Four-layer cylinder with a composite core and piezoelectric external skins. Mechanical and electrical variables described by Mono-models and Variable kinematic models for various radius to thickness ratios R/h . Actuator case.

	$R/h = 100$						$DOFs$
	\hat{w}	$\hat{\sigma}_{\alpha\alpha}$	$\hat{\sigma}_{\alpha z}$	$\hat{\sigma}_{zz}$	$\hat{\Phi}$	\hat{D}_z	
$LW4_a$ [140]	2.4869	-	-	-0.1835	0.5009	-0.3494	
$LW4M_a$ [140]	2.4869	-	-	0.0000	0.5009	-0.3494	
$LW4FM_a$ [140]	2.4869	-	-	0.0000	0.5009	-0.3622	
$LW4$	2.4872	-0.2902	0.0000	0.0000	0.5009	-0.3621	222836
$LW1$	2.4452	-0.2596	-0.0001	0.0318	0.5009	-0.3485	65540
$EL3Z$	43.5403	18.077	-0.0018	-48.670	0.4959	37.190	65540
$EL4$	44.3032	18.006	-0.0163	-48.710	0.5009	37.136	65540
$EL3$	44.8222	18.157	-0.0098	-48.878	0.5001	37.343	52432
$EL2$	1124.5	-91.270	0.0690	53.830	0.5034	-133.35	39324
$EL1$	1029.2	-90.429	0.0657	59.038	0.5000	-134.39	26216
$EL4_{Case 1}$	-12.287	-0.4031	-0.0003	0.0000	0.3224	-0.4440	117972
$EL4_{Case 2}$	22.269	0.7975	-0.0120	-0.1312	0.6784	0.5026	117972
$EL4_{Case 3}$	2.4880	-0.2902	0.0000	0.0000	0.5009	-0.3621	170404
$EL3_{Case 1}$	-17.722	-0.4577	-0.0004	0.0000	0.2562	-0.5169	91756
$EL3_{Case 2}$	34.832	5.1907	-0.0214	-14.279	0.7452	10.731	91756
$EL3_{Case 3}$	2.4889	-0.2902	0.0000	0.0000	0.5009	-0.3621	131080
$EL2_{Case 1}$	-14.717	-0.4399	-0.0003	0.0000	0.2811	-0.5207	65540
$EL2_{Case 2}$	29.364	6.0191	0.0441	-19.827	0.7190	13.997	65540
$EL2_{Case 3}$	2.4880	-0.2903	0.0000	0.0000	0.5009	-0.3621	91756
$EL1_{Case 1}$	-2200.3	-18.715	-0.0044	-1.2398	0.5494	-15.798	39324
$EL1_{Case 2}$	3493.6	-75.394	0.1000	97.022	0.4510	-143.38	39324
$EL1_{Case 3}$	2.4558	-0.2596	0.0000	0.0318	0.5000	-0.3485	52432
	$R/h = 2$						$DOFs$
	\hat{w}	$\hat{\sigma}_{\alpha\alpha}$	$\hat{\sigma}_{\alpha z}$	$\hat{\sigma}_{zz}$	$\hat{\Phi}$	\hat{D}_z	
$LW4_a$ [140]	-1.1542	-	-	0.1416	0.4064	-1.0754	
$LW4M_a$ [140]	-1.1542	-	-	0.0000	0.4064	-1.0754	
$LW4FM_a$ [140]	-1.1542	-	-	0.0000	0.4064	-1.0654	
$LW4$	-1.1534	-0.0894	-0.0022	0.0000	0.3962	-1.0659	222836
$LW1$	-1.2820	0.8799	0.0008	0.9183	0.3900	-0.6169	65540
$EL3Z$	-1.0226	0.3370	0.0031	1.1361	-1.1287	-0.9830	65540
$EL4$	-3.0789	0.7162	-0.0242	-0.2791	0.5529	-0.3374	65540
$EL3$	-0.8279	1.2289	-0.0318	-0.5882	0.4804	0.1053	52432
$EL2$	-12.269	-1.2000	0.0698	1.1274	0.5332	-2.4689	39324
$EL1$	-12.680	-2.6283	0.0818	0.0327	0.5000	-2.7931	26216
$EL4_{Case 1}$	-1.0742	-0.0860	-0.0029	0.0000	0.2769	-1.0667	117972
$EL4_{Case 2}$	-2.9077	0.3489	-0.0195	0.5244	0.6574	-1.0222	117972
$EL4_{Case 3}$	-1.1401	-0.0887	-0.0027	0.0000	0.3962	-1.0659	170404
$EL3_{Case 1}$	-1.1021	-0.0847	-0.0028	0.0022	0.2478	-1.0668	91756
$EL3_{Case 2}$	-3.6975	0.7041	-0.0351	0.3716	0.8013	-0.6621	91756
$EL3_{Case 3}$	-1.1377	-0.0849	-0.0028	0.0022	0.3967	-1.0654	131080
$EL2_{Case 1}$	-0.6215	-0.0647	-0.0062	-0.0171	0.2741	-1.0740	65540
$EL2_{Case 2}$	-7.1876	0.5386	0.0363	-0.4764	0.6981	-0.2952	65540
$EL2_{Case 3}$	-1.1572	-0.0937	-0.0041	-0.0173	0.3943	-1.0729	91756
$EL1_{Case 1}$	-4.6472	0.4951	0.0103	0.8077	0.5429	-0.8084	39324
$EL1_{Case 2}$	-12.137	-2.2188	0.0890	0.9437	0.4528	-2.9806	39324
$EL1_{Case 3}$	-1.0557	0.9225	-0.0045	0.9191	0.4924	-0.6172	52432

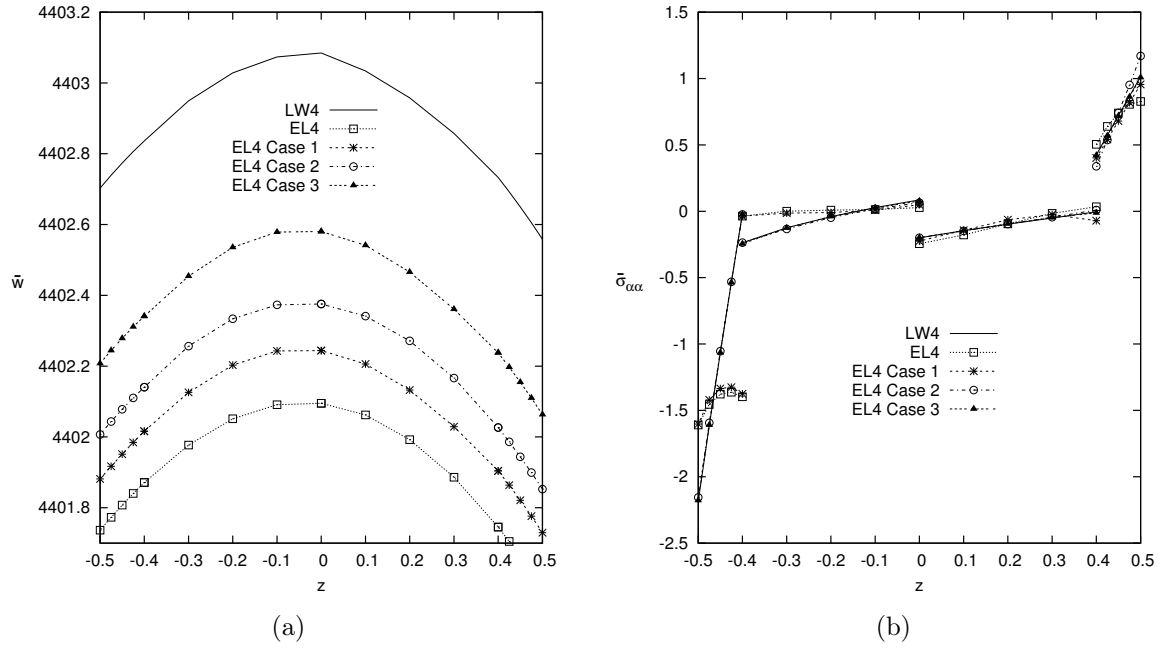


Figure 9.69: Four-layered cylinder, Sensor case, transverse mechanical displacement and in-plane stress, \hat{w} for $R/h = 100$ (a), $\hat{\sigma}_{\alpha\alpha}$ for $R/h = 2$ (b).

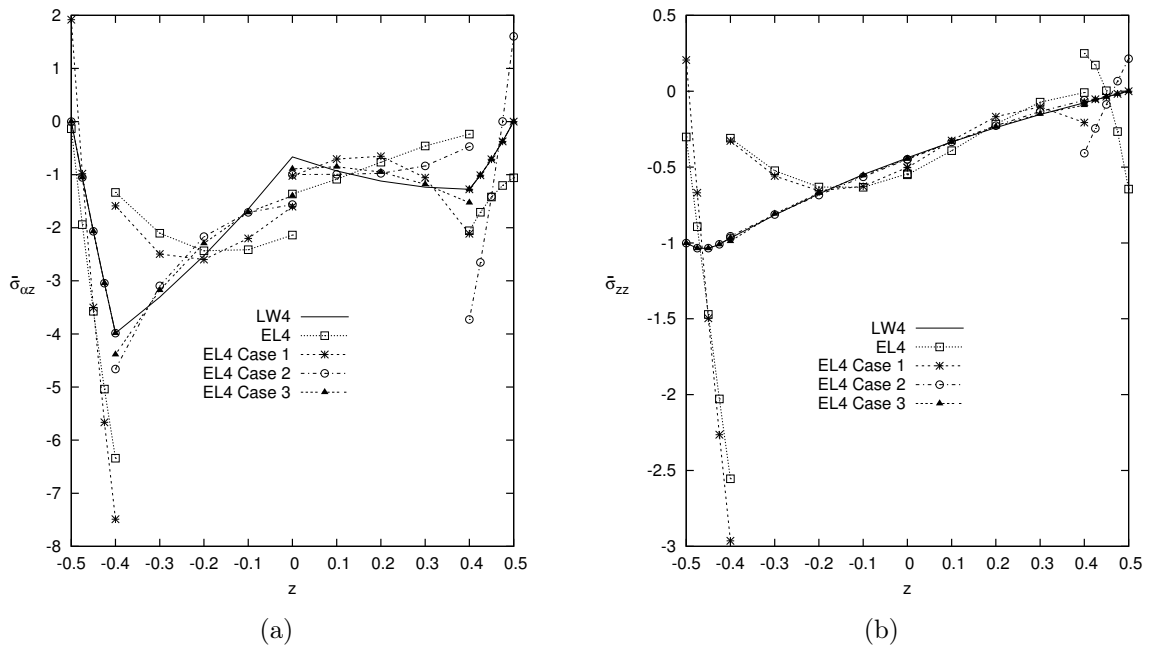


Figure 9.70: Four-layered cylinder, Sensor case, transverse mechanical stresses, $\hat{\sigma}_{\alpha z}$ for $R/h = 100$ ratio (a), $\hat{\sigma}_{zz}$ for $R/h = 2$ ratio (b).

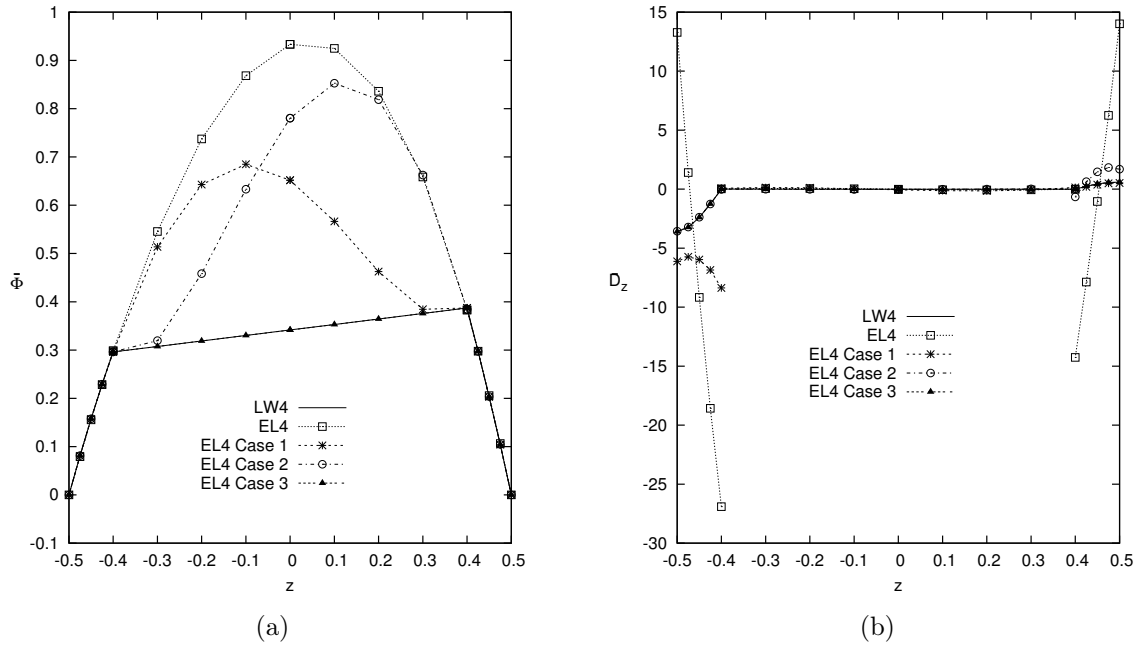


Figure 9.71: Four-layered cylinder, Sensor case, electric potential and transverse electric displacement, $\hat{\Phi}$ for $R/h = 100$ (a), and \hat{D}_z for $R/h = 2$ (b).

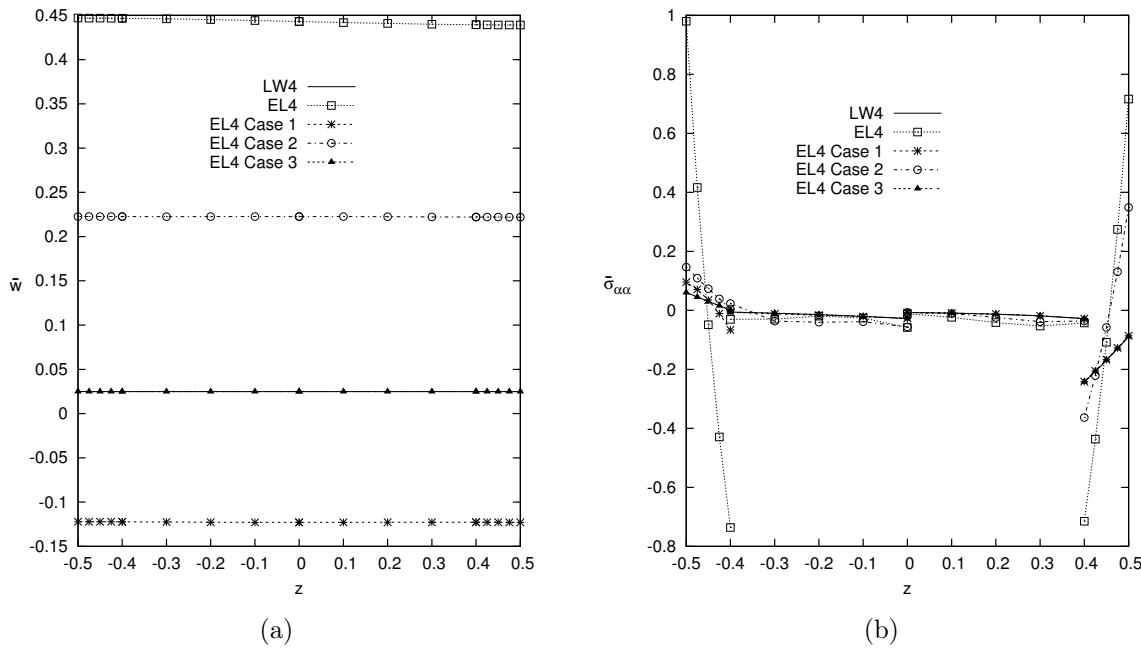


Figure 9.72: Four-layered cylinder, Actuator case, transverse mechanical displacement and in-plane stress, \hat{w} for $R/h = 100$ (a), $\hat{\sigma}_{\alpha\alpha}$ for $R/h = 2$ (b).

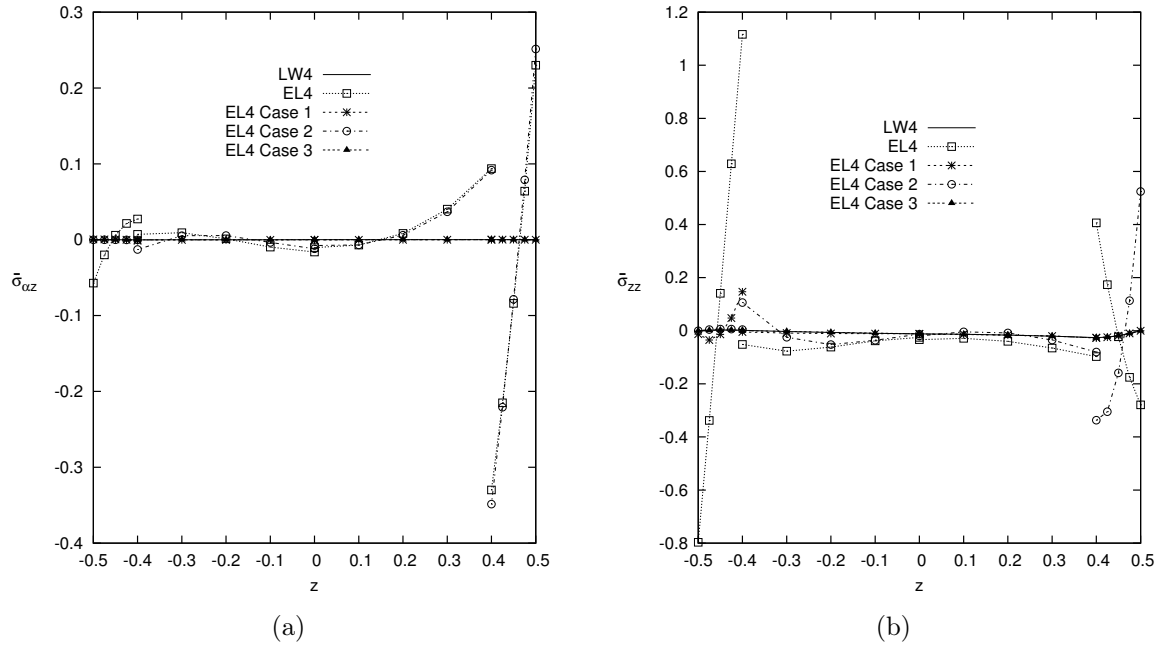


Figure 9.73: Four-layered cylinder, Actuator case, transverse mechanical stresses, $\hat{\sigma}_{\alpha z}$ for $R/h = 100$ ratio (a), $\hat{\sigma}_{zz}$ for $R/h = 2$ ratio (b).

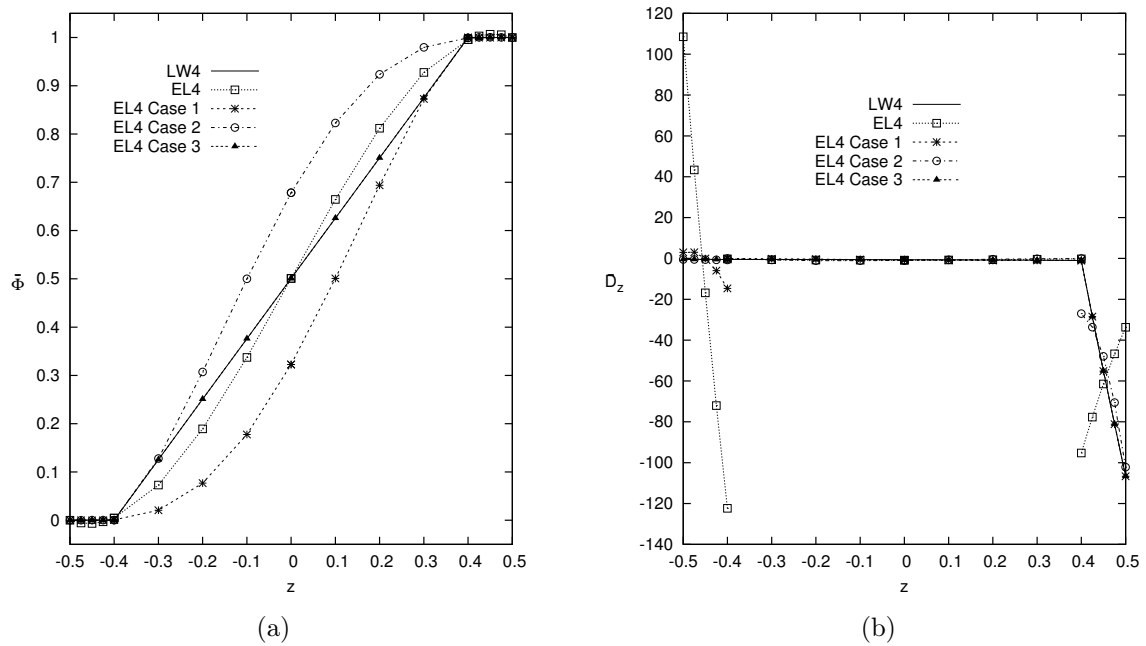


Figure 9.74: Four-layered cylinder, Actuator case, electric potential and transverse electric displacement, $\hat{\Phi}$ for $R/h = 100$ (a), and \hat{D}_z for $R/h = 2$ (b).

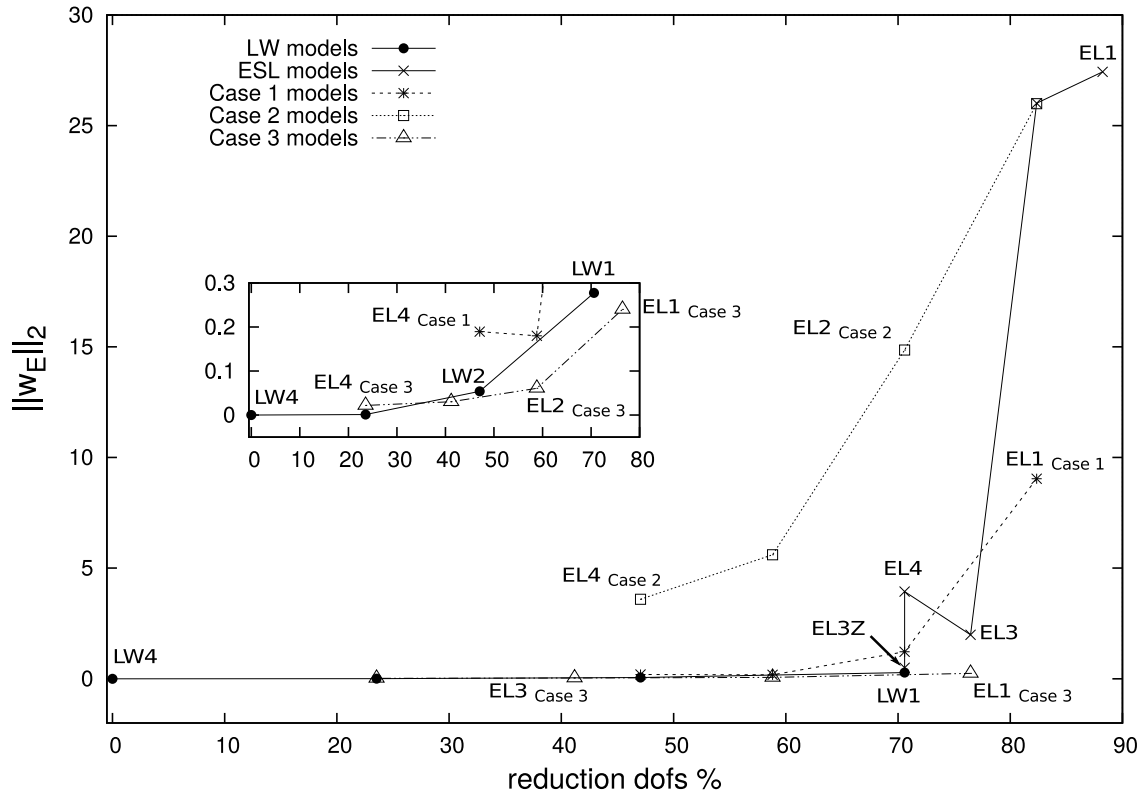


Figure 9.75: Four-layered cylinder, Actuator case, Euclidean Norm Error of the transverse mechanical displacement, \hat{w} for $R/h = 2$.

Chapter 10

Node-Dependent Variable Kinematic

In a global/local scenario, as told in the previous chapter, the limited computational resources can be distributed in an optimal manner to study in detail only those parts of the structure that require an accurate analysis. In general, two main approaches are available to deal with a global/local analysis: refining the mesh or the FE shape functions in correspondence with the critical domain; formulating multi-model methods, in which different subregions of the structure are analysed with different mathematical models. To couple coarse and refined mesh discretizations of different subregions of a structure, adaptive techniques are often used. The h-adaptation method [160] is used when the structure's subregions differ in mesh size, whereas the p-adaptation method [161] can be applied when the subregions vary in the polynomial order of the shape functions. Moreover, the hp-adaptation [113] can allow the implementation of subregions differing in both mesh size and shape functions. The methods mentioned so far can be addressed as single-theory or single-model methods.

In the case of multi-theory methods, in which different subregions of the structure are analysed with different structural theories with kinematically incompatible elements, the compatibility of displacements and equilibrium of stresses at the interface between dissimilar elements have to be achieved. A wide variety of multiple model methods have been reported in the literature. In general, multi-theory methods can be divided into sequential or multistep methods, and simultaneous methods. In a sequential multi-model, the global region is analysed with an adequate model with a cheap computational cost to determine the displacement or force boundary conditions for a subsequent analysis at the local level. The local region can be modeled with a more refined theory, or it can be modeled with 3-D finite elements, see [162–165]. The simultaneous multi-model methods are characterized by the analysis of the entire structural domain, where different subregions are modeled with different mathematical models and/or distinctly different levels of domain discretization, in a unique step. A well-known method to couple incompatible kinematics in multi-model methods, is the use of Lagrange multipliers, which serve as additional equations to enforce compatibility between adjacent subregions. In the three-field formulation by Brezzi and Marini [166], an additional grid at the interface is introduced. The unknowns are represented independently in each sub-domain and at the interface, where the matching is provided by suitable Lagrange multipliers. This method was recently adopted by Carrera *et al.* [167–169] to couple beam elements of different orders and, thus, to develop variable kinematic beam theories. Ben Dhia *et al.* [170–172] proposed the Arlequin method to couple different numerical models by means of a minimization procedure. This method was adopted by Hu *et al.* [173, 174] for the linear and non-linear analysis of sandwich beams modelled via one-dimensional and two-dimensional finite elements, and by Biscani *et al.* [175] for the analysis of beams and by Biscani *et al.* [176] for the analysis of plates. Reddy and Robbins [177] and Reddy [178] presented a multiple-model method on the basis of a variable kinematic theory and on mesh superposition in the sense of Fish [179] and Fish and Markolefas [180]. Coupling was obtained by linking the FSDT variables, which are present in all the considered models, without us-

ing Lagrangian multipliers. The coupling of different kinematics model in the framework of composite beam structure, using the extended variational formulation (XVF), is presented in [181], sinus model and classical kinematics are coupled into non-overlapping domains. In this chapter, the concept of the present node-dependent variable kinematic model is used to develop a new simultaneous multiple-model method, by 2D elements with node-dependent kinematics, for the simultaneous global/local analysis. This node-variable capability enables one to vary the kinematic assumptions within the same finite plate/shell element. The expansion order of the plate/shell element is, in fact, a property of the FE node in the present approach. Therefore, between finite elements, the continuity is ensured by adopting the same expansion order in the nodes at the element interface. In this manner, global/local models can be formulated without the use of any mathematical artifice. As a consequence, computational costs can be reduced assuming refined models only in those zones with a quasi-three-dimensional stress field, whereas computationally cheap, low-order kinematic assumptions are used in the remaining parts of the plate/shell structure.

10.1 Models Coupling

In literature finite elements with different kinematics, see Figure 10.1, can be coupled using additional equations or mathematical artifices, as summerized in the previous introductory section 10. The most common method to couple finite elements with different kinematics are: the Lagrange Multipliers method, and the Arlequin method.

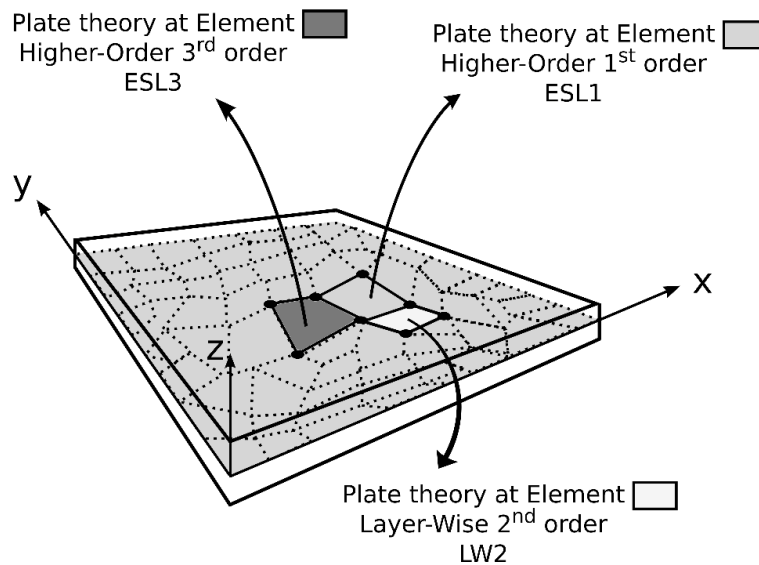


Figure 10.1: Coupling example scheme of finite elements with different kinematics.

In this work a class of new finite elements which allows employing different kinematic assumptions in different subregions of the problem domain is proposed. To highlight the capabilities of the novel formulation, a four-node plate elements with node-dependent kinematics is shown in Figure 10.2. A concentrated load is depicted as P and located at node 7. Global $LW4$ and $ESL4$ zones describe the kinematics around the concentrated load, therefore a local description is given at node 6 and 7 with $LW4$ kinematics and at node 2 and 8 with a refined $ESL4$ higher-order plate theory. Far from the load, global lower-order zones are described as $ESL2$ and $ESL1$. A local approximation is given here at node 3 and 5 with a $ESL2$ parabolical kinematics, and at node 1 and 4 with a linear model $ESL1$. As it will be clear later in this chapter, different kinematics are defined in the global nodes. Shared

nodes between adjacent finite elements have the same kinematics. The coupling of different kinematics is naturally obtained inside the finite element without any mathematical artifice or additional equations.

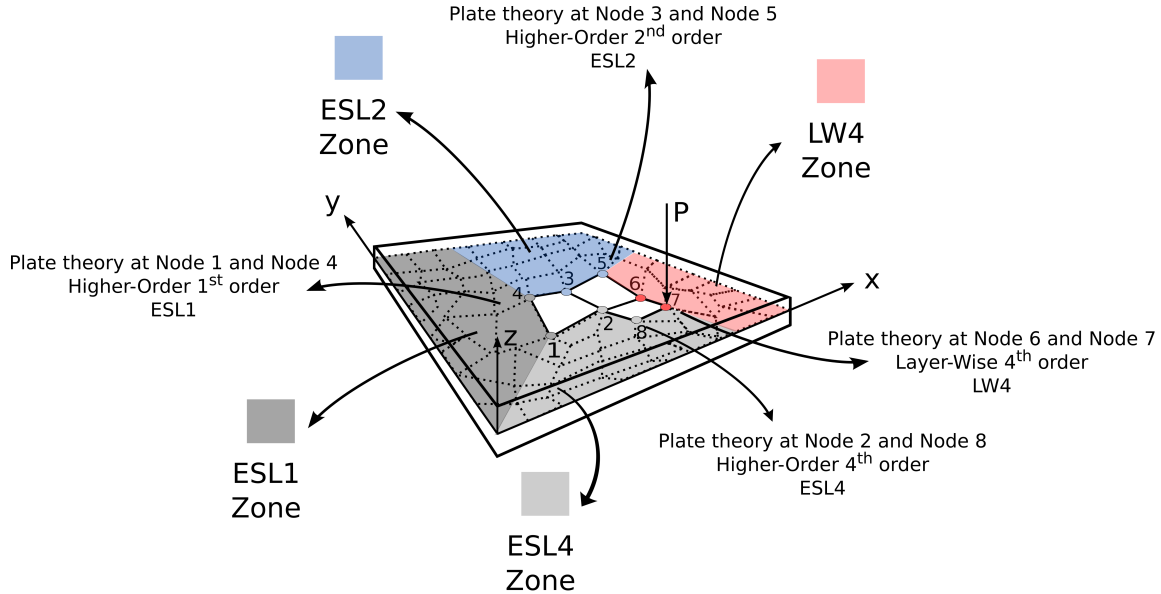


Figure 10.2: Example of finite element with node-dependent kinematics.

The capabilities of the novel formulation can be successfully applied to multifield problems. For example a multilayered structure with piezoelectric patches, sensors and actuators, can be opportunely described in higher-order and lower-order zones, as shown in Figure 10.3.

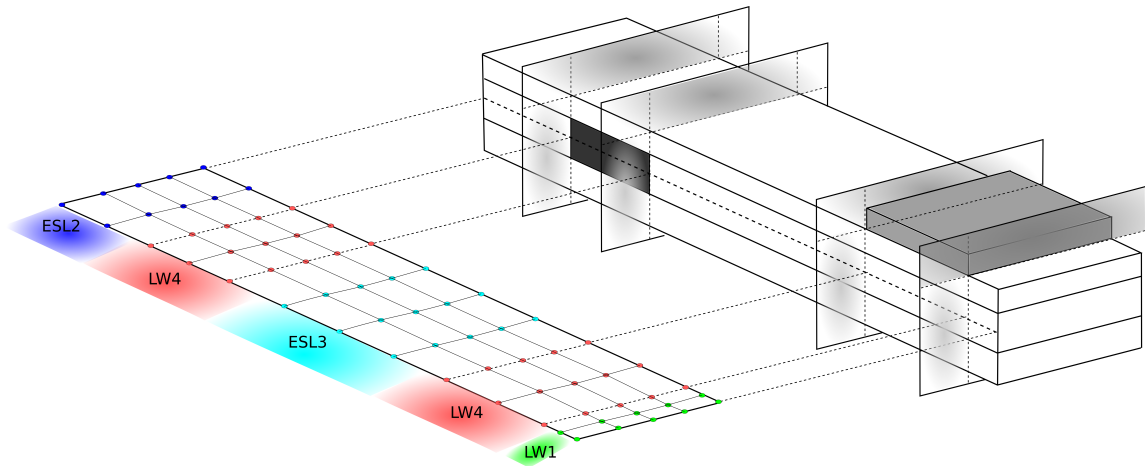


Figure 10.3: Example of finite element with node-dependent kinematics applied to multifield analysis of a multilayered structure with piezoelectric patches.

10.2 Finite elements with node-dependent kinematics

As described in Section 5.1, by utilizing an FEM approximation, the generalized displacements can be expressed as a linear combination of the shape functions, see Equation 5.1, to have:

$$\mathbf{u} = \mathbf{N}_j \mathbf{u}_j \quad \delta \mathbf{u} = \mathbf{N}_i \delta \mathbf{u}_i \quad \text{with } i, j = 1, \dots, (\text{nodes per element})$$

In this work, the thickness functions F_s and F_τ , which determine the plate/shell theory order, are independent variables and may change for each node within the plate/shell element.

Namely, the three-dimensional displacement field and the related virtual variation can be expressed to address FE node-dependent plate/shell kinematics as follows:

$$\begin{aligned} \mathbf{u}(x, y, z) &= F_s^j(z) N_j(x, y) \mathbf{u}_{s_j} \quad s = 0, 1, \dots, N^j \quad j = 1, \dots, (\text{nodes per element}) \\ \delta \mathbf{u}(x, y, z) &= F_\tau^i(z) N_i(x, y) \delta \mathbf{u}_{\tau_i} \quad \tau = 0, 1, \dots, N^i \quad i = 1, \dots, (\text{nodes per element}) \end{aligned} \quad (10.1)$$

where the subscripts τ , s , i , and j denote summation. Superscripts i and j denote node dependency, such that for example F_τ^i is the thickness expanding function and N^i is the number of expansion terms at node i , respectively.

For the sake of clarity, the displacement field of the variable kinematic finite elements as discussed in Figure 10.2 is described in detail hereafter. The darker finite element is represented in Figure 10.4, which also shows the through-the-thickness kinematics at the nodal level. The global displacement field of the element is approximated as follows:

- Node 1 Theory = HOT with $N^1 = 3$ Eq. (3.6)
- Node 2 Theory = LW with $N^2 = 2$ Eq. (3.9)
- Node 3 Theory = HOT with $N^3 = 1$ Eq. (3.6)
- Node 4 Theory = HOT with $N^4 = 3$ Eq. (3.6)

In according to Equation (10.1), it is easy to verify that the displacements at a generic point belonging to the plate element can be expressed as given in Equation (10.2). In this equation, only the displacement component along x -axis is given for simplicity reasons:

$$\begin{aligned} u(x, y, z) &= (u_{0_1} + z u_{1_1} + z^2 u_{2_1} + z^3 u_{3_1}) N_1(x, y) \\ &+ \left[\left(\frac{1+\zeta}{2} \right) u_{0_2} + \left(\frac{1-\zeta}{2} \right) u_{1_2} + \left(\frac{3\zeta^2-1}{2} - 1 \right) u_{2_2} \right] N_2(x, y) \\ &+ (u_{0_3} + z u_{1_3}) N_3(x, y) + (u_{0_4} + z u_{1_4} + z^2 u_{2_4} + z^3 u_{3_4}) N_4(x, y) \end{aligned} \quad (10.2)$$

It is intended that, due to node-variable expansion theory order, the assembling procedure of each finite element increases in complexity with respect to classical mono-theory finite elements. In the present FE approach, in fact, it is clear that both rectangular and square arrays are handled and opportunely assembled for obtaining the final elemental matrices.

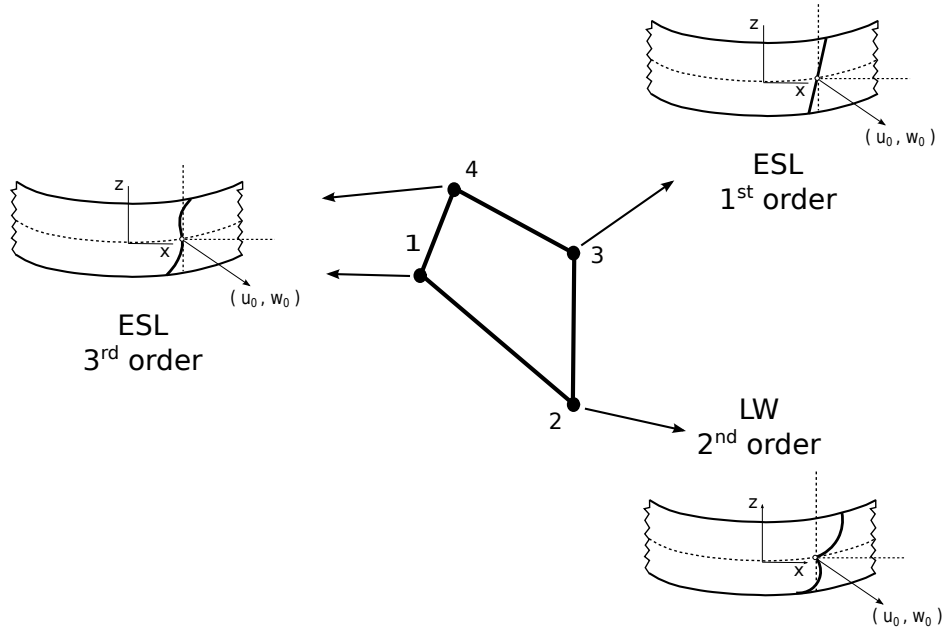


Figure 10.4: Displacement field at the nodal level of the finite element with node-dependent kinematics.

10.2.1 Fundamental nucleus of the stiffness matrix

The governing equations for the static response analysis of the multi-layer plate structure can be obtained by using the principle of virtual displacements, see Section 4.2, which states:

$$\int_{\Omega} \int_A \delta \boldsymbol{\epsilon}^T \boldsymbol{\sigma} \, d\Omega \, dz = \delta L_e \quad (10.3)$$

where the term on the left-hand side represents the virtual variation of the strain energy; Ω and A are the integration domains in the plane and the thickness direction, respectively; $\boldsymbol{\epsilon}$ and $\boldsymbol{\sigma}$ are the vector of the strain and stress components; and δL_e is the virtual variation of the external loadings. By substituting the constitutive equations for composite elastic materials, the linear geometrical relations as well as Equation (10.1) into Equation (10.3), the linear algebraic system in the form of governing equations is obtained in the following matrix expression:

$$\delta \mathbf{u}_{\tau_i} : \mathbf{K}^{\tau s i j} \mathbf{u}_{s_j} = \mathbf{P}^{\tau_i} \quad (10.4)$$

where $\mathbf{K}^{\tau s i j}$ and \mathbf{P}^{τ_i} are the element stiffness and load FE arrays written in the form of *fundamental nuclei*. In particular, $\mathbf{K}^{\tau s i j}$ is a 3×3 matrix whose components are given for the plate case in the following:

$$\begin{aligned} K_{xx}^{\tau s i j} = & \int_{\Omega} N_i N_j \, d\Omega \int_A C_{55} F_{\tau,z}^i F_{s,z}^j \, dz + \int_{\Omega} N_{i,y} N_{j,y} \, d\Omega \int_A C_{66} F_{\tau}^i F_s^j \, dz + \int_{\Omega} N_{i,x} N_{j,y} \, d\Omega \int_A C_{16} F_{\tau}^i F_s^j \, dz + \\ & + \int_{\Omega} N_{i,y} N_{j,x} \, d\Omega \int_A C_{16} F_{\tau}^i F_s^j \, dz + \int_{\Omega} N_{i,x} N_{j,x} \, d\Omega \int_A C_{11} F_{\tau}^i F_s^j \, dz \end{aligned}$$

$$\begin{aligned} K_{xy}^{\tau s i j} = & \int_{\Omega} N_i N_j \, d\Omega \int_A C_{45} F_{\tau,z}^i F_{s,z}^j \, dz + \int_{\Omega} N_{i,y} N_{j,y} \, d\Omega \int_A C_{26} F_{\tau}^i F_s^j \, dz + \int_{\Omega} N_{i,x} N_{j,y} \, d\Omega \int_A C_{12} F_{\tau}^i F_s^j \, dz + \\ & + \int_{\Omega} N_{i,y} N_{j,x} \, d\Omega \int_A C_{66} F_{\tau}^i F_s^j \, dz + \int_{\Omega} N_{i,x} N_{j,x} \, d\Omega \int_A C_{16} F_{\tau}^i F_s^j \, dz \end{aligned}$$

$$\begin{aligned} K_{xz}^{\tau s i j} = & \int_{\Omega} N_i N_{j,y} \, d\Omega \int_A C_{45} F_{\tau,z}^i F_s^j \, dz + \int_{\Omega} N_i N_{j,x} \, d\Omega \int_A C_{55} F_{\tau,z}^i F_s^j \, dz + \int_{\Omega} N_{i,y} N_j \, d\Omega \int_A C_{36} F_{\tau}^i F_{s,z}^j \, dz + \\ & + \int_{\Omega} N_{i,x} N_j \, d\Omega \int_A C_{13} F_{\tau}^i F_{s,z}^j \, dz \end{aligned}$$

$$\begin{aligned} K_{yx}^{\tau s i j} = & \int_{\Omega} N_i N_j \, d\Omega \int_A C_{45} F_{\tau,z}^i F_{s,z}^j \, dz + \int_{\Omega} N_{i,y} N_{j,y} \, d\Omega \int_A C_{26} F_{\tau}^i F_s^j \, dz + \int_{\Omega} N_{i,x} N_{j,y} \, d\Omega \int_A C_{66} F_{\tau}^i F_s^j \, dz + \\ & + \int_{\Omega} N_{i,y} N_{j,x} \, d\Omega \int_A C_{12} F_{\tau}^i F_s^j \, dz + \int_{\Omega} N_{i,x} N_{j,x} \, d\Omega \int_A C_{16} F_{\tau}^i F_s^j \, dz \end{aligned}$$

$$\begin{aligned} K_{yy}^{\tau s i j} = & \int_{\Omega} N_i N_j \, d\Omega \int_A C_{44} F_{\tau,z}^i F_{s,z}^j \, dz + \int_{\Omega} N_{i,y} N_{j,y} \, d\Omega \int_A C_{22} F_{\tau}^i F_s^j \, dz + \int_{\Omega} N_{i,x} N_{j,y} \, d\Omega \int_A C_{26} F_{\tau}^i F_s^j \, dz + \\ & + \int_{\Omega} N_{i,y} N_{j,x} \, d\Omega \int_A C_{26} F_{\tau}^i F_s^j \, dz + \int_{\Omega} N_{i,x} N_{j,x} \, d\Omega \int_A C_{66} F_{\tau}^i F_s^j \, dz \end{aligned}$$

$$\begin{aligned} K_{yz}^{\tau s i j} = & \int_{\Omega} N_i N_{j,y} \, d\Omega \int_A C_{44} F_{\tau,z}^i F_s^j \, dz + \int_{\Omega} N_i N_{j,x} \, d\Omega \int_A C_{45} F_{\tau,z}^i F_s^j \, dz + \int_{\Omega} N_{i,y} N_j \, d\Omega \int_A C_{23} F_{\tau}^i F_{s,z}^j \, dz + \\ & + \int_{\Omega} N_{i,x} N_j \, d\Omega \int_A C_{36} F_{\tau}^i F_{s,z}^j \, dz \end{aligned}$$

$$\begin{aligned}
 K_{zx}^{\tau isj} &= \int_{\Omega} N_i N_{j,y} d\Omega \int_A C_{36} F_{\tau,z}^i F_s^j dz + \int_{\Omega} N_i N_{j,x} d\Omega \int_A C_{13} F_{\tau,z}^i F_s^j dz + \int_{\Omega} N_{i,y} N_j d\Omega \int_A C_{45} F_{\tau}^i F_{s,z}^j dz + \\
 &\quad + \int_{\Omega} N_{i,x} N_j d\Omega \int_A C_{55} F_{\tau}^i F_{s,z}^j dz \\
 K_{zy}^{\tau isj} &= \int_{\Omega} N_i N_{j,y} d\Omega \int_A C_{23} F_{\tau,z}^i F_s^j dz + \int_{\Omega} N_i N_{j,x} d\Omega \int_A C_{36} F_{\tau,z}^i F_s^j dz + \int_{\Omega} N_{i,y} N_j d\Omega \int_A C_{44} F_{\tau}^i F_{s,z}^j dz + \\
 &\quad + \int_{\Omega} N_{i,x} N_j d\Omega \int_A C_{45} F_{\tau}^i F_{s,z}^j dz \\
 K_{zz}^{\tau isj} &= \int_{\Omega} N_i N_j d\Omega \int_A C_{33} F_{\tau,z}^i F_{s,z}^j dz + \int_{\Omega} N_{i,y} N_{j,y} d\Omega \int_A C_{44} F_{\tau}^i F_s^j dz + \int_{\Omega} N_{i,x} N_{j,y} d\Omega \int_A C_{45} F_{\tau}^i F_s^j dz + \\
 &\quad + \int_{\Omega} N_{i,y} N_{j,x} d\Omega \int_A C_{45} F_{\tau}^i F_s^j dz + \int_{\Omega} N_{i,x} N_{j,x} d\Omega \int_A C_{55} F_{\tau}^i F_s^j dz
 \end{aligned}$$

where comma denote partial derivatives and $C_{11}, C_{12}, \dots, C_{66}$ are the material coefficients for a monoclinic lamina as defined in [66].

The fundamental nucleus as given above is the basic building block for the construction of the element stiffness matrix of classical, refined and variable-kinematic theories. In fact, given these nine components, element stiffness matrices of arbitrary plate models can be obtained in an automatic manner by expanding the fundamental nucleus versus the indexes $k, \tau, s, i,$ and j . In the development of both ESL and LW theories, the fundamental nucleus of the stiffness matrix is evaluated at the layer level and then assembled as shown in Figure 10.5. This figure, in particular, illustrates the expansion of the fundamental nucleus in the case of a 9-node Lagrange finite element with node-dependent variable kinematics with different Taylor polynomial expansions, as example.

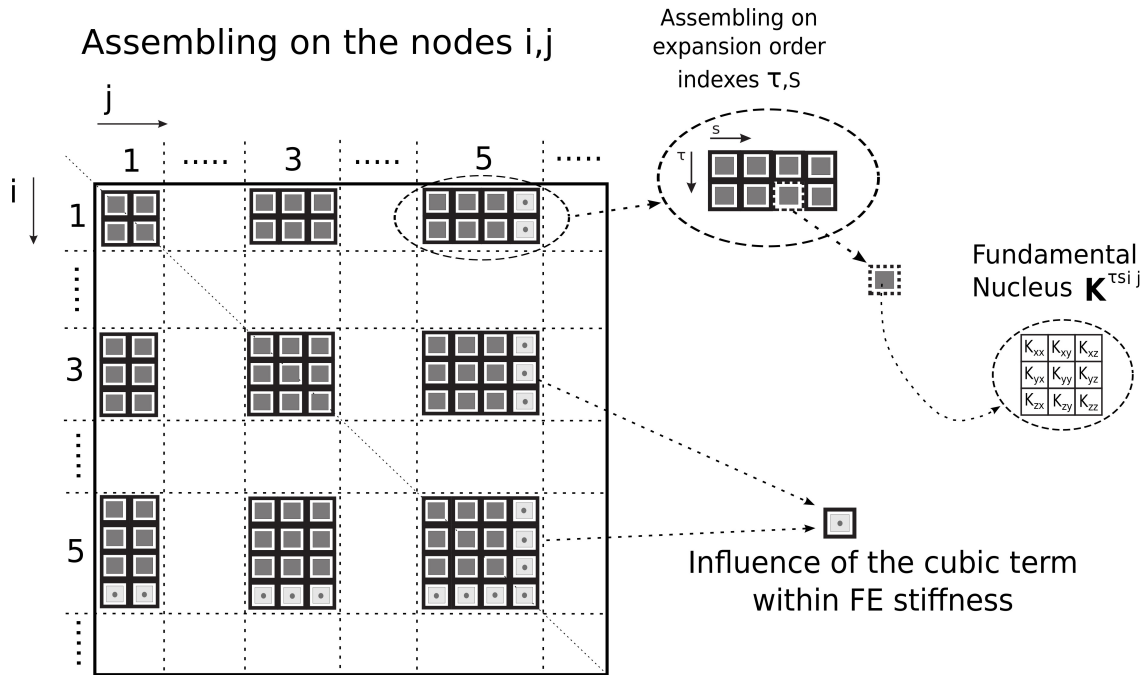
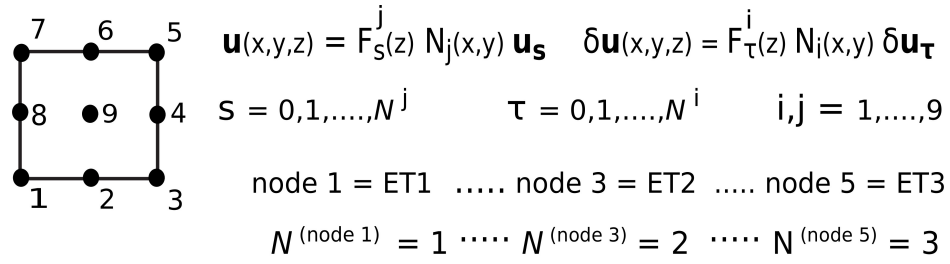


Figure 10.5: Assembling scheme of a 9-node finite element with node-dependent kinematics. Highlights of the influence of the cubic term of a 3rd order Taylor expansion model in the FE stiffness.

10.3 Mechanical Analysis Results

Some problems have been considered to assess the capabilities of the proposed variable-kinematics plate elements and related global/local analysis. These analysis cases comprise:

- Isotropic plate simply-supported, with centered localized uniform pressure
- Eight-layered composite cantilvered plate, with free-tip concentrated load
- Three-layered composite plate simply supported, with centered localized uniform pressure
- Unsymmetrically laminated sandwich rectangular plate simply supported, with centered localized uniform pressure

Whenever possible, the proposed multi-theory models are compared to single-theory from higher-order ESL models, LW models, 3D elasticity solutions and analytical results. Moreover different multi-theory models present in literature are given in some cases. For the sake of clarity, present multi-model theories are opportunely described for each numerical case considered.

10.3.1 Simply-supported isotropic plate under localized pressure load

A simply-supported isotropic plate is analysed. The geometrical dimensions are: $a = 2 m$, $b = h = 0.2 m$. The employed material is isotropic, with the following properties: $E = 75 GPa$, $G = 28,846 GPa$, $\nu = 0,3$. The plate is simply-supported along two opposite sides and free along the remaining two edges. It undergoes a localised uniform pressure, $P = 1 Pa$, acting on the 10% of the length and centered at the mid-span, see Figure 10.6a. The transverse section of the proposed structure is shown in Figure 10.6b, where the verification points at which displacement and stress components are measured are also depicted. The results of the present methodology, in fact, are compared with some solutions from the literature and with an MSC/NASTRAN solid model made of 8-node CHEXA elements. With reference to Figure 10.6b, the in-plane displacements u and shear stress component σ_{xz} are evaluated at $x = 0$, whereas the other two displacement components v and w and the normal stresses σ_{xx} and σ_{zz} are evaluated at plate mid-span. The results are given in the following non-dimensional form:

$$(\hat{u}, \hat{v}, \hat{w}) = \frac{Eh}{a^2 P} (u, v, w) \quad (\hat{\sigma}_{xx}, \hat{\sigma}_{xz}, \hat{\sigma}_{zz}) = \frac{1}{P} (\sigma_{xx}, \sigma_{xz}, \sigma_{zz}) \quad (10.5)$$

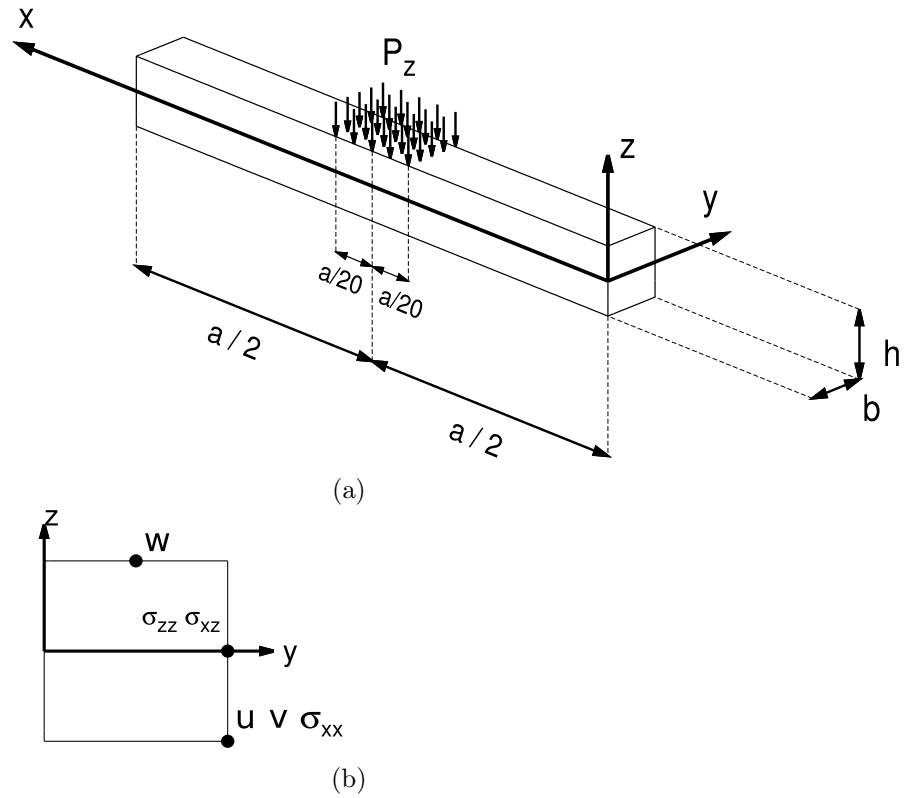


Figure 10.6: Reference system of the isotropic plate (a), and placement of the evaluation points on the transverse section (b).

First, a convergence study is conducted. To serve this scope and as shown in Figure 10.7, the plate structure has been subdivided into 5 zones along the axis x , and they are numbered from 1 to 3 for symmetry reasons. The choice of dividing the structure in this manner was made for allowing fair comparisons with other models from the literature [167, 175]. According to Table 10.1, which shows the converge study of the single-theory *ET4* model for various mesh discretizations and related comparison with different solid models from MSC/NASTRAN, a non-uniform mesh grid of 20×4 elements is enough for ensuring good results. The same mesh is depicted in Figure 10.7 and it is used in the remaining analyses for the definition of the single- and multi-theory models.

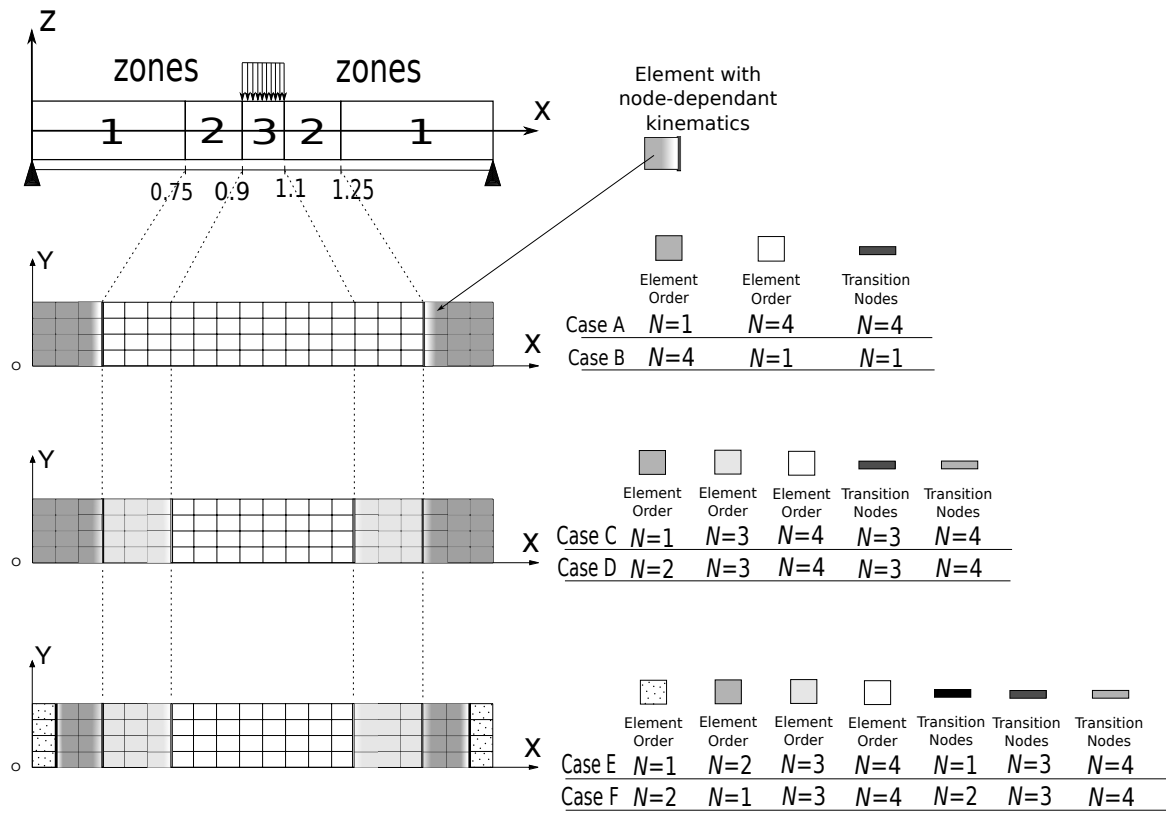


Figure 10.7: Subdivision zones for the isotropic plate, final mesh grid chosen after convergence study, and graphical description of the multi-theory models.

Table 10.1: Convergence study according to the *ET4* model of the isotropic plate structure.

			$(-10)\hat{u}$	$(-10^2)\hat{v}$	$-\hat{w}$	$(10^{-1})\hat{\sigma}_{xx}$	$(-10)\hat{\sigma}_{xz}$	$(-10)\hat{\sigma}_{zz}$	<i>DOFs*</i>
Present Plate Element									
<i>Mesh</i> 10×4									
<i>zone1</i>	<i>zone2</i>	<i>zone3</i>	3.743	2.129	2.544	1.440	8.640	5.287	2835
2×4	2×4	2×4							
<i>Mesh</i> 16×4									
<i>zone1</i>	<i>zone2</i>	<i>zone3</i>	3.744	2.126	2.544	1.431	8.641	5.247	4455
3×4	3×4	4×4							
<i>Mesh</i> 20×4									
<i>zone1</i>	<i>zone2</i>	<i>zone3</i>	3.743	2.126	2.544	1.431	8.641	5.248	5535
4×4	4×4	4×4							
<i>Mesh</i> 20×8									
<i>zone1</i>	<i>zone2</i>	<i>zone3</i>	3.743	2.126	2.544	1.431	8.637	5.254	10455
4×8	4×8	4×8							
<i>Mesh</i> 30×4									
<i>zone1</i>	<i>zone2</i>	<i>zone3</i>	3.743	2.125	2.544	1.429	8.641	5.263	8235
6×4	6×4	6×4							
<i>Mesh</i> 20×4									
<i>zone1</i>	<i>zone2</i>	<i>zone3</i>	3.743	2.125	2.544	1.429	8.641	5.267	5535
3×4	3×4	8×4							
8 node SOLID CHEXA MSC/NASTRAN									
<i>Mesh</i> $100 \times 20 \times 20$			3.788	2.124	2.544	1.352	8.402	5.202	131859
<i>Mesh</i> $100 \times 40 \times 40$			3.667	2.124	2.544	1.389	8.502	5.216	502619
<i>Mesh</i> $80 \times 40 \times 40$			3.440	2.124	2.544	1.388	8.502	5.197	401759
<i>Mesh</i> $100 \times 60 \times 60$			3.776	2.124	2.544	1.402	8.533	5.221	1112579

*: Degrees of freedom of the whole plate structure

Table 10.2 shows the results for the present metallic plate from various single- and multi-theory models. Solutions from the literature [167, 175] are also given for comparison. Multi-theory models are referred to as *Case A* to *Case F*, and they are defined according to Figure 10.7. In particular, in *Case A*, lower-order kinematics is employed at the plate boundaries, whereas 4-th order plate theory is used close to the loading. Vice-versa, in *Case B*, refined approximation orders are utilized close to the boundary. The present *Case A* and *Case B* multi-theory models are analogous to models *Arlequin^A* and *Arlequin^B* from [175], where the Arlequin method was used to mix finite beam elements with different kinematics at the interface, and *LM^A* and *LM^B* from [167], where Lagrange multipliers were used along with 1D beam element to implement variable kinematic beam theories. Results from other original global/local plate models referred to as *Case C* to *Case F* are also given in Table 10.2 and they are graphically explained in Figure 10.7. Therefore the models named TE1-TE4 are beam mono-models with the description of the beam section via Taylor polynomials from order 1 to 4 from [167]. All the multi-theory models, presented here, have been implemented discretizing structural domains with lower- and higher-order theories and coupling them by enforcing the same kinematics at the interface nodes. In this manner, there is no information loss and no need to adopt any mathematical artifice, such as Lagrange multipliers or *overlapping regions*.

Table 10.2: Simply-supported metallic plate. Displacement and stress components from single-theory, multi-theory and reference models.

	$(-10)\hat{u}$	$(-10^2)\hat{v}$	$-\hat{w}$	$(10^{-1})\hat{\sigma}_{xx}$	$(-10)\hat{\sigma}_{xz}$	$(-10)\hat{\sigma}_{zz}$	$DOFs^*$
Reference solutions [175]							
<i>SOLID</i>	3.776	2.124	2.544	1.402	8.533	5.221	558150
<i>Arlequin^A</i>	3.729	2.116	2.537	1.424	5.000	5.217	1197
<i>Arlequin^B</i>	3.716	-0.056	2.547	1.444	8.352	4.807	1197
<i>LM^A</i>	3.699	2.116	2.524	1.420	5.000	6.001	1134
<i>LM^B</i>	3.732	-0.080	2.550	1.419	8.429	4.395	1134
<i>TE4</i>	3.735	2.116	2.542	1.423	8.511	6.003	2745
<i>TE3</i>	3.735	2.092	2.542	1.425	8.462	6.063	1830
<i>TE2</i>	3.729	2.108	2.532	1.409	5.865	4.265	1098
<i>TE1</i>	3.736	-0.080	2.548	1.419	5.000	4.395	549
Present single- and multi-theory models							
<i>ET4</i>	3.743	2.125	2.544	1.429	8.641	5.267	2835
<i>ET3</i>	3.742	2.139	2.544	1.434	8.641	5.286	2268
<i>ET2</i>	3.731	2.097	2.534	1.402	6.262	5.087	1701
<i>ET1</i>	3.402	2.688	2.323	1.414	6.265	4.594	1134
<i>Case A</i>	3.562	2.125	2.460	1.429	6.265	5.267	2349
<i>Case B</i>	3.587	2.688	2.413	1.414	8.708	4.594	1620
<i>Case C</i>	3.561	2.125	2.460	1.429	6.256	5.275	2187
<i>Case D</i>	3.731	2.125	2.537	1.429	6.263	5.276	2349
<i>Case E</i>	3.704	2.125	2.532	1.429	6.358	5.276	2133
<i>Case F</i>	3.591	2.125	2.465	1.429	6.154	5.275	2133

* : for a fair comparison with reference solutions, DOFs are given for half plate structure

Additional results in terms of transverse displacement w , in-plane stress σ_{xx} , transverse shear stress σ_{xz} and transverse normal stress σ_{zz} along the thickness are represented in Figures 10.8, 10.9, 10.10, and 10.11, respectively. The following comments can be drawn from the analysis:

- Single-theory models with lower expansion order, i.e. *ET1* and *ET2*, yield good results in terms of displacements and in-plane stress, σ_{xx} . However, in order to accurately describe the shear and normal transverse stresses σ_{xz} and σ_{zz} , higher-order theories, such as *ET3* and *ET4*, are required.
- Depending on the structural domain of interest, multi-theory models allow us to enrich the solution in a smart and efficient manner. Nevertheless, accurate analysis may require attentive distribution of the kinematics approximation through the problem domain. For example, although *Case E* and *Case F* models have the same number of DOFs and according to Figure 10.8, the distribution of the transverse displacement w through the thickness can vary significantly. Contrarily, the in-plane stress σ_{xx} is not sensitive to variable-kinematic modeling, see Figure 10.9.
- As further guidelines, it is clear from Figure 10.10 that, as far as the accuracy on the transverse shear stress σ_{xz} is concerned, higher-order approximation theories must be placed close to the boundaries. This is the case of the *Case B* model and mono-theory

models *ET3* and *ET4*. Contrarily, if good approximation of the transverse normal stress σ_{zz} is needed, the model kinematic order must be enriched in the loading zone. Except for *Case B* configuration and mono-model *ET1*, all the other cases have a good behaviour in terms of σ_{zz} , see Figure 10.11. It has to be noticed that *Case A* and *Case C* to *Case F*, have the same accuracy as the reference mono-theory model *ET4*.

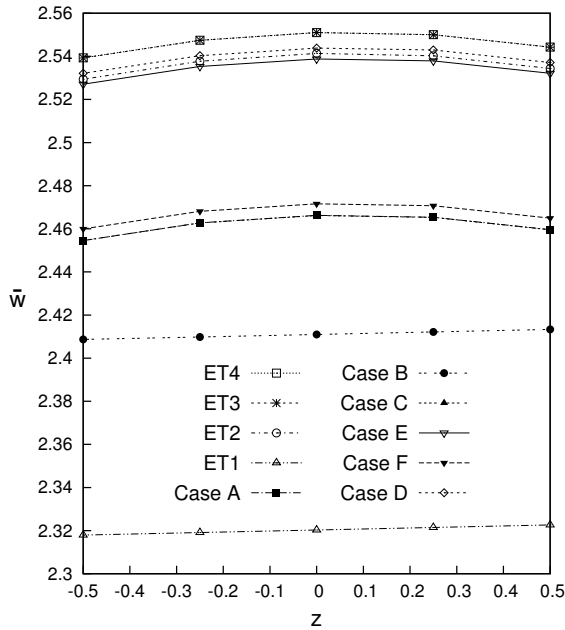


Figure 10.8: Transverse displacement $w(x; y) = w(a/2; b/2)$. Isotropic plate.

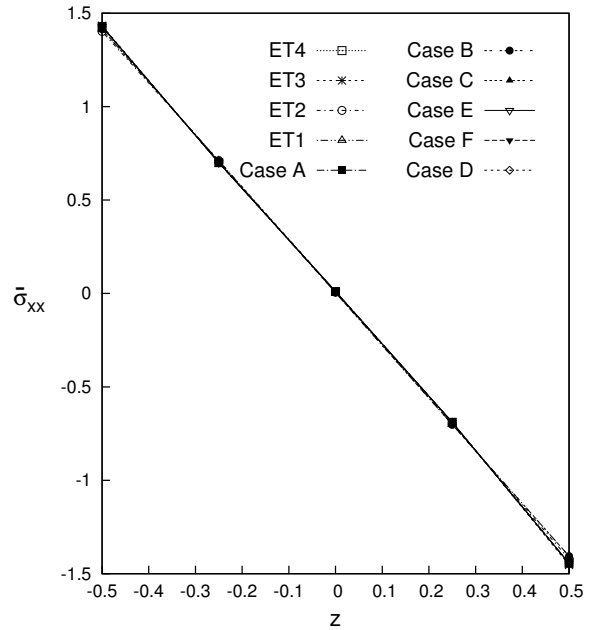


Figure 10.9: In-plane stress $\sigma_{xx}(x; y) = \sigma_{xx}(a/2; b)$. Isotropic plate.

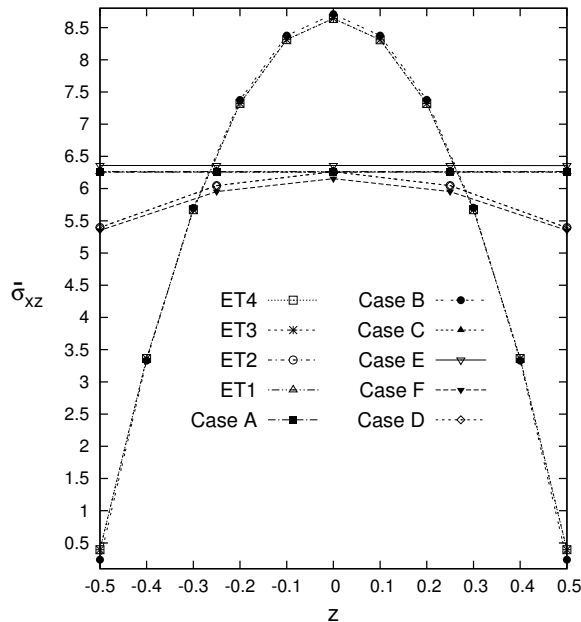


Figure 10.10: Transverse shear stress $\sigma_{xz}(x; y) = \sigma_{xz}(0; b)$. Isotropic plate.

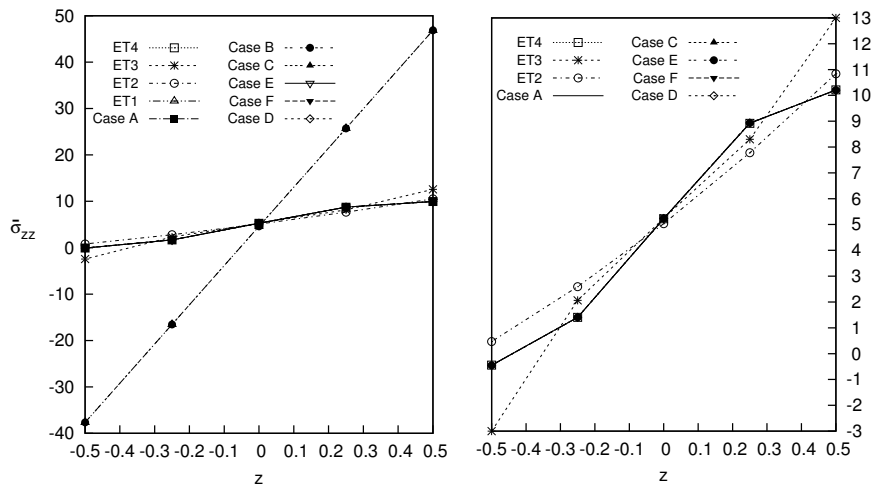


Figure 10.11: Transverse normal stress $\sigma_{zz}(x; y) = \sigma_{zz}(a/2; b)$. Isotropic plate.

For the sake of completeness, the distribution of transverse shear stress σ_{xz} , see Figure 10.12, and transverse normal stress σ_{zz} , see Figure 10.13, along the in-plane x axis are given. The results demonstrate that the *Case A* model can represent the transverse shear stress σ_{xz} accurately only in the loading zone. On the other hand, the same model gives an error of approximately 28% in the remaining part of the domain with respect to *Case B* and *ET4* models. Regarding the transverse normal stress σ_{zz} distribution along x , it is evident that higher-order models are required to describe the solution correctly. Even in this case, *Case A* model can represent a correct behaviour in the loading zone only. Therefore, a convergence analysis on the size of the transition elements is done for the cases represented in Figures 10.12 and 10.13. The convergence analysis was performed keeping the same mesh of the original cases, reducing the size of the transition elements in the x direction (transition element original size in the x direction $El_x = 0,25$), and fixing the transition lines at $x = 0,75$ and $x = 1,25$, see Figure 10.7. For the transverse shear stress σ_{xz} , see Figure 10.14a, the reduction of the transition element in the x direction lead to an increasing of oscillations of the solution in the transition element zones. Differently for the transverse normal stress σ_{zz} , see Figure 10.14b, the reduction of the transition element in the x direction permits to obtain huge reduction of the solution oscillations in the transition element zones.

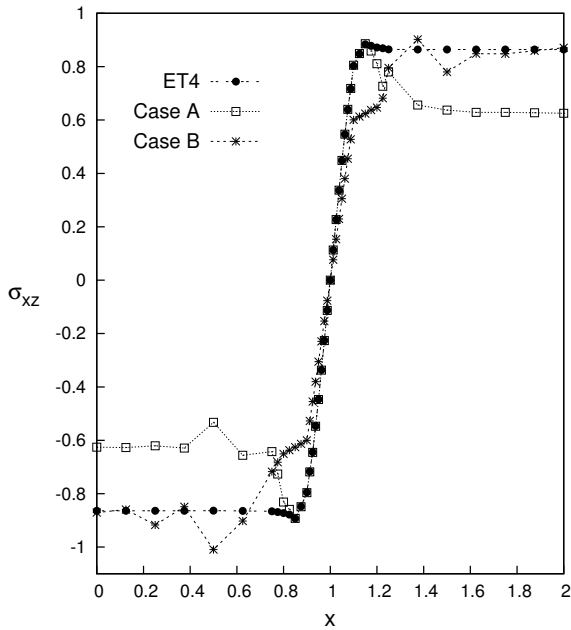


Figure 10.12: Transverse shear stress $\sigma_{xz}(y; z) = \sigma_{xz}(b; 0)$ along the beam axis. Isotropic plate.

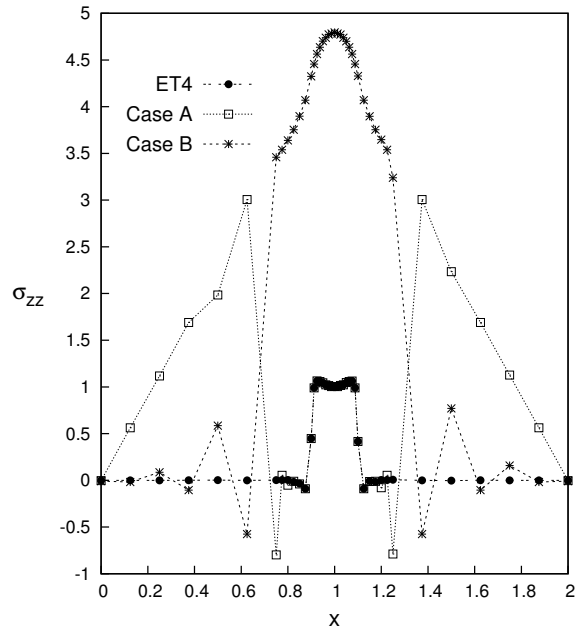
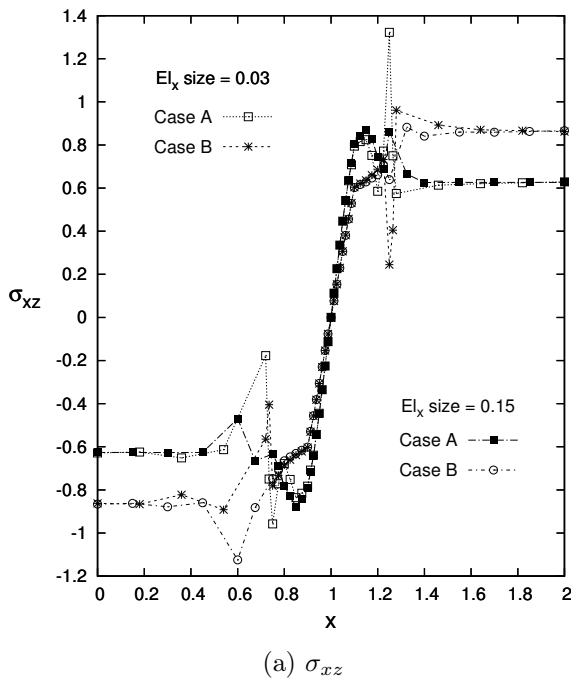
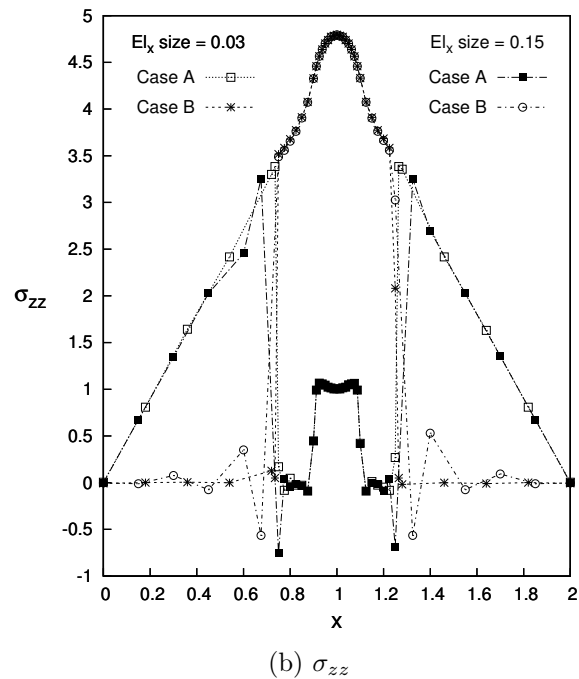


Figure 10.13: Transverse normal stress $\sigma_{zz}(y; z) = \sigma_{zz}(b/2; h/2)$ along the beam axis. Isotropic plate.



(a) σ_{xz}



(b) σ_{zz}

Figure 10.14: Convergence analysis of the transition elements for the transverse shear and normal stresses along the beam axis.

Finally, in order to show the 3D capabilities of the proposed methodology, the three-dimensional distribution of the shear stress σ_{xz} and the normal stress σ_{zz} are shown in Figures 10.15 and 10.16, respectively, where the results from a solid model by Abaqus *C3D20RE* finite element are compared with *ET4* single-theory plate model and *Case A* and *Case B* multi-theory models. From a comparison of the proposed variable-kinematic models with respect to the *ET4* plate model and the solid solution, it is possible to observe a possible reduction of DOFs equal to 18% and 99%, respectively. Moreover, if accurate solutions are needed only

in localized zones of the structure, even more efficient models can be implemented with the present approach.

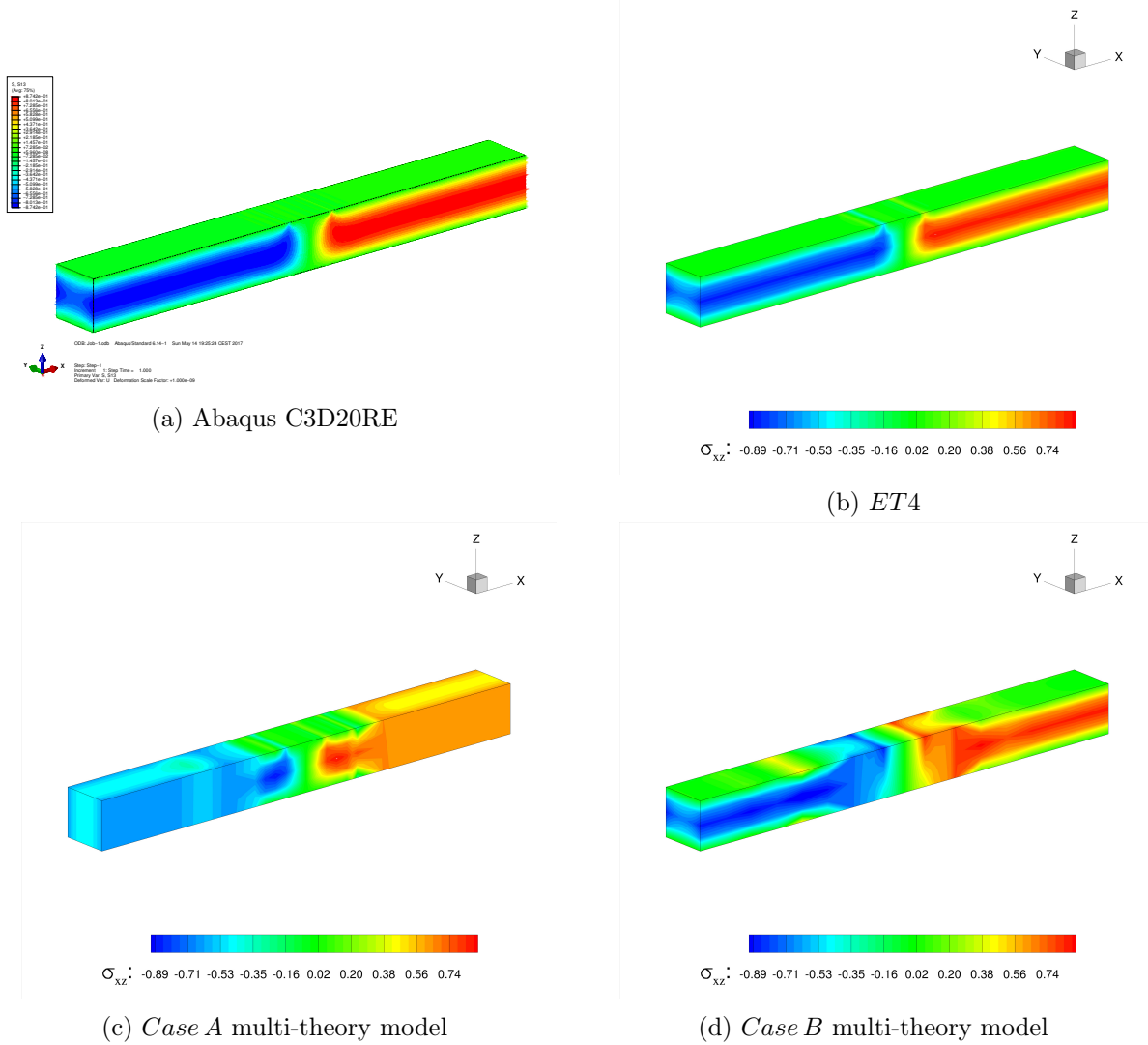


Figure 10.15: Three-dimensional representation of the transverse shear stress σ_{xz} . Isotropic plate.

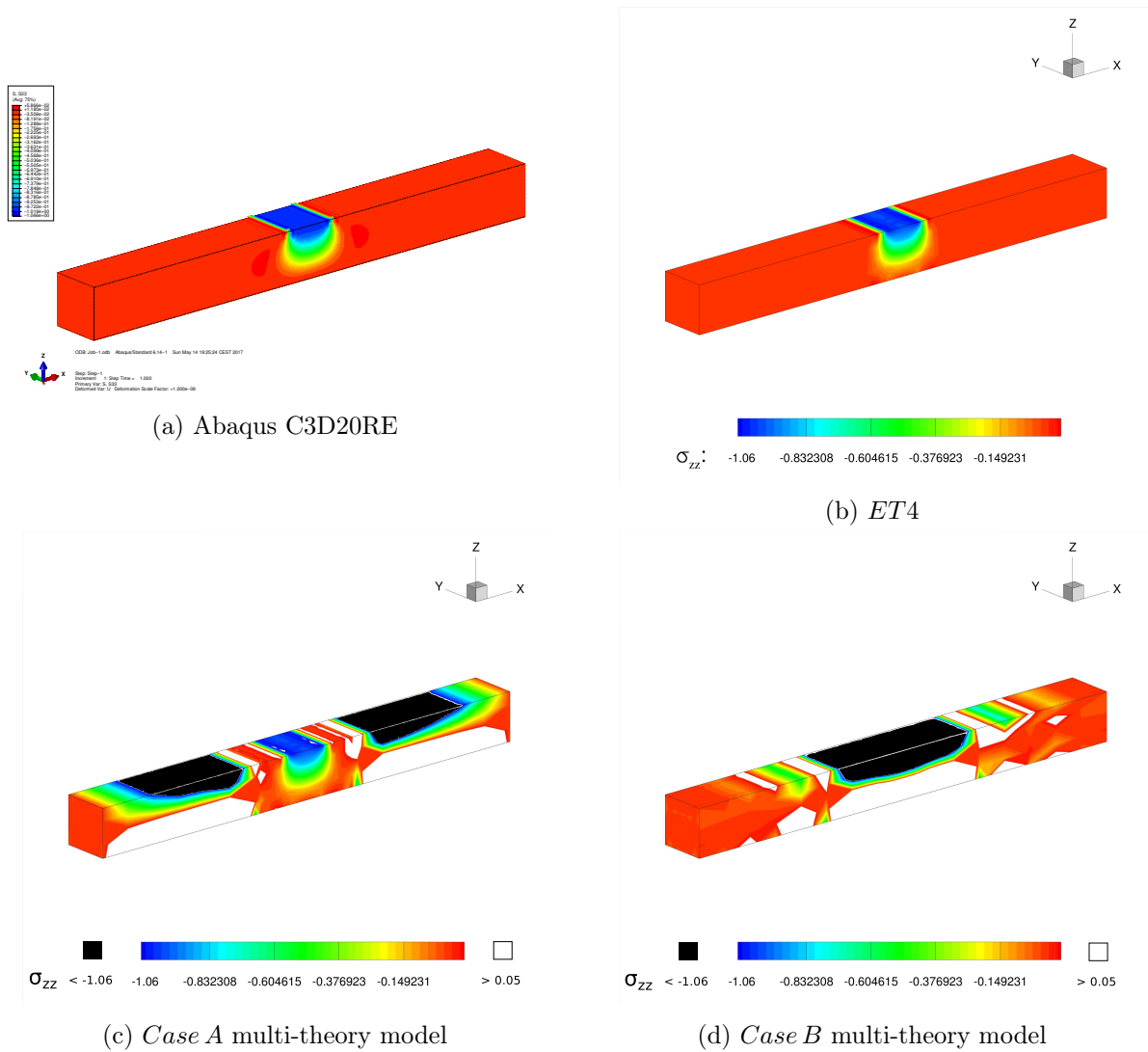


Figure 10.16: Three-dimensional representation of the transverse normal stress σ_{zz} . Isotropic plate.

10.3.2 Eight-layer cantilever plate

The first structure case taken into account is a simple example, that easily permits to describe, through the results, the main capabilities of the present node-dependent plate element. A cantilever eight-layer plate is analysed as shown in Figure 10.17. The structure is loaded at the free end with a concentrated load equal to $P_z = -0.2 N$. The geometrical dimensions are: $a = 90 mm$, $b = 1 mm$, $h = 10 mm$. The mechanical properties of the material labeled with the number 1 are: $E_L = 30 GPa$, $E_T = 1 GPa$, $G_{LT} = G_{TT} = 0.5 GPa$, $\nu_{LT} = \nu_{TT} = 0.25$. On the other hand, the mechanical properties of the material labeled with the number 2 are: $E_L = 5 GPa$, $E_T = 1 GPa$, $G_{LT} = G_{TT} = 0.5 GPa$, $\nu_{LT} = \nu_{TT} = 0.25$. As clear from Figure 10.17, the material stacking sequence is $[1/2/1/2]_s$.

First, a convergence study on single-theory plate models was performed. For both $LW4$ and $ET4$ models, as shown in Table 10.3, a mesh grid of 12×2 elements is enough to ensure convergent results, for transverse mechanical displacement w , in-plane stress σ_{xx} and transverse normal stress σ_{xz} . Various node-variable kinematic plate models have been used to perform the global/local analysis of the proposed plate structure, and they are depicted in Figure 10.18. These models are compared in Table 10.4 with lower- to higher-order single-theory models as well as with various solutions from the literature, including an analytical solution based on the 2D elasticity as presented in Lekhnitskii [148].

It can be observed for the transverse displacements w that mono-theory LW models show a good accuracy solution independently of the polynomial order, differently for single-model ESL with Taylor polynomial yield good results only with higher-order expansion $ET3$ and $ET4$. Moreover multi-theory ESL models *Case A*, *Case B* and *Case C* show an intermediate solution accuracy for all the three considered cases without relevant differences. For the multi-theory ESL-LW models *Case D*, *Case E* and *Case F* the solution is very accurate, due to the partial LW approximation, and it is obtained exactly the same solution for the three considered cases.

Regarding the in-plane stress σ_{xx} the accuracy solution is not sensitive for all the considered single and multi model theories, except for the *Case A* configuration where the transition elements are acting at the evaluation position.

For the transverse shear stress σ_{xz} similar comments respect to the transverse displacement can be drawn. Single theory LW models show a good accuracy solution independently of the polynomial order, otherwise higher-order mono-model ESL theories with Taylor polynomial, $ET3$ and $ET4$, are required to obtained a sufficient solution accuracy. Nevertheless, accurate solutions in localized regions/points can be obtained by using the multi-theory ESL model *Case B*, and with multi-theory ESL-LW models *Case D* and *Case E*.

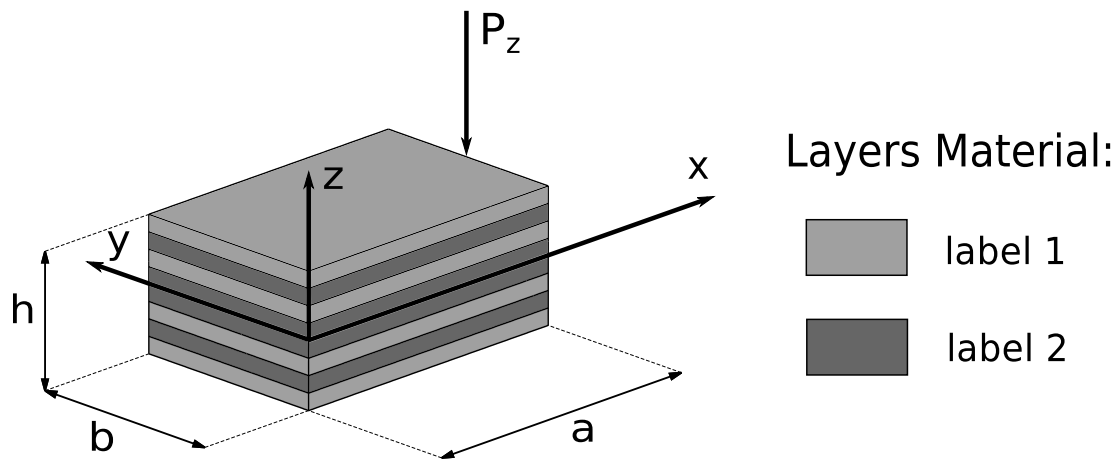


Figure 10.17: Eight-layered plate with concentrated loading. Reference system and material lamination scheme.

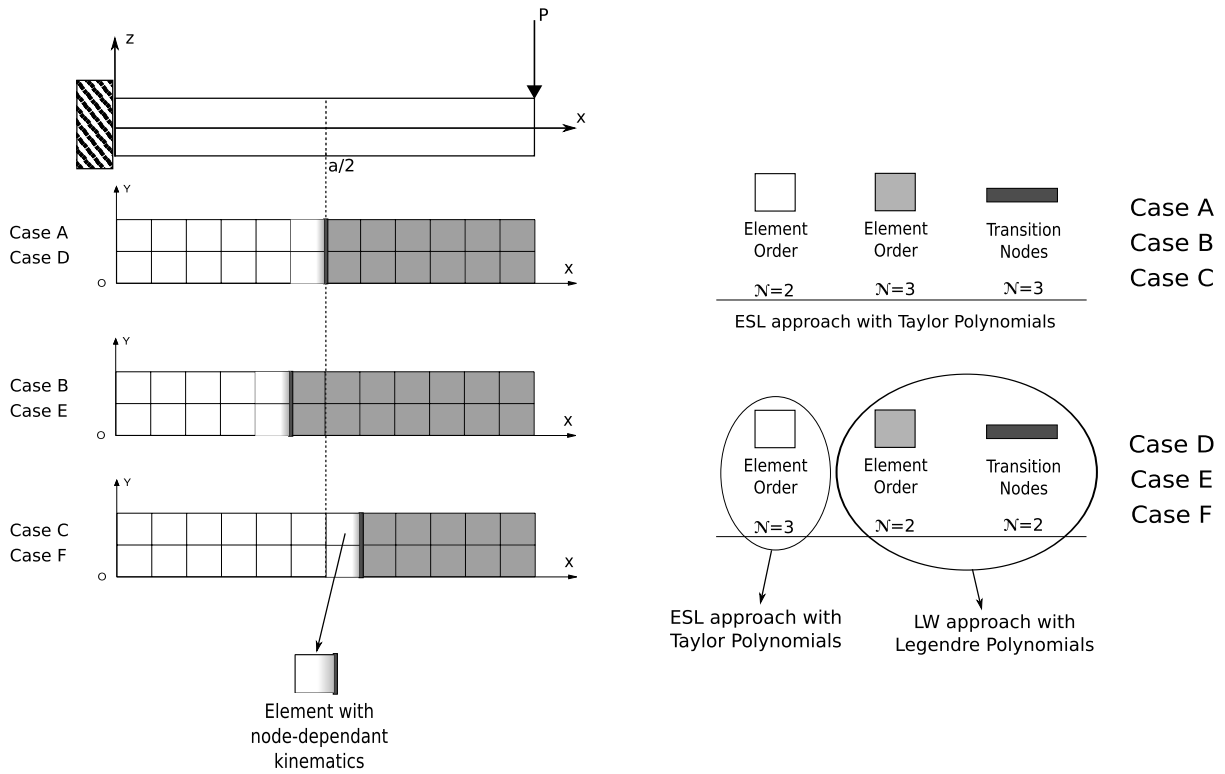


Figure 10.18: Eight-layered plate. Mesh scheme of the adopted multi-theory models with node-dependent kinematics.

Table 10.3: Convergence study of single-theory models of the eight-layer cantilever plate. Transverse displacement $w = -10^2 \times w(a, b/2, 0)$, in-plane principal stress $\sigma_{xx} = 10^3 \times \sigma_{xx}(a/2, b/2, +h/2)$, transverse shear stress $\sigma_{xz} = -10^2 \times \sigma_{xz}(a/2, b/2, 0)$.

	Mesh	2×2	4×2	6×2	8×2	10×2	12×2
<i>LW4</i>	w	3.031	3.032	3.031	3.030	3.030	3.030
	σ_{xx}	651	690	716	725	728	730
	σ_{xz}	2.991	2.797	2.792	2.791	2.790	2.789
<i>ET4</i>	w	3.029	3.029	3.029	3.028	3.028	3.028
	σ_{xx}	684	723	729	730	731	731
	σ_{xz}	3.054	2.829	2.820	2.821	2.822	2.822

Table 10.4: Eight-layer cantilever plate. Transverse displacement $w = -10^2 \times w(a, b/2, 0)$, in-plane normal stress $\sigma_{xx} = 10^3 \times \sigma_{xx}(a/2, b/2, +h/2)$, transverse shear stress $\sigma_{xz} = -10^2 \times \sigma_{xz}(a/2, b/2, 0)$ by various single- and multi-theory models.

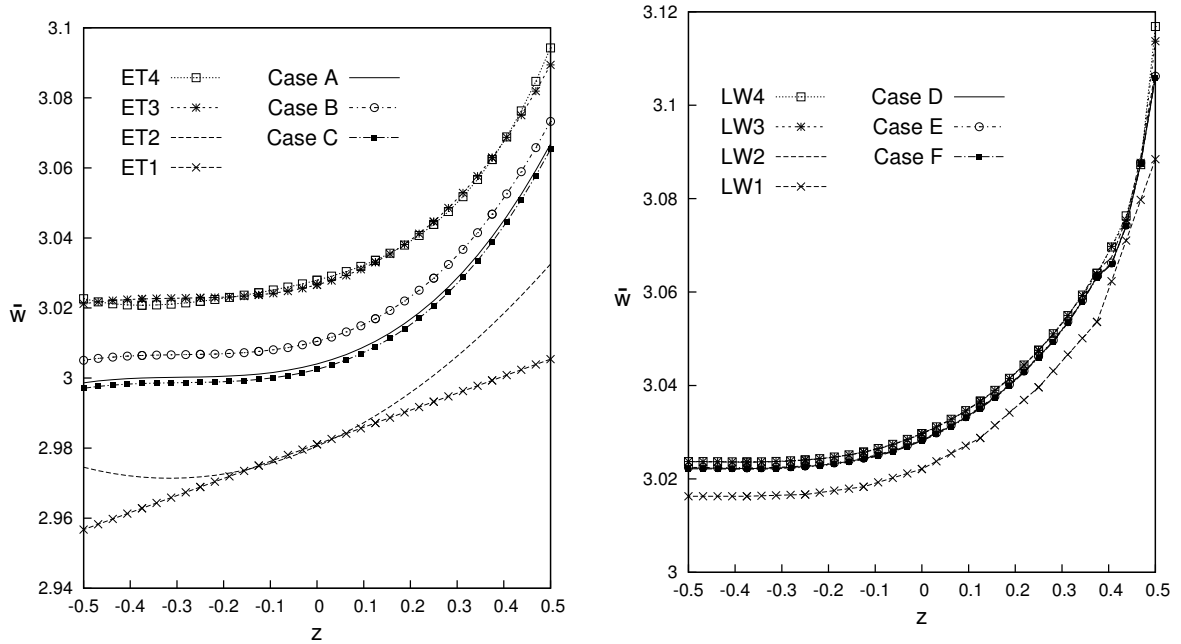
	w	σ_{xx}	σ_{xz}	$DOFs$
Reference solutions				
Nguyen and Surana [149]	3.031	720		
Davalos <i>et al.</i> [150]	3.029	700		
Xiaoshan [151]	3.060	750		
Vo and Thai [152]	3.024			
Lekhnitskii [148]		730	2.789	
Present single- and multi-theory models				
<i>LW4</i>	3.030	730	2.789	12375
<i>LW3</i>	3.030	731	2.788	9375
<i>LW2</i>	3.030	731	2.795	6375
<i>LW1</i>	3.022	731	2.775	3375
<i>ET4</i>	3.028	731	2.822	1875
<i>ET3</i>	3.027	731	2.822	1500
<i>ET2</i>	2.980	731	2.005	1125
<i>ET1</i>	2.981	729	2.000	750
<i>Case A</i>	3.004	808	2.375	1320
<i>Case B</i>	3.010	737	2.781	1365
<i>Case C</i>	3.002	731	2.030	1305
<i>Case D</i>	3.028	732	2.799	4035
<i>Case E</i>	3.028	729	2.799	4425
<i>Case F</i>	3.028	731	2.818	3645

Some results in terms of transverse displacement w and transverse shear stress σ_{xz} along the thickness are represented in Figures 10.19a and 10.19b, 10.20a and 10.20b, respectively. Some more comments can be made:

- As shown in Figure 10.19a, the through-the-thickness distribution of the transverse displacement w , evaluated at the free tip of the plate, is correctly predicted by a third-order ESL model *ET3*. The same accuracy cannot be reached by the proposed ESL models with node-variable kinematics. Differently, as depicted in Figure 10.19b, both LW single theory and ESL-LW theory accuracy is not sensitive of the chosen model, except for the single linear model *LW1*.
- Figure 10.20a shows that the transverse shear stress σ_{xz} , evaluated at the mid-span of the plate, is very sensitive to the position of the transition variable-kinematic elements. *Case B* model has the same accuracy as mono-model *ET3* and *ET4*. On the contrary, the *Case C* configuration has poor accuracy like mono-models *ET1* and *ET2*. Finally, *Case A* model presents a intermediate compromise between the other two multi-theory cases. All the ESL models are not able to reproduce the accurate behaviour of the reference 2D elasticity solution *Lekhnitskii*, presented in [148]. On the contrary, as depicted in Figure 10.20b, the LW single models are able to reach an accurate solution as the reference solution *Lekhnitskii*, except for the linear model *LW1*. Multi-theory

ESL-LW (ET3-LW2) models have a good approximation of the solution where the verification point is described by LW theories, *Case D* and *Case E* models, therefore *Case F* show the same accuracy solution of the model *ET3*.

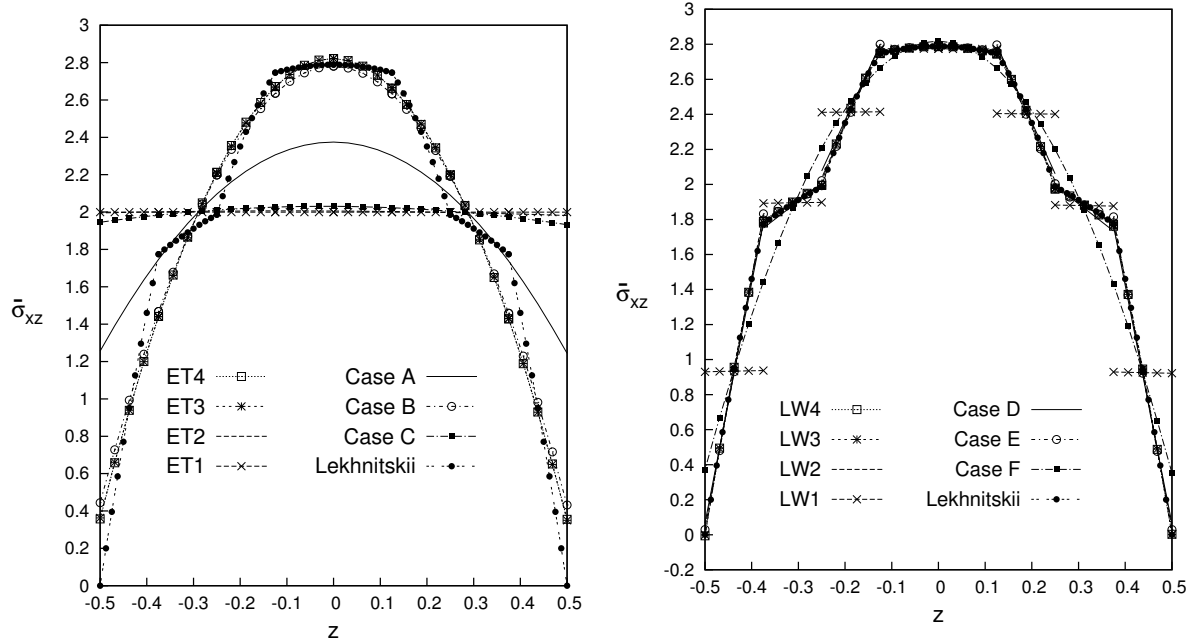
By the evaluation of the various node-variable kinematic models, it is clear that an accurate representation of the stresses in localized zones is possible with DOFs reduction if an accurate distribution of the higher-order kinematic capabilities is performed in those localized zones. Differently, the displacements values are dependent on the global approximation over the whole structure. The DOFs reduction can be moderate or stronger, depending on the structure and the load case configuration.



(a) ESL single and multi model with Taylor Polynomials

(b) LW single model, and ESL model by Taylor Polynomials combined with LW model by Legendre Polynomials

Figure 10.19: Eight-layer composite plate. Transverse displacement $w(x; y) = -10^2 \times w(a; b/2)$.



(a) ESL single and multi model with Taylor Polynomials

(b) LW single model, and ESL model by Taylor Polynomials combined with LW model by Legendre Polynomials

Figure 10.20: Eight-layer composite plate. Transverse shear stress $\sigma_{xz}(x; y) = -10^2 \times \sigma_{xz}(a/2; b/2)$.

10.3.3 Composite plates simply-supported

A simply-supported composite plate is analysed. The geometrical dimensions are: $a = b = 0.1 \text{ m}$, the side-thickness ratio is $a/h = 10$. A symmetric $[0^\circ/90^\circ/0^\circ]$ stacking sequences is considered. The material employed is orthotropic with the following properties: $E_L = 132.5 \text{ GPa}$, $E_T = 10.8 \text{ GPa}$, $G_{LT} = 5.7 \text{ GPa}$, $G_{TT} = 3.4 \text{ GPa}$, $\nu_{LT} = 0.24$, $\nu_{TT} = 0.49$. The plate is simply-supported and a localised uniform transverse pressure, $P_z = -1 \text{ MPa}$, is applied at top face on a square region of side length equal to $a/5 \times b/5$ and centered at the point $(a/2, b/2)$, see Figure 10.22. Due to the symmetry of both the geometry and the load, a quarter of the plate is analyzed and the following symmetry and boundary conditions (simply-supported) are applied:

$$\begin{array}{cc}
 \textit{Boundary} & \textit{Symmetry} \\
 u_s(x, 0) = 0 & w_s(x, 0) = 0 & u_s(a/2, y) = 0 \\
 v_s(0, y) = 0 & w_s(0, y) = 0 & v_s(x, b/2) = 0
 \end{array} \quad (10.6)$$

A convergence study versus the FE element size, i.e. the number of elements, is performed, for the sake of brevity the single-model *ET4* is considered. In order to compare the results with other solutions present in literature [176], the mid-plane domain of the plane structure was subdivided into three zones along the axes x and y and they are shown in Figure 10.21. The results from the convergence analysis are shown in Table 10.5 and they are given in terms of transverse displacement $w = (-10^5) \times w$ and in-plane normal stresses σ_{xx} , σ_{yy} evaluated at $(a/2, b/2, -h/2)$, and transverse shear stress $\sigma_{xz} = (-10) \times \sigma_{xz}$ evaluated at $(5a/12, b/2, 0)$. As it is clear from this preliminary analysis, a non-uniform mesh grid of 10×10 elements ensures the convergence of the solution.

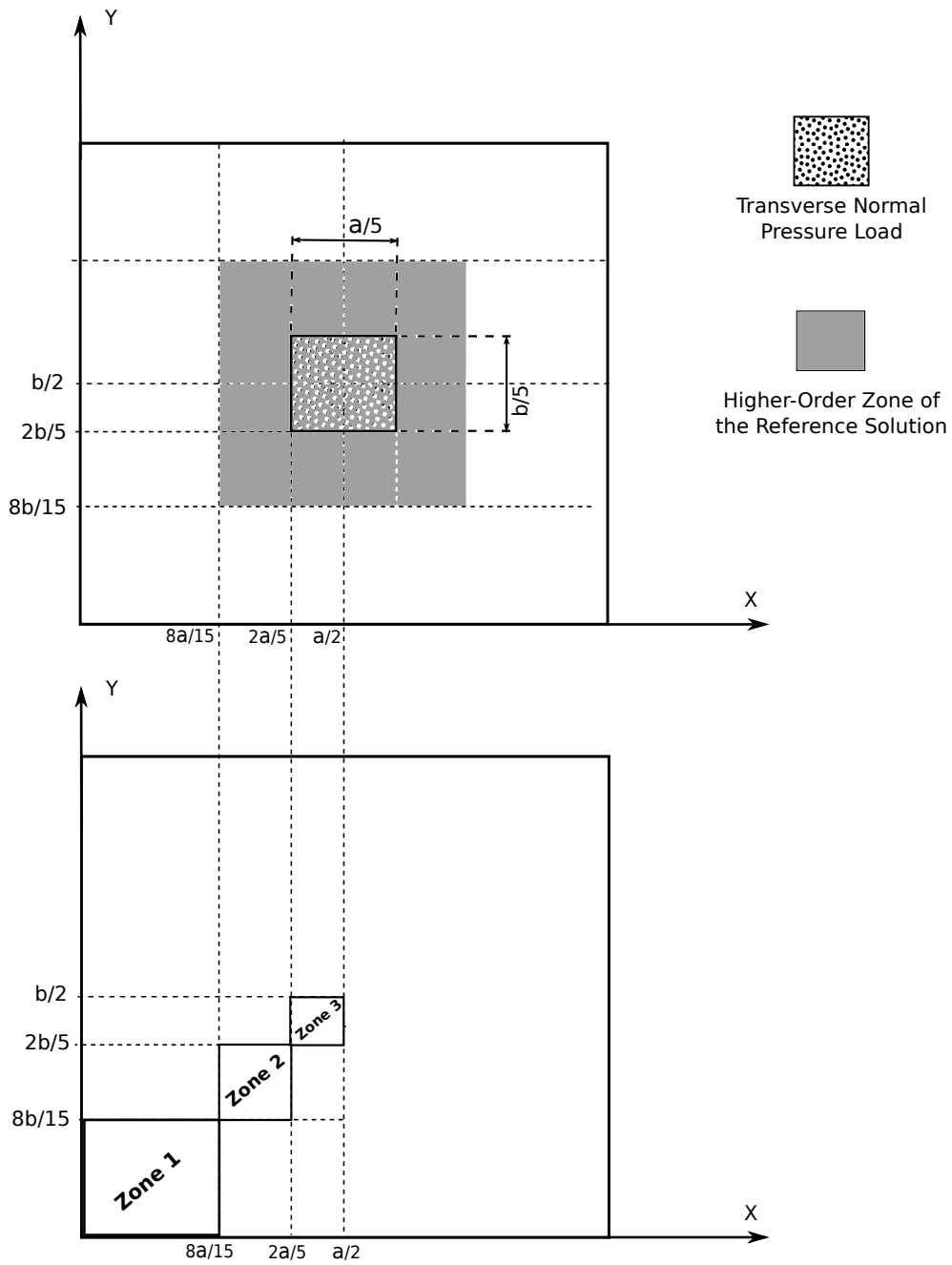


Figure 10.21: Cross-ply laminate subjected to localized pressure load and related FE mesh discretization into 3 zones.

Table 10.5: Convergence study with a *ET4* plate element. Composite plate with $(0^\circ/90^\circ/0^\circ)$ lamination, a quarter of the plate is taken into account.

			w	σ_{xx}	σ_{yy}	σ_{xz}	$DOFs$
<i>Mesh</i> 5×5							
<i>zone1</i>	<i>zone2</i>	<i>zone3</i>	1.661	12.493	2.187	5.977	1815
2×2	2×2	1×1					
<i>Mesh</i> 8×8							
<i>zone1</i>	<i>zone2</i>	<i>zone3</i>	1.660	12.057	2.025	5.754	4335
3×3	3×3	2×2					
<i>Mesh</i> 10×10							
<i>zone1</i>	<i>zone2</i>	<i>zone3</i>	1.660	12.058	2.026	5.756	6615
4×4	4×4	2×2					
<i>Mesh</i> 6×6							
<i>zone1</i>	<i>zone2</i>	<i>zone3</i>	1.660	12.054	2.024	5.744	2535
2×2	2×2	2×2					
<i>Mesh</i> 8×8							
<i>zone1</i>	<i>zone2</i>	<i>zone3</i>	1.660	11.972	2.012	5.853	4335
2×2	2×2	4×4					
<i>Mesh</i> 10×10							
<i>zone1</i>	<i>zone2</i>	<i>zone3</i>	1.660	11.956	2.008	5.847	6615
2×2	2×2	6×6					

The non-uniform adopted mesh and the various node-variable kinematic models, with global/local capabilities used to perform the analysis of the proposed plate structure, are depicted in Figure 10.22, where the mesh grid of a quarter of the plate is analysed. The results are given in terms of transverse displacement w and in-plane normal stresses σ_{xx} , σ_{yy} evaluated at $(a/2, b/2, -h/2)$, transverse shear stress σ_{xz} evaluated at $(5a/12, b/2, 0)$, and transverse normal stress σ_{zz} evaluated at $(a/2, b/2, +h/2)$.

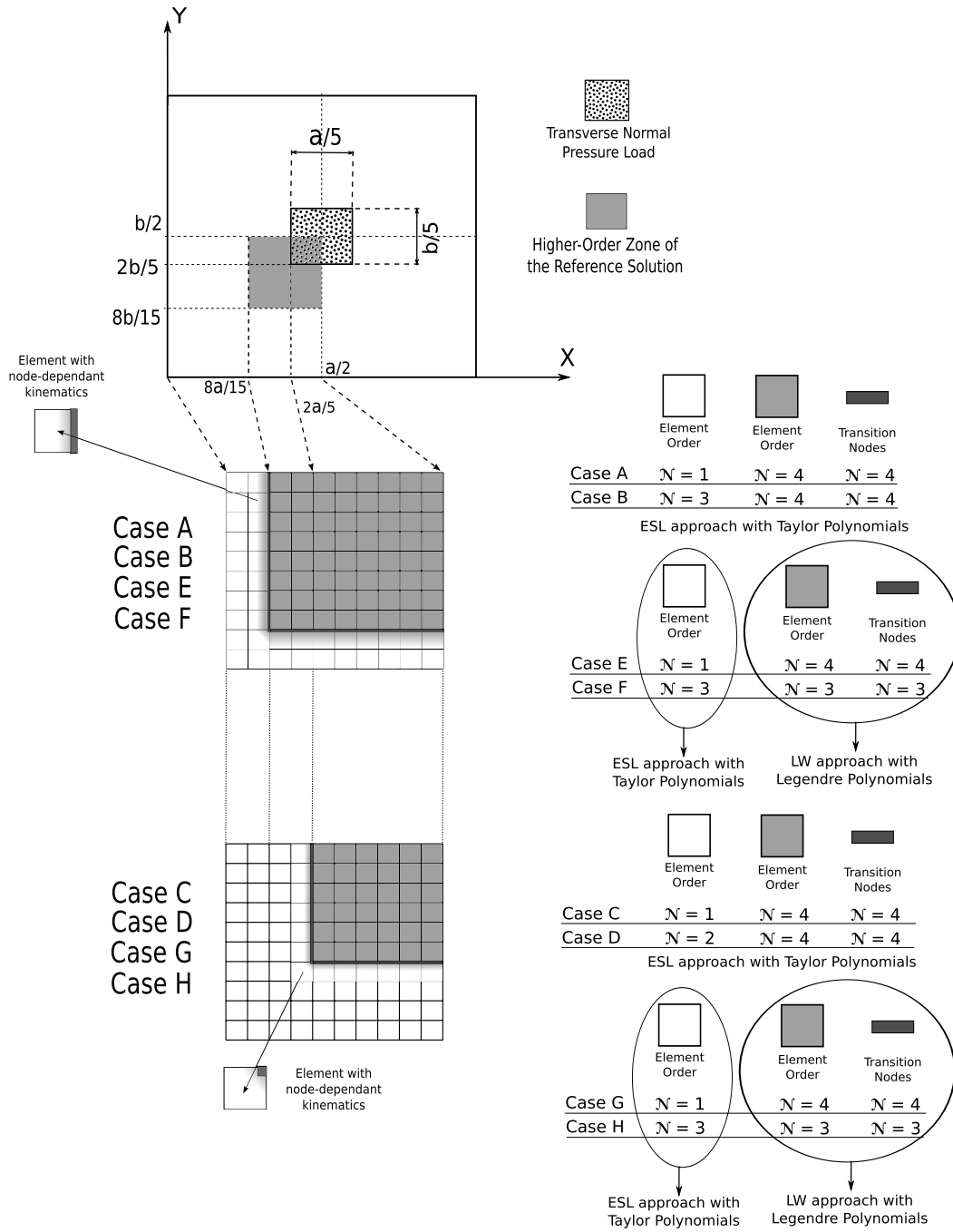


Figure 10.22: Non-uniform adopted mesh on quarter of the plate, and graphical representation of the multi-theory models of the cross-ply plate structure.

For the three-layered plate structure with $[0^\circ/90^\circ/0^\circ]$, mono-theory models are compared with those from the present global/local approach in Table 10.6. The table shows that mono-theory ESL models with lower expansion order, $ET1$ and $ET2$, are not able to describe appropriately the transverse displacements w and the in-plane stresses σ_{xx} and σ_{yy} , otherwise LW mono-models represent these variables with a good accuracy solution for every expansion order. To accurately describe the shear transverse stresses σ_{xz} , ESL higher-order theories are required, or LW mono-models theories. The transverse normal stress σ_{zz} needs higher-order theories to be well described, both linear ESL and LW single-models are not sufficient. Table 10.6 also show solutions for variable kinematic multi-model theories, the cases taken into account are named from *Case A* to *Case H*, and they are explained in Figure 10.22. The cases named as *Case A*, *Case B* and *Case E* are equivalent to the models $(ET1 - ET4)^A$, $(ET3 -$

$ET4)^B$ and $(ET1 - LW4)^E$ taken from [176] and in which, via the Arlequin method and 4-node Lagrangian plate elements, a fourth-order plate theory is used in correspondence of the loading and a first- and third-order kinematics is used outside the loading zone, respectively.

Table 10.6: Composite plate with $[0^\circ/90^\circ/0^\circ]$ lamination. Transverse displacement $w = (-10^5) \times w(a/2, b/2, -h/2)$, in-plane normal stresses $\sigma_{xx} = \sigma_{xx}(a/2, b/2, -h/2)$ and $\sigma_{yy} = \sigma_{yy}(a/2, b/2, -h/2)$, transverse shear stress $\sigma_{xz} = (-10) \times \sigma_{xz}(5a/12, b/2, 0)$, and transverse normal stress $\sigma_{zz} = -\sigma_{xz}(a/2, b/2, +h/2)$ by various single- and multi-theory models.

	w	σ_{xx}	σ_{yy}	σ_{xz}	σ_{zz}	$DOFs$
Reference solutions [176]						
$3D$	1.674	11.94	2.019	6.524		
$LW4_a$	1.675	11.94	2.020	6.523		39
$LW4$	1.672	11.83	1.983	6.464		9984
$ET4_a$	1.660	11.95	2.005	5.865		15
$ET4$	1.657	11.85	1.985	5.830		3840
$(ET1 - ET4)^A$	1.609	11.92	1.962	5.848		2448
$(ET3 - ET4)^B$	1.657	11.84	1.985	5.831		3936
$(ET1 - LW4)^E$	1.617	11.91	1.953	6.481		3984
Present single- and multi-theory models						
$LW4$	1.6745	11.9547	2.0232	6.5557	1.0000	17199
$LW3$	1.6745	11.9624	2.0302	6.5613	1.0108	13230
$LW2$	1.6719	11.9141	2.0458	6.3903	1.0731	9261
$LW1$	1.6369	11.3621	2.1465	6.5881	1.4679	5292
$ET4$	1.6596	11.9556	2.0078	5.8473	0.9905	6615
$ET3$	1.6590	11.9867	2.1164	6.0147	1.2443	5292
$ET2$	1.5625	10.1942	1.7935	3.8521	1.0377	3969
$ET1$	1.4954	10.2867	2.1002	3.7554	1.8261	2646
$Case A$	1.6040	12.0084	1.9821	5.8510	0.9910	5247
$Case B$	1.6596	11.9556	2.0077	5.8473	0.9905	6159
$Case C$	1.5257	11.7328	1.9453	4.9414	0.9938	4167
$Case D$	1.5770	11.8056	1.9510	4.9970	0.9909	4983
$Case E$	1.6103	12.0107	1.9923	6.5254	1.0000	12183
$Case F$	1.6670	11.9699	2.0263	6.5524	1.0108	10494
$Case G$	1.5274	11.7105	1.9474	5.3212	1.0009	8223
$Case H$	1.6613	11.9305	2.0198	6.3616	1.0118	8334

Some results in terms of transverse displacement w , and transverse shear stress σ_{xz} along the thickness are represented in Figures 10.23a, 10.23b, 10.24a and 10.24b. The following remarks can be made:

- The transverse displacement w behaviour can change sensitively depending on the distribution of the kinematic enrichment within the structure plane. Figure 10.23a show that $Case B$ has the same accuracy as the full higher-order $ET4$ mono-model with a 8% DOFs reduction, and an accuracy close to multi-model $Case H$ with a 26% DOFs reduction. It is noticeable that, the choice of the ESL or LW model for the loaded zone is not decisive for the correct description of the transverse mechanical displacement, as

shown for *Case C* and *Case G*. On the contrary a global more refined approximation get better accuracies, as the case of the multi-models *Case A* and *Case E*.

- For the evaluation of the transverse shear stress σ_{xz} , higher-order models are necessary in the regions close to the considered evaluation point. In Figure 10.23b mono-model *LW4* is used as reference solution. It is evident that ESL single-models, for every expansion orders, are not able to correctly describe the transverse shear stress. The ESL multi-model *Case A* has the same poor accuracy of the theory *ET4*. The linear model *LW1* is clearly not sufficient to describe the transverse shear stress, differently from the single value reported in Table 10.6 taken in $z = 0$. In Figure 10.24a the multi-model *Case E* and *Case G*, where in the boundary regions a *ET1* model is used and in the loaded zones a *LW4* model is adopted, the accuracy on the transverse shear stress is not completely guaranteed by the LW model. In particular for the *Case G* the evaluation point is close to the transition element, this position is perturbing the accuracy solution. On the contrary for the *Case E* the evaluation point is not more close to the transition element and the solution accuracy is like the full LW model. Finally in Figure 10.24b the multi-model *Case F* and *Case H* are not suffering any perturbation problem, due to the third-order ESL model of the boundary regions.

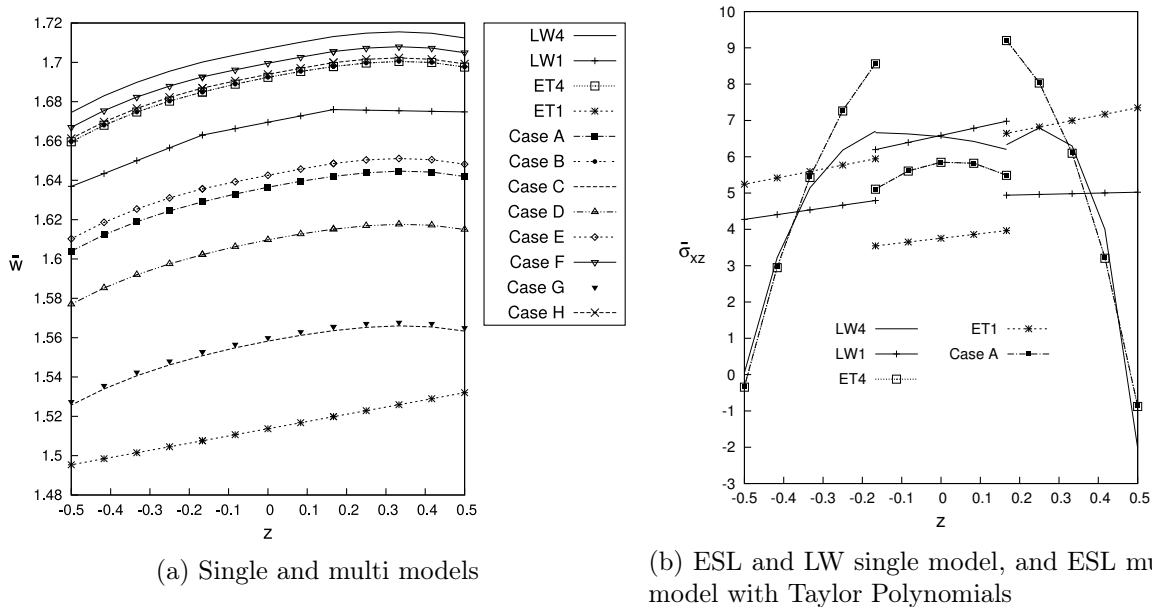


Figure 10.23: Composite plate. Transverse displacement $w(x; y) = -10^5 \times w(a/2; b/2)$, and transverse shear stress $\sigma_{xz}(x; y) = -10 \times \sigma_{xz}(5a/12; b/2)$.

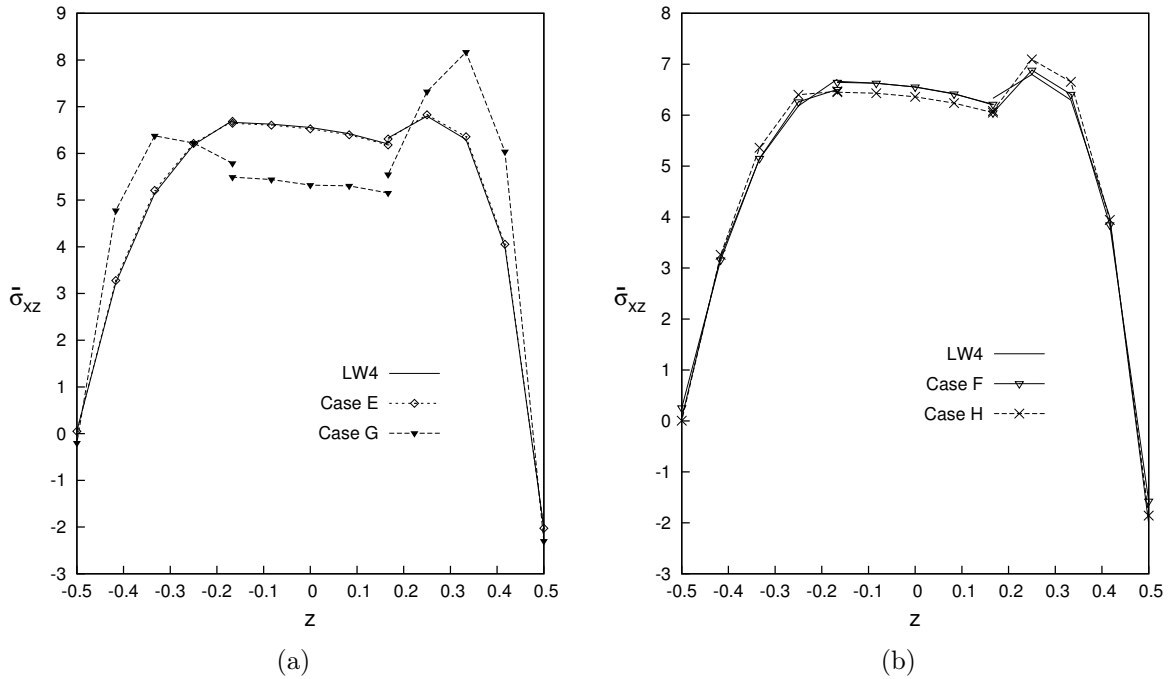


Figure 10.24: Composite plate. Transverse shear stress $\sigma_{xz}(x; y) = -10 \times \sigma_{xz}(5a/12; b/2)$. Multi-theories with ESL model by Taylor Polynomials combined with LW model by Legendre Polynomials.

Results in terms of in-plane stress σ_{xx} , transverse shear stress σ_{xz} and transverse normal stress σ_{zz} along the in-plane x axis are represented in Figures 10.25a, 10.25b and 10.26a respectively.

For the in-plane stress σ_{xx} , see Figure 10.25a, the mono-models *LW4* and *ET4* show the same accuracy solution. Multi-models with ESL approach with Taylor polynomials, *Case A* and *Case C*, produce small oscillations in the transition zone. On the contrary, multi-theories with ESL model by Taylor Polynomials combined with LW model by Legendre Polynomials, *Case E* and *Case G*, show big fluctuations in the transition elements. Moreover it has to be noticed that if the refined polynomials are limited to the loading zone, *Case C* and *Case G*, the solution accuracy in the loading zone is lower respect to the reference *LW4* solution.

For the transverse shear stress σ_{xz} , see Figure 10.25b, the *ET4* mono-model have an accuracy close to the mono-model *LW4* in the loaded zone, differently the *ET4* model reach a maximum value of the shear stress 9% lower than the reference *LW4* solution. For multi-model theories the same comments made for the in-plane stress can be applied for the behaviour description of the transverse shear stress.

For transverse normal stress σ_{zz} , see Figure 10.26a, the mono-models *LW4* and *ET4* show the same accuracy solution. For multi-model theories the same comments made for the in-plane stress can be applied for the behaviour description of the transverse normal stress. It has to be noticed that the oscillations of the transition elements are smaller than those of the in-plane stress and the transverse shear stress.

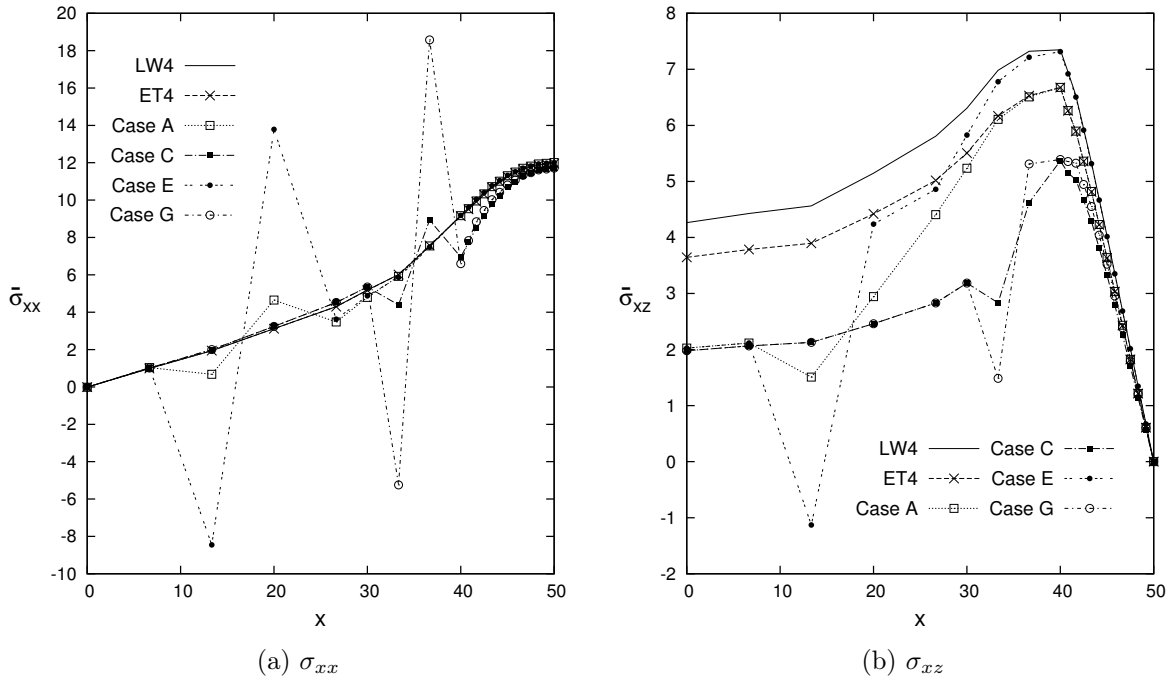


Figure 10.25: Composite plate. In-plane stress $\sigma_{xx}(y; z) = \sigma_{xx}(b/2; -h/2)$, and transverse shear stress $\sigma_{xz}(y; z) = -10 \times \sigma_{xz}(b/2; 0)$ along the in-plane direction X , the axis X is expressed in $[mm]$. Single and Multi-theory models.

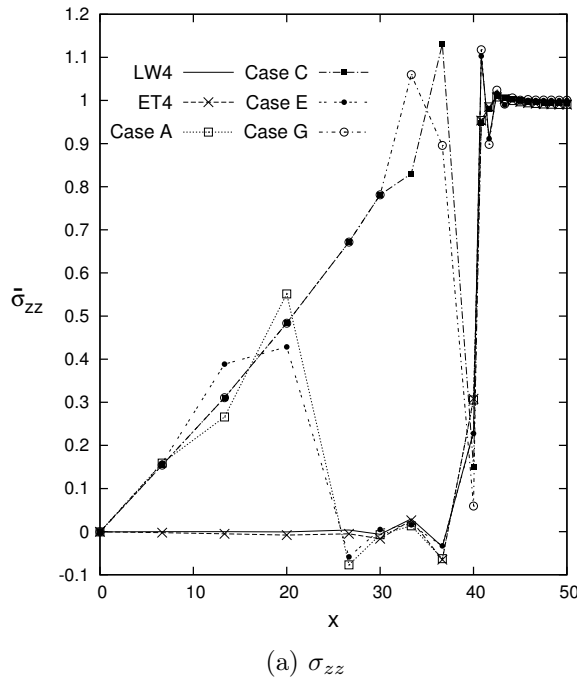


Figure 10.26: Composite plate. Transverse normal stress $\sigma_{zz}(y; z) = -\sigma_{zz}(b/2; +h/2)$ along the in-plane direction X , the axis X is expressed in $[mm]$. Single and Multi-theory models.

Finally, a three-dimensional distributions on a quarter of the plate of the transverse shear stress σ_{xz} is given to underline the global/local capabilities of the presente finite element on the whole domain of the analyzed plate structure. The reference single-model solution $LW4$ is depicted in Figure 10.27a. For a fair results comparison, the extremities of the colorbar values of the $LW4$ model are used to limit the colorbar of the other solutions. The

single-model *ET4* is not able to correctly describe the transverse shear stress behaviour, it is clear from Figure 10.27b that the interlaminar continuity of the transverse shear stress is not satisfied. In Figure 10.28a the multi-model named Case E, (*ET1-LW4*) is represented. It is evident that the transverse shear stress is well represented in the *LW4* zone only. The multi-model Case H, (*ET3-LW3*) is represented in Figure 10.28b, the small *LW3* zone is able to correctly describe the transverse shear stress, on the contrary the *ET3* zone has a comparable behaviour as the single-model *ET4*.

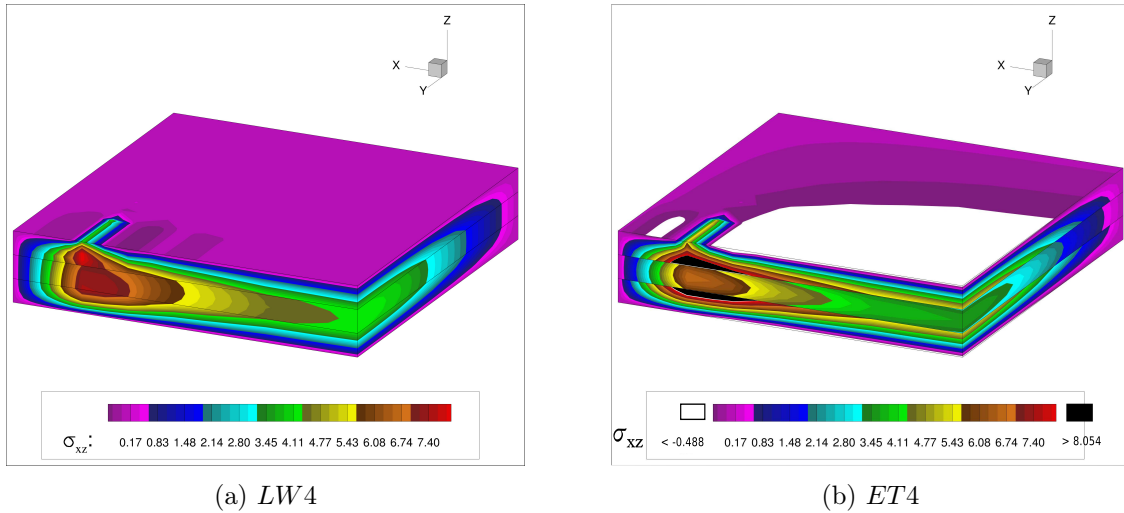


Figure 10.27: Composite plate, three-dimensional view of a quarter of the plate. Transverse shear stress σ_{xz} for single models.

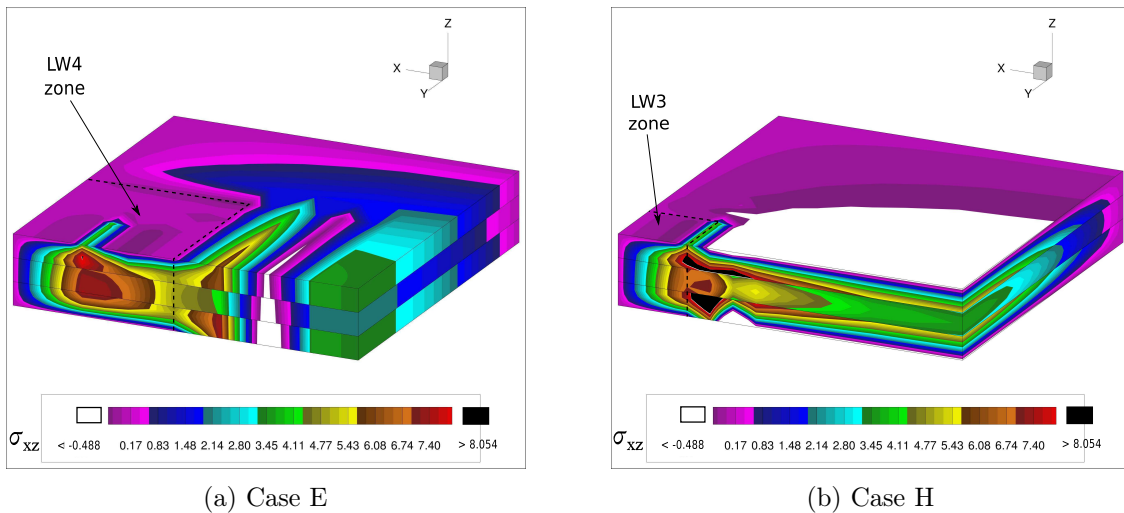


Figure 10.28: Composite plate, three-dimensional view of a quarter of the plate. Transverse shear stress σ_{xz} for multi-models.

10.3.4 Sandwich rectangular plates simply-supported

A simply-supported unsymmetrically laminated rectangular sandwich plate is analysed. The geometrical dimensions are: $a = 100\text{ mm}$, $b = 200\text{ mm}$, the total thickness is $h = 12\text{ mm}$, the top skin thickness is $h_{top} = 0.1\text{ mm}$, the bottom skin is thick $h_{bottom} = 0.5\text{ mm}$, and the core thickness is $h_{core} = 11.4\text{ mm}$. The two skins have the same material properties: $E_1 = 70\text{ GPa}$, $E_2 = 71\text{ GPa}$, $E_3 = 69\text{ GPa}$, $G_{12} = G_{13} = G_{23} = 26\text{ GPa}$, $\nu_{12} = \nu_{13} = \nu_{23} = 0.3$, moreover the metallic foam core has the following material properties: $E_1 = E_2 = 3\text{ MPa}$,

$E_3 = 2.8 MPa$, $G_{12} = G_{13} = G_{23} = 1 MPa$, $\nu_{12} = \nu_{13} = \nu_{23} = 0.25$. The plate is simply-supported and a localised uniform transverse pressure, $P_z = -1 MPa$, is applied at top face on a square region of side length equal to $(a = 5 mm) \times (b = 20 mm)$ and centered at the point $(a/2, b/2)$, see Figure 10.29.

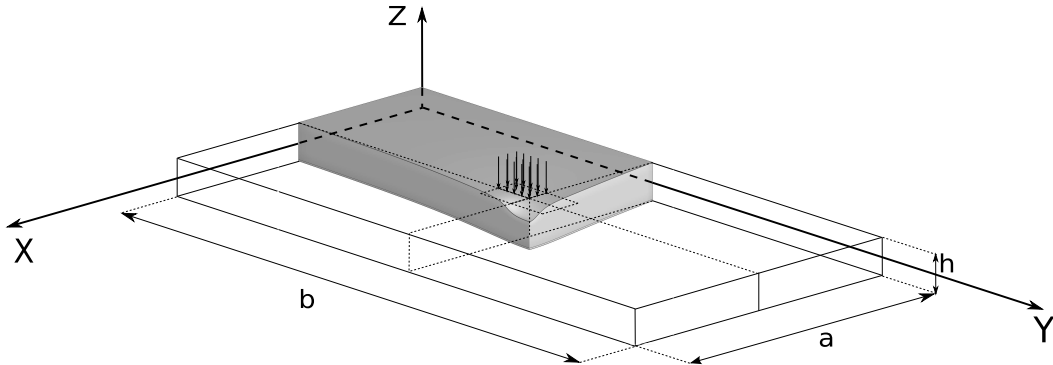


Figure 10.29: Reference system of the sandwich plate. Three-dimensional deflection representation of a quarter of the plate.

Due to the symmetry of both the geometry and the load, a quarter of the plate is analyzed and the following symmetry and boundary conditions (simply-supported) are applied:

$$\begin{array}{ccc}
 \textit{Boundary} & & \textit{Symmetry} \\
 u_s(x, 0) = 0 & w_s(x, 0) = 0 & u_s(a/2, y) = 0 \\
 v_s(0, y) = 0 & w_s(0, y) = 0 & v_s(x, b/2) = 0
 \end{array} \tag{10.7}$$

The present single- and multi-model solutions are compared with other solutions present in literature, three-dimensional analytical and three-dimensional FEM NASTRAN [182], ESL and LW analytical higher-order by the use of Fourier series expansions [183], ESL and LW FEM higher-order [184]. A non-uniform mesh grid of 38×54 elements ensures the convergence of the solution with a *LW4* single-model, see Figure 10.30. For the sake of brevity the study of the convergence is here omitted. The adopted refined mesh is necessary to study the behaviour of the mechanical variables along the whole plate domain, and not in one single point. The difficult task is to obtain a good behaviour of the mechanical stresses, and in particular of the transverse normal stress σ_{zz} along the in-plane directions avoiding strange oscillations due to the changing of the element size.

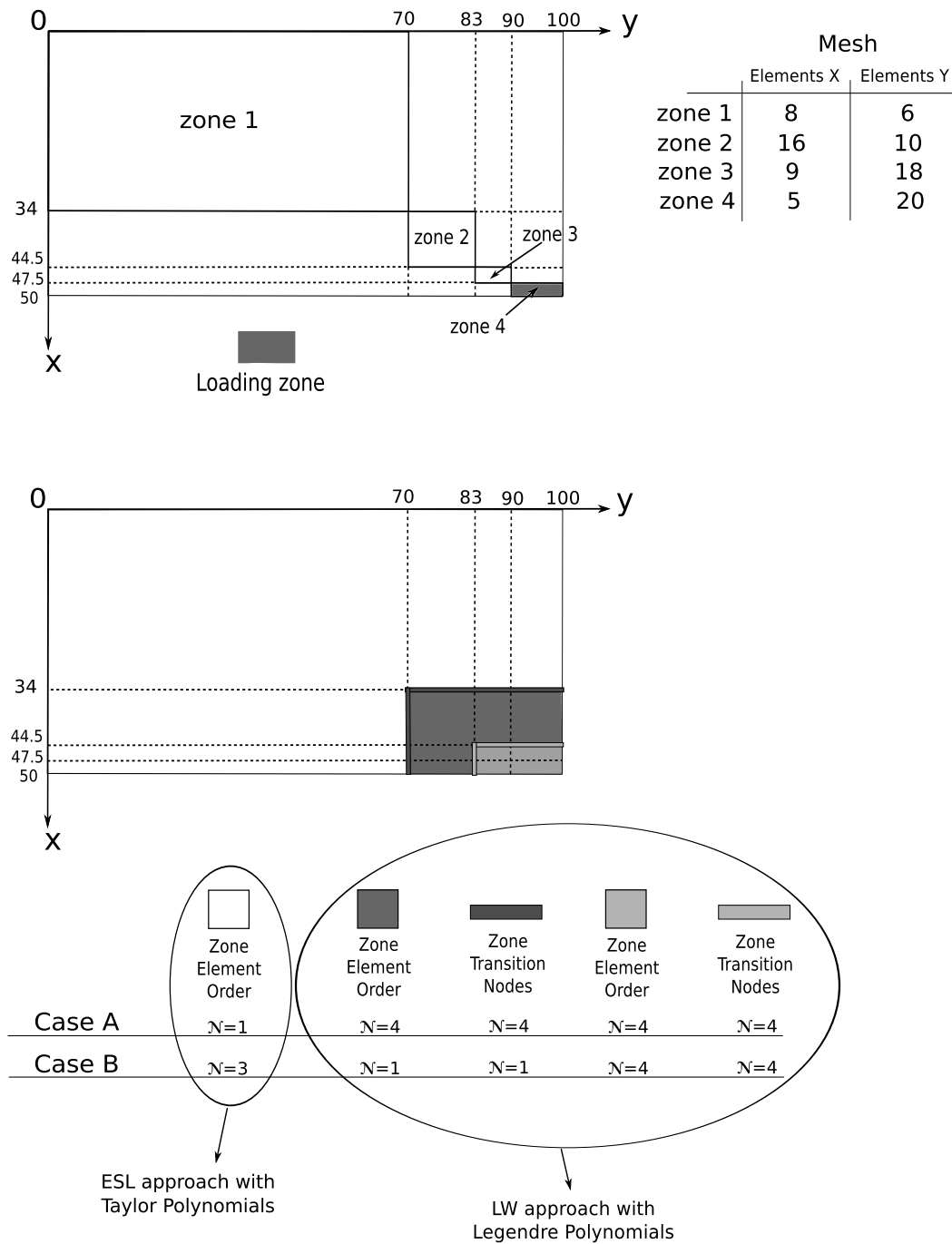


Figure 10.30: Non-uniform adopted mesh and graphical representation of the multi-model cases, for a quarter of the sandwich plate.

For the unsymmetrically laminated rectangular sandwich plate, mono-theory models are compared with those from the present global/local approach in Table 10.7. ESL models are not able to correct describe all the variables, therefore LW theories are necessary to match the reference analytical and 3D results. Table 10.7 also show solutions for variable kinematic multi-model theories. As emerged in the previous numerical sections, the primary variables (displacements) depend on the global domain approximation, in particular the transverse displacement w is better describe in the *Case B* configuration with a $DOFs$ reduction of 34% respect to the *Case A* multi-model. On the contrary the postprocessed variables (stresses) are dependent on the local approximation.

Table 10.7: Unsymmetrically laminated rectangular sandwich plate. Transverse displacement w , in-plane normal stresses σ_{xx} and σ_{yy} , and transverse normal stress σ_{zz} evaluated at $(a/2, b/2)$ by various single- and multi-theory models.

	z	w	σ_{xx}	σ_{yy}	σ_{zz}	$DOFs$
Top Skin						
3D Analytical [182]	Top	-3.78	-624	-241	-	
	Bottom		580	211	-	
3D NASTRAN [182]	Top	-3.84	-628	-237	-	
	Bottom		582	102	-	
LWM2 Analytical [183]	Top	-3.8243	-619.49	-	-	
	Bottom		577.36	-	-	
LWM2 FEM [184]	Top	-3.7628	-595.56	-223.93	-	
	Bottom		556.00	196.37	-	
Top Skin						
<i>LW4</i>	Top	-3.7774	-622.48	-233.39	-0.9649	327327
	Bottom		578.60	203.25	-0.8738	
<i>LW3</i>	Top	-3.7723	-618.14	-232.33	-1.0143	251790
	Bottom		574.87	202.36	-0.8270	
<i>LW2</i>	Top	-3.7552	-601.46	-228.13	-0.9813	176253
	Bottom		559.72	198.73	-0.8710	
<i>LW1</i>	Top	-3.3896	-562.86	-286.15	-242.69	100716
	Bottom		530.98	262.78	240.82	
<i>ET4</i>	Top	-2.5498	-248.99	-38.930	256.87	125895
	Bottom		184.89	-1.7709	-275.80	
<i>ET3</i>	Top	-0.5995	-121.19	-56.428	-21.706	100716
	Bottom		59.439	8.9946	-19.349	
<i>ET2</i>	Top	-0.0238	-29.573	-28.178	-30.655	75537
	Bottom		-27.989	-27.470	-29.934	
<i>ET1</i>	Top	-0.0191	-29.740	-25.448	-25.404	50358
	Bottom		-29.444	-25.211	-25.248	
<i>Case A</i>	Top	-2.1386	-622.21	-220.95	-0.9649	245619
	Bottom		567.44	198.35	-0.8738	
<i>Case B</i>	Top	-2.4177	-609.14	-217.40	-0.9654	161007
	Bottom		563.79	196.16	-0.8663	

Some results in terms of transverse displacement w , and transverse normal stress σ_{zz} along the thickness of the sandwich plate are represented in Figures 10.31a, and 10.31b. The transverse displacement w behaviour can change sensitively depending on the distribution of the kinematic enrichment within the structure plane. Figure 10.31a show that ESL mono-models can vary sensitively their accuracy depending on the expansion order, differently the LW mono-models have almost the same accuracy independently from the adopted expansion. Moreover for the multi-models, it is noticeable that the choice of the LW higher-order models for the loaded zone is not decisive for the correct description of the transverse mechanical displacement, as shown for *Case A* and *Case B*.

On the other hand for the transverse normal stress σ_{zz} , see Figure 10.31b, LW higher-order models are able to correctly predict a good behaviour along the plate thickness. Multi-models theories *Case A* and *Case B* show the same accuracy of the reference solution *LW4* in the considered evaluation point.

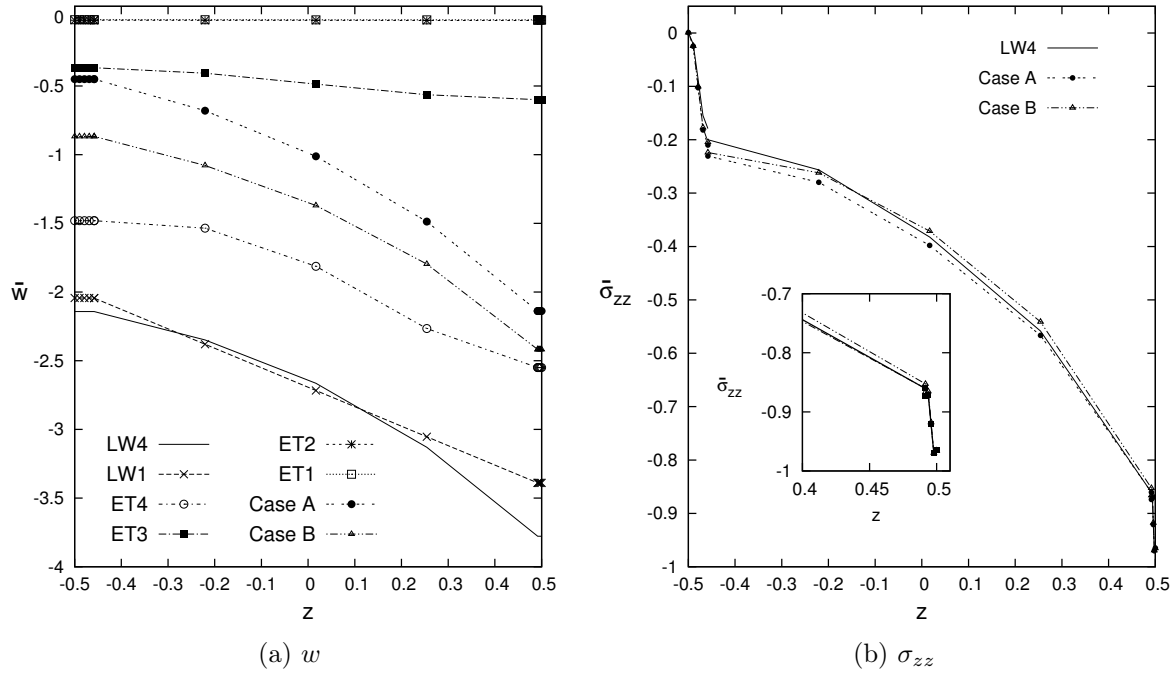


Figure 10.31: Unsymmetrically laminated rectangular sandwich plate. Transverse displacement $w(x; y)$, and transverse normal stress $\sigma_{zz}(x; y)$ evaluated at $(a/2, b/2)$ by various single- and multi-theory models.

Results in terms of the three-dimensional representation of the in-plane stress σ_{xx} and its behaviour along the in-plane x axis are represented in Figures 10.32a and 10.32b respectively. In Figure 10.32a it is noticeable that the maximum values of the in-plane stress are located in the loading zone and its surroundings. Furthermore the behaviour of the in-plane stress σ_{xx} along the the in-plane x axis and evaluated at $(y, z) = (b/2, +h/2)$ is depicted in Figure 10.32b. Mono-models *LW4* and *ET4* and multi-models *Case A* and *Case B* show almost the same accuracy solution. Multi-models *Case A* and *Case B*, produce small oscillations in the transition zone. It is noticeable that the oscillations are small, this is due to a finer mesh respect to the case of the previous numerical section.

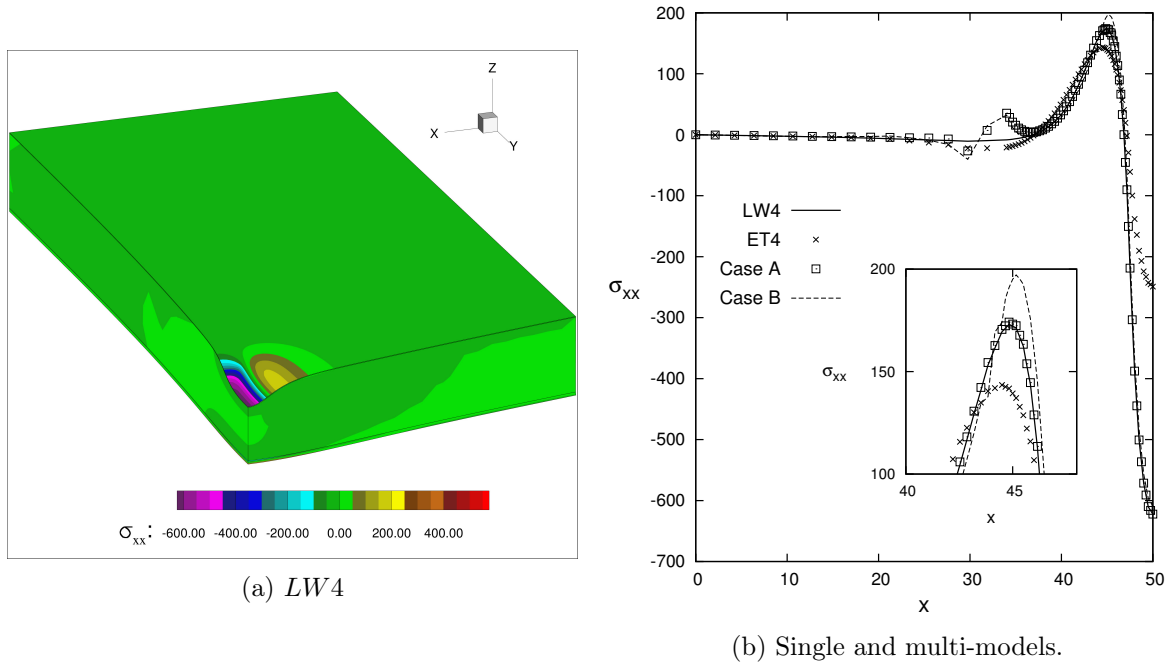


Figure 10.32: Unsymmetrically laminated rectangular sandwich plate. In-plane stress σ_{xx} , three-dimensional view of a quarter of the plate, and in-plane stress along the in-plane axis direction X evaluated at $(y, z) = (b/2, +h/2)$, for single and multi-models.

Finally, a three-dimensional distributions on a quarter of the sandwich plate of the transverse normal stress σ_{zz} is given to underline the global/local capabilities of the present finite element on the whole domain of the analyzed sandwich plate structure. The reference single-model solution *LW4* is depicted in Figure 10.33a. For a fair results comparison, the extremities of the colorbar values of the *LW4* model are used to limit the colorbar of the other solutions. The single-model *ET4* is not able to correctly describe the transverse shear stress behaviour, as shown in Figure 10.33b. Multi-model *Case A* and *Case B* are shown in Figures 10.34a and 10.34b respectively. It is evident that the transverse normal stress is well represented in the *LW4* zone only, closed to the loaded zone.

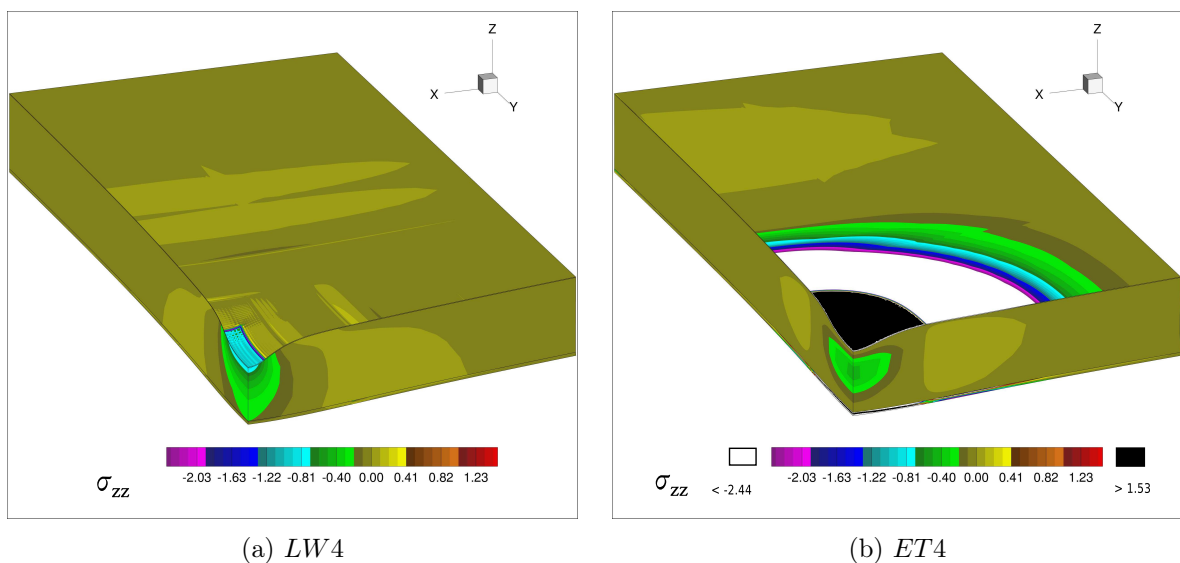


Figure 10.33: Unsymmetrically laminated rectangular sandwich plate, three-dimensional view of a quarter of the plate. Transverse normal stress σ_{zz} for single models.

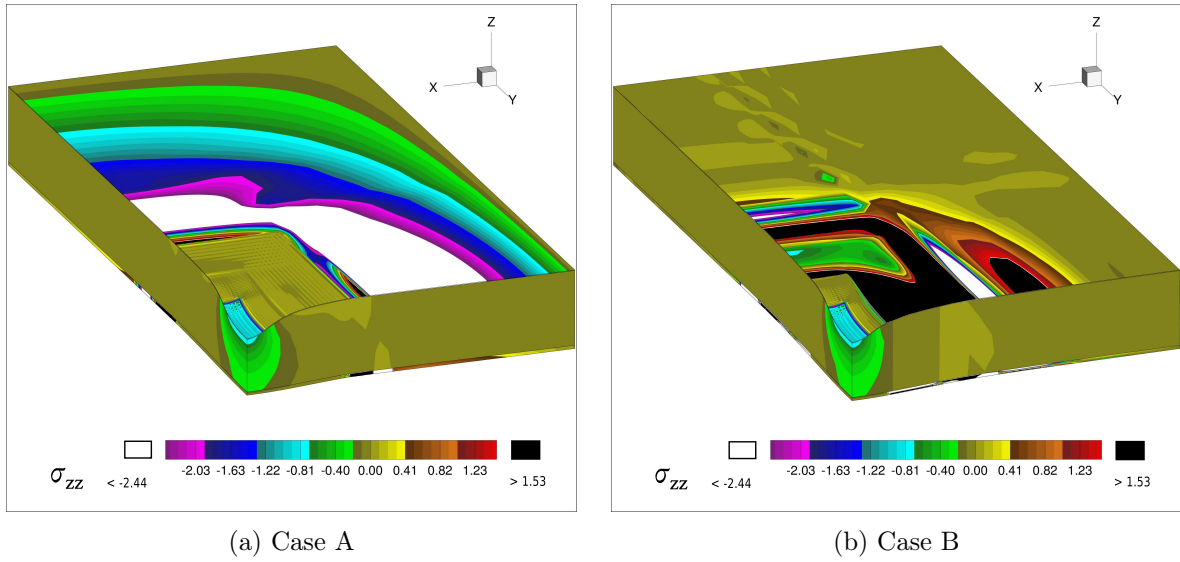


Figure 10.34: Unsymmetrically laminated rectangular sandwich plate, three-dimensional view of a quarter of the plate. Transverse normal stress σ_{zz} for multi-models.

10.4 Electro-Mechanical Analysis Results

Some problems have been considered to assess the capabilities of the proposed variable-kinematics plate elements and related global/local analysis. These analysis cases comprise:

- Composite plate with piezoelectric skins simply-supported, with bi-sinusoidal mechanical and electrical loadings
- Sandwich cantilevered plate with piezoelectric patch shear actuated in mode-15
- Sandwich cantilevered plate with piezoelectric patch under concentrated mechanical load

Whenever possible, the proposed multi-theory models are compared to single-theory from higher-order ESL models, LW models, 3D elasticity solutions and analytical results. Moreover different multi-theory models present in literature are given in some cases. For the sake of clarity, present multi-model theories are opportunely described for each numerical case considered.

10.4.1 Simply-supported cross-ply composite plates with piezoelectric skins

A four-layer cross-ply square plate with a cross-ply Gr/Ep composite core $[0^\circ/90^\circ]$ and PZT-4 piezoelectric external skins, see Figure 10.35, is analyzed. The square plate has the following geometrical data: $a = b = 4.0$, and $h_{tot} = 1.0$. In respect to the total thickness, a single piezoelectric skin is thick $h_p = 0.1h_{tot}$, while the single core layer is thick $h_c = 0.4h_{tot}$. The static analysis of the plate structure is evaluated in sensor and actuator configuration.

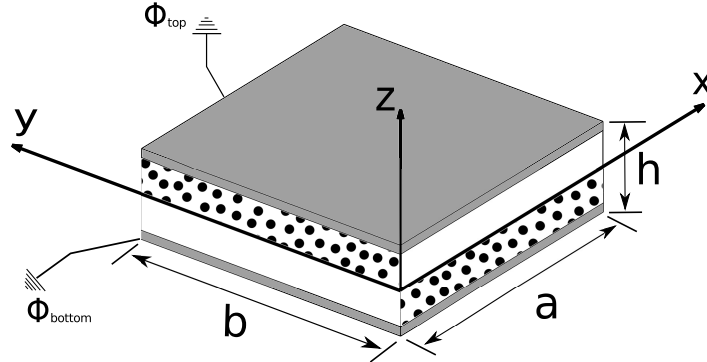


Figure 10.35: Reference system of the composite plate with piezoelectric skins.

For the sensor case, a bi-sinusoidal transverse normal pressure is applied to the top surface of the plate:

$$p(x, y, z_{top}) = p_z^o \sin(m\pi x/a) \sin(n\pi y/b) \quad (10.8)$$

with amplitude $p_z^o = 1$ and wave numbers $m = 1$, $n = 1$. The potential at top and bottom position is imposed $\Phi_t = \Phi_b = 0$. For the actuator case, a bi-sinusoidal electric potential is imposed at top surface:

$$\Phi(x, y, z_{top}) = \phi_z^o \sin(m\pi x/a) \sin(n\pi y/b) \quad (10.9)$$

with amplitude $\phi_z^o = 1$ and wave numbers $m = 1$, $n = 1$. The potential at bottom position is imposed $\Phi_b = 0$. No mechanical load is applied. The material properties of the plate are given in Table 10.8.

Table 10.8: Material data for multilayered plate.

Mechanical Properties									
	E_{11} [GPa]	E_{22} [GPa]	E_{33} [GPa]	ν_{12} [-]	ν_{13} [-]	ν_{23} [-]	G_{12} [GPa]	G_{13} [GPa]	G_{23} [GPa]
<i>Gr/EP</i>	132.38	10.756	10.756	0.24	0.24	0.49	5.6537	5.6537	3.606
<i>PZT - 4</i>	81.3	81.3	64.5	0.329	0.432	0.432	30.6	25.6	25.6

Electrical Properties									
	e_{15} [C/m ²]	e_{24} [C/m ²]	e_{31} [C/m ²]	e_{32} [C/m ²]	e_{33} [C/m ²]	$\tilde{\epsilon}_{11}/\epsilon_0$ [-]	$\tilde{\epsilon}_{22}/\epsilon_0$ [-]	$\tilde{\epsilon}_{33}/\epsilon_0$ [-]	ϵ_0 [C/Vm]
<i>Gr/EP</i>	0	0	0	0	0	3.5	3.0	3.0	$8.85 * 10^{-12}$
<i>PZT - 4</i>	12.72	12.72	-5.20	-5.20	15.08	1475	1475	1300	$8.85 * 10^{-12}$

The plate has simply-supported boundary conditions. Due to the symmetry of both the geometry and the load, a quarter of the plate is analyzed and the following symmetry and boundary conditions (simply-supported) are applied:

$$\begin{array}{ll}
 \textit{Boundary} & \textit{Symmetry} \\
 u_s(x, 0) = 0 & w_s(x, 0) = 0 & u_s(a/2, y) = 0 \\
 v_s(0, y) = 0 & w_s(0, y) = 0 & v_s(x, b/2) = 0 \\
 \Phi_s(x, 0) = 0 & \Phi_s(0, y) = 0 &
 \end{array} \tag{10.10}$$

The boundary condition of the electric potential is taken into account to compare the results with the analytical solution, see [46], where the electric potential has the following Navier-type assumptions $\Phi = \hat{\Phi} \sin(m\pi x/a) \sin(n\pi y/b)$.

In order to compare the results with other solutions present in literature [185](Arlequin method), the mid-plane domain of the plane structure was subdivided into two zones along the axes x and y, as shown in Figure 10.36, and multi-theory models *Case A*, *Case B* and *Case C* are depicted on the FE discretization of a quarter of the plate. The FE mesh on a quarter plate is 10×10 elements, the accounted mesh is the same used in the reference solutions [185]; the difference is that, in the reference solutions, it is used a four-node element and a Reissner Mixed Variational Theorem applied to the transverse electric displacement \mathcal{D}_z (*RMVT - D_z*), the transverse electric displacement is a priori modelled with the mechanical displacements.

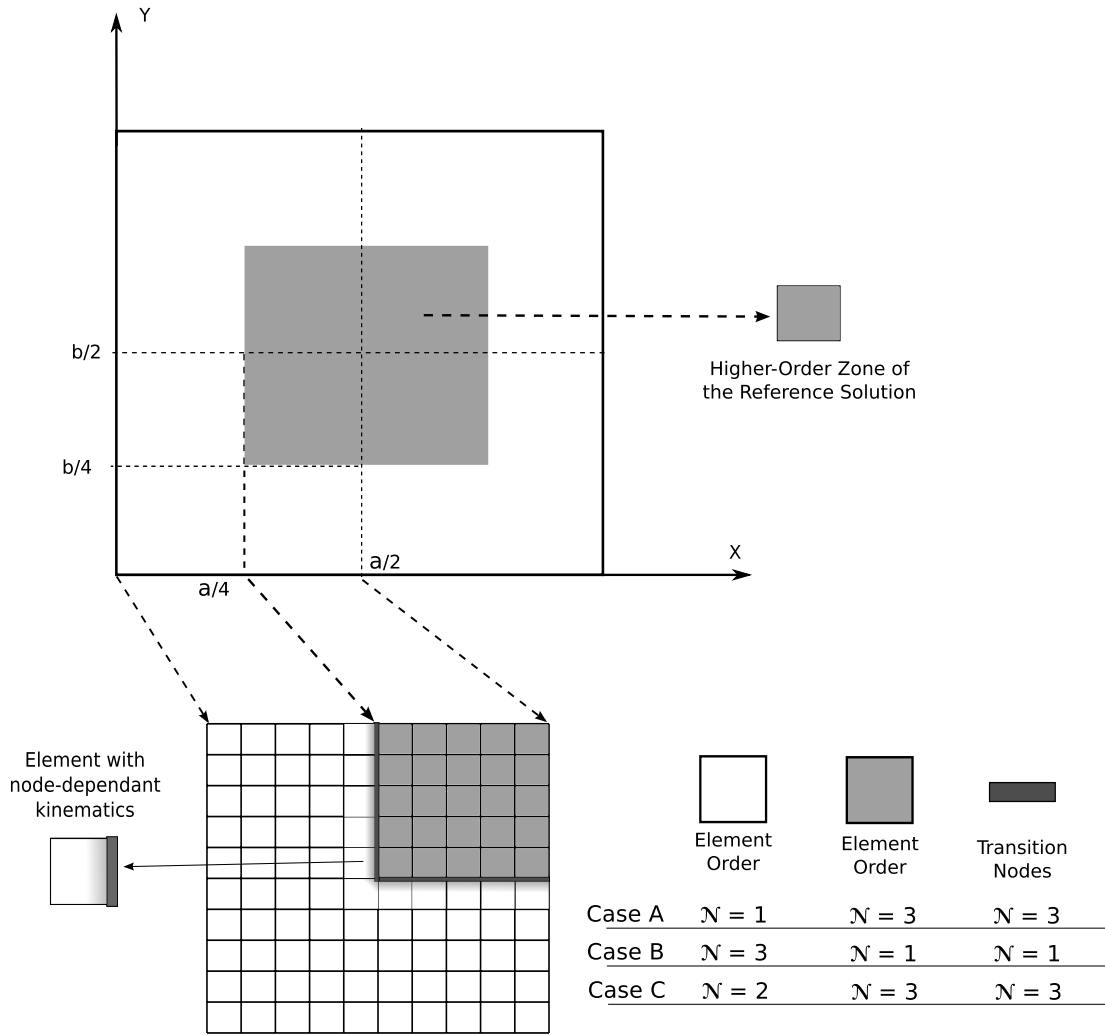


Figure 10.36: Mesh zones of the composite plate with piezoelectric skins and graphical representation of the multi-theory models, based on layer-wise models.

Some results of the transverse mechanical displacement w , in-plane stress σ_{xx} , transverse shear stress σ_{xz} , transverse normal stress σ_{zz} , electric potential Φ , and transverse electric displacement \mathcal{D}_z evaluated along the plate thickness are given in tabular form, see Tables 10.9, 10.10, for the sensor case and the actuator case respectively. Mono-theory models are compared with those from the present multi-model approach, furthermore the exact $3D$ solutions provided by Heyliger [78], the analytical solution with layer-wise mono-models [46], and the multi-model solutions via the Arlequin method [185] are given. For the transverse shear and normal stresses the evaluation point is located between the composite layers, their results are given for the upper layer with upscript $^+$ and for the lower layer with upscript $^-$. It is clear for both sensor and actuator cases that at least a second order expansion order is needed to get good results for all the considered variables.

Table 10.9: Composite four-layered plate with piezoelectric skins. Transverse displacement $\bar{w} = (10^{11}) \times w(a/2, b/2, 0)$, in-plane stress $\bar{\sigma}_{xx} = \sigma_{xx}(a/2, b/2, +h/2)$, transverse shear stress $\bar{\sigma}_{xz} = \sigma_{xz}(0, b/2, 0)$, transverse normal stress $\bar{\sigma}_{zz} = (10) \times \sigma_{zz}(a/2, b/2, 0)$, electric potential $\bar{\Phi} = (10^2) \times \Phi(a/2, b/2, 0)$, and transverse electric displacement $\bar{D}_z = (10^{10}) \times D_z(a/2, b/2, +h/2)$ by various single- and multi-theory models. Sensor Case.

	\bar{w}	$\bar{\sigma}_{xx}$	$\bar{\sigma}_{xz}$	$\bar{\sigma}_{zz}$	$\bar{\Phi}$	\bar{D}_z	<i>DOFs</i>
Reference solutions							
<i>3D Exact</i> [78]	30.027	6.5643	-	4.9831	0.611	0.1606	
<i>LW4_a</i> [46]	30.029	6.5642	0.6872	-	0.6108	0.161	
<i>LW1_a</i> [46]	29.852	6.9995	-	-	0.6030	-0.880	
<i>(LW1 - LWM3)^A</i> [185]	29.91	-	-	4.888 ⁺	0.555	-0.0252	
				5.159 ⁻			
<i>(LW2 - LWM3)^C</i> [185]	29.72	-	-	4.871 ⁺	-	0.1533	
				5.147 ⁻			
Present single- and multi-theory models							
<i>LW4</i>	30.029	6.5739	0.6906 ⁺	4.9844 ⁺	0.6111	0.1321	29988
			0.6886 ⁻	4.9812 ⁻			
<i>LW3</i>	30.029	6.5749	0.6866 ⁺	4.8882 ⁺	0.6110	0.1348	22932
			0.6886 ⁻	5.0648 ⁻			
<i>LW2</i>	29.981	6.5690	0.8162 ⁺	5.2397 ⁺	0.6090	0.1489	15876
			0.7058 ⁻	4.8336 ⁻			
<i>LW1</i>	29.851	7.0132	0.7099 ⁺	5.7912 ⁺	0.6032	-0.8948	8820
			0.6791 ⁻	3.9877 ⁻			
<i>Case A</i>	29.932	6.5694	0.7100 ⁺	4.8889 ⁺	0.6100	0.1365	12692
			0.6798 ⁻	5.0506 ⁻			
<i>Case B</i>	29.926	7.0033	0.6816 ⁺	5.7928 ⁺	0.6025	-0.8936	19060
			0.6863 ⁻	3.9850 ⁻			
<i>Case C</i>	29.999	6.5852	0.8168 ⁺	4.8965 ⁺	0.6108	0.1353	17812
			0.7057 ⁻	5.0601 ⁻			

Table 10.10: Composite four-layered plate with piezoelectric skins. Transverse displacement $\bar{w} = (10^{11}) \times w(a/2, b/2, 0)$, in-plane stress $\bar{\sigma}_{xx} = \sigma_{xx}(a/2, b/2, +h/2)$, transverse shear stress $\bar{\sigma}_{xz} = (10) \times \sigma_{xz}(0, b/2, 0)$, transverse normal stress $\bar{\sigma}_{zz} = (10^3) \times \sigma_{zz}(a/2, b/2, 0)$, electric potential $\bar{\Phi} = \Phi(a/2, b/2, 0)$, and transverse electric displacement $\bar{D}_z = (10^9) \times D_z(a/2, b/2, +h/2)$ by various single- and multi-theory models. Actuator Case.

	\bar{w}	$\bar{\sigma}_{xx}$	$\bar{\sigma}_{xz}$	$\bar{\sigma}_{zz}$	$\bar{\Phi}$	\bar{D}_z	<i>DOFs</i>
Reference solutions							
<i>3D Exact</i> [78]	-1.471	1.1181	-0.2387	-14.612	0.4476	-	
<i>LW4_a</i> [46]	-1.4707	1.1180	-0.239	-	0.4477	-2.4184	
<i>LW1_a</i> [46]	-1.5962	3.3433	-	-	0.4468	-1.3814	
(<i>LW1 - LWM3</i>) ^A [185]	-1.420	1.119	-	-	-	-	
(<i>LW2 - LWM3</i>) ^C [185]	-1.410	-	-	-	-	-	
Present single- and multi-theory models							
<i>LW4</i>	-1.4707	1.1248	-0.2411 ⁺ -0.2391 ⁻	-14.732 ⁺ -14.660 ⁻	0.4477	-2.4186	29988
<i>LW3</i>	-1.4707	1.1261	-0.2270 ⁺ -0.2394 ⁻	-13.541 ⁺ -15.343 ⁻	0.4477	-2.4183	22932
<i>LW2</i>	-1.4662	1.1311	-0.3592 ⁺ -0.2505 ⁻	-20.604 ⁺ -15.978 ⁻	0.4477	-2.4167	15876
<i>LW1</i>	-1.5962	3.3531	-0.0293 ⁺ -0.2980 ⁻	14.188 ⁺ -21.879 ⁻	0.4468	-1.3816	8820
<i>Case A</i>	-1.4729	1.1315	-0.0302 ⁺ -0.2979 ⁻	-12.729 ⁺ -14.223 ⁻	0.4479	-2.4183	12692
<i>Case B</i>	-1.5916	3.3590	-0.2210 ⁺ -0.2385 ⁻	-14.026 ⁺ -21.913 ⁻	0.4467	-1.3818	19060
<i>Case C</i>	-1.4679	1.1250	-0.3599 ⁺ -0.2504 ⁻	-13.641 ⁺ -15.318 ⁻	0.4477	-2.4183	17812

Some results in terms of transverse displacement w , transverse shear stress σ_{xz} and electric transverse displacement D_z along the plate thickness. For the transverse displacement w , in sensor case configuration, the differences between single and multi-models are negligible, see Figure 10.37a. On the contrary for the actuator case, see Figure 10.37b, remarkable differences are present between *LW4* and *LW1* single-model solutions; extending the comparison to the multi-models, it is clear that a more refined expansion is needed in the center plate where the load is higher, see *Case A* and *Case C*, differently *Case B* shows an accuracy very close to *LW1* single-model.

The transverse shear stress σ_{xz} is represented in Figure 10.38a for the actuator configuration. The stress is evaluated in its maximum shear stress value point $(x, y) = (0, b/2)$. The mono-model *LW4* is able to predict the correct behaviour as the 3D Exact reference solution [78]. The higher-order multi-models *Case A* and *Case C* are not sufficient to depict the good representation of the shear stress. Differently *Case B* shows a good accuracy solution due to the higher-order representation in the evaluation zone of the shear stress.

Regarding the electric transverse displacement D_z , represented in Figure 10.38b for the sensor configuration, it is evaluated in the center plate. The mono-model *LW4* is able to predict the correct behaviour as the 3D Exact reference solution [78]. In this case, the multi-models *Case A* and *Case C*, differently from *Case B*, are able to get a good accuracy solution due to the higher-order representation in the center plate zone.

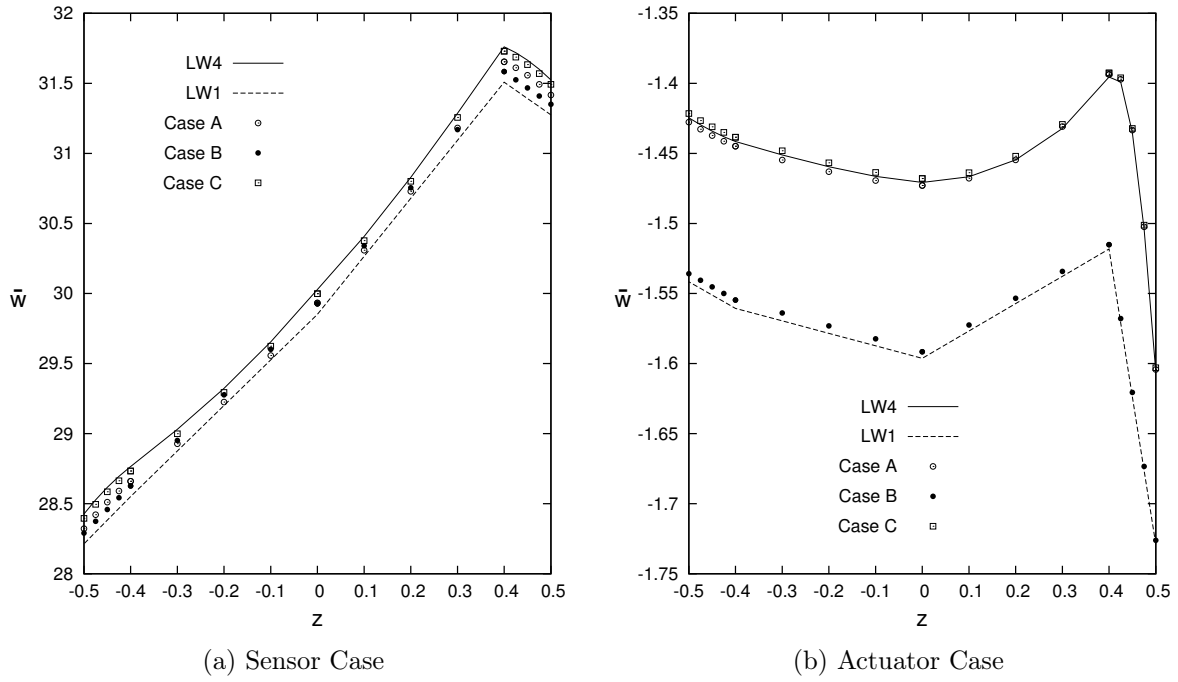


Figure 10.37: Composite plate with piezoelectric skins. Transverse displacement $\bar{w}(x; y) = 10^{11} \times w(a/2; b/2)$. Sensor and Actuator Cases. Single and Multi-theory models.

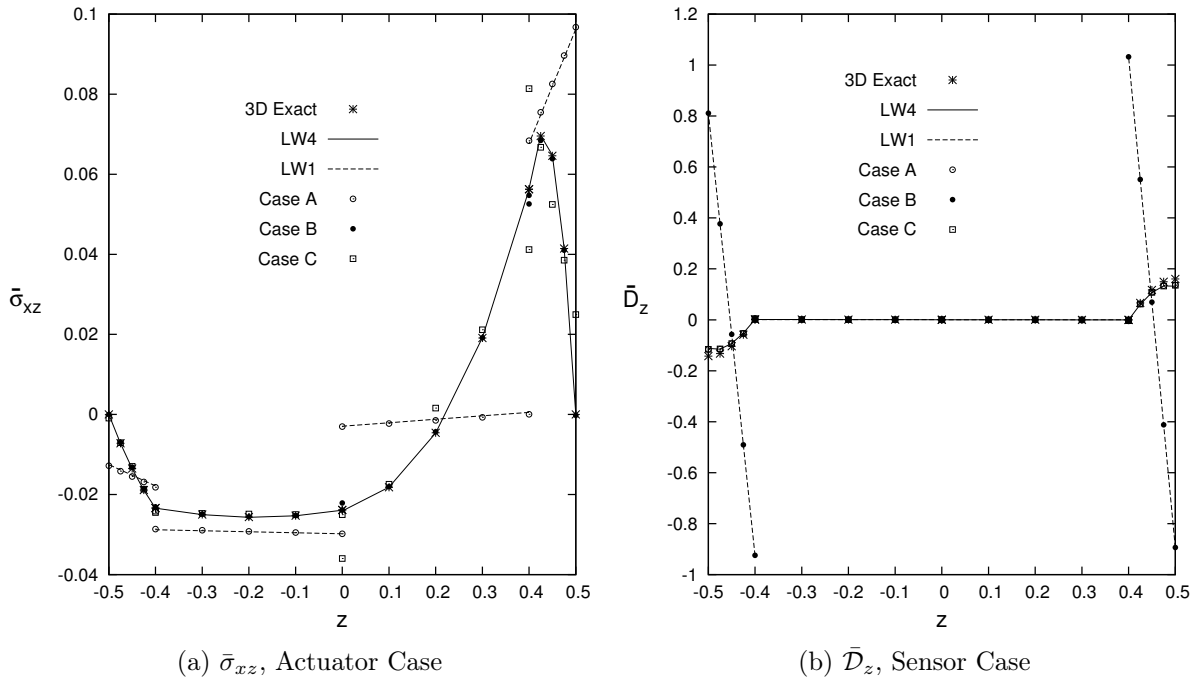


Figure 10.38: Composite plate with piezoelectric skins. Transverse shear stress $\bar{\sigma}_{xz}(x; y) = (10) \times \sigma_{xz}(0, b/2)$ for the Actuator Case, and transverse electric displacement $\bar{D}_z(x; y) = (10^{10}) \times D_z(a/2, b/2)$ for the Sensor Case. Single and Multi-theory models.

Results in terms of in-plane stress $\bar{\sigma}_{xx}(y; z) = \sigma_{xx}$, and transverse electric displacement $\bar{D}_z = (10^{10}) \times D_z$ along the in-plane x axis are represented in Figures 10.39a, 10.39b respectively. For both the depicted variables, the multi-model *Case C* is able to reproduce the correct behaviour along the X axis as the reference solution *LW4*. The linear single model *LW1* and multi-models *Case A* and *Case B* show an incorrect solution in the zone where a

linear approximation is used. In the transition elements small oscillations are present, these oscillations are due to the coarse mesh, if the mesh is more refined the oscillations tend to fade.

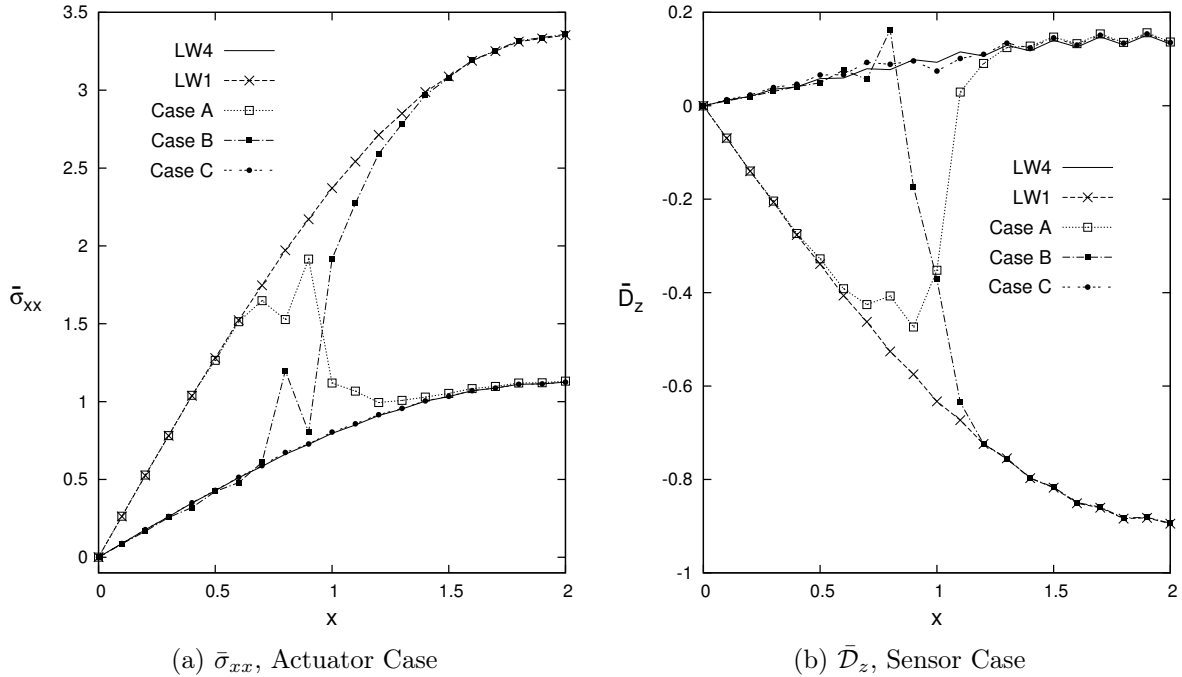


Figure 10.39: Composite plate with piezoelectric skins. In-plane stress $\bar{\sigma}_{xx}(y; z) = \sigma_{xx}(b/2; +h/2)$ for the Actuator Case, and transverse electric displacement $\bar{D}_z(y; z) = (10^{10}) \times \mathcal{D}_z(b/2; +h/2)$ for the Sensor Case, along the in-plane direction X , the axis X is expressed in $[mm]$. Single and Multi-theory models.

Figures 10.40a and 10.40b show the three-dimensional distributions of the transverse normal stress σ_{zz} , in Sensor Case configuration, of the single-model *LW4* and the variable kinematic multi-model *Case A* respectively. The results show the enhanced global/local capabilities of the *Case A* model, which is able to predict correctly the stress state in the center zone where the loading is bigger. Moreover the three-dimensional distributions of the transverse shear stress σ_{xz} , in Actuator Case configuration, is depicted in Figures 10.41a and 10.41b for the single-model *LW4* and the variable kinematic multi-model *Case B* respectively. The results show the enhanced global/local capabilities of the *Case B* model, it represents accurately the maximum shear stress in boundary zone of the plate structure.

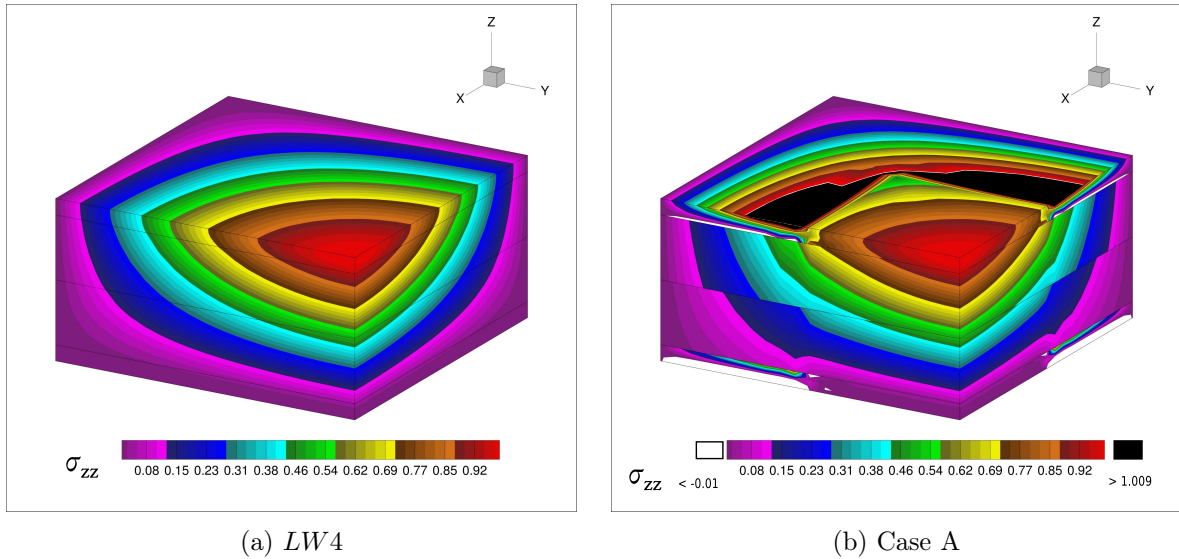


Figure 10.40: Composite plate with piezoelectric skins, three-dimensional view of a quarter of the plate. Transverse normal stress σ_{zz} for single and multi-model. Sensor Case.

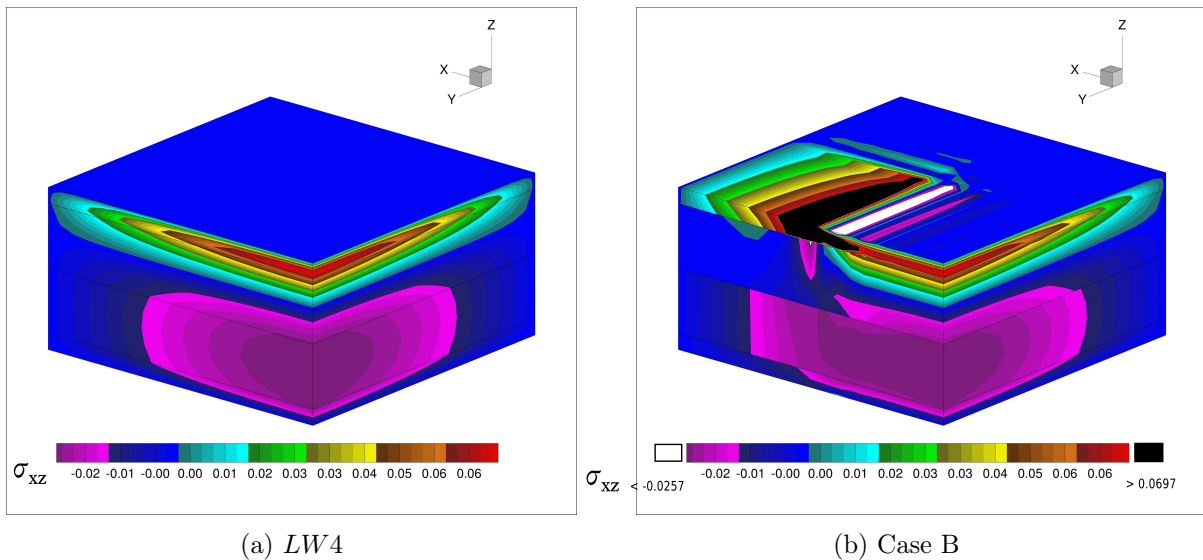


Figure 10.41: Composite plate with piezoelectric skins, three-dimensional view of a quarter of the plate. Transverse shear stress σ_{xz} for single and multi-model. Actuator Case.

10.4.2 Sandwich cantilever plate shear-actuated in mode-15

A cantilever sandwich plate is analysed as second example and it is shown in Figure 10.42. The geometrical dimensions are: $a = 100 \text{ mm}$, $b = 20 \text{ mm}$, $h_{total} = 18 \text{ mm}$. The upper and lower layers are made of Aluminum with the following mechanical properties: $E = 70.3 \text{ GPa}$, $\nu = 0.345$, $\varepsilon = 30.975 \times 10^{-12} \text{ F/m}$; each aluminum layer is thick $h_{Al} = 8 \text{ mm}$. The central layer is thick $h_c = 2 \text{ mm}$, it is made of Foam, with the following properties: $E = 35.3 \text{ MPa}$, $\nu = 0.38$, $\varepsilon = 30.975 \times 10^{-12} \text{ F/m}$; a small PZT-5H piezoelectric patches is introduced in the foam layer with dimension: $a_p = 10 \text{ mm}$, $b_p = 20 \text{ mm}$, $h_p = 2 \text{ mm}$, the PZT-5H material has the following properties: $C_{11} = C_{22} = C_{33} = 126 \text{ GPa}$, $C_{23} = 79.5 \text{ GPa}$, $C_{12} = C_{13} = 84.1 \text{ GPa}$, $C_{44} = C_{55} = C_{66} = 23 \text{ GPa}$, $e_{11} = 23.3 \text{ C/m}^2$, $e_{12} = e_{13} = -6.5 \text{ C/m}^2$, $e_{26} = e_{35} = 17 \text{ C/m}^2$, $\varepsilon_{11} = 1.3 \times 10^{-8} \text{ F/m}$, $\varepsilon_{22} = \varepsilon_{33} = 1.503 \times 10^{-8} \text{ F/m}$. The material PZT-5H is polarized in the x-direction, or in *mode* - 15. The structure is loaded at the upper

and lower surfaces of the piezoelectric patch with a constant uniform electric potential equal to $\Phi_{t/b} = \mp 10.0 V$.

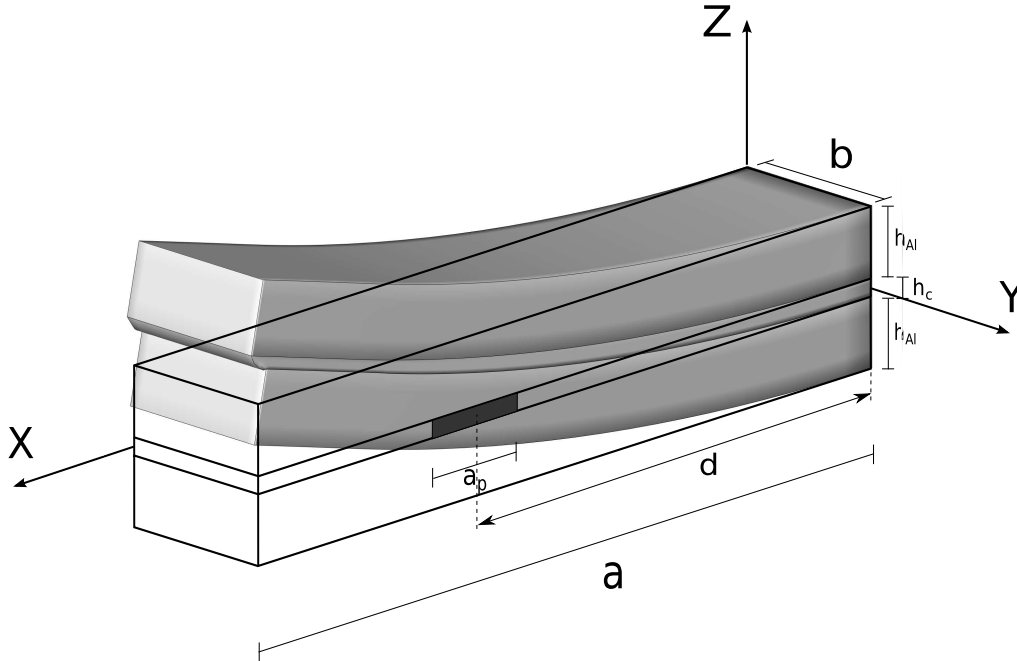


Figure 10.42: Reference system of the sandwich plate with piezoelectric patch, and three-dimensional representation of the deformation under the electric load.

First, a convergence study on a single-theory plate model was performed. As far as an *LW4* model is concerned and as shown in Table 10.11, a non-uniform mesh grid of 56×8 elements, see Figure 10.43 is enough to ensure convergent results. This structural problem has become popular and it is a good benchmark problem for its selectivity. The present plate element model is compared with various solutions from the literature, including those of Zhang and Sun [186,187], Benjeddou et al. [188]. Some results are given varying the actuator position along the x-axis, the deflection at the free edge is investigated for each position of the piezoelectric patch, see Figure 10.44, and compared with the literature solutions [186,188], here named Sun & Zhang, and Benjeddou et al., respectively.

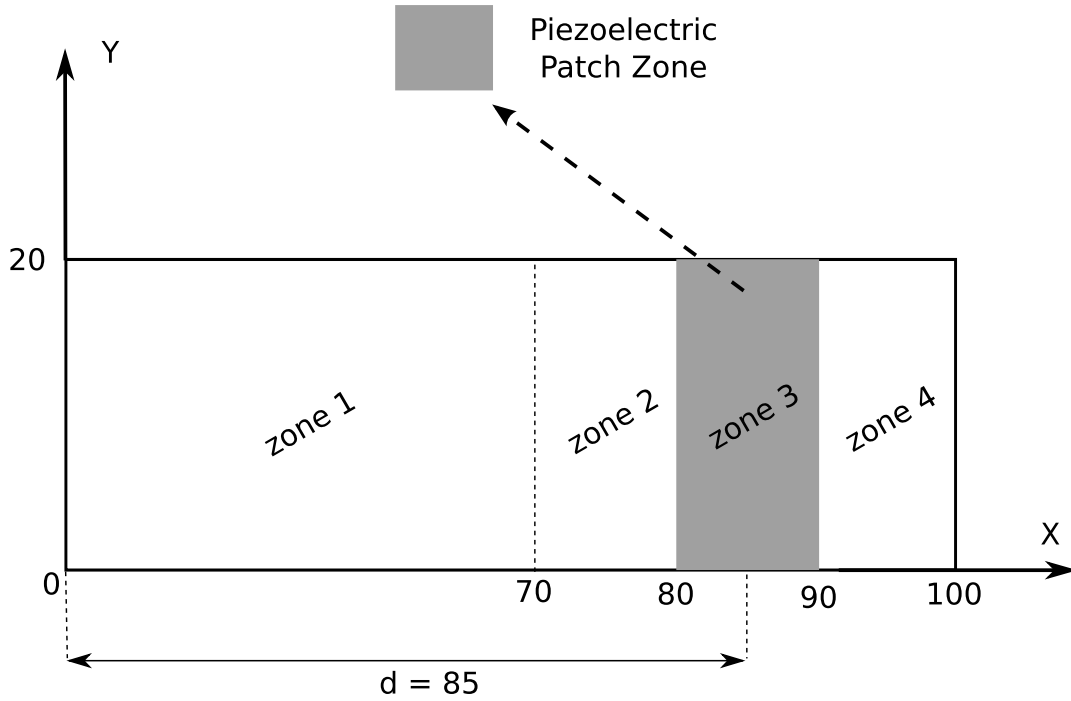


Figure 10.43: Mesh zone subdivisions of the sandwich plate with piezoelectric patch, for the convergence study.

Table 10.11: Convergence study versus the number of elements of the $LW4$ single-theory model of the sandwich cantilever plate. Transverse displacement $w = 10^8 \times w(a, b/2, +h/2)$, electric potential $\Phi = \Phi(d, b/2, -h/2)$, in-plane principal stress $\sigma_{xx} = \sigma_{xx}(d, b/2, -h/2)$, transverse shear stress $\sigma_{xz} = \sigma_{xz}(d, b/2, 0)$, with the center of the piezoelectric patch placed at $d = 85 \text{ mm}$.

				w	Φ	σ_{xx}	σ_{xz}	$DOFs$
<i>Mesh 8 × 2</i>								
<i>zone1</i>	<i>zone2</i>	<i>zone3</i>	<i>zone4</i>	6.7194	0.5852	983.17	-1220.7	4420
2 × 2	2 × 2	2 × 2	2 × 2					
<i>Mesh 16 × 4</i>								
<i>zone1</i>	<i>zone2</i>	<i>zone3</i>	<i>zone4</i>	6.7531	0.1404	1023.7	-959.22	15444
4 × 4	4 × 4	4 × 4	4 × 4					
<i>Mesh 32 × 8</i>								
<i>zone1</i>	<i>zone2</i>	<i>zone3</i>	<i>zone4</i>	6.7673	0.0257	944.61	-967.35	57460
8 × 8	8 × 8	8 × 8	8 × 8					
<i>Mesh 64 × 16</i>								
<i>zone1</i>	<i>zone2</i>	<i>zone3</i>	<i>zone4</i>	6.7738	0.0097	956.82	-981.90	221364
16 × 16	16 × 16	16 × 16	16 × 16					
<i>Mesh 56 × 8</i>								
<i>zone1</i>	<i>zone2</i>	<i>zone3</i>	<i>zone4</i>	6.7661	0.0172	957.65	-983.45	99892
8 × 8	16 × 8	16 × 8	16 × 8					

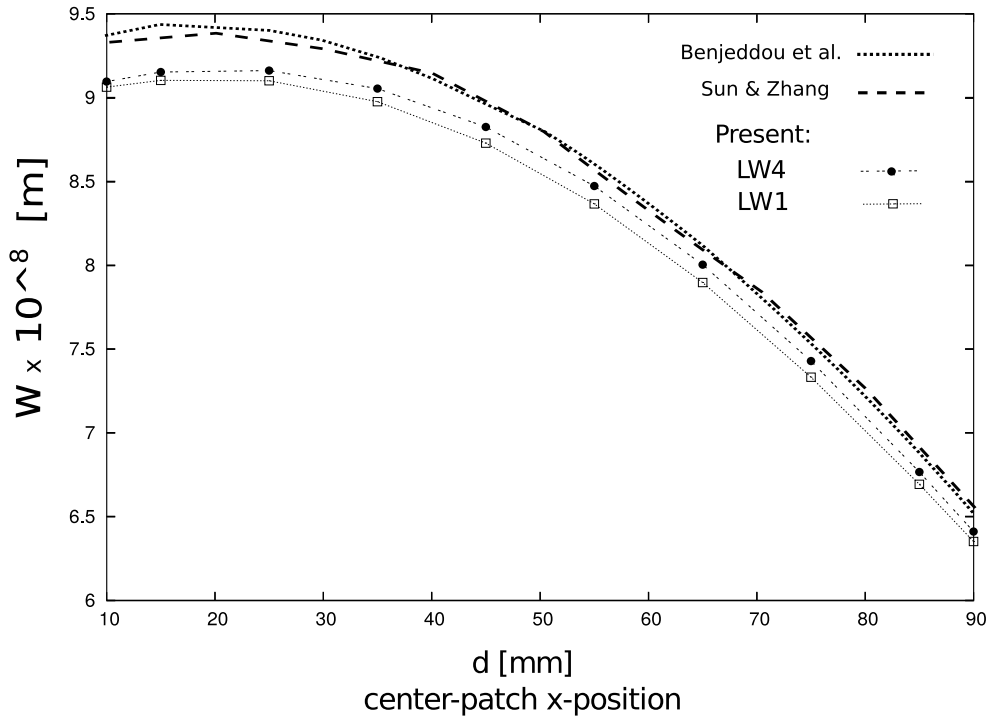


Figure 10.44: Sandwich plate with piezoelectric patch, tip transverse displacement $w(x, y, z) = 10^8 \times w(a, b/2, +h/2)$ for several position of the piezoelectric patch along the x-axis direction.

Various node-variable kinematic models have been used to perform the global/local analysis of the proposed plate structure, with the center of the piezoelectric patch fixed at $d = 85 \text{ mm}$. The mid-plane domain of the plate structure was subdivided into higher-order and lower-order zones along the axes x and y and they are depicted in Figure 10.45. Some results of the transverse mechanical displacement w , in-plane stress σ_{xx} , transverse shear stress σ_{xz} , transverse normal stress σ_{zz} , electric potential Φ , and transverse electric displacement \mathcal{D}_z evaluated along the plate thickness are given in tabular form, see Table 10.12. Monothory models are compared with those from the present multi-model approach, furthermore the FEM 3D solution provided by 3D Abaqus C3D20RE element is given.

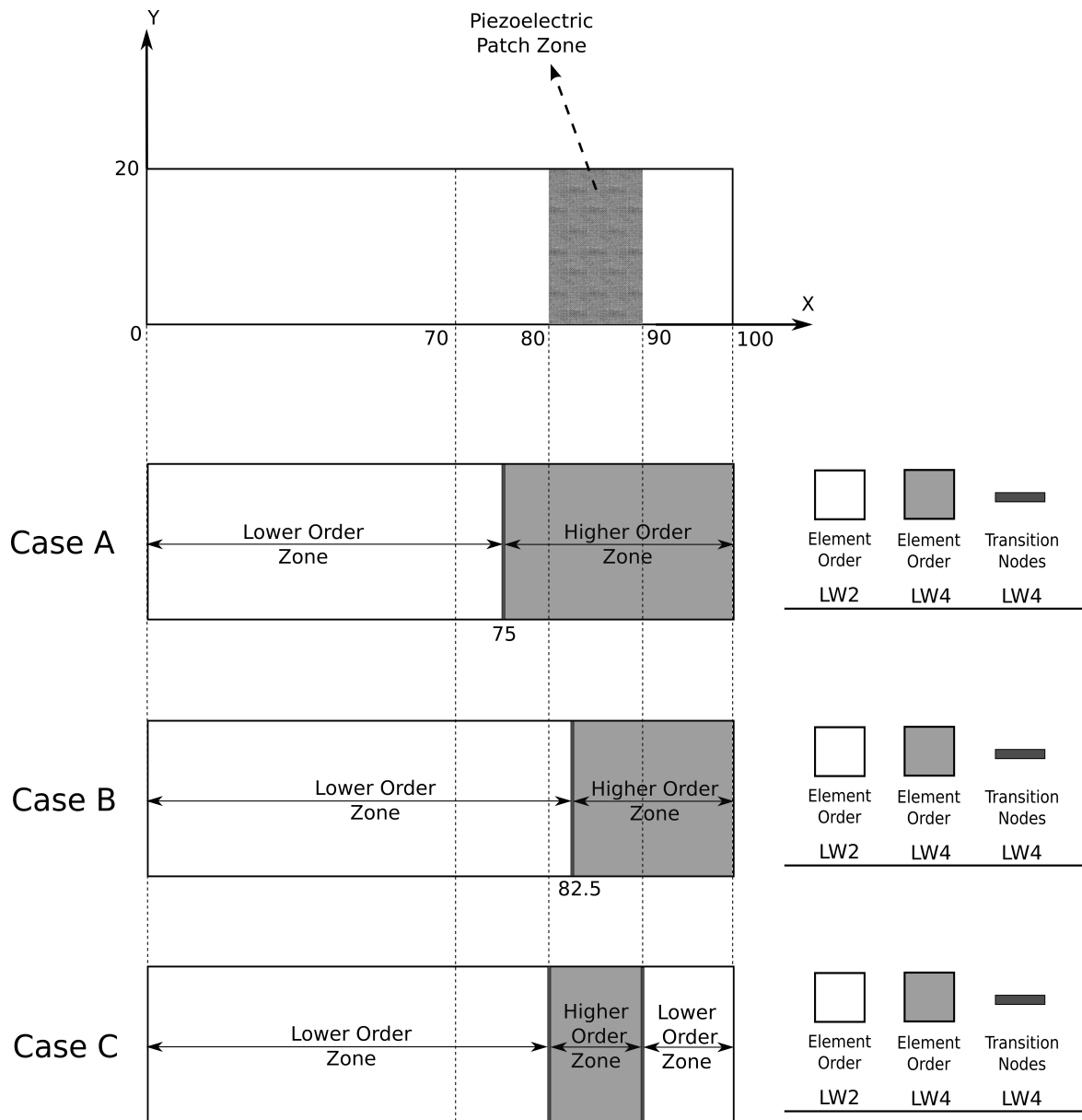


Figure 10.45: Graphical representation of the multi-theory models, based on layer-wise models, of the sandwich plate with piezoelectric patch, for the node-variable kinematic study.

Table 10.12: Single-theory and multi-theory models of the sandwich cantilever plate. Transverse displacement $w = 10^8 \times w(a, b/2, +h/2)$, electric potential $\Phi = \Phi(d, b/2, -h/2)$, in-plane principal stress $\sigma_{xx} = \sigma_{xx}(d, b/2, -h/2)$, transverse shear stress $\sigma_{xz} = \sigma_{xz}(d, b/2, 0)$, transverse normal stress $\sigma_{zz} = \sigma_{zz}(d, b/2, -h/2)$, transverse electric displacement $\mathcal{D}_z = 10^4 \times \mathcal{D}_z(d, b/2, 0)$, with the center of the piezoelectric patch placed at $d = 85 \text{ mm}$.

	w	σ_{xx}	σ_{xz}	σ_{zz}	Φ	\mathcal{D}_z	$DOFs$
3D Abaqus C3D20RE	6.7775	939.50	-1001.1	-3.7539	6.3489	-	627028
<i>LW4</i>	6.7661	957.65	-983.45	36.319	0.0172	2.7523	99892
<i>LW3</i>	6.7716	819.22	-941.32	-262.36	0.0187	2.7526	76840
<i>LW2</i>	6.7957	1163.2	-878.64	354.78	0.0208	2.7530	53788
<i>LW1</i>	6.6923	684.02	-969.41	465.55	0.0443	2.7524	30736
<i>Case A</i>	6.7660	958.91	-984.12	36.388	-0.0116	2.7523	86836
<i>Case B</i>	6.7914	901.61	-858.59	-18.913	-0.0112	2.7532	77044
<i>Case C</i>	6.7738	915.53	-949.66	36.314	-0.0094	2.7526	67252

Some results in terms of transverse displacement w , and electric potential Φ along the thickness are represented in Figures 10.46a and 10.46b, furthermore three-dimensional view of the electric potential Φ is given in Figures 10.47a and 10.47b. Some more comments can be made:

- The through-the-thickness distribution of the transverse displacement w at the free tip, as shown in Figure 10.46a, is correctly predicted by higher-order single-models *LW3* and *LW4*. The same accuracy is reached by the *Case A* multi-model and little losses in accuracy are present in the *Case B* and *Case C* multi-models.
- The behaviour of the electric potential Φ along the thickness, depicted in Figure 10.46b, is well described for every single and multi-models. Furthermore the three-dimensional view of the electric potential Φ , on deformed structure, is given by the finite element 3D Abaqus C3D20RE, see Figure 10.47a, and the present mono-model *LW4*, see Figure 10.47b. It has noticeable that the electric potential calculated by the commercial 3D Abaqus C3D20RE finite element does not tend to zero at the top and bottom positions of the inserted patch zone, differently the present *LW4* model well describe the electric potential behaviour without imposing any boundary conditions at the top and bottom positions.

Furthermore some results in terms of mechanical stresses are given for the in-plane stress σ_{xx} in Figure 10.48a, transverse normal stress σ_{zz} in Figure 10.48b, and transverse shear stress σ_{xz} in Figures 10.49a, 10.49b, 10.50a, 10.50b. Some more comments can be made:

- The through-the-thickness distribution of the in-plane stress σ_{xx} , as shown in Figure 10.48a, is correctly predicted by higher-order single-models *LW3* and *LW4*. The same accuracy is reached by all the considered multi-models, where the evaluation point is described by the *LW4* theory. It has to be noticed that the *Case B* show a little loss in accuracy due to the short distance of the evaluation point from the transition elements.
- The transverse normal stress σ_{zz} , as shown in Figure 10.48b, is well described by the *LW4* single-model. The same accuracy is reached by all the considered multi-models, where the evaluation point is described by the *LW4* theory. As mentioned for the in-plane stress σ_{xx} , the *Case B* show a little loss in accuracy due to the short distance of the evaluation point from the transition elements.
- The three-dimensional view of the transverse shear stress σ_{xz} , on undeformed structure, is given by the finite element 3D Abaqus C3D20RE in Figure 10.49a, by the present

mono-model *LW4* in Figure 10.49b, and by multi-model *Case C* in Figure 10.50a, in which it is possible to notice the differences, at the clamped boundaries and at the transition elements close to the patch zone, respect to the *LW4* solution. Therefore, the through-the-thickness distribution of the transverse shear stress σ_{xz} is given in Figure 10.50b. All the single-model considered are not able to fulfill the interlaminar continuity condition of the shear stress. Regarding the multi-models, they show an accuracy very close to the *LW4* solution, and as mentioned for the in-plane stress σ_{xx} , the *Case B* show a little loss in accuracy due to the short distance of the evaluation point from the transition elements.

By the evaluation of the various node-variable kinematic models, it is clear that an accurate representation of the stresses in localized zones is possible with DOFs reduction if an accurate distribution of the higher-order kinematic capabilities is performed. Differently, the primary variables, mechanical displacements and electric potential, are dependent on the global approximation over the whole structure. The DOFs reduction can be moderate or stronger, depending on the structure and the load case configuration.

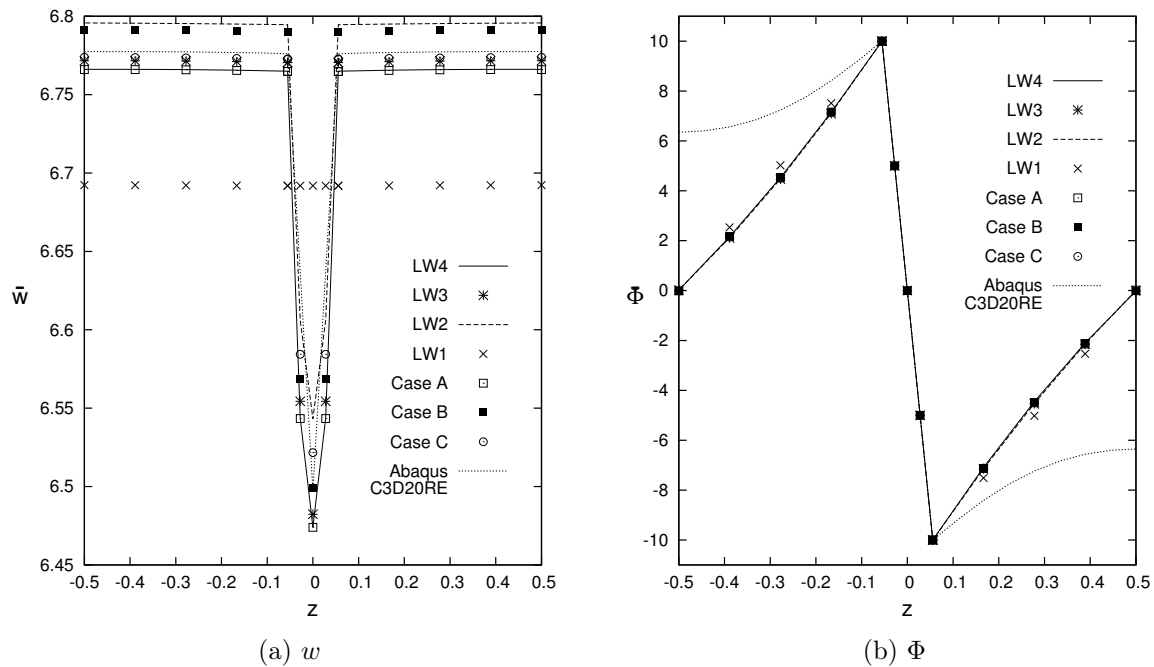
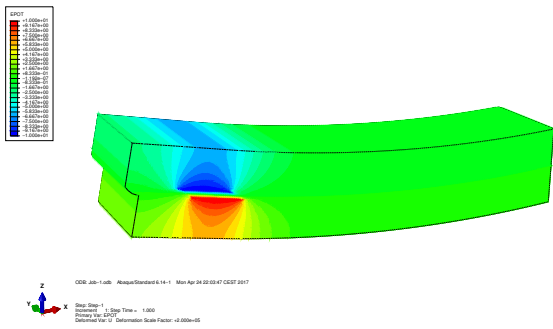
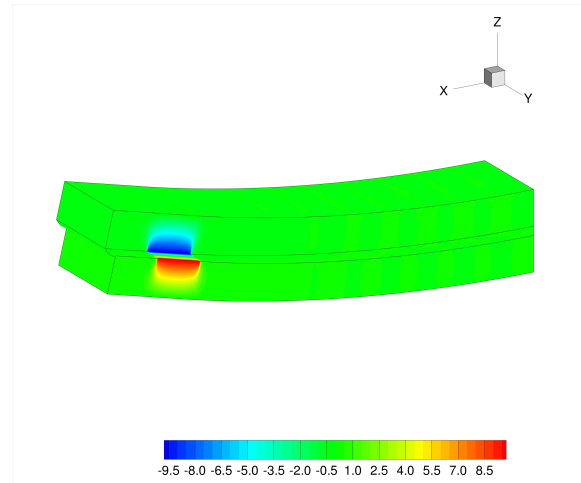


Figure 10.46: Sandwich cantilever plate, transverse displacement $w(x, y) = 10^8 \times w(a, b/2)$, and electric potential $\Phi(x, y) = \Phi(d, b/2)$. Single and Multi-theory models.

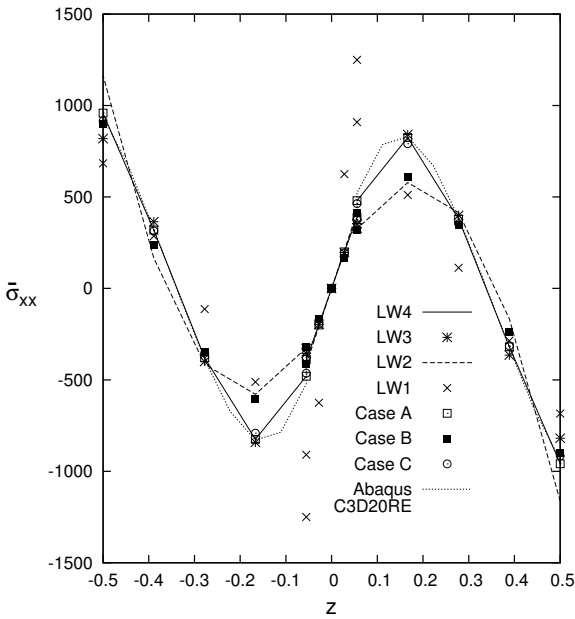


(a) 3D Abaqus C3D20RE

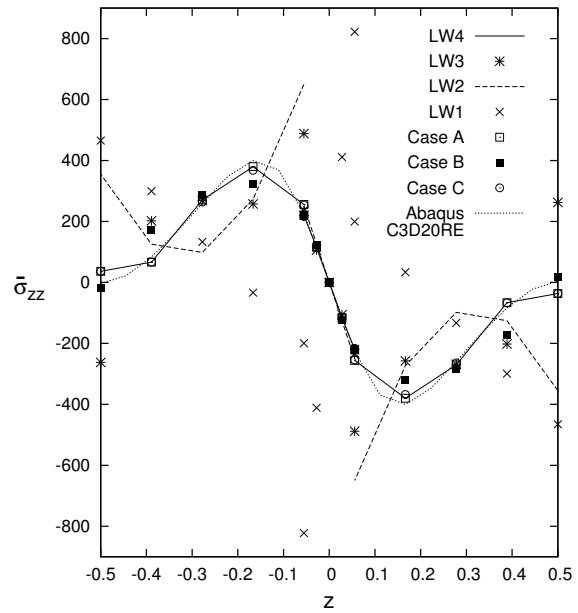


(b) LW4

Figure 10.47: Sandwich cantilever plate, three-dimensional view of the electric potential Φ , on deformed structure. 3D Abaqus C3D20RE and mono-model $LW4$.



(a) σ_{xx}



(b) σ_{zz}

Figure 10.48: Sandwich cantilever plate, in-plane stress $\sigma_{xx}(x, y) = \sigma_{xx}(d, b/2)$, and transverse normal stress $\sigma_{zz}(x, y) = \sigma_{zz}(d, b/2)$. Single and Multi-theory models.

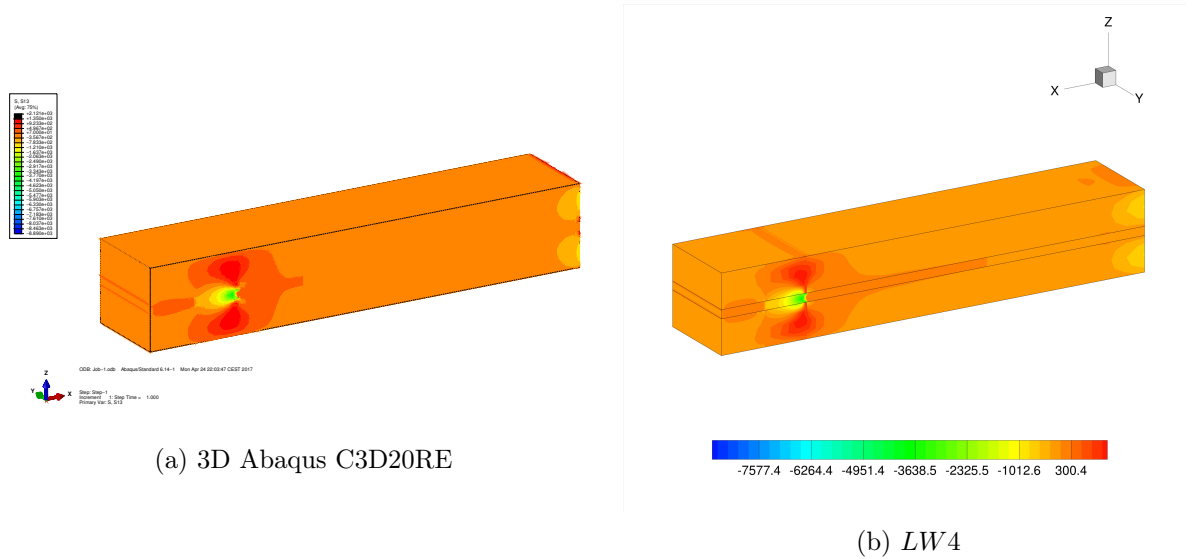


Figure 10.49: Sandwich cantilever plate, three-dimensional view of the transverse shear stress σ_{xz} , on undeformed structure. 3D Abaqus C3D20RE and mono-model LW4.

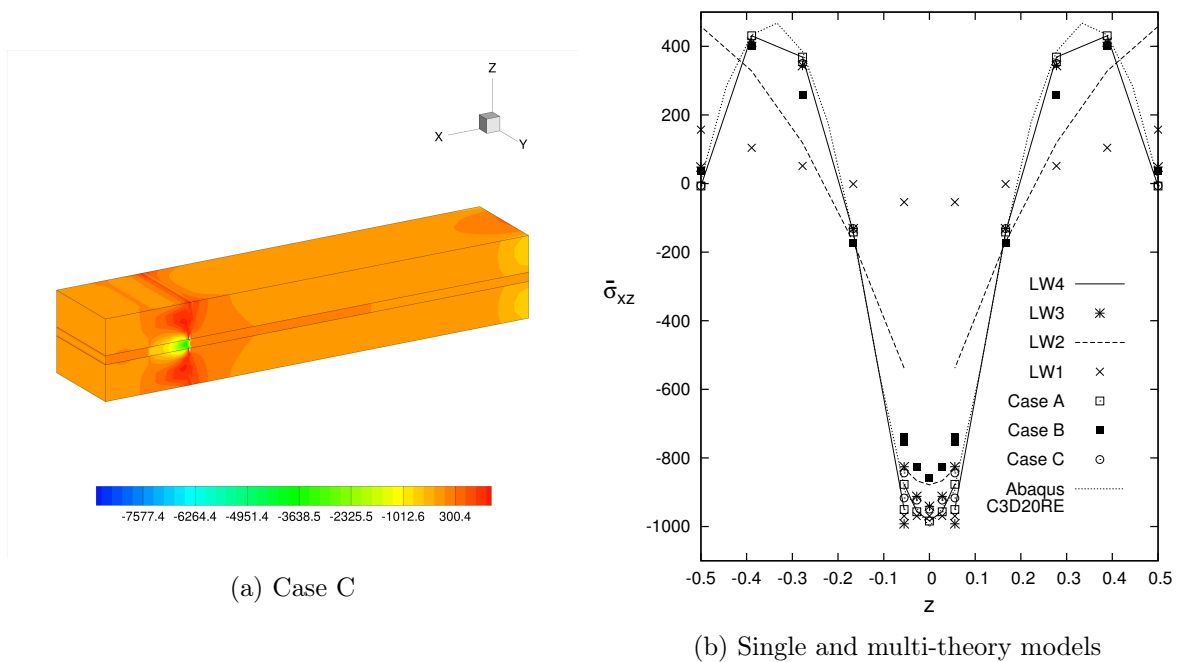


Figure 10.50: Sandwich cantilever plate, transverse shear stress σ_{xz} . Three-dimensional view on undeformed structure by multi-model *Case C*, and behaviour along the thickness $\sigma_{xz}(x, y) = \sigma_{xz}(d, b/2)$ for single and multi-theory models.

10.4.3 Sandwich cantilever plate under mechanical loading

A cantilever sandwich plate is analysed as shown in Figure 10.51. The geometrical dimensions are: $a = b = 20 \text{ mm}$, $h_{total} = 6 \text{ mm}$. The upper and lower layers are made of Aluminum. The central layer is made of Foam, and a PZT-5H piezoelectric patches is introduced in the foam layer with dimension: $a_p = 10 \text{ mm}$, $b_p = 20 \text{ mm}$, $h_p = 2 \text{ mm}$, it is centered at $x = 10 \text{ mm}$. The material properties are the same of the previous numerical example. The three layers have the same thickness $h = 2 \text{ mm}$. The structure is loaded at the free tip $(x, y, z) = (a, b/2, +h/2)$ with a concentrated transverse mechanical load equal to $P_z = -100 \text{ N}$. The piezoelectric patch

is set in open-circuit configuration. The plate is cantilevered and the following boundary condition are applied:

$$\begin{matrix} \text{Boundary} \\ u_s(0, y) = 0 \quad v_s(0, y) = 0 \quad w_s(0, y) = 0 \end{matrix} \quad (10.11)$$

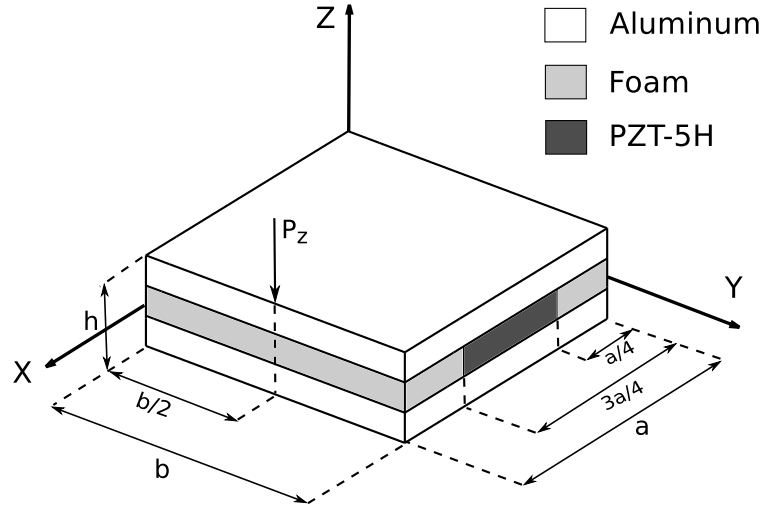


Figure 10.51: Reference system of the sandwich plate with piezoelectric patch under the concentrated mechanical load.

The structure analyzed in this numerical section is taken from the work of Sun and Zhang [186]. The present single- and multi-model solutions are compared with a calculated three-dimensional FEM ABAQUS solution. A non-uniform mesh grid of 60×16 elements ensures the convergence of the solution with a *LW4* single-model, see Figure 10.52. For the sake of brevity the study of the convergence is here omitted. The adopted refined mesh is necessary to study the behaviour of the mechanical and electrical variables along the whole plate domain, and not in one single point. The difficult task is to obtain a good behaviour of the mechanical stresses, electric potential and electric displacements, along the in-plane directions close to the interfaces of the piezoelectric patch, avoiding strange oscillations due to the changing of the element size.

Table 10.13: Single-theory and multi-theory models of the sandwich cantilever plate under concentrated mechanical load. Transverse displacement $w = 10^5 \times w(a, b/2, +h/2)$, electric potential $\Phi = \Phi(3a/4, b/2, +h/6)$, in-plane principal stress $\sigma_{xx} = 10^{-7} \times \sigma_{xx}(a/2, b/2, +h/2)$, transverse shear stress $\sigma_{xz} = 10^{-5} \times \sigma_{xz}(a/2, b/2, +h/6)$, transverse normal stress $\sigma_{zz} = 10^{-5} \times \sigma_{zz}(a/2, b/2, 0)$, transverse electric displacement $\mathcal{D}_z = 10^6 \times \mathcal{D}_z(a/2, b/2, +h/6)$.

	w	σ_{xx}	σ_{xz}	σ_{zz}	Φ	\mathcal{D}_z	$DOFs$
3D Abaqus C3D20RE	-4.8842	1.0599	-5.7298	8.2433	-532.51	-0.0148	338660
<i>LW4</i>	-5.7762	1.0569	-5.7337 ⁺ -5.6823 ⁻	8.2616	-463.46	1.1278 ⁺ 1.0417 ⁻	207636
<i>LW3</i>	-5.0390	1.0529	-5.7392 ⁺ -5.4894 ⁻	8.2657	-477.39	1.1890 ⁺ 0.7684 ⁻	159720
<i>LW2</i>	-4.1148	1.0422	-5.4192 ⁺ -6.0215 ⁻	6.8405	-490.26	1.3531 ⁺ -11.580 ⁻	111804
<i>LW1</i>	-3.1085	1.2066	-2.1940 ⁺ -12.596 ⁻	6.7876	-455.66	1.0372 ⁺ 63.269 ⁻	63888
<i>Case A</i>	-5.7408	1.0558	-5.7982 ⁺ -5.7475 ⁻	8.2646	-462.57	1.1079 ⁺ 1.0072 ⁻	188628
<i>Case B</i>	-3.2147	1.0653	-5.6762 ⁺ -5.6241 ⁻	8.5057	-518.01	1.1309 ⁺ 1.0498 ⁻	141108
<i>Case C</i>	-3.2648	1.0576	-5.6240 ⁺ -5.8244 ⁻	8.2302	-464.57	1.0684 ⁺ 0.9687 ⁻	160116

Some results are given in terms of transverse displacement w , transverse shear stress σ_{xz} , electric potential Φ and electric transverse displacement \mathcal{D}_z along the plate thickness. For the transverse displacement w the differences between single and multi-models are negligible in the lower part of the multilayer, see Figure 10.53a. On the contrary, in the upper part of the multilayer close to the applied concentrated load, remarkable differences are present between *LW4* and *Case A* respect to the other single and multi-model solutions.

The transverse shear stress σ_{xz} is represented in Figure 10.53b. The stress is evaluated in the center patch $(x, y) = (a/2, b/2)$. The mono-model *LW4* is able to predict the correct behaviour satisfying the interlaminar continuity condition, and its accuracy is almost the same of the Abaqus C3D20RE finite element solution. The lower single-models *LW2* and *LW1* are not able to represent correctly the stress behaviour. The higher-order multi-models show a good accuracy solution due to the higher-order representation in the evaluation zone of the shear stress.

Regarding the electric potential Φ , represented in Figure 10.54a, it is evaluated along the side-edge of the patch closer to the applied concentrated load $\bar{\Phi}(x; y) = \Phi(3a/4; b/2)$. Higher-order single-models are needed to well describe to non-linear behaviour of the electric potential and to capture its maximum value located at the interfaces corner $(3a/4; b/2; +h/6)$. The top and bottom position values tend naturally to zero without imposing any boundary conditions. The multi-model solutions have almost the same accuracy of the *LW4* solution, except for the *Case B* multi-model which shows an increase of the maximum value at the interfaces corner, this is due to the influence of the transition zone with the *LW1* zone elements, as shown in Figure 10.52. It has to be noticeable that the present solutions are compared with the Abaqus C3D20RE finite element solution which shows a comparable electric potential description in the center part of the thickness multilayer, on the contrary the top and bottom values does not naturally tend to zero.

Regarding the electric transverse displacement \mathcal{D}_z , represented in Figure 10.54b, it is evaluated in the center patch. The same considerations of the shear stress can be made here. The mono-model *LW4* is able to predict the correct behaviour, its accuracy is almost the same of the Abaqus C3D20RE finite element solution. The lower single-models *LW2* and *LW1* are not able to represent correctly the electric displacement behaviour. The higher-order multi-

models show a good accuracy solution due to the higher-order representation in the evaluation zone.

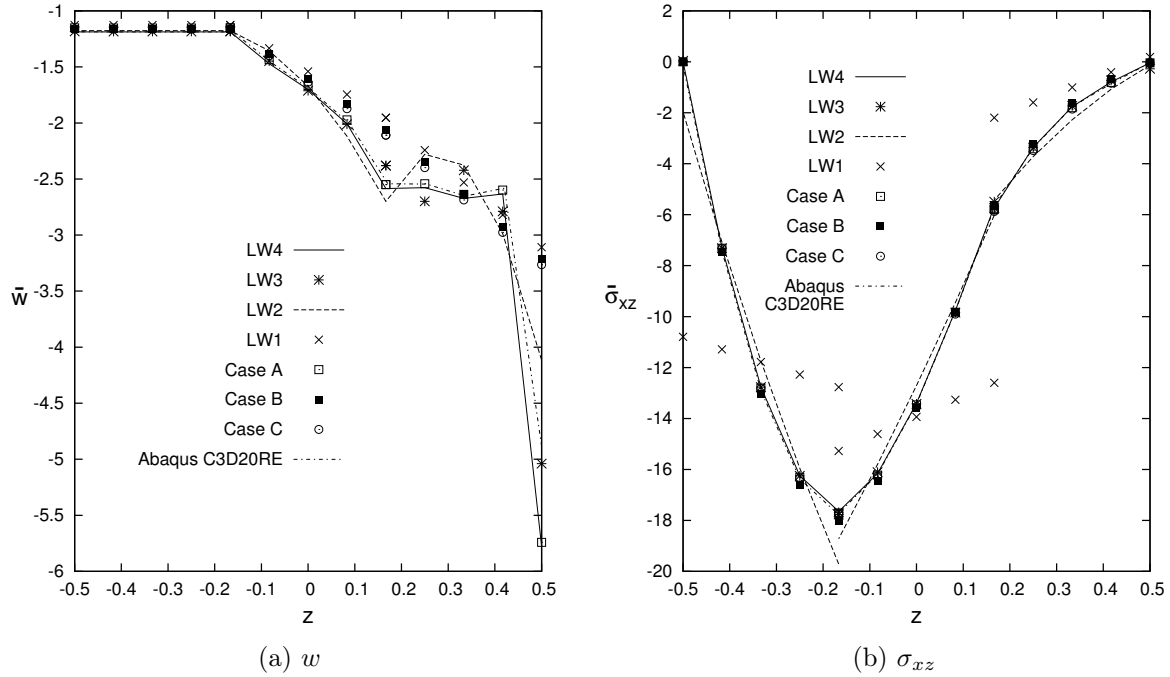


Figure 10.53: Sandwich cantilever plate under concentrated mechanical load. Transverse displacement $\bar{w}(x; y) = 10^5 \times w(a; b/2)$, and transverse shear stress $\bar{\sigma}_{xz}(x; y) = 10^{-5} \times \sigma_{xz}(a/2; b/2)$ along the plate thickness. Single and Multi-theory models.

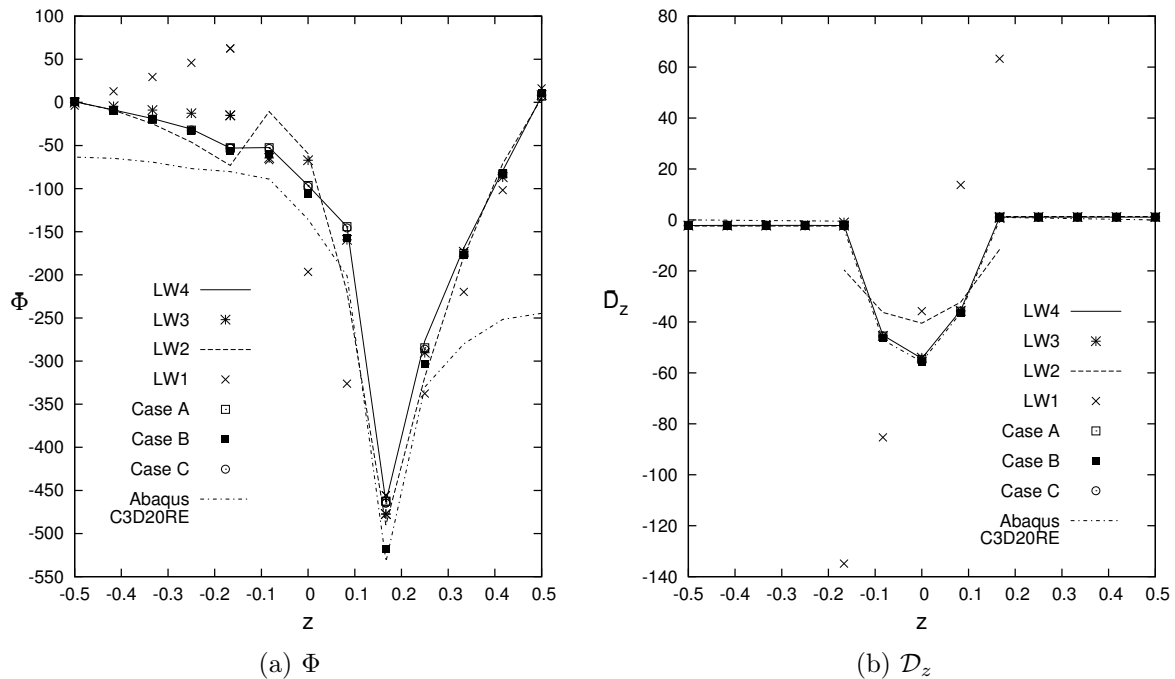


Figure 10.54: Sandwich cantilever plate under concentrated mechanical load. Electric potential $\bar{\Phi}(x; y) = \Phi(3a/4; b/2)$, and transverse electric displacement $\bar{D}_z(x; y) = 10^6 \times D_z(a/2; b/2)$ along the plate thickness. Single and Multi-theory models.

Results in terms of transverse shear and normal stresses $\bar{\sigma}_{xz}(y; z) = (10^{-5}) \times \sigma_{xz}$, $\bar{\sigma}_{zz}(y; z) = (10^{-5}) \times \sigma_{zz}$, electric potential $\bar{\Phi}(y; z) = \Phi$, and transverse electric displacement $\bar{D}_z =$

$(10^5) \times \mathcal{D}_z$, along the in-plane x axis at the interface between the upper skin and the sandwich core, are represented in Figures 10.55a, 10.55b, 10.56a, 10.56b respectively. For both the transverse stress variables, see Figures 10.55a and 10.55b, the *LW4* single-model and higher-order multi-models show the same behaviour and accuracy. Higher peak values are noticeable at the side-edges of the piezoelectric patch $x = 5; 15 \text{ mm}$. The multi-model *Case B* show an increase of the maximum peak value at $x = 15 \text{ mm}$, this is due to the transition zone between *LW4* and *LW1* models, as shown in Figure 10.52. The linear single-model *LW1* completely underestimate the stresses description.

The electric potential is well depicted by all the single and multi-models, as shown in Figure 10.56a. As mentioned before, the multi-model *Case B* show an increase of the maximum peak value at $x = 15 \text{ mm}$, this is due to the transition zone between *LW4* and *LW1* models. Regarding the transverse electric displacement \mathcal{D}_z , the single *LW4* and all the multi-models, as shown in Figure 10.56b, show a well description along the in-plane direction with some small oscillations in the zones close to the side-edge of the patch at $x = 5; 15 \text{ mm}$. It has to be noticed that the linear single-model *LW1* is completely not able to correct describe the transverse electric displacement, at $x = 5 \text{ mm}$ the peak values show an inverse, positive, sign respect to the other single and multi-models, and at $x = 15 \text{ mm}$ the maximum peak value is almost double respect to the other models.

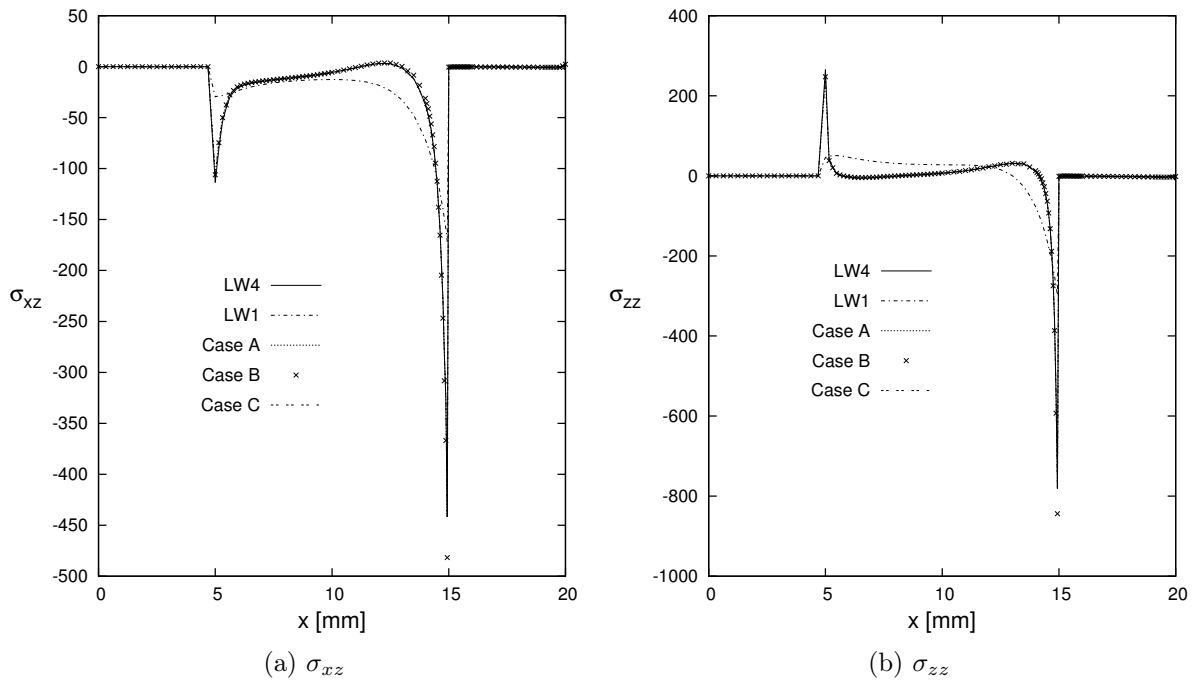


Figure 10.55: Sandwich cantilever plate under concentrated mechanical load. Transverse shear stress $\bar{\sigma}_{xz}(y; z) = 10^{-5} \times \sigma_{xz}(b/2; +h/6)$, and transverse normal stress $\bar{\sigma}_{zz}(y; z) = 10^{-5} \times \sigma_{zz}(b/2; +h/6)$ along the in-plane x -axis. Single and Multi-theory models.

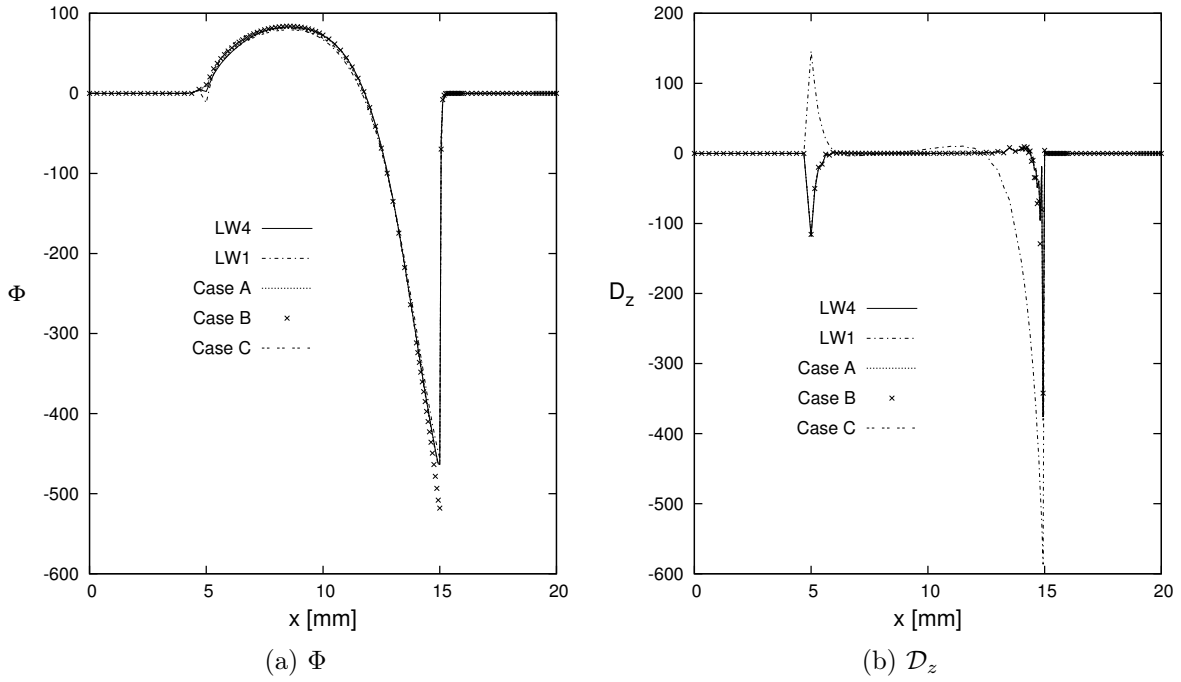
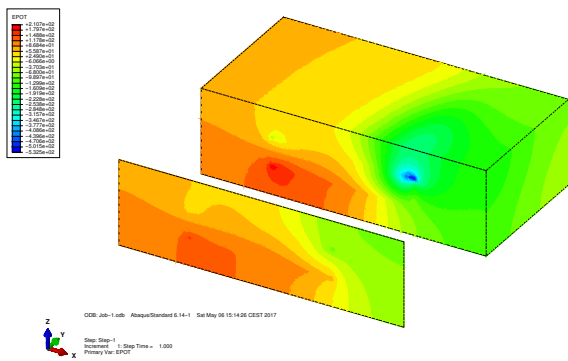


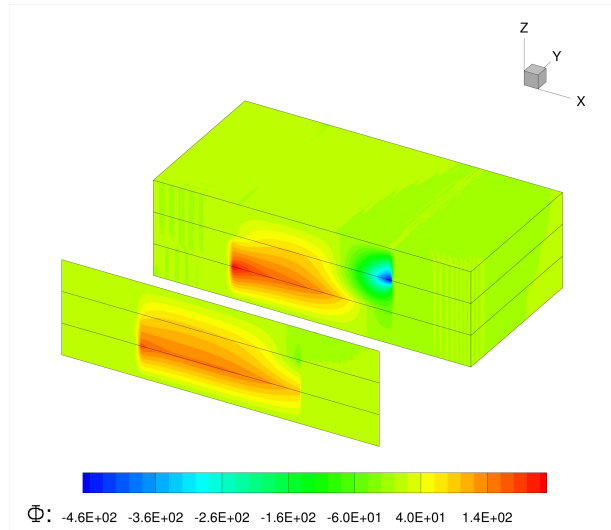
Figure 10.56: Sandwich cantilever plate under concentrated mechanical load. Electric potential $\bar{\Phi}(y; z) = \Phi(b/2; +h/6)$, and transverse electric displacement $\bar{D}_z = 10^5 \times D_z(b/2; +h/6)$ along the in-plane x-axis. Single and Multi-theory models.

Finally in Figures 10.57a and 10.57b the three-dimensional distributions of the electric potential Φ , obtained with the Abaqus 3D finite element C3D20RE and the present *LW4* single-model, respectively are depicted on the entire plate structure, represented with an initial section at $y = 0$ and the middle section at $y = b/2$. It has to be noticed that the present *LW4* single model well describes the phenomena without imposing any boundary condition, the electric potential tend naturally to zero.

The electric in-plane and transverse displacements D_x and D_z are depicted in Figures 10.58a, 10.58b, , 10.59a and , 10.59b, respectively. The present *LW4* single model and the Abaqus 3D finite element C3D20RE are in good agreement on the whole plate structure.

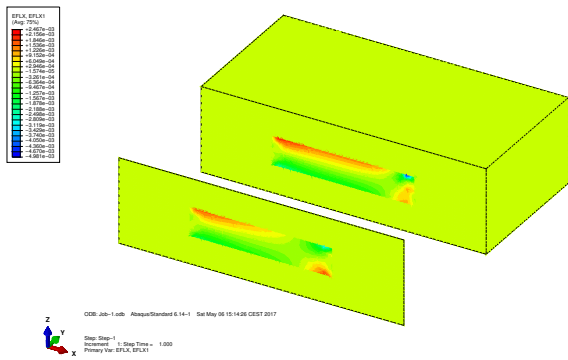


(a) 3D Abaqus C3D20RE

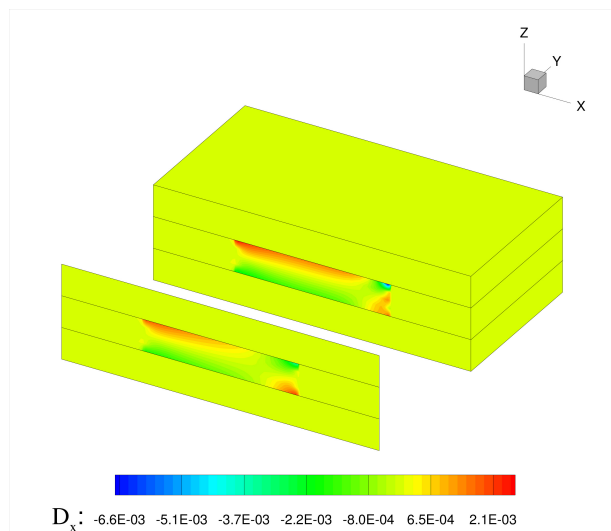


(b) *LW4*

Figure 10.57: Sandwich cantilever plate under concentrated mechanical load. Three-dimensional view of the electric potential Φ , on undeformed structure. 3D Abaqus C3D20RE and mono-model *LW4*.

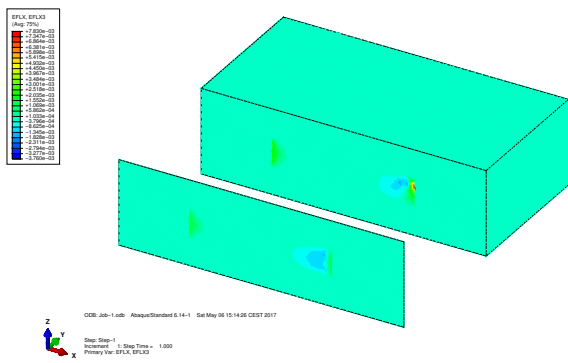


(a) 3D Abaqus C3D20RE

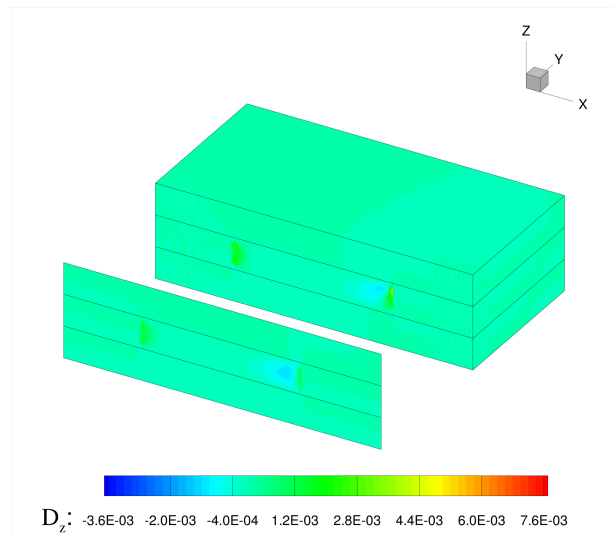


(b) *LW4*

Figure 10.58: Sandwich cantilever plate under concentrated mechanical load. Three-dimensional view of the in-plane electric displacement \mathcal{D}_x , on undeformed structure. 3D Abaqus C3D20RE and mono-model *LW4*.



(a) 3D Abaqus C3D20RE



(b) *LW4*

Figure 10.59: Sandwich cantilever plate under concentrated mechanical load. Three-dimensional view of the transverse electric displacement \mathcal{D}_z , on undeformed structure. 3D Abaqus C3D20RE and mono-model *LW4*.

Conclusions

The benchmarks and assessments proposed in the thesis make it possible to validate the refined and advanced two-dimensional models based on Unified Formulation for multilayered structures and multifield problems. Classical theories, originally developed for conventional structures, result inappropriate for such cases. The conducted analysis makes it possible to investigate the main problems connected to these cases and to recognize the importance of refined/advanced 2D models. The accuracy and the robustness of the present finite element are tested in the first part of the thesis. In the second part, the efficiency of the finite element combined with two different strategies is investigated. The following major, but general conclusions can be drawn from the investigation carried out in this thesis:

- The MITC shell element presents good properties of convergence and robustness; the shell element is completely locking free, even when the shell is very thin.
- The results converge to the exact solution by increasing the number of the elements and the order of expansion of the primary variables (mechanical displacements, electric potential, temperature) in the thickness direction, regardless of the employed function type.
- The combination of the linear contribution with the trigonometric and exponential series is very important for the description of the displacement and stresses field. The linear contribution leads to the reduction of the trigonometric and exponential terms required to reach the reference solution.
- For thermal stress problems applied to composite structure, it is important to accurately model the thermal load. If for very thin structure an assumed linear temperature profile can be sufficiently accurate, differently for moderately-thick and thick structure a calculated thermal profile (solving the Fourier heat conduction equation) is mandatory to avoid erroneous description of the applied thermal load.
- Regarding the coupled electro-mechanical analysis, the use of higher-order Layer-Wise models is necessary to well describe the electric potential and the complicated transverse stress behaviour due to the electric effect.
- Unified Formulation is the ideal tool for the implementation of variable kinematic theories (Mixed ESL/LW, Node-Dependent Variable Kinematic). In fact, the theory approximation order and the modelling technique (ESL, LW) are free parameters of the FEM arrays, which are written in a compact and very general form.
- The present variable kinematic theories (Mixed ESL/LW, Node-Dependent Variable Kinematic) allows to locally improve the solution. Two main aspects can be highlighted: a reduction of computational costs with respect to Layer-Wise single-model solutions, and a simultaneous multi-models global-local analysis can be performed in one-single analysis step.

- The Mixed ESL/LW method has shown all its potentiality in the analysis of sandwich structures, and in the multifield problems. In particular strong reduction of computational costs can be obtained in the electro-mechanical analysis of composite structures embedding piezoelectric layers.
- The Node-Dependent Variable Kinematic method permits to enrich locally the theory approximation accuracy by enforcing the same kinematics at the interface nodes between kinematically incompatible plate/shell elements. The resulting global/local approach is very efficient because it does not employ any mathematical artifice to enforce the displacement and stress continuity, such as those methods based on Lagrange multipliers or overlapping regions.
- An accurate representation of secondary variables (mechanical stresses and electric displacements) in localized zones is possible with DOFs reduction if an accurate distribution of the higher-order kinematic capabilities is performed. On the contrary, the accuracy of the solution in terms of primary variables (mechanical displacements and electric potential) values depends on the global approximation over the whole structure. The efficacy of the node-dependent variable kinematic and global/local models, thus, depends on the characteristics of the problem under consideration as well as on the required analysis type.

Appendix A

Fundamental Nuclei with the MITC method

A.1 PVD for mechanical problems

The explicit expression of the stiffness matrix nuclei are given below with the reinterpolation of the strain components via the MITC method Eq. 5.5. The stiffness matrix $\mathbf{K}_{uu}^{k\tau sij}$ nucleus is defined as follows:

$$\mathbf{K}_{uu}^{k\tau sij} = \begin{bmatrix} K_{uu\alpha\alpha} & K_{uu\alpha\beta} & K_{uu\alpha z} \\ K_{uu\beta\alpha} & K_{uu\beta\beta} & K_{uu\beta z} \\ K_{uu z\alpha} & K_{uu z\beta} & K_{uu zz} \end{bmatrix}^{k\tau sij}$$

In the following equations the new set of Lagrangian shape function of the MITC method are indicated, for example, as \bar{N}_{m1} , where $m1$ indicates the set of new interpolation points, for more details refers to Section 5.2. Therefore, the old node element shape function are evaluated in the new set of interpolation points, for example N_i^{m1} are the old Lagrangian shape element function evaluated in new set $m1$.

$$\begin{aligned} K_{uu\alpha\alpha}^{k\tau sij} = & \tilde{C}_{55}^k N_i^{m1} N_j^{n1} \int_{\Omega^k} \bar{N}_{m1} \bar{N}_{n1} d\alpha^k d\beta^k \int_{A^k} F_{\tau,z} F_{s,z} H_\alpha^k H_\beta^k dz^k - \frac{\tilde{C}_{55}^k}{R_\alpha^k} N_i^{m1} N_j^{n1} \int_{\Omega^k} \bar{N}_{m1} \bar{N}_{n1} d\alpha^k d\beta^k \int_{A^k} F_{\tau,z} F_s H_\beta^k dz^k - \\ & - \frac{\tilde{C}_{55}^k}{R_\alpha^k} N_i^{m1} N_j^{n1} \int_{\Omega^k} \bar{N}_{m1} \bar{N}_{n1} d\alpha^k d\beta^k \int_{A^k} F_\tau F_{s,z} H_\beta^k dz^k + \tilde{C}_{66}^k N_{i,\beta}^{m3} N_{j,\beta}^{n3} \int_{\Omega^k} \bar{N}_{m3} \bar{N}_{n3} d\alpha^k d\beta^k \int_{A^k} F_\tau F_s \frac{H_\alpha^k}{H_\beta^k} dz^k + \\ & + \tilde{C}_{16}^k N_{i,\alpha}^{m1} N_{j,\beta}^{n3} \int_{\Omega^k} \bar{N}_{m1} \bar{N}_{n3} d\alpha^k d\beta^k \int_{A^k} F_\tau F_s dz^k + \tilde{C}_{16}^k N_{i,\beta}^{m3} N_{j,\alpha}^{n1} \int_{\Omega^k} \bar{N}_{m3} \bar{N}_{n1} d\alpha^k d\beta^k \int_{A^k} F_\tau F_s dz^k + \\ & + \tilde{C}_{11}^k N_{i,\alpha}^{m1} N_{j,\beta}^{n1} \int_{\Omega^k} \bar{N}_{m1} \bar{N}_{n1} d\alpha^k d\beta^k \int_{A^k} F_\tau F_s \frac{H_\beta^k}{H_\alpha^k} dz^k + \frac{\tilde{C}_{55}^k}{(R_\alpha^k)^2} N_i^{m1} N_j^{n1} \int_{\Omega^k} \bar{N}_{m1} \bar{N}_{n1} d\alpha^k d\beta^k \int_{A^k} F_\tau F_s \frac{H_\beta^k}{H_\alpha^k} dz^k \end{aligned}$$

$$\begin{aligned} K_{uu\alpha\beta}^{k\tau sij} = & \tilde{C}_{45}^k N_i^{m1} N_j^{n2} \int_{\Omega^k} \bar{N}_{m1} \bar{N}_{n2} d\alpha^k d\beta^k \int_{A^k} F_{\tau,z} F_{s,z} H_\alpha^k H_\beta^k dz^k - \frac{\tilde{C}_{45}^k}{R_\beta^k} N_i^{m1} N_j^{n2} \int_{\Omega^k} \bar{N}_{m1} \bar{N}_{n2} d\alpha^k d\beta^k \int_{A^k} F_{\tau,z} F_s H_\alpha^k dz^k - \\ & - \frac{\tilde{C}_{45}^k}{R_\alpha^k} N_i^{m1} N_j^{n2} \int_{\Omega^k} \bar{N}_{m1} \bar{N}_{n2} d\alpha^k d\beta^k \int_{A^k} F_\tau F_{s,z} H_\beta^k dz^k + \tilde{C}_{26}^k N_{i,\beta}^{m3} N_{j,\beta}^{n2} \int_{\Omega^k} \bar{N}_{m3} \bar{N}_{n2} d\alpha^k d\beta^k \int_{A^k} F_\tau F_s \frac{H_\alpha^k}{H_\beta^k} dz^k + \\ & + \tilde{C}_{12}^k N_{i,\alpha}^{m1} N_{j,\beta}^{n2} \int_{\Omega^k} \bar{N}_{m1} \bar{N}_{n2} d\alpha^k d\beta^k \int_{A^k} F_\tau F_s dz^k + \tilde{C}_{66}^k N_{i,\beta}^{m3} N_{j,\alpha}^{n3} \int_{\Omega^k} \bar{N}_{m3} \bar{N}_{n3} d\alpha^k d\beta^k \int_{A^k} F_\tau F_s dz^k + \\ & + \tilde{C}_{16}^k N_{i,\alpha}^{m1} N_{j,\beta}^{n3} \int_{\Omega^k} \bar{N}_{m1} \bar{N}_{n3} d\alpha^k d\beta^k \int_{A^k} F_\tau F_s \frac{H_\beta^k}{H_\alpha^k} dz^k + \frac{\tilde{C}_{45}^k}{R_\alpha^k R_\beta^k} N_i^{m1} N_j^{n2} \int_{\Omega^k} \bar{N}_{m1} \bar{N}_{n2} d\alpha^k d\beta^k \int_{A^k} F_\tau F_s dz^k \end{aligned}$$

$$\begin{aligned}
 K_{uu\alpha z}^{k\tau sij} &= \tilde{C}_{45}^k N_i^{m1} N_{j,\beta}^{n2} \int_{\Omega^k} \bar{N}_{m1} \bar{N}_{n2} d\alpha^k d\beta^k \int_{A^k} F_{\tau,z} F_s H_\alpha^k dz^k + \tilde{C}_{55}^k N_i^{m1} N_{j,\alpha}^{n1} \int_{\Omega^k} \bar{N}_{m1} \bar{N}_{n1} d\alpha^k d\beta^k \int_{A^k} F_{\tau,z} F_s H_\beta^k dz^k + \\
 &+ \tilde{C}_{36}^k N_{i,\beta}^{m3} \int_{\Omega^k} \bar{N}_{m3} N_j d\alpha^k d\beta^k \int_{A^k} F_\tau F_{s,z} H_\alpha^k dz^k + \tilde{C}_{13}^k N_{i,\alpha}^{m1} \int_{\Omega^k} \bar{N}_{m1} N_j d\alpha^k d\beta^k \int_{A^k} F_\tau F_{s,z} H_\beta^k dz^k - \\
 &- \frac{\tilde{C}_{45}^k}{R_\alpha^k} N_i^{m1} N_{j,\beta}^{n2} \int_{\Omega^k} \bar{N}_{m1} \bar{N}_{n2} d\alpha^k d\beta^k \int_{A^k} F_\tau F_s dz^k - \frac{\tilde{C}_{55}^k}{R_\alpha^k} N_i^{m1} N_{j,\alpha}^{n1} \int_{\Omega^k} \bar{N}_{m1} \bar{N}_{n1} d\alpha^k d\beta^k \int_{A^k} F_\tau F_s \frac{H_\beta^k}{H_\alpha^k} dz^k + \\
 &+ \frac{\tilde{C}_{26}^k}{R_\beta^k} N_{i,\beta}^{m3} N_j^{n2} \int_{\Omega^k} \bar{N}_{m3} \bar{N}_{n2} d\alpha^k d\beta^k \int_{A^k} F_\tau F_s \frac{H_\alpha^k}{H_\beta^k} dz^k + \frac{\tilde{C}_{16}^k}{R_\alpha^k} N_{i,\beta}^{m3} N_j^{n1} \int_{\Omega^k} \bar{N}_{m3} \bar{N}_{n1} d\alpha^k d\beta^k \int_{A^k} F_\tau F_s dz^k + \\
 &+ \frac{\tilde{C}_{12}^k}{R_\beta^k} N_{i,\alpha}^{m1} N_j^{n2} \int_{\Omega^k} \bar{N}_{m1} \bar{N}_{n2} d\alpha^k d\beta^k \int_{A^k} F_\tau F_s dz^k + \frac{\tilde{C}_{11}^k}{R_\alpha^k} N_{i,\alpha}^{m1} N_j^{n1} \int_{\Omega^k} \bar{N}_{m1} \bar{N}_{n1} d\alpha^k d\beta^k \int_{A^k} F_\tau F_s \frac{H_\beta^k}{H_\alpha^k} dz^k \\
 \\
 K_{uu\beta\alpha}^{k\tau sij} &= \tilde{C}_{45}^k N_i^{m2} N_j^{n1} \int_{\Omega^k} \bar{N}_{m2} \bar{N}_{n1} d\alpha^k d\beta^k \int_{A^k} F_{\tau,z} F_{s,z} H_\alpha^k H_\beta^k dz^k - \frac{\tilde{C}_{45}^k}{R_\alpha^k} N_i^{m2} N_j^{n1} \int_{\Omega^k} \bar{N}_{m2} \bar{N}_{n1} d\alpha^k d\beta^k \int_{A^k} F_{\tau,z} F_s H_\beta^k dz^k - \\
 &- \frac{\tilde{C}_{45}^k}{R_\beta^k} N_i^{m2} N_j^{n1} \int_{\Omega^k} \bar{N}_{m2} \bar{N}_{n1} d\alpha^k d\beta^k \int_{A^k} F_\tau F_{s,z} H_\alpha^k dz^k + \tilde{C}_{26}^k N_{i,\beta}^{m2} N_{j,\beta}^{n3} \int_{\Omega^k} \bar{N}_{m2} \bar{N}_{n3} d\alpha^k d\beta^k \int_{A^k} F_\tau F_s \frac{H_\alpha^k}{H_\beta^k} dz^k + \\
 &+ \tilde{C}_{12}^k N_{i,\beta}^{m2} N_{j,\alpha}^{n1} \int_{\Omega^k} \bar{N}_{m2} \bar{N}_{n1} d\alpha^k d\beta^k \int_{A^k} F_\tau F_s dz^k + \tilde{C}_{66}^k N_{i,\alpha}^{m3} N_{j,\beta}^{n3} \int_{\Omega^k} \bar{N}_{m3} \bar{N}_{n3} d\alpha^k d\beta^k \int_{A^k} F_\tau F_s dz^k + \\
 &+ \tilde{C}_{16}^k N_{i,\alpha}^{m3} N_{j,\alpha}^{n1} \int_{\Omega^k} \bar{N}_{m3} \bar{N}_{n1} d\alpha^k d\beta^k \int_{A^k} F_\tau F_s \frac{H_\beta^k}{H_\alpha^k} dz^k + \frac{\tilde{C}_{45}^k}{R_\alpha^k R_\beta^k} N_i^{m2} N_j^{n1} \int_{\Omega^k} \bar{N}_{m2} \bar{N}_{n1} d\alpha^k d\beta^k \int_{A^k} F_\tau F_s dz^k \\
 \\
 K_{uu\beta\beta}^{k\tau sij} &= \tilde{C}_{44}^k N_i^{m2} N_j^{n2} \int_{\Omega^k} \bar{N}_{m2} \bar{N}_{n2} d\alpha^k d\beta^k \int_{A^k} F_{\tau,z} F_{s,z} H_\alpha^k H_\beta^k dz^k - \frac{\tilde{C}_{44}^k}{R_\beta^k} N_i^{m2} N_j^{n2} \int_{\Omega^k} \bar{N}_{m2} \bar{N}_{n2} d\alpha^k d\beta^k \int_{A^k} F_{\tau,z} F_s H_\alpha^k dz^k - \\
 &- \frac{\tilde{C}_{44}^k}{R_\beta^k} N_i^{m2} N_j^{n2} \int_{\Omega^k} \bar{N}_{m2} \bar{N}_{n2} d\alpha^k d\beta^k \int_{A^k} F_\tau F_{s,z} H_\alpha^k dz^k + \tilde{C}_{22}^k N_{i,\beta}^{m2} N_{j,\beta}^{n2} \int_{\Omega^k} \bar{N}_{m2} \bar{N}_{n2} d\alpha^k d\beta^k \int_{A^k} F_\tau F_s \frac{H_\alpha^k}{H_\beta^k} dz^k + \\
 &+ \tilde{C}_{26}^k N_{i,\alpha}^{m3} N_{j,\beta}^{n2} \int_{\Omega^k} \bar{N}_{m3} \bar{N}_{n2} d\alpha^k d\beta^k \int_{A^k} F_\tau F_s dz^k + \tilde{C}_{26}^k N_{i,\beta}^{m2} N_{j,\alpha}^{n3} \int_{\Omega^k} \bar{N}_{m2} \bar{N}_{n3} d\alpha^k d\beta^k \int_{A^k} F_\tau F_s dz^k + \\
 &+ \tilde{C}_{66}^k N_{i,\alpha}^{m3} N_{j,\alpha}^{n3} \int_{\Omega^k} \bar{N}_{m3} \bar{N}_{n3} d\alpha^k d\beta^k \int_{A^k} F_\tau F_s \frac{H_\beta^k}{H_\alpha^k} dz^k + \frac{\tilde{C}_{44}^k}{(R_\beta^k)^2} N_i^{m2} N_j^{n2} \int_{\Omega^k} \bar{N}_{m2} \bar{N}_{n2} d\alpha^k d\beta^k \int_{A^k} F_\tau F_s \frac{H_\alpha^k}{H_\beta^k} dz^k \\
 \\
 K_{uu\beta z}^{k\tau sij} &= \tilde{C}_{44}^k N_i^{m2} N_{j,\beta}^{n2} \int_{\Omega^k} \bar{N}_{m2} \bar{N}_{n2} d\alpha^k d\beta^k \int_{A^k} F_{\tau,z} F_s H_\alpha^k dz^k + \tilde{C}_{45}^k N_i^{m2} N_{j,\alpha}^{n1} \int_{\Omega^k} \bar{N}_{m2} \bar{N}_{n1} d\alpha^k d\beta^k \int_{A^k} F_{\tau,z} F_s H_\beta^k dz^k + \\
 &+ \tilde{C}_{23}^k N_{i,\beta}^{m2} \int_{\Omega^k} \bar{N}_{m2} N_j d\alpha^k d\beta^k \int_{A^k} F_\tau F_{s,z} H_\alpha^k dz^k + \tilde{C}_{36}^k N_{i,\alpha}^{m3} \int_{\Omega^k} \bar{N}_{m3} N_j d\alpha^k d\beta^k \int_{A^k} F_\tau F_{s,z} H_\beta^k dz^k - \\
 &- \frac{\tilde{C}_{44}^k}{R_\beta^k} N_i^{m2} N_{j,\beta}^{n2} \int_{\Omega^k} \bar{N}_{m2} \bar{N}_{n2} d\alpha^k d\beta^k \int_{A^k} F_\tau F_s \frac{H_\alpha^k}{H_\beta^k} dz^k - \frac{\tilde{C}_{45}^k}{R_\beta^k} N_i^{m2} N_{j,\alpha}^{n1} \int_{\Omega^k} \bar{N}_{m2} \bar{N}_{n1} d\alpha^k d\beta^k \int_{A^k} F_\tau F_s dz^k + \\
 &+ \frac{\tilde{C}_{22}^k}{R_\beta^k} N_{i,\beta}^{m2} N_j^{n2} \int_{\Omega^k} \bar{N}_{m2} \bar{N}_{n2} d\alpha^k d\beta^k \int_{A^k} F_\tau F_s \frac{H_\alpha^k}{H_\beta^k} dz^k + \frac{\tilde{C}_{12}^k}{R_\alpha^k} N_{i,\beta}^{m2} N_j^{n1} \int_{\Omega^k} \bar{N}_{m2} \bar{N}_{n1} d\alpha^k d\beta^k \int_{A^k} F_\tau F_s dz^k + \\
 &+ \frac{\tilde{C}_{26}^k}{R_\beta^k} N_{i,\alpha}^{m3} N_j^{n2} \int_{\Omega^k} \bar{N}_{m3} \bar{N}_{n2} d\alpha^k d\beta^k \int_{A^k} F_\tau F_s dz^k + \frac{\tilde{C}_{16}^k}{R_\alpha^k} N_{i,\alpha}^{m3} N_j^{n1} \int_{\Omega^k} \bar{N}_{m3} \bar{N}_{n1} d\alpha^k d\beta^k \int_{A^k} F_\tau F_s \frac{H_\beta^k}{H_\alpha^k} dz^k
 \end{aligned}$$

$$\begin{aligned}
 K_{uu_{z\alpha}}^{k\tau sij} &= \tilde{C}_{36}^k N_{j,\beta}^{n3} \int_{\Omega^k} N_i \bar{N}_{n3} d\alpha^k d\beta^k \int_{A^k} F_{\tau,z} F_s H_\alpha^k dz^k + \tilde{C}_{13}^k N_{j,\alpha}^{n1} \int_{\Omega^k} N_i \bar{N}_{n1} d\alpha^k d\beta^k \int_{A^k} F_{\tau,z} F_s H_\beta^k dz^k + \\
 &+ \tilde{C}_{45}^k N_{i,\beta}^{m2} N_j^{n1} \int_{\Omega^k} \bar{N}_{m2} \bar{N}_{n1} d\alpha^k d\beta^k \int_{A^k} F_\tau F_{s,z} H_\alpha^k dz^k + \tilde{C}_{55}^k N_{i,\alpha}^{m1} N_j^{n1} \int_{\Omega^k} \bar{N}_{m1} \bar{N}_{n1} d\alpha^k d\beta^k \int_{A^k} F_\tau F_{s,z} H_\beta^k dz^k + \\
 &+ \frac{\tilde{C}_{26}^k}{R_\beta^k} N_i^{m2} N_{j,\beta}^{n3} \int_{\Omega^k} \bar{N}_{m2} \bar{N}_{n3} d\alpha^k d\beta^k \int_{A^k} F_\tau F_s \frac{H_\alpha^k}{H_\beta^k} dz^k + \frac{\tilde{C}_{16}^k}{R_\alpha^k} N_i^{m1} N_{j,\beta}^{n3} \int_{\Omega^k} \bar{N}_{m1} \bar{N}_{n3} d\alpha^k d\beta^k \int_{A^k} F_\tau F_s dz^k + \\
 &+ \frac{\tilde{C}_{12}^k}{R_\beta^k} N_i^{m2} N_{j,\alpha}^{n1} \int_{\Omega^k} \bar{N}_{m2} \bar{N}_{n1} d\alpha^k d\beta^k \int_{A^k} F_\tau F_s dz^k + \frac{\tilde{C}_{11}^k}{R_\alpha^k} N_i^{m1} N_{j,\alpha}^{n1} \int_{\Omega^k} \bar{N}_{m1} \bar{N}_{n1} d\alpha^k d\beta^k \int_{A^k} F_\tau F_s \frac{H_\beta^k}{H_\alpha^k} dz^k - \\
 &- \frac{\tilde{C}_{45}^k}{R_\alpha^k} N_{i,\beta}^{m2} N_j^{n1} \int_{\Omega^k} \bar{N}_{m2} \bar{N}_{n1} d\alpha^k d\beta^k \int_{A^k} F_\tau F_s dz^k - \frac{\tilde{C}_{55}^k}{R_\alpha^k} N_{i,\alpha}^{m1} N_j^{n1} \int_{\Omega^k} \bar{N}_{m1} \bar{N}_{n1} d\alpha^k d\beta^k \int_{A^k} F_\tau F_s \frac{H_\beta^k}{H_\alpha^k} dz^k \\
 \\
 K_{uu_{z\beta}}^{k\tau sij} &= \tilde{C}_{23}^k N_{j,\beta}^{n2} \int_{\Omega^k} N_i \bar{N}_{n2} d\alpha^k d\beta^k \int_{A^k} F_{\tau,z} F_s H_\alpha^k dz^k + \tilde{C}_{36}^k N_{j,\alpha}^{n3} \int_{\Omega^k} N_i \bar{N}_{n3} d\alpha^k d\beta^k \int_{A^k} F_{\tau,z} F_s H_\beta^k dz^k + \\
 &+ \tilde{C}_{44}^k N_{i,\beta}^{m2} N_j^{n2} \int_{\Omega^k} \bar{N}_{m2} \bar{N}_{n2} d\alpha^k d\beta^k \int_{A^k} F_\tau F_{s,z} H_\alpha^k dz^k + \tilde{C}_{45}^k N_{i,\alpha}^{m1} N_j^{n2} \int_{\Omega^k} \bar{N}_{m1} \bar{N}_{n2} d\alpha^k d\beta^k \int_{A^k} F_\tau F_{s,z} H_\beta^k dz^k + \\
 &+ \frac{\tilde{C}_{22}^k}{R_\beta^k} N_i^{m2} N_{j,\beta}^{n2} \int_{\Omega^k} \bar{N}_{m2} \bar{N}_{n2} d\alpha^k d\beta^k \int_{A^k} F_\tau F_s \frac{H_\alpha^k}{H_\beta^k} dz^k + \frac{\tilde{C}_{12}^k}{R_\alpha^k} N_i^{m1} N_{j,\beta}^{n2} \int_{\Omega^k} \bar{N}_{m1} \bar{N}_{n2} d\alpha^k d\beta^k \int_{A^k} F_\tau F_s dz^k + \\
 &+ \frac{\tilde{C}_{26}^k}{R_\beta^k} N_i^{m2} N_{j,\alpha}^{n3} \int_{\Omega^k} \bar{N}_{m2} \bar{N}_{n3} d\alpha^k d\beta^k \int_{A^k} F_\tau F_s dz^k + \frac{\tilde{C}_{16}^k}{R_\alpha^k} N_i^{m1} N_{j,\alpha}^{n3} \int_{\Omega^k} \bar{N}_{m1} \bar{N}_{n3} d\alpha^k d\beta^k \int_{A^k} F_\tau F_s \frac{H_\beta^k}{H_\alpha^k} dz^k - \\
 &- \frac{\tilde{C}_{44}^k}{R_\beta^k} N_{i,\beta}^{m2} N_j^{n2} \int_{\Omega^k} \bar{N}_{m2} \bar{N}_{n2} d\alpha^k d\beta^k \int_{A^k} F_\tau F_s \frac{H_\alpha^k}{H_\beta^k} dz^k - \frac{\tilde{C}_{45}^k}{R_\beta^k} N_{i,\alpha}^{m1} N_j^{n2} \int_{\Omega^k} \bar{N}_{m1} \bar{N}_{n2} d\alpha^k d\beta^k \int_{A^k} F_\tau F_s dz^k \\
 \\
 K_{uu_{zz}}^{k\tau sij} &= \tilde{C}_{33}^k \int_{\Omega^k} N_i N_j d\alpha^k d\beta^k \int_{A^k} F_{\tau,z} F_{s,z} H_\alpha^k H_\beta^k dz^k + \frac{\tilde{C}_{23}^k}{R_\beta^k} N_j^{n2} \int_{\Omega^k} N_i \bar{N}_{n2} d\alpha^k d\beta^k \int_{A^k} F_{\tau,z} F_s H_\alpha^k dz^k + \\
 &+ \frac{\tilde{C}_{13}^k}{R_\alpha^k} N_j^{n1} \int_{\Omega^k} N_i \bar{N}_{n1} d\alpha^k d\beta^k \int_{A^k} F_{\tau,z} F_s H_\beta^k dz^k + \frac{\tilde{C}_{23}^k}{R_\beta^k} N_i^{m2} \int_{\Omega^k} \bar{N}_{m2} N_j d\alpha^k d\beta^k \int_{A^k} F_\tau F_{s,z} H_\alpha^k dz^k + \\
 &+ \frac{\tilde{C}_{13}^k}{R_\alpha^k} N_i^{m1} \int_{\Omega^k} \bar{N}_{m1} N_j d\alpha^k d\beta^k \int_{A^k} F_\tau F_{s,z} H_\beta^k dz^k + \tilde{C}_{44}^k N_{i,\beta}^{m2} N_{j,\beta}^{n2} \int_{\Omega^k} \bar{N}_{m2} \bar{N}_{n2} d\alpha^k d\beta^k \int_{A^k} F_\tau F_s \frac{H_\alpha^k}{H_\beta^k} dz^k + \\
 &+ \tilde{C}_{45}^k N_{i,\alpha}^{m1} N_{j,\beta}^{n2} \int_{\Omega^k} \bar{N}_{m1} \bar{N}_{n2} d\alpha^k d\beta^k \int_{A^k} F_\tau F_s dz^k + \tilde{C}_{45}^k N_{i,\beta}^{m2} N_{j,\alpha}^{n1} \int_{\Omega^k} \bar{N}_{m2} \bar{N}_{n1} d\alpha^k d\beta^k \int_{A^k} F_\tau F_s dz^k + \\
 &+ \tilde{C}_{55}^k N_{i,\alpha}^{m1} N_{j,\alpha}^{n1} \int_{\Omega^k} \bar{N}_{m1} \bar{N}_{n1} d\alpha^k d\beta^k \int_{A^k} F_\tau F_s \frac{H_\beta^k}{H_\alpha^k} dz^k + \frac{\tilde{C}_{12}^k}{R_\alpha^k R_\beta^k} N_i^{m1} N_j^{n2} \int_{\Omega^k} \bar{N}_{m1} \bar{N}_{n2} d\alpha^k d\beta^k \int_{A^k} F_\tau F_s dz^k + \\
 &+ \frac{\tilde{C}_{12}^k}{R_\alpha^k R_\beta^k} N_i^{m2} N_j^{n1} \int_{\Omega^k} \bar{N}_{m2} \bar{N}_{n1} d\alpha^k d\beta^k \int_{A^k} F_\tau F_s dz^k + \frac{\tilde{C}_{22}^k}{(R_\beta^k)^2} N_i^{m2} N_j^{n2} \int_{\Omega^k} \bar{N}_{m2} \bar{N}_{n2} d\alpha^k d\beta^k \int_{A^k} F_\tau F_s \frac{H_\alpha^k}{H_\beta^k} dz^k + \\
 &+ \frac{\tilde{C}_{11}^k}{(R_\alpha^k)^2} N_i^{m1} N_j^{n1} \int_{\Omega^k} \bar{N}_{m1} \bar{N}_{n1} d\alpha^k d\beta^k \int_{A^k} F_\tau F_s \frac{H_\beta^k}{H_\alpha^k} dz^k
 \end{aligned}$$

A.2 PVD for electro-mechanical problems

The explicit expression of the stiffness matrix nuclei are given below with the reinterpolation of the strain components via the MITC method Eq. 5.5. The stiffness matrix $\mathbf{K}^{k\tau sij}$ nucleus is defined as follows:

$$\mathbf{K}^{k\tau sij} = \begin{bmatrix} K_{uu\alpha\alpha} & K_{uu\alpha\beta} & K_{uu\alpha z} & K_{u\Phi\alpha} \\ K_{uu\beta\alpha} & K_{uu\beta\beta} & K_{uu\beta z} & K_{u\Phi\beta} \\ K_{uu z\alpha} & K_{uu z\beta} & K_{uu z z} & K_{u\Phi z} \\ K_{\Phi u\alpha} & K_{\Phi u\beta} & K_{\Phi u z} & K_{\Phi\Phi} \end{bmatrix}^{k\tau sij}$$

where the mechanical stiffness matrix nuclei $\mathbf{K}_{uu}^{k\tau sij}$ are the same defined for the pure mechanical problems in the previous appendix section A.1. In the following equations the new set of Lagrangian shape function of the MITC method are indicated, for example, as \bar{N}_{m1} , where $m1$ indicates the set of new interpolation points, for more details refers to Section 5.2. Therefore, the old node element shape function are evaluated in the new set of interpolation points, for example N_i^{m1} are the old Lagrangian shape element function evaluated in new set $m1$.

The pure electric contribution is defined as follows:

$$\begin{aligned} K_{\Phi\Phi}^{k\tau sij} = & -\tilde{\epsilon}_{33}^k \int_{\Omega^k} N_i N_j d\alpha^k d\beta^k \int_{A^k} F_{\tau,z} F_{s,z} H_\alpha^k H_\beta^k dz^k - \tilde{\epsilon}_{22}^k \int_{\Omega^k} N_{i,\beta} N_{j,\beta} d\alpha^k d\beta^k \int_{A^k} F_\tau F_s \frac{H_\alpha^k}{H_\beta^k} dz^k - \\ & - \tilde{\epsilon}_{12}^k \int_{\Omega^k} N_{i,\alpha} N_{j,\beta} d\alpha^k d\beta^k \int_{A^k} F_\tau F_s dz^k - \tilde{\epsilon}_{12}^k \int_{\Omega^k} N_{i,\beta} N_{j,\alpha} d\alpha^k d\beta^k \int_{A^k} F_\tau F_s dz^k - \\ & - \tilde{\epsilon}_{11}^k \int_{\Omega^k} N_{i,\alpha} N_{j,\alpha} d\alpha^k d\beta^k \int_{A^k} F_\tau F_s \frac{H_\beta^k}{H_\alpha^k} dz^k \end{aligned}$$

The stiffness electro-mechanical coupling matrices $\mathbf{K}_{u\Phi}^{k\tau sij}$ and $\mathbf{K}_{\Phi u}^{k\tau sij}$ are defined as follows:

Actuation in 3-1 mode

$$\begin{aligned} K_{u\Phi\alpha}^{k\tau sij} = & \tilde{e}_{25}^k N_i^{m1} \int_{\Omega^k} \bar{N}_{m1} N_{j,\beta} d\alpha^k d\beta^k \int_{A^k} F_{\tau,z} F_s H_\alpha^k dz^k + \tilde{e}_{15}^k N_i^{m1} \int_{\Omega^k} \bar{N}_{m1} N_{j,\alpha} d\alpha^k d\beta^k \int_{A^k} F_{\tau,z} F_s H_\beta^k dz^k + \\ & + \tilde{e}_{36}^k N_{i,\beta}^{m3} \int_{\Omega^k} \bar{N}_{m3} N_j d\alpha^k d\beta^k \int_{A^k} F_\tau F_{s,z} H_\alpha^k dz^k + \tilde{e}_{31}^k N_{i,\alpha}^{m1} \int_{\Omega^k} \bar{N}_{m1} N_j d\alpha^k d\beta^k \int_{A^k} F_\tau F_{s,z} H_\beta^k dz^k - \\ & - \frac{\tilde{e}_{25}^k}{R_\alpha^k} N_i^{m1} \int_{\Omega^k} \bar{N}_{m1} N_{j,\beta} d\alpha^k d\beta^k \int_{A^k} F_\tau F_s dz^k - \frac{\tilde{e}_{15}^k}{R_\alpha^k} N_i^{m1} \int_{\Omega^k} \bar{N}_{m1} N_{j,\alpha} d\alpha^k d\beta^k \int_{A^k} F_\tau F_s \frac{H_\beta^k}{H_\alpha^k} dz^k \end{aligned}$$

$$\begin{aligned} K_{u\Phi\beta}^{k\tau sij} = & \tilde{e}_{24}^k N_i^{m2} \int_{\Omega^k} \bar{N}_{m2} N_{j,\beta} d\alpha^k d\beta^k \int_{A^k} F_{\tau,z} F_s H_\alpha^k dz^k + \tilde{e}_{14}^k N_i^{m2} \int_{\Omega^k} \bar{N}_{m2} N_{j,\alpha} d\alpha^k d\beta^k \int_{A^k} F_{\tau,z} F_s H_\beta^k dz^k + \\ & + \tilde{e}_{32}^k N_{i,\beta}^{m2} \int_{\Omega^k} \bar{N}_{m2} N_j d\alpha^k d\beta^k \int_{A^k} F_\tau F_{s,z} H_\alpha^k dz^k + \tilde{e}_{36}^k N_{i,\alpha}^{m3} \int_{\Omega^k} \bar{N}_{m3} N_j d\alpha^k d\beta^k \int_{A^k} F_\tau F_{s,z} H_\beta^k dz^k - \\ & - \frac{\tilde{e}_{24}^k}{R_\beta^k} N_i^{m2} \int_{\Omega^k} \bar{N}_{m2} N_{j,\beta} d\alpha^k d\beta^k \int_{A^k} F_\tau F_s \frac{H_\alpha^k}{H_\beta^k} dz^k - \frac{\tilde{e}_{14}^k}{R_\beta^k} N_i^{m2} \int_{\Omega^k} \bar{N}_{m2} N_{j,\alpha} d\alpha^k d\beta^k \int_{A^k} F_\tau F_s dz^k \end{aligned}$$

$$\begin{aligned}
 K_{u\Phi_z}^{k\tau sij} &= \tilde{e}_{33}^k \int_{\Omega^k} N_i N_j d\alpha^k d\beta^k \int_{A^k} F_{\tau,z} F_{s,z} H_\alpha^k H_\beta^k dz^k + \frac{\tilde{e}_{32}^k}{R_\beta^k} N_i^{m2} \int_{\Omega^k} \bar{N}_{m2} N_j d\alpha^k d\beta^k \int_{A^k} F_\tau F_{s,z} H_\alpha^k dz^k + \\
 &+ \frac{\tilde{e}_{31}^k}{R_\alpha^k} N_i^{m1} \int_{\Omega^k} \bar{N}_{m1} N_j d\alpha^k d\beta^k \int_{A^k} F_\tau F_{s,z} H_\beta^k dz^k + \tilde{e}_{24}^k N_{i,\beta}^{m2} \int_{\Omega^k} \bar{N}_{m2} N_{j,\beta} d\alpha^k d\beta^k \int_{A^k} F_\tau F_s \frac{H_\alpha^k}{H_\beta^k} dz^k + \\
 &+ \tilde{e}_{25}^k N_{i,\alpha}^{m1} \int_{\Omega^k} \bar{N}_{m1} N_{j,\beta} d\alpha^k d\beta^k \int_{A^k} F_\tau F_s dz^k + \tilde{e}_{14}^k N_{i,\beta}^{m2} \int_{\Omega^k} \bar{N}_{m2} N_{j,\alpha} d\alpha^k d\beta^k \int_{A^k} F_\tau F_s dz^k + \\
 &+ \tilde{e}_{15}^k N_{i,\alpha}^{m1} \int_{\Omega^k} \bar{N}_{m1} N_{j,\alpha} d\alpha^k d\beta^k \int_{A^k} F_\tau F_s \frac{H_\beta^k}{H_\alpha^k} dz^k
 \end{aligned}$$

$$\begin{aligned}
 K_{u\alpha}^{k\tau sij} &= \tilde{e}_{36}^k N_{j,\beta}^{n3} \int_{\Omega^k} N_i \bar{N}_{n3} d\alpha^k d\beta^k \int_{A^k} F_{\tau,z} F_s H_\alpha^k dz^k + \tilde{e}_{31}^k N_{j,\alpha}^{n1} \int_{\Omega^k} N_i \bar{N}_{n1} d\alpha^k d\beta^k \int_{A^k} F_{\tau,z} F_s H_\beta^k dz^k + \\
 &+ \tilde{e}_{25}^k N_j^{n1} \int_{\Omega^k} N_{i,\beta} \bar{N}_{n1} d\alpha^k d\beta^k \int_{A^k} F_\tau F_{s,z} H_\alpha^k dz^k + \tilde{e}_{15}^k N_j^{n1} \int_{\Omega^k} N_{i,\alpha} \bar{N}_{n1} d\alpha^k d\beta^k \int_{A^k} F_\tau F_{s,z} H_\beta^k dz^k - \\
 &- \frac{\tilde{e}_{25}^k}{R_\alpha^k} N_j^{n1} \int_{\Omega^k} N_{i,\beta} \bar{N}_{n1} d\alpha^k d\beta^k \int_{A^k} F_\tau F_s dz^k - \frac{\tilde{e}_{15}^k}{R_\alpha^k} N_j^{n1} \int_{\Omega^k} N_{i,\alpha} \bar{N}_{n1} d\alpha^k d\beta^k \int_{A^k} F_\tau F_s \frac{H_\beta^k}{H_\alpha^k} dz^k
 \end{aligned}$$

$$\begin{aligned}
 K_{\Phi u_\beta}^{k\tau sij} &= \tilde{e}_{32}^k N_{j,\beta}^{n2} \int_{\Omega^k} N_i \bar{N}_{n2} d\alpha^k d\beta^k \int_{A^k} F_{\tau,z} F_s H_\alpha^k dz^k + \tilde{e}_{36}^k N_{j,\alpha}^{n3} \int_{\Omega^k} N_i \bar{N}_{n3} d\alpha^k d\beta^k \int_{A^k} F_{\tau,z} F_s H_\beta^k dz^k + \\
 &+ \tilde{e}_{24}^k N_j^{n2} \int_{\Omega^k} N_{i,\beta} \bar{N}_{n2} d\alpha^k d\beta^k \int_{A^k} F_\tau F_{s,z} H_\alpha^k dz^k + \tilde{e}_{14}^k N_j^{n2} \int_{\Omega^k} N_{i,\alpha} \bar{N}_{n2} d\alpha^k d\beta^k \int_{A^k} F_\tau F_{s,z} H_\beta^k dz^k - \\
 &- \frac{\tilde{e}_{24}^k}{R_\beta^k} N_j^{n2} \int_{\Omega^k} N_{i,\beta} \bar{N}_{n2} d\alpha^k d\beta^k \int_{A^k} F_\tau F_s \frac{H_\alpha^k}{H_\beta^k} dz^k - \frac{\tilde{e}_{14}^k}{R_\beta^k} N_j^{n2} \int_{\Omega^k} N_{i,\alpha} \bar{N}_{n2} d\alpha^k d\beta^k \int_{A^k} F_\tau F_s dz^k
 \end{aligned}$$

$$\begin{aligned}
 K_{\Phi u_z}^{k\tau sij} &= \tilde{e}_{33}^k \int_{\Omega^k} N_i N_j d\alpha^k d\beta^k \int_{A^k} F_{\tau,z} F_{s,z} H_\alpha^k H_\beta^k dz^k + \frac{\tilde{e}_{32}^k}{R_\beta^k} N_j^{n2} \int_{\Omega^k} N_i \bar{N}_{n2} d\alpha^k d\beta^k \int_{A^k} F_{\tau,z} F_s H_\alpha^k dz^k + \\
 &+ \frac{\tilde{e}_{31}^k}{R_\alpha^k} N_j^{n1} \int_{\Omega^k} N_i \bar{N}_{n1} d\alpha^k d\beta^k \int_{A^k} F_{\tau,z} F_s H_\beta^k dz^k + \tilde{e}_{24}^k N_{j,\beta}^{n2} \int_{\Omega^k} N_{i,\beta} \bar{N}_{n2} d\alpha^k d\beta^k \int_{A^k} F_\tau F_s \frac{H_\alpha^k}{H_\beta^k} dz^k + \\
 &+ \tilde{e}_{14}^k N_{j,\beta}^{n2} \int_{\Omega^k} N_{i,\alpha} \bar{N}_{n2} d\alpha^k d\beta^k \int_{A^k} F_\tau F_s dz^k + \tilde{e}_{25}^k N_{j,\alpha}^{n1} \int_{\Omega^k} N_{i,\beta} \bar{N}_{n1} d\alpha^k d\beta^k \int_{A^k} F_\tau F_s dz^k + \\
 &+ \tilde{e}_{15}^k N_{j,\alpha}^{n1} \int_{\Omega^k} N_{i,\alpha} \bar{N}_{n1} d\alpha^k d\beta^k \int_{A^k} F_\tau F_s \frac{H_\beta^k}{H_\alpha^k} dz^k
 \end{aligned}$$

Actuation in 1-5 mode

$$\begin{aligned}
 K_{u\Phi_\alpha}^{k\tau sij} &= \tilde{e}_{35}^k N_i^{m1} \int_{\Omega^k} \bar{N}_{m1} N_j d\alpha^k d\beta^k \int_{A^k} F_{\tau,z} F_{s,z} H_\alpha^k H_\beta^k dz^k - \frac{\tilde{e}_{35}^k}{R_\alpha^k} N_i^{m1} \int_{\Omega^k} \bar{N}_{m1} N_j d\alpha^k d\beta^k \int_{A^k} F_\tau F_{s,z} H_\beta^k dz^k + \\
 &+ \tilde{e}_{26}^k N_{i,\beta}^{m3} \int_{\Omega^k} \bar{N}_{m3} N_{j,\beta} d\alpha^k d\beta^k \int_{A^k} F_\tau F_s \frac{H_\alpha^k}{H_\beta^k} dz^k + \tilde{e}_{21}^k N_{i,\alpha}^{m1} \int_{\Omega^k} \bar{N}_{m1} N_{j,\beta} d\alpha^k d\beta^k \int_{A^k} F_\tau F_s dz^k + \\
 &+ \tilde{e}_{16}^k N_{i,\beta}^{m3} \int_{\Omega^k} \bar{N}_{m3} N_{j,\alpha} d\alpha^k d\beta^k \int_{A^k} F_\tau F_s dz^k + \tilde{e}_{11}^k N_{i,\alpha}^{m1} \int_{\Omega^k} \bar{N}_{m1} N_{j,\alpha} d\alpha^k d\beta^k \int_{A^k} F_\tau F_s \frac{H_\beta^k}{H_\alpha^k} dz^k
 \end{aligned}$$

$$\begin{aligned}
 K_{u\Phi_\beta}^{k\tau sij} &= \tilde{e}_{34}^k N_i^{m2} \int_{\Omega^k} \bar{N}_{m2} N_j d\alpha^k d\beta^k \int_{A^k} F_{\tau,z} F_{s,z} H_\alpha^k H_\beta^k dz^k - \frac{\tilde{e}_{34}^k}{R_\beta^k} N_i^{m2} \int_{\Omega^k} \bar{N}_{m2} N_j d\alpha^k d\beta^k \int_{A^k} F_\tau F_{s,z} H_\alpha^k dz^k + \\
 &+ \tilde{e}_{26}^k N_{i,\alpha}^{m3} \int_{\Omega^k} \bar{N}_{m3} N_{j,\beta} d\alpha^k d\beta^k \int_{A^k} F_\tau F_s dz^k + \tilde{e}_{22}^k N_{i,\beta}^{m2} \int_{\Omega^k} \bar{N}_{m2} N_{j,\beta} d\alpha^k d\beta^k \int_{A^k} F_\tau F_s \frac{H_\alpha^k}{H_\beta^k} dz^k + \\
 &+ \tilde{e}_{16}^k N_{i,\alpha}^{m3} \int_{\Omega^k} \bar{N}_{m3} N_{j,\alpha} d\alpha^k d\beta^k \int_{A^k} F_\tau F_s \frac{H_\beta^k}{H_\alpha^k} dz^k + \tilde{e}_{12}^k N_{i,\beta}^{m2} \int_{\Omega^k} \bar{N}_{m2} N_{j,\alpha} d\alpha^k d\beta^k \int_{A^k} F_\tau F_s dz^k
 \end{aligned}$$

$$\begin{aligned}
 K_{u\Phi_z}^{k\tau sij} &= \tilde{e}_{23}^k \int_{\Omega^k} N_i N_{j,\beta} d\alpha^k d\beta^k \int_{A^k} F_{\tau,z} F_s H_\alpha^k dz^k + \tilde{e}_{13}^k \int_{\Omega^k} N_i N_{j,\alpha} d\alpha^k d\beta^k \int_{A^k} F_{\tau,z} F_s H_\beta^k dz^k + \\
 &+ \tilde{e}_{34}^k N_{i,\beta}^{m2} \int_{\Omega^k} \bar{N}_{m2} N_j d\alpha^k d\beta^k \int_{A^k} F_\tau F_{s,z} H_\alpha^k dz^k + \tilde{e}_{35}^k N_{i,\alpha}^{m1} \int_{\Omega^k} \bar{N}_{m1} N_j d\alpha^k d\beta^k \int_{A^k} F_\tau F_{s,z} H_\beta^k dz^k + \\
 &+ \frac{\tilde{e}_{22}^k}{R_\beta^k} N_i^{m2} \int_{\Omega^k} \bar{N}_{m2} N_{j,\beta} d\alpha^k d\beta^k \int_{A^k} F_\tau F_s \frac{H_\alpha^k}{H_\beta^k} dz^k + \frac{\tilde{e}_{21}^k}{R_\alpha^k} N_i^{m1} \int_{\Omega^k} \bar{N}_{m1} N_{j,\beta} d\alpha^k d\beta^k \int_{A^k} F_\tau F_s dz^k + \\
 &+ \frac{\tilde{e}_{12}^k}{R_\beta^k} N_i^{m2} \int_{\Omega^k} \bar{N}_{m2} N_{j,\alpha} d\alpha^k d\beta^k \int_{A^k} F_\tau F_s dz^k + \frac{\tilde{e}_{11}^k}{R_\alpha^k} N_i^{m1} \int_{\Omega^k} \bar{N}_{m1} N_{j,\alpha} d\alpha^k d\beta^k \int_{A^k} F_\tau F_s \frac{H_\beta^k}{H_\alpha^k} dz^k
 \end{aligned}$$

$$\begin{aligned}
 K_{\Phi u_\alpha}^{k\tau sij} &= \tilde{e}_{35}^k N_j^{n1} \int_{\Omega^k} N_i \bar{N}_{n1} d\alpha^k d\beta^k \int_{A^k} F_{\tau,z} F_{s,z} H_\alpha^k H_\beta^k dz^k - \frac{\tilde{e}_{35}^k}{R_\alpha^k} N_j^{n1} \int_{\Omega^k} N_i \bar{N}_{n1} d\alpha^k d\beta^k \int_{A^k} F_{\tau,z} F_s H_\beta^k dz^k + \\
 &+ \tilde{e}_{26}^k N_{j,\beta}^{n3} \int_{\Omega^k} N_{i,\beta} \bar{N}_{n3} d\alpha^k d\beta^k \int_{A^k} F_\tau F_s \frac{H_\alpha^k}{H_\beta^k} dz^k + \tilde{e}_{21}^k N_{j,\alpha}^{n1} \int_{\Omega^k} N_{i,\beta} \bar{N}_{n1} d\alpha^k d\beta^k \int_{A^k} F_\tau F_s dz^k + \\
 &+ \tilde{e}_{16}^k N_{j,\beta}^{n3} \int_{\Omega^k} N_{i,\alpha} \bar{N}_{n3} d\alpha^k d\beta^k \int_{A^k} F_\tau F_s dz^k + \tilde{e}_{11}^k N_{j,\alpha}^{n1} \int_{\Omega^k} N_{i,\alpha} \bar{N}_{n1} d\alpha^k d\beta^k \int_{A^k} F_\tau F_s \frac{H_\beta^k}{H_\alpha^k} dz^k
 \end{aligned}$$

$$\begin{aligned}
 K_{\Phi u_\beta}^{k\tau sij} &= \tilde{e}_{34}^k N_j^{n2} \int_{\Omega^k} N_i \bar{N}_{n2} d\alpha^k d\beta^k \int_{A^k} F_{\tau,z} F_{s,z} H_\alpha^k H_\beta^k dz^k - \frac{\tilde{e}_{34}^k}{R_\beta^k} N_j^{n2} \int_{\Omega^k} N_i \bar{N}_{n2} d\alpha^k d\beta^k \int_{A^k} F_{\tau,z} F_s H_\alpha^k dz^k + \\
 &+ \tilde{e}_{26}^k N_{j,\alpha}^{n3} \int_{\Omega^k} N_{i,\beta} \bar{N}_{n3} d\alpha^k d\beta^k \int_{A^k} F_\tau F_s dz^k + \tilde{e}_{22}^k N_{j,\beta}^{n2} \int_{\Omega^k} N_{i,\beta} \bar{N}_{n2} d\alpha^k d\beta^k \int_{A^k} F_\tau F_s \frac{H_\alpha^k}{H_\beta^k} dz^k + \\
 &+ \tilde{e}_{16}^k N_{j,\alpha}^{n3} \int_{\Omega^k} N_{i,\alpha} \bar{N}_{n3} d\alpha^k d\beta^k \int_{A^k} F_\tau F_s \frac{H_\beta^k}{H_\alpha^k} dz^k + \tilde{e}_{12}^k N_{j,\beta}^{n2} \int_{\Omega^k} N_{i,\alpha} \bar{N}_{n2} d\alpha^k d\beta^k \int_{A^k} F_\tau F_s dz^k
 \end{aligned}$$

$$\begin{aligned}
 K_{\Phi u_z}^{k\tau sij} &= \tilde{e}_{34}^k N_{j,\beta}^{n2} \int_{\Omega^k} N_i \bar{N}_{n2} d\alpha^k d\beta^k \int_{A^k} F_{\tau,z} F_s H_\alpha^k dz^k + \tilde{e}_{35}^k N_{j,\alpha}^{n1} \int_{\Omega^k} N_i \bar{N}_{n1} d\alpha^k d\beta^k \int_{A^k} F_{\tau,z} F_s H_\beta^k dz^k + \\
 &+ \tilde{e}_{23}^k \int_{\Omega^k} N_{i,\beta} N_j d\alpha^k d\beta^k \int_{A^k} F_\tau F_{s,z} H_\alpha^k dz^k + \tilde{e}_{13}^k \int_{\Omega^k} N_{i,\alpha} N_j d\alpha^k d\beta^k \int_{A^k} F_\tau F_{s,z} H_\beta^k dz^k + \\
 &+ \frac{\tilde{e}_{22}^k}{R_\beta^k} N_j^{n2} \int_{\Omega^k} N_{i,\beta} \bar{N}_{n2} d\alpha^k d\beta^k \int_{A^k} F_\tau F_s \frac{H_\alpha^k}{H_\beta^k} dz^k + \frac{\tilde{e}_{21}^k}{R_\alpha^k} N_j^{n1} \int_{\Omega^k} N_{i,\beta} \bar{N}_{n1} d\alpha^k d\beta^k \int_{A^k} F_\tau F_s dz^k + \\
 &+ \frac{\tilde{e}_{12}^k}{R_\beta^k} N_j^{n2} \int_{\Omega^k} N_{i,\alpha} \bar{N}_{n2} d\alpha^k d\beta^k \int_{A^k} F_\tau F_s dz^k + \frac{\tilde{e}_{11}^k}{R_\alpha^k} N_j^{n1} \int_{\Omega^k} N_{i,\alpha} \bar{N}_{n1} d\alpha^k d\beta^k \int_{A^k} F_\tau F_s \frac{H_\beta^k}{H_\alpha^k} dz^k
 \end{aligned}$$

Appendix B

Publications & Talks

Journal Articles

Cinefra M, Carrera E, **Valvano S** (2015), "Variable kinematic shell elements for the analysis of electro-mechanical problems", *Mechanics of Advanced Materials and Structures* 22(1-2): 77-106

DOI: <http://dx.doi.org/10.1080/15376494.2014.908042>

Cinefra M, **Valvano S**, Carrera E (2015), "Heat conduction and Thermal Stress Analysis of laminated composites by a variable kinematic MITC9 shell element", *Curved and Layered Structures* 2: 301-320

DOI: <http://dx.doi.org/10.1515/cls-2015-0017>

Cinefra M, **Valvano S**, Carrera E (2015), "A layer-wise MITC9 finite element for the free-vibration analysis of plates with piezo-patches", *International Journal of Smart and Nano Materials* 6(2): 85-104

DOI: <http://dx.doi.org/10.1080/19475411.2015.1037377>

Cinefra M, **Valvano S** (2016), "A variable kinematic doubly-curved MITC9 shell element for the analysis of laminated composites", *Mechanics of Advanced Materials and Structures* 23(11): 1312-1325

DOI: <http://dx.doi.org/10.1080/15376494.2015.1070304>

Filippi M, Petrolo M, **Valvano S**, Carrera E (2016), "Analysis of laminated composites and sandwich structures by trigonometric, exponential and miscellaneous polynomials and a MITC9 plate element", *Composite Structures* 150: 103-114

DOI: <http://dx.doi.org/10.1016/j.compstruct.2015.12.038>

Cinefra M, **Valvano S**, Carrera E (2016), "Thermal stress analysis of laminated structures by a variable kinematic MITC9 shell element", *Journal of Thermal Stresses* 39(2): 121-141

DOI: <http://dx.doi.org/10.1080/01495739.2015.1123591>

Pagani A, **Valvano S**, Carrera E (2016), "Analysis of laminated composites and sandwich structures by variable-kinematic MITC9 plate elements", *Journal of Sandwich Structures and Materials*

DOI: <http://dx.doi.org/10.1177/1099636216650988>

Carrera E, **Valvano S** (2017), "A variable kinematic shell formulation applied to thermal stress of laminated structures", *Journal of Thermal Stresses* 40(7): 803-827

DOI: <http://dx.doi.org/10.1080/01495739.2016.1253439>

Carrera E, Pagani A, **Valvano S** (2017), "Shell elements with through-the-thickness variable kinematics for the analysis of laminated composite and sandwich structures", *Composites*

Part B, Engineering 111: 294-314

DOI: <http://dx.doi.org/10.1016/j.compositesb.2016.12.001>

Carrera E, Pagani A, **Valvano S** (2017), "Multilayered plate elements accounting for refined theories and node-dependent kinematics", *Composites Part B, Engineering* 114: 189-210

DOI: <http://dx.doi.org/10.1016/j.compositesb.2017.01.022>

Keshava Kumar S, Harursampath D, Carrera E, Cinefra M, **Valvano S** (2017), "Modal analysis of delaminated plates and shell using Carrera Unified Formulation-MITC9 shell element", *Mechanics of Advanced Materials and Structures*

DOI: <http://dx.doi.org/10.1080/15376494.2017.1302024>

Valvano S, Carrera E (2017), "Multilayered plate elements with node-dependent kinematics for the analysis of composite and sandwich structures", *FACTA UNIVERSITATIS, Series: Mechanical Engineering* 15(1): 1-30

DOI: <http://dx.doi.org/10.22190/FUME170315001V>

Carrera E, **Valvano S** (2017), "Analysis of laminated composite structures with embedded piezoelectric sheets by variable kinematic shell elements", *Journal of Intelligent Material Systems and Structures*

DOI: <http://dx.doi.org/10.1177/1045389X17704913>

Conference Proceedings

Cinefra M, Carrera E, **Valvano S** (2013), "Refined shell elements for the analysis of multilayered structures with piezoelectric layers", *In 6th ECCOMAS Thematic Conference on Smart Structures and Material (SMART2013)*, Torino (Italy), 24-26 June

Cinefra M, Carrera E, **Valvano S** (2013), "Doubly-curved shell finite elements based on MITC-type technique and Unified Formulation for the analysis of multilayered structures", *In International Conference on Science and Technology of Heterogeneous Materials and Structures*, Wuhan University, China, 11-13 October

Cinefra M, **Valvano S**, Carrera E (2014), "A Finite Elements Model embedding Piezoelectric Patches", *In 5th International Symposium on Aircraft Materials*, Marrakech, Morocco, 23-26 April

Cinefra M, **Valvano S**, Carrera E (2014), "A Finite Elements with Continue Transverse Electric Displacement for the Electro-Mechanical Analysis of Shell Structures", *In DeMEASS VI*, Ede, Netherlands, 25-28 May

Cinefra M, Carrera E, **Valvano S** (2014), "Refined shell elements for the thermo-mechanical analysis of multilayered structures", *In First International Conference on Mechanics of Composites (MechComp2014)*, Stony Brook, Long Island (NY), USA, 8-12 June

Cinefra M, **Valvano S**, Carrera E (2014), "Refined Shell Elements for the Analysis of Multifield Problems in Multilayered Structures", *In 11th World Congress on Computational Mechanics WCCM XI, 5th European Conference on Computational Mechanics ECCM V, 6th European Conference on Computational Fluid Dynamics ECFD VI*, Barcelona, Spain, 20-25 July

Cinefra M, **Valvano S**, Carrera E (2015), "A Finite Element with Continuous Transverse Electric Displacement for Static and Free-Vibration Analysis of Piezoelectric Shells", *In 7th ECCOMAS Thematic Conference on Smart Structures and Materials*, Ponta Delgada, Azores,

Portugal, 3-6 June

Cinefra M, Carrera E, **Valvano S** (2015), "Free-Vibration Analysis of Delaminated Shells via Unified Formulation", *In 18th International Conference on Composite Structures*, Lisbon, Portugal, 15-18 June

Pagani A, **Valvano S**, Carrera E (2015), "Analysis of Laminated Structures by combined ESL-LW Variable Kinematics Plate Elements", *In XXIII Congresso - Associazione Italiana di Aeronautica e Astronautica (AIDAA)*, Torino, Italy, 17-19 November

Carrera E, Pagani A, **Valvano S** (2016), "A variable-kinematic plate element including cohesive mechanics", *In 2nd International Conference on Mechanics of Composites*, Porto, Portugal, 11-14 July

Carrera E, Pagani A, **Valvano S** (2016), "CUF-based layered shell elements with mixed LW-ESL assumptions", *In 19th International Conference on Composite Structures*, Porto, Portugal, 5-9 September

Carrera E, **Valvano S**, Kulikov GM (2017), "Node-dependent kinematic shell elements for the analysis of smart structures", *In 8th International Conference DeMEASS VIII*, Moscow, Russia, 21-24 May

Carrera E, Kulikov GM, **Valvano S** (2017), "A multilayered plate element accounting node-dependent kinematics for static analysis of piezoelectric structures", *In VIII ECCOMAS Thematic Conference on Smart Structures and Materials SMART 2017*, Madrid, Spain, 5-8 June

Bibliography

- [1] W T Koiter. On the foundations of the linear theory of thin elastic shell. *Proc. Kon. Nederl. Akad. Wetensch.*, 73:169–195, 1970.
- [2] P G Ciarlet and L Gratie. Another approach to linear shell theory and a new proof of Korn’s inequality on a surface. *C. R. Acad. Sci. Paris*, I,340:471–478, 2005.
- [3] E Reissner and Y Stavsky. Bending and stretching of certain types of heterogeneous aelotropic elastic plates. *Journal of Applied Mechanics*, 28:402–408, 1961.
- [4] E Reissner. The effect of transverse shear deformation on the bending of elastic plates. *Journal of Applied Mechanics*, 12(2):69–77, 1945.
- [5] R D Mindlin. Influence of rotary inertia and shear flexural motion of isotropic, elastic plates. *Journal of Applied Mechanics*, 18:31–38, 1951.
- [6] T Kant, D R J Owen, and O C Zienkiewicz. Refined higher order C^0 plate bending element. *Computer & Structures*, 15:177–183, 1982.
- [7] T Kant and J R Kommineni. Large amplitude free vibration analysis of cross-ply composite and sandwich laminates with a refined theory and C^0 finite elements. *Computer & Structures*, 50:123–134, 1989.
- [8] J N Reddy. Mechanics of laminated composite plates and shells. *Theory and Analysis*, CRC Press, New York (USA), 1997.
- [9] A N Palazotto and S T Dennis. Nonlinear analysis of shell structures. *AIAA Series*, 1992.
- [10] A K Noor and W S Burton. Assessment of computational models for multi-layered composite shells. *Applied Mechanics Review*, 43:67–97, 1990.
- [11] J N Reddy. An evaluation of equivalent-single-layer and layerwise theories of composite laminates. *Composite Structures*, 25:21–35, 1993.
- [12] A S Mawenya and J D Davies. Finite element bending analysis of multilayer plates. *Journal for Numerical Methods in Engineering*, 8:215–225, 1974.
- [13] F G Rammerstorfer, K Dorninger, and A Starlinger. Composite and sandwich shells. *Nonlinear Analysis of Shells by Finite Elements*, 328:131–194, 1992.
- [14] E Carrera. Theories and finite elements for multilayered, anisotropic, composite plates and shells. *Archives of Computational Methods in Engineering*, 9(2):87–140, 2002.
- [15] E Carrera. Theories and finite elements for multilayered plates and shells: a unified compact formulation with numerical assessment and benchmarking. *Archives of Computational Methods in Engineering*, 10(3):215–296, 2003.

-
- [16] E. Carrera. Historical review of Zig-Zag theories for multilayered plates and shells. *Applied Mechanics Reviews*, 56:287–308, 2003.
- [17] T Kant and R K Khare. Finite element thermal stress analysis of composite laminates using a higher-order theory. *Journal of Thermal Stresses*, 17(2):229–255, 1994.
- [18] A A Khdeir and J N Reddy. Thermal stresses and deflections of cross-ply laminated plates using refined plate theories. *Journal of Thermal Stresses*, 14(4):419–438, 1991.
- [19] W Zhen and C Wanji. A global-local higher order theory for multilayered shells and the analysis of laminated cylindrical shell panels. *Composites Structures*, 84(4):350–361, 2008.
- [20] K R Khare, T Kant, and A K Garg. Closed-form thermo-mechanical solutions of higher-order theories of cross-ply laminated shallow shells. *Composite Structures*, 59:313–340, 2003.
- [21] A A Khdeir. Thermoelastic analysis of cross-ply laminated circular cylindrical shells. *International Journal of Solids and Structures*, 33(27):4007–4017, 1996.
- [22] A A Khdeir, M B Rajab, and J N Reddy. Thermal effects on the response of cross-ply laminated shallow shells. *International Journal of Solids and Structures*, 29(5):653–667, 1992.
- [23] A Barut, E Madenci, and A Tessler. Nonlinear thermoelastic analysis of composite panels under non-uniform temperature distribution. *International Journal of Solids and Structures*, 37(27):3681–3713, 2000.
- [24] C J Miller, W A Millavec, and T P Richer. Thermal stress analysis of layered cylindrical shells. *AIAA Journal*, 19(4):523–530, 1981.
- [25] P.C. Dumir, J.K. Nath, P. Kumari, and S. Kapuria. Improved efficient zigzag and third order theories for circular cylindrical shells under thermal load. *Journal of Thermal Stresses*, 31:343–363, 2008.
- [26] Y S Hsu, J N Reddy, and C W Bert. Thermoelasticity of circular cylindrical shells laminated of bimodulus composite materials. *Journal of Thermal Stresses*, 4(2):155–177, 1981.
- [27] K Ding. Thermal stresses of weak formulation study for thick open laminated shell. *Journal of Thermal Stresses*, 31(4):389–400, 2008.
- [28] E Carrera. Temperature profile influence on layered plates response considering classical and advanced theories. *AIAA Journal*, 40(9):1885–1896, 2002.
- [29] E Carrera and A Ciuffreda. Closed-form solutions to assess multilayered-plate theories for various thermal stress problems. *Journal of Thermal Stresses*, 27:1001–1031, 2004.
- [30] A Robaldo and E Carrera. Mixed finite elements for thermoelastic analysis of multilayered anisotropic plates. *Journal of Thermal Stresses*, 30:165–194, 2007.
- [31] S Brischetto and E Carrera. Heat conduction and thermal analysis in multilayered plates and shells. *Mechanics Research Communications*, 38:449–455, 2011.
- [32] DJ Inman, M Ahmadihan, and RO Claus. Simultaneous active damping and health monitoring of aircraft panels. *Journal of Intelligent Material Systems and Structures*, 12:775–783, 2001.

-
- [33] I Chopra. Status of application of smart structures technology to rotorcraft systems. *Journal of the American Helicopter Society*, 45:228–252, 2000.
- [34] P Gaudenzi. Smart Structures: Physical Behaviour, Mathematical Modelling and Applications. *John Wiley & Sons, Ltd, UK*, 2009.
- [35] A Preumont, R Bastait, and G Rodrigues. Active optics for large segmented mirrors: scale effects. *In Proceedings of the IV ECCOMAS Thematic Conference on Smart Structures and Materials*, 2009.
- [36] D Foster. The bridge to smart technology. *In Bloomberg Businessweek*, 2009.
- [37] CA Roger. Intelligent material systems and structures. *In Proceedings of US Japan Workshop on Smart/Intelligent Materials and Systems*, 2009.
- [38] R D Mindlin. Forced thickness-shear and flexural vibrations of piezoelectric crystal plates. *Journal of Applied Physics*, 23:83–91, 1952.
- [39] E P EerNisse. Variational method for electroelastic vibration analysis. *IEEE Transactions on Sonics and Ultrasonic*, 14(4):153–160, 1967.
- [40] H F Tiersten and R D Mindlin. Forced vibrations of piezoelectric crystal plates. *Quarterly of Applied Mathematics*, 20(2):107–126, 1962.
- [41] H F Tiersten. *Linear Piezoelectric Plate Vibrations*. Plenum, New York (USA), 1969.
- [42] D Saravanos and P R Heyliger. Mechanics and computational models for laminated piezoelectric beams, plates, and shell. *Applied Mechanics Reviews*, 52(10):305–320, 1999.
- [43] S Kapuria. A coupled zig-zag third-order theory for piezoelectric hybrid cross-ply plates. *Journal of Applied Mechanics*, 71:604–618, 2004.
- [44] C Ossadzow-David and M Touratier. A multilayered piezoelectric shell theory. *Composites Science and Technology*, 64:2121–2158, 2004.
- [45] P R Heyliger, K Pei, and D Saravanos. Layerwise mechanics and finite element model for laminated piezoelectric shells. *AIAA Journal*, 34(11):2353–2360, 1996.
- [46] D Ballhause, M D’Ottavio, B Kröplin, and E Carrera. A unified formulation to assess multilayered theories for piezoelectric plates. *Computers & Structures*, 83(15-16):1217–1235, 2005.
- [47] M D’Ottavio, D Ballhause, B Kroplin, and E Carrera. Closed-form solutions for the free-vibration problem of multilayered piezoelectric shells. *Computers & Structures*, 84:1506–1524, 2006.
- [48] A Benjeddou, J Deu, and S Letombe. Free vibrations of simply-supported piezoelectric adaptive plates: An exact sandwich formulation. *Thin-walled structures*, 40:573–666, 2002.
- [49] M Robaldo, E Carrera, and A Benjeddou. A unified formulation for finite element analysis of piezoelectric adaptive plates. *Computers and Structures*, 84:1494–1505, 2006.
- [50] E Carrera, M Boscolo, and A Robaldo. Hierarchic multilayered plate elements for coupled multifield problems of piezoelectric adaptive structures: formulation and numerical assessment. *Archives of Computational Methods in Engineering*, 14(4):383–430, 2007.

-
- [51] E Carrera and P Nali. Classical and Mixed Finite Plate Elements for the Analysis of Multifield Problems and Smart Layered Structures. *Acta Mechanica Sinica*, 23:115–121, 2010.
- [52] E Carrera and S Brischetto. Analysis of thickness locking in classical, refined and mixed multilayered plate theories. *Composite Structures*, 82(4):549–562, 2008.
- [53] E Carrera and S Brischetto. Analysis of thickness locking in classical, refined and mixed theories for layered shells. *Composite Structures*, 85(1):83–90, 2008.
- [54] E Carrera, S Brischetto, and P Nali. Variational statements and computational models for multifield problems and multilayered structures. *Mechanics of Advanced Materials and Structures*, 15(3):182–198, 2008.
- [55] G A Altay and M C Dokmeci. Fundamental variational equations of discontinuous thermopiezoelectric fields. *International Journal of Engineering Sciences*, 34(7):769–782, 1996.
- [56] G A Altay and M C Dokmeci. Coupled thermoelastic shell equations with second sound for high-frequency vibrations of temperature-dependent materials. *International Journal of Solids and Structures*, 38(16):2737–2768, 2001.
- [57] R D Mindlin. Equations of high-frequency vibrations of thermopiezoelectric crystal plates. *International Journal of Solids and Structures*, 10:625–632, 1974.
- [58] J L Nowinski. *Theory of Thermoelasticity with Applications*. Sijthoff & Noordhoff, The Netherlands, 1978.
- [59] T Ikeda. *Fundamentals of Piezoelectricity*. Oxford University Press, Oxford (UK), 1990.
- [60] A W Leissa. *Vibration of Shells*. NASA SP-288, Washington, D.C. (USA), 1973.
- [61] A W Leissa. *Vibration of Plates*. NASA SP-160, Washington, D.C. (USA), 1969.
- [62] E Kreyszig. *Advanced Engineering Mathematics*. John Wiley & Sons, Inc., New York (USA), 1968.
- [63] V Z Vlasov. *Osnovnye Differentsialnye Uravnemia Obshche Teorii Uprugikh Obolochek*. Pinkl. Mat. Mekh. (English Translation: NACA TM-1241, Basic Differential Equations in General Theory of Elastic Shells, 1951), 1944.
- [64] I S Sokolnikoff. *Mathematical Theory of Elasticity*. McGraw-Hill, Book Company Inc., New York (USA), 1956.
- [65] E Carrera, S Brischetto, and P Nali. *Plates and Shells for Smart Structures: Classical and Advanced Theories for Modeling and Analysis*. John Wiley & Sons, 2011.
- [66] E Carrera, M Cinefra, and E Petrolo M. abd Zappino. *Finite Element Analysis of Structures through Unified Formulation*. John Wiley & Sons, 2014.
- [67] E Carrera. Multilayered shell theories accounting for layerwise mixed description, Part 1: governing equations. *AIAA Journal*, 37(9):1107–1116, 1999.
- [68] E Carrera. Multilayered shell theories accounting for layerwise mixed description, Part 2: numerical evaluations. *AIAA Journal*, 37(9):1117–1124, 1999.
- [69] H Murakami. Laminated composite plate theory with improved in-plane responses. *Journal of Applied Mechanics*, 53:661–666, 1986.

- [70] M Cinefra, S Valvano, and E Carrera. Heat conduction and Thermal Stress Analysis of laminated composites by a variable kinematic MITC9 shell element. *Curved and Layered Structures*, 1:301–320, 2015.
- [71] M Cinefra, S Valvano, and E Carrera. Thermal Stress Analysis of laminated structures by a variable kinematic MITC9 shell element. *Journal of Thermal Stresses*, 39(2):121–141, 2016.
- [72] M Cinefra, E Carrera, and S Valvano. Variable Kinematic Shell Elements for the Analysis of Electro-Mechanical Problems. *Mechanics of Advanced Materials and Structures*, 22(1-2):77–106, 2015.
- [73] M Cinefra, S Valvano, and E Carrera. A layer-wise MITC9 finite element for the free-vibration analysis of plates with piezo-patches. *International Journal of Smart and Nano Materials*, 6(2):85–104, 2015.
- [74] A Robaldo. Classical and Mixed Finite Elements for Thermoelectromechanical Analysis of Multilayered Anisotropic Plates. *PhD Thesis, Politecnico di Torino*, 2006.
- [75] K Xu, A K Noor, and Y Y Tang. Three-dimensional solutions for free vibrations of initially-stressed thermoelectroelastic multilayered plates. *Computational Methods in Applied Mechanics and Engineering*, 141(1-2):125–139, 1997.
- [76] E Pan. Exact solution for simply supported and multilayered magneto-electro-elastic plates. *Journal of Applied Mechanics*, 68(4):608–618, 2001.
- [77] X Y Li, H J Ding, and W Q Chen. Three-dimensional analytical solution for functionally graded magneto-electro-elastic circular plates subjected to uniform load. *Composite Structures*, 83(4):381–390, 2008.
- [78] P Heyliger. Static behavior of laminated elastic/piezoelectric plates. *AIAA Journal*, 32(12):2481–2484, 1994.
- [79] C Q Chen, Y P Shen, and X M Wang. Exact solution of orthotropic cylindrical shell with piezoelectric layers under cylindrical bending. *International Journal of Solids and Structures*, 33(30):4481–4494, 1996.
- [80] P C Dumir, G P Dube, and S Kapuria. Exact piezoelastic solution of simply-supported orthotropic circular cylindrical panel in cylindrical bending. *International Journal of Solids and Structures*, 34(6):685–702, 1997.
- [81] P Heyliger. Exact solutions for simply supported laminated piezoelectric plates. *Journal of Applied Mechanics*, 64(2):299–306, 1997.
- [82] P C Dumir, G P Dube, and S Kapuria. Dynamic analysis of thick laminated shell panel with piezoelectric layer based on three dimensional elasticity solution. *Computer & Structures*, 84(22-23):1519–1526, 2006.
- [83] V Tungikar and B K M Rao. Three dimensional exact solution of thermal stresses in rectangular composite laminates. *Composite Structures*, 27(4):419–430, 1994.
- [84] Z Q Cheng and R C Batra. Three-dimensional thermoelastic deformations of a functionally graded elliptic plate. *Composites Part B: Engineering*, 31(2):97–106, 2000.
- [85] J N Reddy and Z N Chen. Three-dimensional thermomechanical deformations of functionally graded rectangular plates. *European Journal of Mechanics A/Solids*, 20(5):841–855, 2001.

-
- [86] R Rolfes, J Noack, and M Taeschner. Three-dimensional thermomechanical deformations of functionally graded rectangular plates. *Composite Structures*, 46(4):367–379, 1999.
- [87] J G Ren. Exact solutions for laminated cylindrical shells in cylindrical bending. *Composite Science and Technology*, 29(3):169–187, 1987.
- [88] T K Varadan and K Bhaskar. Bending of laminated orthotropic cylindrical shells - an elasticity approach. *Composite Structures*, 17(2):141–156, 1991.
- [89] M Kashtalyan and M Menshykova. Three-dimensional elasticity solution for sandwich panels with a functionally graded core. *Composite Structures*, 87(1):36–43, 2009.
- [90] E Reissner. On a certain mixed variational theory and a proposed application. *International Journal for Numerical Methods in Engineering*, 20(7):1366–1368, 1984.
- [91] E Carrera. Developments, ideas and evaluation based upon Reissner’s Mixed Variational Theorem in the Modeling of Multilayered Plates and Shells. *Applied Mechanics Review*, 54:301–329, 2001.
- [92] D C Ossadzow and M Touratier. Multilayered piezoelectric refined plate theory. *AIAA Journal*, 41(1):90–99, 2003.
- [93] W Q Chen and K Y Lee. Alternative state space formulations for magnetoelectric thermoelasticity with transverse isotropy and the application to bending analysis of non-homogeneous plate. *International Journal of Solids Structures*, 40(21):5689–5705, 2003.
- [94] T Weller and C Licht. Modeling of linearly electromagneto-elastic thin plates. *Comptes Rendus Mecanique*, 335(4):201–206, 2007.
- [95] H Murakami. Assessment of plate theories for treating the thermomechanical response of layered plates. *Composites Engineering*, 3(2):137–143, 1993.
- [96] K Bhaskar, T K Varadan, and J S M Ali. Thermoelastic solutions for orthotropic and anisotropic composite laminates. *Composites: Part B*, 27(5):415–420, 1996.
- [97] J S M Ali, K Bhaskar, and T K Varadan. A new theory for accurate thermal/mechanical flexural analysis of symmetric laminated plates. *Composite Structures*, 45(3):227–232, 1999.
- [98] A K Noor and W S Burton. Computational models for high-temperature multilayered composite plates and shells. *Applied Mechanics Reviews*, 45(10):419–446, 1992.
- [99] L Librescu and W Lin. Non-linear response of laminated plates and shells to thermo-mechanical loading: implications of violation of interlaminar shear traction continuity requirement. *International Journal of Solids and Structures*, 36(27):4111–4147, 1999.
- [100] S Brischetto and E Carrera. Thermal Stress Analysis by Refined Multilayered Composite Shell Theories. *Journal of Thermal Stresses*, 32(1):165–186, 2009.
- [101] S Brischetto, R Leetsch, E Carrera, T Wallmersperger, and B Kröplin. Thermo-mechanical bending of functionally graded plates. *Journal of Thermal Stresses*, 31(3):286–308, 2008.
- [102] A Suleman and V B Venkayya. A simple finite element formulation for a laminated composite plate with piezoelectric layers. *Journal of Intelligent Material Systems and Structures*, 6(6):776–782, 1995.

- [103] D A Saravanos, P R Heyliger, and D A Hopkins. Layerwise mechanics and finite element for the dynamic analysis of piezoelectric composite plates. *International Journal of Solids and Structures*, 34(3):359–378, 1997.
- [104] A Benjeddou. Advances in piezoelectric finite element modeling of adaptive structural elements: a survey. *Computers & Structures*, 76(1-3):347–363, 2000.
- [105] P R Heyliger and D A Saravanos. Exact free vibration analysis of laminated plates with embedded piezoelectric layers. *Journal Acoustical Society of America*, 98(3):1547–1557, 1995.
- [106] H Allik and T J R Hughes. Finite element method for piezoelectric vibration. *International Journal for Numerical Methods in Engineering*, 2(2):151–157, 1970.
- [107] M Kögl and M L Bucalem. Analysis of smart laminates using piezoelectric mitc plate and shell elements. *Computers & Structures*, 83(15-16):1153–1163, 2005.
- [108] R Lammering and S Mesecke-Rischmann. Multi-field variational formulations and related finite elements for piezoelectric shells. *Smart Materials and Structures*, 12(6):904–913, 2003.
- [109] D H Jr Robbins and I Chopra. The effect of laminated kinematic assumptions on the global response of actuated plates. *Journal of Intelligent Material Systems and Structures*, 17(4):273–299, 2006.
- [110] R Garcia Lage, C M M Soares, C A M Soares, and J N Reddy. Layerwise partial mixed finite element analysis of magneto-electro-elastic plates. *Computers & Structures*, 82(17-19):1293–1301, 2004.
- [111] M D’Ottavio and B Kröplin. An extension of Reissner mixed variational theorem to piezoelectric laminates. *Mechanics of Advanced Materials and Structures*, 13(2):139–150, 2006.
- [112] G Kirchhoff. Über das Gleichgewicht und die Bewegung einer elastischen Scheibe. *Journal für die reine und angewandte Mathematik*, 40:51–88, 1850.
- [113] K J Bathe. Finite element procedure. *Prentice Hall*, 1996.
- [114] O C Zienkiewicz, R L Taylor, and J Z Zhu. *The Finite Element Method*. Elsevier Butterworth Heinemann, New York (USA), 2005.
- [115] T J R Hughes, M Cohen, and M Horaun. Reduced and selective integration techniques in the finite element methods. *Nuclear Engineering and Design*, 46:203–222, 1978.
- [116] H Parisch. A critical survey of the 9-node degenerated shell element with special emphasis on thin shell application and reduced integration. *Computer Methods in Applied Mechanics and Engineering*, 20:323–350, 1979.
- [117] O C Zienkiewicz, R L Taylor, and J M Too. Reduced intergration technique in general analysis of plates and shells. *International Journal for Numerical Methods in Engineering*, 3:275–290, 1973.
- [118] E D L Pugh, E Hintonand, and O C Zienkiewicz. A study of quadrilater plate bending elements with reduced integration. *International Journal for Numerical Methods in Engineering*, 12:1059–1079, 1978.
- [119] C Chinosi and C Lovadina. Remarks on partial selective reduced integration method for Reissner-Mindlin plate problem. *Computers & Structures*, 73:73–78, 1999.

- [120] D S Malkus and T J R Hughes. Mixed finite element methods - reduced and selective integration techniques: a unified concepts. *Computer Methods in Applied Mechanics and Engineering*, 15:63–81, 1978.
- [121] K J Bathe and E Dvorkin. A formulation of general shell elements - the use of mixed interpolation of tensorial components. *International Journal for Numerical Methods in Engineering*, 22:697–722, 1986.
- [122] K J Bathe and F Brezzi. A simplified analysis of two plate bending elements-the MITC4 and MITC9 elements. *Proceedings, Numerical Methods in Engineering: Theory and Applications*, 1987.
- [123] K J Bathe, F Brezzi, and S W Cho. The MICT7 and MITC9 plate bending elements. *Computers & Structures*, 32(3-4):797–814, 1989.
- [124] M L Bucalem and E Dvorkin. Higher-order MITC general shell elements. *International Journal for Numerical Methods in Engineering*, 36:3729–3754, 1993.
- [125] N.N. Huang. Influence of shear correction factors in the higher-order shear deformation laminated shell theory. *International Journal of Solids and Structures*, 31:1263–1277, 1994.
- [126] X P Shu. A refined theory of laminated shells with higher-order transverse shear deformation. *International Journal of Solids and Structures*, 34(6):673–683, 1997.
- [127] G Giunta, F Biscani, S Belouettar, and E Carrera. Hierarchical modelling of doubly curved laminated composite shells under distributed and localised loadings. *Composites Part B*, 42(4):682–691, 2011.
- [128] N J Pagano. Exact solutions for rectangular bidirectional composites and sandwich plate. *Journal of Composite Materials*, 4:20–34, 1970.
- [129] E Carrera and L Demasi. Classical and advanced multilayered plate elements based upon PVD and RMVT. Part 2: Numerical Implementations. *International Journal for Numerical Methods in Engineering*, 55:253–291, 2002.
- [130] W J Liou and C T Sun. A three-dimensional hybrid stress isoparametric element for the analysis of laminated composite plates. *Computers and Structures*, 25:241–249, 1985.
- [131] K Moriya. Laminated plate and shell elements for finite element analysis of advanced fiber reinforced composite structures. *Transactions of the Japan Society of Mechanical Engineering (Series A)*, 52(478):1600–1607, 1986.
- [132] J N Reddy. A simple higher-order theory for laminated composite plates. *Journal of Applied Mechanics*, 51:745–752, 1984.
- [133] H J Jing and M L Liao. Partial hybrid stress element for the analysis of thick laminated composite plates. *International Journal for Numerical Methods in Engineering*, 28:2813–2827, 1989.
- [134] J N Reddy and W C Chao. A comparison of closed-form and finite-element solutions of thick laminated anisotropic rectangular plates. *Nuclear Engineering Design*, 64:153–167, 1981.
- [135] B N Pandia and T Kant. Flexural analysis of laminated composites using refined higher-order C^0 plate bending elements. *Computer Methods in Applied Mechanics and Engineering*, 66:173–198, 1985.

- [136] S Di and E Ramm. Hybrid stress formulation for higher-order theory of laminated shell analysis. *Computer Methods in Applied Mechanics and Engineering*, 109:359–376, 1993.
- [137] F Auricchio and E Sacco. A mixed-enhanced finite element for the analysis of laminated composite plates. *International Journal for Numerical Methods in Engineering*, 44:1481–1504, 1999.
- [138] K M Liew, B Han, and M Xiao. Differential quadrature method for thick symmetric cross-ply laminates with first-order shear flexibility. *International Journal of Solids and Structures*, 33:2647–2658, 1996.
- [139] E Carrera and A Ciuffreda. A unified formulation to assess theories of multilayered plates for various bending problems. *Composite Structures*, 69:271–293, 2005.
- [140] E Carrera and S Brischetto. Piezoelectric shell theories with a priori continuous transverse electromechanical variables. *Journal of Mechanics of Materials and Structures*, 2(2):377–399, 2007.
- [141] M Y Yasin, N Ahmad, and M N Alam. Finite element analysis of actively controlled smart plate with patched actuators and sensors. *Latin American Journal of Solids and Structures*, 7:227–247, 2010.
- [142] A S D Wang and F W Crossman. Calculation of Edge Stresses in Multi-Layer by Sub-Structuring. *Journal of Composite Materials*, 12:76–83, 1978.
- [143] N J Pagano and S R Soni. Global-Local Laminate Variational Model. *International Journal of Solids and Structures*, 19(3):207–228, 1983.
- [144] R Jones, R Callinan, K K Teh, and K C Brown. Analysis of Multi-Layer Laminates Using Three-Dimensional Super Elements. *International Journal for Numerical Methods in Engineering*, 20(3):583–587, 1984.
- [145] M Botshekanan Dehkordi, M Cinefra, S M R Khalili, and E Carrera. Mixed LW/ESL models for the analysis of sandwich plates with composite faces. *Composite Structures*, 98:330–339, 2013.
- [146] M Botshekanan Dehkordi, S M R Khalili, and E Carrera. Non-linear transient dynamic analysis of sandwich plate with composite face-sheets embedded with shape memory alloy wires and flexible core- Based on the mixed LW (Layer-wise)/ESL (Equivalent single layer) models. *Composites Part B*, 87:59–74, 2016.
- [147] M Petrolo, M Cinefra, A Lamberti, and E Carrera. Evaluation of Mixed Theories for Laminated Plates through the Axiomatic/Asymptotic Method. *Composites Part B*, 76:260–272, 2015.
- [148] S G Lekhnitskii. Anisotropic Plates. In *Tsai, S W and Cheron, T editors (Translated from 2nd Russian Edition)*. Gordon & Branch, 1968.
- [149] S H Nguyen and K S Surana. Two-dimensional curved beam element with higher-order hierarchical transverse approximation for laminated composites. *Computers & Structures*, 36:499–511, 1990.
- [150] J F Davalos, Kim Y, and Barbero E J. Analysis of laminated beams with a layerwise constant shear theory. *Computers & Structures*, 28:241–253, 1994.
- [151] Y Z Xiaoshan Lin. A novel one-dimensional two-node shear-flexible layered composite beam element. *Finite Elements in Analysis and Design*, 47:676–682, 2011.

- [152] T P Vo and H T Thai. Static behavior of composite beams using various refined shear deformation theories. *Computers & Structures*, 94:2513–2522, 2012.
- [153] M Petrolo and A Lamberti. Axiomatic/asymptotic analysis of refined layer-wise theories for composite and sandwich plates. *Mechanics of Advanced Materials and Structures*, 23(1):28–42, 2016.
- [154] J.N. Reddy and C.F. Liu. A higher-order shear deformation theory of laminated elastic shells. *International Journal of Engineering Science*, 23(3):319—330, 1985.
- [155] A. Kumar, A. Chakrabarti, and M. Ketkar. Analysis of laminated composite skew shells using higher order shear deformation theory. *Latin American Journal of Solids and Structures*, 10:891—919, 2013.
- [156] S. Kapuria, P.C. Dumir, and S. Sengupta. Nonaxisymmetric exact piezothermoelastic solutions for laminated cylindrical shell. *AIAA Journal*, 35:1792—1795, 1997.
- [157] Y.M. Yasin and S. Kapuria. An efficient layerwise finite element for shallow composite and sandwich shells. *Composite Structures*, 98:202—214, 2013.
- [158] A Pagani, S Valvano, and E Carrera. Analysis of laminated composites and sandwich structures by variable-kinematic MITC9 plate elements. *Journal of Sandwich Structures and Materials*. DOI: 10.1177/1099636216650988.
- [159] E Carrera, A Pagani, and S Valvano. Shell elements with through-the-thickness variable kinematics for the analysis of laminated composite and sandwich structures. *Composites Part B*, 111:294–314, 2017.
- [160] R E Bank. Adaptive computational methods for partial differential equations. *SIAM*, 1983.
- [161] B A Szabo and I Babuska. Finite element analysis. *John Wiley & Sons*, 1991.
- [162] D M Thompson and O H Jr Griffin. 2-D to 3-D Global/Local Finite Element Analysis of Cross-Ply Composite Laminates. *Journal of Reinforced Plastics and Composites*, 9:492–502, 1990.
- [163] K M Mao and C T Sun. A Refined Global-Local Finite Element Analysis Method. *International Journal for Numerical Methods in Engineering*, 32:29–43, 1991.
- [164] J D Whitcomb and K Woo. Application of Iterative Global/Local Finite Element Analysis. Part 1: Linear Analysis. *Communications in Numerical Methods in Engineering*, 9(9):745–756, 1993.
- [165] J D Whitcomb and K Woo. Application of Iterative Global/Local Finite Element Analysis. Part 2: Geometrically Non-Linear Analysis. *Communications in Numerical Methods in Engineering*, 9(9):757–766, 1993.
- [166] F Brezzi and L D Marini. The three-field formulation for elasticity problems. *GAMM Mitteilungen*, 28:124–153, 2005.
- [167] E Carrera, A Pagani, and M Petrolo. Use of Lagrange multipliers to combine 1D variable kinematic finite elements. *Computers & Structures*, 129:194–206, 2013.
- [168] E. Carrera and A. Pagani. Analysis of reinforced and thin-walled structures by multi-line refined 1D/beam models. *International Journal of Mechanical Sciences*, 75:278–287, 2013.

- [169] E. Carrera and A. Pagani. Multi-line enhanced beam model for the analysis of laminated composite structures. *Composites: Part B*, 57:112–119, 2014.
- [170] H Ben Dhia. Multiscale mechanical problems: the Arlequin method. *Comptes Rendus de l'Academie des Sciences Series IIB Mechanics Physics Astronomy*, 326(12):899–904, 1998.
- [171] H Ben Dhia. Further insights by theoretical investigations of the multiscale Arlequin method. *International Journal for Multiscale Computational Engineering*, 6(3):215–232, 2008.
- [172] H Ben Dhia. The Arlequin method as a flexible engineering tool. *International Journal for Numerical Methods in Engineering*, 62(11):1442–1462, 2005.
- [173] H Hu, S Belouettar, M Potier-Ferry, and E M Daya. Multi-scale modelling of sandwich structures using the Arlequin method. Part I: linear modelling. *Finite Elements in Analysis and Design*, 45(1):37–51, 2008.
- [174] H Hu, S Belouettar, M Potier-Ferry, E M Daya, and A Makradi. Multi-scale nonlinear modelling of sandwich structures using the Arlequin method. *Finite Elements in Analysis and Design*, 92(2):515–522, 2010.
- [175] F Biscani, G Giunta, S Belouettar, E Carrera, and H Hu. Variable kinematic beam elements coupled via Arlequin method. *Composite Structures*, 93(2):697–708, 2011.
- [176] F Biscani, G Giunta, S Belouettar, E Carrera, and H Hu. Variable kinematic plate elements coupled via Arlequin method. *International Journal for Numerical Methods in Engineering*, 91:1264–1290, 2012.
- [177] J N Reddy and D H Robbins. Theories and computational models for composite laminates. *Applied Mechanics Review*, 47:147–165, 1994.
- [178] Junuthula N Reddy. Mechanics of laminated composite plates- Theory and analysis(Book). *Boca Raton, FL: CRC Press, 1997.*, 1997.
- [179] J Fish. The s-version of the finite element method. *Computers and Structures*, 43(3):539–547, 1992.
- [180] J Fish and S Markolefas. Adaptive s-method for linear elastostatics. *Computer Methods in Applied Mechanics and Engineering*, 103:363–396, 1993.
- [181] C Wenzel, P Vidal, M D'Ottavio, and O Polit. Coupling of heterogeneous kinematics and Finite Element approximations applied to composite beam structures. *Composite Structures*, 116:177–192, 2014.
- [182] H R Meyer-Piening. Experiences with 'exact' linear sandwich beam and plate analyses regarding bending, instability and frequency investigations. In *Proceedings of the Fifth International Conference on Sandwich Constructions, Vol. 1, edited by H.R. Meyer-Piening and D. Zenkert*, pages 37–48, EMAS Publishing, Zurich, 2000.
- [183] E Carrera and A Ciuffreda. Bending of composites and sandwich plates subjected to localized lateral loadings: a comparison of various theories. *Composite Structures*, 68:185–202, 2005.
- [184] E Carrera and L Demasi. Two benchmarks to assess two-dimensional theories of sandwich, composite plates. *AIAA Journal*, 41(7):1356–1362, 2003.

- [185] F Biscani, P Nali, S Belouettar, and E Carrera. Coupling of hierarchical piezoelectric plate finite elements via Arlequin method. *Journal of Intelligent Material Systems and Structures*, 23(7):749–764, 2012.
- [186] C T Sun and X D Zhang. Use of thickness-shear mode in adaptive sandwich structures. *Smart Materials and Structures*, 4:202–206, 1995.
- [187] X D Zhang and C T Sun. Formulation of an adaptive sandwich beam. *Smart Materials and Structures*, 5:814–823, 1996.
- [188] A Benjeddou, M Trindade, and R Ohayon. A unified beam finite element model for extension and shear piezoelectric actuation mechanisms. *Journal of Intelligent Material Systems and Structures*, 8:1012–1025, 1997.